Myonuclear alterations in ageing syndromes

Levy, Yotam

Awarding institution:
King's College London

MYONUCLEAR ALTERATIONS IN AGEING SYNDROMES

A thesis submitted for the degree of Doctor of Philosophy at King's College London

Yotam Levy

Centre for Human & Applied Physiological Sciences

School of Basic & Medical Biosciences

Faculty of Life Sciences & Medicine

King's College London

· 2019 ·

Abstract

Sarcopenia, a condition characterised by progressive loss of skeletal muscle mass and strength, has been associated with an intrinsic deterioration of the force-generating capacity of individual myofibres. As the reduction in force-generation is greater than the loss of muscle fibre volume (specific force loss), a decrease in cellular quality may contribute to the aforementioned weakness. The work presented in this thesis aimed to further elucidate the mechanisms by which myofibre force is depressed during the ageing process, using a plethora of animal and human models, with specific reference to myonuclear proteins and organisation.

Existent *ex vivo* methods to study myonuclear organisation in single muscle fibres did not fulfil the methodological necessities of this project. Thus, methods of varying degrees of automation were developed to study the (i) three-dimensional nuclear organisation, and (ii) nuclear pixel intensities of a range of antibodies, in confocal image stacks of isolated skinned single muscle fibres. Analyses were performed using custom-made MATLAB scripts and Fiji macros. Both methods were used in the present thesis and various related publications.

Physiological and premature ageing are frequently associated with an accumulation of prelamin A, a precursor of lamin A, in the nuclear envelope of various cell types. The current work aimed to underpin the hitherto unknown mechanisms by which accumulation of prelamin A in the nucleus alters myonuclear organisation and muscle fibre function. By applying the methods developed in this work on single muscle fibres from various mouse models of lamin A misprocessing, results indicated that postnatal accumulation of farnesylated prelamin A and absence of *Zmpste24* in myonuclei can lead to a low number of nuclei and enlarged myonuclear domains in single muscle fibres, concomitant with decreased transcriptional activity, reduction in contractile protein content and low specific force.

Scientific studies on human ageing are limited by inclusion of sedentary cohorts. Hence, the role of myonuclear organisation is unknown in biological ageing, i.e. ageing that is not contaminated by inactivity-related pathologies. The final objective in this thesis was to verify whether levels of activity and age can lead to changes in nuclear organisation in single muscle fibres. Results showed an elevated number of nuclei in single muscle fibres from physically inactive patients and nuclear mispositioning in all the elderly cohorts. Transcriptional activity in the active cohort was >2x that of all other groups, revealing a possible association between level of physical activity, but not age.

Consequently, biological ageing and muscle disuse do not share the same myonuclear alterations, demonstrating the importance of differentiating between the two conditions in ageing research. Future work should deepen the understanding of the mechanisms by which the persistence of farnesylated prelamin A and absence of *Zmpste24* in myonuclei lead to a smaller nuclear population in single muscle fibres. Moreover, research should continue to characterise the specific contribution of muscle disuse to human ageing. Importantly, future studies should identify whether any correlation exists between the existence of prelamin A and progerin in single muscle fibres, and age and physical activity.

For my parents

For my grandfather

28.1.1933 – 6.2.2019

Preface & acknowledgements

The text presented in this thesis owes its existence to many people from whom I have learnt a great deal over the years. However, I would firstly like to thank King's College London for having been a home for me for nearly a decade, beginning with a Science Foundation course that had provided me with the scientific and lingual skills required for a Bachelor's degree in the UK, all the way to a PhD in muscle physiology and a few grey hairs collected along the way. It was the stimulating environment and sheer beauty of the Maughan Library, to which I was exposed on my first week at King's, that had opened the gates of boundless curiosity, which had swept over my life and resulted in this thesis. As beautifully stated by the Ancient Roman philosopher and orator, Marcus Tullius Cicero –

"To be ignorant of what occurred before you were born is to remain always a child. For what is the worth of human life, unless it is woven into the life of our ancestors by the records of history?"

My research thus builds upon the works of others, without whose ideas and hard labour my own notions could not have existed. In this context, I would like to thank my primary supervisor, Dr. Julien Ochala, who had agreed to draft an overly eager undergraduate student to his cohort and was willing to quietly tolerate my energy levels, whilst tacitly preventing my explorations from wasting precious time. Unfortunately, there is not enough space (or words!) to thank Julien for all his actions, incredible guidance and support over the last five years. Nevertheless, I indeed wish to thank Julien for placing me at the fore of every opportunity, challenging me to excel and helping to see the forest from the trees, be it in my PhD or in life. For his open mind, ambitious ideas and mainly – for always being there, ready to answer my every question, no matter the time or day. Thanks for everything, Julien! You have made this PhD an incredible experience.

A sincere gratitude also goes to my secondary supervisor, Prof. Steve Harridge, whose experienced advice, patience and welcoming manner have never gone unnoticed. Thank you for all the time and effort invested in all aspects of this thesis! I owe a significant part of my PhD to Steve, as it was his willingness to set time aside from his extremely busy schedule to teach me the various routes to a PhD, that had set my mind to pursue a doctorate in muscle physiology. Most importantly, I would like to thank Steve for his show of elation at hearing of my engagement, and I promise to always remember – "happy wife happy life!".

I am deeply indebted to Dr. Vladimir Snetkov for countless intriguing conversations and for sharing his vast knowledge and experience with me. From his artful humour to child-like curiosity, every moment of conversing with Vlad is a joy to the heart and a challenge to the intellect. I would also like to thank both Vlad and his wife, Goutta, for the pleasurable evenings we spent together, filled with insightful discussions.

My grateful thanks to Dr. Anthea Rowlerson, whose readiness to lend an attentive ear and a helpful hand have been guiding me in different aspects of life since the second year of my Bachelor's degree. To Anthea's inquisitive mind and sharp practicality there is no second and it is solely my privilege to have met her. Also, I never had the opportunity to thank Anthea for helping me to plant potted plants in the department!

Many thanks go to the technical and academic staff at the Centre for Human & Applied Physiological Sciences who, together, have helped making the department a friendly workspace. I would additionally like to thank our Chief Technician, Lindsey Marjoram, who through no fault of her own was required to endure my daily requests and cheeky humour. Lindsey has proven to be a worthy opponent in banter!

I would additionally like to express my gratitude to the past and present PhD students and postdoctoral researchers in our department, namely (and in order of date of acquaintance!), MJ, Julia, Phil, Oihane, Katie, Tom, Jacob, PJ, Abbi and Ben, for having been there at all times, sharing their major successes and endless minor setbacks, for their ever-lasting inclination to advise and help and most of all, for being great friends. I would especially like to thank Tom for flying to my wedding in Israel and for joining dinner at Carluccio's every time my mother visits. I would also like to thank Maria, a visiting research fellow from the beautiful Cetara, Italy, who had taught me to swear in Italian during long hours on the microscope! Additional thanks to the many BSc and MSc students whom I had the pleasure to mentor in our laboratory and who sharpened my scientific knowledge.

To my dear talented friend, Ofir Levi, who had read through this entire manuscript, despite not having a science degree(!), yet through his brilliance had somehow managed to make not only valid comments, but challenge complete ideas altogether – I hope this says more about him than about my work! His extreme genius, musical ability and good nature never cease to amaze me. Thank you for being there all these years!

A long overdue expression of gratitude goes to my incredible parents, Anna and Doron, as well as my sisters, Inbar, Yifat and Sapir, who had always been the core of my happiness, guiding compass and infinite source of inspiration, without whose shouldering and encouragement no part of this decade could have materialised this way. My family has always been my first contact for a friendly chat and have taught me, through example, how to strive for success and self-fulfilment, whilst maintaining humility and content. I owe a great deal of my personality to them.

I would especially like to thank a girl I met seven years ago (now my wife) on the second month of my Bachelor's degree, Miss Keren Amroussi (now Mrs. Levy). I have a friend who says a man goes to university to find an intelligent wife. I always thought the notion was senseless in its essence – yet, the opportunity to disprove him had sailed! Since our first date in Winter Wonderland, Keren has had the misfortune to accompany me throughout my academic endeavours and dilemmas. In her loving heart I found an oasis of serenity and goodness, without whom I would not have had the will to journey into new lands. Thank you for having been the essential pivot and inspiration of my life. Here, I would also like to thank Keren's parents, Batya and Zvi Amroussi, as well as her brothers Orani, Yoseph and Dan for having been my second family in London all these years. I am incredibly in debt to them for their constant support that has never wavered. I will forever vividly remember all the Friday nights we have spent together.

An expression of gratitude must go to my examiners, Dr. Sue Shackleton and Prof. Winnok De Vos, without whose detailed examination this thesis could not have reached its current level.

Final thanks go to any person from whom I have ever drawn inspiration, be it scientists, philosophers, visual artists, authors, musicians, athletes, businesspersons, politicians, historical figures or my neighbour. Lastly, to the reader, if you have reached this part of the preface, I commend your patience!

"Just as food eaten without appetite is a tedious nourishment, so does study without zeal damage the memory by not assimilating what it absorbs" – Leonardo da Vinci

- Yotam Levy

List of publications

Levy Y, Ross JA, Niglas M, Snetkov VA, Lynham S, Liao CY, Roy-Packelwartz MJ, Hsu YM, McNally EM, Alsheimer M, Harridge SDR, Fong LG, Español Y, López-Otín C, Kennedy BK, Lowe DA & Ochala J (2018). Prelamin A causes aberrant myonuclear arrangement and results in muscle fiber weakness. *JCI Insight* **3**(19), 120920. PMID: 30282816

Buono S, Ross J, Tasfaout H, **Levy Y**, Kretz C, Tayefeh L, Matson J, Guo S, Kessler P, Monia BP, Bitoun M, Ochala J, Laporte J & Cowling BS (2018). Reducing dynamin 2 (DNM2) rescues DNM2-related dominant Centronuclear Myopathy. *PNAS* **115**(43), 11066-11071. PMID: 30291191

Ross JA*, **Levy Y***, Svensson K*, Philip A, Schenk S & Ochala J (2018). SIRT1 regulates nuclear number and domain size in skeletal muscle fibres. *J Cell Physiol* **233**(9), 7157-7163. PMID: 29574748 ***Contributed equally**

Ross JA, Pearson A, **Levy Y**, Cardel B, Handschin C & Ochala J (2017). Exploring the role of PGC-1α in Defining Nuclear Organisation in Skeletal Muscle Fibres. *J Cell Physiol* **232**(6), 1270-1274. PMID: 27861863

Lindqvist J, **Levy Y**, Pati-Alam A, Hardeman EC, Gregorevic P & Ochala J (2016). Modulating myosin restores muscle function in a mouse model of nemaline myopathy. *Ann Neurol* **79**(5), 717-725. PMID: 26891371

Abbreviations & acronyms

AcH3	Acetyl histone H3
ACN	Acetonitrile
ANOVA	Analysis of variance
ATP	Adenosine triphosphate
BSA	Bovine serum albumin
CCD	Charge-coupled device
CMT2B1	Charcot-Marie-Tooth neuropathy type 2B1
CPU	Central processing unit
CSA	Cross-sectional area
DAPI	4',6-diamidino-2-phenylindole
DCM-CD	Dilated cardiomyopathy with conduction disease
DTT	Dithiothreitol
ECM	Extracellular matrix
ECRL	Extensor carpi radialis longus
EDL	Extensor digitorum longus
EDMD	Emery-Dreifuss muscular dystrophy
EM	Electron microscopy
Fab	Antibody-binding domain
Fc	Constant domain
FPLD	Dunnigan-type familial partial lipodystrophy
FTase	Farnesyltransferase
FTI	Farnesyltransferase inhibitor
FWHM	Full-width half-maximum
GPU	Graphics processing unit
HCD	Higher-energy C-trap dissociation
HF	Hip fracture
HGPS	Hutchinson-Gilford progeria syndrome
HP1	Heterochromatin-associated protein 1
IAA	Iodoacetamide
ICMT	Isoprenylcysteine carboxylmethyl transferase
IF	Immunofluorescence
IHC	Immunohistochemistry

INM	Inner nuclear membrane
KO	Knockout
LAP1	Lamina-associated protein 1
LAP2α	Lamina-associated polypeptide 2α
LBR	Lamin B receptor
LC-MS	Liquid chromatography mass spectrometry
LGMD1B	Limb-Girdle muscular dystrophy type 1B
LINC	Linkers of nucleo-skeleton to the cytoskeleton
MADA	Mandibuloacral dysplasia type A
MND	Myonuclear domain
MS	Mass spectrometry
MTJ	Myotendinous junction
MTOC	Microtubule organising centre
MU	Motor unit
NA	Numerical aperture
NE	Nuclear envelope
NETs	Nuclear envelope transmembrane proteins
NN	Nearest neighbour
ONM	Outer nuclear membrane
PBS	Phosphate-buffered saline
PFA	Paraformaldehyde
PSF	Point spread function
RCE1	Ras-converting enzyme 1
RD	Restrictive dermopathy
RI	Refractive index
RP	Rhodamine phalloidin
RT	Room temperature
SC	Satellite cell
SD	Standard deviation
SD-NN	Standard deviation of nearest neighbour
SEM	Scanning electron microscopy
SNR	Signal-to-noise ratio
SPS	Synchronous precursor scan
SR	Sarcoplasmic reticulum
TA	Tibialis anterior
TBS	Tris-buffered saline
TEAB	Tetraethylammonium bromide
TMT	Tandem mass tag
TMT6plex	Tandem mass tag 6-plex
VSMC	Vascular smooth muscle cell
WT	Wild-type
Zmpste24	Zinc metallopeptidase STE24

Table of contents

Figures & tables

Figures

Tables

Chapter 1: Literature review

1.1. General aims

In many countries, life expectancy and the number of people in older age have increased significantly in the last decades. However, healthspan, that is the length of time one lives without ageing-associated chronic disease, has remained virtually the same since the middle of the 20th century, despite the significant increase in life expectancy in that period. As a result, governments are required more than ever to medically and financially support an increasing number of older unhealthy citizens, who at the present time could be living with ageing-related chronic diseases for 20 years or longer, which current figures show is ~23% of one's life expectancy at birth in the UK (ONS, 2017; Harridge & Lazarus, 2017). The goal for health services should therefore be to maximise health expectancy to match life expectancy. This would result in a significant reduction in the number of years one is found in a state of morbidity, improve quality of life and save a tremendous amount of money to health services and citizens alike.

Ageing can be defined as an exponential accumulation of a variety of adverse alterations to normal physiology that together increase the risk of mortality. The process of ageing takes place in every cell of the human body. As cellular damage accumulates, the amount of biological reserves reduces. Upon diminishment of reserves, the ageing process accelerates, ultimately leading to accelerated organ failure. In skeletal muscle, ageing manifests as a gradual decline in muscle mass and strength (sarcopenia) and in line with other organs and tissues, the ageing-induced impairments are irreversible (Fries, 1980; Seals *et al.*, 2016).

For various reasons, the scientific community has yet to reach a conclusive definition of muscle ageing. A major reason for that is the contamination of scientific studies with assumptions rooted in Western cultural norms. As human ageing encompasses a combination

of biological ageing and environmental factors, such as sedentarity and muscle disuse, is the typical sedentary older person the appropriate model for ageing? It has been argued that being physically active is the default position for maintaining good physiological function throughout life and that the results obtained in many ageing studies, human or otherwise, are contaminated by muscle inactivity. In this context, it is also intriguing that muscle strength is predictive of age of mortality and that exercise can prevent the detrimental effects typically associated with ageing (Kallman *et al.*, 1990; Bassey & Harries, 1993; Lazarus & Harridge, 2010; Harridge & Lazarus, 2017).

At the cellular level, sarcopenia is often associated with general changes to cell organelles, such as mitochondria and lysosomes (López-Otín *et al.*, 2013), as well as reductions in type II muscle fibre size and strength, however, the causes remain rather obscure (Frontera & Larsson, 1997; Frontera *et al.*, 2000; Ochala *et al.*, 2007). It appears that age-related alterations to the function of single muscle fibres are of qualitative (function of cross-bridges) and quantitative (number of cross-bridges) nature, both of which may be affected by physical activity (Bottinelli, 2001; D'Antona *et al.*, 2003, 2006, 2007*b*; Canepari *et al.*, 2005). The latter has been proposed to relate to an ageing-induced reduction in the concentration of myosin heavy chain (MHC) in single muscle fibres (D'Antona *et al.*, 2003), which could be associated predominantly with level of physical activity rather than ageing *per se* (D'Antona *et al.*, 2007*b*). Though the cellular reasons for the reduction in MHC concentrations are unknown, they could possibly be explained by altered myonuclear distribution in single muscle fibres (Cristea *et al.*, 2010).

Interestingly, genetic modifications to nuclear envelope-associated genes result in a myriad of muscle disorders, including premature ageing, whereby the maturation process of the nuclear scaffold protein lamin A is perturbed, leading to shared molecular and cellular mechanisms with many ageing-associated diseases (Janin *et al.*, 2017; Kubben & Misteli, 2017). Such similarities with ageing are thought to originate from faulty expression of lamin A in multiple tissues, mainly of mesenchymal origin (e.g. skin, bone, adipose and muscle tissue), that occurs during normal ageing (Scaffidi & Misteli, 2006; McClintock *et al.*, 2007; Rodriguez *et al.*, 2009; Ragnauth *et al.*, 2010; Cristea *et al.*, 2010; Olive *et al.*, 2010*a*; De La Rosa *et al.*, 2013; Kubben & Misteli, 2017; Ross *et al.*, 2018). Misprocessing of lamin A has been associated with numerous cellular and nuclear defects, such as reduced cell motility, increased apoptosis under mechanical strain (Verstraeten *et al.*, 2008) and altered transcription of mechano-sensitive genes (Bertrand *et al.*, 2014). However, it is unkown whether these could explain the reduced myonuclear distribution witnessed in single muscle fibres from elderly individuals (Cristea *et al.*, 2010), and whether the

latter could in turn explain the reduced MHC concentration and low specific force associated with ageing.

Consequently, this PhD project aimed to further characterise the mechanisms that link the processing of lamin A with myonuclear organisation and functional capabilities of single muscle fibres in health, biological ageing and disuse, using a variety of animal and human models.

1.2. Skeletal muscle structure and function

1.2.1. Compartmentalisation of skeletal muscles

Skeletal muscles can be studied at many different levels, ranging from gross anatomy, to physiological studies of structure and function, extending to the functioning of individual molecular motors, their biochemical and metabolic properties. Their functions are wide and include active roles, such as metabolic health and maintenance of posture, as well as inactive roles, as padding of the skeleton (beneficial for falls). Numerous muscular disorders, including ageing, have been documented to manifest from various biological origins and are often accompanied by muscle weakness and premature mortality (Jones *et al.*, 2004).

Skeletal muscles are multinucleated cells that connect to bones *via* fibrous collagenous connective tissue called tendons, or a sheet of fibrous tissue termed aponeurosis. They are classically described to consist of the following compartments, each constitutes part of the preceding compartment: muscle bundle > fascicles > fibres > fibrils > filaments (Figure 1.1 and Figure 1.2). Extracellular matrix (ECM) of collagenous connective tissue circumscribes each muscle (epimysium), fascicle (perimysium) and muscle fibre (endomysium). Muscle fibroblasts, blood vessels, motor neurons and muscle spindles (specialised sensory organs that detect changes in muscle length), are embedded within the perimysium (Jones *et al.*, 2004; Gillies *et al.*, 2014). As will become clear in subsequent sections, the force-generating capacity of a given muscle is proportional to its physiological cross-sectional area (Haxton, 1944; Jones *et al.*, 2004).

Beneath the endomysium lies a layer of ECM material (basement membrane) that is contiguous with the plasma membrane (sarcolemma) of the fibre, except for locations where muscle stem cells (satellite cells) can be found between the two layers. Directly underneath the sarcolemma, reside muscle nuclei and a network of smooth endoplasmic reticulum, called the sarcoplasmic reticulum (SR), which envelops each myofibril; the SR is the predominant storage

of calcium in skeletal muscle fibres (Mauro, 1961; Endo *et al.*, 1970). The sarcolemma contains numerous invaginations of transverse membranous tubules (T-tubules), which penetrate into the cytoplasm of the muscle fibre and terminate adjacently to the SR as a triad (Peachey, 1965). On either side of the T-tubules are enlargements of the SR, termed terminal cisternae, where calcium exchange with myofibrils takes place during muscle contraction and relaxation (Endo, 1977).

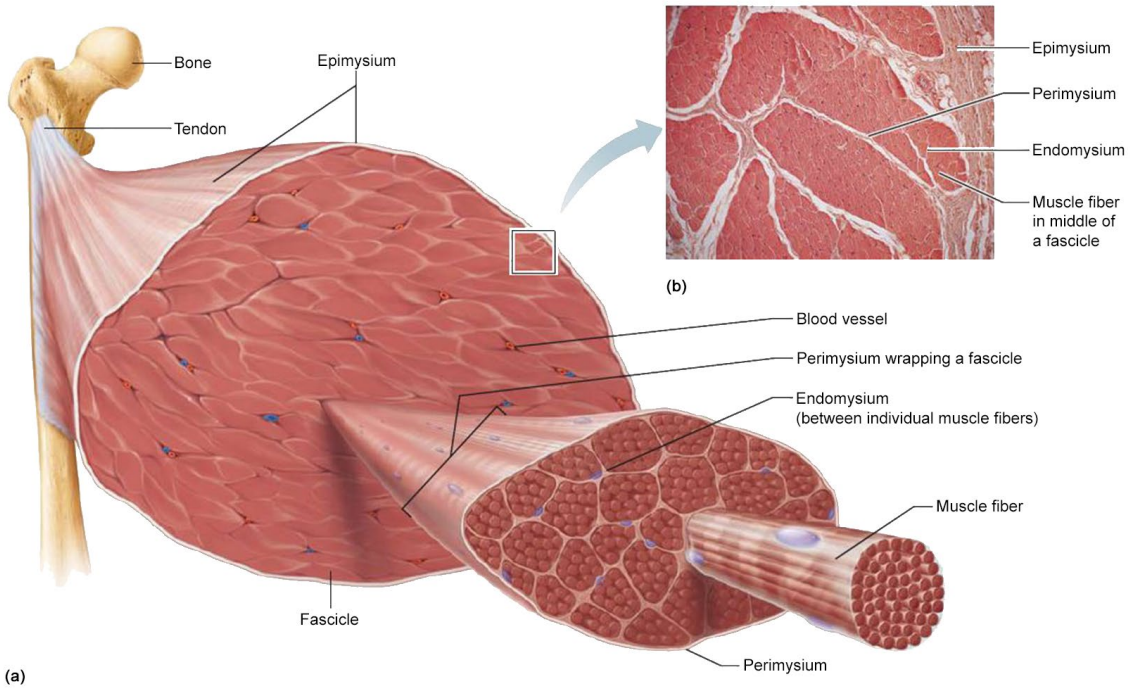

Figure 1.1: Structure of skeletal muscles
(a) Skeletal muscles originate from and insert into bones *via* tendons. The muscle is composed of fascicles, which consist of numerous muscle fibres. Connective tissue surrounds the muscle (epimysium), fascicles (perimysium) and individual muscle fibres (endomysium). Each muscle fibre consists of numerous myofibrils, which are in turn, composed of myofilaments. (b) Photomicrograph of a cross-section of part of a skeletal muscle (30x magnification). Adopted from Marieb & Hoehn (2015). Copyright © 2015, Pearson Education, Inc.

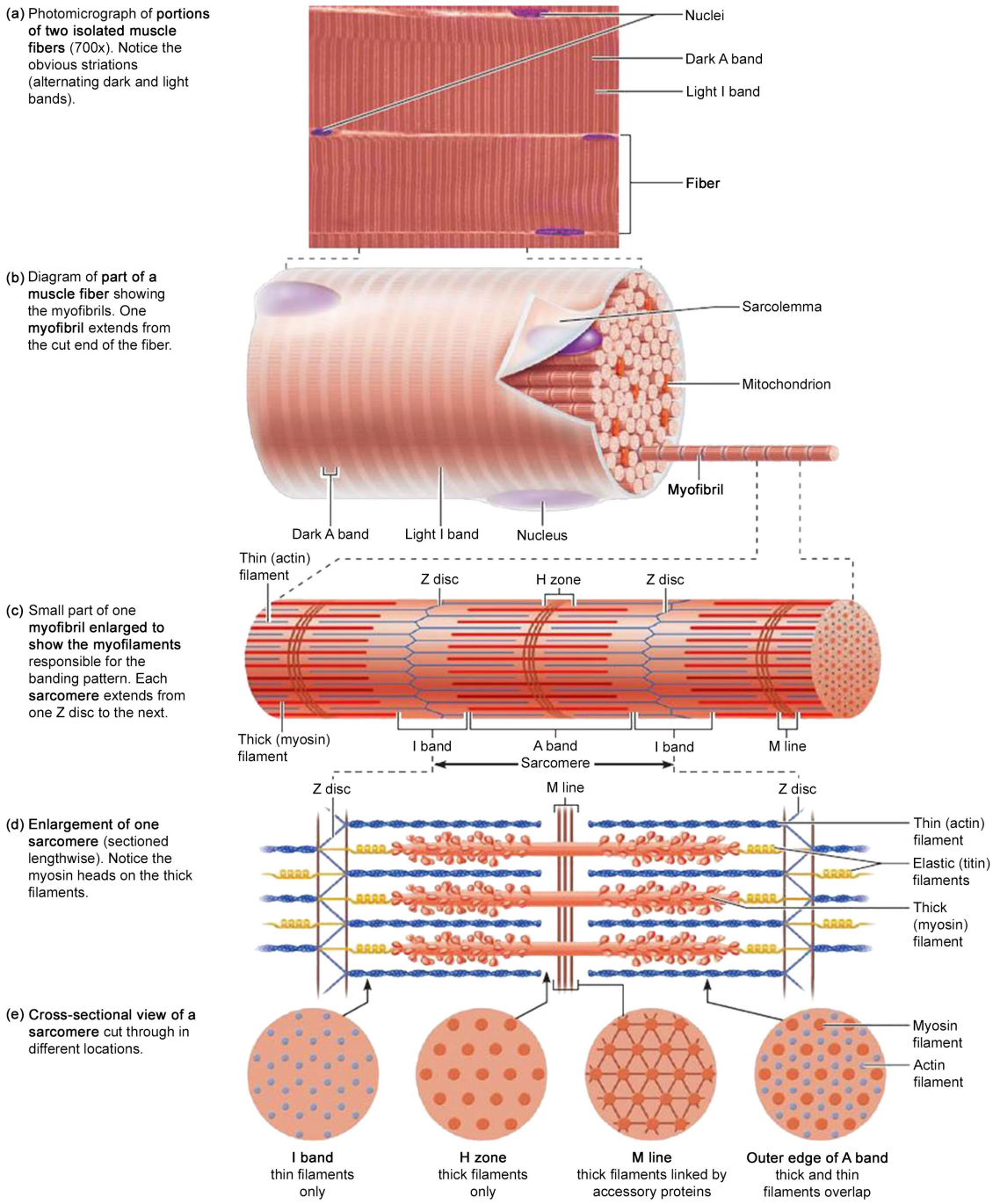

Figure 1.2: Structure of muscle fibres

The sarcomere, positioned in series within myofibrils, is the basic contracting unit of a muscle fibre. Adopted from Marieb & Hoehn (2015). Copyright © 2015, Pearson Education, Inc.

1.2.2. Sarcomeres

Each muscle fibre consists of approximately two thousand myofibrils, which contain the basic contractile units (sarcomeres) of skeletal muscles, positioned in series within each myofibril (Figure 1.2 and Figure 1.3). A single sarcomere is predominantly composed of actin and myosin filaments, running in parallel, such that actin filaments are situated between myosin filaments. Myosin filaments are held in parallel by M-line proteins and titin, whereas actin filaments adhere to the Z-lines of the sarcomere *via* Z-line proteins and α-actinin (Ehler & Gautel, 2008). The area between two Z-lines is the sarcomere. Laterally, Z-lines of adjacent sarcomeres are mostly contiguous (Figure 1.3) and connected together by the structural protein desmin, which in turn, additionally attaches nuclei to the Z-line (Goldfarb & Dalakas, 2009; Kirby & Lammerding, 2018). Thus, muscle fibres can produce a roughly homogeneous contraction within a cross-sectional area (CSA).

The attachment of myosin heads to actin filaments is termed a cross-bridge. During muscle contraction, myosin heads repetitively and sequentially attach, pull (power stroke) and detach from actin filaments in a cycle termed the cross-bridge cycle (Huxley, 1957; Huxley & Simmons, 1971). The process requires the hydrolysis of adenosine triphosphate (ATP) by the ATPase activity of myosin heads and thus, myosin heads are the motor that produces muscle contraction, by converting chemical energy into mechanical work (Gautel & Djinovic-Carugo, 2016). All things being equal, the larger the number of myosin heads that can bind actin filaments, the larger the cumulative force produced. Therefore, sarcomeres possess a force-length relationship (Figure 1.4), whereby isometric force is low at short and long sarcomere lengths and optimal in-between. Low force in the former is due to overlapping of actin filaments, whereas in the latter as cross-bridges cannot form when actin filaments are overly spread apart (Gordon *et al.*, 1966; Jones *et al.*, 2004).

Contraction of a sarcomere results in shortening of the distance between two adjacent Z-lines. When all sarcomeres in a series contract simultaneously, contraction velocity is additive. Thus, longer muscles have a faster contraction velocity (e.g. biceps brachii) than shorter muscles. Conversely, the larger the number of sarcomeres in parallel, the larger the force produced by a single muscle fibre. As a result, maximum isometric force of a muscle fibre is proportional to its CSA and not to its length; force produced per unit CSA is termed specific force.

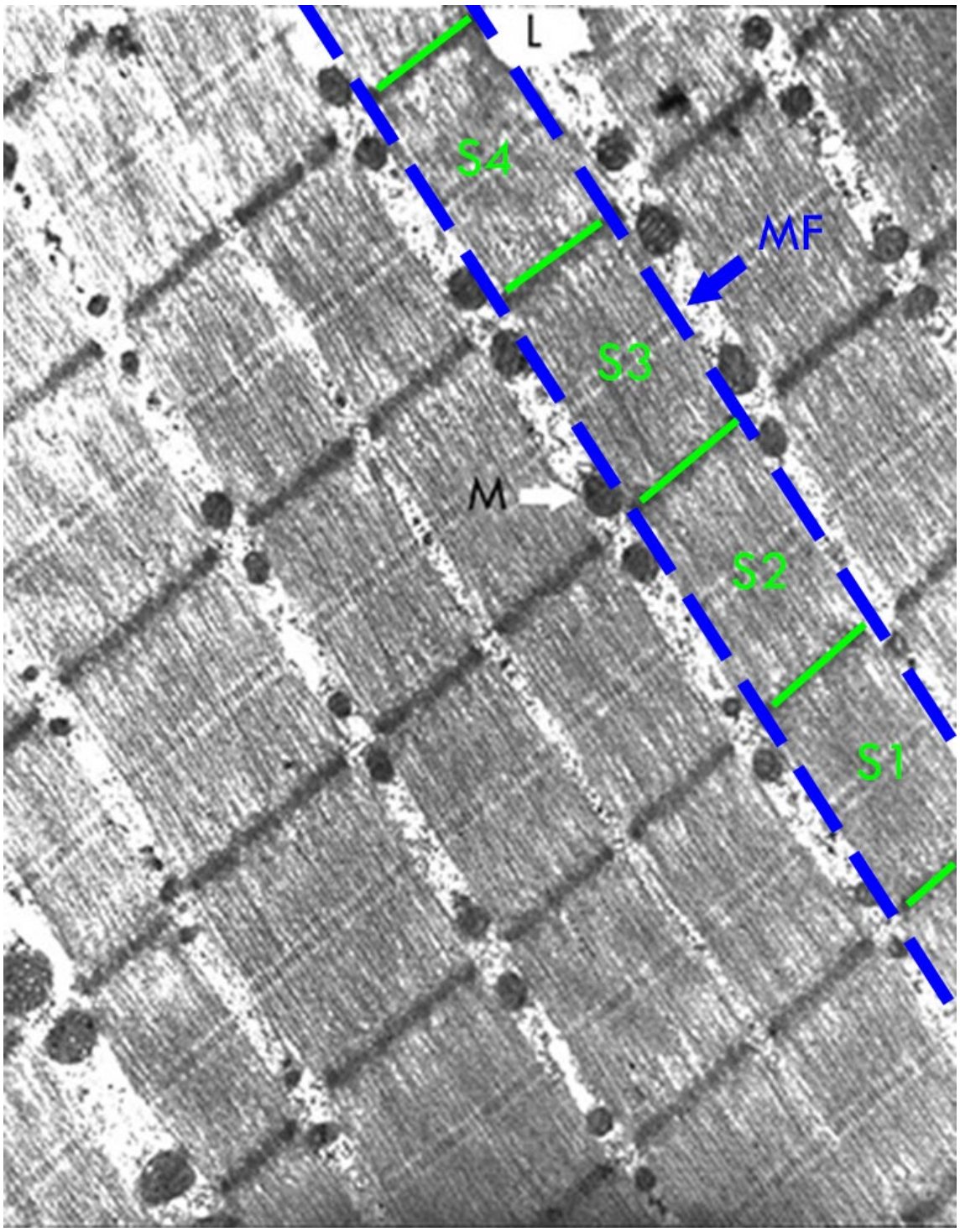

Figure 1.3: Longitudinal electron micrograph of healthy human muscle tissue
MF denotes a myofibril (area between blue dotted lines) and its associated sarcomeres (S1-4), defined by the area between two Z-lines (green lines). L shows a lipid droplet. M shows a mitochondrion. Original magnification 8400x. Adapted from Sprott *et al.* (2004). Copyright © 2004, BMJ Publishing Group Ltd.

Power is the rate of work performed and hence, power is an indication of a muscle's functional performance (Hill, 1938). Power of a muscle fibre is the product of both force and velocity. As the former depends on muscle fibre CSA and the latter on length, power is proportional to fibre volume. As muscles have varying functions and are of different lengths and CSA, optimal sarcomere length for power generation is muscle and species dependent (Burkholder & Lieber, 2001; Gollapudi & Lin, 2009).

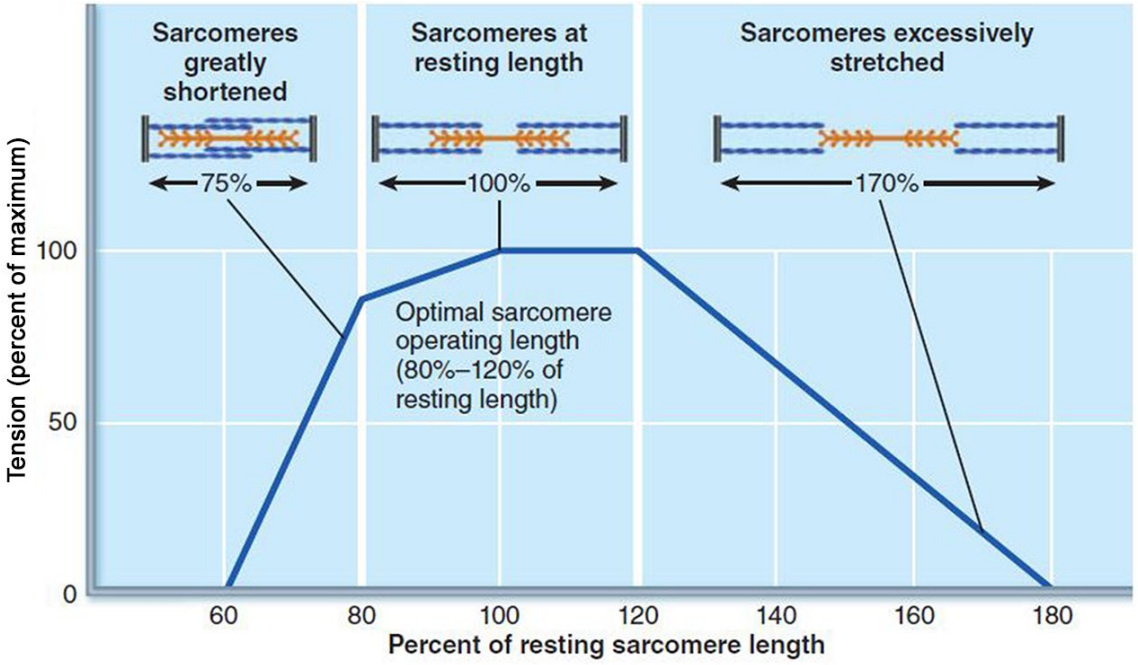

Figure 1.4: Force-length relationship in skeletal muscle fibres
A muscle generates maximum force when it is between 80% and 120% of its optimal resting length. Alterations in length beyond this optimal range reduce its force and ability to generate tension. Changes in isometric force are predominantly due to alterations in the number of actomyosin interactions. Adopted from Marieb & Hoehn (2015). Copyright © 2015, Pearson Education, Inc.

1.2.3. Muscle fibre types

Skeletal muscles are composed of a heterogeneous population of muscle fibres of mixed enzymatic and contractile properties. Enzymatic properties are determined by the myosin ATPase (Brooke & Kaiser, 1970), whose activity is predominantly governed by the innervation of the muscle fibre (Buller *et al.*, 1960; Kugelberg, 1973; Nemeth *et al.*, 1986; Sieck *et al.*, 1996). Thus, muscle fibres are classically classified as type I (slowest), IIa, IIx (fast) and IIb (fastest), as determined by their myosin heavy chain (MHC) enzymatic activity.

The mechanical properties of muscle fibres are determined by their MHC isoform, as MHCs dictate the maximum shortening velocity and maximal force, and therefore power, of single muscle fibres (Larsson & Moss, 1993; Ennion *et al.*, 1995; Geiger *et al.*, 2000; Argüello *et al.*, 2001). In mammals, muscle fibres with MHC I IIa, IIx, IIb and hybrids can be found, with the exception of MHC IIb that is absent in humans (Larsson & Moss, 1993; Ennion *et al.*, 1995; Roy *et al.*, 1999; Bottinelli & Reggiani, 2000; Ochala *et al.*, 2007). Sarcomere shortening velocity decreases in the order of MHC IIb > IIx > IIa > I (Larsson & Moss, 1993; Harridge *et al.*, 1996; Bottinelli & Reggiani, 2000; D'Antona *et al.*, 2006), predominantly as a result of the varying ability of the myosin head to release its ADP, which depends on the specific MHC isoform; longer attachment time prevents the myosin head from reattaching to actin and produce another power-stroke (Canepari *et al.*, 2010; Caremani *et al.*, 2015). On a cellular level, assuming identical MHC isoforms, the force produced by myosin heads is determined by modulating the number of myosin motors, rather than force of a motor or the size of its stroke, to match a given load (Piazzesi *et al.*, 2002, 2007). Therefore, specific force of single muscle fibres is greatly dependent on their MHC content (Roy *et al.*, 1999; Geiger *et al.*, 2000; D'Antona *et al.*, 2003).

1.3. Myonuclear domains in single myofibres

Since the observation that when cells are taken from an embryonic myotome, they differentiate into muscle fibres (Harrison *et al.*, 1907), researchers have been intrigued by the dynamics of perinatal muscle growth. This had led to numerous studies in the topics of muscle development, regeneration and growth (Schiaffino & Partridge, 2008). The introduction of cell culture techniques in the 1950s (Evans *et al.*, 1951; Dulbecco, 1952) had laid the groundwork for the first example of perinatal muscle development, in cell culture, showing that mononucleated myoblasts proliferate and fuse into multinucleated myotubes (Konigsberg, 1963). However, how muscles grow postnatally and why and how their number of nuclei was increasing had remained a mystery until the early 1970s.

1.3.1. Postnatal nucleation of skeletal muscle

Early researchers investigating the relationship between muscle fibres and their nuclei had initially focused on correlating number of nuclei with muscle weight and size. For instance, Enesco & Puddy (1964) had demonstrated in muscle cryosections of growing rats (15-94 days) a

concomitant increase in number of nuclei with muscle weight and myofibre CSA in the biceps brachii, extensor carpi radialis longus (ECRL), gastrocnemius and tibialis anterior (TA) muscles. Similarly, Moss (1968) had shown in muscle cryosections of growing chickens (0-266 days) that the number of nuclei in the pectoral and gastrocnemius muscles increased in proportion to muscle weight and muscle fibre CSA. Such studies had led to the conclusion that number of nuclei increases in proportion to muscle fibre size.

A central question originating from the aforementioned studies was how the number of nuclei was increasing in skeletal muscle postnatally, as it was known, or believed, that muscle nuclei do not divide (MacConnachie *et al.*, 1964; Moss & Leblond, 1970). Key to answering this question, was the discovery of SCs in 1961 (Mauro, 1961). Using EM in muscle samples from adult fruit bats and postnatal mice, SCs were characterised with a fusiform shape, which makes them easy to recognise (Muir *et al.*, 1965). They were noted to contain few organelles and a nucleus, their cytoplasmic matrix contained numerous dense granules (found to be ribosomes) and the cells were osmotically depended on the muscle fibre. Significantly, SCs were found in muscles from postnatal mice (3 days) more often (up to 20% of total nuclei) than in mature fruit bats (up to 10% of total nuclei), alluding to the possibility that SCs may in fact give rise to, or proliferate into, muscle nuclei. In support, myofibrils were found within some of the SCs, as observed by EM muscle sections, suggesting SCs can generate myofibrils (Muir *et al.*, 1965). Later studies in mice had also confirmed in heat injury-induced regenerating muscles that SCs were found much more frequently in wounded areas than in non-wounded parts of the regenerating muscle fibres, and that they appear to give rise to new myoblasts (Shafiq & Gorycki, 1965); this was also noticed in muscular dystrophy patients, whose muscles are in constant state of regeneration (Shafiq *et al.*, 1967). Thus, it had become clear that SCs have certain unknown functions in muscle, with a possible role in nuclear formation during postnatal development.

As viewed by a series of publications through the 1960s to the early 1970s (Messier & Leblond, 1960; Enesco & Puddy, 1964; MacConnachie *et al.*, 1964; Shafiq *et al.*, 1968; Moss, 1968*a*, 1968*b*; Moss & Leblond, 1970, 1971; Bridge & Allbrook, 1970), the origin of the increasing number of nuclei with increasing muscle fibre size had remained largely unknown until the early 1970s, when Moss & Leblond (1970) demonstrated in TA muscles of 17-days-old rats that thymidine-^{3}H (a radiolabelled nucleotide that is only incorporated into nuclei during DNA synthesis) was incorporated into SCs, but not into true muscle nuclei (hereafter myonuclei), as confirmed by EM, and concluded that only SCs, but not myonuclei, can synthesise DNA. Ultimately, Moss & Leblond (1971) concluded, “the results confirm the classical view that true

muscle nuclei do not divide… The satellite cells associated with muscle fibers are capable of undergoing mitosis in growing animals; and such mitoses are followed by the incorporation of one or both daughter nuclei into the associate fiber. Satellite cells thus function as myoblasts" (Moss & Leblond, 1970:460). This had therefore provided a satisfactory explanation to the witnessed increase in number of nuclei with increasing muscle fibre size during postnatal development, a model that is held to this day.

1.3.2. Postnatal nucleation of single muscle fibres

The studies above describe a decade wherein muscle researchers were attempting to shed more light into the different functions of the newly discovered SCs and understand how they differ from myonuclei. The accumulating knowledge about both had provided the necessary platform to explain how number of myonuclei increases during neonatal growth.

Though researchers had indeed reached definitive conclusions regarding the different functions of SCs and myonuclei, it had remained unknown how nuclei were functioning as a population. The predominant research techniques used at the time to study nuclei, EM and immunohistochemistry (IHC), had not provided the required spatial view of muscle fibres to efficiently study their myonuclear population (Schmalbruch & Hellhammer, 1976, 1977). As a result of such technological limitations, researchers were not able to accurately study the topic using existing techniques; EM and IHC simply harboured too many limitations (Schmalbruch & Hellhammer, 1977). As admitted by Bridge & Allbrook (1970:293), "The results are subject to considerable error, owing to the difficulty of deciding which nucleus belonged to which fibre, and also distinguishing between peripheral myonuclei and adjacent fibroblast nuclei".

Researchers had therefore pivoted to another modality, isolated single muscle fibres or segments of fibres, to study the relationship between number of nuclei and size of single muscle fibres. Such transition was made possible by the development of single muscle fibre isolation techniques, as well as improved technology of light microscopy (Bischoff, 1975, 1986; Konigsberg *et al.*, 1975; Viguie *et al.*, 1997; Roy *et al.*, 1999). The advancements in both fields enabled something which was extremely difficult to achieve previously, studying muscle fibres and their nuclei in three dimensions (3D). Thus, a gradual rise in the number of publications investigating this relationship, in single muscle fibres, may be witnessed since the 1970s.

For example, Konigsberg *et al.* (1975) and Bischoff (1975, 1986), the pioneers of the single muscle fibre isolation techniques, were the first to provide conclusive proof that SCs directly

give rise to myoblasts in isolated muscle fibres, a conclusion subsequently confirmed by others (Rosenblatt *et al.*, 1995; Yablonka-Reuveni, 1995).

In 1997, Viguie *et al.* (1997) attempted to study the effects of chronic denervation on rat single muscle fibres from the extensor digitorum longus (EDL) muscle. Upon dissecting the muscle, single muscle fibres were manually isolated, their nuclei were stained with propidium iodide and the fibres were mounted on coverslips, prior to producing *z* stack images of the fibres, using a laser scanning confocal microscope. Their technique had achieved the desirable results, i.e. they were able to accurately calculate fibre volume and number of nuclei. Roy *et al.* (1999) had taken this technique a step further and showed in functionally-overloaded rats (daily endurance training for 10-weeks) that number of nuclei had increased linearly with muscle fibre volume. That number of nuclei correlates with muscle fibre CSA (and in some occasions circumference) was later confirmed *in vivo* in EDL and soleus muscles of young (2 months) and old (23 months) mice, but the relationship was lost in middle-aged mice (14 months) (Bruusgaard *et al.*, 2006) (more on this topic in the next section).

In a study published in 2002 (Wada *et al.*, 2002), the authors isolated single muscle fibres of young and mature mice using a new method, NaOH maceration, and had taken a more traditional approach than the studies above in their imaging and analysis; they did not acquire *z* stacks, but had instead acquired a few images per fibre, in different focal planes. They had then calculated fibre CSA from its diameter ($CSA = 3.14 \times \left(\frac{diameter}{2}\right)^2$), instead of determining the CSA from measurements of fibre diameter and depth. Had they done the latter, they would have discovered that single muscle fibres are in fact elliptical and not circular, as per their calculation.

Thus, studies were beginning to show a transition from 2D imaging of muscle sections to 3D imaging of single muscle fibres, using advanced light microscopy. This was partly made possible by the advancements in isolation techniques of single muscle fibres (e.g. NaOH maceration, collagenase) and the continual improvement of manual dissection (Konigsberg *et al.*, 1975; Bischoff, 1986; Frontera & Larsson, 1997; Roy *et al.*, 1999; Wada *et al.*, 2002; Moyle & Zammit, 2014). Moreover, technological developments in light microscopy had allowed biologists to study nuclear behaviour in muscles *in vivo* (Bruusgaard *et al.*, 2003, 2006; Bruusgaard & Gundersen, 2008), whereupon researchers could study entire muscle fibres, with a significant reduction in the confounding factors found in whole muscle cryosections (e.g. connective tissue). All of these had together resolved some of the difficulties faced by research

groups, such as Schmalbruch & Hellhammer (1977), for all the nuclei observed belonged to the studied fibre and not to any other fibre or another type of cell (e.g. fibroblast).

The transition from 2D to 3D imaging was also noted in the analysis of data. It is my personal opinion that although both research groups (Viguie *et al.*, 1997; Wada *et al.*, 2002) had produced some novelty in their approach, their analysis of the acquired image stacks was rather traditional, for they had used a 2D approach to analyse 3D data. As the authors had shown in their respective studies, they had successfully measured the volume of muscle fibres (3D data). They had then progressed onto using their measurements of fibre length (2D data) to standardise their data of number of nuclei, in order to compare between fibres. Classically, such normalisation with fibre length was correctly performed, as the data was acquired in 2D muscle cryosections where CSA (transverse sections) and length (longitudinal sections) were the predominant measurements of fibre size. However, if one has the capacity to acquire 3D data about the volume of a single muscle fibre, and had already done so, there is no place for standardising nuclear number to mm fibre length (2D data), as such normalisation ignores fibre volume, the most physiologically relevant parameter of fibre dimensions.

Nevertheless, normalising number of nuclei with fibre volume is not a perfect method for characterising the relationship between nuclei and single muscle fibres either. This is because relying solely on this parameter assumes that only the number of nuclei, and not their distribution on a fibre, is essential for optimal function of the single muscle fibre. If fibre A and fibre B have each 10 nuclei per unit fibre volume, but all the nuclei in fibre A are concentrated in a small region of the fibre, are both fibres similar in function? Possibly, but arguably unlikely. Additional parameters are required to unravel this relationship.

1.3.3. Myonuclear organisation

Muscle nuclei had been traditionally believed to be randomly distributed on single muscle fibres (Muir *et al.*, 1965). Towards the end of the 1980s, a series of publications had emerged, all aiming to answer the following questions: “Do these (muscle) nuclei interact, and do their products completely intermingle? Or is a muscle fiber constructed of a mosaic of domains, each dominated by a single nucleus?” (Hall & Ralston, 1989:771). These questions had served as the origin of a theory (Figure 1.5) that asserts that each nucleus in a muscle fibre controls the gene expression in a finite volume, or domain, of the fibre (Hall & Ralston, 1989; Bruusgaard *et al.*,

2003; Qaisar & Larsson, 2014). The following sections will explore the answers to these questions and show how the theory of a myonuclear domain had originated.

1.3.3.1. Inter-nuclear interaction – organisation of information

The first in this series of publications had demonstrated, in transfected C2 mouse muscle cells, that the localisation of the mRNA encoding the human T-lymphocyte antigen CD8 was restricted to the surroundings of the nucleus encoding it and to its neighbouring nuclei. This was in contrast to the protein, which was distributed over the entire surface of the myotube (Ralston & Hall, 1989*a*, 1992). Such results, they asserted, proved that cytoplasmic proteins can be transported throughout a myofibre and that the mRNAs encoding them remain near their origin.

Conversely, Pavlath *et al.* (1989) showed in the same cell-type that proteins targeted to the golgi apparatus and the contractile machinery had remained in the vicinity of their nucleus of origin and its neighbouring nuclei (i.e. similarly to mRNA); these findings were also supported by a second study by Ralston & Hall (Ralston & Hall, 1989*b*). In the latter publication, the authors had explained the discrepancy between these studies by stating that the case for surface proteins is different than cytoplasmic proteins (Hall & Ralston, 1989). Thus, it appears as the spreading of mRNA and cytoplasmic proteins within single muscle fibres is rather contained, relatively to surface proteins. This was later confirmed *in vivo* by other groups (Merlie & Sanes, 1985; Sanes *et al.*, 1991; Gundersen *et al.*, 1993).

On a scale of an entire population of nuclei on a muscle fibre, the results above had led Ralston & Hall to theorise that in order to maintain uniform protein synthesis of immobile elements (e.g. myofibrils), the proportion of nuclei that are active is likely to be dictated by the distance these proteins must travel from each nucleus (Hall & Ralston, 1989). The distance would be "determined by the relative rates of diffusion, association with a target, and metabolic breakdown" (Hall & Ralston, 1989:772). Hence, it would be expected that the transcriptional activity of each nucleus differs from another and could even be specialised for the transcriptional requirements of their location on the fibre. As the half-life of a protein may be determined by its rate of diffusion, it would not be implausible to assert that to attain optimal function of a single muscle fibre, nuclei should control a domain, or a finite volume of a myofibre. However, for such a system to perform efficiently, nuclear positioning on single muscle fibres should be well-ordered and not random.

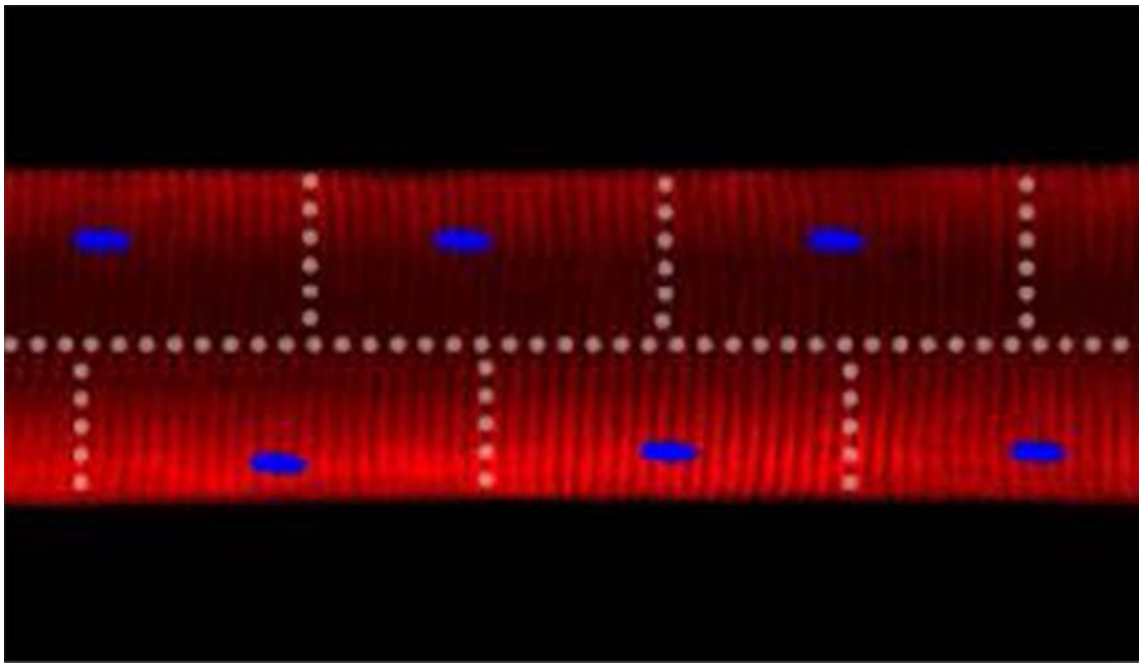

Figure 1.5: Myonuclear domains in a single muscle fibre
According to the myonuclear domain theory, a muscle fibre (red) consists of a mosaic of domains, each dominated by a single nucleus (blue). Each volume governed by a single nucleus is termed a myonuclear domain. Adapted from Qaisar & Larsson (2014).

1.3.3.2. Nuclear distribution

In 2003, Kristian Gundersen's laboratory (University of Oslo), published a research paper in *The Journal of Physiology* wherein they described a novel method for studying nuclear distribution in mouse single muscle fibres *in vivo* (Bruusgaard *et al.*, 2003; Bruusgaard & Gundersen, 2008). That publication marked the beginning of a highly valuable series of publications about nuclear organisation in health (Bruusgaard *et al.*, 2003, 2006), overload exercise (Bruusgaard *et al.*, 2010), inactivity (Bruusgaard *et al.*, 2012) and even testosterone doping (Egner *et al.*, 2013) in mice and rats. Their technique enabled the visualisation of muscle nuclei *in vivo,* by injecting labelled DNA into nuclei of single muscle fibres and tracking them with time-lapse confocal microscopy. By doing so, the movement of nuclei may be monitored over several days and even weeks (Gundersen & Bruusgaard, 2008) and conclusions about nuclear movement and distribution may be reached, *in vivo*.

The Gundersen laboratory's approach differed to the studies mentioned above not only as the study was conducted *in vivo*, but also as it was specifically concerned with nuclear distribution. In their publication from 2003 (Bruusgaard *et al.*, 2003), the group measured nuclear organisation on single muscle fibres using parameters such as myonuclear domain

(MND) and 3D co-ordinates of nuclear positioning on the fibres. They had additionally introduced a parameter, "order-score", that is the result of computer simulations, which compare the experimental nuclear positioning against random and optimal positioning to ascertain whether nuclei are distributed randomly or optimally on muscle fibres (Figure 1.6). Thus, whereas MND provided information about the average volume of a fibre each nucleus may have governed (calculated as $\frac{Fibre\ volume}{No.nuclei}$), order-score is a measure of the randomness of the nuclear distribution.

As the researchers wished to answer the question whether myonuclear organisation in healthy muscle fibres is random or optimal, best (optimal) and worst (random) mathematical conditions had to be formed as controls. As all comparisons are performed against an ideal or random distribution, the order-score should be treated as a value of "performance" or improvement from random distribution; 0% equals completely random distribution, 100% equals optimal distribution (Bruusgaard *et al.*, 2003).

From the perspective of the work undertaken in this thesis, their main results on single muscle fibres from EDL and soleus muscles of adult mice had revealed the following: a) nuclei did not alter their position over several days; b) the endplate and myotendinous junction (MTJ) are specialised regions of the fibre, wherein nuclei reside in high density; c) extrasynaptic nuclei (muscle nuclei that do not reside at the neuromuscular junction) are not randomly distributed and repel each other, presumably to minimize transport distances (~40% improvement from random distribution); d) number of nuclei was approximately proportional to the muscle fibre's cytoplasmic volume and surface area (Bruusgaard *et al.*, 2003).

That nuclei do not spread randomly and are positioned more or less evenly on a single muscle fibre has been shown numerous times in rodents (Bruusgaard *et al.*, 2003, 2006, 2012; Bruusgaard & Gundersen, 2008; Folker & Baylies, 2013) and as mentioned above, their number correlates more strongly with fibre size during muscle growth, hypertrophy and ageing than in adulthood (Bruusgaard *et al.*, 2006, 2012; Egner *et al.*, 2013). Thus, it appears that not only are nuclei situated in an orderly manner on single muscle fibres, groups of nuclei with specialised distribution exist (endplate and MTJ), alluding to the possibility for speciality of protein synthesis in such nuclei as well (Cutler *et al.*, 2018).

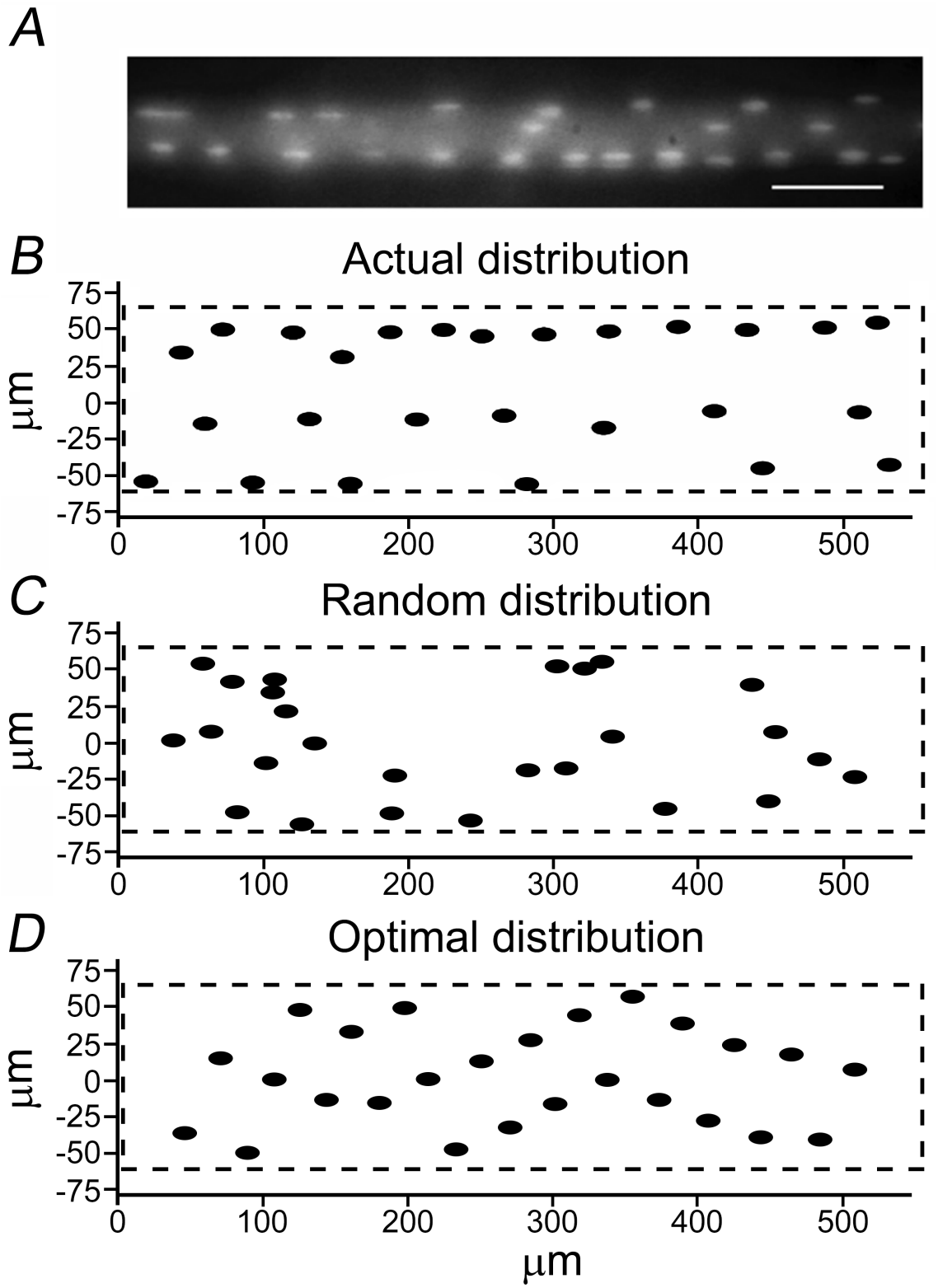

Figure 1.6: Distribution patterns of nuclei in by computer simulations

A, averaged micrograph of 17 focal planes of the segment. Scale bar = 50 µm. B, observed nuclear positions on the surface foldout. C, a computer simulation where the same number of nuclei were positioned randomly on the same surface. D, a computer simulation where nuclei were assumed to repel each other and distances were measured directly through the cytosol. Adapted from Bruusgaard *et al.*, (2003).

1.3.3.3. MND – specialised maintenance tool of single myofibres

As stated above, two conditions should be met in order to support the theory of MNDs; (i) nuclei should be relatively evenly spaced; (ii) the transcriptional activity of each nucleus differs from another and could even be specialised for the transcriptional requirements of their location on the fibre. Hitherto, it has been established that myonuclei are not randomly ordered. The final part in discerning the existence of a MND is, therefore, to verify whether the transcriptional activity in each nuclear domain, of nuclei with the same speciality (i.e. extrasynaptic), is unique, or rather that all nuclei have an identical profile of transcription.

In this regard, it has been documented *in vitro* that only a portion of myoblasts accumulate NFATc1 (Abbott *et al.*, 1998), NFAT5 (O'Connor *et al.*, 2006), myogenin (Ishido *et al.*, 2004; Ferri *et al.*, 2009), MyoD (Ishido *et al.*, 2004; Yamamoto *et al.*, 2008), Myo18B (Salamon *et al.*, 2003) or myostatin (McPherron *et al.*, 1997; Artaza *et al.*, 2002). Moreover, it has been demonstrated *in vivo* that nuclei within a muscle fibre do not have equivalent gene expression, as determined by *in situ* hybridisation of α-skeletal actin and troponin I slow into sections of regenerating muscles (Newlands *et al.*, 1998); similar findings were also made for myostatin (Artaza *et al.*, 2002), as well as for JunB, a transcription factor that maintains skeletal muscle mass and promotes hypertrophy (Raffaello *et al.*, 2010). Lastly, level of acetylation of Histones H3 and H4 correlates with the activity level of gene transcription (Hebbes *et al.*, 1988). Though the authors of another publication (Gnocchi *et al.*, 2011) claim nuclei in single muscle fibres showed homogeneous immunostaining of acetylated histone H3, their confocal images show otherwise; using western blots, they had not measured acetylation in each nucleus, but relied solely on global measurements for each muscle fibre. They had additionally not quantified pixel intensities of the staining in their images and relied solely on qualitative analysis of those images, which to me show heterogeneous immunostaining. Such heterogeneity of histone H3 acetylation was confirmed using pixel quantification of single nuclei in confocal images of muscle cryosections, showing metabolically labelled nascent RNA (5-ethynyl uridine) and immunostained with histone 3 lysine 9 acetylation as a marker of transcriptional activity (Kirby *et al.*, 2016).

The above literature reveals that nuclei in single muscle fibres maintain compartmentalisation of gene expression, which probably facilitates regional production of proteins (Cutler *et al.*, 2018). This may add to the notion of MNDs in demonstrating that each nucleus provides varying levels of transcripts to the cell. Nevertheless, this could also imply that each extrasynaptic nucleus specialises in the synthesis of different proteins and all extrasynaptic

nuclei, altogether as a population, provide stable synthesis of transcripts across the muscle fibre. However this is unlikely for, as previously stated, mRNAs and cytoplasmic proteins were only found in the general area of their nucleus of origin and its neighbouring nuclei (Ralston & Hall, 1989*b*; Hall & Ralston, 1989). Furthermore, it has been shown in lateral transverse muscles and body wall muscles of *Drosophila* that sarcomere assembly initiates near the nucleus, by synthesising a complex of proteins (called I-Z-I), composed of Z-line (e.g. ZASP) and F-actin proteins (Rui *et al.*, 2010; Auld & Folker, 2016). This once again demonstrates nuclei control their proximal environment. These findings further support the concept of a nucleus synthesising proteins for its domain.

The notion of a MND is additionally attractive as single muscle fibres may be of extreme length (e.g. sartorius muscle). Transporting proteins across centimetres of dense tissue could be very slow and energetically costly and thence significantly increase chances for post-transcriptional modifications of proteins (Hershko, 1998; Ciechanover, 2005, 2015; Bojkowska *et al.*, 2011; Braten *et al.*, 2016; Ciechanover & Kwon, 2017). Furthermore, it is unlikely that the requirements of a single muscle fibres in the proximal edge of a fibre are the same as those at the distal edge, as may be epitomised by the existence of specialised populations of nuclei on muscle fibres; is it a coincidence that the number of nuclei in the MTJ is significantly greater than in the rest of the muscle fibre, particularly as it is known that the MTJ is highly vulnerable to damage during stretch or eccentric work? (Tidball, 1991; Frenette & Côté, 2000; Bruusgaard *et al.*, 2003; Wang *et al.*, 2013).

In conclusion, research appears to support the existence of MNDs in single muscle fibres. A model whereby each nucleus acts as a governor of its own province and provides the required services for that specific district promptly and efficiently, whilst aiding other nuclei when necessary, thereby sharing some of the municipal load, is likely the most relevant; overlapping domains are supported by the finding that proteins encoded from myonuclei were found near neighbouring nuclei as well (Ralston & Hall, 1989*b*; Hall & Ralston, 1989). Therefore, the model of a fibre as a city with distinct borders (as seen in Figure 1.5), previously suggested by other research groups (Karlsson, 2008; Van der Meer *et al.*, 2011; Qaisar & Larsson, 2014), does not fit these findings. More likely, and supported by the studies above, is that the appropriate model is one whereby a nucleus governs a volume of the fibre that overlaps to a certain extent with the volume of other nuclei; the territories simply overlap at the edges.

Consequently, suggested answers to Ralston & Hall's questions (Ralston & Hall, 1989*a*) would be that muscle nuclei indeed interact in some way and their products may intermingle to an extent between the myonuclear domains. Furthermore, a muscle fibre does not seem to be constructed of a mosaic of domains *per se*, but rather a mosaic whereby each domain slightly overlaps with its nearest domains. Such organisation supports the stochastic nature of the nuclear transcriptional activity seen in single muscle fibres (Newlands *et al.*, 1998; Cutler *et al.*, 2018).

1.3.3.4. Evidence for organised nuclear distribution in humans

By the end of the 2000s, an increasing number of studies on nuclear organisation in mature single muscle fibres had begun to emerge, each with a slightly different approach. Some studies were still focusing on the number of nuclei within single muscle fibres, whereas others on their spatial distribution; nonetheless, all were conducted in animals (Bruusgaard *et al.*, 2006, 2012; Zhang *et al.*, 2007*b*, 2009; Bruusgaard & Gundersen, 2008; Lei *et al.*, 2009; Egner *et al.*, 2013; Chapman *et al.*, 2014). The first study, to the best of the author's knowledge, to investigate nuclear distribution *per se* in single muscle fibres from human samples came from the laboratory of Lars Larsson (Uppsala University), wherein a comparison of myonuclear organisation was performed between humans and other species, such as mouse, rat, pig horse and rhinoceros (Liu *et al.*, 2009). Building upon their method, a year later, they published a research paper in *Aging Cell* (Cristea *et al.*, 2010), investigating the effect of ageing and gender on nuclear organisation in human single muscle fibres. In that study, as well as their following study (Qaisar *et al.*, 2013), they were investigating two main parameters: MND and nearest neighbour (NN).

As previously stated, the typical method to calculate MNDs is to divide fibre volume by the number of nuclei on the fibre, which results in the average volume of a fibre each nucleus governs. This measure provides useful information in conjunction with other parameters, however, by itself is rather crude. Therefore, Larsson's group had used an additional parameter to investigate the spatial arrangement of nuclei on muscle fibres, nearest neighbour (NN). NN is an algorithm that finds, for each nucleus, the neighbouring nucleus that resides in its closest proximity. The average of the NN distances for all nuclei on a fibre, therefore, allows investigating whether nuclei on a muscle fibre are situated remotely from one another, or in close proximity (e.g. aggregates). Perhaps more important is the standard deviation of NN (SD-NN), as it reflects the regularity of these distances and therefore, reflects the level of order in the nuclear population.

The approach to analysis between the studies by Cristea *et al.* (2010) and Bruusgaard *et al.* (2003) was similar, as NN, used in the former publication, is the core of order-score, used in the latter publication. In the work published by Bruusgaard *et al.* (2003), the experimental NN is measured, followed by calculations of the optimal and random NN distances. The result is the improvement in the experimental NN distances from random distribution. Hence, while Cristea *et al.* (2010) had compared between biological samples, Bruusgaard *et al.* (2003) had compared to an ideal value; the latter approach has the additional advantage in cases where a control group is non-existent. In any case, the two approaches of analysis are similar in their essence.

From a biological perspective, comparing nuclear organisation in human single muscle fibres to a control group may produce errors and it might be that a comparison to an ideal might be more reliable. As will be shown in the next section, MNDs are dynamic and are affected by age, activity level and disease, even in young healthy controls, as reviewed by Van der Meer *et al.* (2011) and Murach *et al.* (2018). Generally, the heterogeneity of human samples provides a platform less controlled than that of animal models and a comparison of nuclear organisation with an ideal may produce results that are more reliable.

1.3.3.5. Dynamics of MNDs

Average MND in muscle fibres depends on both number of nuclei and volume of the fibre they inhabit. As it is well-established that myonuclei do not divide, SCs are the source of new myonuclei in single muscle fibres (Moss & Leblond, 1971). SCs have been documented in literature to be involved in numerous situations of muscle fibre adaptation, including postnatal growth, regeneration, hypertrophy and re-growth following atrophy (Zammit *et al.*, 2006; Scharner & Zammit, 2011; Relaix & Zammit, 2012). However, how the incorporation of myonuclei specifically affects MNDs in various situations remains in conflict (Gundersen, 2016; Murach *et al.*, 2018).

Claims suggesting MNDs are fixed and that nuclei have a transcriptional “ceiling” have been made in numerous publications (I. Wada *et al.*, 2003; Brack, 2005; Bruusgaard *et al.*, 2006; Mantilla *et al.*, 2008; Van der Meer *et al.*, 2011; Pallafacchina *et al.*, 2013; Qaisar & Larsson, 2014; Gundersen, 2016; Murach *et al.*, 2018). In order for this to be true, two assumptions should be made: (i) muscle fibres cannot undergo hypertrophy above a certain threshold without prior incorporation of nuclei into the fibre, and; (ii) muscle fibre atrophy is accompanied

by a reduction in nuclear number, to maintain a constant MND. The text below will discuss the dynamics of MNDs in various situations.

Postnatal muscle growth

During postnatal muscle growth, muscle fibres increase in size and weight and myonuclear number increases drastically, by the activation of SCs (Moss & Leblond, 1971). It has therefore been suggested that MND in growing muscle fibres ought to be rather tightly maintained (I. Wada *et al.*, 2003; Brack, 2005; Bruusgaard *et al.*, 2006; Mantilla *et al.*, 2008; Van der Meer *et al.*, 2011; Pallafacchina *et al.*, 2013; Qaisar & Larsson, 2014; Gundersen, 2016; Murach *et al.*, 2018). Nevertheless, evidence suggests the contrary during postnatal development. Single muscle fibres from the soleus muscle, taken from rats aged 4-49 days, have demonstrated a simultaneous increase in myofibre CSA, nuclear number and MND; i.e. though number of nuclei was indeed rising, it was not sufficient to prevent the growing MNDs in postnatal development (Ohira *et al.*, 2001). This is supported by another study in growing mice (0 days to 6 months), which showed in TA single muscle fibres that MND was increasing up to 6 months of age, but plateaued between 6-18 months (I. Wada *et al.*, 2003). Further support is provided from single muscle fibres from the diaphragm muscle in growing rats, wherein MND had increased significantly from P14 to P28 in type I, type IIa and type IIx muscle fibres (Mantilla *et al.*, 2008).

As seen in Figure 1.7, adapted from White *et al.* (2010), postnatal growth in mouse EDL single muscle fibres is biphasic: 1) muscle growth accompanied by incorporation of myonuclei (<P21); 2) muscle growth without accretion of myonuclei (>P21) (White *et al.*, 2010; Pallafacchina *et al.*, 2013). This was accompanied by a concomitant decrease in the number (Figure 1.7b) and proportion of SCs (Figure 1.7c) in the fibre. Importantly, MND was shown to increase sharply up to P56 (Figure 1.7d), and possibly beyond, as P56 was the oldest group in the study (White *et al.*, 2010).

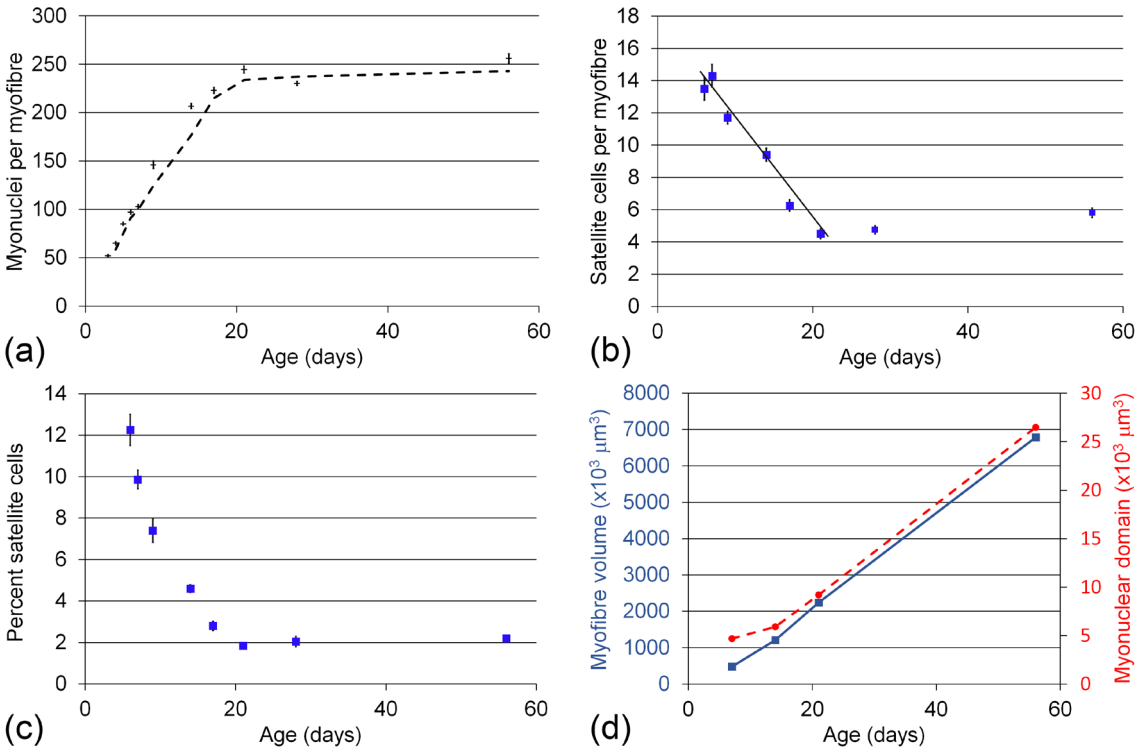

Figure 1.7: Postnatal growth dynamics of EDL myofibres and associated nuclei

(a) Myonuclei were counted on isolated EDL myofibres from Myf5$^{nlacZ/+}$ and/or *3F-nlacZ-E* mice and there was a 4-fold increase in myonuclei number per myofibre between P3 and P14 from ~50 to ~200. The adult complement of myonuclei (~250) was reached by P21. Then, (d) mean total myofibre volume was calculated by multiplying mean length by mean cross- sectional area and increased in a linear fashion between P7 to P56 (blue line). Myonuclear domain during postnatal development was calculated by dividing mean total myofibre volume by the mean number of myonuclei per myofibre (dashed red line). (b) Satellite cell number steadily decreased from P6, to reach the adult level by P21. Satellite cells were identified and counted on isolated *Myf5$^{nlacZ/+}$* and *3F-nlacZ-E* myofibres and pooled at each age to give a mean ± SEM. The number of satellite cells per myofibre decreased by 0.66 satellite cells per day ($R^2 = 0.98$) to reach the adult level by P21, when it remained unchanged until 10 months, the oldest age analysed. (c) The same data with satellite cells expressed as a percentage of total myofibre nuclei (myonuclei plus satellite cells). Due to the rapidly increasing myonuclear number, there is an exaggerated fall from P6 until P21. Data shown are mean ± SEM (n > 30 myofibres from at least 6 mice at P7, P14, P21 and P56, and at least 2 mice per age at all other stages), except for (d), which is mean; trend line in (a) depicts the moving average (n > 30 myofibres from each of at least 2 mice at each age). Adapted with legend from White *et al.* (2010).

Consequently, as proposed by others, a linear relationship indeed exists between number of nuclei and muscle fibre volume during postnatal growth (Enesco & Puddy, 1964; Moss, 1968*a*, 1968*b*; I. Wada *et al.*, 2003; Brack, 2005; Bruusgaard *et al.*, 2006; Mantilla *et al.*, 2008). Nevertheless, whereas other studies inferred that the increase in nuclear number is proportional to the muscle fibre size in that stage of development (Enesco & Puddy, 1964; Moss, 1968*a*, 1968*b*; Bruusgaard *et al.*, 2006), the studies above do not support such claims. As a result, sufficient evidence shows that MNDs increase during postnatal growth and are thus, not fixed during postnatal development.

That MND is not fixed during postnatal growth does not necessarily falsify the notion of a transcriptional ceiling. It is possible that the only reason muscle growth is permitted at such a high rate during postnatal development is because the process of laying the foundation for growth had already been ahead of development to permit such growth; i.e. the mouse genetics had "predicted" the forthcoming growth and had ensured a sufficient number myonuclei was found in the fibre to support the forthcoming event. Hence, it is possible that the number of nuclei in single muscle fibres did not alter in White *et al.* (2010) after P21 because the number of incorporated nuclei should have sufficed to support growth of fibres to adulthood.

Such a pre-programmed prediction of biological necessities and outcomes is not alien to normal biology, as observed by a significant rise in growth hormone (GH) and insulin-like growth hormone-1 (IGF-1) during adolescence (Ashpole *et al.*, 2015; Richmond & Rogol, 2016), as well as the cartilaginous epiphyseal growth plate that is often used to predict bone morphology (Carriero *et al.*, 2011; Castro-Abril *et al.*, 2016; Yadav *et al.*, 2016). Assuming the environment provides perfect conditions for one to reach their potential height, that is dictated by their genes, the factors (e.g. GH, epiphyseal plate) performing the day-to-day work, which are pre-programmed as well, will be the predominant regulators of height. In the case for muscles, the inherited genetic traits perhaps predict a target for muscle size in adulthood and, in the absence of environmental interference (e.g. laboratory conditions), the factors controlling muscle size, myonuclei, are thus pre-programmed to support muscle growth up to that potential. Thus, it is plausible that pre-programmed genes aim to reach a certain muscle size and the pre-laid myonuclei are simply the tool to acquire that.

That epigenetics can control muscle growth in response to environmental factors has been shown in rats, where postnatal malnutrition had led to significant retardation in muscle growth, possibly due to low GH and IGF-1 (Gautsch *et al.*, 1999; Bayol *et al.*, 2004; Fiorotto *et al.*, 2014;

Ferraz-Pereira *et al.*, 2015). It has additionally been demonstrated in pigs (Stickland *et al.*, 1975) and rats (Bayol *et al.*, 2004) that postnatal malnutrition may lead to a low number of myonuclei and that number of SCs is reduced in malnourished infants (Hansen-Smith *et al.*, 1979). Lastly, studies show IGF-1 controls SC activation, number of nuclei, MND volume, ribosome abundance and protein synthesis in adult and neonatal mouse and rat single muscle fibres (McCall *et al.*, 1998; Hameed *et al.*, 2002; Hill & Goldspink, 2003; Qaisar *et al.*, 2012; Fiorotto *et al.*, 2014). Therefore, if epigenetics can tune the size of muscles by using biological factors to affect it (e.g. IGF-1, myonuclei, SCs), is there a genetic baseline that is the potential of muscle growth waiting to be realised in the absence of interference? In the context of MNDs during postnatal development, a mouse is born with a large pool of SCs that are mostly there to be turned into myonuclei, unless it is unfavourable by the environment (e.g. malnutrition). Thus, it seems plausible that the larger the initial pool of SCs, the larger the number of myonuclei in the myofibre. If the myofibre is not expected to grow drastically to a large size, what could be the purpose for such a superfluous act of nuclear accretion? Biology typically acts for self-preservation and energy conservation, not the contrary.

There are numerous mechanisms by which genetics and the environment can alter muscle fibre size and number of myonuclei; I have merely named a few. Nevertheless, it seems that when the environment is not beneficial for growing large muscles at the neonatal stage, genes somehow control muscle size, possibly by controlling regulators of number of nuclei (e.g. IGF-1 and SCs). It would have been interesting had White *et al.* (2010) continued their study for a few additional months, followed by ablation of SCs and muscle overload to see whether the number of nuclei found in the muscle at P21 was sufficient to support muscles to adult-size, but no further in the absence of SCs. Such a study could provide an experimental answer to this theory. As it stands, though, it is not possible to support or otherwise the theory of a transcriptional ceiling in neonates. It can only be asserted that MNDs are clearly not fixed during postnatal development.

Hypertrophy, atrophy and re-growth.

It is imperative to state at this stage that whether SCs are a pre-requisite for hypertrophy in adulthood is irrelevant from the perspective of the work in this thesis. This section will simply address whether MNDs are fixed in adulthood and whether sufficient evidence exists to support the theory of a transcriptional ceiling in single muscle fibres. At first glance both seem tightly connected with incorporation of myonuclei. However, this is not necessarily so from the

perspective of my work, for it would be enough to observe research that demonstrates muscles can grow drastically (e.g. >30%) without incorporating any nuclei and retain their functional capacity to disprove both claims. Of course, it could also be evident that if in some cases muscles grow and in others do not, without incorporating nuclei, there is reason to believe some regulation of muscle size occurs independently from myonuclei. Nevertheless, even in such a case, it would remain a possibility to claim MNDs are not fixed and that evidence of a ceiling is lacking. Thus, it would suffice to mention that numerous hypertrophic conditions have been documented in literature to include incorporation of myonuclei into muscle fibres (Enesco & Puddy, 1964; Moss, 1968*b*; Moss & Leblond, 1970, 1971; Cheek *et al.*, 1971; Seiden, 1976; Schiaffino *et al.*, 1976; Lipton & Schultz, 1979; Cabrić & James, 1983; Winchester & Gonyea, 1992; Giddings & Gonyea, 1992; McCall *et al.*, 1998; Kadi *et al.*, 1999; Roy *et al.*, 1999; Allen *et al.*, 1999, 2013; Bruusgaard *et al.*, 2010).

It has been demonstrated *in vivo* that the addition of myonuclei precedes overload-induced hypertrophy by up to 5 days, in mouse single muscle fibres (Bruusgaard *et al.*, 2010). This goes against the notion of a fixed MND in adult muscle, as at least temporarily, MNDs must have been smaller (16% reduction in their study) prior to the increase in fibre volume. Following 2 weeks of overload, myofibre hypertrophy had plateaued, and increases of 54% were observed in number of nuclei and 35% in single muscle fibre CSA. The MNDs acquired following those 2 weeks were similar to the beginning of the study, suggesting the theory of a transcriptional ceiling may be possible. A large increase in muscle fibre CSA concomitant with maintenance, and even reduction, in MND volume in response to overload-induced hypertrophy has also been noted in the plantaris (Roy *et al.*, 1999) and soleus (McCall *et al.*, 1998) in rats, as well as in fast MHC-containing fibres of cat plantaris muscle (Allen *et al.*, 1995). Moreover, when >75% of SCs were conditionally depleted in overload-induced adult mice, muscle hypertrophy was prevented, serving as further support that a transcriptional ceiling may exist in single muscle fibres (Egner *et al.*, 2016; Goh & Millay, 2017).

In another study by a different group, 2-weeks overload-induced hypertrophy was not prevented in adult mice, where 90% of SCs were ablated using an inducible Pax7-diphtheria toxin transgene; new myonuclei were not incorporated during fibre hypertrophy and MND had therefore increased by 32% (McCarthy *et al.*, 2011). Specific force of single muscle fibres (max force relative to fibre CSA) was unchanged, but specific force of the whole muscle was reduced by 20%, and expression of embryonic myosin was only raised by 7%, compared to 29% in controls (McCarthy *et al.*, 2011). The group had repeated their study for longer term (8 weeks)

and reached similar results for the first 2 weeks of the experiment (Fry *et al.*, 2014*a*). Nevertheless, following the first 2 weeks of overload, muscles with ablated SCs ceased to hypertrophy, whereas controls continued to hypertrophy throughout the 8 weeks of the study. They additionally found increased accumulation of extracellular matrix (ECM) in SC-depleted single muscle fibres, but not in controls, by an inhibitory effect of SCs on muscle fibroblasts, which lowers secretions of collagen and fibronectin (Fry *et al.*, 2014*a*). As fibronectin-secreting muscle fibroblasts may be involved in peripheral myonuclear positioning (Roman *et al.*, 2018), further effect of SCs' ablation may be carried through altered nuclear positioning, which none of the studies above had investigated.

It is intriguing the two research groups (Bruusgaard *et al.*, 2010; McCarthy *et al.*, 2011; Fry *et al.*, 2014*a*; Egner *et al.*, 2016) had reached conflicting results, yet their approach was rather alike. The debate between the two groups on this matter may be found in the following reference (McCarthy *et al.*, 2017). It certainly seems that the synergistic ablation technique used by Bruusgaard *et al.* (2010) and Egner *et al.* (2016) had consistently produced a more potent SC activation than McCarthy *et al.* (2011) and Fry *et al.* (2014), as shown by an increase in abundance of Pax7+ cells of 420%-650% (Egner *et al.*, 2016), compared with 360% (McCarthy *et al.*, 2011) and ∼100% (Fry *et al.*, 2014*a*), respectively, following surgery. It also seems that single muscle fibres reached larger CSAs in the former group (30-50%), compared with the latter group (10%-30%). It is therefore possible that simply altering the level of protein synthesis in nuclei in the latter group was sufficient to increase fibre volume, by increasing the amount of ECM more so than myofibrillar proteins, but that crossing a certain threshold of fibre volume would have resulted in low specific force in the fibres themselves and not just in the muscle as a whole (Kadi, 2008; Gundersen, 2016). Enhanced production of ECM is abundant in numerous muscle disorders associated with altered myonuclear organisation, SC-depletion and low specific force of single muscle fibres (Wallgren-Pettersson *et al.*, 1988; Sanoudou *et al.*, 2003; Nikolova *et al.*, 2004; Brack *et al.*, 2007; Puckelwartz *et al.*, 2009; Risson *et al.*, 2009; Gillies & Lieber, 2011; Wu *et al.*, 2011; Banerjee *et al.*, 2014; Azibani *et al.*, 2014; Falcone *et al.*, 2014; Chapman *et al.*, 2014; Duddy *et al.*, 2015; McGreevy *et al.*, 2015; Hardy *et al.*, 2016; Lindqvist *et al.*, 2016; Goh & Millay, 2017; Gillies *et al.*, 2017).

That increase in fibre volume can result in 20-40% elevation in MND and low specific force of single muscle fibres has been demonstrated numerous times in genetically modified mice wherein the expression of proteins involved in muscle hypertrophy, through alterations in the myostatin signalling pathway, is altered (Bruusgaard *et al.*, 2005; Amthor *et al.*, 2007, 2009;

Welle *et al.*, 2007; Sartori *et al.*, 2009; Raffaello *et al.*, 2010; Qaisar *et al.*, 2012). The low specific force in such conditions has been partly attributed to increased ECM volume in single muscle fibres, that occurs in conjunction with large MNDs (Bruusgaard *et al.*, 2005). In other conditions that indeed induce incorporation of myonuclei, e.g. IGF-1 signalling pathway, specific force is typically retained (McCall *et al.*, 1998; Barton-Davis *et al.*, 1999; Petrella *et al.*, 2006; Kadi, 2008; Qaisar *et al.*, 2012; Egner *et al.*, 2013).

In response to exercise, a known stimulator of nuclear accretion through IGF-1 signalling, it certainly seems that incorporation of myonuclei in rodents is part of a robust hypertrophic response, concomitant with maintenance of MND volume (McCall *et al.*, 1998; Roy *et al.*, 1999). However, the case for humans is rather confusing (Kadi *et al.*, 2005), as at times, MND is maintained during exercise-induced muscle fibre hypertrophy (Snijders *et al.*, 2016; Damas *et al.*, 2018), whereas in other times, hypertrophy increases the domains (Kadi *et al.*, 2004). Conflicting results from studies investigating the impact of prolonged resistance exercise training on muscle fibre MND have been summarised in Table 3 in the following review paper (Snijders *et al.*, 2009). Nevertheless, the majority of publications seem to support the notion that MND remains similar in response to exercise training. Moreover, as for the cases wherein MND had indeed increased, researchers suggested the reason was that subjects were untrained individuals whose muscles relied on the ability of their nuclei to increase muscle fibre volume simply by upregulating gene expression rather than nuclear accretion (Kadi, 2008; Snijders *et al.*, 2009). In support, when Snijders *et al.* (2016) had selected participants who are recreationally active, performing sports on a non-competitive basis between 2 and 5 h per week, no difference in MND was noted during and following 12-weeks of resistance exercise, despite 20-40% increase in muscle fibre CSA.

It therefore appears that homeostasis of MNDs is a significant determinant in preserving muscle function. Evidence also suggests that single muscle fibres that are oxidative, either type I or genetically modified to be oxidative, require a larger population of myonuclei for optimal function, presumably due to the additional requirements of mitochondrial protein synthesis (Roy *et al.*, 1999; Bruusgaard *et al.*, 2003; Fry *et al.*, 2014*b*; Kirby *et al.*, 2016; Keeling *et al.*, 2017; Ross *et al.*, 2017*b*, 2018; Murach *et al.*, 2018). It is important to state here that it is recognised that the sole mechanism of regulating muscle size is not simply alteration of number of nuclei, as it is clear from the genetically modified animals mentioned above that muscle volume may indeed increase in the absence of additional myonuclei. Nevertheless, as the functional capacity

of hyper-hypertrophied (>30%) single muscle fibres from these animals is typically not retained, I suggest MND as one of the determinants of functional quality of single muscle fibres.

It is additionally clear that if McCarthy *et al.* (2011) and Fry *et al.* (2014) had successfully increased muscle fibre CSA by 10-30%, with >80% ablation of SCs, some redundancy in the number of myonuclei exists, otherwise it would be difficult to imagine the complex mechanisms whereby few nuclei can somehow control centimetres of muscle fibres, without jeopardising specific force. Such redundancy is not rare in biology (Gundersen & Bruusgaard, 2008; Schiaffino *et al.*, 2013). Various animal models of muscle hypertrophy, atrophy and regrowth have shown that single muscle fibres can alter their volume simply by altering protein synthesis and degradation, without altering number of nuclei (Allen *et al.*, 1995; Kadi *et al.*, 2004, 2005; Verheul *et al.*, 2004; Aravamudan *et al.*, 2006; Bruusgaard *et al.*, 2006, 2010, 2012; Bruusgaard & Gundersen, 2008; Gundersen & Bruusgaard, 2008; Pallafacchina *et al.*, 2013; Egner *et al.*, 2013; Kirby *et al.*, 2016; Schwartz *et al.*, 2016). In fact, it was found that, though during postnatal development and ageing a significant correlation exists between number of nuclei and fibre CSA, the correlation is lost in adulthood (Bruusgaard *et al.*, 2006). Moreover, it has been suggested that the number of myonuclei in a single muscle fibre may represent the largest fibre volume in the history of that fibre ("muscle memory"), as nuclei acquired during overload were not lost in detraining, demonstrating some redundancy in the number of nuclei in a myofibre (Gundersen & Bruusgaard, 2008; Bruusgaard *et al.*, 2010; Gundersen, 2016); this has also been confirmed in humans (Kadi *et al.*, 2004). It additionally seems that myonuclei possess a significant reserve capacity to upregulate (up to 7x) transcription during overload-induced hypertrophy, when SCs are ablated, supporting 25% increase in CSA of single muscle fibres (Kirby *et al.*, 2016).

All these studies firmly confirm that MND is flexible at all times; in postnatal development, adulthood, hypertrophy, atrophy and regrowth following atrophy. The notion that a MND is fixed as number of nuclei increases in the neonatal with fibre CSA is simply false. It is my presumption that previous researchers were struggling to reach this conclusion due to their inability to calculate MNDs in histological sections and were led to the assumption that MNDs are fixed as number of nuclei increases linearly with fibre CSA, at least up to P21. Nevertheless, as demonstrated above, MND increases linearly with fibre volume in the neonatal, most likely well into adulthood, when the correlation of MND and fibre volume is lost.

Caution is required with regards to the conclusion on a transcriptional ceiling. Numerous studies have demonstrated that maintenance of MND during significant hypertrophy preserves

muscle function, and that without this mechanism (e.g. myostatin signalling inhibition) specific force is reduced. Nevertheless, it has also been shown that fibre CSA may increase by 10-30% simply by upregulating gene transcription, increasing MND by up to 40% (Allen *et al.*, 1995; Kadi, 2008). It therefore certainly seems that some hypertrophy is possible without the activation of SCs and that some redundancy exists in preservation of MNDs (Allen *et al.*, 1995; Gundersen, 2016; Murach *et al.*, 2018). However, the evidence that alterations in protein balance sufficiently preserve muscle function in cases of fibre hypertrophy beyond ∼30% in CSA is not convincing.

It is the opinion of the author that the inability to conclude whether a transcriptional ceiling indeed exists originates from the capability of muscle fibres to change their volume by altering the balance of protein synthesis and degradation, as well as due to the aforementioned "muscle memory". It is therefore suggested that when striving to resolve this conundrum, the model used should be exercised animals and human participants, where MNDs are more likely to be pushed to their maximum capacity (assuming such a capacity exists); or at the very least it could be claimed that the correlation between number of nuclei and fibre volume is significant in exercised muscles (Allen *et al.*, 1995, 1999; Kadi *et al.*, 1999; Roy *et al.*, 1999; Kadi, 2008; Bruusgaard *et al.*, 2010; Egner *et al.*, 2013). Thus, any alterations in fibre CSA would be less likely to be due to simple changes in protein balance. I believe a model such as this would perform better in ascertaining whether a transcriptional ceiling exists in single myofibres. Alternatively, I maintain my suggestion to study neonates for several months, followed by ablation of SCs and muscle overload, to see whether the number of nuclei found in the muscle at P21 is sufficient to support muscles to adult-size, but no further in the absence of SCs.

The ultimate aspect to discuss in this regard is the possible redundancy in this system. It is my interpretation that if muscle fibres do not rely solely on increasing number of myonuclei to increase fibre volume, the process of incorporating myonuclei is likely to be quite energetically costly. I also believe that the fact that following atrophy and regrowth, or training and detraining, the newly acquired nuclei are not lost for a prolonged period of time, is another factor leading me to assert that incorporating myonuclei is energetically costly. If muscles atrophy simply due to reduced activity levels, it is clear that biology is not allowing muscles to retain proteins unnecessary to their function. It therefore seems to me that it is costlier to incorporate myonuclei than to retain existing ones. If true, it makes sense why muscle fibres can rely on altering protein balance to change in size; it simply costs less energy and can respond more promptly to cellular requirements. In addition, retaining this "muscle memory" in the form of nuclei (Gundersen, 2016) may be beneficial, for if the environment had previously required

large muscles for survival, it might require it again. In such a case, the foundation had already been laid to return to the previous muscle size, aiding the survival of the animal.

Lastly, it seems to me that muscles may indeed be able to predict the necessity in additional nuclei, even in adulthood. The studies above have demonstrated that additional nuclei are not necessarily required to support fibre hypertrophy of up to 30% in CSA, yet above that nuclei are incorporated, possibly even prior to the rise in CSA (Bruusgaard *et al.*, 2010). The process of muscle growth in adulthood does not appear to me overly dissimilar to that of postnatal development from the perspective of MNDs. Assuming a large increase in fibre CSA is predicted, nuclei are incorporated into the fibre, either prior to or during muscle hypertrophy. Following, the remainder of hypertrophy is carried by alterations in protein balance. The possible difference between postnatal development and adulthood is that, in adulthood, the prediction might not be so much as a prediction, as much as the muscle fibres sensing the future cellular requirements based on the applied mechanical overload and selecting the "programme" to activate accordingly. A mechanism capable of such function indeed exists in single muscle fibres and is termed mechano-transduction (discussed in following sections).

1.4. Nuclear structure and function

1.4.1. Structure of the nuclear membrane

Myonuclei contain the genome of the cell and therefore play a key role in providing protein transcripts to the muscle fibre. Hence, preservation of optimal nuclear structure and function are of great importance for the maintenance of a healthy cell.

Each nucleus in a muscle fibre is surrounded by a nuclear membrane, termed the nuclear envelope (NE), which serves as an anchoring location for numerous proteins that connect the cytoskeleton to the nucleus (Figure 1.8). The NE is composed of two lipid bilayers, namely the inner nuclear membrane (INM) and outer nuclear membrane (ONM). The two layers jointly form a physical barrier between the nucleoplasm and the cytoplasm, thereby creating distinct environments inside and outside the nucleus. Whereas the ONM is contiguous with the endoplasmic reticulum, the INM is not. The two membranes are separated by a thin lumen and are joined at intervals to create nuclear pore complexes that are used as selective channels for transport of molecules across the NE (e.g. mRNA, proteins above 40 kDa) (Shimi *et al.*, 2008;

Elosegui-Artola *et al.*, 2017; Cutler *et al.*, 2018). The nucleoplasmic side of the INM is lined by a nuclear lamina, composed of A-type lamins (mainly lamins A/C) and B-type lamins (lamins B1, B2 and B3) that form meshworks underneath the membrane (Shimi *et al.*, 2015). In concert with other proteins integrated into the INM, e.g. lamin B receptor (LBR), lamina-associated protein 1 (LAP1) and heterochromatin-associated protein 1 (HP1), the nuclear lamina provides structural stability to the NE and aids in protection, anchoring and folding of heterochromatin (Solovei *et al.*, 2013; Turgay *et al.*, 2017; van Steensel & Belmont, 2017; de Leeuw *et al.*, 2018).

The NE encompasses integral proteins that tether the nucleus to the cell, thereby providing the nucleus with structural integrity and mechanical connectivity with the cell (Schirmer & Gerace, 2005; Kirby & Lammerding, 2018). Amongst such proteins is the intermediate filament protein, desmin (Figure 1.8). Desmin associates with the nucleus *via* plectin 1 and nesprin-3 (nuclear envelope spectrin repeat-3, also known as Syne-3, synaptic nuclear envelope) and thus, connects the nucleus to the sarcolemma through the dystroglycan protein complex, as well as to Z-lines of sarcomeres (Staszewska *et al.*, 2015; Kirby & Lammerding, 2018). Loss of desmin from mouse single muscle fibres has been shown to alter nuclear shape and localisation on the muscle fibre, as well as to perturb myofibrillar connectivity and physiological function (Shah *et al.*, 2004). Similarly, lack of plectin 1 from mouse single muscle fibres may lead to adverse alterations in nuclear morphology, positioning and movement on the muscle fibre, as well as causing chromatin modifications that mediate mechanotransduction (Staszewska *et al.*, 2015). Thus, desmin-dependent nuclear connectivity with the muscle fibre is of great importance for the maintenance of optimal nuclear organisation and myofibre physiological function.

The INM is further physically linked to the cytoskeleton by a group of proteins termed the LINC complex (linkers of nucleo-skeleton to the cytoskeleton), composed of Sad1/UNC84 (SUN) domain-containing proteins on the INM and nesprins on the ONM that together form a direct link between chromatin and the cytoskeleton (Zhang *et al.*, 2007*a*; Puckelwartz *et al.*, 2009; Wilkie *et al.*, 2011). The LINC complex has numerous cellular functions, including but not limited to, cell division (Chi *et al.*, 2009*b*; Link *et al.*, 2014; Zhou *et al.*, 2017; Wang *et al.*, 2018), centrosome association with the nucleus (Saunders *et al.*, 2017), chromatin remodelling (Tajik *et al.*, 2016), export of mRNA from the nucleus (Li *et al.*, 2017), NE remodelling (Denais *et al.*, 2016; Raab *et al.*, 2016; Robijns *et al.*, 2016), cell-surface remodelling (Lautscham *et al.*, 2015; Haase *et al.*, 2016), cell migration (Folker *et al.*, 2011), nuclear migration (Folker *et al.*, 2011; Meinke *et al.*, 2014; Lautscham *et al.*, 2015; Gimpel *et al.*, 2017) and sarcomere assembly (Auld & Folker, 2016).

On the INM, SUN proteins (predominantly SUN1 and SUN2) form trimers and bind lamin A with their N-terminal domain (Haque *et al.*, 2006; Zhou *et al.*, 2012). Within the perinuclear space, SUN proteins associate through their C-terminal domain with the KASH (Klarsicht/ANC-1/Syne homologue) domain of nesprins, which in turn, bind intermediate filaments, microtubules and the actin cytoskeleton, depending on the nesprin isoform attaching the cellular compartments, as depicted in Figure 1.8 (Padmakumar *et al.*, 2005; Rajgor *et al.*, 2012; Wilson & Holzbaur, 2015; Gimpel *et al.*, 2017; Kim *et al.*, 2017). The link between nesprins and the cytoskeleton has lately been shown to be a mechanically rich system of high sensitivity to the magnitude of force applied to it (Balikov *et al.*, 2017).

Through alternative splicing, multiple tissue-specific isoforms of nesprins can be transcribe, each with its own unique function (Rajgor *et al.*, 2012). For instance, nesprin-1α, a shorter variant preferentially located in striated muscles, has recently been demonstrated to be important for nuclear organisation in myotubes, by associating with microtubules *via* Akap450, Pcm1, Pericentrin and kinesin 1 motor protein (Gimpel *et al.*, 2017). As already mentioned, nesprin-3 can associate with desmin *via* the protein plectin 1 (Wilhelmsen *et al.*, 2005). Both nesprin-1α and nesprin-2 have been shown to bind both lamin A and emerin (Mislow *et al.*, 2002; Zhang *et al.*, 2005). Hence, alternative splicing of nesprins allows the LINC complex, and therefore nuclei, to partner with a variety of cytoskeletal networks.

Adverse alterations in the protein composition of the LINC complex results in diverse effects on the formation of the complex. Specifically, the localisation of nesprins depends upon redundant SUN1/2 interactions, which in turn depend upon lamins; i.e. correct localisation of the LINC complex proteins depends on directionality, from inside to outside of the nucleus (Padmakumar *et al.*, 2005; Crisp *et al.*, 2006; Lei *et al.*, 2009; Méjat *et al.*, 2009; Chen *et al.*, 2014*b*; Zhou *et al.*, 2017).

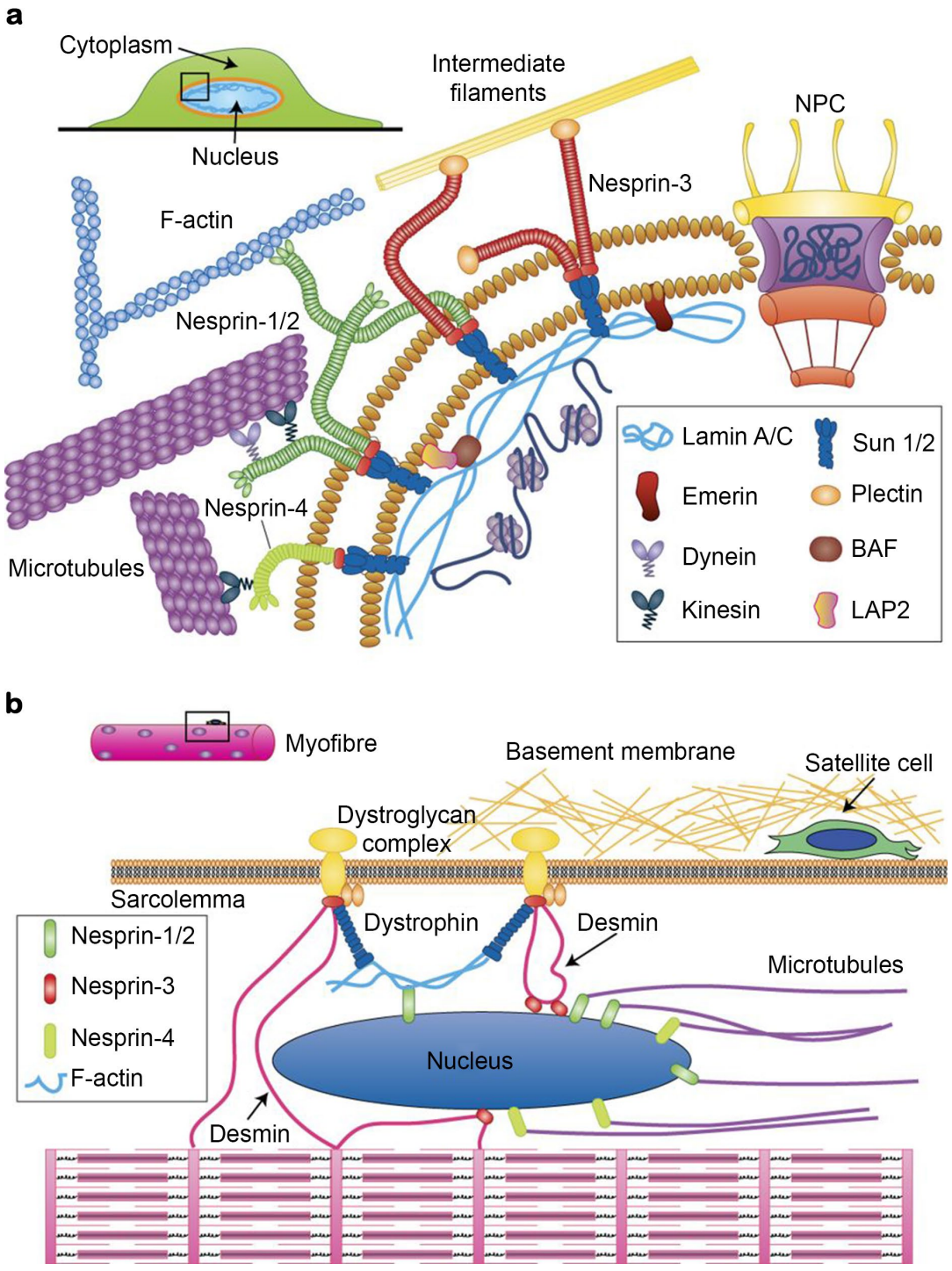

Figure 1.8: Linkers of nucleo-skeleton to the cytoskeleton (LINC) complex

(a) The complex physically bridges between the cytoskeleton and the nuclear envelope. The SUN proteins are at its core, where they interact with KASH-domain proteins (nesprins) on the cytoplasmic side, and lamins on their nucleoplasmic side. As lamins are attached to chromatin, movement of the nuclear envelope alters chromatin packing and gene expression and hence, the LINC complex serves as a major part of mechano-sensing in muscle fibres. (b) LINC complex proteins interact with actin filaments, dystrophin and desmin to anchor the nucleus to the sarcolemma and Z-lines of sarcomeres, respectively. Adapted from Kirby & Lammerding (2018).

In mammalian muscle, adverse alterations of the LINC complex have been shown to lead to nuclear mispositioning on muscle fibres, disrupted nuclear anchorage and altered nuclear morphology (Crisp *et al.*, 2006; Zhang *et al.*, 2007*b*, 2007*a*; Lei *et al.*, 2009; Puckelwartz *et al.*, 2009; Stroud *et al.*, 2017; Zhou *et al.*, 2017, 2018; Gimpel *et al.*, 2017). These are thought to manifest as a blunted response to mechanical tension, possibly leading to abrogated expression of biomechanical genes (Banerjee *et al.*, 2014) and perturbed myogenesis, accompanied by reduced expression of myogenic transcription factors (e.g. MyoD, myogenin and MHC) (Zhang *et al.*, 2007*a*; Zhou *et al.*, 2017).

Thus, structural maintenance of the NE is essential for integration of mechanical cues from the cytoskeleton in order to regulate gene expression and cellular adaptations, a process termed mechano-sensing (Guilluy *et al.*, 2014; Alam *et al.*, 2016; Hatch & Hetzer, 2016; Ungricht & Kutay, 2017).

1.4.2. Nuclear lamina

As mentioned above, lamina lines the INM and comprises of meshworks of lamins type A and lamins type B (Shimi *et al.*, 2015). Three differentially expressed lamin genes have been recognised in mammals, *LMNA*, *LMNB1* and *LMNB2*. A-type lamins are generally thought to be expressed upon cell differentiation and are alternatively spliced from *LMNA*, located on chromosome 1q21.2–q21.3, to synthesise lamin A, C, AΔ10 and C2. In mammalian muscle, the two main products of the *LMNA* gene are lamin A and lamin C, produced in roughly equal amounts, with an alternative splice site in intron 10 to produce lamin C (Lin & Worman, 1993; Wydner *et al.*, 1996). B-type lamins can be found in all developmental stages and are expressed from *LMNB1* (lamin B1) and *LMNB2* (lamins B2 and B3) (Liu *et al.*, 2000; Delbarre *et al.*, 2006; Shimi *et al.*, 2008, 2015; Goldberg *et al.*, 2008; Xie *et al.*, 2016; de Leeuw *et al.*, 2018).

Similarly to other intermediate filaments, lamins constist of an N-terminal head domain, a coiled-coil central rod domain and a C-terminal tail domain. However, unlike other intermediate filaments, lamins possess a nuclear localisation signal, an immunoglobulin-fold domain and a CAAX motif at their C-terminal tail domain.

Lamins share some similarities in their maturation process. Lamins A, B1 and B2 are firstly produced as prelamins, which to mature must undergo sequential enzymatic cleavages in their their CAAX motifs (Figure 1.9). Firstly, the cysteine residue on the CAAX motif is farnesylated by farnesyltransferase (FTase). Then the -AAX is cleaved by zinc metallopeptidase STE24

(ZMPSTE24) and/or Ras-converting enzyme 1 (RCE1). Following, the exposed farnesylcysteine is methylated by isoprenylcysteine carboxylmethyl transferase (ICMT). Processing of prelamin A (immature lamin A) differs to other lamins, due to an additional step, whereby the last 15 amino acid residues of its C-terminal domain are trimmed by ZMPSTE24, to release a mature and functional protein, lamin A (Bergo *et al.*, 2002; Pendás *et al.*, 2002; Navarro *et al.*, 2004; Corrigan *et al.*, 2005; Young *et al.*, 2006; Spear *et al.*, 2018). Thus, lamin A does not remain farnesylated. Farnesylation of the CAAX motif is a crucial step in the maturation of prelamin A, as the farnesylcysteine methyl ester is thought to localise lamin A to the nuclear lamina (Izumi *et al.*, 2000; Toth *et al.*, 2005; Young *et al.*, 2005; Davies *et al.*, 2009).

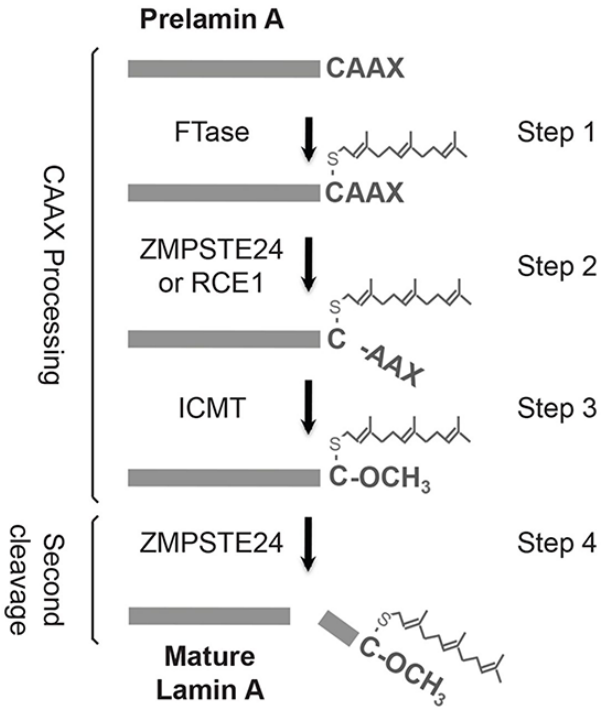

Figure 1.9: Post-translational modifications of prelamin A

Prelamin A is matured to lamin A by undergoing successive modifications by farnesyltransferase (FTase; step 1), the proteases zinc metallopeptidase STE24 (ZMPSTE24) and Ras-converting enzyme 1 (RCE1; step 2) and isoprenylcysteine carboxylmethyl transferase (ICMT; step 3). ZMPSTE24 is absolutely necessary for step 4. Loss of ZMPSTE24 leads to accumulation of farnesylated prelamin A in the nucleus. In Hutchinson-Gilford progeria syndrome (HGPS), a 50 amino acid deletion in the cleave site for ZMPSTE24 in prelamin A leads to the inability of ZMPSTE24 to recognise the protein, resulting in accumulation of mutated prelamin A (progerin) in the nucleus. Adopted from Spear *et al.* (2018).

Each of the lamins A, C, B1 and B2 forms meshworks that, though indeed interact to an extent at the nuclear lamina, are distinct from each other. Using super-resolution microscopy, it has been suggested that lamin B1 has a higher edge length and edge connectivity than lamins A and C, as well as a higher number of edges per face when compared with lamin B2. Moreover, lamin A has been shown to have more edge connectivity than lamin C (Shimi *et al.*, 2015). Interestingly, in the absence of lamin A, nuclear pore complexes appear to localise in areas rich in lamin C, whereas the inverse may not occur in the absence of lamin C, presumably because the smaller C-terminal domain of lamin C poses smaller steric hindrance than the larger domain of lamin A (Shimi *et al.*, 2015). In any case, these suggest lamin A and lamin C form separate meshworks that do not overlap with B-type lamin meshworks (Xie *et al.*, 2016).

Although the majority of A-type lamins are found in the nuclear lamina, a small fraction indeed exists in the nucleoplasm (Dechat *et al.*, 2008, 2010; Gruenbaum & Aebi, 2014; de Leeuw *et al.*, 2018). Their function is yet to be fully comprehended, however, studies suggest an important role in chromatin regulation, gene expression and mechano-signalling (Naetar *et al.*, 2017). Localisation of A-type lamins to the nucleoplasm is thought to be regulated by several mechanisms, including post-translational modifications that likely regulate ther solubility (Zhang & Sarge, 2008; Buxboim *et al.*, 2014; Snider & Omary, 2014; Moriuchi *et al.*, 2016). Additional factors have been suggested to regulate the assembly and post-translational modifications of lamin A, including associations with proteins, such as lamina-associated polypeptide 2 α (LAP2α) (Dechat *et al.*, 2000, 2004; Snider & Omary, 2014; Gesson *et al.*, 2016; Naetar *et al.*, 2017).

1.4.3. Functions of lamin A at the NE

The key functions of lamin A at the NE are to (i) provide structural stability to the nucleus and, (ii) serve as a bridge between the cytoskeleton and chromatin, in order to affect the expression of mechano-sensitive genes and subsequently, allow the cell to adapt to mechanical stress. It is, hence, not surprising that lamins have been documented to control numerous processes that lead to cellular adaptations, such as cell proliferation (Song *et al.*, 2013), cell division (Gonzalez-Suarez *et al.*, 2009; Swift *et al.*, 2013), myogenesis (Frock *et al.*, 2006), chromatin remodelling (Tajik *et al.*, 2016; Serebryannyy & Misteli, 2018), regulation of transcription through modulation of nuclear and cytoskeletal actin polymerisation (Ho *et al.*, 2013), NE remodelling (Denais *et al.*, 2016; Robijns *et al.*, 2016), cell-surface remodelling (Lautscham *et al.*, 2015; Haase *et al.*, 2016), cell motility (Booth-Gauthier *et al.*, 2013), focal

adhesion formation and cytoskeletal tension (Corne *et al.*, 2017), nuclear movement (Folker *et al.*, 2011; Folker & Baylies, 2013; Lautscham *et al.*, 2015), resistance to mechanical strain (Verstraeten *et al.*, 2008), control of reductive stress and autophagy (Dialynas *et al.*, 2015), as well as control of oxidative stress and mitochondrial dysfunction (Sieprath *et al.*, 2015). These are but merely examples to show the vast involvement of A-type lamins in cellular processes.

Lamin levels, especially those of lamin A/C, determine the stiffness of the nucleus and its susceptibility to mechanical strain (Broers *et al.*, 2004; Verstraeten *et al.*, 2008; Swift *et al.*, 2013; Buxboim *et al.*, 2017). Optimal compliance of the nuclear membrane is important for nuclear movement through narrow gaps (Thiam *et al.*, 2016; Denais *et al.*, 2016), such as between myofibrils (Roman *et al.*, 2017), as well as for efficient gene expression, due to the interaction between lamin A and chromatin (Schreiner *et al.*, 2015; Stephens *et al.*, 2017). Complete ablation of *LMNA* has been shown to result in a highly compliant nuclear membrane (Davidson *et al.*, 2015; Thiam *et al.*, 2016) that can respond defectively to mechanical changes of the cytoskeleton (Broers *et al.*, 2004). Such nuclei demonstrate altered gene expression and high incidence of NE ruptures (Lammerding *et al.*, 2004; Denais *et al.*, 2016; Houthaeve *et al.*, 2018).

The ability of lamins to bind and regulate chromatin has been demonstrated numerous times, as reviewed by Naetar *et al.* (2017). A-type lamins and chromatin typically associate through large domains on chromatin, termed lamina-associated domains. Such association of the NE with chromatin physically facilitates tissue-specific gene repression (Kind *et al.*, 2013; Therizols *et al.*, 2014; Robson *et al.*, 2016). However, binding of chromatin with the NE is not necessarily dependent on the existence of A-type lamins, likely due to the numerous additional proteins on the INM that interact with and regulate chromatin organisation, e.g. LBR, HP1 and tissue-specific nuclear envelope transmembrane proteins (NETs) (Solovei *et al.*, 2013; Robson *et al.*, 2016; de Las Heras *et al.*, 2017; Serebryannyy & Misteli, 2018).

Muscle tissue is highly adaptable to various stressors. One benefit of having many nuclei on a muscle fibre is to satisfy the transcriptional requirements of the cell. However, as muscles are highly responsive to mechanical conditions (Latouche *et al.*, 2013), a second benefit arises. As a muscle fibre stretches, the shape of the NE is modified, resulting in changes in chromatin packing (Tajik *et al.*, 2016) and activation of many processes, including Ca^{2+} ions entry into the nucleus (Itano *et al.*, 2003) and gene expression of mechano-sensitive genes (Maniotis *et al.*, 1997; Wang *et al.*, 2009; Méjat & Misteli, 2010; Elosegui-Artola *et al.*, 2017; Kirby & Lammerding, 2018). As muscle fibres are multinucleated, each muscle fibre essentially possesses a large number of

monitors of mechanical tension, scattered on its surface, with the ability to promptly alter gene expression according to the sensed mechanical condition of the fibre. The ability to monitor the entire length of a muscle fibre and affect gene expression in each specific MND is a huge benefit for maintaining optimal muscle function. It is therefore not surprising that when the nucleus-cell attachment is faulty, muscle disorders arise; muscle fibres simply cannot sense the current mechanical condition of the fibre (Lammerding *et al.*, 2004; Verstraeten *et al.*, 2008; Janin *et al.*, 2017; Janin & Gache, 2018).

1.4.4. Hutchinson-Gilford progeria syndrome and ageing

Genetic mutations in NE components have been shown to result in many types of dystrophies, myopathies and progeria syndromes, collectively called nuclear envelopathies, as summarised in Figure 1.10. In line with this, various heritable diseases originating from mutations in lamin genes are termed laminopathies (Shackleton *et al.*, 2005; Zhang *et al.*, 2007*a*; Méjat *et al.*, 2009; Puckelwartz *et al.*, 2009; Navarro *et al.*, 2013; Banerjee *et al.*, 2014; Meinke *et al.*, 2014; Wang *et al.*, 2016; Zhou *et al.*, 2017; Janin *et al.*, 2017; Brayson & Shanahan, 2017; Spear *et al.*, 2018).

Mutations in *LMNA* may result in a variety of phenotypes, including Emery-Dreifuss muscular dystrophy (EDMD), Limb-Girdle muscular dystrophy type 1B (LGMD1B), dilated cardiomyopathy with conduction disease (DCM-CD), Charcot-Marie-Tooth neuropathy type 2B1 (CMT2B1), restrictive dermopathy (RD), Dunnigan-type familial partial lipodystrophy (FPLD), mandibuloacral dysplasia type A (MADA), atypical Werner's syndrome and Hutchinson-Gilford progeria syndrome (HGPS). Mutations in the *ZMPSTE24* gene have been reported to result in RD, HGPS and MADB (Janin *et al.*, 2017).

Muscle laminopathies (e.g. EDMD, LGMD1B) are characterised by joint contractures, predominantly affecting the elbows, ankles and neck, as well as progressive muscle weakness and wasting. Death is typically caused by cardiac conduction defects with dilated cardiomyopathy (Lattanzi *et al.*, 2011). In Hutchinson-Gilford progeria syndrome, children appear normal at birth, however, the symptoms of accelerated ageing become apparent during the first year of life. Symptoms include growth retardation, alopecia, delayed dentition, sclerodermatous skin changes and severe atherosclerosis (Worman & Michaelis, 2018). Average lifespan is 13 years of age, with the main death cause (90% of patients) being progressive atherosclerosis of the coronary and cerebrovascular arteries (Eriksson *et al.*, 2003).

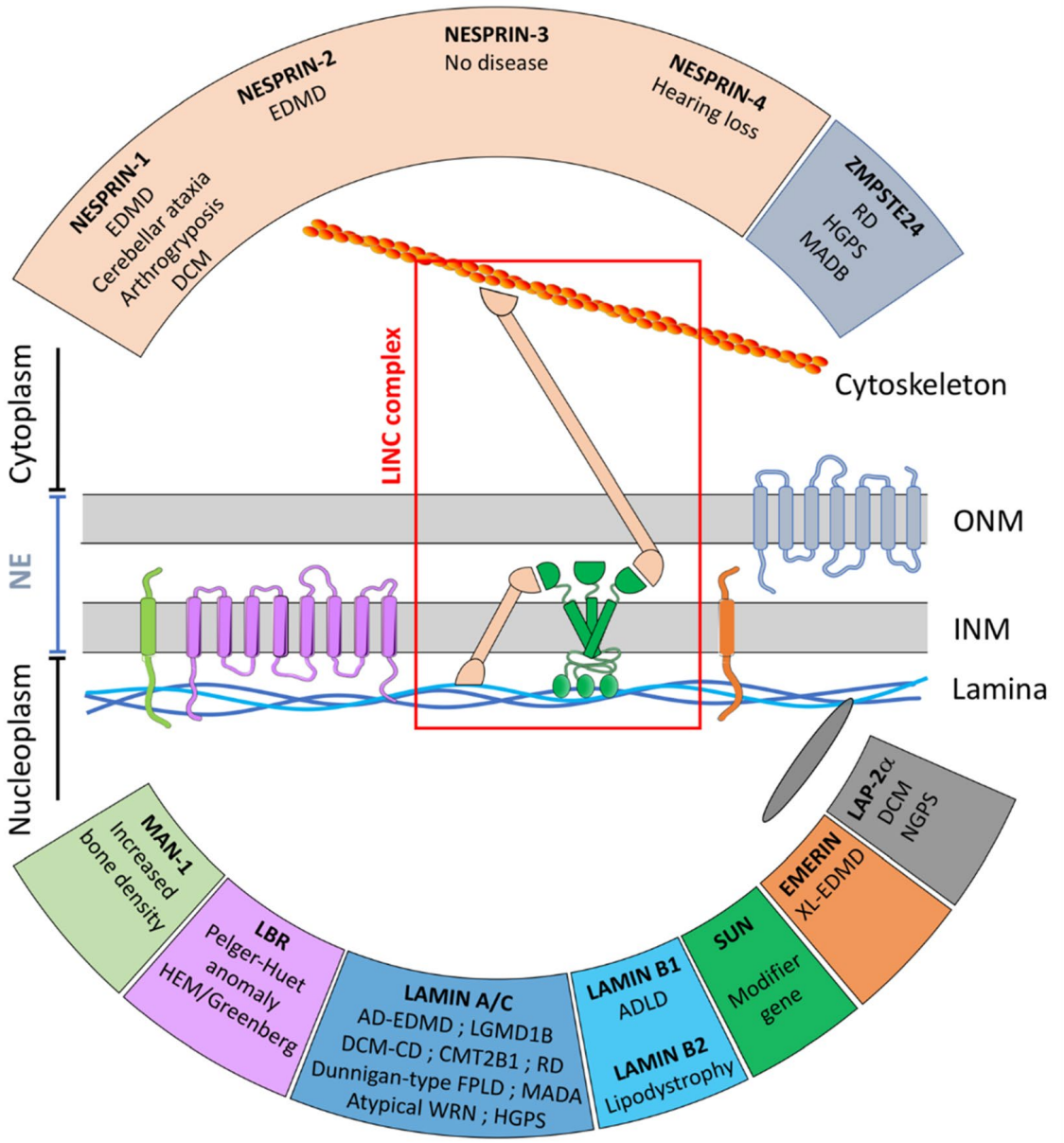

Figure 1.10: Nuclear envelopathies

Schematic representation of the different nuclear envelope components and their interactions. The pathologies associated with mutations in the related genes are indicated in the corresponding boxes. LINC complex components (SUN proteins in green and Nesprins in light brown) are highlighted in the red box. EDMD: Emery-Dreifuss Muscular Dystrophy, RD: Restrictive Dermopathy, HGPS: Hutchinson-Gilford Progeria Syndrome, MADA: Mandibuloacral Dysplasia type A, MADB: Mandibuloacral Dysplasia type B, DCM: Dilated Cardiomyopathy, DCM-CD: Dilated Cardiomyopathy with Conduction Defects, NGPS: Nestor-Guillermo Progeria Syndrome, ADLD: Autosomal Dominant Leukodystrophy, LGMD: Limb-Girdle Muscular Dystrophy, CMT: Charcot-Marie-Tooth, FPLD: Familial Partial Lipodystrophy, WRN: Werner's Syndrome. Adapted with legend from Janin *et al.* (2017).

To date, over 600 mutations have been documented in the *LMNA* gene, typically transmitted by autosomal dominant inheritance (de Leeuw *et al.*, 2018). Most of these are missense mutations distributed all along the *LMNA* gene. As different missense mutations of the same residue may lead to different diseases, the severity of the phenotypes can vary between individuals (Worman, 2012; de Leeuw *et al.*, 2018).

The main cause of HGPS is abnormal splicing of the *LMNA* primary transcript, most often caused by a *de novo* point mutation within exon 11 of the *LMNA* gene (c.1824C > T, p.G608G) that activates a cryptic splice site. This leads to a deletion of 50 amino acids at the C-terminal domain and to the accumulation of a truncated farnesylated form of prelamin A, progerin, at the INM (De Sandre-Giovannoli *et al.*, 2003; Davies *et al.*, 2009). However, point mutations in *LMNA* that cause progeria, but do not lead to accumulation of prelamin A variants, such as p.T528M, p.M540T, p.E55K and p.E55G, have also been reported (Verstraeten *et al.*, 2006; Soria-Valles *et al.*, 2016). Autosomal recessive mutations in *ZMPSTE24* that cause HGPS (e.g. N265S) are thought to directly interefere with the catalytic function of ZMPSTE24 (Quigley *et al.*, 2013), reducing its function to 25-30% of a fully functional ZMPSTE24 (Spear *et al.*, 2018), leading to reduced levels of mature lamin A and increased levels of native farnesylated prelamin A (Shackleton *et al.*, 2005).

At the cellular level, expression of progerin or farnesylated prelamin A has been shown to induce a variety of cellular defects, such as reduced cell motility (Booth-Gauthier *et al.*, 2013), abnormal chromosome segregation during mitosis (Cao *et al.*, 2007), decreased viability and increased apoptosis under mechanical strain (Verstraeten *et al.*, 2008), enhanced oxidative stress and cell senescence (Varela *et al.*, 2005; Sieprath *et al.*, 2015), as well as reductive stress and autophagy upregulation (Dialynas *et al.*, 2015).

Nuclear conditions associated with abnormal lamin processing include aberrant nuclear shapes (Goldman *et al.*, 2004; Shackleton *et al.*, 2005), reduced nuclear deformation in response to mechanical stress (Dahl *et al.*, 2006), altered transcription of mechano-sensitive genes including defected signalling of yes-associated protein (YAP) (Bertrand *et al.*, 2014), DNA damage and abnormal chromatin structure (Scaffidi & Misteli, 2006, 2008), constantly activated DNA damage checkpoints (Liu *et al.*, 2006), unsynchronized DNA endoreplication (Wang *et al.*, 2018), loss of heterochromatin (Shumaker *et al.*, 2006), genome-wide loss of spatial compartmentalisation of active and inactive chromatin domains (McCord *et al.*, 2013) and chromosome aberrations (Liu *et al.*, 2005).

In order to explain how such varations in lamin processing could lead to laminopathies, three models are have been suggested. The mechanical model dictates that lamin A misprocessing alters the ability of nuclei to respond to mechanical strain (highly applicable to muscle tissue), leading to nuclear fragility and senescence. The second model states that lamin mutations alter the expression of mechano-sensitive genes, due to the association of lamins with chromatin. The final model states that the toxicity of progerin leads to cell death (Liu *et al.*, 2005; Davies *et al.*, 2011; de Leeuw *et al.*, 2018).

A wide spectrum of strategies to correct HGPS-associated defects have been proposed. The main aims are: (i) to directly repair the disease-causing mutation; (ii) to inhibit pre-mRNA aberrant splicing leading to progerin mRNA production; (iii) to decrease the toxicity of iso-prenylated and methylated progerin; (iv) to induce progerin clearance; (v) to decrease the noxious downstream effects linked to progerin accumulation. Proposed methods include inhibitors of prelamin A isoprenylation and methylation (e.g. Lonafarnib and Pravastatin), autophagy-activating drugs (e.g. Rapamycin), down-regulation of prelamin A aberrant splicing (e.g. Metformin) and reduction of the downstream toxic effects of progerin (e.g. reactive oxygen species scavengers). Though a growing body of promising therapeutic candidates indeed exists, the ability of current therapies to alleviate the progeroid phenotype unfortunately remains inadequate (Burtner & Kennedy, 2010; Olive *et al.*, 2010*a*; Harhouri *et al.*, 2018; Mattioli *et al.*, 2019; Piekarowicz *et al.*, 2019). For a current review on existing treatment strategies for HGPS see Harhouri *et al.* (2018).

Interestingly, blocking the farnesylation of progerin and native prelamin A in mice, using farnesyltransferase inhibitors (FTIs), and therefore, altering their localisation to the nucleoplasm (Wang *et al.*, 2012), has been demonstrated to partially reverse the cellular abnormalities associated with their accumulation on the INM and alleviate the progeria-associated cellular phenotypes (Toth *et al.*, 2005; Yang *et al.*, 2005, 2010; Capell *et al.*, 2005; Young *et al.*, 2005, 2006; Fong *et al.*, 2006*a*; Verstraeten *et al.*, 2008). This has also been confirmed in genetically engineered mice expressing a non-farnesylated version of progerin (Yang *et al.*, 2011). The incomplete rescue by administration of FTIs has been suggested to be due to the FTIs' inability to improve cellular sensitivity to mechanical strain (Verstraeten *et al.*, 2008).

As many clinical and molecular features of HGPS resemble the physiological ageing process, many researchers have expressed interest in the molecular mechanism by which progerin promotes ageing (Scaffidi & Misteli, 2006; Burtner & Kennedy, 2010; Olive *et al.*, 2010*a*;

Folgueras *et al.*, 2018). The reason for the phenotypic similarity between HGPS and ageing is thought to be the expression of progerin in multiple tissues, mainly of mesenchymal origin (e.g. skin, bone, adipose and muscle tissue), that occurs during normal ageing (Scaffidi & Misteli, 2006; McClintock *et al.*, 2007; Rodriguez *et al.*, 2009; Ragnauth *et al.*, 2010; Olive *et al.*, 2010*a*).

In support, the atherosclerotic plaques in HGPS were reported to be similar to those found in ageing individuals. In the same study, researchers reported that progerin staining increased by an average of 3.34% per year in coronary arteries of non-HGPS individuals between the ages of 1 month and 97 years (Olive *et al.*, 2010*b*). Moreover, the vascular stiffening witnessed in progeria was claimed to be similar to that of human ageing, as seen by increased pulse wave velocity (Gerhard-Herman *et al.*, 2012). In human aortic vascular smooth muscle cells (VSMCs), prelamin A has been shown to promote calcification, by inducing persistent DNA damage signalling (Liu *et al.*, 2013). Another study on human VSMCs showed that prelamin A accumumlated in older individuals, especially in atherosclerotic lesions, coinciding with nuclear morphology defects, causing accelerated cell senecesnce (Ragnauth *et al.*, 2010). In human dermal fibroblasts, it has been shown that progerin levels may increase during human ageing and that the cellular defects associated with ageing are similar to those of HGPS (McClintock *et al.*, 2007). Lastly, *Zmpste24* KO mice, an accelerated ageing model that lacks Zmpste24 and therefore accumulates farnesylated prelamin A, were documented with severe defects in skeletal muscle contractility and low force-generating capacity of soleus, plantaris, gastrocnemius and extensor digitorum longus (EDL) muscles, resembling muscular defects seen in human ageing (Frontera *et al.*, 2008; Greising *et al.*, 2012). Thus, a significant body of research suggests HGPS and normal ageing share molecular and phenotypic similarities with regards to prelamin A, possibly rendering *Zmpste24* KO and *Lmna* (G609G) viable candidates to be used as models of human ageing (Olive *et al.*, 2010*a*; Vidak & Foisner, 2016; Folgueras *et al.*, 2018).

1.5. Skeletal muscle ageing and disuse

1.5.1. Definition of ageing in skeletal muscle

Ageing can be defined as an exponential accumulation of a variety of adverse alterations to normal biology that together increase the risk of mortality. The process of ageing takes place in every cell of the human body. As of the third decade of life, a gradual decay in the function of

physiological systems is noted, which at later decades (typically sixth and seventh decades) accelerates upon exhaustion of biological reserves. The increased rate of ageing typically leads to frailty/morbidity, a condition characterised by accelerated failure of homeostatic systems (Harman, 1998; Seals *et al.*, 2016).

In many countries, life expectancy and the number of people in older age have increased significantly in the last decades. This has been majorly achieved by improving the fields of medicine, sanitation and nutrition, which have collectively risen life expectancy at birth to a significantly higher age than our ancestors', predominantly due to a reduction in early mortality (Fries, 1980; Seals *et al.*, 2016). It is hence not surprising that the average lifespan in the United States had risen from 47 years in the early 1900s to 73 years by 1980 (Fries, 1980).

However, healthspan, that is the length of time one lives without ageing-associated chronic disease, has remained virtually unfaltering since the middle of the 20th century, despite the significant increase in life expectancy in that period. As a higher percentage of humans live to advanced ages, the prevalence of chronic degenerative diseases, such as Type 2 diabetes, cardiovascular disease and some types of cancer, has increased simultaneously with life expectancy (Hex *et al.*, 2012; Bartlett *et al.*, 2012). These are collectively known as comorbidities of ageing, for they are all driven by the ageing process itself (Booth *et al.*, 2012; Seals *et al.*, 2016). As a result, governments are required more than ever to medically and financially support an increasing number of older unhealthy citizens, who could nowadays be living with ageing-related chronic diseases for 20 years, which current figures show is ∼20% of one's life expectancy at birth in the UK (ONS, 2017; Harridge & Lazarus, 2017). The goal for health services should therefore be to maximise health expectancy to match life expectancy (Figure 1.11). This would result in a significant reduction in the number of years one is found in a state of morbidity, improve quality of life and save a tremendous amount of money to health services and citizens alike.

For various reasons, the scientific community has yet to reach a conclusive definition of muscle ageing. A major reason for that is the contamination of scientific studies with assumptions rooted in Western cultural norms. As human ageing encompasses a combination of biological ageing and environmental factors, such as sedentarity and muscle disuse, is the typical sedentary older person the appropriate model for ageing? Probably not. It has been argued that being physically active is the default position for maintaining good physiological function throughout life and that the results obtained in many ageing studies, human or

otherwise, are contaminated by muscle inactivity (Harridge & Lazarus, 2017). In this context, it is also intriguing that muscle strength is predictive of age of mortality and that exercise can prevent the detrimental effects typically associated with ageing.

In such a case, if a physically active lifestyle is indeed met, assuming an absence of acute life-threatening illnesses/accidents, healthspan is predominantly affected by genetics. Consequently, an alternative approach to ageing research is required. Instead of studying the beneficial effects of exercise in the elderly population, one should study the adverse effects of muscle disuse. Altering the thought process would require an alternative ageing model, active elderly individuals, for their biology represents ageing that is clear from the adverse effects associated with muscle disuse. Consequently, it is not solely the increase in life expectancy that had led to the current prevalence of comorbidities of ageing, but also the shift from a physically active to sedentary lifestyle, as lack of physical activity has been shown to accelerate the process of ageing and lead to early and prolonged morbidity (Fries, 1980; Booth *et al.*, 2012; Seals *et al.*, 2016; Harridge & Lazarus, 2017).

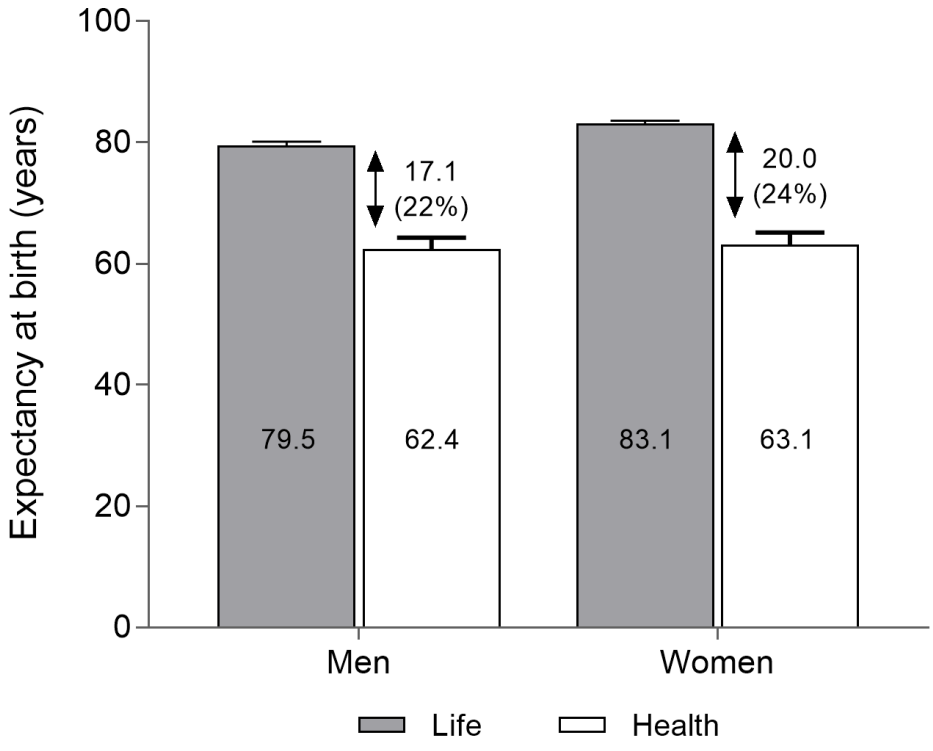

Figure 1.11: Life and healthy life expectancy at birth in the UK, 2014-2016
Reproduced from ONS (2017).

By studying physically active populations, the unsurprising result is revealed, that muscle activity is not a cure for the decline in physical performance seen in ageing. This decay may be epitomised by the longer performance times with increasing age in world-records for 100 m and 10,000 m track events of both men and women, especially after the eighth decade of life (Rittweger *et al.*, 2009; Lazarus & Harridge, 2017); a similar trend is observed in weightlifting competitions (Pearson *et al.*, 2002). Hence, though it is indeed clear that physical activity cannot produce immortality, such populations are the true representatives of ageing, for they lack the confounding effects of muscle inactivity. Importantly, it appears that the accelerated decline in performance later in life also takes place in trained individuals, demonstrating ageing, without disuse, can cause such decline; disuse would merely lead to this state earlier in life, ∼20 years earlier according to the weightlifting study! (Pearson *et al.*, 2002). It certainly seems that trained individuals show better physical performance than sedentary (Sapey *et al.*, 2014; Bartlett *et al.*, 2016, 2018; Duggal *et al.*, 2018; Pollock *et al.*, 2018*b*), regardless of their age, and thus, trained individuals are rendered unidentifiable by their age (Lazarus & Harridge, 2010).

While the relationship between health and physical activity is accepted, the volume of exercise necessary to maintain good health is unclear (Powell *et al.*, 2011; Kennedy *et al.*, 2018; Bakker *et al.*, 2018; Yamamoto *et al.*, 2018). How much training is required to achieve one's potential healthspan? It has been suggested that individuals may have a set-point for the required physical activity capable of maintaining such potential; training above that set-point would lead to a compression of morbidity, whereas exercising below it would hamper one's ability to reach the full healthspan potential (Lazarus & Harridge, 2017). It is important to note here that the accelerated decline in performance after the 8th decade witnessed in the world-records discussed above hardly demonstrates frailty, as this population can sprint 100 m within 15-30 seconds and lift 50 kg above their head in their eighth and ninth decades. It is thus expected that physical activity above their individual set-points had compressed their time in a state of morbidity and had therefore increased their individual healthspan.

There is, however, another significant limitation in the literature on ageing; the predominance of cross-sectional studies in the field. Therefore, literature on human ageing is not only limited by the typical differences between individuals in genetics, nutrition, healthcare and socioeconomic position (Kuh *et al.*, 2014), but is also skewed by the relative lack of longitudinal studies (Harridge & Lazarus, 2017). The current situation worsens by the 20th and 21st centuries' presumption that sedentary elderly cohorts are a typical representation of ageing in humans, as they rely on populations with significant dissimilarities in levels of physical activity

between individuals (Harridge & Lazarus, 2017), adding to the already existing variance in performance observed when studying solely highly trained individuals (Pollock *et al.*, 2015). Similarly, studies of ageing in animal models, which are not free from limitations, regardless of physical activity (Demetrius, 2005), show a similar trend by involving inactive animals as a model for ageing (Harridge & Lazarus, 2017). Consequently, research groups should strive to conduct longitudinal studies in addition to their cross-sectional publications and focus solely on active populations for research on muscle ageing.

1.5.2. Properties of sarcopenia

1.5.2.1. Age-related adaptations in whole muscles

For a review on the general hallmarks of ageing see López-Otín *et al.* (2013). Ageing manifests in skeletal muscle as a gradual decline in contractile function (dynapenia) and loss of muscle tissue mass (sarcopenia) (Power *et al.*, 2013). In line with other biological systems, sarcopenia encompasses a phase of accelerated ageing, which eventually causes the irreversible induction of immobility (frailty) (Seals *et al.*, 2016). However, the causes leading to frailty are not well characterised (Buch *et al.*, 2016; Harridge & Lazarus, 2017).

Muscular performance in humans reaches its peak during the third decade of life. Longitudinal studies indicate a constant decrease in strength of approximately 1-5% per year following the third decade, depending on the age, gender and muscle group (Aniansson *et al.*, 1992; Winegard *et al.*, 1996; Frontera *et al.*, 2000, 2008; Kim *et al.*, 2018). Loss of force production has been shown to be linear until the sixth-seventh decades, followed by an accelerated phase thereafter, in sedentary (Larsson *et al.*, 1979; Kim *et al.*, 2018) and highly trained individuals (Pearson *et al.*, 2002; Korhonen *et al.*, 2003; Michaelis *et al.*, 2008; Lazarus & Harridge, 2017). Higher rate of force loss in women in that period has also been demonstrated in both sedentary (Kim *et al.*, 2018) and trained individuals (Korhonen *et al.*, 2003). Anaerobic exercise has been shown to be superior to aerobic exercise in decelerating such loss in muscle function (Michaelis *et al.*, 2008; Rittweger *et al.*, 2009).

However, maximal force is merely one determinant of muscle function in older age. Older age is associated with a reduced rate of force development (Harridge *et al.*, 1996; Korhonen *et al.*, 2003). The ability to produce force rapidly is of great significance to the elderly population, as it is a major factor in their ability to avoid falls and consequently, a major determinant of risk

of frailty (Aagaard *et al.*, 2002). Rate of force development may be significantly improved by resistance exercise in sedentary young cohorts (Aagaard *et al.*, 2002) and thus, the alternative perspective is that inactivity significantly reduces one's rate of force development even at a young age, further demonstrating the importance of leading a physically active lifestyle in both young and elderly populations.

On a whole muscle level, the changes in function have frequently been attributed to loss of muscle mass and CSA, loss of MUs and infiltration of connective tissue into muscles (Frontera *et al.*, 1991; Parise & Yarasheski, 2000; Yarasheski, 2003; Agley *et al.*, 2013; Buch *et al.*, 2016; Hepple & Rice, 2016). This has often been reported to result in loss of whole muscle specific force and therefore, it is suggested the quality of muscles is altered in such cases (Men *et al.*, 1985; Overend *et al.*, 1992; Klein *et al.*, 2001; Frontera *et al.*, 2008).

1.5.2.2. Age-related adaptations in single muscle fibres

The changes in whole muscles may be in part due to selective atrophy of type II muscle fibres (Larsson *et al.*, 1979; Lexell *et al.*, 1988; Andersen, 2003; Nilwik *et al.*, 2013), as well as the aforementioned loss of their MUs, typically leading to a shift towards type I fibres (Andersen, 2003; Hepple & Rice, 2016). However, it seems as life-long exercise may ameliorate such loss of MUs, at least until the seventh decade, as number of MUs in the TA leg muscle, did not differ between master long-distance runners (>45 km/week for >30 years, age 61-67 years) and young sedentary individuals, but was ∼30% lower in the older sedentary cohort (Power *et al.*, 2010).

Though such age and disuse-related changes may account for a reduction in absolute force generation, they do not explain the specific force-loss documented in single myofibres of elderly individuals (Frontera & Larsson, 1997; Frontera *et al.*, 2000; Ochala *et al.*, 2007), that is exacerbated by immobility (D'Antona *et al.*, 2003). Loss of specific force in aged single fibres is typically accounted for by numerous molecular alterations, including but not limited to conversion of MHC towards slow (Andersen, 2003) or fast isoforms (Baldwin & Haddad, 2001; D'Antona *et al.*, 2003; Degens & Alway, 2006), slower sliding velocity of actin on MHC I (Höök *et al.*, 2001; D'Antona *et al.*, 2003) and MHC IIx (D'Antona *et al.*, 2003), reduced number of myosin heads in the strong-binding state that results in low yield of force per cross-bridge (Lowe *et al.*, 2001, 2002), post-translational modifications of myosin molecules (Lowe *et al.*, 2001; Höök *et al.*, 2001; Ramamurthy *et al.*, 2001) and low concentration of MHC isoforms (D'Antona *et al.*, 2003, 2007*b*).

It therefore appears that age-related alterations to the function of single muscle fibres are of qualitative (function of cross-bridges) and quantitative (number of cross-bridges) nature, both of which may be affected by physical activity (Bottinelli, 2001; D'Antona *et al.*, 2003, 2006, 2007*b*; Canepari *et al.*, 2005). Of specific interest to my work is the relationship between MHC concentration and specific force of single muscle fibres, for the strong association between the two factors (D'Antona *et al.*, 2003). As demonstrated by D'Antona *et al.* (2003), myosin concentration is a strong determinant of specific force in both type I and IIa single muscle fibres and appears to be modulated by age and inactivity. Interestingly, in a later study, the specific force of both fibre types is suggested to be predominantly modulated by physical activity, but not necessarily by ageing, as specific force was similar between young and elderly endurance trained individuals, but reduced in the order of elderly endurance trained > elderly sedentary > elderly immobilised (D'Antona *et al.*, 2007*b*). However, the reasons for the reduction in MHC concentrations are unknown. Nevertheless, the contrasting results between the two studies demonstrate the importance of matching the level of activity between populations and not simply studying the elderly population because its individuals are older and therefore "must" be representative of ageing.

Myonuclear organisation in ageing single muscle fibres

As discussed in section 1.3, the distribution of myonuclei in single muscle fibres is rather even at a young age and deviations from such distribution are typically associated with muscle disorders (Bruusgaard *et al.*, 2003, 2005; Ross *et al.*, 2017*b*, 2018). As a reminder, a strong association between number of nuclei and CSA of single muscle fibres exists in rodents at young and older ages, but possibly not in adulthood (Bruusgaard *et al.*, 2006). In older age, myonuclear distribution has been demonstrated to be less ordered in the EDL muscle (and a trend for the soleus) of rodents (Bruusgaard *et al.*, 2006) and the vastus lateralis muscle in humans (Cristea *et al.*, 2010). In humans, the change in myonuclear organisation has been suggested to be more prominent in type IIa muscle fibres, especially in older women (65-96 years), coinciding with reduced MND volumes and smaller fibre CSA (Cristea *et al.*, 2010). Nevertheless, another study by Karlsen *et al.* (2015) had not found a difference between MND volumes of sedentary young, trained young, sedentary elderly and trained elderly individuals and had thus concluded aerobic training and ageing do not affect MNDs; the effect on nuclear distribution had not been investigated.

A major limitation in most of the studies mentioned above is their sedentary lifestyle, be it animals or humans. It is known that numerous conditions characterised by muscle hypertrophy include incorporation of myonuclei into muscle fibres (Seiden, 1976; Schiaffino *et al.*, 1976; Winchester & Gonyea, 1992; Giddings & Gonyea, 1992; McCall *et al.*, 1998; Kadi *et al.*, 1999; Roy *et al.*, 1999; Allen *et al.*, 1999, 2013; Bruusgaard *et al.*, 2010). More specifically, it has often been demonstrated that overload exercise-induced muscle hypertrophy can lead to increased number of nuclei in muscle fibres from humans (Kadi *et al.*, 1999, 2005; D'Antona *et al.*, 2006), and rodents (Bruusgaard *et al.*, 2010; Egner *et al.*, 2013); however, the specific effect of that on nuclear distribution is unknown. It has additionally been shown that ageing (Bruusgaard *et al.*, 2006) and inactivity (Bruusgaard *et al.*, 2012) do not necessarily lead to loss of myonuclei in rodents; though, once again, the specific effect of that on nuclear distribution is unknown. Lastly, the strong relationship of nuclear number and muscle fibre CSA can be seen in trained young (Kadi *et al.*, 1999) and older cohorts (Hikida *et al.*, 2000), but not necessarily in untrained elderly individuals (Hikida *et al.*, 1998).

Taken together, it is clear that physical activity is capable of changing the size of single muscle fibres and their associated number of nuclei. However, how such cellular alterations in response to physical activity impact myonuclear distribution in older age is unknown. It would be therefore difficult to elucidate from the studies of MNDs in sedentary ageing populations whether the myonuclear changes attributed to ageing are indeed of ageing or inactivity. It is the author's assumption that if myonuclear distribution is indeed less ordered in single muscle fibres from elderly individuals (Cristea *et al.*, 2010), it could be one potential explanation for the ageing-induced muscle atrophy, as well as the reduced concentration of MHC, that have been suggested to take part in ageing and inactivity (D'Antona *et al.*, 2003, 2007*b*), as basal rates of muscle protein synthesis were found to be similar between young and elderly men (Cuthbertson *et al.*, 2005). Therefore, it is not simply the number of nuclei that dictates protein synthesis, but their localisation on the muscle fibre as well, as discussed in section 1.3. Lastly, as discussed above, work with genetically engineered mice and human muscle samples have typically associated the progeroid phenotype to the mutations in *ZMPSTE24* and *LMNA* in those samples. Whereas samples with such genetic mutations have indeed been described with cellular adaptations that mimic those of ageing (e.g. nuclear alterations and senescence), and have indeed demonstrated nuclear movement alterations (Folker *et al.*, 2011; López-Otín *et al.*, 2013), the applicability to MND research in biological ageing is unknown, as to the best of my knowledge, MNDs have not been investigated in accelerated ageing disorders.

1.6. Techniques used to study MNDs

1.6.1. Introduction

The current project aimed to connect ageing and disuse-related nuclear envelope alterations with myonuclear organisation and concentration of MHC in isolated single muscle fibres. The following section aims to provide the reader with the essential background to the method developed here to accomplish the aims of the project (aims are detailed in section 1.7). Specifically, this section will discuss the methodological aspects of myonuclear organisation research and will explore the progression of the field from its early days to current methods. It will then examine the rationale behind these methods, along with the technical limitations for which a researcher should account when studying single muscle fibres (section 1.6.4.1).

1.6.2. Humans vs animal models

The choice of species on which to conduct a study depends on a variety of considerations, encompassing aspects from biology (e.g. physiological similarity), methodology (e.g. ability to acquire a bundle of muscle from tendon-to-tendon), economy (e.g. high expenditure of animal research) and ethics. Consequently, studying any species has its own myriad of advantages and disadvantages that must be considered at the planning phase of any research project. From the purely scientific perspective, possibly the most important factor of all is the ability to infer conclusions from the model studied to humans, the primary beneficiary.

The use of animals to study human physiology is vast. Hitherto, numerous animal models have been developed for muscle research, ranging from small animals, e.g. *Drosophila*, to mid-sized animals, e.g. rodents, and even large-sized animals, e.g. rhino (Liu *et al.*, 2009). In fact, the use of animal models in muscle research is so prevalent that, for instance, Duchenne Muscular Dystrophy, solely, encompasses more than 60 different animal models associated with the disorder (McGreevy *et al.*, 2015).

If only a couple of reasons were to be distilled in favour of using animal models for human research, they would likely be the descriptive nature and absence of tight control that are inherent to *in vivo* muscle research in humans. For obvious reasons, major alterations to muscle physiology in humans are unethical, causing human research to be relatively descriptive. It is

therefore mainly possible to describe a process, which is important in itself, rather than isolate the constituents of that process to unravel the function of individual factors in the larger context.

In contrast to humans, animal research permits alterations of normal biology, as well as enhanced ability to conduct *in vivo* and *ex vivo* work that are not normally available, or are unethical, in human research. For example, in humans, it would be impossible to study nuclear organisation in muscle fibres, *in vivo*, in response to chronic high-dosage administration of a certain drug (e.g. testosterone), or knocking-out of satellite cells, followed by excision of the entire muscle, tendon-to-tendon, isolating its muscle fibres and running functional tests on them *ex vivo*; all of these have already been performed in rodents (Bruusgaard & Gundersen, 2008; Bruusgaard *et al.*, 2012; Egner *et al.*, 2016).

Moreover, animals allow for tight control of both experimental conditions (e.g. nutrition, temperature, age, activity level) and genetics (e.g. studying siblings), to a grade that is impossible to achieve in humans. The absence of such control in humans often complicates conclusion-drawing. For instance, is the difference in lean muscle mass observed following 6-weeks' weightlifting due to the environment or genetics? Environmental factors, such as nutrition, sleep and pain tolerance, on the one hand, and genetic factors, as muscle fibre types, ability to activate SCs and testosterone levels, symbiotically affect all the results of such studies. The use of animal models simplifies such concerns, as for the most part, the environmental factors may be controlled. Moreover, though inter-animal differences indeed exist, even between siblings (Akhtar, 2015), genetic control is nonetheless greater when compared with humans.

Animal research has its caveats as well, however, mainly when attempting to infer results from animals to humans. Numerous biological dissimilarities exist between humans and animals in various aspects, such as anatomy, metabolism, immune and inflammatory responses, genetic responses to stresses and others (Akhtar, 2015), that may lead to inferring results from one species to another somewhat of a struggle at times. Additionally, the phenotype of a disease in humans may differ from that of an animal model (McGreevy *et al.*, 2015; Akhtar, 2015). Therefore, caution should be exercised when studying animal models and attempting to conclude a biological process in a specific model is undeniably the same in humans.

Studying animal models and humans, together, holds great potential for muscle research. The use of animal models to mimic human diseases may aid in isolating variables and by using sufficient amount of validation, results from animals may advance our knowledge about such diseases in human biology.

1.6.3. Use of stereology in nuclear organisation

1.6.3.1. Histological sections – muscle bundles

Two parameters have traditionally served as the basis for nuclear organisation research in single muscle fibres: muscle fibre size and number of myonuclei (the broad-term "size" is used here intentionally, as fibre size may be represented in various ways). Both parameters have been traditionally achieved by studying 2D histological sections of frozen muscle bundles, or human biopsies. As 2D histological sections are limited in their ability to infer information about a 3D object, a sequential series of sections is ordinarily acquired using a method termed stereology, i.e. a 3D interpretation of a structure represented by a series of 2D cross-sections. When using stereology for muscle cryosections of whole muscle bundles, systematic uniform random sampling is used, whereby the researcher chooses the location of the first cross-section at random (though of course that section must satisfy the requirements of the researcher) and any following sections are cut at equal intervals. All the acquired slices are then collectively used to represent the structure of the entire muscle bundle.

However, the use of stereology in histological sections is limited in its accuracy and efficiency for nuclear organisation research in muscle fibres. The primary reason is the small size of nuclei (~10-20 μm in length) relative to that of a muscle bundle. If the bundle is undersampled to detect single nuclei, numerous nuclei could be missed within each section, leading to false conclusions regarding the number of nuclei in the muscle. This then dictates that sampling frequency should be sufficiently high to detect each individual nucleus. Such a solution is impractical, however, as hundreds to thousands of sections would need to be cut. At worst, it could be a highly inaccurate task, for it requires perfect matching of the series of sections, supplemented by the impossibility to discard of any sections, i.e. information, and making slicing errors (though to a certain extent it is possible to account for missing sections). At best, it is a laborious task indeed.

In fact, even from the perspective of simply counting nuclei in 2D, muscle cross-sections are not optimal. Firstly, it is not simple to determine which nucleus belongs to which single muscle fibre. Secondly, not all nuclei viewed in cross-sections by traditional staining are muscle nuclei (myonuclei). As admitted by Bridge & Allbrook (1970:293), "The results are subject to considerable error, owing to the difficulty of deciding which nucleus belonged to which fibre, and also distinguishing between peripheral myonuclei and adjacent fibroblast nuclei". Though

regarding the latter difficulty, Winje *et al.* (2018) have recently developed a method to identify myonuclei using an antibody against pericentriolar material 1 (PCM1), a protein localised at the nuclear membrane of post-mitotic cells, .e.g. single muscle fibres, to be used on muscle cryosections; as single muscle fibres are surrounded by dividing cells (e.g. fibroblasts), only myonuclei should be tagged by the antibody. This however does not aid in identifying which nucleus belongs to which fibre.

Hence, although 2D sections have indeed proven a highly valuable tool for certain aspects of single muscle fibre research (e.g. measuring CSA, fibre-typing), more reliable techniques are prompted for studying nuclear organisation. Most importantly, the uncertainty in associating a nucleus to a single muscle fibre, together with the fact that, to the author's knowledge, it is impossible to perform a series of cross-sections on single myofibres to account for this, render histological sectioning unsuitable for studying nuclear organisation on single muscle fibres.

1.6.3.2. Fluorescence microscopy – single muscle fibres

Advancements in microscopy techniques have greatly enhanced the field of single muscle fibre research. The development of a confocal microscope has greatly reduced the out-of-focus light that is inherent to visualising thick samples (Fischer *et al.*, 2011; Jonkman *et al.*, 2014; Jonkman & Brown, 2015). In addition to the discovery and improvement of fluorescent proteins and dyes along the years, such advancements have led to significantly enhanced optical sectioning of thick samples, making confocal microscopy a resourceful tool for researching single muscle fibres (Heintzmann & Ficz, 2013; Johnson & Straight, 2013).

The concept of stereology applies to fluorescence microscopy as well, as the representation of a 3D volume in confocal microscopy is performed by acquiring a succession of single-plane images. However, in contrast to histology that is limited by the amount and quality of manual labour required by the researcher to acquire an appropriate number of cross-sections to study myonuclear organisation, fluorescence microscopy is fast and reproducible. Thus, an adequate sampling frequency of *z* slices is easily achievable, leading to an accurate calculation of number of nuclei and volume of single muscle fibres. Fluorescence microscopy is therefore superior to conventional histology, firstly as single muscle fibres may be studied, and secondly, as sampling frequency of slices is much more easily achieved.

Nevertheless, image analysis is not perfect for studying nuclear organisation on single muscle fibres either, for two main reasons. Firstly, accurate representation of a muscle fibre is

limited by the ability of light to penetrate such a thick, dense and heterogeneous sample. Secondly, the ease with which image analysis is performed is depended on the quality of staining. Thus, though this method may indeed be beneficial for researching myonuclear organisation, it is not without faults (this topic will be discussed further in following sections).

1.6.4. Commonly-used techniques for isolating single myofibres

The use of single muscle fibres for muscle research has been gradually growing in popularity, since the development of their isolation techniques in the 1970s (Bischoff, 1975, 1986; Collins & Zammit, 2009). A major benefit of studying isolated muscle fibres relies on the lower number of confounding factors needed to be considered compared with whole muscles (e.g. connective tissue and pennation angles). Moreover, the ability to isolate single muscle fibres has opened a vast range of opportunities, not previously available. This is especially true for functional studies in muscles wherein the quality of myofibrillar proteins is in question, e.g. actomyosin mutations, or when nuclear organisation is altered (D'Antona *et al.*, 2003; Lindqvist *et al.*, 2016; Ross *et al.*, 2018).

Since its emergence, the field of single muscle fibre research has greatly progressed alongside scientific technological advancements. A variety of techniques involving single muscle fibres exist to date, each with its own plethora of advantages and disadvantages. Some of these techniques have successfully connected fields of single muscle fibre research, by incorporating the ability to simultaneously study functional (e.g. passive tension) and structural aspects (e.g. nuclear organisation) of single muscle fibres.

Generally, the method of choice for isolating muscle fibres depends on the goals of the study. The initial predominant choice for a researcher wishing to study isolated muscle fibres is whether the sarcolemma should be intact. Intact sarcolemma exists only when a fibre is isolated from both ends of the muscle bundle (tendon-to-tendon) (Konigsberg *et al.*, 1975; Collins & Zammit, 2009). Hence, single muscle fibres isolated from tendon-to-tendon are referred to as intact fibres. The existing alternative to intact fibres is membrane-permeabilised, also called "skinned", muscle fibres, where the basement membrane of the fibres is loosened, or even stripped at times, thereby causing its permeabilisation (Konigsberg *et al.*, 1975).

Both single fibre isolation methods offer advantages. For instance, to study the delivery of action potentials into the neuromuscular junction and the resultant muscle contraction, the sarcolemma of the fibre must be intact to permit action potential propagation (Stålberg, 1979).

Thus, contraction, in this case, is produced by an electrical stimulus. Conversely, if one wishes to bypass action potentials, in order to focus on the contractile mechanism *per se*, e.g. to study actomyosin interactions, the loss of membrane is beneficial, as electrical stimulation is no longer required to contract the fibre. Contraction in this case may be initiated by immersing the fibre in a solution containing high [Ca^{2+}] (Shah & Lieber, 2003; Ochala *et al.*, 2007; Curtin *et al.*, 2015).

In order to isolate single muscle fibres, whilst maintaining the sarcolemma intact, a couple of typical methods prevail; maceration in NaOH (typically 40%, 3h) (Wada *et al.*, 2002; Zhang *et al.*, 2009; McCarthy *et al.*, 2011; Jackson *et al.*, 2012; Fongy *et al.*, 2019) or enzymatic digestion (collagenase, 1-2h) (Bischoff, 1975; Rosenblatt *et al.*, 1995; Nagata *et al.*, 2006; Collins & Zammit, 2009; Gnocchi *et al.*, 2011; Falcone *et al.*, 2014; Roman *et al.*, 2018). Using these isolation techniques, fibres maintain their sarcolemma, SCs and other non-muscle nuclei (Mauro, 1961; Konigsberg *et al.*, 1975; Bruusgaard & Gundersen, 2008; Pallafacchina *et al.*, 2010; Winje *et al.*, 2018). Single muscle fibres isolated this way may be used for functional (e.g. maximum force production) and structural studies (e.g. nuclear organisation), as well as in cases where a very high yield of fibres is required. Enzymatic digestion by collagenase has the additional benefit of preserving the biological function of single muscle fibres and is therefore often used for culturing satellite cells (Rosenblatt *et al.*, 1995; Collins & Zammit, 2009).

When the presence of a sarcolemma is of little importance, or is indeed disruptive to the study, mechanical isolation may be used. Mechanical isolation requires an initial step of loosening the basement membrane of the muscle fibres in a skinning-solution, containing relaxing solution and glycerol 1:1 (v/v), for 24 hours. Only then can manual excision of fibres begin, using fine dissection tweezers (Konigsberg *et al.*, 1975; Eastwood *et al.*, 1979; Place *et al.*, 2015; Ross *et al.*, 2018; Levy *et al.*, 2018; Buono *et al.*, 2018). Single muscle fibre isolation must be performed in relaxing solution, otherwise the fibres hypercontract (more on this below). When single muscle fibres are isolated mechanically, isolated fibres are considered permeabilised and devoid of satellite cells (Konigsberg *et al.*, 1975; Ross *et al.*, 2018). An additional advantage of mechanical isolation is that, at times, the isolation methods mentioned above are inapplicable; for instance, when studying human muscle biopsies, as it is typically impossible to acquire a muscle from tendon-to-tendon from a living human.

Mechanical isolation of single muscle fibres is commonly used for functional studies, which necessitate bypassing the neuromuscular junction to study the contractile machinery of the fibre (Ochala *et al.*, 2007; Li *et al.*, 2015; Lindqvist *et al.*, 2016). Importantly, these fibres do not show

any loss of force as a result of this procedure, when compared with intact fibres (Curtin *et al.*, 2015), in spite of showing expanded gaps between myofibrils and partial denuding of the basement membrane (Konigsberg *et al.*, 1975). Lastly, this technique permits simultaneous research of structural proteins (e.g. desmin) and myonuclear organisation (Shah & Lieber, 2003; Cristea *et al.*, 2010; Ross *et al.*, 2017*b*, 2018; Levy *et al.*, 2018; Buono *et al.*, 2018).

1.6.4.1. Technical aspects of preparing single myofibres for microscopy

In order to comprehend the rationale behind the isolation techniques mentioned above, and their application for nuclear organisation studies in fluorescence microscopy, it would be necessary to familiarise the reader with the complications faced when manually handling single muscle fibres and how they are typically tackled. Importantly, as the topic of this thesis is nuclear organisation in single muscle fibres, the technical limitations mentioned below are from the perspective of one who wishes to study this topic; limitations depend on one's aim and perspective and as such, a thorough examination of these techniques, from all conceivable angles, for all possible applications, is beyond the scope of this work. The information below will therefore focus on the main considerations required for studying MNDs in single muscle fibres.

Hypercontraction

Intact single muscle fibres may hypercontract into rigor-state when handled with tweezers, likely due to injuring the membrane of the fibre or the fibre itself (Roth *et al.*, 2000; Collins & Zammit, 2009). It has therefore been recommended to use large-diameter heat-polished Pasteur pipettes instead (Collins & Zammit, 2009). Whereas for some studies hypercontracted fibres may not pose a significant issue, it would be better to avoid them altogether when studying nuclear organisation, for the following reasons.

Firstly, hypercontracted human skeletal muscle fibres have been documented *ex vivo* with spreading of Z discs in EM (Roth *et al.*, 2000); the consequence of that to nuclear organisation is unknown. Additionally, whenever hypercontracted fibres have been documented *in vivo*, it is usually in association with a severe muscle disease and injured muscle fibres (Fridén & Lieber, 1998). For a review of the topic see Roth *et al.* (2000).

Secondly, nuclei rely on muscle contraction for spatial repositioning in muscle fibres (Roman *et al.*, 2017). Nuclear movement that results from successive fibre contractions is a phenomenon also noticed by the author whilst experimenting in the laboratory. If myonuclei indeed alter their location as a result of physiological muscle contractions, it would be difficult

to envision what could happen as a result of a hypercontraction. A simplistic view would be that the distance between nuclei is simply shortened (as may arguably be seen in the contracted fibre in Figure 1.12, middle arrow); however, that is probably an over-simplistic view, as Roman *et al.* (2017) demonstrated that nuclei can travel from the centre of a muscle fibre to its periphery, in response to physiological fibre contractions. If nuclei are indeed capable of such vast spatial movements in the fibre, it would be virtually impossible to retrace their movement in a hypercontracted myofibre and understand their pre-contraction positions.

Thirdly, fibre contraction can alter nuclear shape (Shah & Lieber, 2003; Shah *et al.*, 2004; Zhang *et al.*, 2009; Chapman *et al.*, 2014). It may initially seem as a change in nuclear shape is an insignificant matter for its localisation. However, the studies mentioned above reveal that nuclei do not all respond to changes in sarcomere length in a similar manner. This is especially true when comparing elongated and round nuclei. Consequently, it would be possible that the centroid of each nucleus deviates from its original location to a different unknown extent. Any analysis of nuclear organisation is erroneous in such a state, or at the very least, inaccurate.

Lastly, imaging of single muscle fibres is not always conducted from one tendon to another, due to a variety of considerations. One consideration is the sensor area of the camera, as it limits the area of the fibre that can be imaged. Thus, assuming muscle fibres are typically a few mm in length, but the segment of the fibre that can be imaged is limited by the sensor to 0.5 mm, that segment, hopefully chosen at random, would be likely regarded as a representation of the entire fibre; that segment would include all the nuclei on that 0.5 mm of a fibre. However, when a fibre is hypercontracted, sarcomere length is significantly shortened, inhomogenously (as seen in Figure 1.12). Therefore, a greater number of nuclei could be found within the 0.5 mm of the fibre, as the distance between nuclei is likely shortened (or altered), and thence a larger number of nuclei could fit in the image. Hence, comparisons between this hypercontracted fibre and a normal fibre are impossible, as the conditions are dissimilar.

Thus, hypercontracted fibres may lead to numerous complications, assumptions and errors and as a result, should not be regarded as normal. It would be therefore better to discard of them altogether when studying nuclear organisation; that is, of course, unless one wishes to specifically study the effect of hyper-contractility on nuclear organisation.

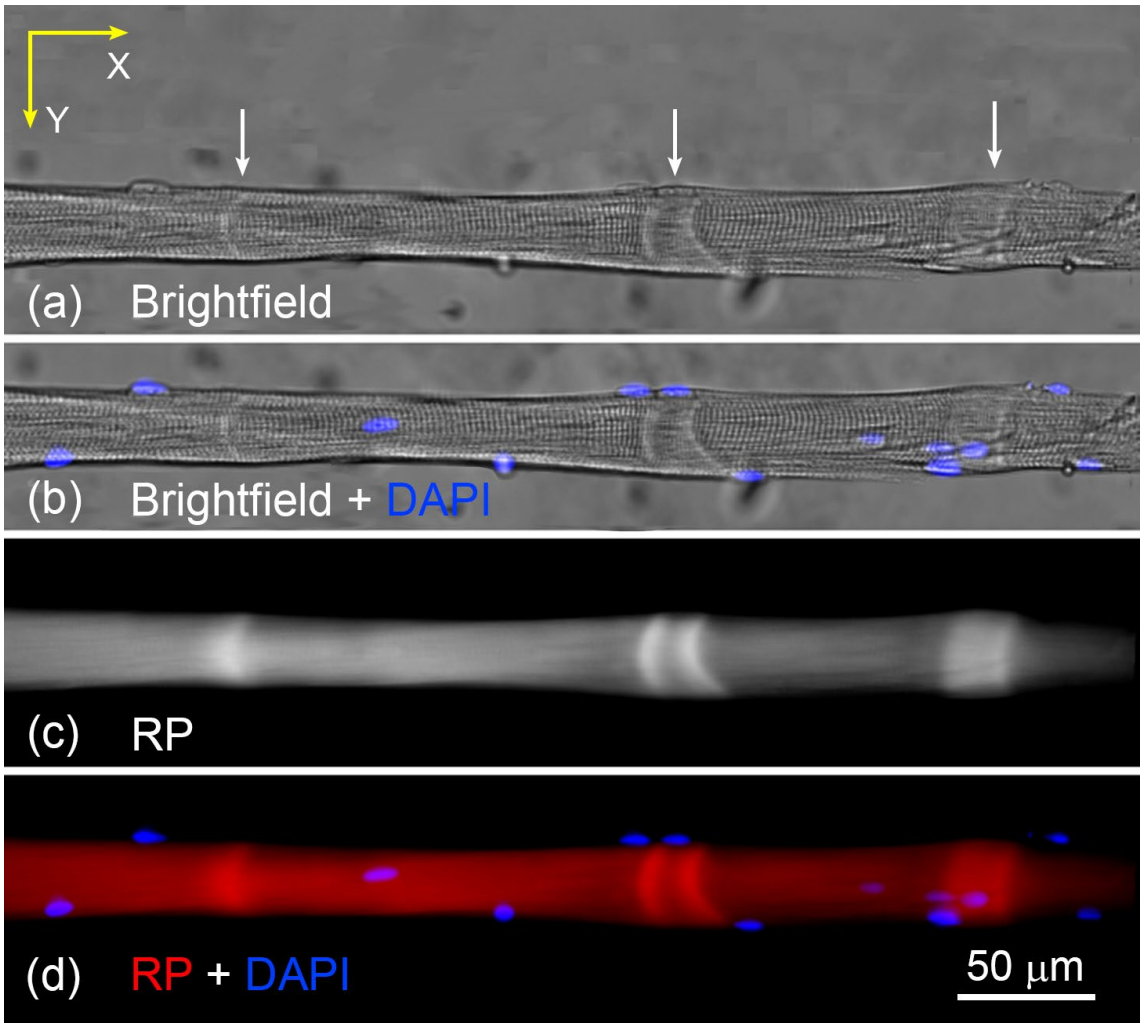

Figure 1.12: Hypercontraction in a single muscle fibre
(a) Brightfield image of a single muscle fibre, with arrows pointing to hypercontracted areas; (b) Same image as in (a), with DAPI overlaid to show location of nuclei; (c) Rhodamine phalloidin (RP) view of the fibre, showing hypercontracted areas; (d) Same image as (c), with DAPI overlaid to show location of nuclei.

Modality of choice

Preparation of non-muscle cells, e.g. fibroblasts, for fluorescence imaging *in vitro* is typically rather simple. The cells are normally thin and adherent to the surface of the slide or coverslip. Unless the surface of the coverslip is over-confluent with cells, or binding of the antibody is non-specific, imaging should be simple. However, upon isolation, single muscle fibres are not adhered to a dish or coverslip and therefore, alternative techniques should be used when preparing single muscle fibres for fluorescence microscopy.

Intact single muscle fibres

The typical method to prepare intact single muscle fibres for imaging is by pipetting them (to avoid damaging the fibres) onto a coverslip and mounting with a mounting medium, prior to imaging (Viguie *et al.*, 1997; Roy *et al.*, 1999; Zhang *et al.*, 2007*b*, 2009; Lei *et al.*, 2009; Gnocchi *et al.*, 2011; Chapman *et al.*, 2014; Roman *et al.*, 2018). This method, however, poses some difficulties non-existent in other types of cells.

As stated, single muscle fibres are not cultured on the surface of a coverslip and are, therefore, not well-adhered to it. In addition, their morphology is highly compliant, allowing significant movement and flotation when suspended in solution. Taken together, fibres may acquire bends and curves and tend to clump when pipetted onto a coverslip (Figure 1.13). Examples may be seen in images of numerous publications that had studied intact single muscle fibres (Duddy *et al.*, 2011; Gnocchi *et al.*, 2011; Chapman *et al.*, 2014; Sawano *et al.*, 2016).

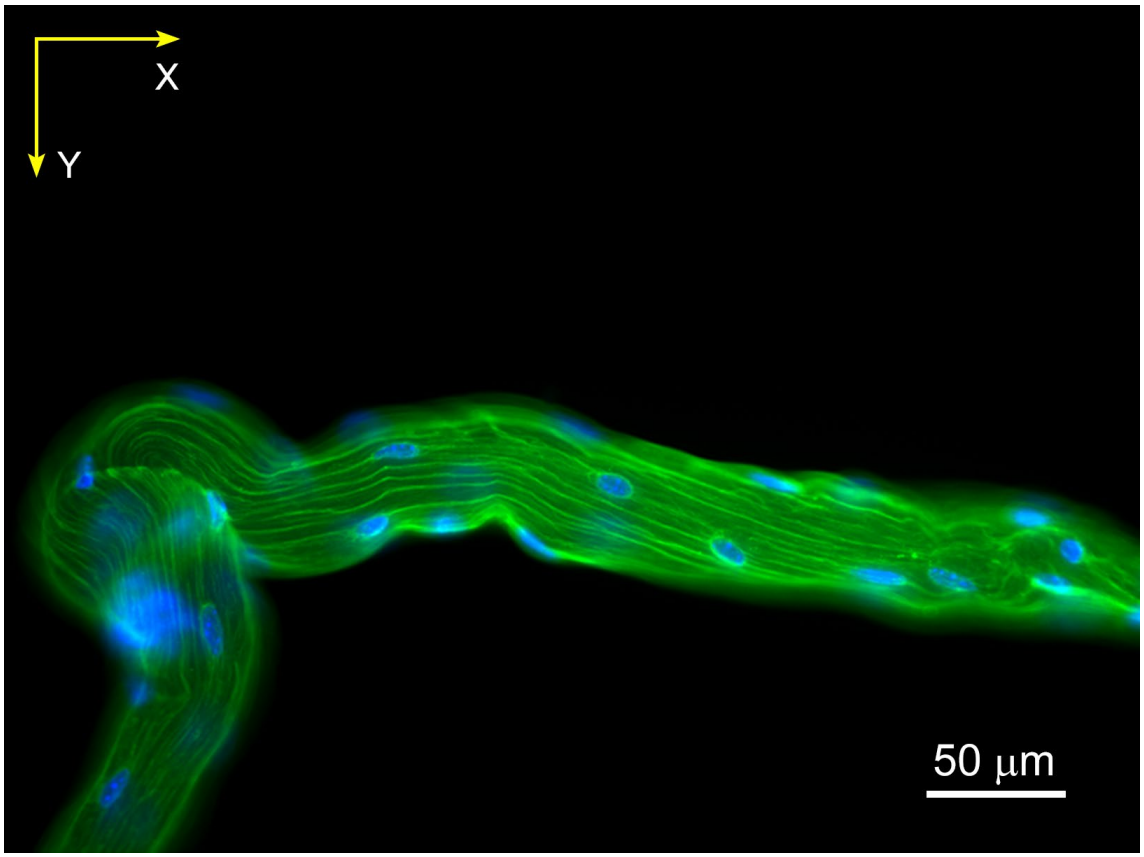

Figure 1.13: High compliance of intact single myofibres in IF microscopy
Intact single muscle fibres were pipetted onto a coverslip, nuclei were stained with DAPI (blue) and β-tubulin (green), prior to mounting in Fluoromount-G™ mounting medium. Immunofluorescent (IF) image was acquired with a spinning disk confocal microscope, 20x/0.75 air objective lens. Courtesy of Dr. Jacob A. Ross, Ochala laboratory, King's College London.

Fibre-clumping and high compliance are detrimental for studying nuclear organisation, as they may lead to changes in the distance between individual nuclei in the fibre. For this reason, the common practice for studying nuclear organisation is to use a viscous mounting medium to prevent fibres from moving, with the additional benefit of improving image quality during microscopy (discussed below). Another common practice is to identify a linear section of the fibre and image the area. It is easy to see, then, why this method requires a significant number of fibres, and time.

The final major obstacle when imaging intact fibres is the inherent inability to control sarcomere length, as manual handling of the fibres typically leads to hypercontraction. As discussed above, this may lead to significant discrepancies in correlations of nuclear organisation and fibre size.

Skinned single muscle fibres

When imaging skinned muscle fibres, none of the limitations mentioned thus far for preparation to microscopy, but others, should be considered. To the author's knowledge, the common method for imaging membrane-permeabilised muscle fibres using confocal microscopy was developed by Shah & Lieber (2003), who combined confocal microscopy with functional tests of fibres. Such potential was made possible by attaching skinned single muscle fibres between connectors leading to a force transducer and a lever arm system, on a stage of a confocal microscope (Shah & Lieber, 2003; Cristea *et al.*, 2010; Qaisar *et al.*, 2013). This system is highly beneficial for demonstrating a causal effect of structure-function within each single muscle fibre, rather than per population. Information is thence less likely to be engulfed by statistical averages and, possibly, a lower number of samples is thus required. Additionally, setting of sarcomere length is made possible, providing better normalisation of the fibres.

As is the case for any method, Shah and Lieber's system is not immune to imperfections. Though simultaneous imaging and functional testing has its uses, the technique is time-consuming for only one single muscle fibre may be clamped between the connectors and undergo functional tests and imaging at any given moment; only once testing is complete can another fibre be attached between connectors and replace the other. This method can become rather lengthy, especially when fibres occasionally tear during functional tests and the process must restart anew with a different fibre. Consequently, though this method is highly useful for correlating structure with function, considerable time is required to achieve a high yield of single muscle fibres.

Overcoming optical challenges

Lateral and axial resolution

A major variable to factor when imaging any biological specimen, especially thick samples in 3D, is the required resolution that should and could be achieved. In simple terms, resolution is a measure of the possibility to resolve two adjacent points, situated in space closely together; hence, high resolution means two adjacent points can be recognised as two individual entities, whereas in cases of low resolution, the points appear as one. Resolution is inversely proportional to the distance it represents; thus, the higher the resolution, the shorter the distance between adjacent points that can be resolved (Murphy & Davidson, 2012; Heintzmann & Ficz, 2013).

A widely accepted method to calculate spatial (x, y) resolution is the Rayleigh Criterion, which defines two diffraction spots (Airy discs) as resolved when the maximum of a disc overlaps with the first minimum of another (Murphy & Davidson, 2012). See Figure 1.14 for a visual clarification. The Rayleigh Criterion for confocal microscopy can be defined as:

$$r_{x,y} = \frac{0.4\ \lambda_{exc}}{NA} \quad (1)$$

Where *r* is the achievable optical spatial resolution, λ is the excitation wavelength and *NA* is the numerical aperture of the objective lens.

Axial resolution for confocal microscopy can be defined as:

$$r_z = \frac{1.4\ \lambda_{exc}\ \eta}{NA^2} \quad (2)$$

Where *η* is the refractive index of the objective medium and the rest as before.

Thus, the formulas above show that (i) spatial resolution depends on the excitation wavelength and NA of the objective lens, but not magnification. Thus, the lower the excitation wavelength, the higher the resolution for a given NA; (ii) when imaging samples in 3D, lateral resolution is significantly greater than axial resolution (Waters & Wittmann, 2014).

Importantly, when an optical device projects an image onto a detector (e.g. camera), the resolution of the detector should closely match that of the optical device (Salmon *et al.*, 2013). In order to match them, the magnification and NA of the objective lens should be considered, as well as the size of the smallest object, the nucleus (short axis = ~5 μm). According to the

Nyquist theorem, sampling frequency should be at least double the highest sample frequency (Murphy & Davidson, 2012). Therefore, the size of a pixel and thickness of optical sections should be at least half the size of a nucleus.

That axial resolution worsens through deeper sections is best demonstrated by the shape of the point spread function (PSF), i.e. 3D diffraction spread of a point source viewed through the objective, which appears to be stretching in the *xz* dimension of reconstructed *z*-stacks (Figure 1.15). Such stretching is the result of light diffraction in the tissue that results from a number of factors, such as distance of the focal plane from the coverslip, spherical aberration, photonic interaction with the sample and light scattering from fluorophores (Ntziachristos, 2010; Murphy & Davidson, 2012; Salmon *et al.*, 2013; Goodwin, 2014). Consequently, when imaging thick samples, such as single muscle fibres, the choice of a microscope should be one that is capable of an accurate representation of the fibre, without distorting the biological morphology (Fischer *et al.*, 2011; Jonkman & Brown, 2015).

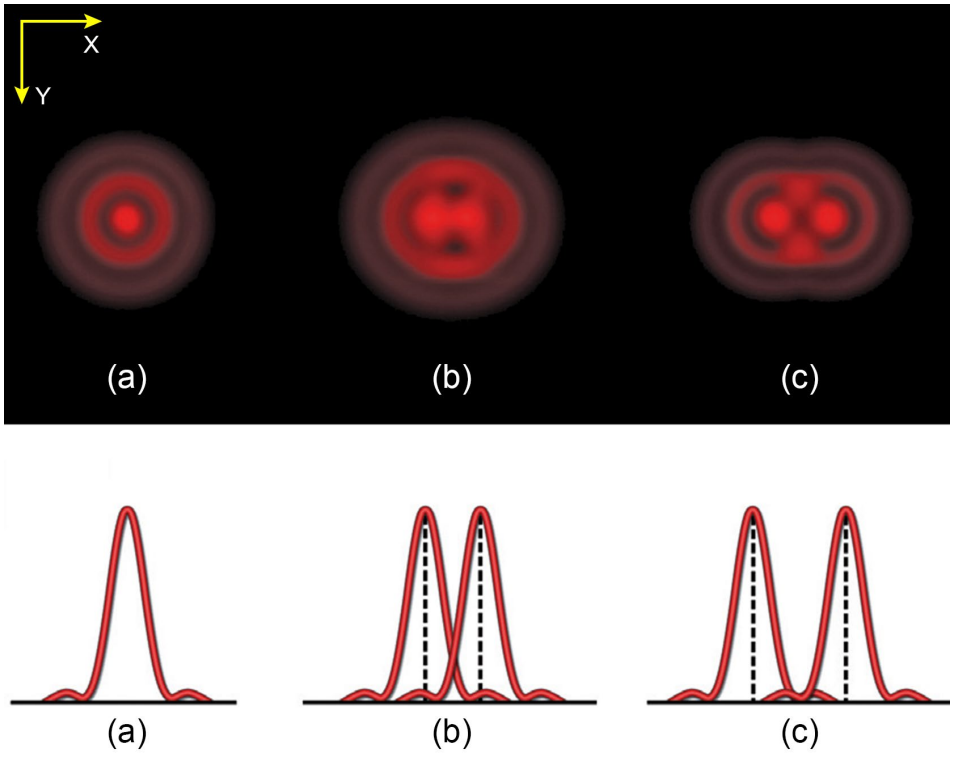

Figure 1.14: Rayleigh criterion for spatial resolution
(a) Diffraction pattern and profile of an Airy disc, showing first and second diffraction rings; (b) two barely resolved discs meeting the Rayleigh limit, with the maximum of the left disc overlapping with the first minimum of the second disc; (c) two resolved Airy discs, with the maximum of the left disc overlapping with the second minimum of the other disc. Adapted from Murphy & Davidson (2012). Copyright © 2012, John Wiley and Sons.

The development of a confocal microscope, and especially laser-scanning microscope, has greatly reduced the out-of-focus light that is inherent to visualising thick samples (Figure 1.16). Such microscopes rely on pinholes to reject photons from out-of-focus areas, thereby reducing photonic interaction with the sample (Fischer *et al.*, 2011; Jonkman *et al.*, 2014; Jonkman & Brown, 2015). Confocal microscopes have been documented to be used for sample depth similar to that of single muscle fibres (roughly 20-50 µm) numerous times, are relatively readily available in many laboratories and require simple preparation of samples (Fischer *et al.*, 2011; Oreopoulos *et al.*, 2014; Jonkman & Brown, 2015). Consequently, confocal microscopy is frequently the method of choice when imaging single muscle fibres. An in-depth comparison between the various confocal microscopy techniques may be found in the following reference (Jonkman & Brown, 2015). In addition, multiphoton microscopes have been documented to reliably penetrate samples of up to 350-600 µm depth, due to the use of 2 photons of lower power, and may therefore be very useful for imaging of single muscle fibres (Theer *et al.*, 2003; Monici, 2005; Corbin *et al.*, 2014); this is despite the slightly reduced lateral resolution of a multiphoton microscope in comparison with confocal, due to the absence of pin holes and the longer wavelength used in this system (Ntziachristos, 2010).

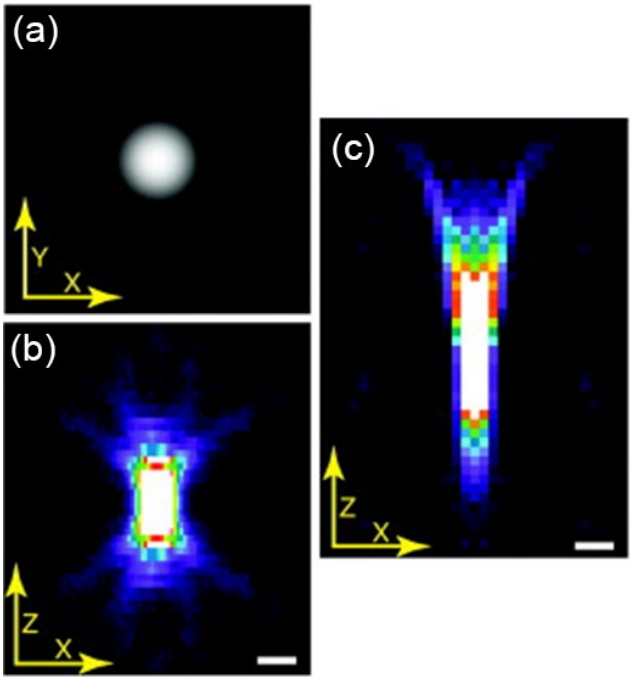

Figure 1.15: Point spread function (PSF) in inverted confocal microscopy
(a) Idealised diffraction pattern of a point source; (b) Z-stack of a fluorescent bead in aqueous medium focused at 5 µm from the coverslip; (c) Z-stack of a fluorescent bead in collagen gel focused at 150 µm from the coverslip. Note the elastic asymmetrical stretching in the *z* axis. Scale bar = 0.25 µm. Adapted from Fischer *et al.* (2011). Copyright © 2011, Elsevier.

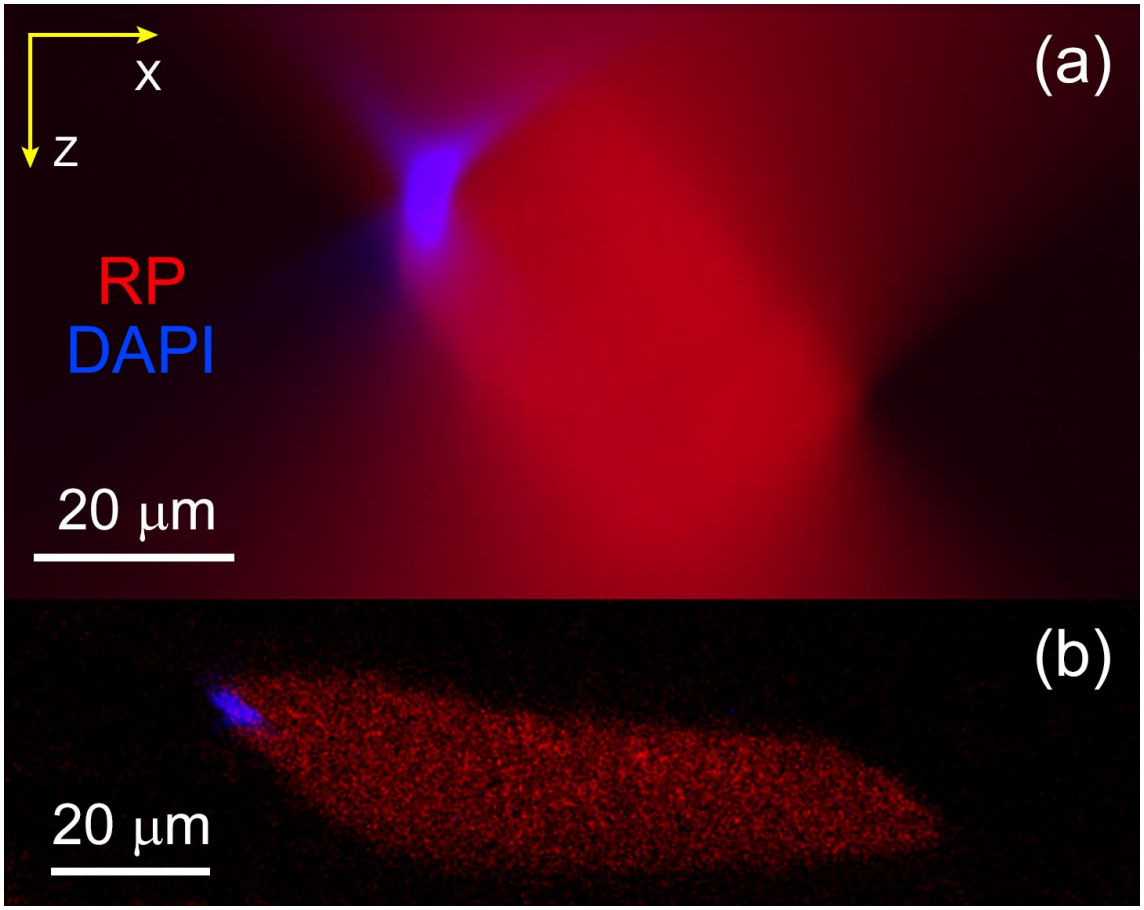

Figure 1.16: Microscope performance in single muscle fibres
(a) Raw image of a transverse section of a single muscle fibre in PBS, taken with an inverted wide-field microscope, Zeiss Fluar 20x/NA 0.75 air objective lens; (b) Raw image of a transverse section of a single muscle fibre in PBS, taken with an upright laser scanning confocal microscope, Zeiss Plan-Apochromat 20x/NA 1.3 water objective lens; DAPI = nuclei, RP = rhodamine phalloidin (actin). Though the altered objective lens reduces light scattering, the improvement in PSF is primarily due to the microscope.

Spherical aberration

Spherical aberration may severely contribute to the degradation of PSF in deeper focal planes. In a perfect lens (a rare case indeed), all incoming light rays are focused at the focal point (Figure 1.17). However, because light penetrates different materials (e.g. air, glass, water) on its way to the sample and the geometry of the sample is usually not positioned in perfect parallel to the objective, light rays may not necessarily converge at the same focal plane, leading to spherical aberrations (Murphy & Davidson, 2012; Wolf, 2013). In such a case, when a bright fluorescent spot (e.g. a fluorescent bead) is viewed at best focus, the spot would appear surrounded by bright halo. Unless corrected, this could lead to inaccurate measurements of areas of interest, as the measured area appears larger than its actual size with additional out-of-focus light.

In order to optimise the light path to the sample, thereby correcting spherical aberration, the best starting point is the set-up of the experiment. Firstly, the type of objective lens chosen for the experiment is crucial. Achromatic objectives are the simplest lenses used in fluorescence microscopy and, though they indeed correct for chromatic aberration in two wavelengths, do not correct spherical aberration. Fluorite objectives, slightly more advanced, correct for both chromatic and spherical aberration. Plan apochromatic objective lenses are the best choice, for they correct for spherical aberration to the highest degree, as well as chromatic aberration in three wavelengths. Moreover, Plan objectives correct for flatness of field and therefore, a flat specimen appears sharp over the entire field of view, rather than only at the centre (Murphy & Davidson, 2012; Ross *et al.*, 2014).

Secondly, spherical aberration may also be caused by using a coverslip other than 0.17 mm (No. 1.5) thickness, for which most objective lenses are optimised (Figure 1.18). Simply changing from No. 1.5 to 1.0 (0.13-0.16 mm) coverslip may increase full-width half-maximum (FWHM), a typically used measure of intensity distribution, by ∼3 times, resulting in significant spherical aberrations (Keller, 2006; Waters, 2009).

Lastly, spherical aberration may also result from the sample preparation. As light crosses through dissimilar media, e.g. oil to water, it bends (refracts) at the interface between the media and changes its path upon entry to the latter medium, resulting in axial and marginal spherical aberrations (Figure 1.17). Refraction occurs as the velocity of light changes between different media, despite its frequency remaining unchanged. The ratio of velocity of light in a vacuum to its velocity in a specified medium is expressed as a Refractive Index (RI; Table 1.1) (Helmchen &

Denk, 2005; Keller, 2006; Murphy & Davidson, 2012; Heintzmann & Ficz, 2013; Oreopoulos *et al.*, 2014; Jonkman & Brown, 2015). Thus, when preparing intact single muscle fibres for confocal microscopy, it is imperative to strive to match the RIs of the objective lens, mounting medium and the sample; the closer they match, the better the achieved PSF (Jonkman *et al.*, 2014). In this regard, tissue clearing to homogenise the RI of the specimen could also improve tissue penetration (Pan *et al.*, 2016; Ariel, 2017). Nevertheless, the use of mounting media and tissue clearing may not always be possible, as their use could lead to morphological alterations of the specimen (Murphy & Davidson, 2012; Ertürk *et al.*, 2014; Richardson & Lichtman, 2015; Decroix *et al.*, 2015; Pan *et al.*, 2016; Ariel, 2017; Fankoua *et al.*, 2017).

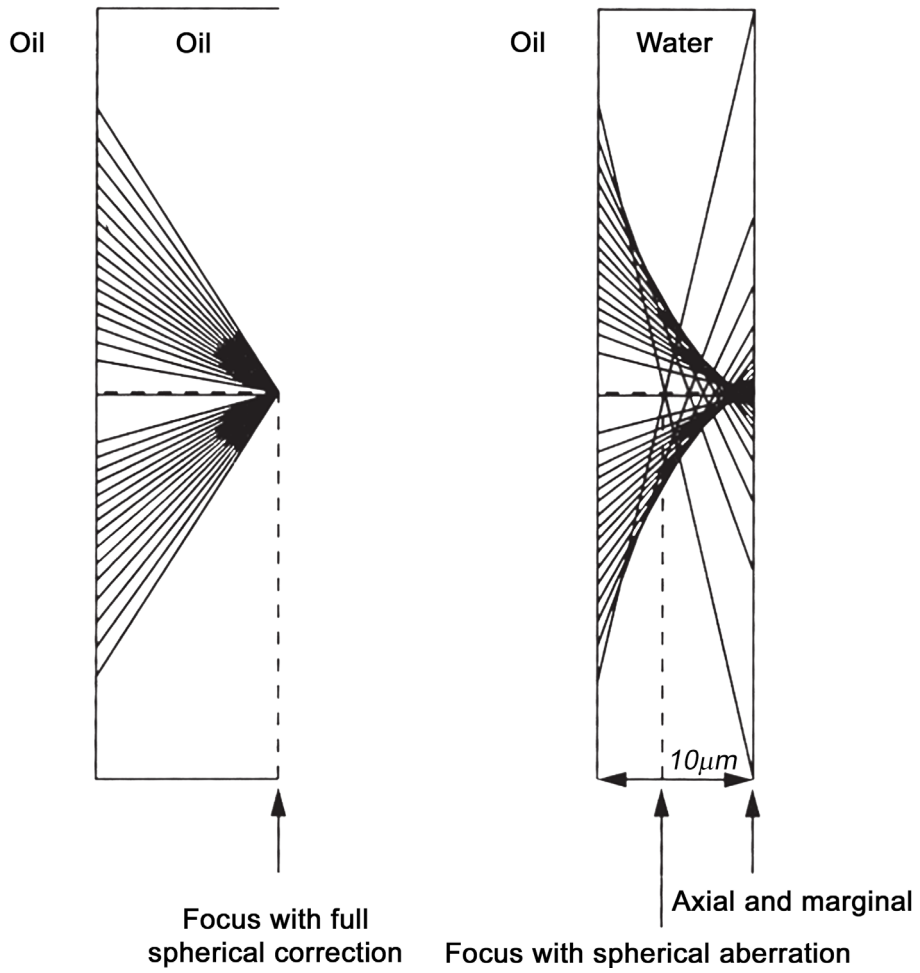

Figure 1.17: Spherical aberration due to refractive index mismatch
Ray diagram of a NA 1.3 oil-immersion objective, focusing into oil (left) versus focus 10 μm in water (right). Adopted with legend from Keller (2006). Copyright © 2006, Springer Science.

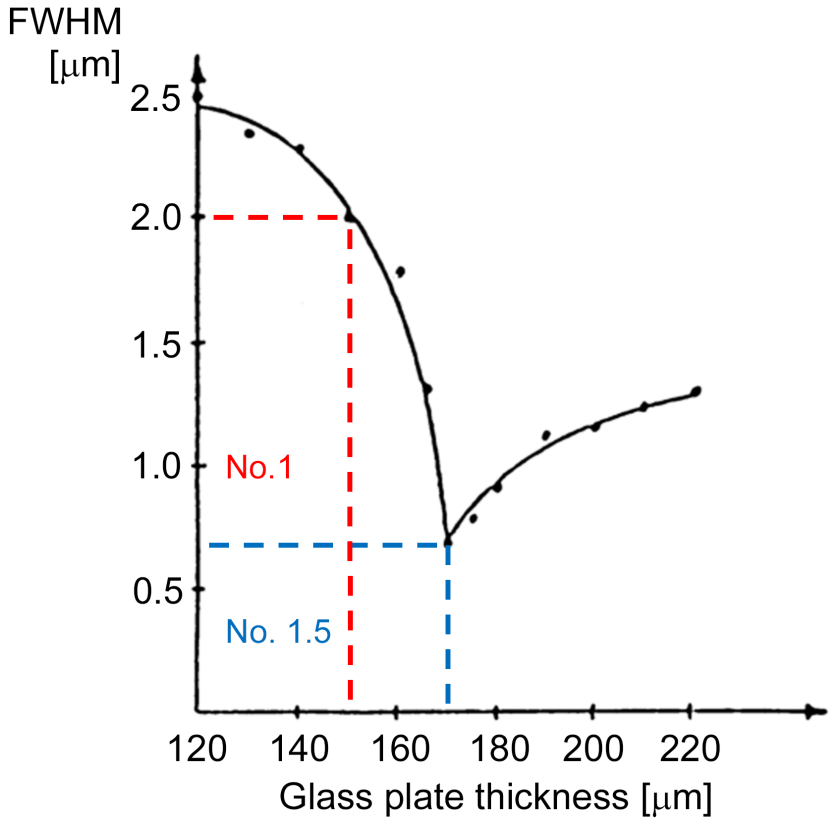

Figure 1.18: Changes in resolution with various coverslip thicknesses
Measured with Plan-Neofluar 63x, NA 1.2 water. Note the great difference in full-width half-maximum (FWHM) when changing from No. 1.5 coverslip (0.16-0.19 mm) to the next standardised thickness, No. 1 (0.13-0.16 mm). Adapted from Keller (2006). Copyright © 2006, Springer Science.

Table 1.1: Refractive indices of media typically used in fluorescence microscopy

Medium	Refractive index
Air	1.00
Water	1.33
Fluoromount-G™ mounting medium	1.40
ProLong™ Gold mounting medium (48h incubation)	1.46
75% Glycerol	1.44
Glass	~1.50
Low autofluorescence immersion oil	~1.52
Muscle fibres (Huxley & Niedergerke, 1958; Dirckx *et al.*, 2005; Chen *et al.*, 2014*a*)	1.36 - 1.41
Airway smooth muscle cells (Curl *et al.*, 2005)	1.36

Photonic interaction and light scattering

In cases of thick samples, photonic interaction (autofluorescence) and light scattering may be significant contributors to degradation of signal-to-noise ratio (SNR) and PSF (Figure 1.19 and Figure 1.20). When a sample is illuminated, photons interact with various cellular proteins, leading to autofluorescence and elastic scattering (stretching of PSF in the *z* dimension) (Ntziachristos, 2010). Autofluoresce may significantly reduce the SNR of an image, especially when the sample is illuminated with UV (360-380 nm) excitation wavelength, as flavins, reduced NAD(P)H, lipofuscins, reticulin fibres, collagen and elastin are all excited with UV light, emitting fluorescence in the 420-560 nm (violet-green) wavelengths (Viegas *et al.*, 2007; Oliveira *et al.*, 2010).

Fluorophores on secondary antibodies may also contribute to light scattering and degradation of SNR. While a sample is illuminated with an excitation wavelength corresponding to that of the fluorophore, the latter becomes excited and emits light. The light emitted by the fluorophore adds up to that of autofluorescence (Figure 1.19), further degrading the SNR (Fischer *et al.*, 2011; Murphy & Davidson, 2012). Thus, background in 2D fluorescent images is the result of autofluorescence plus light scattering from the fluorophore (Waters, 2009). As may be seen from Figure 1.19, autofluorescence-induced background in single muscle fibres may constitute >1/3 of peak measured intensity and overall background may reach >50% of peak intensity. Background must therefore be removed if any measurements of intensity are to be made.

Interaction of light with cellular structures additionally leads to light attenuation through deeper planes (Figure 1.20). Hence, the focal plane that is closest to the objective lens is normally brighter than the other extreme of the specimen (Edlund & Lindblad, 2008; Waters, 2009, 2013).

In order to counteract the effects of photonic interactions with the sample, it is often advisable to use bright long wavelength synthetic fluorophores, such as Alexa Fluor™ or DyLight™, as they typically reduce autofluorescence and require lower illumination intensities, further reducing the amount of photonic interaction with the sample (Monici, 2005; Waters, 2013; Wolf, 2013; García-Plazaola *et al.*, 2015).

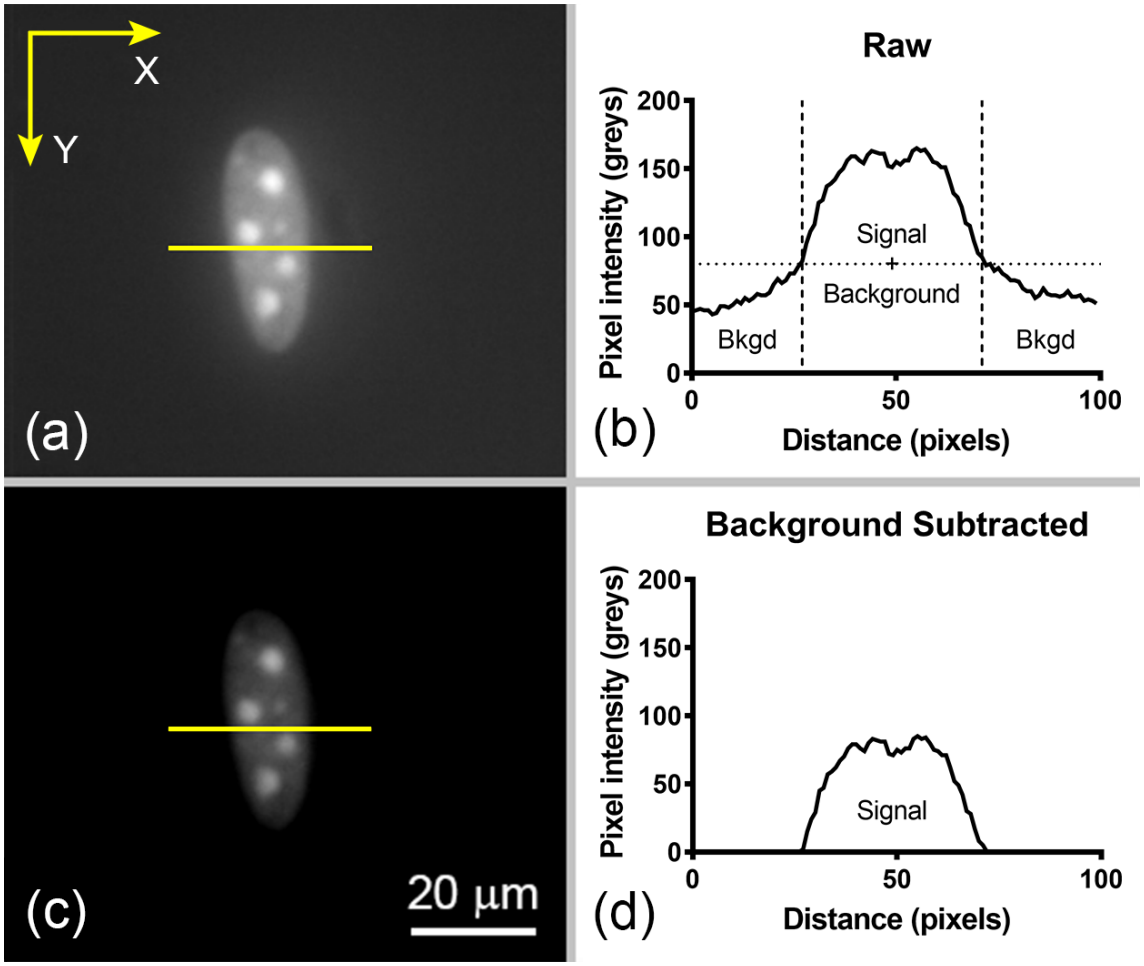

Figure 1.19: Photonic interaction with sample in single muscle fibres

(a) 8-bit image of a nucleus on the periphery of a single muscle fibre. Image was taken with an inverted spinning disk confocal microscope, equipped with a Zeiss Fluar 100x/NA 1.30 oil objective lens. Sample was stained for nuclei with DAPI and mounted with Fluoromount-G™ mounting medium (refractive index 1.40); (b) Horizontal line-scan histogram crossing the centre of the nucleus in raw image (a). Note that the histogram (marked by vertical dotted lines) consists of both background (bkgd) and signal. Background is mostly due to autofluorescence, but also due to light scattering from the fluorophore (note that the background intensity increases proximally to the nucleus, as a result of fluorophore-emitted light); (c) same image as in (a) following background subtraction of 80 greys (horizontal dotted line in (b)); (d) Horizontal line-scan histogram crossing the centre of the nucleus in image (c). Note that both peak and mean intensity are lowered, as the intensity of the nucleus in the raw image was a combination of signal plus background. Following background subtraction, the signal from the nucleus is clear and background noise is eliminated.

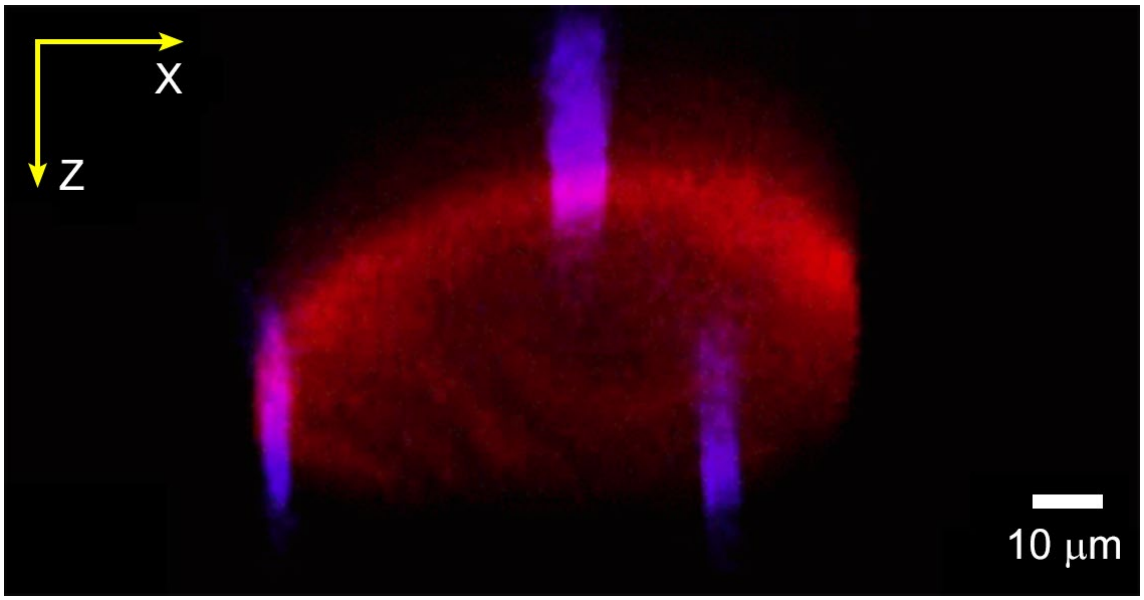

Figure 1.20: Cross-section of fluorescent Z-stack images of a single muscle fibre
Stack was acquired with an upright laser scanning confocal microscope. Red = actin; blue = nuclei. Note the elastic stretching and light attenuation at deeper planes. Adapted from Edlund & Lindblad (2008). Copyright © 2008, IEEE.

Fixatives

Fixatives that cause cross-linking of proteins (e.g. paraformaldehyde), thereby preserving the current condition of a cell, have been demonstrated to enhance autofluorescence, for they readily form covalent bonds between amine-containing groups through Schiff acid-base reactions (Monici, 2005; Allen *et al.*, 2013; Davis *et al.*, 2014; García-Plazaola *et al.*, 2015). As a consequence, the aldehyde groups autofluoresce in the violet-blue wavelengths and may even react with antibodies (Viegas *et al.*, 2007; Oliveira *et al.*, 2010). Autofluorescence at such wavelengths can remarkably degrade the image SNR and mask typically used stains for tagging nuclei, e.g. DAPI, rendering objects of interest indistinguishable from the background (Figure 1.21).

Numerous approaches have been suggested to account for fixation-induced autofluorescence, including a reduction in the concentration of aldehyde-based fixatives, or their avoidance altogether by fixing with 20% methanol (Tokumasu & Dvorak, 2003; Allen *et al.*, 2013; Davis *et al.*, 2014). Other reagents, aiming to quench the reactions of formaldehyde with amine groups, have been demonstrated to reduce autofluorescence in cells, including 50 mM glycine (Allen *et al.*, 2013), 50 mM NH_4Cl (Shtengel *et al.*, 2014), 0.1-0.5% $NaBH_4$, ammonia, proteolytic digestion with proteinase K and Sudan Black B (Viegas *et al.*, 2007; Oliveira *et al.*,

2010). Finally, photo-bleaching of excitable molecules (UV, T30W/G30T8, Philips), for 2 hours at room temperature, has been demonstrated to reduce autofluorescence-derived signal, especially when combined with Sudan Black B (Viegas *et al.*, 2007; Oliveira *et al.*, 2010). An highly-recommended perspective paper about sample preparations, with exemplary protocols, may be found in Allen *et al.*, (2013).

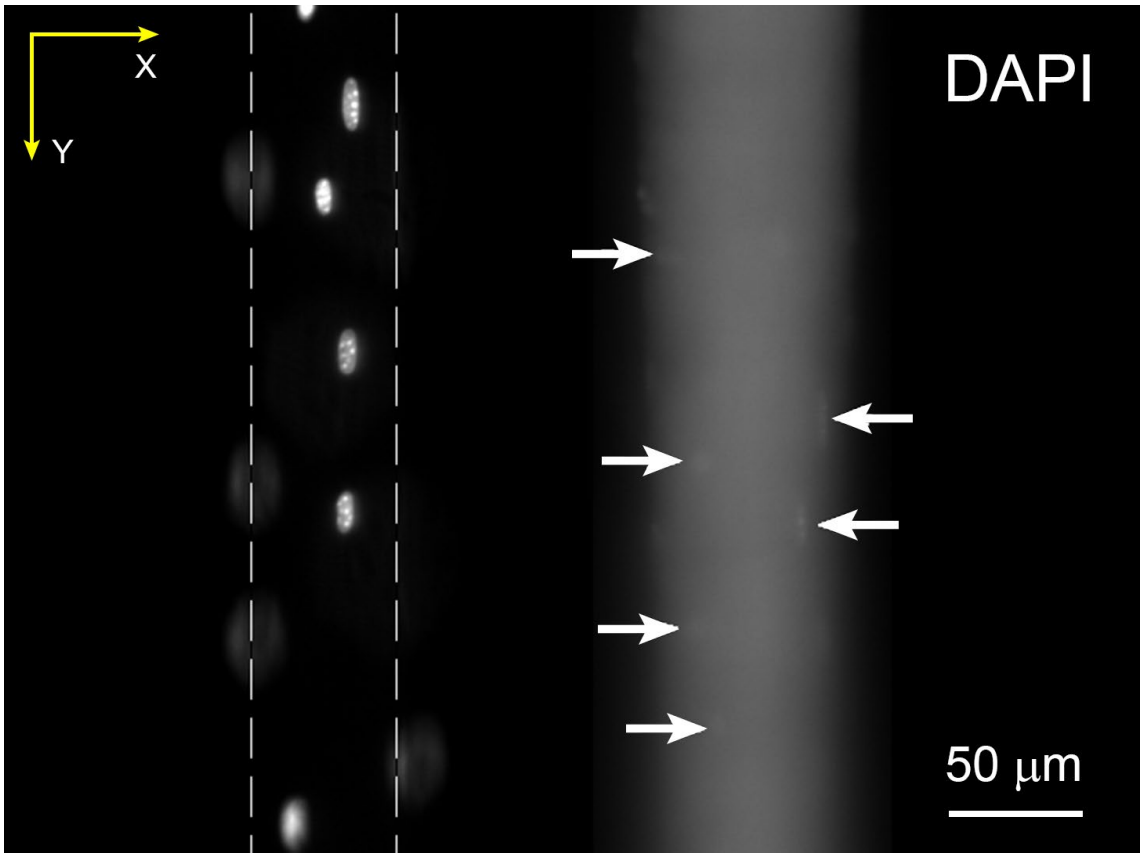

Figure 1.21: Effect of paraformaldehyde on autofluorescence in single myofibres
Confocal image of a single focal plane of two different single muscle fibres following fixation with 4% paraformaldehyde in PBS (left: 10 min; right: 25 min) and staining for nuclei with DAPI (5 min incubation in 1:1000 DAPI/PBS). Each fibre was treated and imaged individually, and imaging conditions were similar (UV excitation, stock blue filter emission, similar illumination intensity and camera exposure). Raw images of fibres were merged into this figure. Pixel intensities within fibres remained untouched, but to enhance clarity, background was removed from the compiled image with simple arithmetic (subtracted 170 grey values; 8-bit image). Arrows point at individual nuclei on the prolonged fixation fibre; note the near impossibility to recognise nuclei.

Image processing

Optimisation of the sample is always the best means for producing valuable images with reliable information. Nevertheless, further processing is possible, and at times required, for improving images that suffer from various optical aberrations. Typically, the basic corrections required for imaging thick sections involve improvement of SNR, which entail enhancing the contrast between the object of interest and background (Waters, 2009). Excluding basic procedures that do not produce major improvements of SNR (e.g. subtracting camera noise), though are indeed required for quantitative imaging, most improvements in SNR typically result from deconvolution and background subtraction.

Focal planes, especially those farthest from the objective, may be subject to significant out-of-focus light. Assuming an image is of sufficiently high SNR, this can be attenuated by reversing (i.e. deconvoluting) the image distortion caused by the microscope, using obtained or calculated PSF, to adjust each image to reflect the true state of the sample (Figure 1.22 and Figure 1.23). Deconvolution can, therefore, lead to improvements in SNR, spatial resolution and accuracy of quantitative measurements (Biggs, 2010; Swedlow, 2013; Goodwin, 2014).

Background subtraction can lead to a significant increase in SNR by enhancing the contrast between the object of interest and the background. It is best performed in/near object to avoid errors originating from inhomogeneity in images (Waters, 2009). Background subtraction is often performed during the deconvolution procedure, immediately before it commences, to reduce the length of time required to process each image. Depending on the necessities of the study, background subtraction may also be performed arithmetically (see Figure 1.19 for an example).

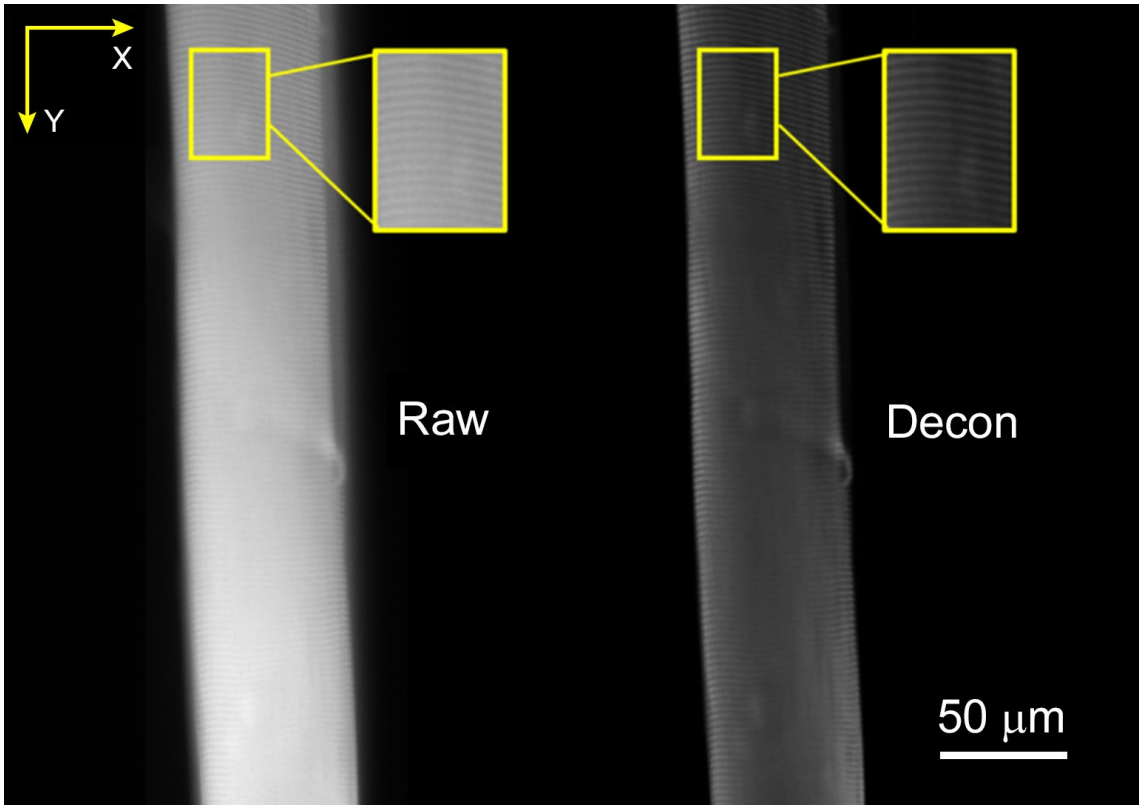

Figure 1.22: Effect of deconvolution on resolution in a single muscle fibre
Image of a single muscle fibre stained with rhodamine phalloidin (actin) and mounted in Fluoromount-G™ mounting medium, before (left) and after deconvolution (right). Raw image was acquired with an inverted wide-field microscope, Zeiss Fluar 20x/NA 0.75 air objective lens. Inserts are zoomed images of the matching area on the corresponding fibre. Deconvolution improved the contrast between the signal (striations) and noise (area between striations).

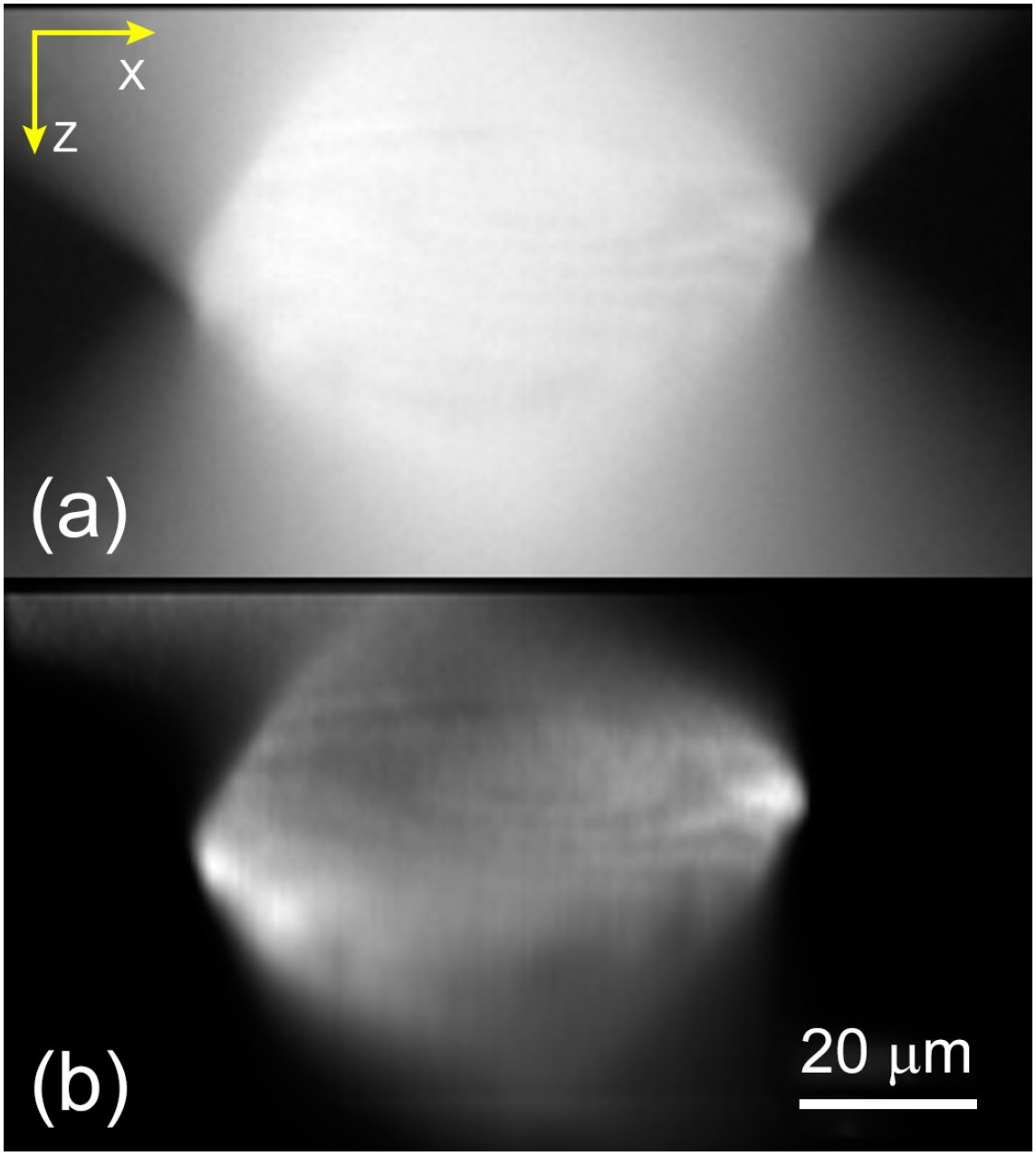

Figure 1.23: Effect of deconvolution on the axial view of a single muscle fibre
(a) Transverse section of the raw single muscle fibre from Figure 1.22; (b) Same image as in (a) following deconvolution. Note the absence of an hourglass-shaped out-of-focus light and the sharper details. Light attenuation through the sample may be observed when comparing the shallow areas of the fibre (right and left edges in x axis), with the intensity through the thickest area in the *z* axis.

1.7. Project aims

Given that research on ageing is confounded with that of muscle inactivity, informative studies of MND in sarcopenic single muscle fibres are scarce. To the best of the author's knowledge, no studies that differentiate sarcopenia from muscle inactivity, in the context of myonuclear distribution on single muscle fibres, and not simply MND, have ever been published. In addition, the source of sarcopenia-related low specific force, MHC concentration and their association with lamin A misprocessing in single muscle fibres is unknown. Thus, this project aimed to characterise the connection between ageing and disuse-related lamin A misprocessing with myonuclear organisation and concentration of MHC in isolated single muscle fibres.

Overall working hypothesis: the nuclear lamina is disrupted in response to biological ageing, a condition exacerbated by muscle disuse. This modifies myonuclear positioning in individual muscle fibres and ultimately affects synthesis and content of contractile proteins, leading to low specific force in single muscle fibres.

Specific aim 1: as a method to determine the 3D spatial organisation of myonuclei in skinned single muscle fibres using confocal microscopy was not within reach for this project, method development was the first objective of this work (chapter 3);

Hypothesis 1: skinned single muscle fibres are devoid of non-muscle nuclei. Confocal microscopy can fulfil the project's necessities, following an optimised sample preparation procedure. Custom-made scripts allow for great flexibility, speed and reliability of data analysis.

Specific aim 2: determine whether the presence of prelamin A can modulate myonuclear positioning and functional capacity of mouse single muscle fibres (chapter 4);

Hypothesis 2: single myofibres from prelamin A-accumulating Zmpste24 KO *mice exhibit altered myonuclear number and positioning in the presence of prelamin A, coinciding with reduced MHC content and depressed specific force.*

Specific aim 3: determine whether biological ageing and muscle disuse lead to altered myonuclear organisation in human isolated myofibres (chapter 5).

Hypothesis 3: single muscle fibres from individuals of varying ages and activity levels show altered nuclear organisation that is predominantly related to muscle activity, but also to age.

Chapter 2: General methods

The general methods and techniques presented below were used in chapters 4 and 5 in this thesis. Though these protocols are commonplace in the field of skinned single muscle fibres, they were all evaluated and optimised prior to their use, to guarantee homogenous treatment of the samples. For a discussion on the method developed specifically for this project, to evaluate nuclear organisation in single muscle fibres, see chapter 3.

2.1. Excision of muscle samples

In order to study nuclear organisation in skinned single muscle fibres *ex vivo*, muscle bundles should be firstly acquired and then membrane-permeabilised in 50% glycerol. As the author of the current work studied muscle fibres from both mice (chapter 4) and humans (chapter 5), the protocols for both are provided below.

2.1.1. Mice – TA and EDL muscle dissection

Early thorough preparation, care and precision are required to acquire muscle samples of high quality. The following is a standard dissection process, similar to that described by Moyle & Zammit (2014). It explains how to isolate the tibialis anterior (TA) and extensor digitorum longus (EDL) muscles from hindlimbs of mice. Importantly, any handling of the muscles was done by their extremities and not the muscles themselves to avoid muscle damage.

Firstly, quality tools were collected: corkboard, metal dissection pins, scalpel blade, micro scissors, fine toothed forceps and 2x fine forceps (Figure 2.1a). Solutions required for muscle dissection included 70% ethanol and a relaxing solution (4 mM Mg-ATP, 1 mM free Mg^{2+}, 20 mM

imidazole, 7 mM ethylene glycol tetraacetic acid (EGTA), 14.5 mM creatine phosphate and KCl to adjust the ionic strength to 180 mM and pH to 7.0) pre-cooled to 4°C.

The mouse was euthanised by cervical dislocation to prevent muscles from becoming hypoxic, as occurs when using CO_2 inhalation (Moyle & Zammit, 2014). Hindlimbs were cleaned with 70% ethanol and thoroughly shaved with the scalpel, followed by further cleaning with 70% ethanol to remove leftovers of shaven hair.

To avoid damaging the anterior side of the hindlimb, an incision was made with the scalpel through the skin at the posterior side of the leg, from the area proximal to the knee, all the way to the heel, while paying careful attention not to cut deep into soft tissue. Using the toothed forceps, the skin was pulled on one side of the incision to the posterior dorsal side of the mouse, to reveal the musculature and tendons on the anterior side of the hindlimb (Figure 2.1b). The forelimb contralateral to the dissected hindlimb was pinned to the corkboard through the palm with a dissection pin. The dissected hindlimb was pinned through the dorsal paw and the tail was stretched underneath the pinned limb (Figure 2.1b); the other hindlimb was also stretched to the opposite side.

The TA muscle (black arrow in Figure 2.1b) and the distal 4 tendons of the EDL muscle were located on the dorsal side of the paw (white arrow in Figure 2.1b). The distal tendons of the EDL were cut near the insertion points on the third phalanx of digits two to five. The TA and EDL muscles were then carefully detached using forceps, by gently tearing the connective tissue between them, while avoiding the application of excessive force. The proximal EDL tendons laterally to the TA muscle were located and rescued from underneath the annular ligament.

The distal tendon of the TA was held with forceps just proximal to its insertion on the first cuneiform and first metatarsal. The tendon was then cut closest to the bone with micro scissors. While still gripping the TA tendon, the muscle was gently pulled backwards to release it from other tissues and the EDL muscle (Figure 2.1c). The musculature around the knee was moved and the origin of the proximal TA tendon on the proximal lateral surface of the tibia was located. The proximal tendon of the TA closest to its origin was cut using micro scissors and the muscle was placed in a petri dish containing the pre-cooled relaxing solution on ice (Figure 2.1d).

The four distal tendons of the EDL muscle were held and their two tendons on the side of the knee were located, on the lateral epicondyle of the femur. Finally, the two proximal tendons of the EDL were cut with micro scissors and the muscle was placed in a petri dish containing pre-cooled relaxing solution on ice.

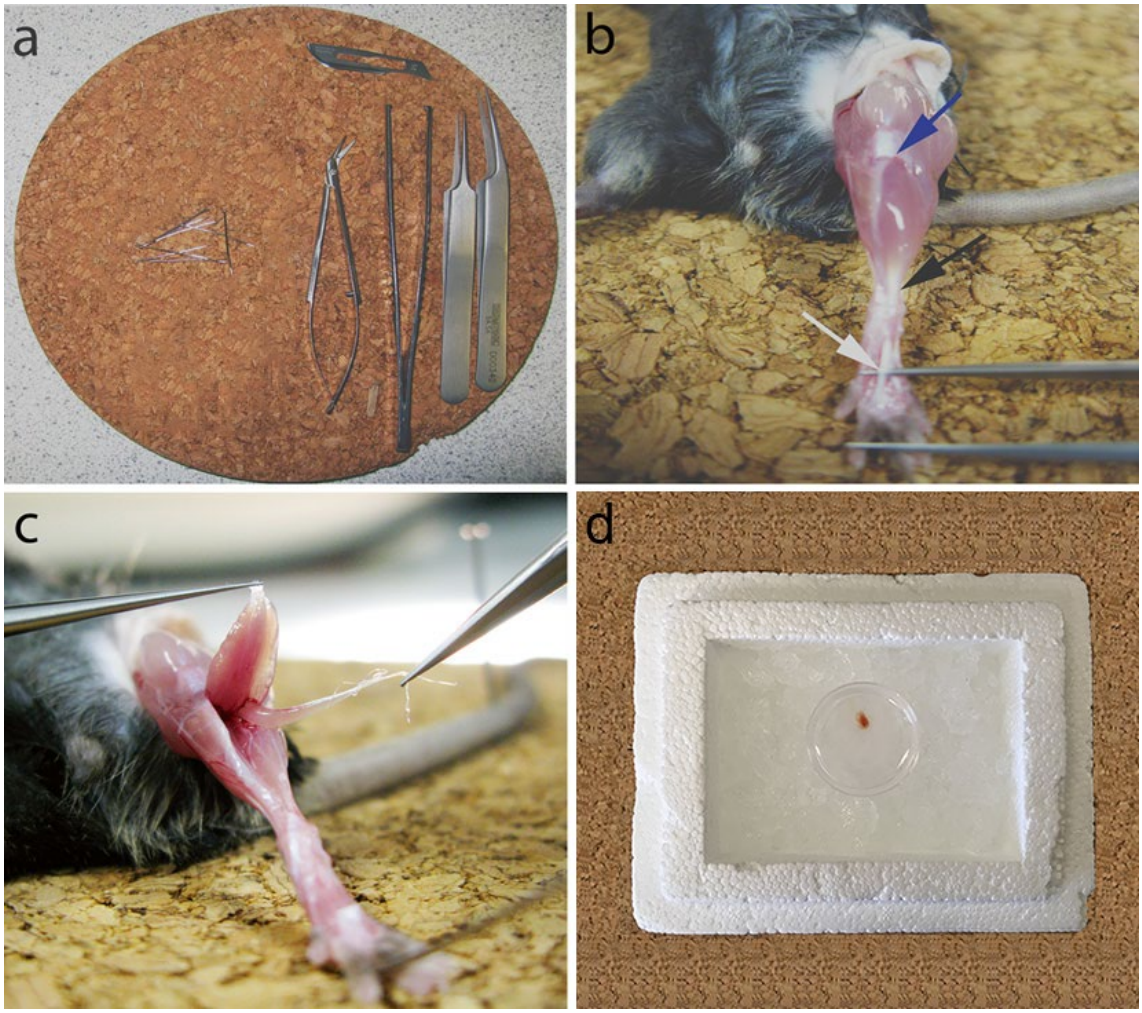

Figure 2.1: Dissection and isolation of mouse muscles
(a) Instruments and equipment for dissecting muscle bundles. From top left: corkboard, metal dissection pins, scalpel blade, micro scissors, fine toothed forceps, x2 fine forceps; (b) Mouse pinned in cross arrangement with skin removed for dissection of the left TA/EDL muscles. Distal EDL tendons have been lifted with forceps (indicated by a white arrow). The tendon lies on the tail side of the distal TA tendon (indicated by a black arrow), and this is where the cut EDL tendons should be grasped and looped out. The approximate location of the proximal TA and EDL tendons is indicated by a blue arrow; (c) Partially removed EDL muscle held by the four distal EDL tendons (right), with the TA held to reveal relative locations (left); (d) Isolated muscle placed in a small petri dish with relaxing buffer, maintained on ice. Adapted from Moyle & Zammit (2014).

2.1.2. Humans – vastus lateralis muscle biopsy

The portion of skin on the mid-thigh (vastus lateralis) of the participant's leg was shaved and cleaned using chlorhexidine gluconate, prior to injecting an anaesthetic (2% lidocaine) to the area, using a 23G needle. A 5 mm incision overlying the biopsy site was performed with a scalpel, avoiding damaging the underlying muscle. A Bergström biopsy needle was then inserted through the incision and suction was used to acquire the biopsy. The aim was to yield a sample of approximately 200 mg. The biopsy was subsequently placed in a petri dish containing pre-cooled relaxing solution on ice.

2.2. Skinning procedure

2.2.1. Preparation of muscle bundles

The petri dish holding the muscle was placed on ice, under a dissection microscope, and the muscle was split into 2-3 bundles of approximately 50 to 100 muscle fibres. In order to prevent tissue damage, muscles were always manipulated with caution, held only by the extremities to avoid unnecessary damage.

2.2.2. Membrane-permeabilisation process

Immediately following the dissection of bundles (still on ice), bundle-ends were tied onto a glass capillary tube, using loops of surgical silk. Following, each attached bundle was slightly stretched (approximately 110% of original length). The distance between the two attachment points (loops) was about 4 mm (Figure 2.2).

The glass capillaries with bundles were subsequently placed into 1.5 ml Eppendorf tubes, containing relaxing solution with 50% (v/v) glycerol, at 4°C for 24h. Chemical skinning permeabilises the single muscle fibre by disrupting the lipid bilayer of the sarcolemma, leaving the myofilament lattice functionally intact (Wood *et al.*, 1975; Konigsberg *et al.*, 1975; Stienen, 2000). Following the 24h period, each tube was transferred to -20°C for short-term storage or continued to be processed for long-term storage.

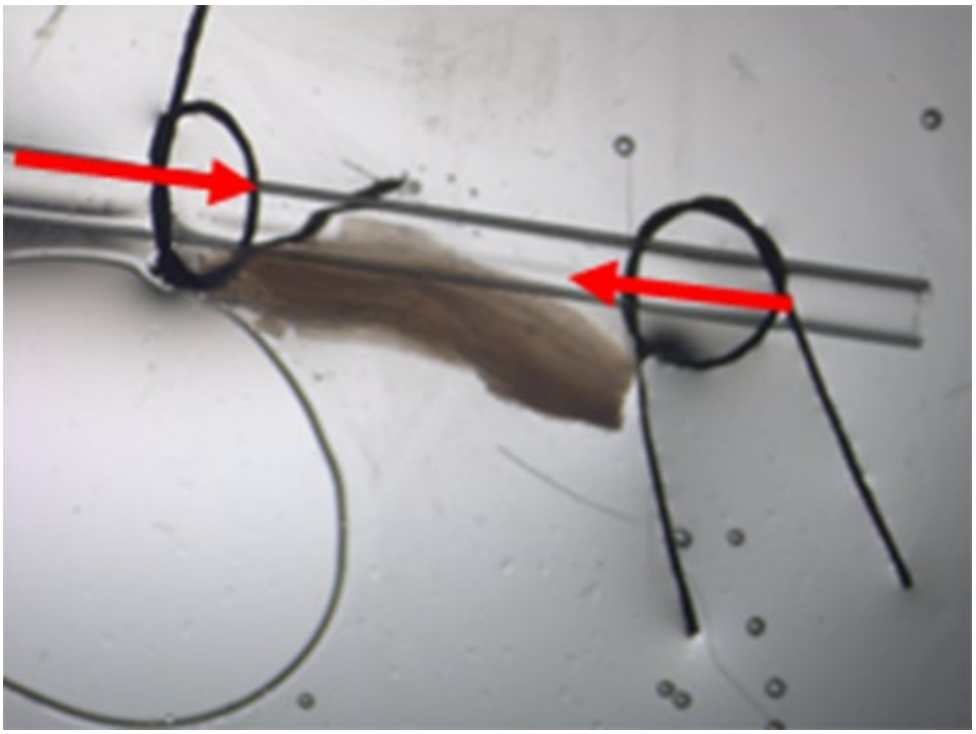

Figure 2.2: Addition of surgical silk loops to a capillary tube
Using fine forceps, two loops of surgical silk were made and slid onto the capillary. The loops were positioned in the approximate location of the muscle bundle.

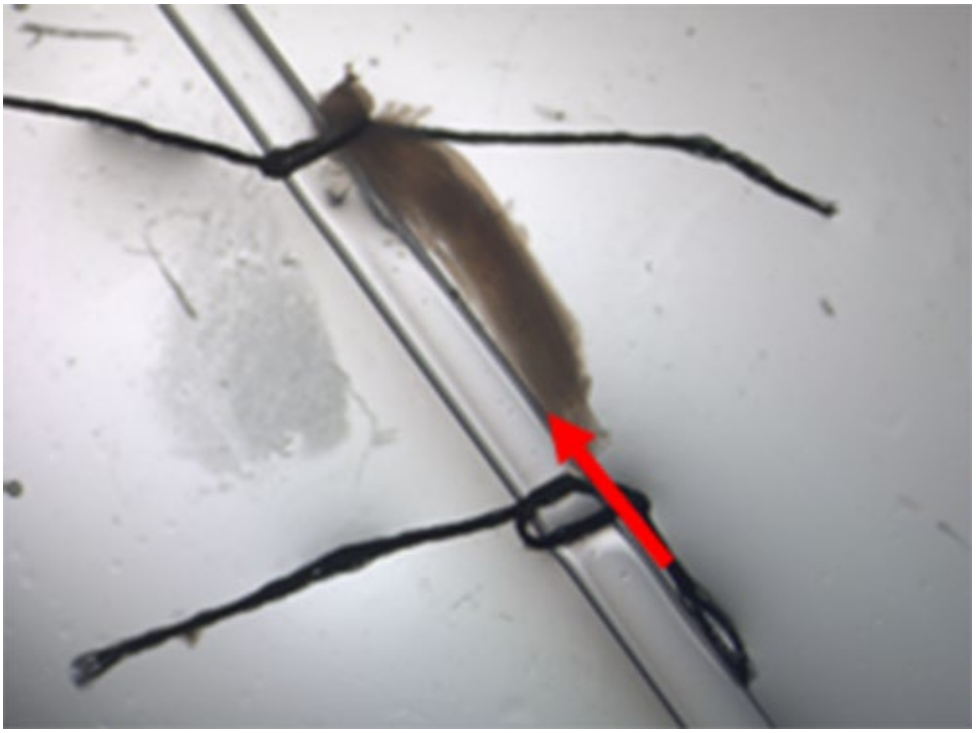

Figure 2.3: Attachment of a muscle bundle to a capillary tube
One side of the bundle was firstly tied securely onto the glass capillary. The other end of the bundle was then tied to the tube, whilst ensuring the bundle was slightly overstretched.

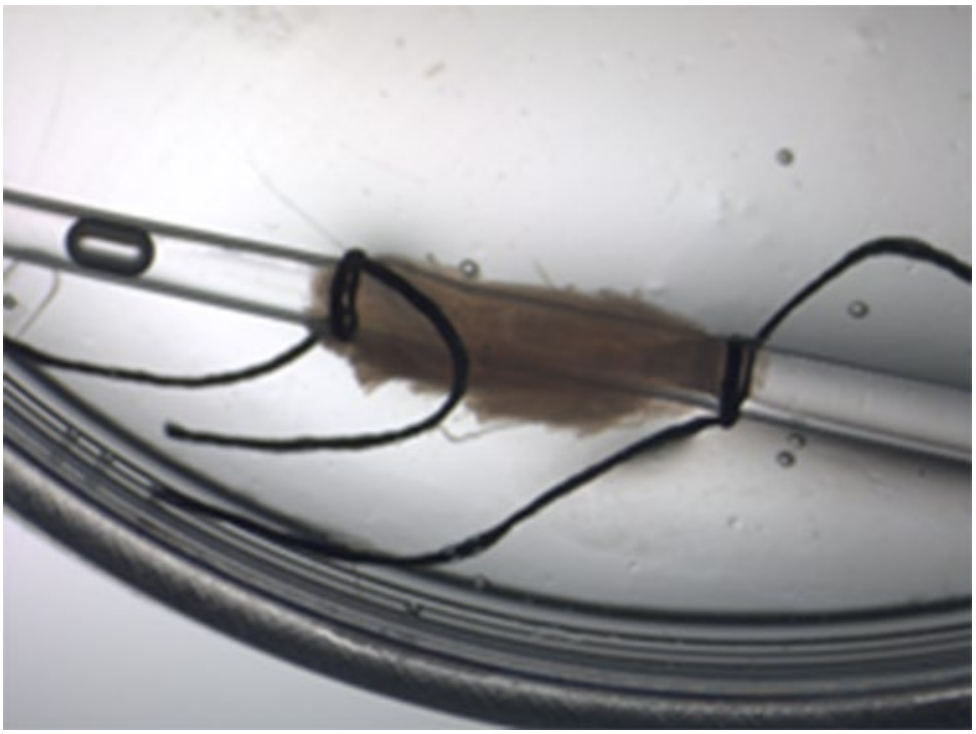

Figure 2.4: Muscle bundle attached to a capillary tube

2.2.3. Long-term storage

Directly moving the muscles to -80°C could lead to cryo-damage to the samples. Therefore, sucrose treatment was performed prior to freezing (Frontera & Larsson, 1997). Each bundle was placed in relaxing solution, maintained at 4°C, containing ascending concentrations of sucrose: 0.5 M, 1.0 M, 1.5 M and 2.0 M sucrose. Under a dissection microscope, within the 2.0 M sucrose in relaxing solution, each bundle was detached from the glass capillary. This step is crucial and requires caution; bundles may be shortened but cannot be overstretched. Subsequently, within the 2.0 M sucrose solution at 4°C, one end of each free bundle was reattached with a single loop of surgical silk. Thus, during the forthcoming freezing process, all manipulations were performed *via* the loop, to avoid damaging the bundles. Each sucrose-treated bundle was then snap-frozen with nitrogen-chilled isopentane, placed in a pre-cooled Eppendorf tube and stored at -80°C. On the day of an experiment, a bundle was de-sucrosed by incubating it for 30 minutes in each sucrose solution, in reverse to the above order, ultimately placing the bundle in relaxing solution.

2.3. Staining protocols

In order to study nuclei in single muscle fibres using confocal microscopy, the fibres and their associated nuclei should be firstly tagged using fluorescent labels. Thus, a method was developed for mounting single muscle fibres on a copper mesh for electron microscopy and processing them for immunofluorescence, as described in sections 3.2 and 3.3, respectively. Thus, the protocols below are only described briefly.

For staining, a pipette and a suction pump (or a second pipette) were required. This allowed one hand to add the necessary solution onto the set-up with the fibres, while the other hand applied suction to empty the solution from the set-up. This way, a liquid current was produced from the pipette administering the solution to the pipette collecting the waste. This technique was performed unless staining solutions were added, in which case the solution on the set-up had initially been emptied and only then were the 300 µl of the staining solution added. Nevertheless, a small volume of the solution should be kept on the set-up at any time, as its removal could either cause the fibres to hypercontract or significantly increase surface tension on the coverslip, possibly injuring the fibres when adding the subsequent solution.

2.3.1. Direct staining of single muscle fibres and nuclei

The protocol detailed below is for direct staining of actin (rhodamine phalloidin; RP) and nuclei (DAPI); this protocol was at the core of the method developed in the following chapter for studying myonuclear domains (MNDs). Solutions used for direct staining can be found in Table 2.1. All procedures were performed at room temperature (RT).

Fibres were fixed with freshly thawed 4% paraformaldehyde (PFA) (10 min, RT) and washed with 50 mM glycine in 1x tris-buffered saline (TBS) to quench the previous reaction with PFA (3x5 min, RT). The fibres were incubated in 300 µl staining solution, containing RP (1:100) and DAPI (1:1000) in TBS (1h, RT), followed by 3x5 min washes in TBS at RT. The solution was then emptied from the set-up and quickly, yet cautiously, 70 µl Fluoromount-G® mounting medium (RI 1.40) were added onto the set-up; this volume is appropriate only when using a 22 X 50 mm rectangular coverslip to cover the sample and should be modified according to the size of coverslip used, otherwise the fibres could be crushed between the coverslips. As an inverted confocal microscope was used, the overlaying coverslip was not positioned in the light path.

Therefore, the thickness of the coverslip did not matter, only its size. The set-up was ultimately placed in 4°C overnight and imaged the following day to avoid fading of the fluorophores.

The most appropriate mounting medium chosen for this project was experimentally found to be Fluoromount-G™. This is in contrast to the typical recommendation that the mounting medium should match the RI of the immersion medium of the objective (Waters, 2009). One potential reason was that the media closely resembles the RI of muscle fibres (1.36-1.41) and hence, light is majorly refracted only once between the coverslip and the media, rather than twice if media of higher RI is used (once between glass and media and once between media and sample). In any case, images acquired with Fluoromount-G™ were consistently of better quality than with mounting media of higher RIs (e.g. ProLong™ Gold with 48h incubation) and was thence selected as the medium of choice for the project.

The mounting media was added almost in parallel with the coverslip (i.e. same *xy* plane as the fibres), but perpendicularly to fibres. As this mounting medium is not highly viscous, the medium was able to flow underneath the fibres, with minimal formation of air bubbles; this was unachievable with ProLong™ (RI 1.46), due to its extreme viscosity.

Table 2.1: Reagents required for direct staining of single myofibres and nuclei

Reagent	Company	Catalogue #
TBS 20x	Thermo Scientific™	28358
Paraformaldehyde (PFA)	Boster	AR1068
Glycine	Sigma	G8898
Rhodamine phalloidin (RP)	Biotium	#00027
4',6-Diamidino-2-Phenylindole, Dilactate (DAPI)	Molecular Probes	D3571
Fluoromount-G®	SouthernBiotech	0100-01

2.3.2. Indirect staining of single muscle fibres and nuclei

Various antibodies were used in this project to tag various nuclear components (Table 2.2 and Table 2.3). The antibodies were used in conjunction with commonplace techniques to reduce background and non-specific binding (e.g. blocking buffer), as well as the methods described in section 1.6.4.1. This style of tagging nuclear components is described in greater depth in section 3.3.2, as it was used in this thesis for quantifying nuclear pixel intensities in confocal images of myonuclei (section 3.5.2).

Briefly, single muscle fibres were fixed with freshly thawed 4% PFA (10 min, RT) and washed with 50 mM glycine in 1x TBS, to quench the previous reaction with PFA (3x5 min, RT). The fibres were then incubated in 300 µl primary antibody cocktail (primary antibody plus 10% blocking solution that matches host species of secondary antibody in TBS) for 3h at RT, followed by a washing step in TBS (3x5 min, RT). Finally, the set-up was incubated in 300 µl secondary antibody cocktail (secondary antibody plus 10% blocking buffer) mixed with DAPI (1:1000) for 1h at RT, followed by a washing step in TBS (3x5 min, RT) and mounting in Fluoromount-G® mounting medium, as stated in the previous section.

Table 2.2: Primary antibodies used for immunofluorescence

Antibody	Company / model	Host species	Target species	Isotype / clonality	Localisation	Concentration
PAX7	DHSB / AB 528428	Mouse	Mouse, rat, human, others	IgG1 / Monoclonal	Satellite cells	1:5
Prelamin A (clone 7G11)	Millipore / MABT345	Rat	Mouse, human	IgG2 / Monoclonal	Nuclei	1:500
Acetyl-Histone H3 (Lys9/Lys14)	Cell Signalling / #9677	Rabbit	Mouse, rat, human	IgG / Polyclonal	Nuclei (Histone H3)	1:200
Histone H3 (tri methyl K27) (EPR18607)	Abcam / ab192985	Rabbit	Mouse, rat, human	IgG / Monoclonal	Nuclei (Histone H3)	1:200

Table 2.3: Secondary antibodies used for immunofluorescence

Antibody	Company / model	Host species	Target species	Isotype	Ex./Em. λ*	Concentration
Alexa Fluor® 488	Invitrogen / A-11001	Goat	Mouse	IgG (H+L)	495/519	1:1000
Alexa Fluor® 488	Invitrogen / A-11008	Goat	Rabbit	IgG (H+L)	495/519	1:1000
Alexa Fluor® 594	Jackson Labs. / 712-585-150	Donkey	Rat	IgG (H+L)	591/614	1:1000
Alexa Fluor® 594	Invitrogen / A-11005	Goat	Mouse	IgG (H+L)	590/617	1:1000
Alexa Fluor® 594	Invitrogen / A-11012	Goat	Rabbit	IgG (H+L)	590/617	1:1000

* Ex./Em. λ = approximate fluorescence excitation (Ex) and emission (Em) maxima, in nm, as noted in manufacturer's website.

2.4. Imaging and analysis

Fluorescence microscopy was used in this project for three purposes: (i) calculations of nuclear organisation in single muscle fibres; (ii) quantification of pixel intensities in nuclei to evaluate overall transcriptional activity; (iii) quantification of pixel intensities in single muscle fibres to assess differences in concentration of actin between fibres. Whereas the first two experiments were performed in both chapter 4 and chapter 5, quantification of pixel intensities of actin in single muscle fibres was only performed in chapter 4 and will be therefore discussed within that chapter. A thorough discussion of the imaging procedures mentioned below can be found in section 3.4; only a brief summary will be provided here. See Table 2.4 for specifications of the analysis computer and Table 2.5 for a list of equipment used for image acquisition.

Table 2.4: Specifications of analysis computer

Part	Model
Computer	Dell XPS 8700
Processor	Intel Core i7 4790 / 3.6GHz
Motherboard	Dell 0KWVT8 A03
Memory	12 GB DDR3L 1600MHz
Graphics card	NVIDIA GeForce GTX 745 4GB
Solid-state drive	Samsung 850 EVO 500GB
Secondary hard drive	Seagate Barracuda 7200.14 1TB
Operating system	Windows 10 Ultimate 64 bit
Monitor 1	Dell UltraSharp 24” U2414H
Monitor 2	Dell UltraSharp 24” U2414H

Table 2.5: Equipment used for image acquisition

Equipment		Model
Microscope		Zeiss Axiovert 200
Spinning disk		BD CARV II confocal imager with Nipkow disk
Light source		EXFO X-Cite® 120 mercury halide arc lamp
Filter sets	DAPI	Semrock Inc., Rochester, New York, Brightline™ series
	E-GFP	
	Texas Red®	Chroma ET 49008
Z motor controller		Physik Instrumente E-662 LVPZT Piezo Controller
Objective lenses	20x	Zeiss FLUAR 20x/0.75 air
	100x	Zeiss FLUAR 100x/1.30 oil
Camera	CCD 12-bit	Photometrics CoolSNAP HQ
Computer	Power supply unit	Corsair CX750
	Processor	Intel Core i5 4460 / 3.2GHz
	Motherboard	Asus H87-PLUS
	Memory	Kingston HyperX Savage 4 GBx2 kit DDR3 1600MHz
	Graphics card	Intel® HD Graphics 4600
	Solid-state drive	Samsung 850 EVO 500GB
	Operating system	Windows 7 Ultimate 64 bit
	Acquisition software	Metamorph v7.8.12 (Molecular Devices)
	Monitor	Dell UltraSharp 24” U2414H

2.4.1. Nuclear organisation in single muscle fibres

Single muscle fibres were mounted on copper meshes for electron microscopy, as described in section 3.2. Arrays of approximately nine fibres were then stained with DAPI (nuclei) and RP (actin), by following the procedures described above and in section 3.3.1.

Imaging was conducted as detailed in section 3.4.1. Briefly, imaging consisted of an inverted spinning disk confocal microscope (Zeiss Axiovert 200), equipped with a 20x objective lens (Zeiss FLUAR 20x/0.75, air) and an EXFO X-Cite® 120 mercury halide arc lamp as the illumination source. Images were acquired by a charge-coupled device (CCD) camera (CoolSNAP HQ, Photometrics), attached to a CARV II confocal imager (BD Bioscience) and a PC running Metamorph v7.8.12 (Molecular Devices). To visualise muscle fibres in 3D, stacks of 100 fluorescent images were acquired for each channel (1 µm *z* increments), using a Z motor controller (E-662 LVPZT Piezo Controller, Physik Instrumente). Sarcomere length was determined from a single image per fibre, taken in the brightfield view. Images were analysed using a custom-made MATLAB script (MATLAB® R2017a, MathWorks, Inc.), as described in section 3.5.1. Figures were made using Prism v7 (GraphPad Software), Fiji (Schindelin *et al.*, 2012; Rueden *et al.*, 2017) and Photoshop CS6 (Adobe Systems, Inc.).

Data from individual muscle fibres and animals/subjects was pooled together for each condition, in line with common practice in the field of both humans and animals (D'Antona *et al.*, 2003, 2007*b*, 2007*a*; Bruusgaard *et al.*, 2005, 2006, 2010, 2012; Frontera *et al.*, 2008; Cristea *et al.*, 2010; McCarthy *et al.*, 2011; Egner *et al.*, 2013, 2016; Karlsen *et al.*, 2015; Ross *et al.*, 2017*b*, 2018; Levy *et al.*, 2018; Buono *et al.*, 2018; Fongy *et al.*, 2019; Dungan *et al.*, 2019). In chapter 4, number of animals and number of single muscle fibres per animal were generally normalised between groups. In chapter 5, due to the nature of human research, only number of single muscle fibres per individual was possible to normalise between groups.

Statistical analysis and production of graphs were performed using Prism v7 (GraphPad Software) and included normality tests, t-tests (chapter 4), Analyses of Variance (ANOVAs; chapter 5) and Pearson product moment correlation to evaluate linear relationships. Statistical significance was set to $p < 0.05$. Data are presented as mean ± SEM and as individual data points.

2.4.2. Nuclear pixel intensity quantification

Single muscle fibres were mounted on copper meshes for electron microscopy, as described in section 3.2. Arrays of approximately nine fibres were then stained with the appropriate antibodies (sections 2.3.2 and 3.3.2). Imaging was conducted as detailed in section 3.4.2.

In chapter 4, imaging consisted of the same equipment mentioned in the previous section. In order to image single nuclei, situated in parallel with the objective, at the periphery of the fibre, in the focal plane closest to the objective, a stack of 50 images, 0.1 µm *z* steps around the nucleus, was acquired in the respective channel for each nucleus, using a 100x objective lens (Zeiss FLUAR 100x/1.30, oil) and a spinning disk optimised for the lens, with fixed illumination settings. Linearity of increasing camera exposure to a fixed antibody concentration, as well as *vice versa* was validated (De Vos *et al.*, 2010), as described in section 3.4.2.

In chapter 5, imaging consisted of an inverted spinning disk confocal microscope (Yokogawa CV1000), with a disk pinhole size of 25 µm, optimised for a 60x objective lens (Olympus UPlanSApo 60x/1.35, oil). The microscope was equipped with excitation lasers of 405 nm and 488 nm, matched with BP447/60 and BP525/50 emission filters. Images were acquired by an electron multiplying charge-coupled device (EM-CCD) camera (ImagEM-1K C9100-14, Hamamatsu), attached to a PC running CellVoyager™ CV1000 Software (Yokogawa). In order to image single nuclei, situated in parallel with the objective, at the periphery of the fibre, in the focal plane closest to the objective, a stack of 50 images, 0.1 µm *z* steps around the nucleus, was acquired in the respective channel for each nucleus, using fixed illumination settings. Linearity of increasing camera exposure to a fixed antibody concentration, as well as *vice versa* was validated (De Vos *et al.*, 2010), as described in section 3.4.2.

Images were analysed using a custom-made Fiji macro (section 3.5.2), Huygens Deconvolution (Scientific Volume Imaging) and Prism v7 (GraphPad Software). Statistical analysis of nuclei was performed as in previous section.

Chapter 3: Method development

3.1. Introduction and rationale

For the general methods used in this thesis see chapter 2. The current chapter will present the method developed by the author to evaluate nuclear organisation in single muscle fibres.

A major objective of this PhD project was to determine whether the presence of prelamin A can modulate myonuclear positioning and functional capacity of single muscle fibres. The methods required to study the functional capacity of single muscle fibres, i.e. specific force, were already routinely performed in the Ochala laboratory at the commencement of this project. However, this was not the case for evaluating nuclear positioning on single muscle fibres, a core aspect of the work described here. Therefore, a method had to be acquired or created.

At the time, the only laboratories performing such experiments were those of Kristian Gundersen (Bruusgaard *et al.*, 2003), who studied mouse single muscle fibres *in vivo*, and Lars Larsson (Cristea *et al.*, 2010), who studied human single muscle fibres *ex vivo*. Nevertheless, neither of their methods could have materialised for the current project. Firstly, Gundersen's technique, albeit achieving excellent results, was performed *in vivo*. As this PhD was self-funded, maintaining mouse colonies was unfeasible under such economic constraints. Secondly, Larsson's technique, though indeed allowed using the same muscle bundle for studying nuclear organisation and measuring functional physiological parameters of single muscle fibres, was slow to perform, as only one muscle fibre could have been processed at a given time, due to its attachment between connectors. Therefore, by using Larsson's method only a fraction of the fibres studied here could have been investigated. Nevertheless, Larsson's image analysis

algorithm was promising, and was indeed requested, alas it could not be provided. Hence, it was required to develop a method that was suitable for the necessities of the current work.

The requirements of the method comprised of: (i) *ex vivo* imaging, as it would enable obtaining muscle samples from various collaborating laboratories and process them in the Ochala laboratory, thereby reducing costs; (ii) speed, to allow for larger *n* numbers; (iii) accuracy and precision when obtaining results. Thus, the author invented a set-up whereby up to nine manually teased single muscle fibres could be clamped simultaneously to a copper mesh for electron microscopy that is glued to a coverslip. This significantly reduced the time required for imaging and normalised the treatment of the fibres; i.e. all fibres underwent exactly the same procedures. For analysis, the author developed a custom-made MATLAB script that utilises previously extracted nuclear and fibre co-ordinates from confocal images to calculate fibre and nuclear parameters (e.g. fibre volume and nearest neighbour distances between nuclei). The MATLAB script used by Bruusgaard *et al.* (2003) was then acquired, from Jo Bruusgaard, University of Oslo, to add calculations of order score to the software. As a result, the *ex vivo* imaging approach described here is similar to that of Larsson's laboratory, as single muscle fibres are clamped between attachment points and studying both nuclear organisation and functional parameters are possible using the same muscle bundle. Additionally, the approach for analysis is similar to that of Gundersen's laboratory, as nuclear organisation is investigated not only using the standard deviation of nearest neighbour distances, but by comparing to an ideal using an order-score that compares the experimental nearest neighbour distances with computed optimal and random distances.

As often occurs in research, developing the method has led to the development of additional tools. The most significant of those is a method for quantifying nuclear pixel intensities in confocal stacks of single muscle fibres. Imaging for this purpose is described in section 3.4 and its method for analysis, a Fiji macro, is provided in section 3.5.2. Both methods were used in publications from the Ochala laboratory (Ross *et al.*, 2017*a*, 2017*b*, 2018).

3.2. Mounting of single myofibres on grids

As high compliance of single muscle fibres is a significant issue when aiming to calculate MNDs from confocal images (Figure 1.13; section 1.6.4.1), there was a necessity to develop a

system whereby single muscle fibres are situated linearly on a coverslip, to allow accurate fluorescence imaging of the fibre and its associated nuclei. This was achieved using a coverslip glued to a copper mesh for electron microscopy, to which single muscle fibres were clamped in parallel with the coverslip, as described below.

On the day of experiments, muscle bundles were de-sucrosed, as described in section 2.2.3, and placed into a relaxing solution, in which single muscle fibres were manually dissected. Using a stereomicroscope, fine dissection tweezers and a scalpel, a copper mesh for electron microscopy (SPI G100 2010C-XA, width, 3 mm; Figure 3.1) was halved to reveal its free ends (Figure 3.3) and glued with superglue onto a No. 1.5 (0.17 mm thickness) high-precision coverslip (Figure 3.4). Using a hydrophobic pen, a circle of ~1 cm in diameter was drawn around the glued mesh, into which ~0.5 ml relaxing solution was pipetted. Arrays of nine single muscle fibres were then prepared at room temperature (RT; Figure 3.6), by attaching each muscle fibre to the opposing free ends of the grid, by clamping the respective free end onto the fibre. The myofibres were mounted at a fixed sarcomere length of ≈2.20 µm. This was a prerequisite for exact determination of nuclear spatial organisation as it allowed accurate comparisons between myofibres (Cristea *et al.*, 2010; Qaisar *et al.*, 2012). It was paramount that the area of the fibre found between the two halves of the grid was not the myotendinous junction, as nuclei in that area were found to be specialised regions of nuclear organisation (Bruusgaard *et al.*, 2003). Maximum prudence was exercised to prevent damaging the single muscle fibres in the process.

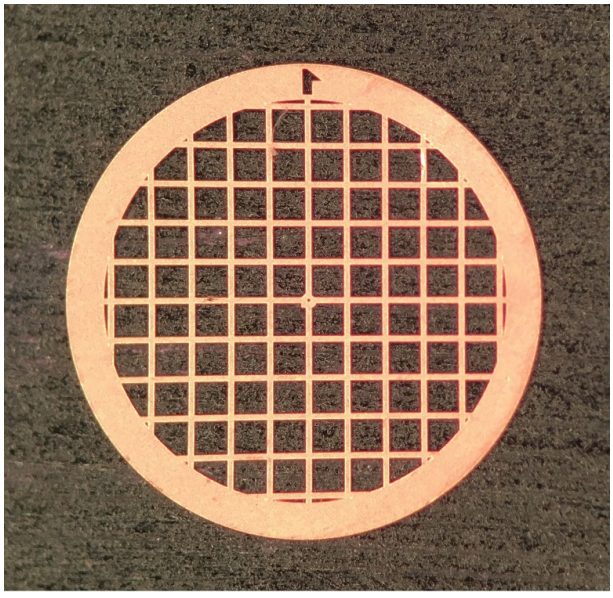

Figure 3.1: Grid used to prepare single muscle fibres for fluorescence microscopy

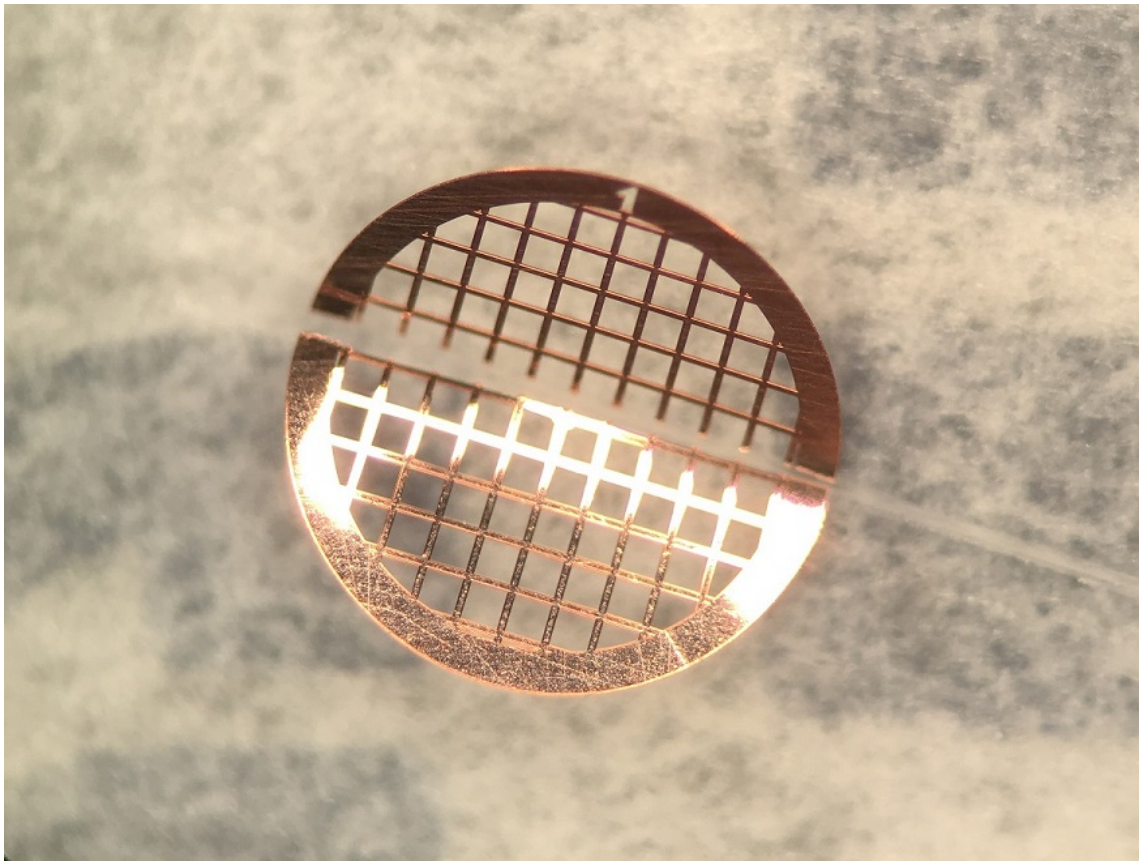

Figure 3.2: Cutting of the grid in half
Note that the top half (marked with '1' on its top) of the grid differs from the bottom half, as its ends are exposed. The same should be done for the bottom half.

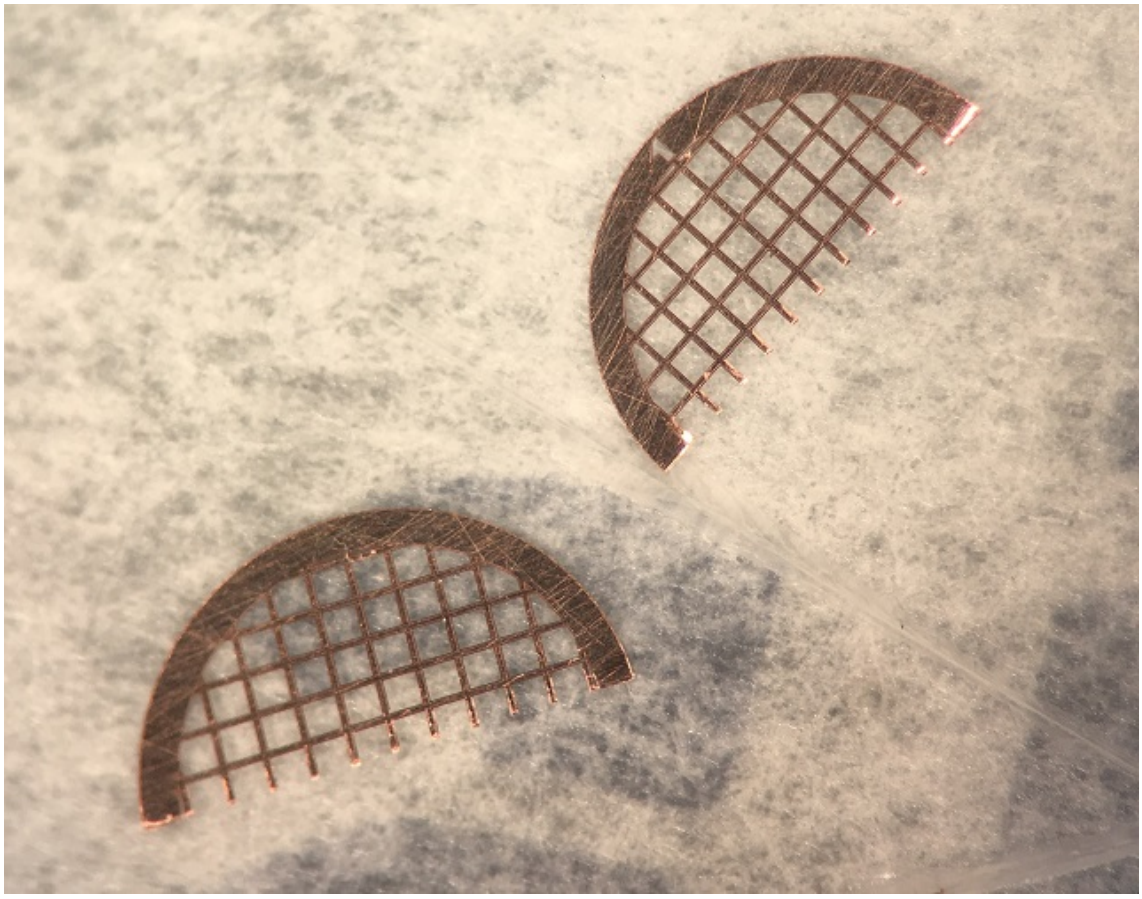

Figure 3.3: Two halves of the grid ready to be glued onto the coverslip

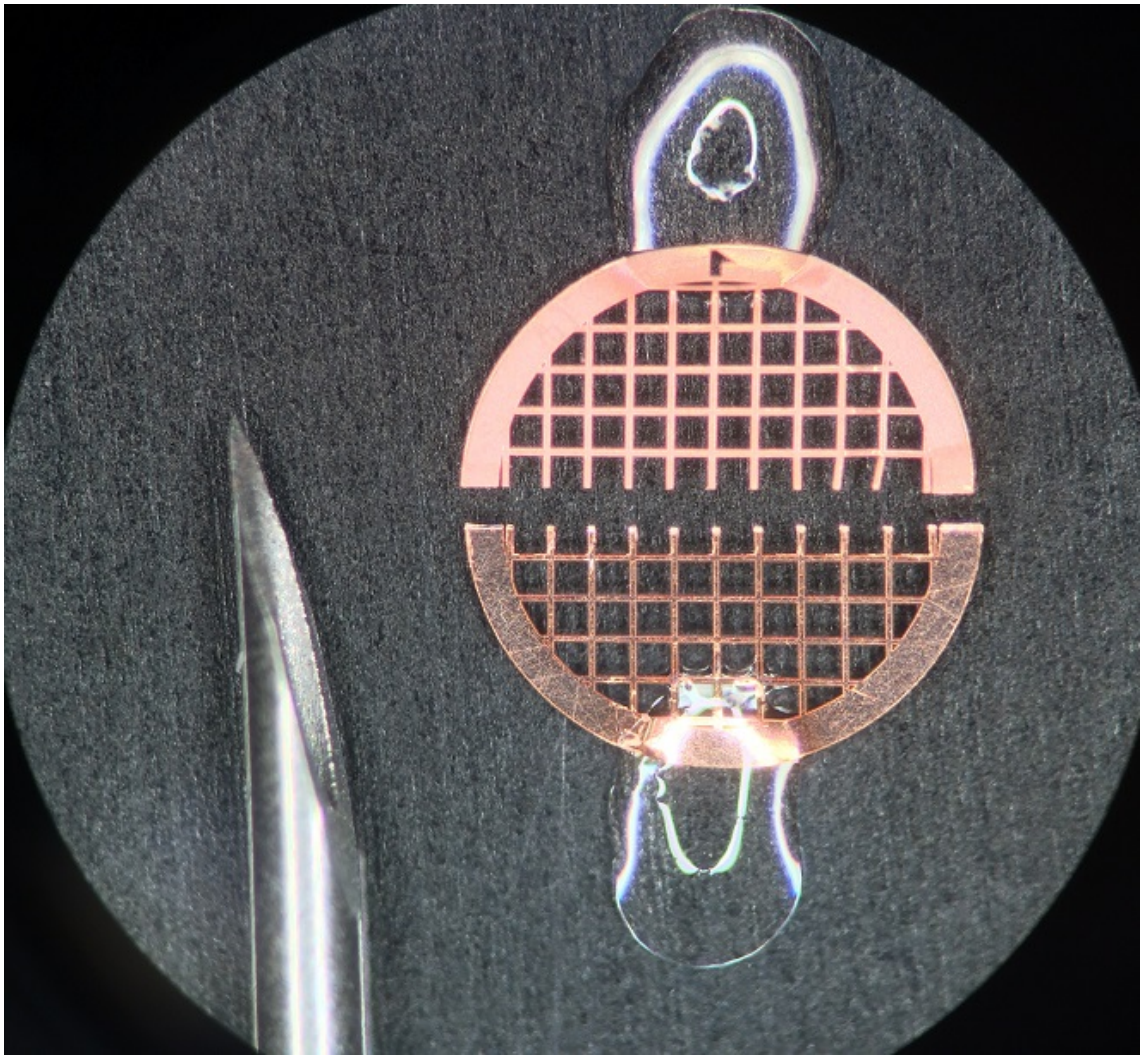

Figure 3.4: Attachment of the halved grid onto the coverslip
The two halves of the grid should be positioned on a No. 1.5 coverslip, as in the picture. A small amount of superglue was collected from the tube with a thin needle and the drop of glue was placed on either side of the halves. 23G needle (left) is provided for scale.

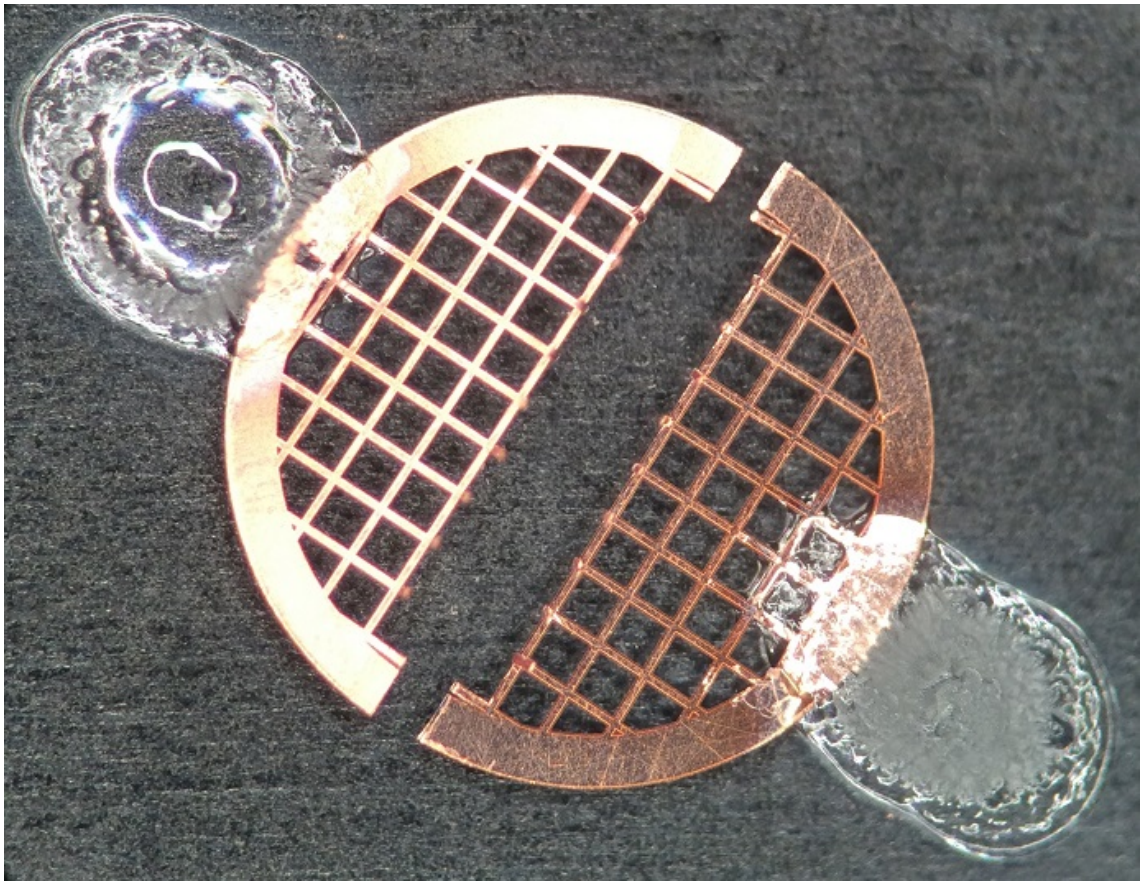

Figure 3.5: Partial folding of the free-ends of the grid to 90° angles

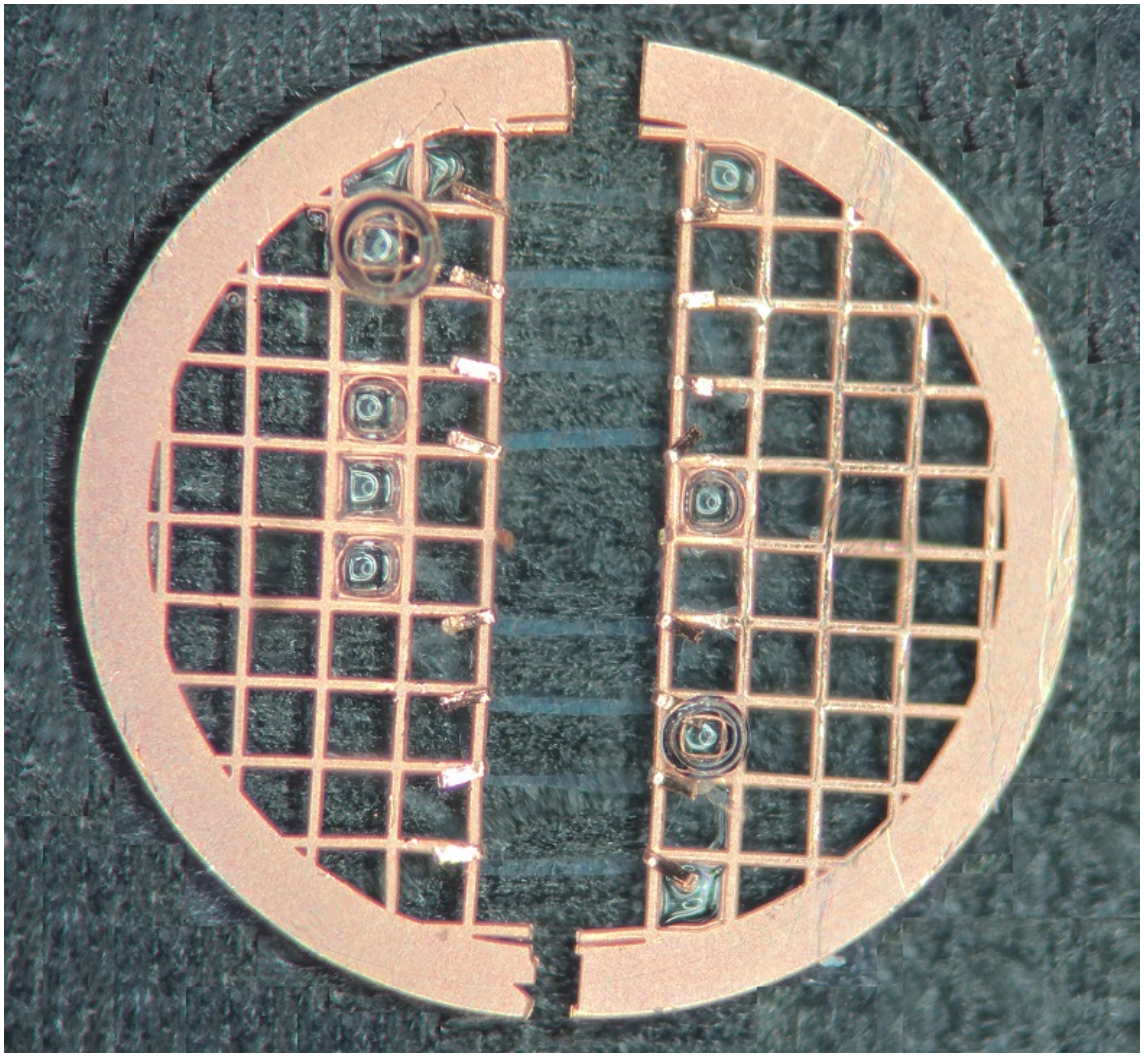

Figure 3.6: Grid with mounted single muscle fibres in solution
Each single muscle fibre was firstly clamped on one side, by folding the free-end of the grid on the fibre. Then the second end of the fibre was clamped on the opposing side.

3.3. Staining protocols

3.3.1. Direct staining of single muscle fibres and nuclei

For the purposes of MND research, resolving nuclei accurately is of high importance. However, due to the thickness of muscle fibres, a certain balance should be met between the required resolution, the ability of the illumination wavelength to penetrate the sample and the microscopy hardware at hand (Table 2.5). The only possible wavelengths for use in the microscope used here were those in the range of DAPI, rhodamine phalloidin (RP) and Texas Red®, as the illumination intensity of green and far red-shifted wavelengths using mercury halide arc lamps is overly weak for imaging single muscle fibres (Figure 3.7 and Figure 3.8).

As only 2-3 wavelengths were possible for simultaneous use, it was required to decide which wavelength should be allocated to each cellular structure, whilst balancing the inverse relationship between the ability of a wavelength to penetrate tissues and achieving maximal resolution. Due the thickness of single muscle fibres and the use of a spinning disk microscope, it was decided to designate red-shifted dyes to fibres, to increase the level of tissue penetration. Consequently, nuclei and muscle fibres were tagged with DAPI and RP, respectively.

To account for the reduced tissue penetration when using DAPI, a Zeiss Fluar objective lens (Murphy & Davidson, 2012; Ross *et al.*, 2014), corrected for spherical aberration and optimised for ultraviolet transmission, was used. It was hypothesised that a Fluar objective, being more efficient than other objectives for such wavelengths, would allow for a reduction in illumination intensity and thence, reduced autofluorescence and increased signal-to-noise ratio (SNR).

RP was selected as the excitation wavelength of RP is sufficiently far from DAPI (Figure 3.8), which prevents bleed-through between channels, but not so far that resolution markedly suffers. Bleed-through from one channel to another may lead to increased background, causing a reduction in SNR and resolution, which in the context of single muscle fibres would visually appear like autofluorescence; as seen in Figure 3.8, the excitation spectrum of RP is virtually zero in the spectrum of DAPI. Moreover, a mercury halide arc lamp is more efficient in the spectrum of RP (~540 nm) than that of Alexa Fluor 594 (~580 nm) for instance, permitting a relative reduction in illumination intensity, possibly reducing photonic interaction with the sample.

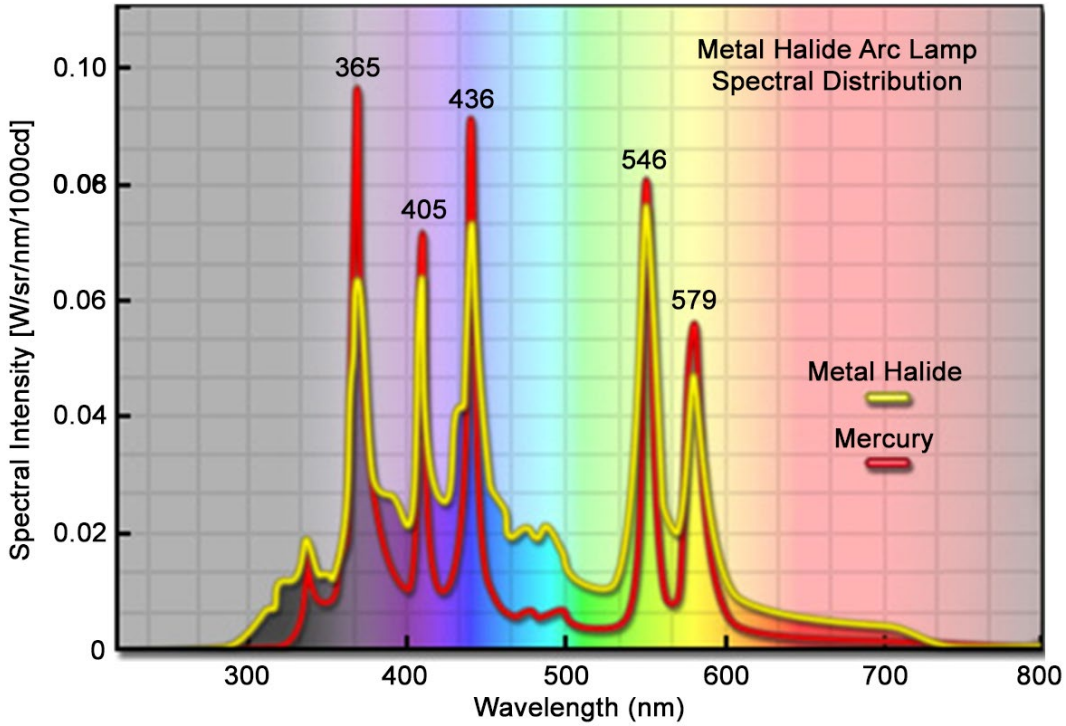

Figure 3.7: Spectral distribution of mercury and metal halide arc lamps
Adopted from Murphy & Davidson (2012). Copyright © 2012, John Wiley and Sons.

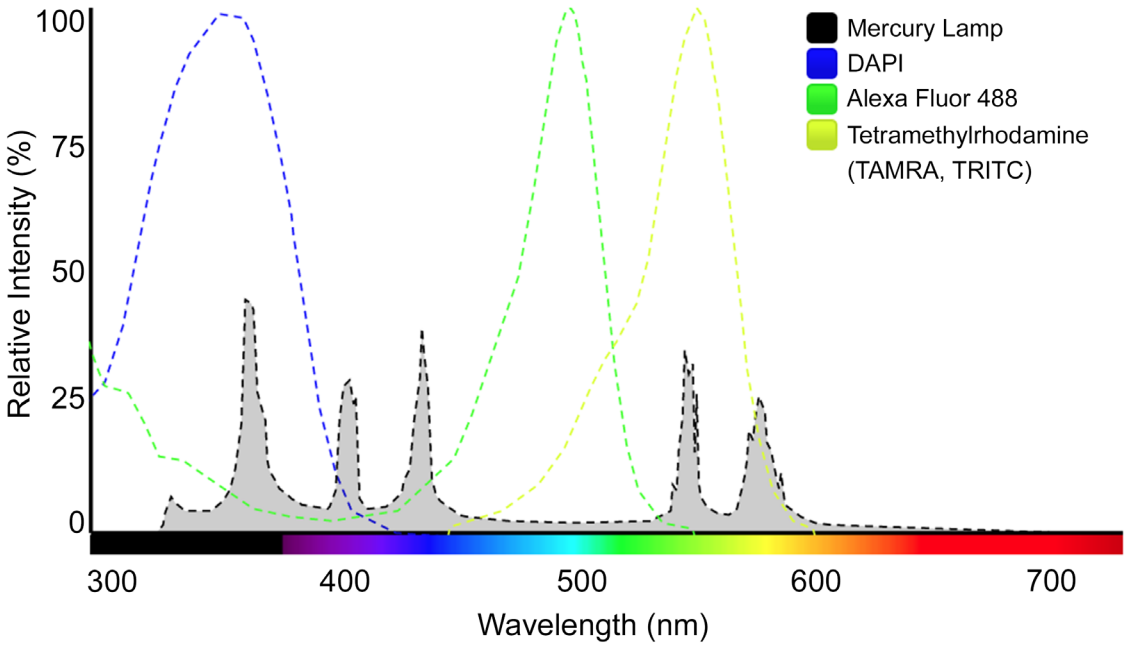

Figure 3.8: Excitation wavelengths of common fluorescent dyes
Figure produced using the 'Fluorescence SpectraViewer' online tool (Thermo Fisher Scientific). Adapted from https://goo.gl/PA37JM.

In theory, the use of red and far red-shifted dyes could have been advantageous for improving light penetration through the sample. However, regarding red dyes, the difference in wavelength between RP and red dyes is rather small and it is the opinion of the author that their use would have counterbalanced the beneficial effects of the longer wavelength, as such wavelengths necessitate increased illumination power when using mercury halide arc lamps. With regards to far red dyes, there is no doubt that the use of such wavelengths could have provided significantly greater tissue penetration, however, as seen in Figure 3.7, the spectral intensity of a mercury halide lamp is extremely low at that spectrum and was hence impractical.

The staining procedure commenced with a fixation step, performed by incubating the fibres in freshly thawed 4% paraformaldehyde (PFA) (10 min, RT), as this concentration and incubation time produced the best balance between the level of fixation and autofluorescence (see Figure 1.21 for an example); 50 mM glycine in 1x tris-buffered saline (TBS) was used to quench the reaction (3x5 min, RT) (Allen *et al.*, 2013). The fibres were then incubated in 300 µl staining solution (1h, RT), containing RP (1:100) and DAPI (1:1000) in TBS, followed by 3x5 min washes in TBS at RT; the use of 300 µl staining solution was to standardise the number of antibodies contained within the solution of constant concentration.

Ultimately, the bubble of solution atop the fibres was removed and quickly, yet cautiously, 70 µl Fluoromount-G® mounting medium (RI 1.40) were added onto the set-up, which was then placed in 4°C overnight and imaged the following day to avoid fading of the fluorophores. This volume of mounting medium should be modified according to the size of the coverslip used to cover the sample, as the appropriate volume should prevent the fibres from being crushed between the coverslips; 70 µl are therefore only appropriate when using a 22 X 50 mm rectangular coverslip. Noteworthy, the media was added almost in parallel with the coverslip, but perpendicularly to fibres. As this mounting medium is not highly viscous, as ProLong™ for example, the medium was able to flow underneath the fibres with minimal formation of air bubbles; this was unachievable with ProLong™ (RI 1.46), due to its extreme viscosity. Due to the use of an inverted microscope, the overlaying coverslip was not positioned in the light path. Therefore, the thickness of the coverslip did not matter, only its size.

The author's choice of Fluoromount-G™ was following experimental tests on the current set-up. This is in contrast to the typical recommendation that the mounting medium should match the RI of the immersion medium of the objective (Waters, 2009). One potential reason

was that the media closely resembles the RI of muscle fibres (1.36-1.41) and hence, light is majorly refracted only once between the coverslip and the media, rather than twice if media of higher RI is used (once between glass and media and once between media and sample). In any case, images acquired with Fluoromount-G™ were consistently of better quality than with mounting media of higher RIs (e.g. ProLong™ Gold with 48h incubation) and was thence selected as the medium of choice for the project.

3.3.2. Indirect staining of single muscle fibres and nuclei

In addition to the direct staining approach, used previously for studying MNDs in single muscle fibres, tagging various nuclear components was performed in this thesis using an indirect method (antibodies). The staining procedures described below were typically performed for quantitation of pixel intensities within nuclei, from which information could be inferred about the level of the investigated nuclear structure. Quantifying pixel intensities requires great care in every step, from muscle dissection all the way to results, for mistakes along the way may lead to false conclusions. Therefore, already at the planning stage of the experiment, it was extremely important that a standard procedure was produced and accurately followed. A list of antibodies used in this thesis can be found in Table 2.2 and Table 2.3.

Several methods for blocking have been tested here, yielding relatively similar results. For the most part, these included different blocking buffers, such as bovine serum albumin and sera, as well as their administration at different steps for various lengths of time. Results were quite similar between methods and it was, therefore, decided to simplify the staining procedures by creating separate primary and secondary antibody cocktails, each containing 10% sera that matches the host species of the secondary antibody. Thus, for example, if using goat secondary antibody, a solution containing 10% normal goat serum and the required concentration of primary antibody in TBS was prepared. When using human fibres (chapter 5) this step was obsolete, as it has been shown that goat serum does not bind human F_c receptors (Alexander & Sanders, 1977). Antibodies made in mouse were avoided when studying mouse fibres (chapter 4), to reduce cross-reactivity with endogenous antibodies. In all cases, whenever possible, rabbit monoclonal primary antibodies were used, for their high affinity and specificity (Ramos-Vara & Miller, 2014).

Shah & Lieber (2003) experimented with incubation times of antibodies against α-actinin in single muscle fibres and showed sufficient antibody binding at the periphery of the fibre after 3-4 hours in 4°C. Thus, it was decided 3 hours incubation at RT should suffice for tagging nuclei.

Hence, as before, staining procedures commenced with a fixation step in freshly thawed 4% PFA (10 min, RT), followed by washing in 50 mM glycine in 1x TBS (3x5 min, RT) (Allen *et al.*, 2013). Next, the fibres were incubated in 300 µl primary antibody cocktail (primary antibody plus 10% blocking solution) for 3h at RT, followed by a washing step in TBS (3x5 min, RT). Finally, the set-up was incubated in 300 µl secondary antibody cocktail (secondary antibody plus 10% blocking buffer) mixed with DAPI (1:1000) for 1h at RT, followed by a washing step in TBS (3x5 min, RT) and mounting in Fluoromount-G® mounting medium, as stated in the previous section.

3.4. Quantitative imaging of single myofibres

Once single muscle fibres were mounted and stained as described, imaging commenced for two main purposes: calculation of myonuclear domains (MNDs) and quantitation of nuclear pixel intensities for various nuclear structures. Though both objectives are of quantitative nature, studying MNDs in single muscle fibres necessitates optical optimisations that are different to those of measuring nuclear pixel intensity. In the former, light intensity should be optimised for best appearance, allowing for easy edge recognition of nuclei (i.e. easy recognition of pixel locations, not intensity). In the latter, fluctuations in pixel intensity should reflect changes in antibody abundance, not changes that originate from methodological aspects (e.g. increased power of illumination). Consequently, the different goals were reflected in both the staining and imaging protocols. Strategy for analysis also differed significantly in this thesis and will be discussed in sections 3.5.1 and 3.5.2, respectively.

For a list of equipment used for image acquisition see Table 2.5. Originally, the microscope used here was composed of parts that, though were in perfect condition, were from the early 2000s. As the ageing parts and the computer to which they were connected were placing a halt on speed of acquisition, a custom-built computer was assembled and parts of the microscope (e.g. filter sets) were upgraded, with three aims in mind – compatibility, speed and reliability.

The main purpose of the computer was image acquisition. Thus, once a compatible motherboard was purchased and installed, the aim was to support speed of acquisition. It was

achieved by firstly purchasing a faster camera card that supports Microsoft Windows versions newer than XP. In addition, a solid-state drive (as opposed to the slower classical hard drive) was purchased to increase the speed of the computer, as well as high-speed memory to allow the imaging software, Metamorph, to use memory for streaming images directly from the camera, instead of saving them immediately on a hard drive, thereby increasing speed of acquisition. As the processing rate of the memory was faster than the rate at which the camera was sending information to the memory, upgrading the memory had ultimately turned the camera into the new limiting factor in rate of acquisition. Thus, acquisition was set directly to the solid-state drive, which proved to be faster than the camera as well, making the camera the new limiting factor in speed of acquisition.

Ultimately, the laborious task of building a new computer that is compatible with an ageing microscope was highly successful. Most parts were in perfect condition and their entire flaw was their lack of compatibility with newer hardware and software. The new computer was able to harness and augment the reliability and speed of acquisition. This was especially noticed at times of heavy transfer of information between the computer and the microscope, which had previously limited the speed of acquisition (predominately rate of changing a *z* slice and camera frame-rate). The microscope may now be used for at least another decade of research.

3.4.1. Fluorescence imaging of MNDs in single myofibres

General set-up – one to two single muscle fibres were captured per image. Acquisition was set to 2 wavelengths, DAPI and RP, as discussed in section 3.3.1, and another for brightfield (for sarcomere length calculations). Images were acquired using a spinning disk confocal microscope (see section 3.5.1.3 for a discussion). The highest NA (0.75) 20x Fluar objective lens available was chosen, as described above. The lens provided adequate balance between the required working distance, resolution and the size of the randomly selected representative area of the fibre to be imaged. The area imaged should be sufficiently large to include a high number of nuclei in each image; the larger the number of sampled nuclei, the lower the error and hence, the better the representation of ground truth. Alternatively, a montage of images could have been produced, however, acquisition time would have been remarkably extended, the extent of bleaching would have greatly increased and analysis would have become more complex.

The size of each camera pixel used here was 6.45 μm^2. To satisfy the Nyquist limit for spatial resolution when imaging nuclei (short axis = ~5 µm), the required magnification was (12.9/5) = 2.6. Together with the tube magnification (1.1x), the magnification used here was of 22x, or more than 8 times the required magnification. Required axial resolution was based on a typical nuclear thickness of 3-4 µm. To satisfy the Nyquist limit for axial resolution when imaging with DAPI (358 nm), the theoretical achievable resolution with a 0.75 NA objective lens is 1.247 µm. However, due to sample thickness, crosstalk of pinholes and mismatching of the objective's refractive index (RI 1.00) with that of the sample (RI 1.40), actual resolution was likely closer to 2 µm (Heintzmann & Ficz, 2013).

A range of *z* steps was tested for studying MNDs in single muscle fibres. The same single muscle fibre was imaged with different *z* steps each time (0.2 µm, 0.4 µm and 1 µm); results of MND demonstrated no significant difference between them. No difference was also noted in the morphology of the fibre. Thus, to save computational power, it was decided to use 1 µm *z* steps, 50 below the fibre and 50 above the fibre, to ensure the entire depth of the fibre was imaged (from the author's experience, bleaching is negligible in single muscle fibres stained with DAPI and RP, especially when used with Fluoromount-G™ mounting medium). As a side note, another study performing a similar method had used *z* steps of 4.3 µm (Cristea *et al.*, 2010).

Light intensity – imaging of myonuclear organisation does not require quantification of pixel intensity. Therefore, altering illumination intensity, or camera exposure, between samples did not change the results, as the intensity would not alter the localisation of a nucleus. The most significant goal here was to eliminate background noise. In the microscope used for this work, intensity was typically set to 25%; it provided good balance between autofluorescence and camera exposure time.

Camera exposure – this should be judged in conjunction with light intensity. Again, the aim was to enhance signal, while eliminating background noise. It was possible to alter exposure between each fibre; however, for the sake of saving time during imaging, most, but not all, of the camera's dynamic range (4096 greys) was used, as this provided a degree of tolerance to increases and decreases of intensity between fibres.

Acquisition – for best accuracy, the system was set to acquire a single image per channel as each *z* step is set. For instance, once the *z* drive reached the first *z* step, the system acquired an image of the nuclei in the DAPI channel, switched to the RP channel, and acquired another

image at the same *z* step. Only then would the z drive travel another step and so on. This removed the precision of the z drive as a factor in calculations. Following acquisition of all 100 steps per channel, a brightfield image was acquired at the centre of the fibre (i.e. place of best focus); this could be done automatically or manually depending on the system at hand. Finally, each stack of images (or the brightfield image) was saved as an individual metafile.

Analysis – a programme for analysing nuclear co-ordinates from the acquired images was developed in MATLAB, as thoroughly described in section 3.5.1 and Appendix 1.

3.4.2. Fluorescence imaging of individual nuclei in single myofibres

Important note – this section will not cover general guidelines for quantitative microscopy, as these are beyond the scope of this work. An excellent checklist for optimising images for quantitative analysis may be found in Waters (2009). As the method below can be applied in numerous ways to many cellular structures (e.g. nuclei, fibre), only the concept of this type of imaging will be discussed here. Importantly, it is vital that fluctuations in pixel intensity should reflect changes in antibody abundance, not changes that originate from methodological aspects. Thus, it is crucial that a standard microscopy pipeline is produced.

General set-up – acquisition was set for a single wavelength (DAPI), or multi-wavelength if additional protein tags were used, and another 2D image for brightfield (to be used for sarcomere length calculations). The illumination source was turned on ~1h before acquisition, to allow the intensity to normalise (Waters, 2009). A single nucleus was acquired per stack of images, using a 100x/NA 1.30 oil immersion objective, matched with a disk that is optimised for the lens. Selected nuclei were only those that were situated at the periphery of the fibre, on the closest focal plane to the objective lens, and residing in parallel to the lens, as this should produce the highest achievable resolution with the lowest requirement for tissue penetration.

Maximum resolution was required for this section. Thus, an objective lens with the highest available NA (1.30) was selected. Maximum lateral resolution when using DAPI (358 nm) and Alexa Fluor 594 (561 nm), for example, with such an objective lens is ~0.165 µm and ~0.259 µm, respectively. Nevertheless, it is nearly impossible to attain spatial resolution lower than ~0.2 µm even under near perfect conditions and all images are likely to be diffraction limited

(Murphy & Davidson, 2012; Wolf, 2013; Jonkman *et al.*, 2014). Therefore, this lens provided the highest potential for diffraction-limited resolution, that could only be overcome by super-resolution microscopy (Jonkman & Brown, 2015).

The size of each camera pixel used here was 6.45 μm^2. To satisfy the Nyquist limit for spatial resolution for imaging nuclei with DAPI (358 nm) and Alexa Fluor 594 (561 nm), for example, the required magnification was ∼78x and ∼50x, respectively. It is hence clear that the lower resolution in longer wavelengths requires reduced power of magnification. Nevertheless, when making comparisons between two wavelengths, the objective lens should match the channel with the highest resolution (DAPI); the secondary channel would simply be oversampled, which causes no harm to the results, and might even be beneficial for later processing (e.g. deconvolution). Therefore, the objective lens used for this part of the thesis was 100x/NA 1.30 oil immersion objective. Maximum axial resolution under such conditions is ∼0.415 µm and ∼0.651 µm, respectively. As from the author's experience oversampling *z* steps can often lead to improved resolution following post-processing, images of a single nucleus per stack of 50 images, 0.1 µm *z* steps apart, were acquired.

Light intensity and camera exposure – using a pilot sample, the best parameters that use the entire dynamic range of the camera, whist leading to the lowest possible background, were identified. It is important to note here that the quantum efficiency of a camera, i.e. its ability to convert each photon that hits the chip into an electron, is of high importance, as high quantum efficiency improves the SNR of an image. Nevertheless, no alternative exists to good sample preparation in achieving high SNR. Once settings have been selected, they should never be changed again, otherwise results would be false. Saturated pixels were prevented by monitoring the histogram and using pseudo-colour view while setting exposure times.

Acquisition – for best accuracy, the system was set to acquire a single image per channel as each *z* step is set, for reasons explained in the previous section. Although bleaching in this set-up is negligible, illuminating the sample for reasons other than acquisition was avoided and the histogram was always monitored. Prior to acquiring a stack, once a nucleus had already been chosen, it was ensured no light passed to the sample for about 1 min to allow the fluorophore to recover. Each image was saved as an individual 16-bit Tif file.

Dark-field correction – camera noise was later removed from the images, as noise is incorporated non-uniformly into the value of each pixel. Consequently, some pixels may be

brighter than others, but not due to actual signal, simply as a result of additional noise. Hence, a dark image was always acquired, by blocking any light from arriving at the camera, with exposure matching that of the sample (Waters & Wittmann, 2014). The image was later used for analysis.

Flat-field correction – illumination of any sample is typically inhomogeneous in light microscopy. Therefore, pixels that appear on the periphery of the image could be of lower intensity, but not necessarily as the sample itself is weaker, but because light intensity is more focused and therefore brighter in that area. Using a fluorescent slide of the required wavelength (AG2273, Agar Scientific), 100 consecutive images were acquired, with 1 ms exposure. Following, an average intensity projection image was produced from the stack (Waters & Wittmann, 2014). This was used for analysis.

Feasibility of pixel quantitation – verifying the linearity of different antibody concentrations with fixed camera exposure times is paramount for determining the feasibility of pixel quantification (De Vos *et al.*, 2010). This was done by making RP concentrations of 1:50, 1:75, 1:100, 1:150, 1:200, 1:250, 1:500 and blank (TBS) and pipetting 250 μl of each solution onto a separate coverslip, prior to imaging with fixed illumination intensity (50%) and camera intensity (200 ms) (Figure 3.9a). Dynamic range showed a significant linear correlation with increasing concentrations of RP ($R^2 = 0.9938$).

Camera linearity – that the camera is sensitive to a varying antibody concentration was validated previously. However, this does not mean that changes in camera exposure times would be reflected linearly and should therefore be evaluated. In a well-calibrated system, it is expected that any changes in camera exposure times would be linear with pixel intensity, when the antibody concentration is fixed. This was tested using blue (DAPI / Indo / Fura, AG2273, Agar Scientific) and red (Rhodamine / Texas Red, AG2273, Agar Scientific) fluorescent slides, with increasing exposure times (Figure 3.9b and Figure 3.9c, respectively). Dynamic range showed a significant linear correlation with exposure times ($R^2 = 0.9983$; $R^2 = 0.9964$, respectively). It is important to note here that it is best to evaluate such relationship in a range that is relevant to the actual acquisitions. However, the minimum illumination intensity (12%) of the mercury halide arc lamp used here was overly bright and it was therefore not possible to reduce the illumination intensity to the required extent for real-life acquisitions.

Analysis – a macro for analysing the acquired images was developed in Fiji, as described in section 3.5.2 and Appendix 3.

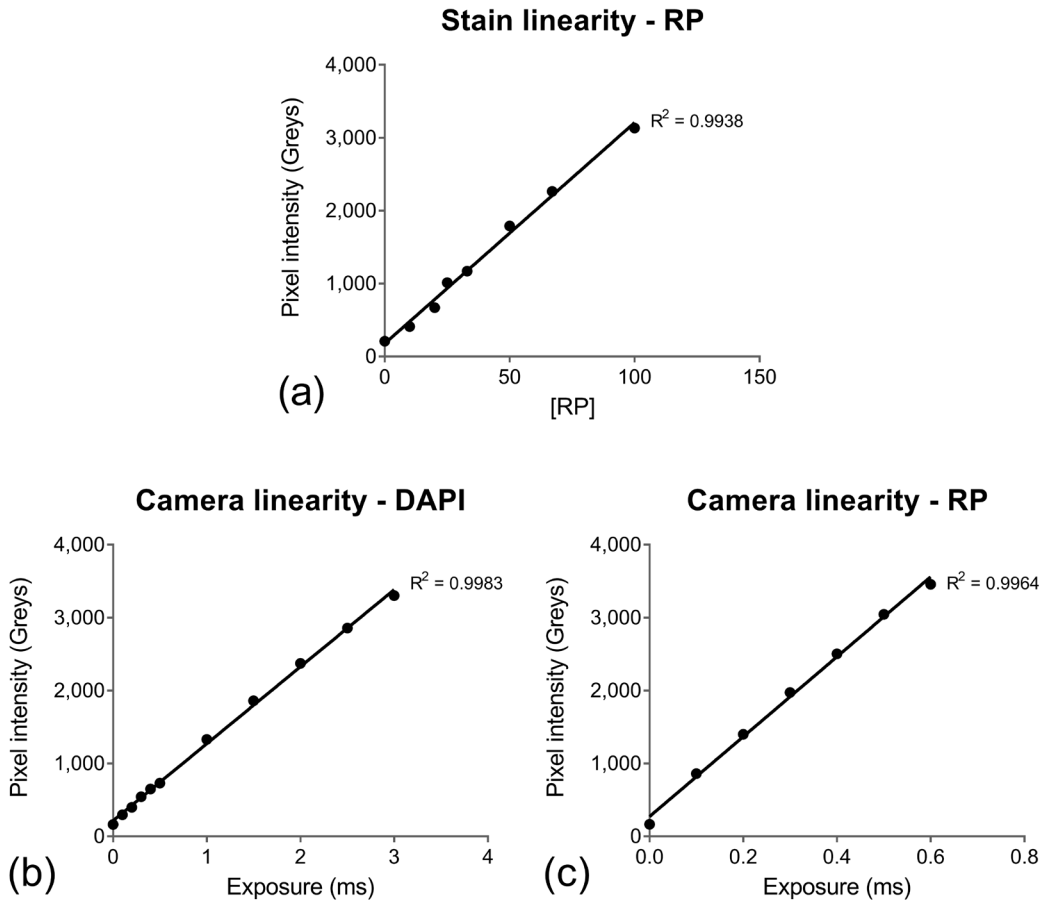

Figure 3.9: Camera and stain linearities

(a) Solutions of varying concentrations of rhodamine phalloidin (RP) were prepared immediately prior to pipetting 250 μl of each solution onto a coverslip and imaging with fixed illumination intensity (50%) and camera exposure time (200 ms). (b) Dynamic range and increasing camera exposure times (0-3 ms with fixed illumination intensity of 12%) shows a linear relationship, using a DAPI fluorescent slide. Pixel saturation was noted > 3 ms exposure. (c) Dynamic range and increasing camera exposure times (0-0.6 ms with fixed illumination intensity of 12%) shows a linear relationship, using a RP fluorescent slide. Pixel saturation was noted > 0.6 ms exposure.

3.5. Analysis

The following sections will describe the main programmes developed for studying nuclei in single myofibres. The first method of analysis, developed at the beginning of this PhD, is for analysing nuclear organisation in confocal stacks of single myofibres using MATLAB (section 3.5.1). Upon completion of its development, an interest in global nuclear transcriptional activity had emerged. Therefore, a second script was developed, in Fiji, to analyse nuclear pixel intensities in confocal images (section 3.5.2).

All the data in this project was analysed using the same computer, as described in Table 2.4. During the development of the scripts to measure pixel intensity (section 3.5.2), the slow read/write rate of the traditional hard drive (155/136 MB/s) initially used, was proving to be a significant hindrance to speed of analysis. To alleviate the computer off the bottleneck, the primary hard drive was replaced with a solid-state drive with a read/write rate of 540/520 MB/s; the original hard drive was then only used to retain unused data. Running of the programme following the replacement had significantly increased speed of analysis.

3.5.1. 3D nuclear organisation

As it was known from the commencement of this PhD that myonuclear organisation would be the core of any study conducted within the project, it was aimed to develop a method that is not only accurate and precise, but also one that is fast and as automatic as possible. To accomplish this, single muscle fibres were processed as described in previous sections. Once 3D stacks were produced, nuclear and fibre pixel co-ordinates were manually extracted, on which calculations were performed in MATLAB. The method is a high throughput, semi-automatic process; the extraction of nuclear co-ordinates from confocal images required short-term manual labour (minutes), followed by fully automatic computations (seconds). This precise method was used in publications from the author's laboratory (Ross *et al.*, 2017*a*, 2017*b*, 2018; Levy *et al.*, 2018). A systematic description of the script can be found in the section below. The original script, in coding language, can be found in Appendix 1.

The reason behind the choice to keep the analysis semi-automatic is that while the microscope used here, spinning disk confocal microscope, was usually sufficient for imaging of

nuclei, it was sub-optimal for imaging of fibre depth. Such microscopes are typically used for samples of thickness up to 30-40 μm, although have been documented to be used in samples >100 μm thickness (Fischer *et al.*, 2011; Jonkman *et al.*, 2014; Oreopoulos *et al.*, 2014). As thickness of single muscle fibres typically ranges between 20-80 μm (primarily depending on the species studied), the images acquired here were not simple to analyse automatically; this was mainly an issue for identifying fibre thickness, rather than for identifying nuclear locations. Considering the rudimentary coding abilities of the author at the time this programme was developed, accounting for this using automatic methods was not simple. This is especially true when one considers that light scattering worsens with increasing fibre thickness, which means different fibres are affected to a different extent, requiring a programme that can adapt to a range of situations rather than a script that is composed of a simple pipeline. Consequently, it was decided that nuclear and fibre co-ordinates would be manually extracted from images and any processing that follows would be fully automatic.

3.5.1.1. Systematic description of analysis

Analysis of myonuclear organisation is divided here into two primary parts: (i) co-ordinate extraction from images to Microsoft Excel and (ii) computations in MATLAB. The following sections will describe the precise process of how both parts were performed in this project.

Nuclear co-ordinate extraction

Using Metamorph, *xyz* coordinates of the centroid of nuclei are manually selected in the blue channel, using the "measure pixel" tool (Figure 3.10), and automatically transferred to Excel, with additional custom-made macros made for Metamorph; the additional macros are mainly made for speed of transfer, but are not required and do not alter the data. They will therefore not appear here.

The next step is to determine the fibre edges in 2D (*xy* plane) from the red channel (Figure 3.11). To accomplish that, the middle of the fibre, in the axial (*z*) plane, must be found first and only then can the following extremes of the myofibre, in the *xy* plane, be acquired: bottom left, top left, bottom right and top right corners. Moreover, as the objective was to compute calculations in 3D, the top and bottom of the fibre, in the *z* plane, are acquired as well.

The final laborious step is to specify the sarcomere length of the fibre. This is done on a brightfield image, acquired in the axial middle of the fibre. The first band and a band that is ten bands' distance from the first band is then selected (Figure 3.12); this serves as the basis for calculations of sarcomere length. Once all the co-ordinates have been copied to Excel, the script may be initiated.

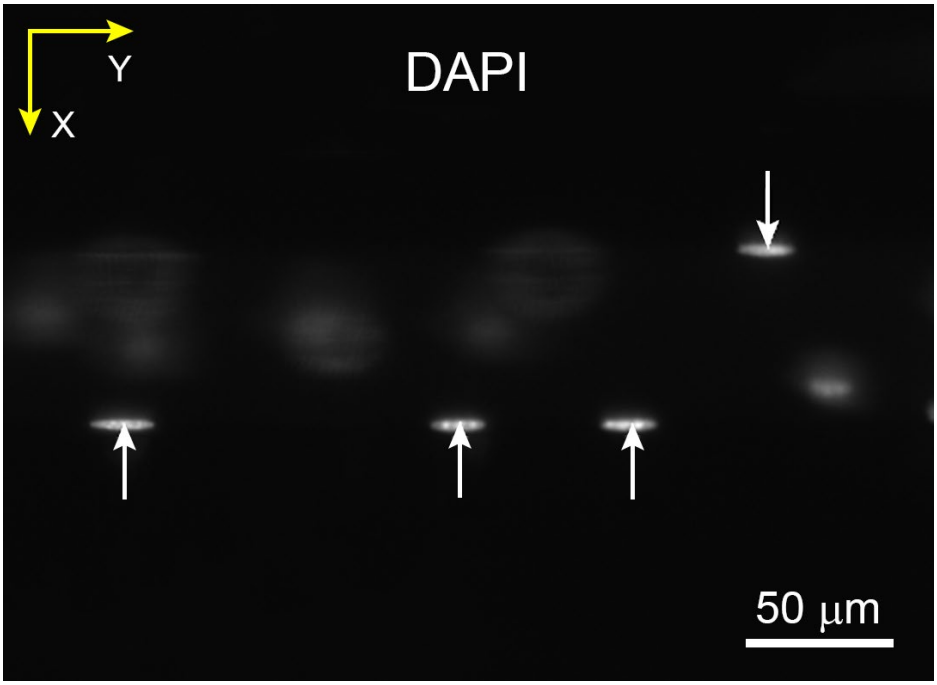

Figure 3.10: Single muscle fibre stained with DAPI
Arrows point to the centroid of nuclei in best focus. Once clicked, centroid co-ordinates are transferred automatically to a Microsoft Excel spreadsheet. Nuclei that do not reside within the current *z* step are ignored, until they are in best focus, in another *z* step.

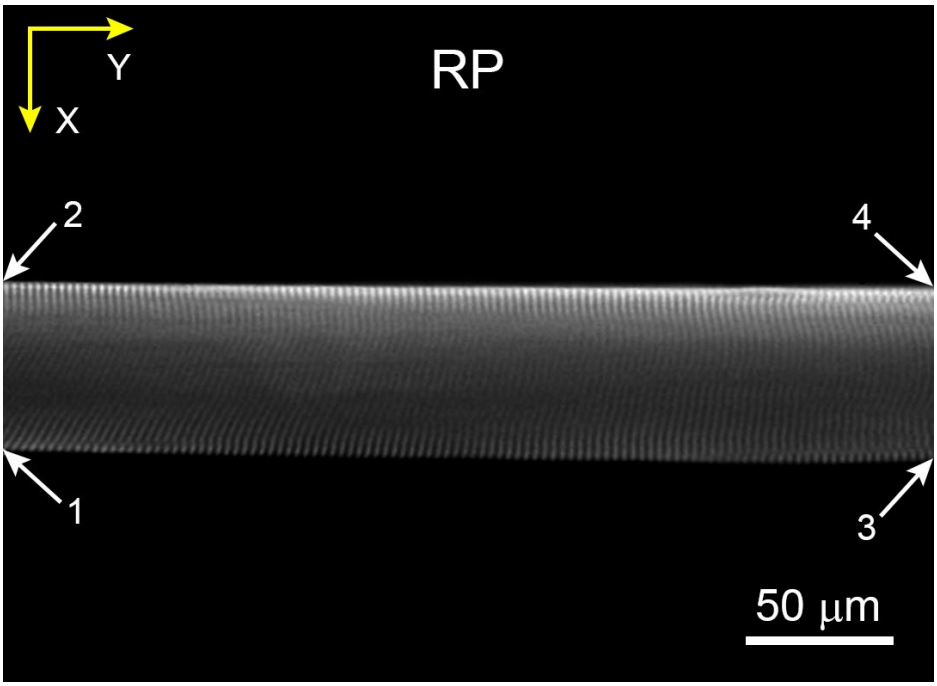

Figure 3.11: Single muscle fibre stained with rhodamine phalloidin (RP)
Numbered arrows point to the order and locations selected by the user to extract the co-ordinates of the fibre. Following the selection in the *xy* plane, the axial boundaries of the fibre are found.

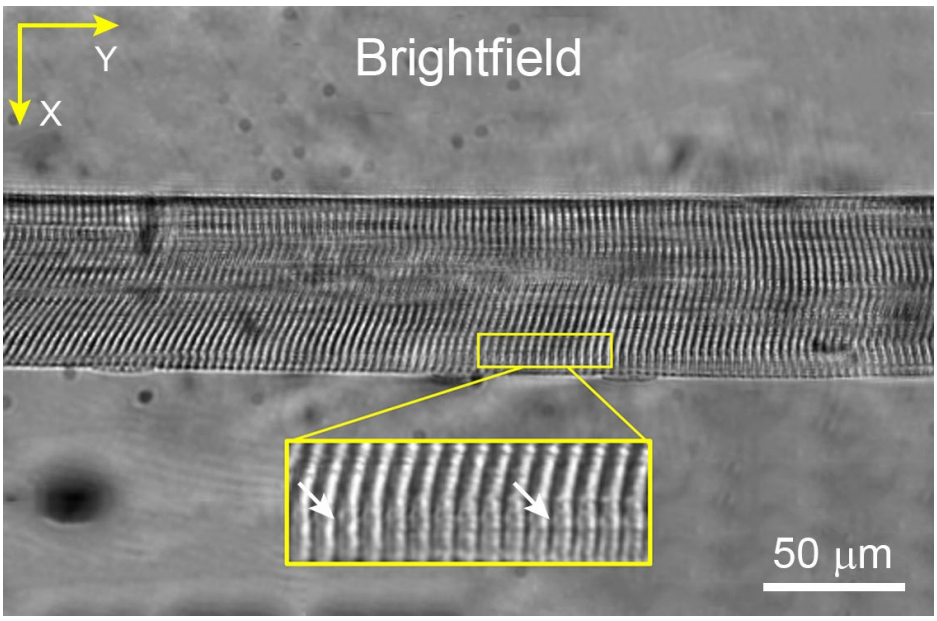

Figure 3.12: Single muscle fibre in brightfield view
The co-ordinates of the first and tenth bands are extracted by the user, providing the required data for measuring average sarcomere length.

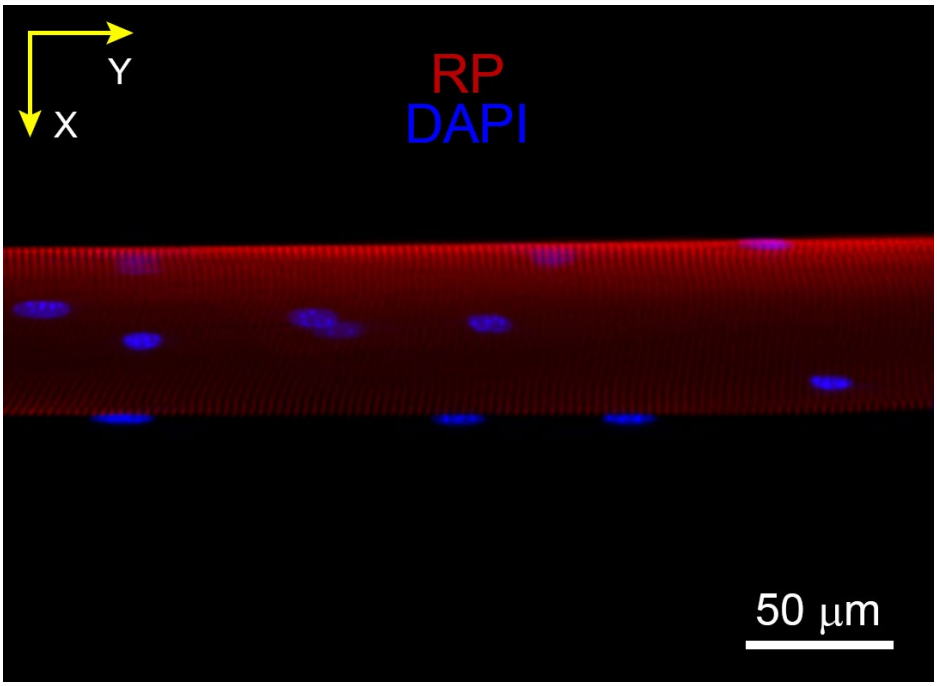

Figure 3.13: Overlay of a single muscle fibre and its nuclei
Fibre was stained for actin using rhodamine phalloidin (RP) and nuclei using DAPI.

Coding language – MATLAB

The extracted co-ordinates should be treated automatically and in the same manner. A script to compute the data was therefore required. For that, an overview on computer programming (also called coding) was conducted to select the most suitable coding language for this project. The language of choice was MATLAB (MathWorks, Inc.) for three main reasons:

1. MATLAB excels in matrix calculations – extracted data from images is in the form of matrices, composed of nuclear and fibre co-ordinates. The use of MATLAB was advantageous as the software was specifically developed to run calculations on matrices. Hence, I believed the code (also called script) should be able to run faster, as MATLAB is highly efficient at running such computations;
2. MATLAB has built-in functions – it was believed MATLAB would likely be more suitable for a beginner, as basic functions that must normally be coded anew are already built-in. This was assumed to significantly shorten the time of development;
3. The use of MATLAB is abundant in Life Sciences – it was believed learning this language would be advantageous to the author's future career.

Automatic analysis of co-ordinations in MATLAB

File definition: the script begins by defining the file to be analysed. From that file, it extracts the *xyz* coordinates of the nuclei and muscle fibre and stores them as two separate variables; one variable for nuclei ('nn_xyz' in the script) and one for the fibre ('fibre_xyz' in the script).

Nearest neighbour: the first part of the programme concerns with nuclei (Figure 3.14). For each nucleus, the script detects another nucleus to which the three-dimensional Euclidean distance is the shortest (D_{min}), as described below:

$$D_{min} = Min\ d(p,q) \tag{3}$$

Where D_{min} is the minimum distance between two nuclei (*p* and *q*) in a Euclidean three-dimensional space and *d(p,q)* is defined as:

$$d(p,q) = \sqrt{(x_2 - x_1)^2 + (y_2 - y_1)^2 + (z_2 - z_1)^2} \tag{4}$$

Where $X_1Y_1Z_1$ and $X_2Y_2Z_2$ are the co-ordinates of nuclei *p* and *q*, respectively.

Nearest neighbour standard deviation (SD): whereas nearest neighbour provides information about the average shortest distance between two nuclei, its SD is a measure of regularity. This is a crucial measure of nuclear organisation, as it tests the regularity of the nearest neighbour distance around the fibre. It uses MATLAB's built-in formula for SD:

$$NNSD = \sqrt{\frac{1}{N-1}\sum_{i=1}^{N}\left|D_{min_{i-\mu}}\right|^2} \tag{5}$$

Where *N* is the number of observations (i.e. nuclei) in the sample, D_{min} is a variable vector (i.e. varying nearest neighbour distance) and μ is the mean of D_{min}, defined as:

$$\mu = \frac{1}{N}\sum_{i=1}^{N} D_{min_i}. \tag{6}$$

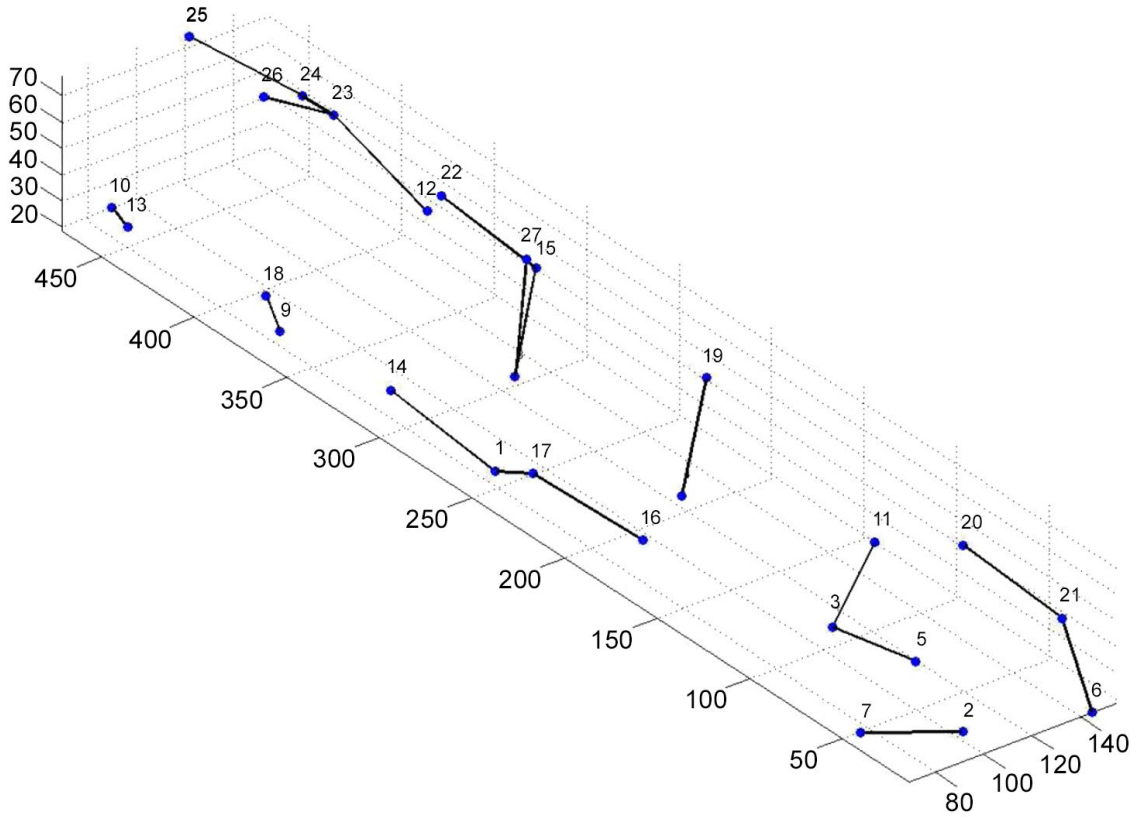

Figure 3.14: Visualisation of nearest-neighbour calculations in a single muscle fibre
For each nucleus, the script detects another nucleus to which the three-dimensional Euclidean distance is the shortest. Adapted from Karlsson (2008).

Total number of nuclei: total number of nuclei is derived in the script by counting the total number of *xyz* co-ordinates present in the main variable of nuclei.

Average sarcomere length: the second part of the programme extracts information about the muscle fibre. This part is initiated by calculating the distance from the *xy* co-ordinates of a first band to the tenth band, in the brightfield view. Hence, it uses the formula for distance between two points in a two-dimensional space. The distance is subsequently divided by ten bands, to return the average length of a single sarcomere, as below:

$$d = \frac{\sqrt{(x_2 - x_1)^2 + (y_2 - y_1)^2}}{10} \qquad (7)$$

Fibre length: to calculate fibre length, the script computes the Euclidean distance, in the *xy* plane of the fibre, between the top left and bottom right ends of the fibre and performs an identical operation for the bottom left and top right ends (Figure 3.15); the distances are then averaged. The resultant average is considered the average fibre length.

Fibre diameter: this section uses a similar approach to the previously discussed fibre length. The script calculates the Euclidean distance between the bottom left and top left of the fibre (*xy* plane) and then repeats the process for the bottom right to top right of the fibre (Figure 3.16); as before, the distances are averaged, and the result is considered the average fibre diameter.

Fibre depth: depth is derived from the distance between the co-ordinates of the top and bottom of the fibre, in the *xz* plane.

Fibre cross-sectional area (CSA): preliminary confocal images had revealed that single muscle fibres are structured as an elliptical cylinder. As a result, calculations of CSA in the script are for area of an *ellipse*:

$$A = \pi ab \tag{8}$$

Where *a* is the semi-major axis (1/2 of diameter) and *b* is the semi-minor axis (1/2 of depth).

Fibre volume: once fibre CSA has been derived, calculation of volume becomes as simple task of multiplying CSA by fibre length:

$$V = CSA \times L \tag{9}$$

Where *L* is the length of the muscle fibre.

Fibre circumference: although fibre circumference *per se* is not considered a highly useful measure, it provides additional information about the size of a fibre, as well as serves as a stepping stone towards calculation of fibre surface area. As muscle fibres are elliptical cylinders, fibre circumference was defined as circumference of an ellipse. Therefore, the following formulae were used for the approximation:

$$h = \frac{(a-b)^2}{(a+b)^2} \tag{10}$$

$$C \approx \pi(a+b)\left(1 + \frac{3h}{10+\sqrt{4-3h}}\right) \tag{11}$$

Where *a* is the semi-major axis (1/2 of diameter) and *b* is the semi-minor axis (1/2 of depth).

Fibre surface area: as mentioned, fibre surface area may be derived from fibre circumference. It is done in a similar fashion to calculation of fibre volume from CSA:

$$SA = C \times L \tag{12}$$

Where *C* is the fibre circumference and *L* is the fibre length.

Nearest neighbour per fibre volume: allows for comparisons of nearest neighbour distances, normalised for fibre volume:

$$NNV = \frac{NN}{V} \tag{13}$$

Where *NN* denotes the nearest neighbour and *V* denotes the fibre volume.

Nearest neighbour per fibre CSA: allows for comparisons of nearest neighbour distances, normalised for fibre CSA:

$$NNA = \frac{NN}{CSA} \tag{14}$$

Where *NN* denotes the nearest neighbour and *CSA* denotes the fibre CSA.

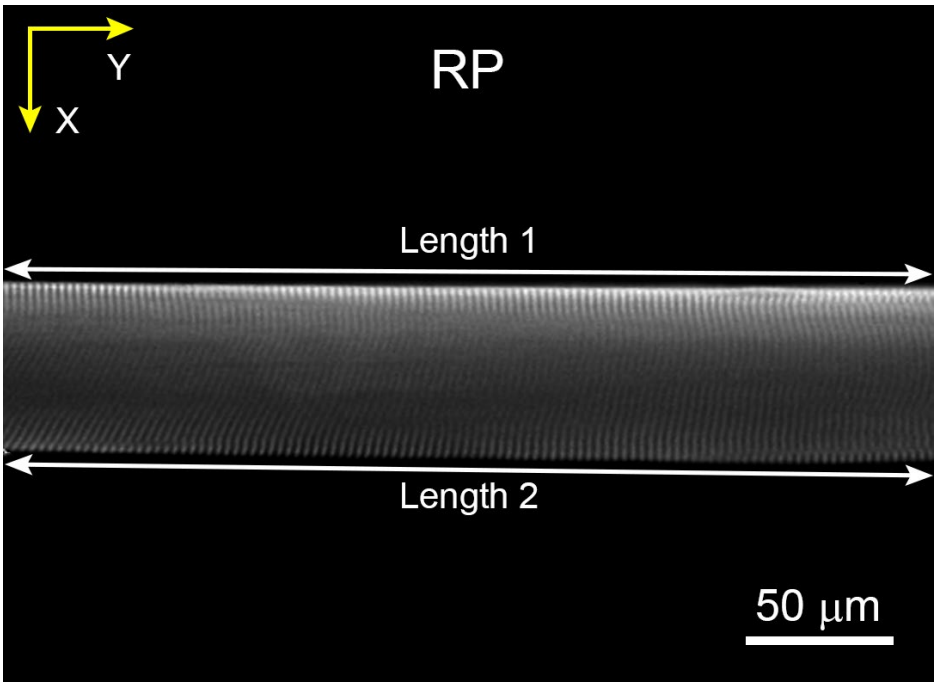

Figure 3.15: Length calculations in a myofibre stained with rhodamine phalloidin (RP)
Length 1 and Length 2 are averaged to produce the average fibre length.

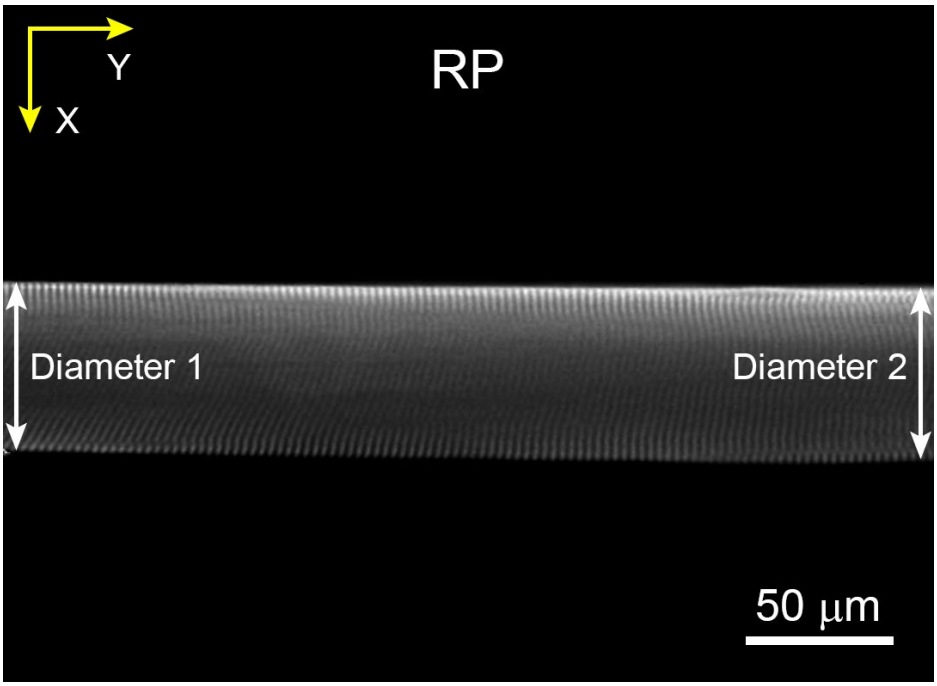

Figure 3.16: Diameter calculations in a myofibre stained with rhodamine phalloidin (RP)
Diameter 1 and Diameter 2 are averaged to produce the average fibre diameter.

Nearest neighbour SD per fibre CSA: allows for comparisons of the SD of nearest neighbour distances, normalised for fibre CSA:

$$NNSDA = \frac{NNSD}{CSA} \quad (15)$$

Where *NNSD* denotes the nearest neighbour and *CSA* denotes the fibre CSA.

Nearest neighbour SD per fibre volume: allows for comparisons of the SD of nearest neighbour distances, normalised for fibre volume:

$$NNSDV = \frac{NNSD}{V} \quad (16)$$

Where *NNSD* denotes the nearest neighbour and *V* denotes the fibre volume.

Total number of nuclei per fibre volume: normalisation for fibre volume provides the ability to compare the number of nuclei between fibres, regardless of the different fibre volumes. It is defined as:

$$NcV = \frac{Nc}{V} \quad (17)$$

Where *Nc* is the total number of nuclei in the fibre and *V* is the volume of the fibre.

Total number of nuclei per fibre CSA: normalisation for fibre CSA provides the ability to compare the number of nuclei between fibres, regardless of the different fibre CSA. It is defined as:

$$NcA = \frac{Nc}{CSA} \quad (18)$$

Where *Nc* is the total number of nuclei in the fibre and *CSA* is the volume of the fibre.

Total number of nuclei per fibre length: using the same rationale as for normalisation of nuclei for fibre volume, the resultant figure represents normalisation for length. The relationship is expressed as:

$$NcL = \frac{Nc}{L} \tag{19}$$

Where *Nc* is the total number of nuclei in the fibre and *L* is the length of the fibre.

Total number of nuclei per fibre surface area: similarly to the previous calculation, allows for comparisons of number of nuclei between fibres with different surface areas:

$$Z = \frac{Nc}{SA} \tag{20}$$

Where *Nc* is the total number of nuclei in the fibre and *SA* is the surface area.

Average myonuclear domain (MND) volume: provides information about the average volume of the fibre each nucleus controls. The average MND in the script is expressed as:

$$MNDV = \frac{V}{Nc} \tag{21}$$

Where *V* is the volume of the fibre and *Nc* is the total number of nuclei in the fibre.

Average MND surface area: describes the average portion of the surface area of the fibre, controlled by individual nuclei. It is derived similarly to MND volume:

$$MNDSA = \frac{SA}{Nc} \tag{22}$$

Where *SA* is the surface area of the fibre and *Nc* is the total number of nuclei in the fibre.

MND volume per fibre CSA: the purpose of this correlation is to demonstrate the relationship between average MND volumes and fibre size and is expressed as:

$$R = \frac{MNDV}{CSA} \tag{23}$$

Where *MNDV* is the average MND volume.

MND surface area per fibre CSA: a similar comparison to MND volume, but compares fibre surface area with CSA instead. This relationship is defined as:

$$R = \frac{MNDSA}{CSA} \tag{24}$$

Where *MNDSA* is the average MND surface area.

Order Score: this part was incorporated in this programme with permission from Jo Bruusgaard, University of Oslo (Bruusgaard *et al.*, 2003). Order score utilises the already known nearest neighbour average distance, fibre radius and fibre length to produce an idealised cylinder. Using these parameters, the experimental average distance of nearest neighbour is then compared with simulated random and optimal nuclear arrangements on the cylinder. As this part of the script was not coded by the author, only the core formula will be presented here. A full description of this part, written by Andreas V. Solbrå, Jo Bruusgaard's collaborator who had coded the order score script, may be found in Appendix 1 and Appendix 2.

$$g(M_E, M_R, M_O) = \frac{M_E - M_R}{M_O - M_R} \tag{25}$$

Where the mean experimental, random and optimal nearest neighbour distances are denoted by M_E, M_R and M_O, respectively.

Ultimately, the programme collects all the results and copies them into two separate Microsoft Excel files; one that summarises the calculated information from all the previously analysed fibres and one for the specific fibre.

3.5.1.2. Tests of data reliability

Several crucial tests have been added to the programme, to avoid errors in the data. Noteworthy, the order of tests below is not representative of the order in the script.

Discarded fibre

The script tests whether the fibre chosen for analysis had been discarded. If it had indeed been discarded, the programme adds a row of zeros to the collective data file, to state the fibre had been discarded. This way, the user is aware of fibres that are discarded when considering *n* numbers for the study and data about a specific fibre is not missing. This parameter was useful for monitoring the physical condition of the muscle bundles and their associated fibres (the main reason for discarding of fibres).

Discrepancies between fibre depth and nuclear organisation

Nuclei are typically situated at the periphery of muscle fibres. Assuming a fibre exhibits numerous nuclei, it would be likely that the distance (in the *xz* plane) between the top nucleus and the bottom nucleus should be roughly similar to the distance between the top and bottom surfaces of the fibre. Therefore, in such situations, it would be possible to infer that the axial distance from top-bottom nuclei would be the same as the fibre depth.

The test compares the distance in *z* between the top and bottom nuclei (in the *xz* plane) with fibre depth. If the distance in *z* between the nuclei is greater than the fibre depth, the script converts the fibre depth to the measured *z*-distance between the top and bottom nuclei and adds 3 µm to that distance; 3 µm is the average thickness of a nucleus, as found by the author. As the extracted co-ordinates of nuclei are of the centroid of each nucleus, and nuclei lay under the sarcolemma, 1.5 µm per nucleus must be added to the new measure of fibre depth to make the measurement physiologically relevant.

This course of action was decided upon as the rather large thickness of muscle fibres occasionally produced difficulties to accurately extract the fibre depth from confocal images and the axial distance between top-bottom nuclei adds a second layer of protection from mistakes in such cases.

Previously analysed fibre

After the programme computes all the different variables, a vector with all the results is created. The vector is then compared with the last line of the collective data file; if matched, the user is warned that the fibre had already been analysed and its file will not be updated. This feature is highly useful in preventing errors due to duplication of results. In a large dataset, such a mistake would be almost impossible to find.

Comparison of original summary sheet with the altered

Some bugs may arise in the process of analysis and therefore caution is required prior to overwriting the original sheet. Without such a checkpoint, potential errors may be extremely difficult to recognise and resolve. If the comparison fails, the dataset would not be altered and the user is warned.

3.5.1.3. Discussion

Set-up for mounting single muscle fibres

The greatest benefit of using the *ex vivo* fibre mounting technique described here is the ability to mount up to nine single muscle fibres on the same set. This significantly shortened the time of image acquisition, in comparison with the *ex vivo* technique used by Cristea *et al.* (2010), which studied one muscle fibre at a given time. This technique additionally has the benefit that all muscle fibres on the same set shared the same treatment, thereby reducing variations originating from methodological origins, such as pipetting errors.

Similarly to Larsson's technique, whereby a single muscle fibre is clamped between micromanipulators, the fibres are situated linearly and in parallel with the coverslip, significantly increasing the ease with which images are acquired, as the fibres cannot bend and are found directly above the objective lens. Moreover, such linear positioning has the potential to greatly increase the reliability of MND analysis, firstly as the fibre is linear and, secondly, as sarcomere length can be controlled; however, unlike the method used by Larsson's laboratory, sarcomere length is manually adjusted and requires significant human dexterity and practice to perfect the technique. Nevertheless, once practised, high precision of mounting with a rather fixed sarcomere length is attainable. In this regard, it would have been beneficial to alter the set-up invented here to include micromanipulators for each fibre, or a system of micromanipulators

that could be used on each single muscle fibre prior to clamping, to standardise sarcomere length in a more precise manner that requires lower level of skill on the part of the scientist.

Lastly, also similarly to Larsson's technique, the same muscle bundle can be used for studying nuclear organisation and measuring functional physiological parameters of single muscle fibres, as only some of the fibres in a bundle are isolated for the purpose of studying nuclear organisation.

Reliability of analysis

The inclusion of various tests had prevented numerous human errors, which are an unfortunate consequence of handling large databases. Apart from the manual extraction of nuclear co-ordinates, the script does not require any user input other than the location and name of the file to be analysed. This way, the data is protected from human error from the moment the programme is run on a file. Consequently, all the data is operated through the exact same pipeline, which guarantees homogeneous handling of the data.

Speed of analysis

Another major benefit of using the MATLAB script is speed. It had immensely shortened and improved data collection for this project. On average, without the programme, it had taken up to 5 hours to analyse a single muscle fibre, or up to 2 hours when using Excel spreadsheets with built-in formulae. Using this programme, it is possible to extract up to 29 different parameters on each muscle fibre in 3-20 min, whilst minimising human error considerably. This has permitted an analysis of thousands of fibres over the period of this PhD and significantly reduced the workload that was required for each part of the project. Large *n* numbers were therefore possible to collect, with a significant reduction in error.

Semi versus fully automatic analysis

As explained in section 3.5.1, this method was decided to be semi-automatic and not fully automatic for methodological reasons, i.e. the sub-optimal microscope available to the author and the rudimentary coding abilities of the author at the time this programme was developed. Due to such limitations, it was decided that co-ordinates should be acquired manually and only then allow the programme to compute the data, rather than produce a programme for image processing. This MATLAB script was more reliable than any image processing script attempted

by the author. Nevertheless, the existence of such limitations did not prevent the author from bidding to improve the method, as described below.

Early in this PhD, new filter sets, lamps and liquid light guides were purchased to optimise the light path to the sample. These were all purchased with the intention of improving the optical path through the microscope and because using a liquid light guide can increase the uniformity of illumination across the field of view (Nolte *et al.*, 2006; Waters, 2009). This action has increased the SNR of images and the ability of the illumination to penetrate the fibres. It was additionally aimed to purchase a new light source, LEDs, to replace the mercury halide arc lamp used as the illumination source, alas it could not be afforded. This could have enabled the simultaneous use of far-red dyes to tag F-actin in single muscle fibres, e.g. Alexa Fluor® 647 phalloidin (Invitrogen™), and red-shifted dyes to tag nuclei, e.g. SYTO™ 85 (Invitrogen™), thereby greatly enhancing the tissue penetration and point spread function (PSF). It was believed that such dyes would have resulted in improved image quality, possibly simplifying image processing to the extent that an image processing script could be achieved; though, of course, the most significant improvement in image quality would have resulted from the use of a more suitable microscope for the task (e.g. multi-photon microscopy).

It is noteworthy that deconvolution of images was tested, to resolve some of the light scattering. However, while inarguably the images were easier to process, deconvolution is a lengthy process. This is especially true for thick samples, the primary samples of interest for deconvolution, as processing of each stack of images, which contains up to 100 images per channel, means processing of up to 200 images per muscle fibre. Deconvolution of each fibre could take up to 1 hour under these conditions (depending on computer power), which, if results were superior to those acquired previously, might convince one to follow this route of analysis. However, performing deconvolution produced results that were similar to the method of processing matrices. Thus, though high SNR images that had indeed enabled automatic processing were obtained using deconvolution, there was no clear benefit to the accuracy of the results, whilst the process was significantly prolonged. It was thence decided to keep the method in its current state.

A comparison was conducted between the microscope used here and other more suitable microscopes (e.g. laser scanning confocal microscope) – for that, the same fibre was imaged sequentially in all microscopes, on the same day. Although at first glance the acquired images

indeed appeared dissimilar, mainly in the *xz* plane (better PSF), analysis showed no significant difference between them (<5%). Whilst analysing the fibres, blindness to the result of each fibre was ensured (it is required to open the Excel file to see the results from analysis). Nonetheless, the images were probably possible to analyse using image processing, which could have simplified analysis had the microscope been available for constant use.

It is certainly interesting that results were not dissimilar when using the spinning disk microscope and deconvolution of its acquired stacks, or a more suitable microscope. This could be interpreted in several ways. Firstly, it could be attributed to the author's experience in viewing images acquired by the spinning disk microscope and to the latter's adequate ability for the task. In such a case, a better microscope may have produced more accurate images, but not better interpretation, as the interpretation of fibre depth lays with the person performing the analysis. Nevertheless, though the analysis of images acquired using various microscopes was unbiased in the sense that the results were not known to the author at the time of analysis, it is possible that the analysis was indeed bias because the same person analysed the images. Though even in such a case, the superior microscope should not have allowed for personal interpretations, due to its ability to accurately represent ground truth, leading to results that were different to those acquired by the spinning disk, had the interpretation of the latter been inaccurate; that is assuming the ability of the superior microscope was sufficient for representing ground truth. Thus, it is possible that the experience of the author may have contributed to the lack of differences between microscopes and that the microscope was suitable for the task.

Another explanation for the similarity between the results could be that the spinning disk microscope was indeed suitable for the task and the ability of the author was irrelevant, as the initial resolution requirements were quite low. For instance, typical measurements of nuclear organisation in mice are such that the distance between adjacent nuclei is ∼20-40 μl; hardly a high resolution requirement. In cases of nuclear aggregations, the resolution of the microscope could be challenged, however, even then, most nuclei in the conditions studied in this thesis were not aggregated. It might be then that very subtle changes in organisation cannot be recognised by this method. It is noteworthy here that this method has not been benchmarked using dummy samples of defined size. Therefore, the actual resolution achieved by this method is unfortunately unknown. Thus, it is possible that there was in fact a difference between the

images acquired by the various microscopes, however, as the conditions studied in this project were not of nuclear aggregates, the superiority of the better microscopes was not reflected in the results.

Lastly, the fact that nuclei are manually selected may produce an error sufficiently large to hide subtle differences, as nuclei are selected based on their appearance, i.e. best focus of the small fluorescent dots within DNA wherein DAPI binds, as opposed to an automatic segmentation method to find centre of mass. Thus, the ability to select the appropriate "centroid" is, firstly, based on the ability of the microscope to represent ground truth and, secondly, though not detached, on the *z* steps, which means the accuracy of choosing the "centroid" is depended on whether the location of best focus is on or between the *z* steps.

For all the reasons mentioned above, it is clear that the method could greatly benefit from switching the semi-automatic approach to fully automatic image processing. This should be accompanied by benchmarking the results using dummy samples of defined size.

Use of Fiji to replace Metamorph

The method worked well using Metamorph. However, Metamorph is not a freeware and thus, data analysis is limited to a specific computer. As a result, if a couple of students, for instance, wish to analyse fibres simultaneously, two licenses of Metamorph are required, one for each machine. This reduces the efficiency of the laboratory as a whole.

The author has lately replaced Metamorph with Fiji. The tools used in Metamorph to mark locations of pixels are simple and are not a unique feature of Metamorph. In Fiji, specific pixels were marked using the "Multi-point" tool, with small yellow crosshairs. All options found in "Set measurements" were removed (leaving only *xyz* and counter). Once all nuclear co-ordinates were extracted, followed by fibre and sarcomere co-ordinates, all in one table, "Measure" was selected and the results were saved as a ".csv" file.

Processing in MATLAB remained simple, as the programme was adapted to process the .csv file instead of the .xlsx file that was used with Metamorph. Location of groups (nuclei, fibre and sarcomere) of co-ordinates in the list was always constant. Sarcomere co-ordinates were extracted from the two bottom lines in the list, as sarcomere co-ordinates are always last to be extracted. Once removed from the overall list of co-ordinates, the final six co-ordinates are of the fibre (four for *xy* margins and two for *z*), leaving the list with only nuclear co-ordinates.

Ultimately, nuclei, fibre and sarcomere co-ordinates are separated into three separate variables. The rest of the MATLAB script remained the same.

It is strongly believed that using Fiji to extract co-ordinates should replace Metamorph. From the scientific perspective, no difference would be observed; nonetheless, this is not the sole parameter to consider when developing a method. Fiji is free, less taxing on the computer (Fiji has a minimalistic layout) and can be used on any computer. Therefore, anyone could use it from any location using a laptop and the efficiency of the laboratory could be significantly augmented with a virtually infinite number of students analysing fibre co-ordinates from home. Fiji is therefore the currently used method for analysing nuclear spatial organisation of single muscle fibres in the Ochala laboratory. As it was not used to acquire co-ordinates for this project, a walkthrough of its MATLAB script is not provided.

3.5.1.4. Future directions

The method developed here to calculate 3D nuclear organisation in single muscle fibres has achieved desirable results. However, it could benefit from various improvements. Firstly, it would be beneficial to alter the set-up invented here to include micromanipulators for each fibre, or a system of micromanipulators that could be used on each single muscle fibre prior to clamping. This would standardise sarcomere length in a more precise manner and the method would not require such a high level of dexterity on the part of the scientist.

Moreover, as previously stated, the future of the method described here relies on full automation. Analysis would therefore entail direct image processing instead of processing of matrices of co-ordinates. As a result, batches of images could be processed automatically without the requirement for user input and supervision. This type of analysis could greatly benefit the high-throughput imaging developed here. At the moment, analysis is the lengthy part of this technique, however, if analysis is automated, the efficiency of the method could significantly increase and thence, the Ochala laboratory as a whole.

In order to realise that, greater light penetration through tissue and better representation of ground truth are warranted, as stacks of higher quality and precision would be easier to analyse using automatic image analysis algorithms. This could be achieved using a variety of approaches, including using a microscope with greater tissue penetration (e.g. multi-photon), for reasons mentioned previously in this report, as well as by using far-red dyes to tag F-actin in

single muscle fibres, e.g. Alexa Fluor® 647 phalloidin (Invitrogen™), and red-shifted dyes to tag nuclei, e.g. SYTO™ 85 (Invitrogen™). Using longer wavelengths, autofluorescence would additionally be reduced, as various cellular structures that emit fluorescence at shorter wavelengths (360-560 nm) could be avoided (Viegas *et al.*, 2007; Oliveira *et al.*, 2010; Ntziachristos, 2010). Lastly, a better objective lens should be used, preferably a Plan apochromatic, as they correct for spherical and chromatic aberrations to the highest degree, as well as flatness of field (Murphy & Davidson, 2012; Ross et al., 2014). Importantly, for a true quantitative nature, the results acquired should be benchmarked using dummy samples of defined size.

Following, automatic processing could commence. Currently, the greatest difficulty is image segmentation. If the acquired PSF is improved for both the muscle fibre and nuclei, automatic segmentation would become much simpler and lead to sub-resolution accuracy of a centre of mass. This would represent the true centroid of both and thus, the accuracy of nuclear organisation and fibre depth measurements would greatly increase. Altogether, analysis would become not only more accurate, but also faster.

3.5.2. Nuclear pixel intensity

Upon completion of the method discussed above, an interest in global nuclear transcriptional activity had emerged. Therefore, a second script was developed to analyse nuclear pixel intensities in confocal images of single muscle fibres. In contrast to the programme for nuclear distribution, this programme was developed directly in Fiji (Schindelin *et al.*, 2012; Rueden *et al.*, 2017) and is capable of processing stacks of images of single nuclei. The MATLAB script mentioned in the previous section runs calculations on previously-acquired co-ordinates of nuclei. Therefore, MATLAB is unaware of the origin (images) of those co-ordinates. Conversely, the Fiji script discussed below reads the original images to analyse data. Thus, unlike the MATLAB programme, the Fiji script is specifically aimed at image processing and, depending on the quality of images, may be semi or fully automatic.

Every set of images has a unique set of characteristics, which to handle requires a certain level of creativity on behalf of the programmer, as well as a significant level of flexibility of the coding language. The nature and relative ease of creating macros in Fiji enables just that.

Image processing of pixel intensities encompasses knowledge in biology, microscopy and computers and is therefore not a simple task. Importantly, it requires great care in every step of the process, from the muscle dissection phase, all the way to the results, for mistakes along the way may lead to false conclusions. Therefore, in essence, the more knowledgeable and experienced the researcher in these topics, the more reliable will be the conclusions. The following section will provide background to image processing of nuclei in single muscle fibres.

3.5.2.1. Imperfections in digital images

Raw images of fluorescence microscopy suffer from various types of imperfections inherent to the sample and camera. They require corrections before any quantifications of pixel intensities may take place. The main corrections performed in this project were for camera offset, noise, non-uniform illumination and background.

Camera offset

When light is completely blocked, i.e. zero photons, from reaching a camera, the average value of pixels in an acquired image is never zero. This is done to allow a user to capture fluctuations in intensity that result from noise; if an offset is not present, these fluctuations would be cut-off, thereby eliminating information from the image. Therefore, cameras have a certain offset to increase their pixel values so data is not cut-off from the image (Lambert & Waters, 2014). In the camera used here, offset was constant and measured as 165 greys. Offset can be removed from an image by subtracting a dark image, i.e. image acquired in complete absence of light, from the original image.

Types of noise

The aim in quantitative microscopy is to quantify the ground truth of a sample. However, if a sample is imaged twice, using the same configurations, measured pixel intensities will not be the same. Such changes are due to noise originating from the sample and camera. The main four types of noise found in raw confocal images are Poisson noise, read noise, dark (thermal) noise and fixed-pattern noise.

Poisson noise

Poisson noise results from the fact that the arrival of photons at the camera is a stochastic process. Poisson noise encompasses both signal and background photons (Waters, 2009). It cannot be altered with camera exposure or number of photons collected and as the process is stochastic, it cannot be removed from the image. However, its effects can be limited by increasing the SNR of the image, as its share in the total signal intensity becomes relatively lower than the signal itself (Lambert & Waters, 2014).

Read noise

Read noise results from imprecision in the measurement of each photoelectron charge packet (accumulated charge in each photodiode of the camera chip) by the read amplifier in a charge-coupled device (CCD) camera. It is the predominant type of noise in cooled CCD cameras (Waters, 2009). Read noise increases with read rate, as a faster reading rate reduces the available time for measurements. Like Poisson noise, read noise cannot be reduced, as it is independent from camera exposure and number of collected photons. Its effects can be limited by increasing SNR (Lambert & Waters, 2014).

The camera used in this project is officially documented with read noise of 8 e^- root mean square (RMS) at 20 MHz, i.e. the standard deviation (SD) of the mean of each pixel is 8 e^-. According to Waters (2013: 142), "For live-cell fluorescence imaging, readout noise of eight electrons or less is acceptable". Readout noise can be translated into grey values:

$$G = \frac{e^-}{\left(\frac{Full\ well\ capacity}{\max grey\ scale\ value}\right)} \quad (26)$$

Where G is the grey scale value, e^- is the number of electrons of noise (8 in my camera), full well capacity per pixel in my camera is 15,000 e^- and max grey scale value in the 12-bit camera used here is 2^{12} = 4,096 greys. Therefore:

$$G = \frac{8}{\left(\frac{15{,}000}{4{,}096}\right)} = 2.185$$

According to this value it is expected that each pixel in an image had a SD of 2.185 greys, which contributed to the overall noise.

Dark (thermal) noise

Dark (thermal) noise results from heat-induced release of electrons in the silicon chip. It is only considered to be an issue with cameras that do not run under cold temperatures (Lambert & Waters, 2014). Cooled CCD cameras have negligible thermal noise and are therefore preferable for pixel quantification studies (Waters, 2013). The camera used here operates at -30°C and has a negligible thermal noise of 0.05 e^-/pixel/second.

Fixed-pattern noise

Fixed-pattern noise results from the different efficiency of each photodiode to collect photons and increases in direct proportion to the signal (Janesick, 1997). As this type of noise is spatially consistent, it is called fixed-pattern. Fixed-pattern noise can be enhanced by alien particles in the light path (e.g. dust) and as such, consistent non-uniform illumination may also be considered as fixed-pattern (Lambert & Waters, 2014). As fixed-pattern noise is spatially consistent, it may be corrected using flat-field correction (Lambert & Waters, 2014).

Illumination non-uniformity

Because of the way light travels from its source, a completely even illumination of a sample is unlikely. This may be seen not only in microscopy, but also in many backlit screens (e.g. phones, computer monitors), where the non-uniformity manifests as darker areas in the screen, due to their distance from the light source. In microscopy, non-uniformity of illumination may manifest as the appearance of one part of the image brighter from the other, when in reality, such difference does not exist in the biological sample (Murray, 2013). This must be corrected.

As seen in Figure 3.17, illumination in this example is brightest in the top centre and weakest at the bottom left. It is likely that that the illumination source is not calibrated perfectly in this image and the lamp should probably be lowered slightly and aimed more towards the left side of the image. In the microscope used here, a liquid light-guide was used in conjunction with a light source that does not required calibration (Waters, 2009). Though this may produce an image with illumination that is more even, it will not resolve the gradual reduction in light

intensity from the centre of the light beam to the periphery. Flat-field correction is required to correct this deformity.

Background

A common source of background in fluorescence 3D microscopy is the sample itself (e.g. autofluorescence) and out-of-focus light (Waters, 2009). Background in confocal images should be removed as it adds to the value of each pixel in the image; even those within the area of interest (Figure 3.18). In order to reduce out-of-focus light in images, an algorithm-based process called deconvolution was performed on all stacks prior to analysis of pixel intensities; background subtraction near-object was performed simultaneously. Near-object background subtraction is considered most accurate, as it ensures important information is not subtracted from the object of interest (Waters & Wittmann, 2014). If background is removed, the SNR of an image would increase.

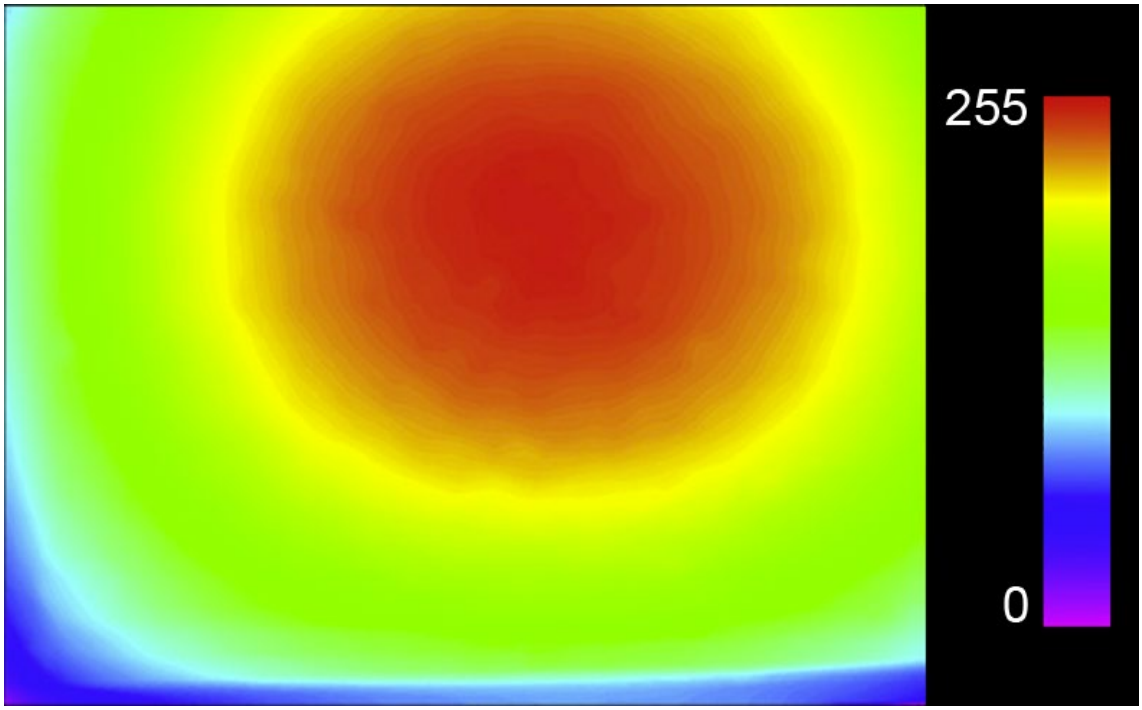

Figure 3.17: Illumination non-uniformity in a spinning disk confocal microscope
Image of a uniformly fluorescent thin specimen, presented as pseudo-colour (spectrum). Adapted from Murray (2013). Copyright © 2013, John Wiley and Sons.

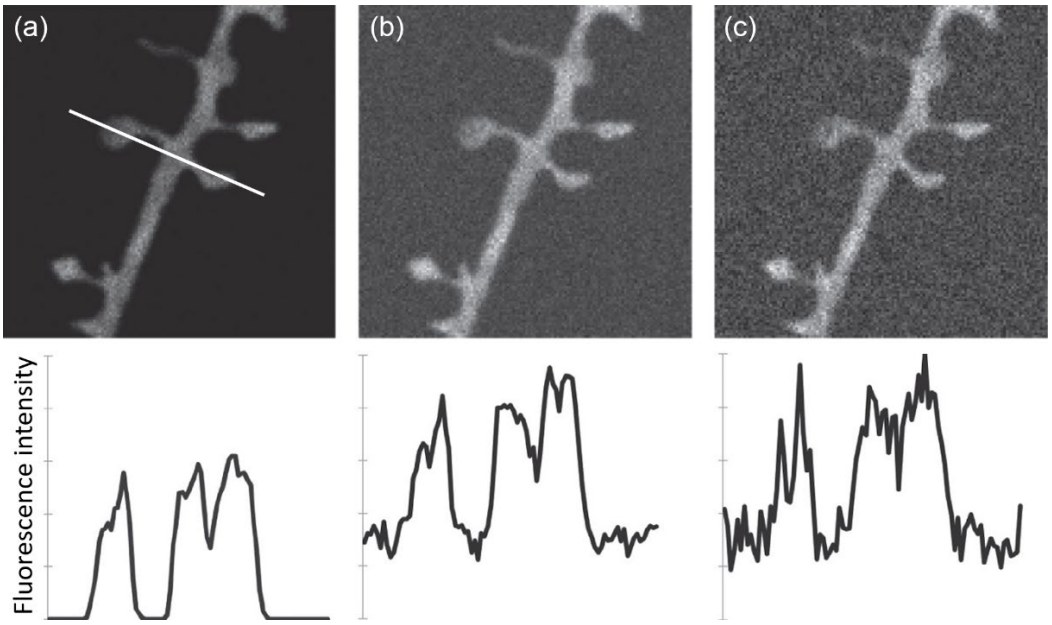

Figure 3.18: Effect of background and noise in a confocal image
Simulated images and corresponding line scans with (a) signal of 150 photons/pixel and Poisson noise, (b) signal of 150 photons/pixel, 50 photons/pixel background and Poisson noise, and (c) signal of 150 photons/pixel, 50 photons/pixel background, Poisson noise, and 10 e^- RMS read noise. Line scans represent the same pixels in each image (white line in a). Adapted with legend from Waters & Wittmann (2014). Copyright © 2014, John Wiley and Sons.

3.5.2.2. Correcting imperfections in digital images

In an ideal scenario, any alterations in fluorescent intensity would be purely due to changes in fluorophore concentration. However, all the non-uniformities discussed above contribute to changes in pixel intensity. Such imperfections should therefore be removed prior to quantification of pixel intensities.

Noise, offset and illumination non-uniformity

As discussed above, thermal noise in the camera used for this project was negligible and can therefore be disregarded as an imperfection. The effect of Poisson and read noise have both been minimised by ensuring the SNR of images was high. This was done in three time-points: sample preparation, imaging and deconvolution.

The sensitivity, or efficiency, of each photodiode is constant. Therefore, the variability in spatial sensitivity is constant in an image and as a result, pixels can be adjusted to a reference,

by flat-fielding the image. Dividing images by a flat-field image additionally corrects non-uniform illumination. Camera offset was removed during the process.

The following formula was used for flat-field correction (Waters & Wittmann, 2014):

$$I'(x,y) = \frac{I_{image}(x,y) - I_{bkg}(x,y)}{I_{ref}(x,y) - I_{bkg}(x,y)} \times \frac{\sum_{x,y}\left(I_{ref}(x,y) - I_{bkg}(x,y)\right)}{xy} \qquad (27)$$

Where *I'(x,y)* is the resultant image that is corrected for dark and flat-field, $I_{image}(x,y)$ is the processed image, $I_{bkg}(x,y)$ is the dark image and $I_{ref}(x,y)$ is the flat-field image.

Each pixel in an image, I_{image}, and flat-filed image, I_{ref}, firstly goes through dark-field subtraction by its corresponding pixel in the I_{bkg} image. The pixel in image I_{image} that has been dark-field corrected is then divided by the corresponding pixel in the flat-field image, I_{ref}. Once the pixel is corrected, it is presented as a ratio. To obtain a similar range of intensity, the resultant pixel ratio value is multiplied by a scaling factor, i.e. the average intensity of the flat-field image, I_{ref}. To avoid data clipping, the entire calculation was performed as a floating point. The result is a stack of images that are corrected for fixed-pattern noise, evenly illuminated and lack camera offset.

Deconvolution and SNR

Following the corrections discussed above, SNR of the image stacks can be increased by deconvolution and near-object background removal, using the software Huygens Deconvolution (Scientific Volume Imaging). Removal of background had also reduced the interference of Poisson noise, as Poisson noise equals the square root of signal photons, plus background photons (Waters, 2009).

Deconvolution is an excellent method to reduce out-of-focus light, subtract background and thence, reduce the interference of Poisson noise in an image. On balance, in contrast to the author's decision to avoid deconvolution for studying nuclear distribution, it was beneficial to deconvolve the images in this part of the project, despite of the significant amount of time it took to process each stack (~30 min).

The benefit of using Huygens Deconvolution, as opposed to other available solutions, was not only for the scientific perspective, but also for speed. The software can run heavy computations in parallel on the thousands of cores available on the graphics processing unit (GPU), instead of using the central processing unit (CPU) of the computer, which in most laboratories only holds 4-8 cores. In the analysis computer used for this project, the CPU had 4 cores (Intel Core i7-4190) and the GPU was GeForce GTX 745 (Table 2.4). According to the Huygens' benchmarking system, using this hardware combination, running deconvolution on the GPU should result in an increase in speed of ~4x that of the CPU. When considering high *n* numbers, this can lead to a reduction of days from analysis.

3.5.2.3. Systematic description of the method

Two separate scripts were written to process all image stacks. The approach was simple: firstly, correct all images for non-uniformities as discussed above, then prepare the stacks for deconvolution, run deconvolution and use the resulting corrected stacks for analysis. Original scripts may be found in Appendix 3.

Dark-field and flat-field corrections

Stacks of images for each nucleus, and each channel, were saved as separate metafiles during acquisition. There was therefore no need to split channels at the beginning of processing. All images in a folder were batch processed. The process below is described for a single channel. Where additional channels were used, the process was repeated for that channel.

Dark and flat-field images were produced prior to running the script. Using Fiji, the dark-field image was subtracted from the flat-field image, to correct the latter for noise and camera offset; both the dark-field and dark-corrected flat-field images were used later in the script.

Folder and suffix definitions: a dialogue is created for the user to select the input and output folders. The suffix depends on the channel to be processed (e.g. DAPI) and requires the file extension (e.g. DAPI.TIF).

Dark and flat-field images: a dialogue is created for the user to select the dark-field image, followed by a dark-corrected flat-field image. The latter image depends on the channel to be processed, as a different flat-field image was created for each channel.

Processing of folder: the input folder is scanned for files containing the suffix and a file list is produced.

Processing of file: nested within the function for processing of folder. When a file containing the appropriate suffix is found, the 'processFile' function is initiated as below.

Dark-field correction: the chosen dark image is opened and stored using its name and ID. A stack of images opens and, using the built-in function 'imageCalculator', the dark-field image is subtracted from each image in the stack.

Flat-field correction: using the 'Calculator Plus' function, each image in a stack is divided by the dark-corrected flat-field image and multiplied by the mean pixel intensity of the flat-field image. The entire calculation is done in floating-point.

Save and exit: the corrected stack of images is then saved as 16-bit tiff in the output folder with its original name, plus the suffix 'backflat_corr'. Though this requires extra storage space, it is important to keep the original images. All open images are then closed and the process can repeat on a new stack of images.

Cropping of stacks

Each stack of images was acquired with an *x,y,z* area much larger than that of a nucleus, as it was more convenient during acquisition. As the next step is rather lengthy (deconvolution), it was decided to crop each stack in Fiji to reduce the size of files, thereby quickening the deconvolution. This was done manually for each stack. It was not performed prior to the previous corrections, as the area of each image would not match that of the correcting images. Thus, corrections could not have been performed.

Deconvolution

For each wavelength (e.g. DAPI, Alexa Fluor 594), stacks of corrected images were fed into the software to undergo slice-by-slice deconvolution. A template containing information about the microscopy set-up (e.g. illumination wavelength, fluorophore wavelength, objective etc.) was produced and applied to each wavelength. PSF for each wavelength was estimated from an average of a training set of 50 images. Deconvoluted stacks of images were saved as 16-bit tiffs. See Figure 1.22 and Figure 1.23 in the literature review for examples of deconvolution.

Pixel intensities

Once pre-processing is completed, the rest of the process is rather quick. Speed of analysis greatly depends on the quality of images. Very high-quality images, i.e. no background and high signal, are the easiest and most accurate to compute. The script written for this in Fiji is fully automatic and uses auto-threshold for segmentation of regions of interest (ROIs). Images that cannot be processed with auto-threshold should be analysed manually; however, even in such cases, once threshold is performed manually the rest can be run in a macro.

Several assumptions are made in order for the script to run successfully. Firstly, it is assumed that the input folder contains images of two channels that were saved as separate files following deconvolution. Therefore, the script expects to read images that were corrected for non-uniformities. Secondly, channel 1 should contain a corrected stack of images of a nucleus stained with a bright nuclear stain (e.g. DAPI or Hoechst). It is this channel from which the ROI of the nucleus is produced and a bright reliable stain is extremely important for enhancing the reliability of the ROI. Once the script is run, the following major steps take place:

Set configurations: as the aim of this script was that it could be used on any computer, and computers do not necessarily share the same Fiji settings, certain configurations must be set prior to analysis. Three categories of configurations are set: binary options, measurements to perform on images and structure of final results table.

Dialogues: four simple dialogues are created for the user to select the input folder, output folder, channel 1 suffix (e.g. DAPI.tif) and channel 2 suffix (e.g. AF594.tif).

Processing of folder: the input folder is scanned for files containing channel 1 suffix and a file list is produced.

Processing of file: nested within the function for processing of folder. When a file containing the appropriate suffix is found the 'processFile' function is initiated as below.

Maximum intensity *z* projections (MIPs): stacks are read one channel at a time and a MIP image is produced for each channel (Figure 3.19a). The process entails "flattening" of a *z* stack into a single 2D image. In the process of producing a MIP image, for each *x,y* location, the brightest pixel in the axial dimension is chosen to remain in that location in the resulting image; all lower values are discarded. The result is that only the brightest pixels, through *z*, in each *x,y*

co-ordinate, are transferred to the new MIP image. A disadvantage of this process is that it may increase background. However, as background had already been removed during deconvolution this was not an issue.

Creation of ROIs: the MIP image of channel 1 (e.g. DAPI) is duplicated. The duplicate is thresholded to an 8-bit binary image (Figure 3.19b), wherein nucleus = 1 (white) and background = 0 (black). Using Fiji's ROI Manager, an ROI of the nucleus is created and saved in the manager (Figure 3.19c).

Measurement of nuclear pixel intensities: once an ROI is saved, it is applied onto the MIP image of channel 1 (Figure 3.19d). Measurements are then made within the region and summarised in a results table (Table 3.1). The same is then done for channel 2. The following measurements are made: min, max, mean and SD of pixel intensity.

Save and exit: for each channel, the ROI-containing MIP image is saved as 16-bit tiff in the output folder with its original name, plus the suffix '_ROI'. All open windows are then closed and the process can repeat on new stacks of images. Final results for each channel are saved as separate '.csv' files, corresponding to their respective channel.

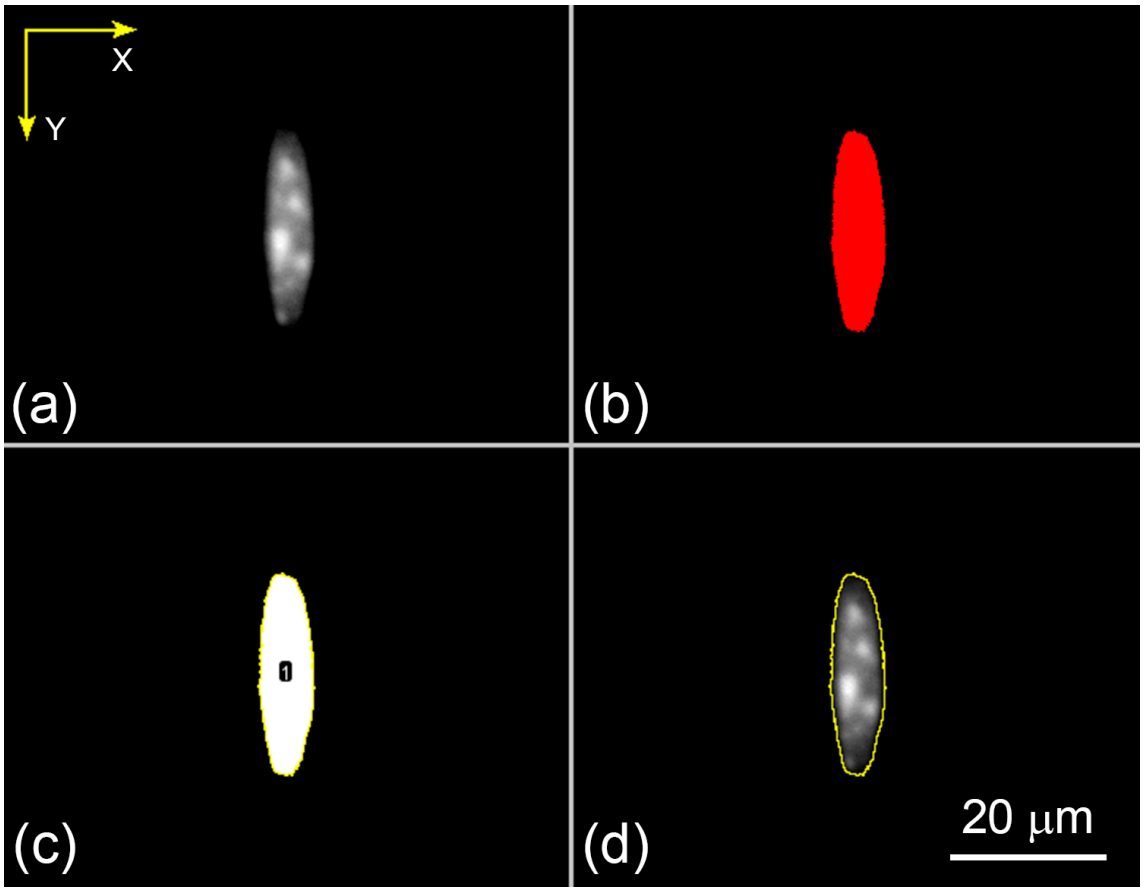

Figure 3.19: Method for measuring nuclear parameters
(a) MIP of an image stack acquired with a spinning disk confocal microscope, Zeiss Fluar 100x/1.30 objective lens. Nuclei were stained with DAPI. Image was corrected for background and uneven illumination as described in the text; (b) Duplicate image of (a) with a threshold mask of 3-255 greys (8-bit); (c) Binary image with a ROI created with the 'Analyse Particles' function in Fiji; (d) ROI from image (c) applied to the original image in (a). Measurements from this image can be found in the table below.

Table 3.1: Pixel intensity measurements acquired from figure above

Parameter	Value
Label	Nucleus
Min	1
Max	654
Mean	232.2289
SD	142.1594

3.5.2.4. Discussion

The scripts above are examples of codes used in this project to measure global nuclear transcriptional activity from confocal images of single myonuclei. The scripts were successful in shortening the time of pre-processing and processing of stacks, due to their automation and the ability to process folders in batch. They were, therefore, used as the core to many studies in the Ochala laboratory, both for pre-processing and for pixel quantification.

The greatest advantage of these programmes is their high level of adaptability and speed. The fact that the method of quantifying pixel intensities is split into different scripts provided great flexibility between projects and requirements, as different parameters were adjusted individually without affecting the rest of the script. Depending on the project, the scripts were adapted to accommodate the necessary changes, resulting from using different microscopes, stains and users.

Ultimately, high-speed analysis is predominantly made possible by high quality of images and strong computer hardware. Better quality of images allowed for full automation of analysis and therefore the time it had taken to initially optimise quality of samples was well-spent. Lower quality images required a more manual approach and additional time. In such cases, the script was adapted accordingly, to begin after manually thresholding the images; the rest of the process was the same as in full automation.

Processing of data with this method was significantly different to that of nuclear organisation. The data analysed for nuclear organisation was matrices, whereas here image stacks *per se* were analysed. Matrices are very small in size (a few kilobytes) and their analysis is mainly performed on the computer's processor. Deconvolution requires more significant computations, which could indeed be performed by the processor, however, as it was chosen to use Huygens Deconvolution, it was possible to divert the task to the much faster memory of the graphics card and hence, remarkably enhance rate of analysis.

Both deconvolution and the script for quantifying nuclear parameters, i.e. image processing, required high-speed file reading and writing. Image processing is challenging for a traditional hard drive, as its read/write rate is not up to scale, when compared with the processor, memory or graphics card. A slow hard drive, therefore, produces a bottleneck on rate of analysis, as it limits the speed of file processing. As mentioned in section 03.5, the slow

read/write rate of the traditional hard drive (155/136 MB/s) originally found in the analysis computer was proving to be a significant hindrance to speed of analysis. To alleviate the computer off the bottleneck, the primary hard drive was replaced with a solid-state drive with a read/write rate of 540/520 MB/s (>3x speed) and only used the hard drive to retain unused data. The scripts were additionally optimised to open one stack at a time and keep only the necessary files open, instead of closing all only at the end of analysis. This was done to reduce the memory requirement.

Running the programme this way had significantly increased speed of analysis during image processing. Interestingly, a number of bugs, presumed to have originated from unsynchronised reading/writing of files, were also eliminated. If that was indeed the case, it was a bug in Fiji itself and not the code created by the author, as the situation was resolved following the change to a solid-state drive. If the issue had not been resolved by replacing the hard drive, the function 'wait()' would have had to be added every time an image is read/written, in order to halt the running of the script for a certain number of ms until loading/saving of the image is complete.

3.6. Conclusion

New methods for imaging and analysing confocal images of single muscle fibres and their nuclei have been described in this thesis. Similarly to other studies (Shah & Lieber, 2003; Zhang *et al.*, 2009; Cristea *et al.*, 2010; Chapman *et al.*, 2014), the set-up used in this project for mounting single muscle fibres prevented any movements of the fibres and therefore simplified and shortened image acquisition. To the author's knowledge, hereto, no other studies have used a set-up that permits imaging of more than one single muscle fibre at a time. Future directions should focus on adding micromanipulators to the set-up, converting the method described here to a fully automatic image processing pipeline and compare results against an object of known size to validate the actual resolution. Altogether, these are thought to greatly increase the accuracy and speed of the method. A fully-automated method was also created for measuring global nuclear transcriptional activity from confocal images of single myonuclei. The programme follows a standard pipline for image processing of such images and acquired the desirable results. Both the methods described in this chapter will be used in the following chapters.

Chapter 4: Effects of prelamin A on mouse myonuclear and myofibre function

4.1. Introduction

The current thesis endeavoured to characterise the connection between ageing and disuse-related misprocessing of lamin A with myonuclear organisation and muscle weakness in isolated single muscle fibres. Premature ageing syndromes share molecular and cellular mechanisms with many ageing-associated diseases (Janin *et al.*, 2017; Kubben & Misteli, 2017). Thus, the work performed in this chapter aimed to use mouse models of Hutchinson-Gilford progeria syndrome (HGPS), wherein lamin A is misprocessed, a condition noted during normal ageing (Scaffidi & Misteli, 2006; López-Otín *et al.*, 2013; Kubben & Misteli, 2017), to investigate whether a link indeed exists between myonuclear organisation and muscle weakness in premature ageing conditions and ageing; results from this chapter were recently published (Levy *et al.*, 2018).

Biological ageing encompasses complex dysfunctional cellular processes with unclear underlying mechanisms, including a potential involvement of alterations at the nuclear level in a wide range of tissues (Scaffidi & Misteli, 2006; López-Otín *et al.*, 2013). Normal nuclear function requires lamin A, an intermediate filament scaffold protein of the inner nuclear membrane (INM) that is expressed from *LMNA* by alternative splicing, noted to regulate nuclear integrity and architecture, as well as chromatin organisation (Shumaker *et al.*, 2006; Broers *et al.*, 2006; Uhler & Shivashankar, 2017). Unlike other lamins, lamin A is firstly translated as a

precursor, prelamin A, which to mature must undergo trimming of the last 15 amino acid residues from its C-terminal domain by zinc metallopeptidase STE24 (ZMPSTE24) (Michaelis & Hrycyna, 2013). Misprocessing of lamin A can lead to numerous disorders, collectively termed laminopathies (Janin *et al.*, 2017), as described in section 1.4.4 and Figure 1.10.

The main cause of HGPS is abnormal splicing of the *LMNA* primary transcript, most often caused by a *de novo* point mutation within exon 11 of the *LMNA* gene (c.1824C>T, p.G608G) that activates a cryptic splice site. This leads to a deletion of 50 amino acids at the C-terminal domain and to the accumulation of a truncated farnesylated form of prelamin A, called progerin, at the INM (De Sandre-Giovannoli *et al.*, 2003; Davies *et al.*, 2009). However, point mutations in *LMNA* that cause progeria, but do not lead to accumulation of prelamin A variants, such as p.T528M, p.M540T, p.E55K and p.E55G, have also been reported (Verstraeten *et al.*, 2006; Soria-Valles *et al.*, 2016). Autosomal recessive mutations in *ZMPSTE24* that cause HGPS (e.g. N265S) are thought to directly interfere with the catalytic function of ZMPSTE24 (Quigley *et al.*, 2013), reducing its function to 25-30% of a fully functional ZMPSTE24 (Spear *et al.*, 2018), leading to reduced levels of mature lamin A and increased levels of native farnesylated prelamin A (Shackleton *et al.*, 2005).

Interestingly, premature ageing syndromes share molecular and cellular mechanisms with many ageing-associated diseases (Janin *et al.*, 2017; Kubben & Misteli, 2017). Such similarities with ageing are thought to originate from faulty expression of lamin A in multiple tissues, mainly of mesenchymal origin (e.g. skin, bone, adipose and muscle tissue), that leads to accumulation of prelamin A or progerin, as occurs during normal ageing (Scaffidi & Misteli, 2006; McClintock *et al.*, 2007; Rodriguez *et al.*, 2009; Ragnauth *et al.*, 2010; Cristea *et al.*, 2010; Olive *et al.*, 2010*a*; De La Rosa *et al.*, 2013; Kubben & Misteli, 2017; Ross *et al.*, 2018). For a review of the shared mechanisms see Kubben & Misteli (2017). As a significant body of research suggests HGPS and normal ageing share molecular and phenotypic similarities with regards to prelamin A processing, mouse models of HGPS are often used to study the ageing process (Folgueras *et al.*, 2018). These include *Zmpste24* KO mice, which lack Zmpste24 and therefore accumulate farnesylated prelamin A, as well as *Lmna* (G609G) mice, whose mutation activates a cryptic splicing donor site that leads to the accumulation of progerin and share a common transcriptional signature with the *Zmpste24* KO progeria model (Olive *et al.*, 2010*a*; Osorio *et al.*, 2011; Vidak & Foisner, 2016; Folgueras *et al.*, 2018).

At the cellular level, adverse effects of lamin A misprocessing include reduced cell proliferation (Song *et al.*, 2013), reduced cell motility (Booth-Gauthier *et al.*, 2013), deregulation of focal adhesion formation and cytoskeletal tension (Corne *et al.*, 2017), decreased viability and increased apoptosis under mechanical strain (Verstraeten *et al.*, 2008), enhanced cell senescence (Varela *et al.*, 2005), reductive stress and autophagy upregulation (Dialynas *et al.*, 2015), as well as oxidative stress and mitochondrial dysfunction that respectively lead to apoptosis and senescence (Sieprath *et al.*, 2015).

Associated nuclear conditions include aberrant nuclear shape (Fong *et al.*, 2004), reduced nuclear deformation in response to mechanical stress (Dahl *et al.*, 2006), increased frequency of nuclear envelope ruptures (Robijns *et al.*, 2016), altered transcription of mechano-sensitive genes including defected signalling of yes-associated protein (YAP) (Bertrand *et al.*, 2014), DNA damage (Scaffidi & Misteli, 2006), constantly activated DNA damage checkpoints (Liu *et al.*, 2006), unsynchronised DNA endoreplication (Wang *et al.*, 2018), chromosome aberrations (Liu *et al.*, 2005), heterochromatin disorganisation (Nikolova *et al.*, 2004), increased heterochromatin and telomere dynamics (Makhija *et al.*, 2016) and telomere shortening (Gonzalez-Suarez *et al.*, 2009).

A wide spectrum of strategies to correct HGPS-associated defects have been proposed. Noteworthy, blocking the farnesylation of progerin and native prelamin A, using farnesyltransferase inhibitors (FTIs), and therefore, altering their localisation to the nucleoplasm (Wang *et al.*, 2012), has been demonstrated to partially reverse the cellular abnormalities associated with their accumulation on the INM and alleviate the progeria-associated cellular phenotypes in mice (Toth *et al.*, 2005; Yang *et al.*, 2005, 2010; Capell *et al.*, 2005; Young *et al.*, 2005, 2006; Fong *et al.*, 2006*a*; Verstraeten *et al.*, 2008). This has also been confirmed in genetically engineered mice expressing a non-farnesylated version of progerin (Yang *et al.*, 2011). The incomplete rescue by administration of FTIs has been suggested to be due to the FTIs' inability to improve cellular sensitivity to mechanical strain (Verstraeten *et al.*, 2008). Lastly, administration of the FTI Lonafarnib to HGPS patients, the vast majority of which had the typical c.1824C>T; p.G608G mutation in *LMNA*, has been associated with a lower mortality rate after 2.2 years of follow-up (Gordon *et al.*, 2018). Therefore, a growing body of promising therapeutic candidates indeed exists. Nevertheless, the ability of current therapies to alleviate

the progeroid phenotype unfortunately remains rather inadequate (Burtner & Kennedy, 2010; Olive *et al.*, 2010*a*; Harhouri *et al.*, 2018; Mattioli *et al.*, 2019; Piekarowicz *et al.*, 2019).

As discussed in section 1.3, myofibres contain several hundreds of peripherally located nuclei, each controlling protein synthesis in a defined volume of cytoplasm termed the myonuclear domain (MND). Regular positioning of myonuclei is essential for optimal nuclear cooperation, MND size and efficient regulation and distribution of gene products (Qaisar & Larsson, 2014). However, apart from a single case whereby reduced myonuclear distribution was witnessed in single muscle fibres from elderly individuals (Cristea *et al.*, 2010), it is generally unknown whether myonuclear positioning is altered in ageing and HGPS, in humans or otherwise. Moreover, it is unknown whether the severe defects in skeletal muscle contractility and low force-generating capacity found in the HGPS mouse models, *Zmpste24* KO (Greising *et al.*, 2012) and *Lmna* (G609G) (Gnocchi *et al.*, 2011), are somehow related to the existence of nuclear disorganisation and reduced MHC concentration, noted previously in single muscle fibres from elderly individuals (D'Antona *et al.*, 2003; Frontera *et al.*, 2008; Cristea *et al.*, 2010; Greising *et al.*, 2012).

In the current study, it was hypothesised that accumulation of prelamin A in nuclei would alter nuclear number, MND sizes and optimal nuclear positioning, leading to reduced myosin content and disrupted ability of myofibres to generate force. To test this, various genetically engineered mouse models that mimic premature ageing syndromes were used, wherein normal processing of lamin A is disrupted (i.e. *Zmpste24* KO, *Zmpste24*$^{-/-}$ *Hprt*$^{Z24/+}$, *Lmna* KO and *Lmna*$^{G609G/G609G}$). Single muscle fibres were, therefore, isolated and membrane-permeabilised, on which a series of contractile and morphological analyses were performed, including an evaluation of the 3D organisation of nuclei, as described in the previous chapter.

4.2. Methods

4.2.1. Animals

Various female mouse models of lamin misprocessing were used in the present study and were selected based on the severity of the phenotype associated with each genetic condition,

as well as age of morbidity (Table 4.1). The mice were euthanised and the Extensor Digitorum Longus (EDL) skeletal muscles were dissected, as described in section 2.1.1.

Zmpste24 KO mice, a model of HGPS, lack the enzyme Zmpste24 and therefore accumulate prelamin A in nuclei. This model was chosen for its numerous histopathological defects that phenocopy those of accelerated ageing (Bergo *et al.*, 2002; Pendás *et al.*, 2002), as well as its tendency to accumulate prelamin A as has been documented during normal ageing (Scaffidi & Misteli, 2006; Ragnauth *et al.*, 2010; Liu *et al.*, 2013). Specifically, this model has been described with severe defects in skeletal muscle contractility and low force-generating capacity of soleus, plantaris, gastrocnemius and extensor digitorum longus (EDL) muscles, resembling muscular defects seen in human ageing (Frontera *et al.*, 2008; Greising *et al.*, 2012). The mice were harvested at the age of their typical lifespan (4 months), an age normally accompanied by severe muscular weakness (Greising *et al.*, 2012). The mice were age and gender-matched with wild-type (WT) controls.

In order to ascertain whether the phenotype of single muscle fibres from *Zmpste24* KO mice originates from the absence of Zmpste24 and whether partial rescue of the model would be accompanied by simultaneous alterations in MND volumes and single fibre specific force, *Zmpste24* mosaic animals that lack a progeroid phenotype were studied (De La Rosa *et al.*, 2013). These mice are null for the autosomal *Zmpste24* locus, but contain an extra copy of the *Zmpste24* gene introduced at the *Hprt* locus of their X chromosome. Because of random X inactivation, single muscle fibres from *Zmpste24* mosaic mice have equal proportions of *Zmpste24*-deficient (prelamin A accumulating) and *Zmpste24*-proficient (mature lamin A containing) myonuclei (De La Rosa *et al.*, 2013). The mice were harvested at the age of 2 months, as no difference between any progeroid markers in these mice was noted between 2 to 12 months of age (De La Rosa *et al.*, 2013). Additionally, number of nuclei in single muscle fibres has been demonstrated to stabilise to adult levels as of P21 in mice (White *et al.*, 2010), allowing for nuclear organisation investigations at the age the mice were euthanised. The mice were age and gender-matched with WT controls.

Further, it was wished to compare the nuclear organisation in muscle fibres from *Zmpste24* KO mice with that of another established model of HGPS, *Lmna* (G609G) (hereafter $Lmna^{G609G}$), for this model has been noted to share a common transcriptional signature with the *Zmpste24* KO progeria model (Osorio *et al.*, 2011), as well as because similarly to native prelamin A,

progerin has been suggested to accumulate in cells during the ageing process (Scaffidi & Misteli, 2006; Cao *et al.*, 2007; Burtner & Kennedy, 2010; López-Otín *et al.*, 2013). In *Lmna*^{G609G} mice, a mutant allele carries the c.1827C>T;p.G609G mutation, which is equivalent to the HGPS c.1824C>T;p.G608G mutation in the human *LMNA* gene. This results in the activation of a cryptic splicing donor site, causing the accumulation of progerin, a truncated and farnesylated protein with an internal deletion of 50 amino acids encompassing the target sequence for cleavage by the enzyme Zmpste24 (Osorio *et al.*, 2011). The mice were harvested at the age of 3 months, the typical age of their lifespan, and were age and gender-matched with WT controls.

Lastly, *Zmpste24* KO single muscle fibres accumulate prelamin A, but also lack lamin A. Therefore, any myofibre alterations noted in the mice might originate from either or from both. To further investigate the effects of a specific lamin A deficiency, without the confounding effects of high levels of prelamin A, a mouse model lacking A-type lamins (*Lmna* KO), which shows significant muscle dysfunction, including reduced specific force of the EDL muscle, was studied (Gnocchi *et al.*, 2011). The mice were harvested at 5 weeks of age, the typical age of their most severe pathology and lifespan, and were age and gender-matched with WT controls.

4.2.2. Farnesyltransferase inhibitor

Studies have demonstrated that blocking the farnesylation of progerin and native prelamin A, using farnesyltransferase inhibitors (FTIs), and therefore, altering their localisation to the nucleoplasm (Wang *et al.*, 2012), partially reverses the cellular abnormalities associated with their accumulation on the inner nuclear membrane and alleviate the cellular phenotypes of progeria (Toth *et al.*, 2005; Yang *et al.*, 2005, 2010; Capell *et al.*, 2005; Young *et al.*, 2005, 2006; Fong *et al.*, 2006*a*; Verstraeten *et al.*, 2008). It was, therefore, wished to investigate whether keeping the same levels of prelamin A, but reducing the fraction that is farnesylated, could rescue MND volumes and specific force in *Zmpste24*-deficient single muscle fibres.

Thus, an established farnesyltransferase inhibitor (FTI), ABT-100 (Gu *et al.*, 2005; Young *et al.*, 2006; Fong *et al.*, 2006*a*; Yang *et al.*, 2010, 2011), was mixed in drinking water containing 0.4% hydroxy methyl propyl cellulose and 1% ethanol, at a concentration of 0.3 mg/ml, so as to deliver a dose of 39 mg/kg/day. The vehicle control consisted of drinking water with 0.4% hydroxy methyl propyl cellulose and 1% ethanol. Mice drank the vehicle or ABT-100 for 15 weeks

starting at five weeks of age before being euthanised and their muscles dissected (Fong *et al.*, 2006*a*). The mice were age and gender-matched with *Zmpste24* KO control mice.

4.2.3. Solutions

Relaxing and activating solutions contained 4 mM Mg-ATP, 1 mM free Mg^{2+}, 20 mM imidazole, 7 mM EGTA, 14.5 mM creatine phosphate, and KCl to adjust the ionic strength to 180 mM and pH to 7.0. The concentrations of free Ca^{2+} were $10^{-9.00}$ M (relaxing solution) and $10^{-4.50}$ M (activating solution).

4.2.4. Muscle fibre permeabilisation

Muscle fibres were permeabilised as described in section 2.2. Briefly, following dissection of the EDL muscle, muscle samples were placed in relaxing solution at 4°C. Bundles of approximately 50 myofibres were dissected free and then tied with surgical silk to glass capillary tubes at slightly stretched lengths. They were then treated with skinning solution (relaxing solution containing glycerol; 50:50 v/v) for 24 hours at 4°C, after which they were transferred to -20°C or processed further with sucrose, snap frozen in liquid nitrogen-chilled propane and stored at -80°C for long-term storage.

Table 4.1: Genetically modified mice studied in this chapter

Mouse	Modification	Zygosity	Age	Reference
Zmpste24	Knockout	Homozygous	4 months	(Greising *et al.*, 2012)
Zmpste24$^{-/-}$ *Hprt*$^{Z24/+}$	Knockout + knock-in	Mosaic	2 months	(De La Rosa *et al.*, 2013)
Lmna	Knockout	Homozygous	5 weeks	(Gnocchi *et al.*, 2011)
Lmna$^{G609G/G609G}$	Knock-in	Homozygous	3 months	(Osorio *et al.*, 2011)

4.2.5. Force production measurements in single myofibres

On the day of experiments, bundles were de-sucrosed, transferred to a relaxing solution and single muscle fibres were dissected using fine dissection tweezers (Ideal-tek High Precision 5.SA) and a stereomicroscope (Zeiss Stemi 2000-C with a Zeiss SteREO CL 1500 ECO light source). Isolated myofibres were then individually attached between connectors leading to a force transducer (model 400A; Aurora Scientific) and a lever arm system (model 308B; Aurora Scientific). Sarcomere length was set to ≈2.50 µm and the temperature to 15°C (Ochala *et al.*, 2012*b*; Lindqvist *et al.*, 2013, 2016; Ross *et al.*, 2018). Number of samples studied is available in Table 4.2.

Fibre CSA was estimated from the width and depth of the fibre, assuming an elliptical circumference (Equation 8). The absolute maximal isometric force generation was calculated as the difference between the total tension in the activating solution (pCa 4.50) and the resting tension measured in the same myofibre while in the relaxing solution (pCa 9.0). Specific force was defined as absolute force divided by CSA (Ochala *et al.*, 2007). Note that myofibres included in the analysis: (i) were able to sustain three consecutive maximum activations without any force depression >10%; and (ii) had preserved sarcomere structures after the three maximum activations.

The measurement of the apparent rate constants of force redevelopment (k_{tr}) involved a mechanical slack-restretch manoeuvre. Each muscle fibre was transferred from the relaxing to the activating solution and allowed to generate steady-state force. The fibre was then rapidly slackened (within 1-2 ms) by 25% of its original length, resulting in a rapid reduction of force to near zero. This was followed by a brief period of unloaded shortening (20 ms) after which the preparation was rapidly re-stretched to its original length. k_{tr} was estimated by linear transformation of the half-time of force redevelopment ($k_{tr} = 0.693/t_{1/2}$), as described previously (Ochala *et al.*, 2007).

Table 4.2: Number of samples studied in force production experiments

Condition	No. animals	No. myofibres	Control	No. animals	No. myofibres
Zmpste24 KO	5	39 (18 rigor)	Wild-type	5	38 (17 rigor)
Mosaic	3	12	Wild-type	3	12
Zmpste24 KO FTIs	2	12	*Zmpste24* KO vehicle	2	12
Lmna KO	4	21	Wild-type	4	21
$Lmna^{G609G}$	4	12	Wild-type	4	12

4.2.6. Nuclear organisation in single myofibres

Single muscle fibres were dissected and mounted at a fixed sarcomere length of ≈2.20 µm on copper meshes for electron microscopy (SPI G100 2010C-XA, width, 3 mm), which had been glued to No. 1.5 (0.17 mm thickness) high-precision coverslips, using a stereomicroscope (Zeiss Stemi 2000-C with a Zeiss SteREO CL 1500 ECO light source) and fine dissection tweezers (Ideal-tek High Precision 5.SA) (chapter 3). The fibres were then incubated in a solution containing rhodamine phalloidin (RP; 1:100, Cat. #00027, Biotium) and DAPI (1:1000, Cat. #D3571, Molecular Probes) (section 2.3.1). Image stacks of 100 fluorescent images were acquired for each channel (1 µm *z* increments), using an inverted spinning disk confocal microscope (Zeiss Axiovert 200) equipped with a 20x objective lens (Zeiss FLUAR 20x/0.75, air) and an EXFO X-Cite® 120 mercury halide arc lamp (Table 2.5 and section 2.4.1). Sarcomere length was determined from a single brightfield image per fibre. Images were analysed as described in sections 3.5.1 and 2.4.1, using a custom-made MATLAB script (MATLAB® R2017a, MathWorks, Inc.). Figures were made using Prism v7 (GraphPad Software), Fiji (Schindelin *et al.*, 2012; Rueden *et al.*, 2017) and Photoshop CS6 (Adobe Systems, Inc.). Number of samples can be found in Table 4.3.

4.2.7. Immunofluorescence

Single muscle fibres were dissected and mounted on grids, as described above. Protocol and antibodies used for indirect immunofluorescence (IF) can be found in section 2.3.2. Number of samples studied is available in Table 4.4. In order to quantify fluorescent intensity of rhodamine phalloidin (RP) in single muscle fibres, imaging was performed as for nuclear organisation, with the exception of using a single channel and fixed illumination settings. In order to determine global nuclear transcriptional activity in single nuclei, a stack of 50 images, 0.1 µm *z* steps, was acquired in the respective channel for each nucleus, using a 100x objective lens (Zeiss FLUAR 100x/1.30, oil) and fixed illumination settings (section 3.4.2). Linearity of increasing camera exposure to a fixed antibody concentration, as well as *vice versa* was validated (De Vos *et al.*, 2010) (section 3.4.2). Skinned muscle fibres did not display any Pax7 positive satellite cells, in line with the literature (Konigsberg *et al.*, 1975; Cristea *et al.*, 2010; Ross *et al.*, 2018). Images were analysed using a custom-made Fiji macro (section 3.5.2), Huygens Deconvolution (Scientific Volume Imaging) and Prism v7 (GraphPad Software).

Table 4.3: Number of samples studied for nuclear organisation measurements

Condition	No. animals	No. myofibres	Control	No. animals	No. myofibres
Zmpste24 KO	5	53	Wild-type	5	44
Mosaic	3	22	Wild-type	3	16
Zmpste24 KO FTIs	2	36	*Zmpste24* KO vehicle	2	32
Lmna KO	4	81	Wild-type	4	51
$Lmna^{G609G}$	4	33	Wild-type	4	21

Table 4.4: Number of samples studied for quantification of pixel intensity

	Rhodamine phalloidin		**Acetyl-histone H3 (Lys9/Lys14)**		**Histone H3 (tri methyl K27)**	
Condition	*Zmpste24* KO	Wild-type	*Zmpste24* KO	Wild-type	*Zmpste24* KO	Wild-type
No. animals	2	2	1	2	2	2
No. myofibres	21	16	9	18	18	18
No. nuclei	N/A	N/A	64	153	51	94

4.2.8. Proteomics

Proteomics experiments were performed to measure the contractile protein density in *Zmpste24* KO single muscle fibres. Following isolation and suspension of *Zmpste24* KO single muscle fibres in buffer solution, all proteomics procedures were performed as summarised in the figure below, by Steven Lynham, Proteomics Facility, Centre of Excellence for Mass Spectrometry, King's College London, London, SE5 9NU, UK.

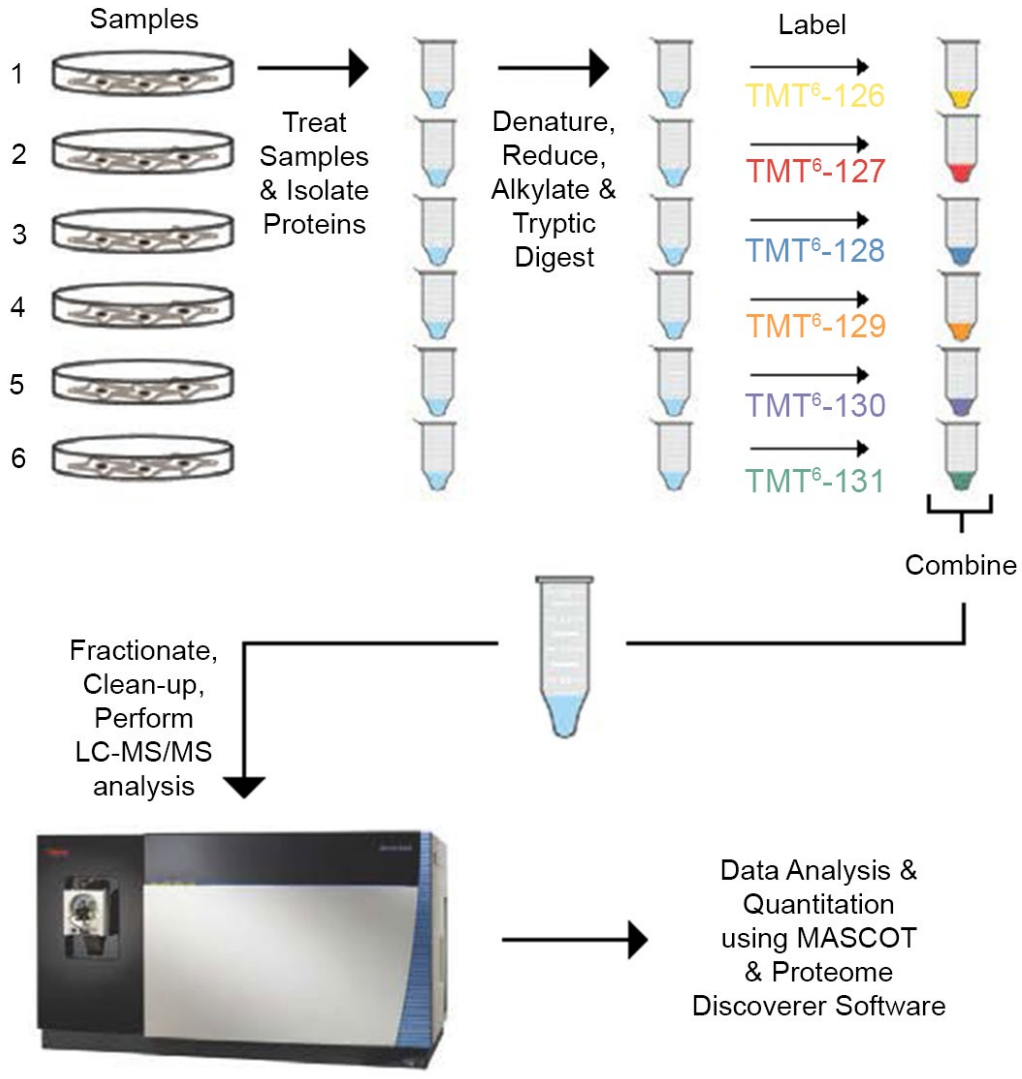

Figure 4.1: Summary of procedures for proteomics experiments
Twelve single muscle fibres (6 WT, 6 *Zmpste24* KO) were isolated and prepared for liquid chromatography mass spectrometry – mass spectrometry (LC-MS/MS), using tandem mass tag 6-plex (TMT^6) labelling. Adapted from https://goo.gl/gWLdSY.

4.2.8.1. Sample Preparation

Twelve 3 mm-long *Zmpste24* KO single muscle fibres were dissected, using fine dissection tweezers (Ideal-tek High Precision 5.SA) and a stereomicroscope (Zeiss Stemi 2000-C with a Zeiss SteREO CL 1500 ECO light source), and individually placed in labelled 0.5 ml Eppendorf tubes containing 25 µl Tris-Triton lysis buffer (10 mM Tris (pH 7.4), 100 mM NaCl, 1 mM EDTA, 1 mM EGTA, 1% Triton X-100, 10% Glycerol, 0.1% SDS, 0.5% Deoxycholate). CSA of each individual muscle fibre was calculated as per Equation 8. Samples were loaded into a stack gel for clean-up of lysis buffer, in order to eliminate chemical interference at the labelling stage and to compress the whole proteome into a single band. Enzymatic digestion and labelling were performed thereafter. Sample volumes were reduced by 50% in a SpeedVac™ (Thermo Scientific™) and the volume was replaced by Laemmli buffer (2x), prior to boiling for 10 min at 96°C. Reduced samples were loaded onto a NuPAGE™ 10% Bis-Tris Protein Gel (10 well, 1.0 mm, Cat. #NP0301BOX, Invitrogen™) and resolved for 10 minutes (100 volts; 59 mA; 6 watts) to 'stack' the whole sample into a single band. Protein bands were visualised using Imperial™ Protein Stain (Cat #24615, Thermo Scientific™).

4.2.8.2. Enzymatic digestion and peptide extraction

In-gel reduction, alkylation and digestion with trypsin were performed on all the samples, prior to subsequent isobaric mass tag labelling (Shevchenko *et al.*, 2006).

Reagents

- 100 mM Tetraethylammonium bromide (TEAB; Cat. #86608, Sigma-Aldrich) – 500 µl 1 M TEAB in 4500 µl water;
- 50 mM TEAB – 1 ml 100 mM TEAB added to 1 ml water;
- 41.05 g/mol Acetonitrile (ACN; Cat. #900667, Sigma-Aldrich);
- 10 mM Dithiothreitol (DTT; Cat. #D0632, Sigma-Aldrich) – 15 mg in 1 ml 100 mM TEAB for 100 mM stock;
- 55 mM Iodoacetamide (IAA; Cat. #I6125, Sigma-Aldrich) – 10 mg in 1 ml 100 mM TEAB;

- 13 ng/µl Trypsin – 250 µl 0.1% trifluoroacetic acid were added to a 25 µg vial of trypsin (Bovine, Cat. #TRYPSEQ-RO; Roche) and 30 µl were removed to a new tube. 200 µl 50mM TEAB were added to achieve the required concentration of 13 ng/µl. Addition of 40 µl to each sample resulted in a total of 520 ng trypsin per sample.

Enzymatic digestion

Bands of interest were excised, chopped into ~2 mm^2 pieces and transferred individually into 1.5 ml Eppendorf tubes. At RT, gel cubes were washed in excess volume of 100 mM TEAB for 5 mins and decanted. ACN was added in excess, decanted after one round and same volume was added again to fully and quickly dehydrate the gel pieces. Tubes were decanted and dried in a SpeedVac™ (Thermo Scientific™) for 5 mins. Gels were rehydrated with 10 mM DTT and heated at 56°C for 30 min. DTT was then decanted, followed by dehydration with ACN and SpeedVac™, as before. 55 mM IAA were added to the samples following dehydration and samples were left to incubate at RT for 20 mins in the dark. Supernatant was discarded, samples were washed briefly with 100mM TEAB buffer then replaced and washed for further 5 mins, before discarding of the buffer. Following, the liquid was decanted and dehydrated with ACN and SpeedVac™, as before. Gels were then rehydrated in 40 µl trypsin solution at 4°C for 20 mins, unabsorbed trypsin was removed and 40 µl 50 mM TEAB were added to cover the gel pieces and keep them wet during enzyme cleavage. Finally, samples were incubated at 37°C for 2 hours, followed by overnight incubation at RT.

Peptide extraction

The supernatants were decanted from the gel pieces and individually collected into new centrifuge tubes. Gels were washed in 40 µl 50 mM TEAB at 37°C for 5 mins, decanted and pooled into the new centrifuge tube from previous step. The gel pieces were then dehydrated with 40 µl ACN at 37°C for 10 mins, decanted and the supernatant was pooled into the new centrifuge tube from previous step. Ultimately, peptide extract was frozen and the pooled supernatants were dried to completion using a SpeedVac™. Samples were then stored at -80°C.

4.2.8.3. Peptide labelling with tandem mass tag 6-plex (TMT6plex™)

Each sample was treated individually with labels added at a 1:1 ratio (Table 4.5). TMT6plex™ labels (Cat. #90066, Thermo Scientific™) were resuspended in 41 µl ACN, vortexed and centrifuged for 1 min at 14,000 rpm. Each vial of TMT reagent was added to the appropriate sample, vortexed and briefly centrifuged at 14,000 rpm before incubation at RT for 1 hour. Reaction was stopped by adding 8 µl of 5% hydroxylamine (Cat. #467804, Aldrich) to each sample and incubating for a further 15 min at RT. All 6 samples for each TMT6plex were combined and incubated at RT for a further 15 min. Finally, combined samples were frozen at -80°C and dried to completion in a SpeedVac™.

Table 4.5: Sample labelling strategy for TMT6plex experiments

Condition	TMT6plex label	Individual label mass (Daltons)
Control 1	126_1	126.1277
Control 2	127_1	127.1247
Control 3	128_1	128.1344
Disease 7	129_1	129.1315
Disease 8	130_1	130.1411
Disease 9	131_1	131.1382
Control 4	126_2	126.1277
Control 5	127_2	127.1247
Control 6	128_2	128.1344
Disease 10	129_2	129.1315
Disease 11	130_2	130.1411
Disease 12	131_2	131.1382

4.2.8.4. Liquid chromatography mass spectrometry – tandem mass spectrometry (LC-MS/MS)

The combined TMT labelled peptide samples were resuspended in a solution containing water, acetonitrile and trifluoroacetic acid (98%, 2% and 0.05%, respectively) and analysed by LC-MS/MS. Chromatographic separations were performed using an UltiMate™ 3000 UHPLC system (Thermo Scientific™). A 10 µl injection of peptides was resolved by reversed phase chromatography on a 75 µm C18 column (50 cm) using a three-step linear gradient of acetonitrile in 0.1% formic acid. The gradient was delivered to elute the peptides at a flow rate of 250 nL/min over 120 min. The eluate was ionised by electrospray ionisation using an Orbitrap Fusion™ Lumos™ (Thermo Scientific™) operating under Xcalibur™ v4.1 (Thermo Scientific™). The system was programmed to acquire in automated data-dependent switching mode, selecting precursor ions based on their intensity for sequencing by higher-energy C-trap dissociation (HCD) for peptide identification and reporter ion fragmentation. Selection of precursor ions was based on their intensity for sequencing by HCD in a TopN method. MS/MS analyses were conducted using higher than normal collision energy profiles that were chosen based on the mass-to-charge ratio (m/z) and the charge state of the peptide. To increase fragmented peptide coverage and reporter ion intensities, a further synchronous precursor scan (SPS) of the top 5 most intense peaks using MS^3 was performed.

4.2.8.5. Database Searching

Raw MS data were processed into peak list files using Proteome Discoverer™ v2.2 (Thermo Scientific™). The raw data file was processed and searched using the Mascot database search algorithm v2.6.0 (Matrix Science; www.matrixscience.com) and the Sequest search algorithm (Eng *et al.*, 1994), against the current Mouse database curated within the UniProt protein knowledgebase (www.uniprot.org).

4.2.8.6. Bioinformatics

Following processing with Proteome Discoverer™ v2.2 (Thermo Scientific™), the result file was exported into Perseus v1.6.3 (www.perseus-framework.org) for qualitative and quantitative data analysis. Quantitative measurement filters in the Proteome Discoverer software were set to the low stringency (p = 0.05) when extracting the quantitative data. The TMT reporter ion signal (area under the peak) was used to measure the abundance of the detected peptides across the TMT6plex. Contractile proteins (i.e. myosin, actin, tropomyosin, troponin I, C and T) were identified and protein content was quantified for each sample. One of the *Zmpste24* KO samples was discarded due to methodological reasons. Results were exported to Microsoft Excel, wherein normalisation of protein content to sample volume was performed, as per Equation 9. Normalised data was exported to Prism v7 (GraphPad Software) for statistical analysis.

4.2.9. Statistical analysis

Statistical analysis and production of graphs were performed using Prism v7 (GraphPad Software), as described in section 2.4. Data from individual muscle fibres and animals was pooled together for each condition, in line with common practice in the field of both humans and animals (D'Antona *et al.*, 2003, 2007*b*, 2007*a*; Bruusgaard *et al.*, 2005, 2006, 2010, 2012; Frontera *et al.*, 2008; Cristea *et al.*, 2010; McCarthy *et al.*, 2011; Egner *et al.*, 2013, 2016; Karlsen *et al.*, 2015; Ross *et al.*, 2017*b*, 2018; Levy *et al.*, 2018; Buono *et al.*, 2018; Fongy *et al.*, 2019; Dungan *et al.*, 2019). Data are presented as mean ± SEM and as individual data points.

4.2.10. Study approval

All animal procedures were approved by the Institutional Animal Care and Use Committees of the University of Minnesota, University of Oviedo, University of California Los Angeles, the Buck Institute for Research on Aging, the University of Würzburg and the Northwestern University.

4.3. Results

The results section is composed of a rather large number of figures associated with each mouse model studied in this chapter. Therefore, overview figures will be presented here; large versions of individual graphs within such figures may be found in Appendix 4.

Zmpste24-deficient mice, a model of HGPS, lack the enzyme Zmpste24 and therefore accumulate farnesylated prelamin A in nuclei (Bergo *et al.*, 2002; Pendás *et al.*, 2002; Greising *et al.*, 2012), as seen in Figure 4.2. This model was used here as a model of ageing for its tendency to accumulate prelamin A, as has been documented during normal ageing (Scaffidi & Misteli, 2006; Ragnauth *et al.*, 2010; Liu *et al.*, 2013), as well as its severe phenotype in skeletal muscle contractility, resembling muscular defects seen in human ageing (Frontera *et al.*, 2008; Greising *et al.*, 2012). The following sections attempt to identify whether prelamin A is associated with alterations in myonuclear organisation and disrupted ability of myofibres to generate force.

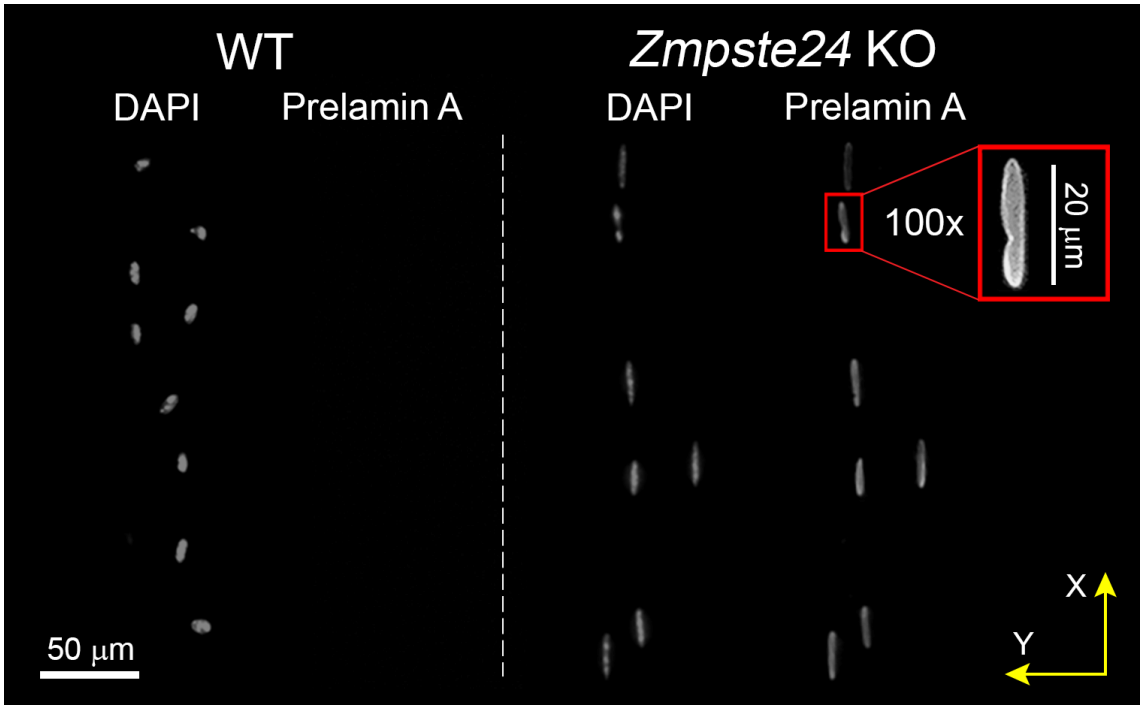

Figure 4.2: Prelamin A accumulation in *Zmpste24*-deficient myonuclei
Maximum intensity projections of typical EDL myofibres immunostained for nuclei and prelamin A. Images were acquired using x20 objective lens, apart from the insert (100x objective). Note that all the nuclei from *Zmpste24* KO fibres were prelamin A positive whilst none of the WT nuclei exhibited prelamin A.

4.3.1. Effect of prelamin A on various nuclear and myofibre parameters

4.3.1.1. Altered nuclear organisation

As detailed in chapter 3, the methodological approach described in this work allows for accurate enumeration of nuclei and their distribution within single muscle fibres. Thus, 97 individual myofibres (44 WT, 53 *Zmpste24* KO) were isolated, imaged using confocal microscopy (Figure 4.3) and 3D image reconstructions were analysed using a custom-made MATLAB script, as described in section 3.5.1.

The data showed that the overall number of nuclei per mm fibre length was significantly lower in mice lacking *Zmpste24* than in WT animals. As observed previously in WT animals (Ross *et al.*, 2017*b*), the number of nuclei per mm fibre length was positively and linearly correlated with their fibre CSA (Figure 4.4A) and volume (Figure 4.4B). However, in *Zmpste24*-deficient mice, as the number of nuclei per mm fibre length did not increase with fibre CSA and volume, MND volumes were significantly greater than in WT rodents, with larger fibres being more severely affected (Figure 4.4C and D).

MND measurements provide valuable information on the average volume of cytoplasm controlled by each myonucleus; however, they do not allow characterisation of the overall spatial distribution of myonuclei within the whole fibre. To evaluate this parameter, nearest neighbour distances (NNs) were calculated between nuclei using the 3D co-ordinates of individual nuclei within each single muscle fibre. In WT mice, NN was unrelated to fibre CSA (Figure 4.4E) and volume (Figure 4.4F), and remained constant at ∼34 µm. On the other hand, NN was significantly dependent on CSA and volume in *Zmpste24*-deficient animals, supporting once again the notion that larger fibres are more severely affected. To further assess the regularity of nuclear positioning within muscle fibres, an order score was calculated to compare the nuclear positioning within a fibre, with that of calculated optimal (100%) and random (0%) organisation on the fibre (Bruusgaard *et al.*, 2003). Interestingly, this parameter was not affected by the absence of *Zmpste24* (Figure 4.4G), implying that regular nuclear spacing was maintained, despite differences in nuclear number, MND and NN distance.

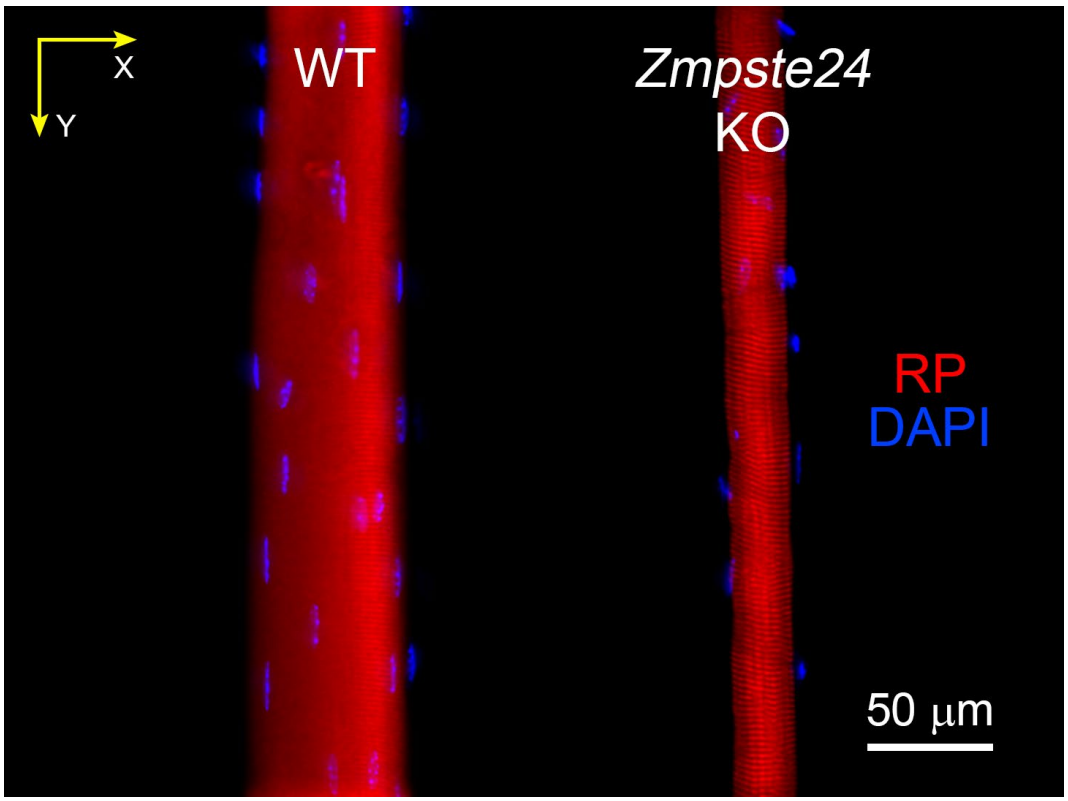

Figure 4.3: Typical confocal images of WT and *Zmpste24* KO single myofibres
Maximum intensity projection of muscle fibres stained for nuclei (DAPI, blue) and actin (Rhodamine Phalloidin; RP, red) and imaged using 20x objective lens.

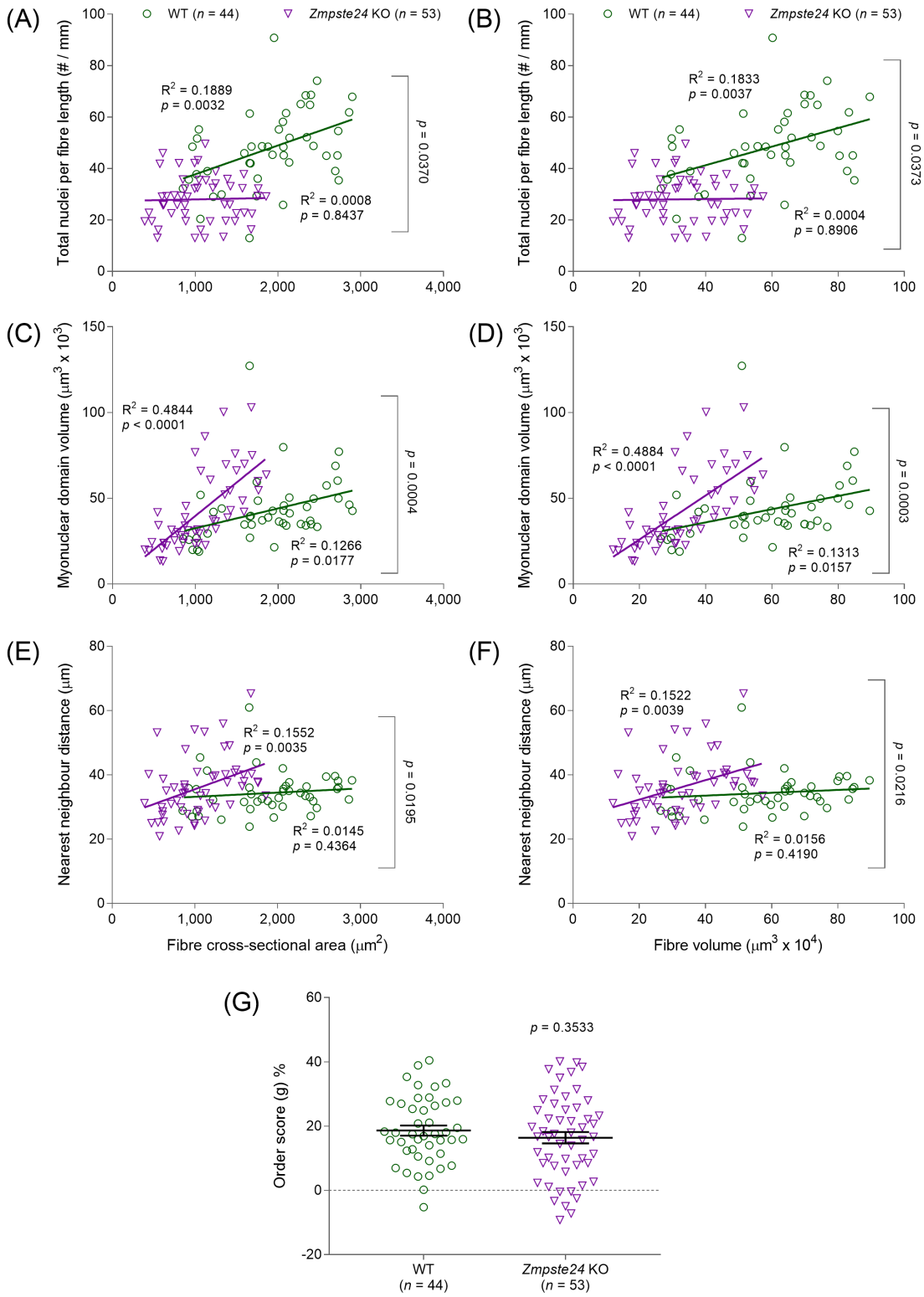

Figure 4.4: Nuclear organisation in *Zmpste24*-deficient single myofibres

Data points represent single myofibres. Graphs show various myonuclear parameters per fibre CSA (A, C, E) and volume (B, D, F). Pearson correlation was performed to evaluate linear relationships; (G) Nuclear distribution in fibres. Error bars show mean ± SEM. Statistical tests included normality tests and t-tests.

4.3.1.2. Changes in transcriptional activity

Such abnormalities in number of nuclei and MND sizes could be accompanied by modified global gene transcription. As myonuclei may alter their transcriptional activity according to cellular demands (Kirby *et al.*, 2016), it was theorised that in *Zmpste24*-deficient muscle fibres, the low number of nuclei should increase their individual transcriptional activity to support such large MNDs. To address this possibility, muscle fibres were incubated in antibodies against acetyl histone H3 (AcH3; Lys9/Lys14; Figure 4.5) and H3K27me3 (Figure 4.6), to be used as markers of activation and repression of transcriptional activity, respectively (Gnocchi *et al.*, 2011; López-Otín *et al.*, 2013; Zane *et al.*, 2014). The mean positive AcH3 intensity, measured by setting a cut-off point for nuclei above 500 greys of background level (12.2% of 12-bit dynamic range), was significantly reduced in *Zmpste24*-deficient compared to WT counterparts (Figure 4.7A), suggesting a possible decrease in overall transcription (Figure 4.7B). However, no significant differences were observed for H3K27me3 (Figure 4.7C and D). Overall, this data potentially suggests that the global transcriptional activity of nuclei in *Zmpste24*-deficient muscle fibres is reduced, which in turn, may affect contractile protein synthesis and content.

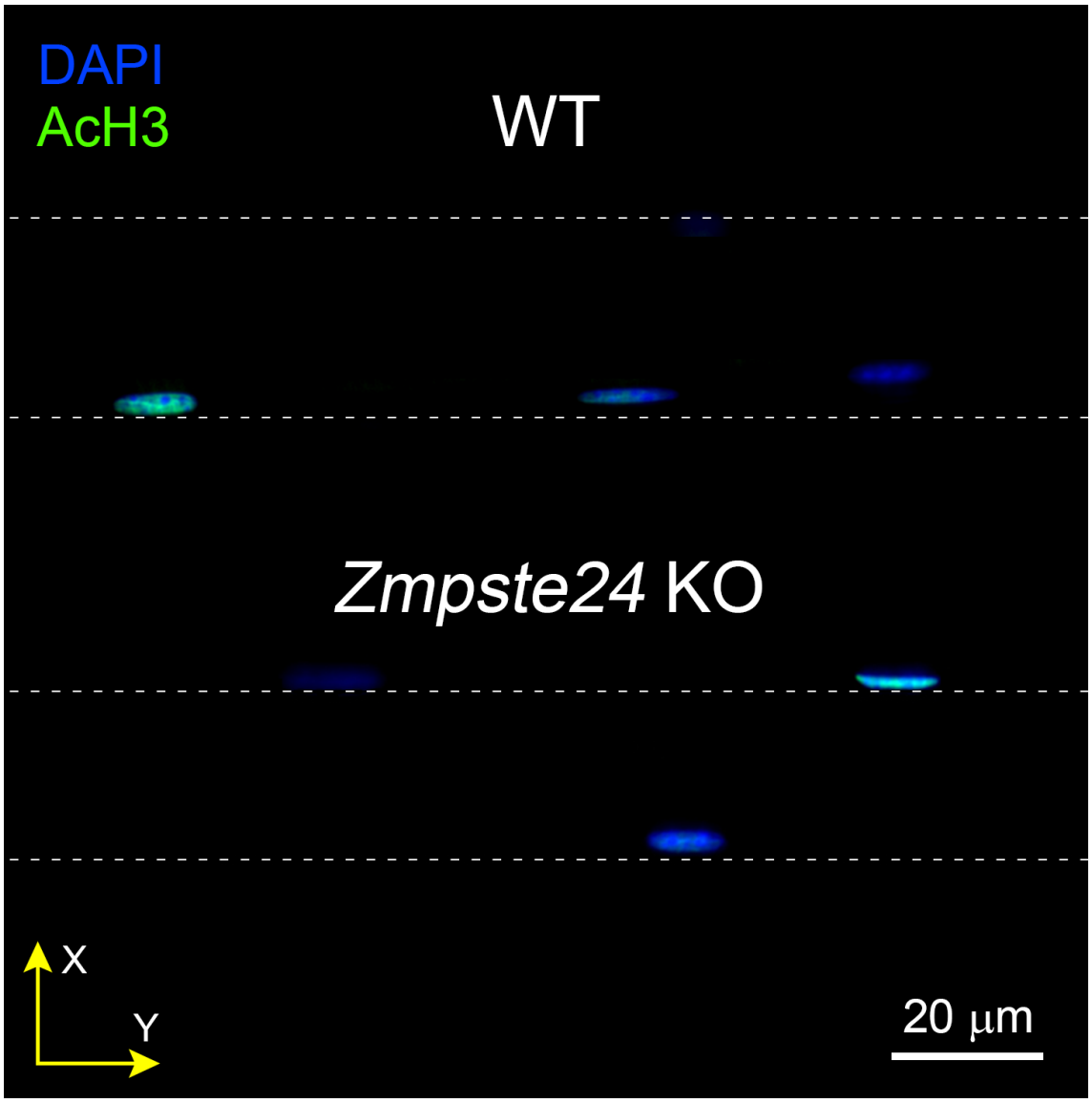

Figure 4.5: Typical heterogeneity of DNA acetylation in nuclei lacking *Zmpste24*
Sections of WT and *Zmpste24* KO muscle fibres (space enclosed between contour lines) stained for nuclei (DAPI, blue) and acetyl histone H3 (AcH3, green), imaged using a 40x objective lens.

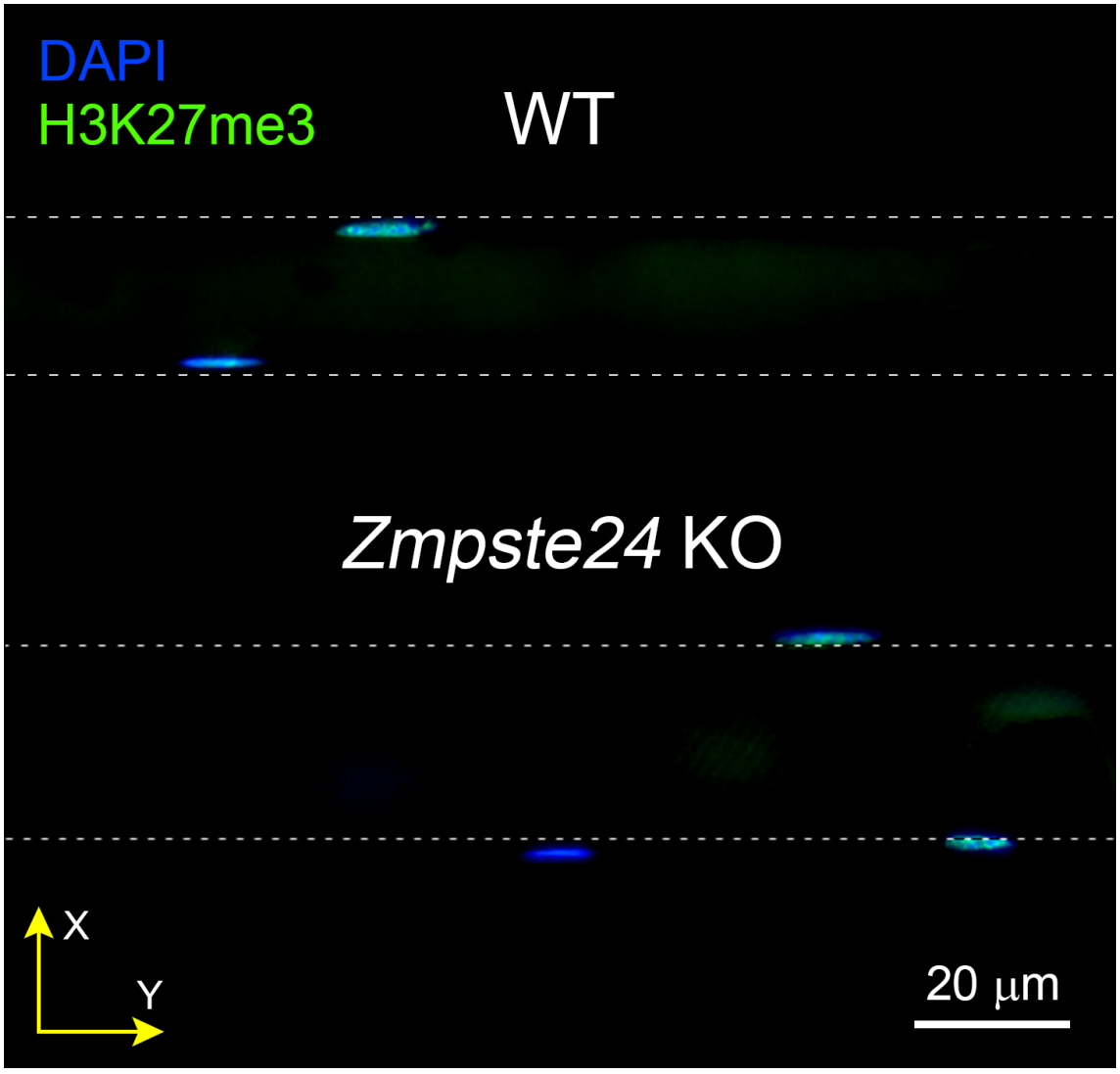

Figure 4.6: Typical heterogeneity of DNA methylation in nuclei lacking *Zmpste24*
Sections of WT and *Zmpste24* KO muscle fibres (space enclosed between contour lines) stained for nuclei (DAPI, blue) and histone H3 methylation (H3K27me3, green), imaged using a 40x objective lens.

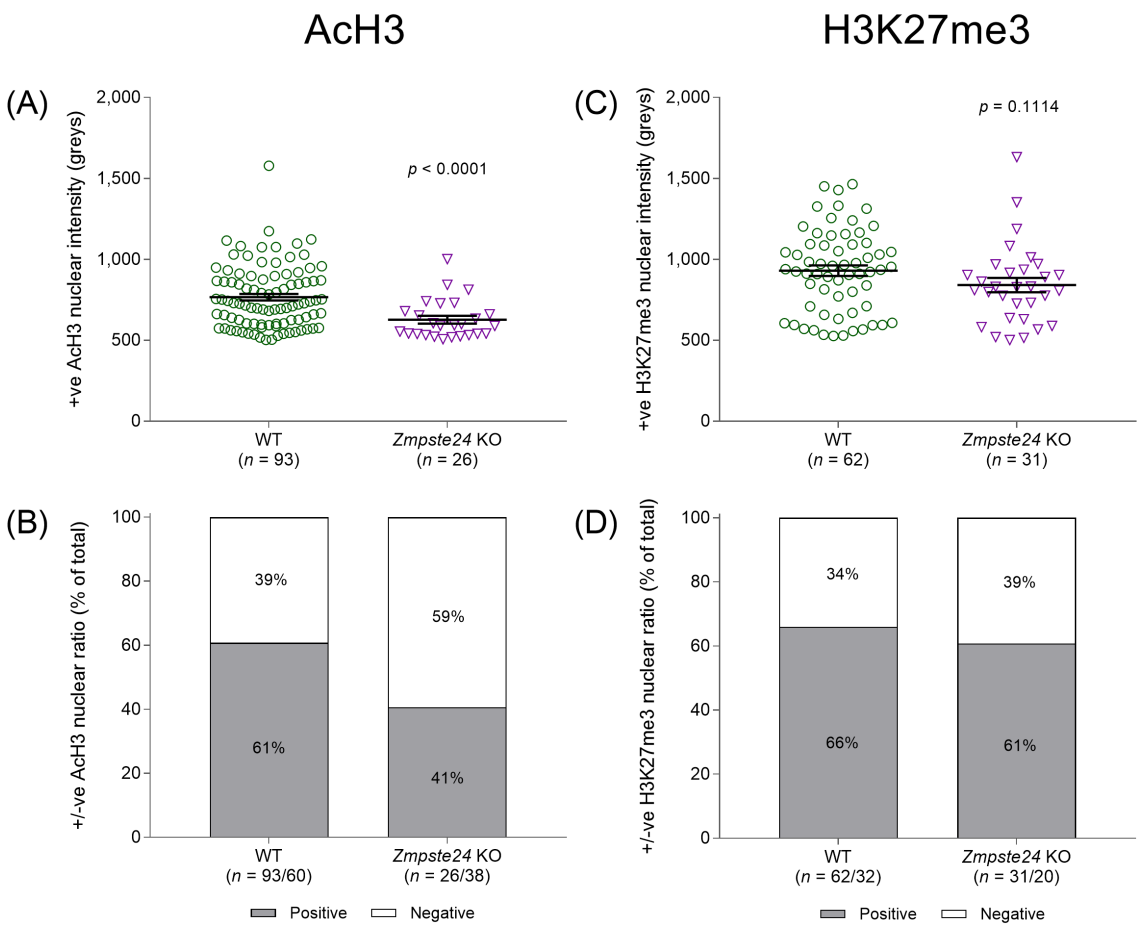

Figure 4.7: Altered transcriptional balance in nuclei lacking *Zmpste24*

(A, C) Data points represent individual nuclei with positive (+ve) levels (>500 greys) of (A) acetyl-histone H3 (AcH3) and (C) H3K27me3. Error bars show mean ± SEM. Statistical tests included normality tests and t-tests; (B, D) Positive nuclei (+ve; >500 greys) versus negative nuclei (-ve; <500 greys) ratio. The cut-off point of 500 greys was selected based on measured background levels of all studied single muscle fibres.

4.3.1.3. Reduced content of contractile proteins

Mean pixel intensity was measured in confocal images of *Zmpste24*-deficient single muscle fibres stained with rhodamine phalloidin (RP) to indirectly ascertain whether levels of actin are reduced in the cell, alongside the myonuclear alterations discovered above. Results revealed that the mean pixel intensity of RP within individual myofibres was lower in the absence of *Zmpste24* (Figure 4.8). To support these findings, proteomics analyses (TMT6plex experiments) were performed on 11 single muscle fibres (6 WT and 5 *Zmpste24* KO), focussing on contractile protein content (myosin, actin, tropomyosin, troponin I, C and T). Protein content was normalised to single muscle fibre volume, by calculating the fibre CSA from the measured fibre diameter (assuming elliptical shape; Equation 8), multiplied by fibre length (Equation 9). The contents of myosin and total contractile proteins were lower in myofibres from mice lacking *Zmpste24* when compared to fibres from WT mice; this was dependent on fibre volume, with a greater effect observed in fibres with larger volumes (Figure 4.9). Altogether, these results suggest that mechanisms related to (i) myonuclear number (ii) contractile protein content are likely to be involved in the aetiology of muscle fibre dysfunction in the absence of *Zmpste24*.

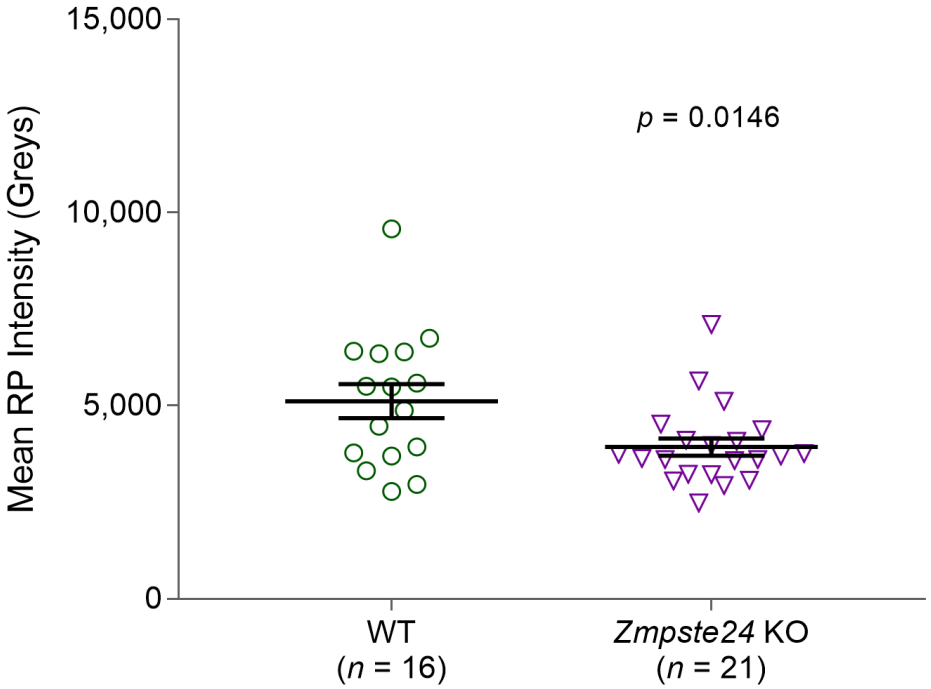

Figure 4.8: Lower mean PR intensity in *Zmpste24*-deficient single myofibres
RP = rhodamine phalloidin. Data points represent individual single muscle fibres. Error bars show mean ± SEM. Statistical tests included normality tests and t-tests.

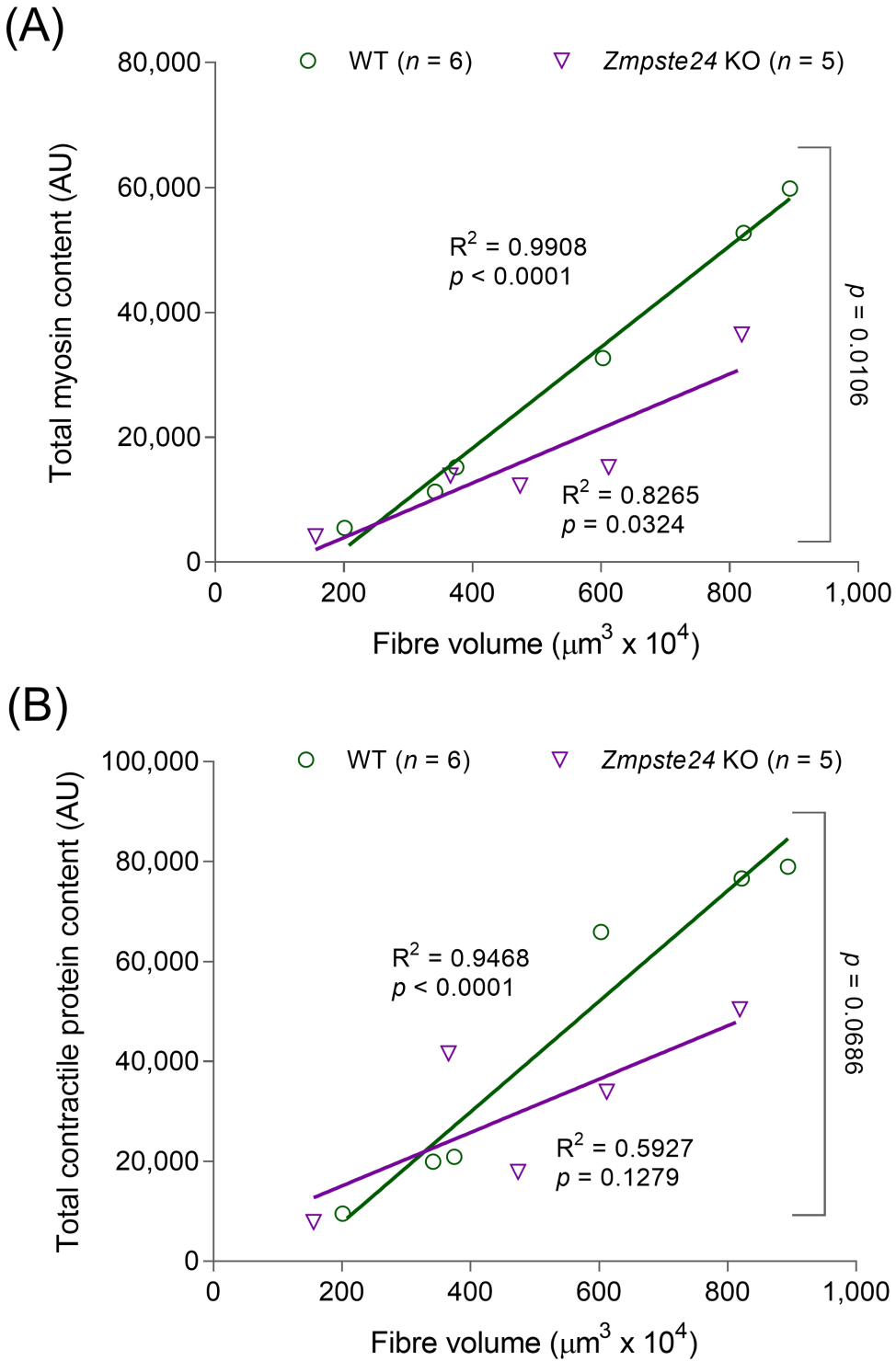

Figure 4.9: Reduced content of contractile proteins in the absence of *Zmpste24*
Data points represent individual single muscle fibres studied using proteomics analysis. Pearson product moment correlation was performed to evaluate linear relationships.

4.3.1.4. Reduced production of force

Due to the above findings, it was wished to evaluate whether a reduction in myosin content would be accompanied by lower specific force in muscle fibres lacking *Zmpste24*. To measure the force-generating capacity of myofibres, at the contractile level, without the confounding effects of possible disrupted sarcoplasmic reticulum Ca^{2+} handling or sarcolemmal excitability, absolute steady-state isometric force at saturating [Ca^{2+}] (pCa 4.50) was measured in 38 WT and 39 *Zmpste24* KO membrane-permeabilised fibres. In WT mice, absolute force was strongly related to CSA and a positive linear relationship was observed; no such relationship was observed in mice lacking *Zmpste24* (Figure 4.10A). This demonstrates that larger fibres with disproportionately greater MND sizes and lower contractile protein content were more severely impaired. In line with these results, specific force, defined as absolute (maximal) force divided by CSA, was significantly lower in mice lacking *Zmpste24* than in WT animals (Figure 4.10B).

Such force depression can be due to changes in the total number of available myosin molecules, their recruitment upon Ca^{2+} activation and/or their intrinsic cycling and mechanical properties in binding to actin. To distinguish between these, rigor force (maximum force in the absence of ATP) was measured, yielding significantly lower force in rodents lacking *Zmpste24* than in WT mice (Figure 4.11A). As rigor force and specific force were depressed to a similar extent, and as under rigor conditions, all myosin heads are attached because of a very slow dissociation rate (Brenner, 1986), it is suggested that the Ca^{2+} recruitment of myosin molecules was not affected in the absence of *Zmpste24*.

Rate of force development (k_{tr}) was measured to evaluate cross-bridge cycling. *Zmpste24*-deficiency did not have any negative effect on this parameter (38.40 ± 3.00 s^{-1} for *Zmpste24* KO versus 39.10 ± 2.50 s^{-1} for WT mice; (Figure 4.11B). As k_{tr} depends on f_{app} + g_{app}, with f_{app} being the rate constant for attachment and g_{app} being the rate constant for detachment (Ochala *et al.*, 2012*a*), the force depression in *Zmpste24* KO muscle fibres was not associated with significant changes in myosin cross-bridge cycling properties. Hence, the specific force depression was most likely related to a quantitative reduction in the content of contractile proteins (total number of myosin molecules available) observed in the *Zmpste24* mutant mice (Figure 4.9). Altogether, these findings unravel, for the first time, a potentially novel link between sub-optimal nuclear number and/or MND volumes and functional contractile efficiency of muscle fibres.

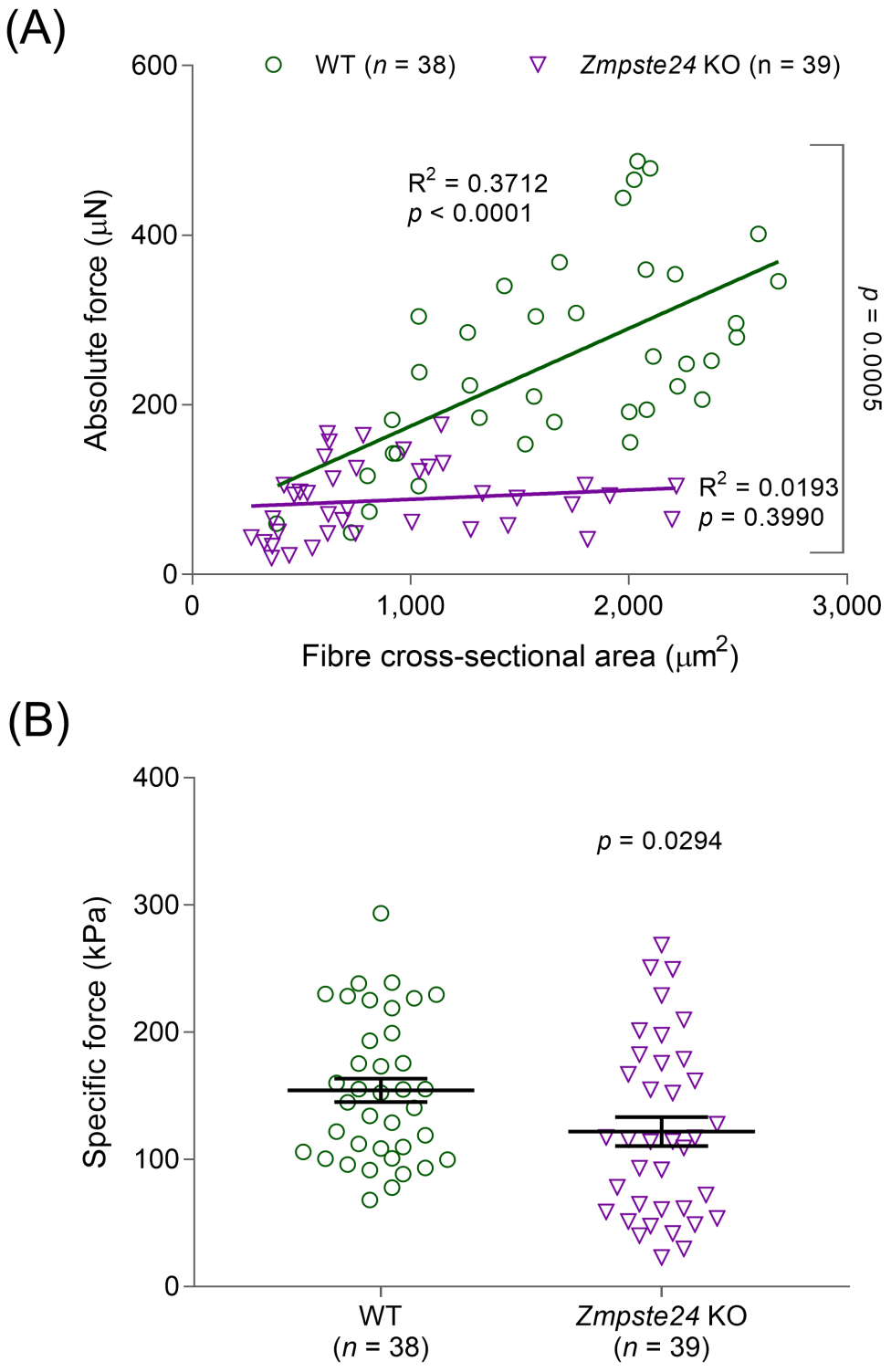

Figure 4.10: Reduced force production in *Zmpste24*-deficient single myofibres

Data points represent individual single muscle fibres. (A) Pearson product moment correlation was performed to evaluate linear relationships; (B) Error bars show mean ± SEM. Statistical tests included normality tests and t-tests.

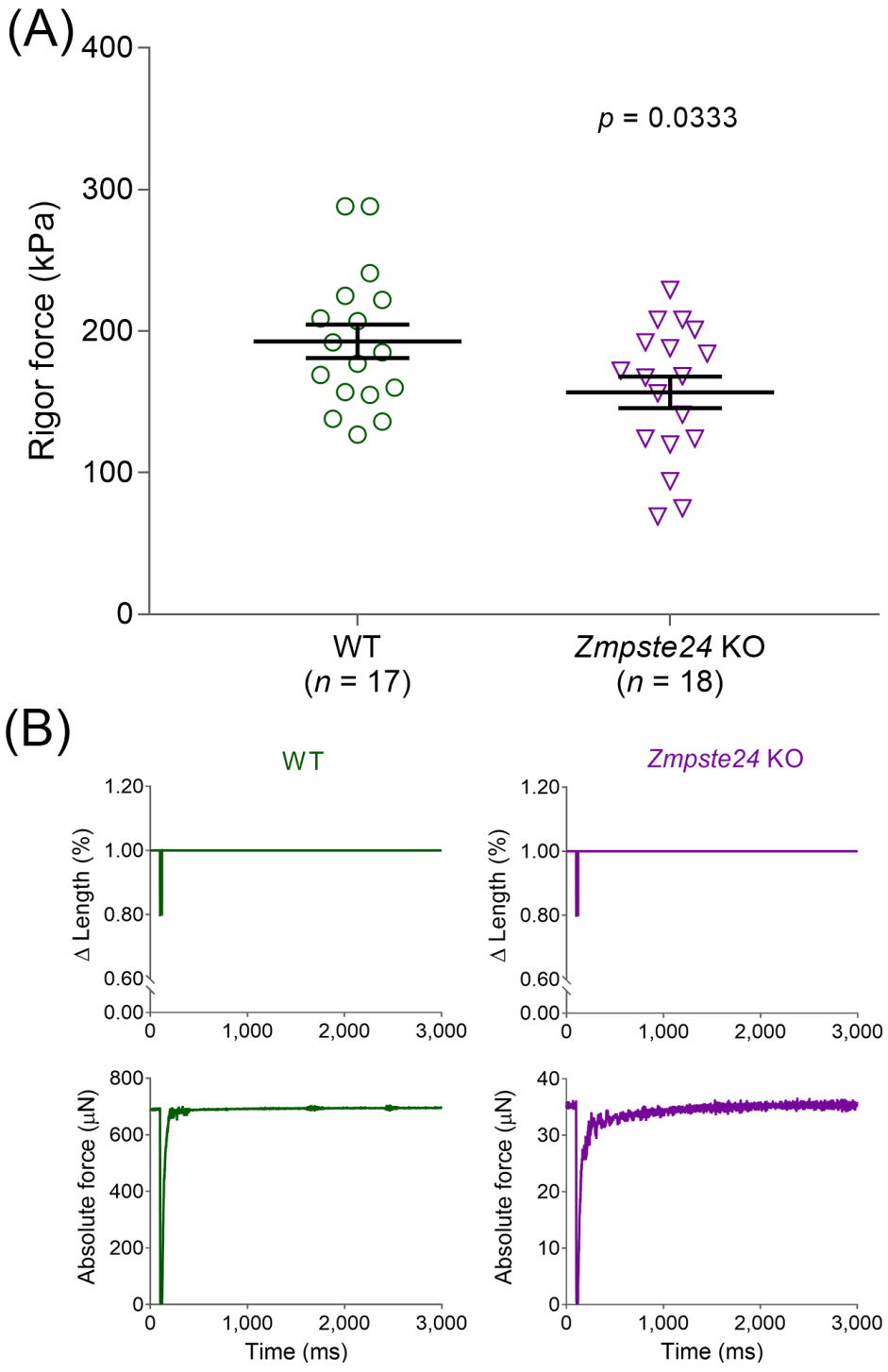

Figure 4.11: Functional parameters of single myofibres lacking *Zmpste24*

(A) Reduced rigor force in *Zmpste24*-deficient single myofibres. Error bars show mean ± SEM. Statistical tests included normality tests and t-tests; (B) Length and force signals of myofibres from one WT and one *Zmpste24* KO mice, used for the calculation of rate of force redevelopment. Time to half force recovery was 16 ms for WT and 18 ms for *Zmpste24* KO. Hence, the rate of force redevelopment was 43.30 s^{-1} for WT and 38.50 s^{-1} for *Zmpste24* KO. Note also that the force recovery is close to 100% for these original recordings as well as for most of all the other myofibres.

4.3.2. Reducing the amount of prelamin A rescues myofibre parameters

Studies on various *Zmpste24* mouse models have shown that reducing the amount of prelamin A in nuclei can partially rescue the progeroid phenotype. An example was achieved in *Zmpste24* KO mice heterozygous for *Lmna* (Fong *et al.*, 2004, 2006*b*; Varela *et al.*, 2005), demonstrating that a partial rescue is attainable simply by reducing the total amount of prelamin A in nuclei. The current section aimed to further ascertain whether (i) a correlation exists between myonuclear number, MNDs and force production in single muscle fibres; and, (ii) specific accumulation of farnesylated prelamin A, and not simply prelamin A or loss of lamin A, can lead to the above adverse myofibre alterations.

To support the proposal of a correlation between myonuclear number, MNDs and force production, single muscle fibres from WT mice and *Zmpste24* mosaic animals that lack a progeroid phenotype were studied (Figure 4.12). *Zmpste24* mosaic mice are null for the autosomal *Zmpste24* locus, but contain an extra copy of the *Zmpste24* gene introduced at the *Hprt* locus of their X chromosome. Because of random X inactivation, single muscle fibres from *Zmpste24* mosaic mice have equal proportions of *Zmpste24*-deficient (prelamin A accumulating) and *Zmpste24*-proficient (mature lamin A containing) myonuclei (De La Rosa *et al.*, 2013). Results revealed that number of nuclei, MND volumes and specific force were similar between the two mouse lines, demonstrating rescue of specific force in single muscle fibres from *Zmpste24* KO mice may be associated with a reduction in MND volumes (Figure 4.12 through Figure 4.14). However, the study also demonstrates that the rescue of myofibre parameters in the mosaic mice could have been due to either a reduction in nuclear prelamin A or increase in lamin A content. Thus, though this set of experiments demonstrates a possible connection between MND volumes and specific force in *Zmpste24*-deficient single muscle fibres, the results are inconclusive as to whether clearance of prelamin A *per se* is associated with a reduction in MND volumes and elevated specific force.

Studies have demonstrated that using FTIs to block the farnesylation of progerin and native prelamin A partially reverses the cellular abnormalities associated with their accumulation on the INM and alleviates the cellular phenotypes of progeria in mice (Toth *et al.*, 2005; Yang *et al.*,

2005, 2010; Capell *et al.*, 2005; Young *et al.*, 2005, 2006; Fong *et al.*, 2006*a*; Verstraeten *et al.*, 2008). Hence, it was wished to investigate whether reducing the amount of farnesylated prelamin A *per se* in *Zmpste24*-deficient single muscle fibres could rescue MND volumes and specific force. Thus, the effects of 15 weeks' FTI administration (ABT-100) on *Zmpste24* KO mice were investigated, starting at five weeks of age (Fong *et al.*, 2006*a*). Results showed that myofibres from FTI-treated rodents exhibited rescued MND sizes and specific force, when compared with vehicle-treated animals (Figure 4.15 through Figure 4.17). Whether the rescue is indistinguishable from WT mice remains to be established, unfortunately, as WT counterparts were not available for this study. Nevertheless, a link between accumulation of farnesylated prelamin A, large MNDs and low specific force in *Zmpste24*-deficient myofibres has been indeed established.

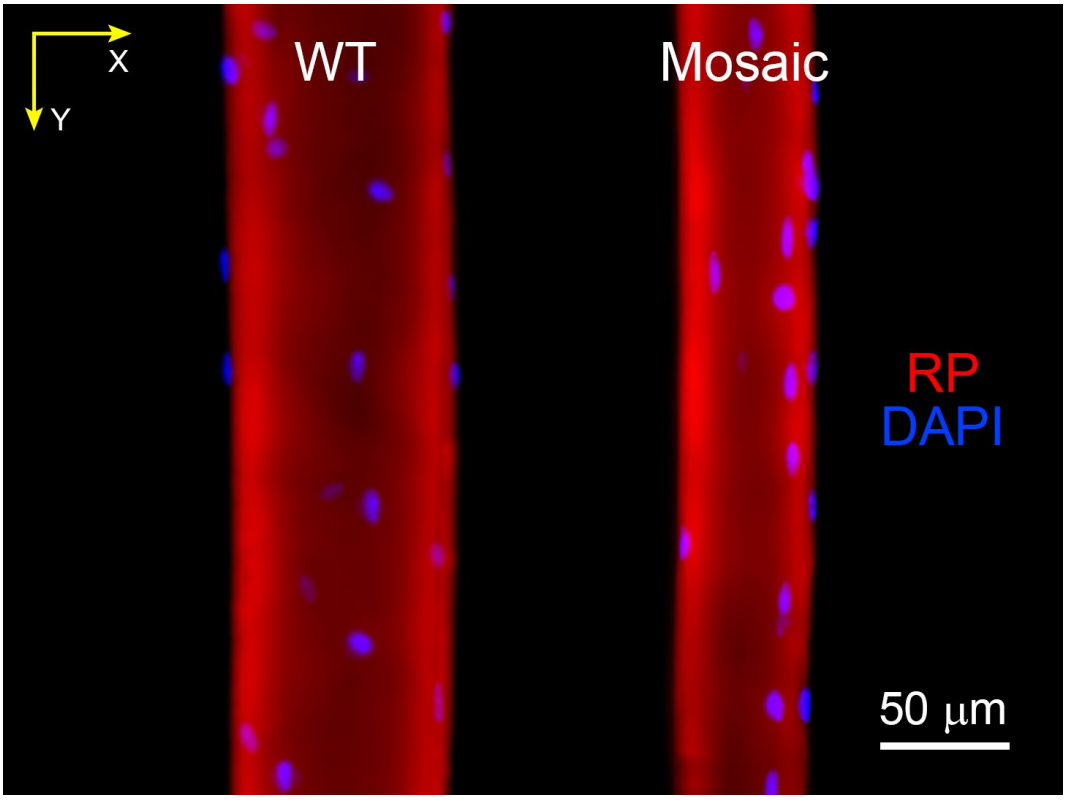

Figure 4.12: Typical confocal images of WT and mosaic single myofibres
Maximum intensity projection of muscle fibres stained for nuclei (DAPI, blue) and actin (Rhodamine Phalloidin; RP, red) and imaged using 20x objective lens.

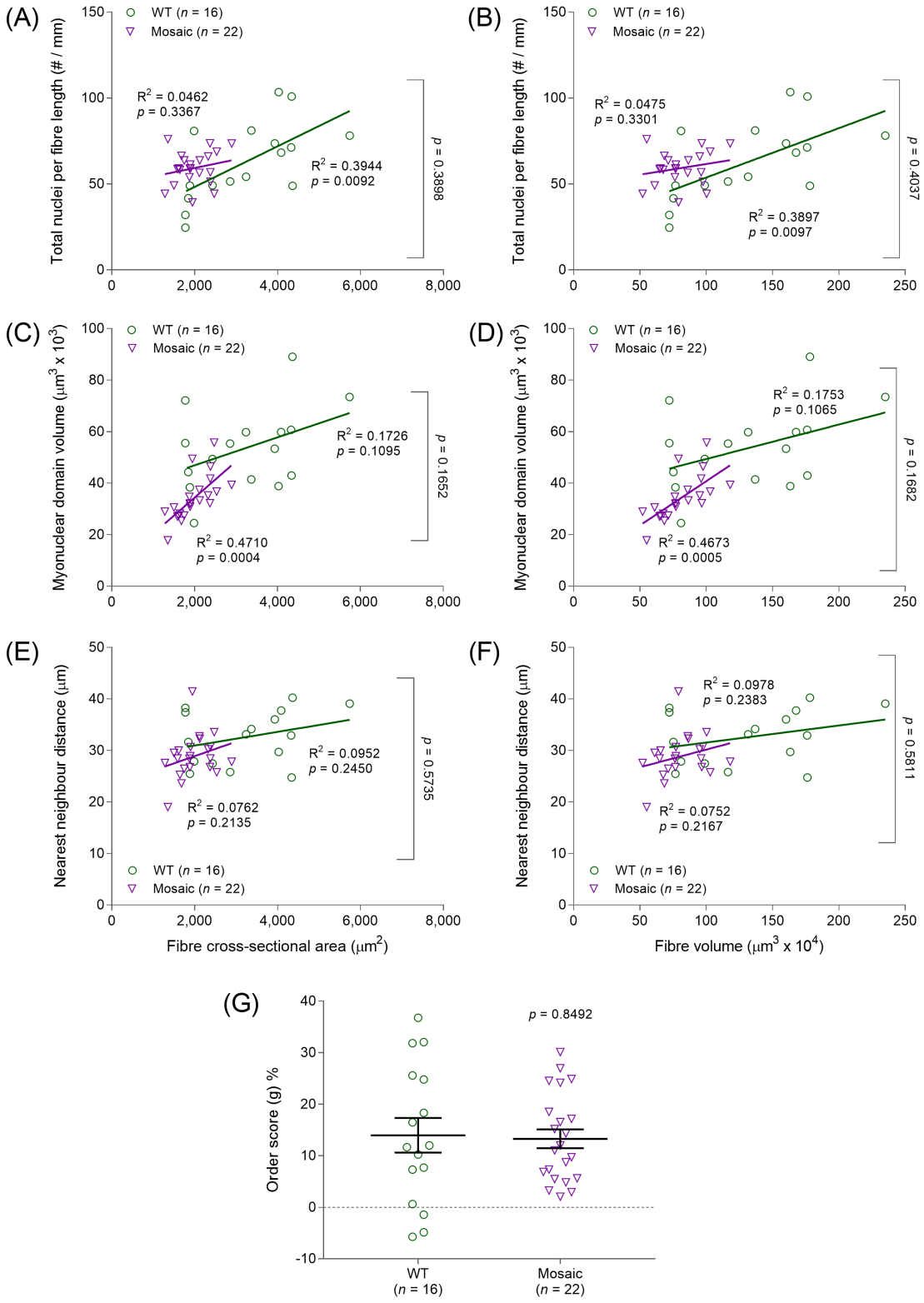

Figure 4.13: Nuclear organisation in mosaic single myofibres

Data points represent single myofibres. Graphs show various myonuclear parameters per fibre CSA (A, C, E) and volume (B, D, F). Pearson correlation was performed to evaluate linear relationships; (G) Nuclear distribution in fibres. Error bars show mean ± SEM. Statistical tests included normality tests and t-tests.

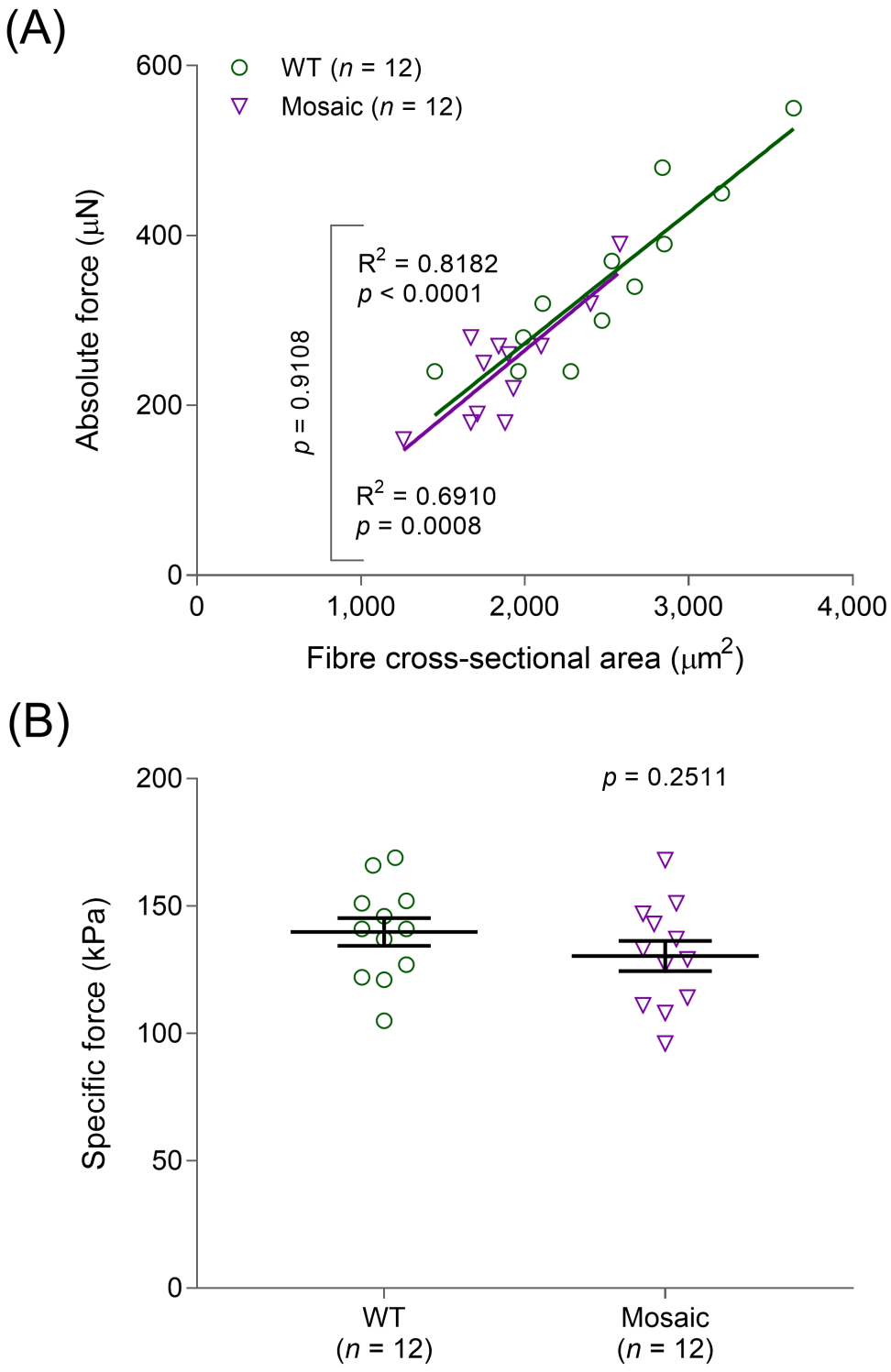

Figure 4.14: Normal force production in mosaic single myofibres

Data points represent individual single muscle fibres. (A) Pearson product moment correlation was performed to evaluate linear relationships; (B) Error bars show mean ± SEM. Statistical tests included normality tests and t-tests.

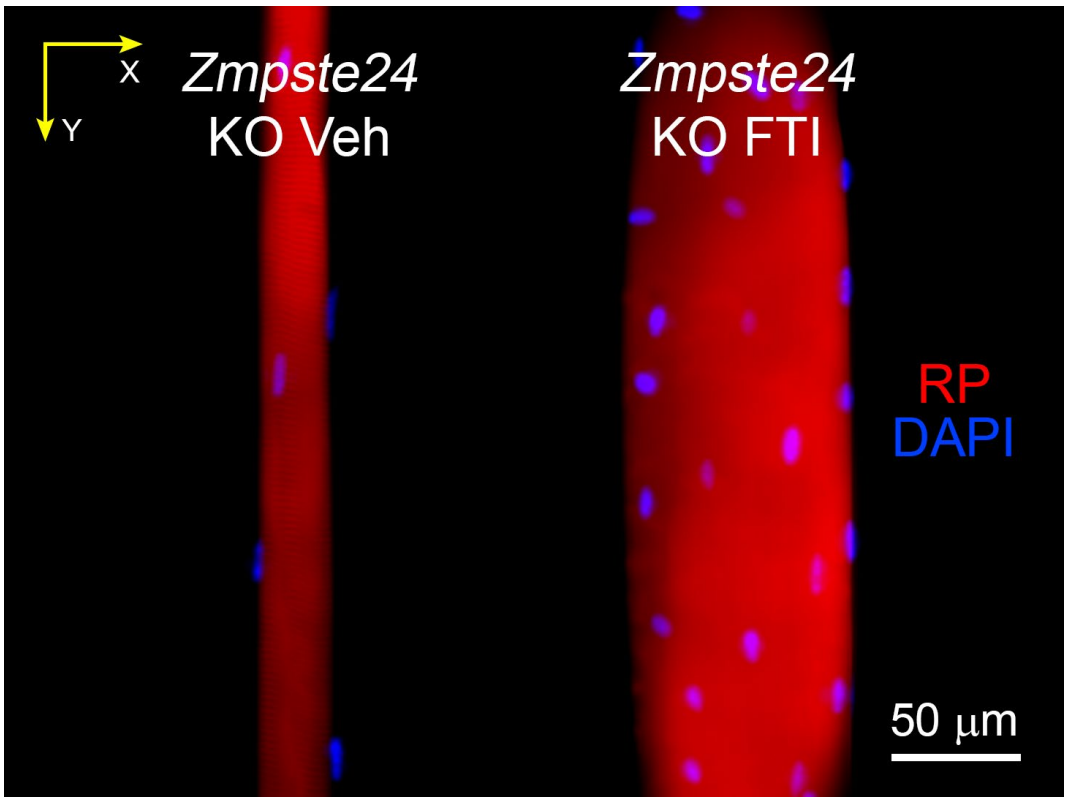

Figure 4.15: *Zmpste24*-deficient myofibres treated with vehicle or FTIs
Maximum intensity projection of muscle fibres stained for nuclei (DAPI, blue) and actin (Rhodamine Phalloidin; RP, red) and imaged using 20x objective lens. FTI = farnesyltransferase inhibitor; Veh = vehicle.

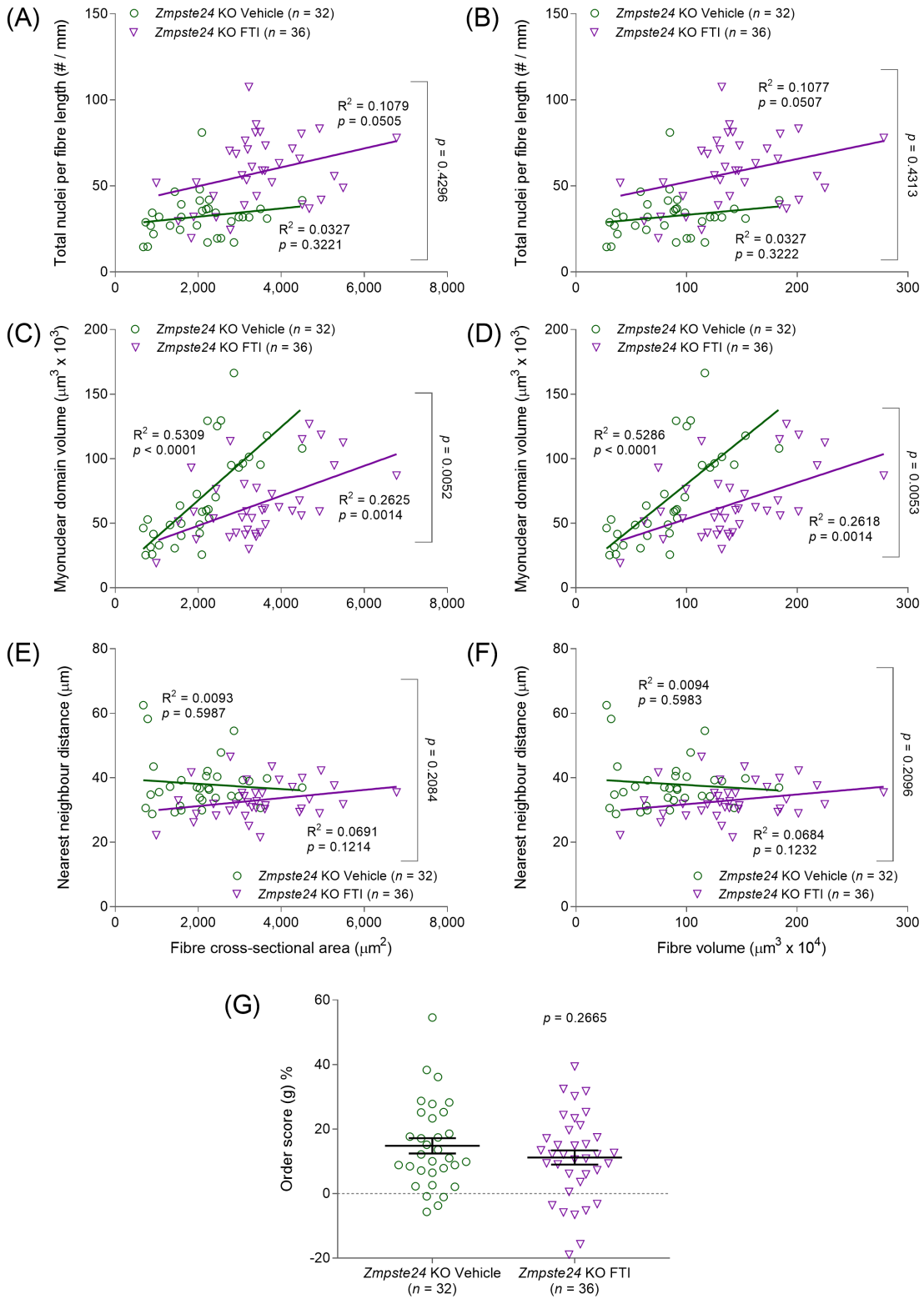

Figure 4.16: Nuclear organisation in FTI-treated *Zmpste24*-deficient single myofibres

Data points represent single myofibres. Graphs show various myonuclear parameters per fibre CSA (A, C, E) and volume (B, D, F). Pearson correlation was performed to evaluate linear relationships; (G) Nuclear distribution in fibres. Error bars show mean ± SEM. Statistical tests included normality tests and t-tests.

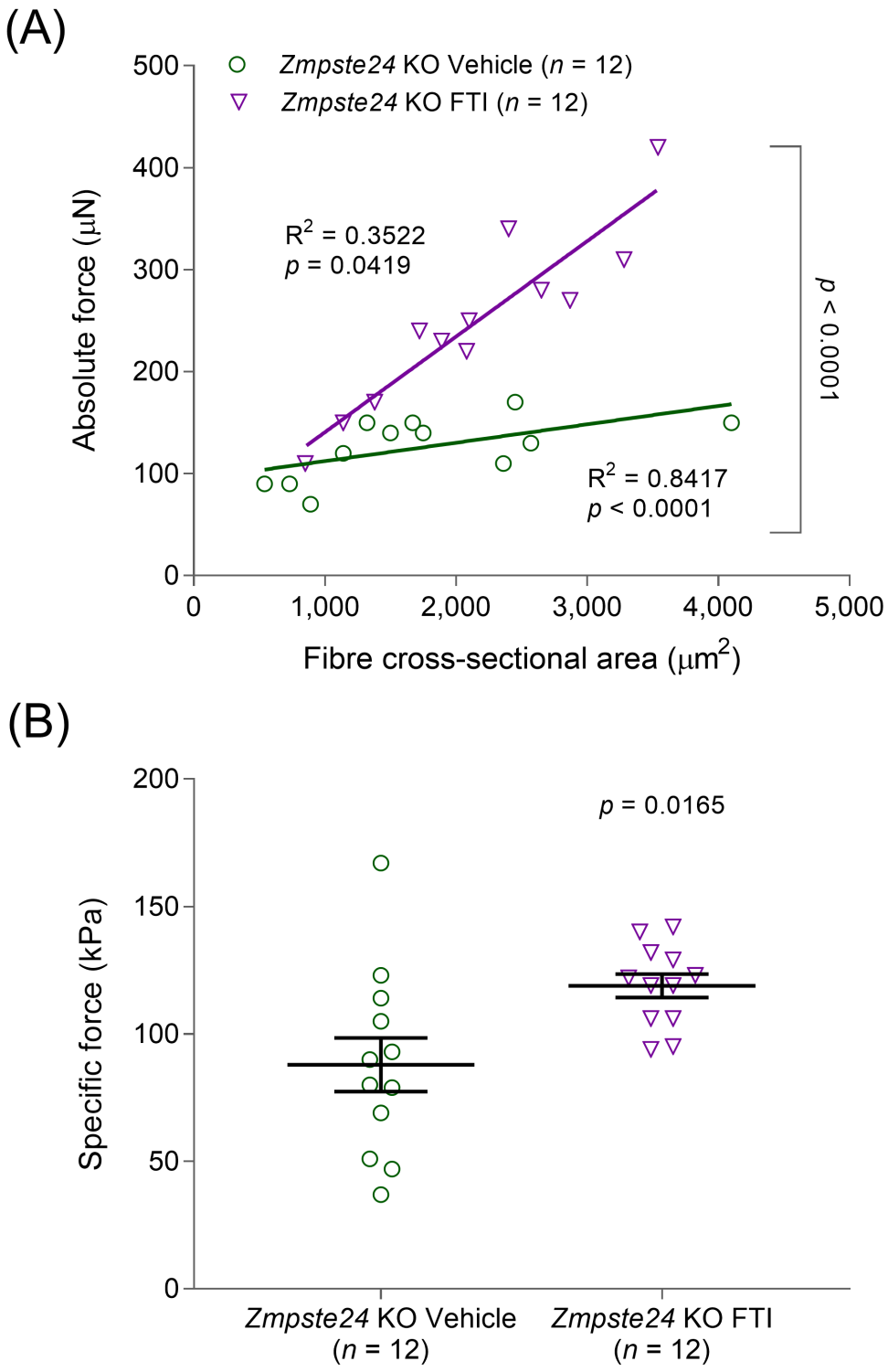

Figure 4.17: Increased force production in FTI-treated *Zmpste24*-deficient myofibres
Data points represent individual single muscle fibres. (A) Pearson product moment correlation was performed to evaluate linear relationships; (B) Error bars show mean ± SEM. Statistical tests included normality tests and t-tests.

4.3.3. Lamin A deficiency subtly alters myofibre parameters

Prior work has shown that *Zmpste24*-deficient mice display an accumulation of farnesylated prelamin A and a deficiency of lamin A (Bergo *et al.*, 2002; Greising *et al.*, 2012). Thus, the results acquired here in *Zmpste24*-deficient mice may originate from either of these two alterations or from both. To further investigate the effects of a specific lamin A deficiency, without the confounding effects of high levels of prelamin A, a mouse model lacking A-type lamins (*Lmna* KO) was studied (Gnocchi *et al.*, 2011) (Figure 4.18). Although myofibres from lamin A-deficient mice had a significantly lower number of nuclei per mm fibre length than their counterparts, MNDs, NN, order score and specific force were normal (Figure 4.18 through Figure 4.20).

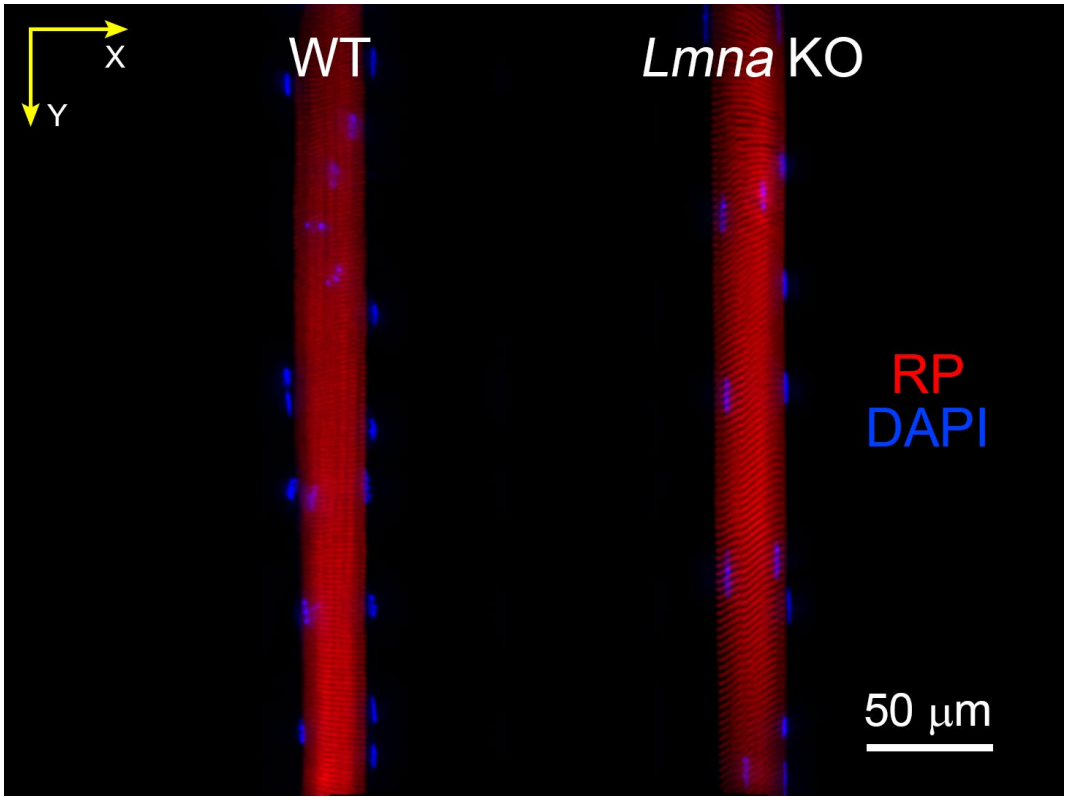

Figure 4.18: Typical confocal images of WT and lamin A-deficient single myofibres
Maximum intensity projection of muscle fibres stained for nuclei (DAPI, blue) and actin (Rhodamine Phalloidin; RP, red) and imaged using 20x objective lens.

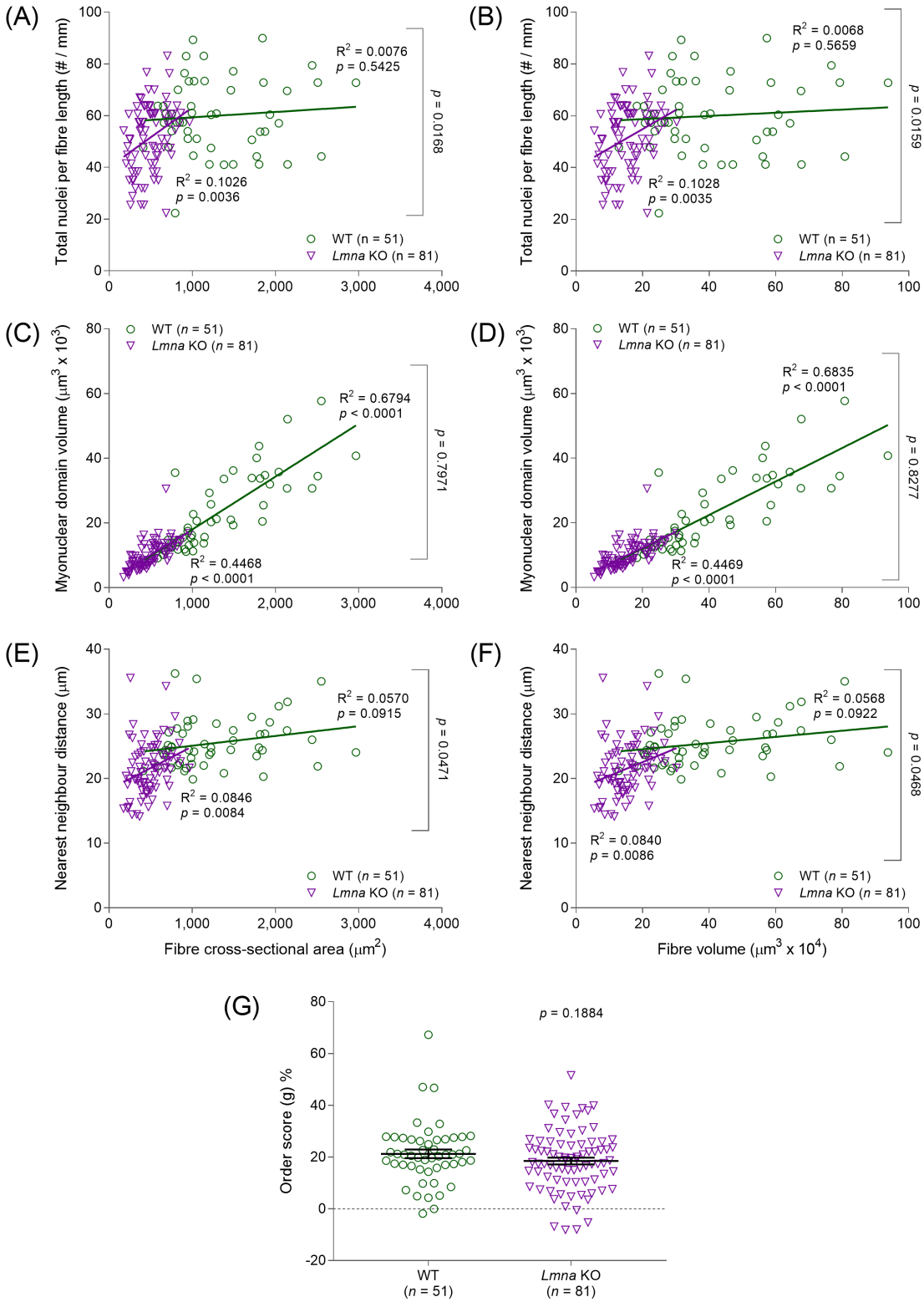

Figure 4.19: Nuclear organisation in lamin A-deficient single myofibres

Data points represent single myofibres. Graphs show various myonuclear parameters per fibre CSA (A, C, E) and volume (B, D, F). Pearson correlation was performed to evaluate linear relationships; (G) Nuclear distribution in fibres. Error bars show mean ± SEM. Statistical tests included normality tests and t-tests.

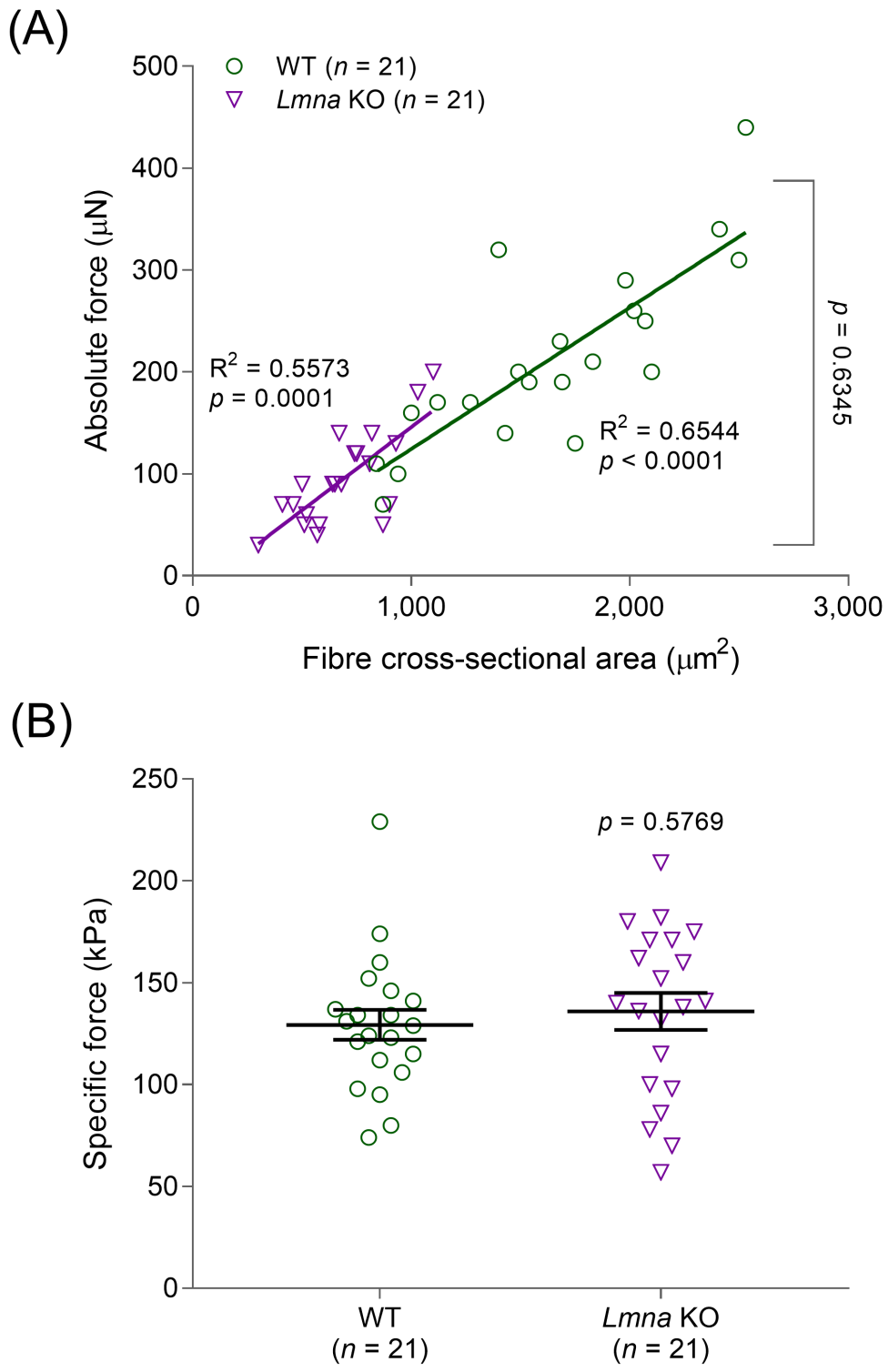

Figure 4.20: Normal force production in lamin A-deficient single myofibres

Data points represent individual single muscle fibres. (A) Pearson product moment correlation was performed to evaluate linear relationships; (B) Error bars show mean ± SEM. Statistical tests included normality tests and t-tests.

4.3.4. Progerin does not alter measured myofibre parameters

As the *Lmna*^{G609G} mouse model of HGPS has been noted to share a common transcriptional signature with the *Zmpste24* KO progeria model (Osorio *et al.*, 2011), as well as because similarly to native prelamin A, progerin (a truncated and farnesylated form of prelamin A, resulting from this mutation) has been suggested to accumulate in cells during the ageing process (Scaffidi & Misteli, 2006; Cao *et al.*, 2007; Burtner & Kennedy, 2010; López-Otín *et al.*, 2013), it was wished to investigate whether progerin is associated with abnormalities in single muscle fibres, similar to those described above in *Zmpste24* KO muscle fibres. No alterations in measured fibre and nuclear parameters were observed in these mice (Figure 4.21 through Figure 4.23).

Taken together, the results acquired from the various mouse models above suggest that the observed defects in *Zmpste24*-deficient mice resulted primarily from loss of *Zmpste24* and accumulation of farnesylated prelamin A in single muscle fibres, rather than the lack of lamin A/C. Strikingly, the defects are not phenocopied by the expression of progerin, which like prelamin A retains a farnesylated C-terminal CAAX domain that alters a number of other functional parameters of the intermediate filament protein.

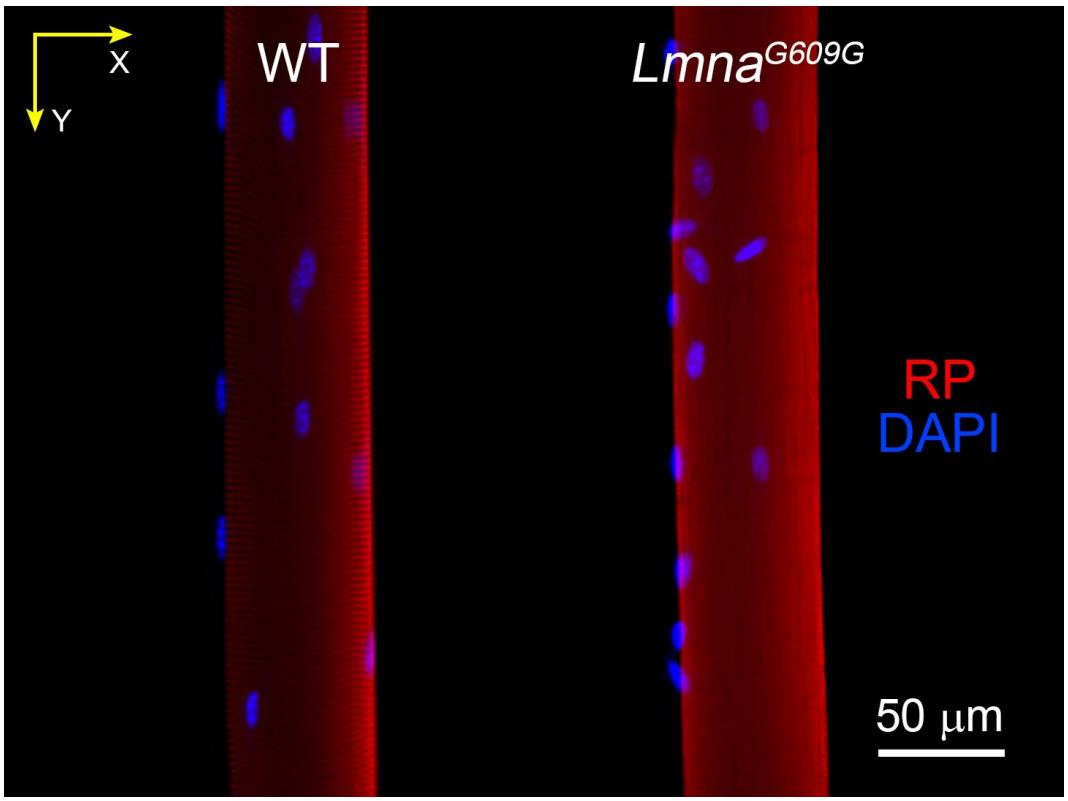

Figure 4.21: Typical confocal images of WT and *Lmna*^{G609G} single myofibres
Fibres were stained for nuclei (DAPI, blue) and actin (Rhodamine Phalloidin; RP, red) and imaged using 20x objective lens.

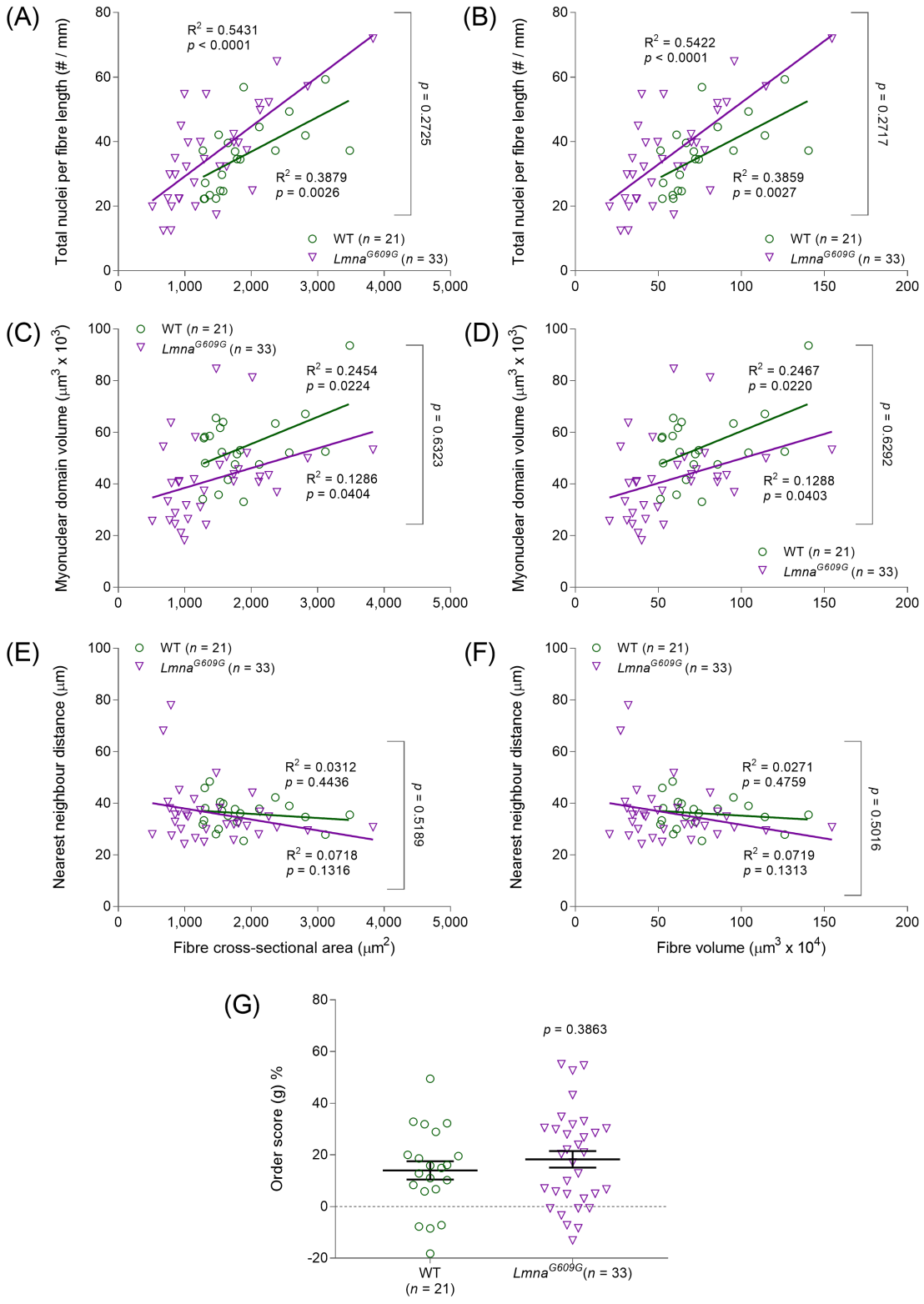

Figure 4.22: Nuclear organisation in *Lmna*^{G609G} single myofibres

Data points represent single myofibres. Graphs show various myonuclear parameters per fibre CSA (A, C, E) and volume (B, D, F). Pearson correlation was performed to evaluate linear relationships; (G) Nuclear distribution in fibres. Error bars show mean ± SEM. Statistical tests included normality tests and t-tests.

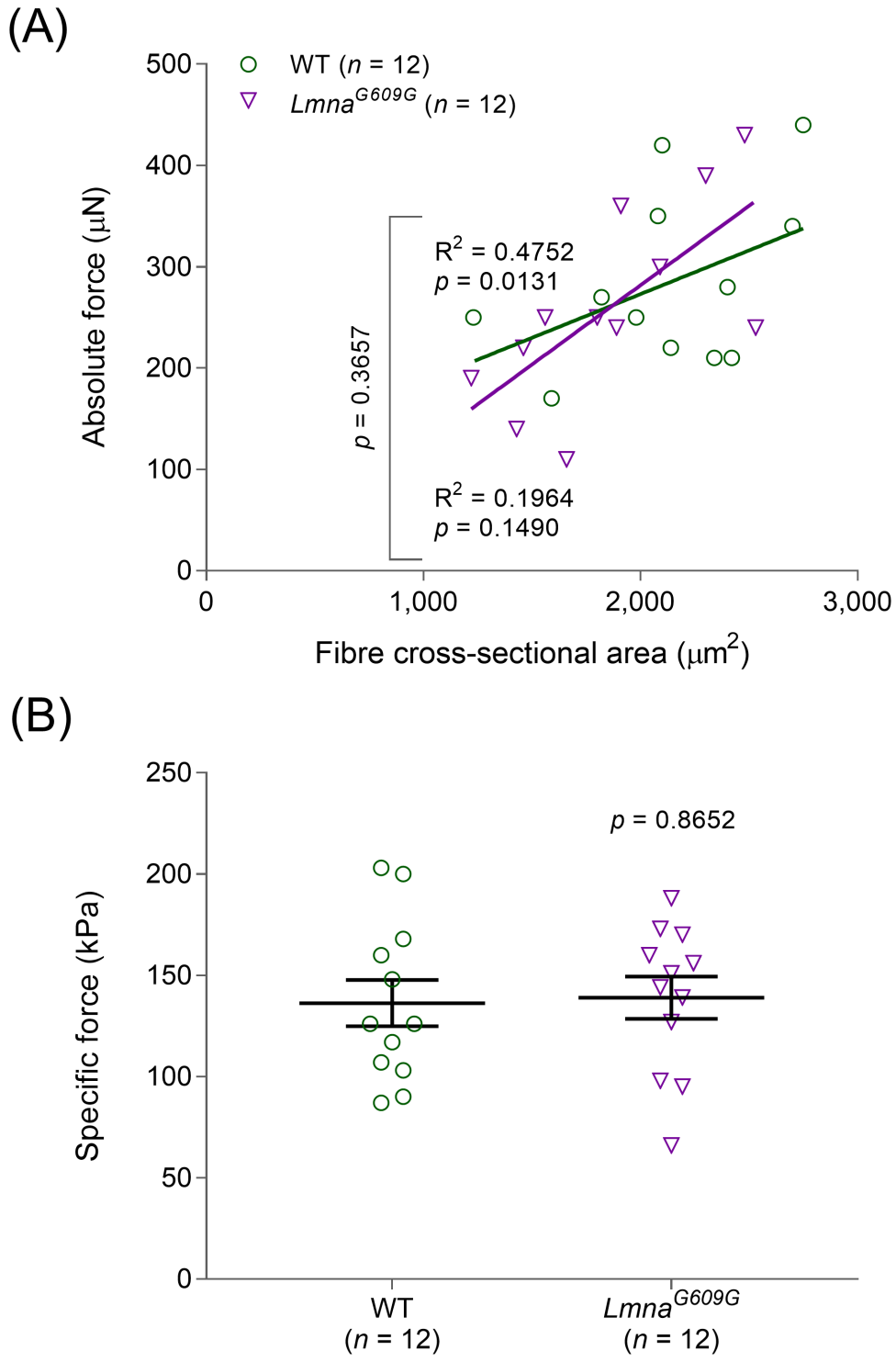

Figure 4.23: Normal force production in *Lmna*^{G609G} single myofibres

Data points represent individual single muscle fibres. (A) Pearson product moment correlation was performed to evaluate linear relationships; (B) Error bars show mean ± SEM. Statistical tests included normality tests and t-tests.

4.4. Discussion

The present work was performed to unravel the mechanisms that link the processing of lamin A with myonuclear organisation and functional capabilities of single muscle fibres in HGPS and normal ageing. Results revealed that a major reason for the low force-generating capacity of *Zmpste24*-deficient single muscle fibres may be associated with reduced contractile protein content, possibly caused by lower number of nuclei, larger MNDs, increased NN distances and lower transcriptional activity of nuclei, alluded to by the lower AcH3 levels found in this model. By altering levels of *Zmpste24* expression (mosaic mice), farnesylation of prelamin A (FTIs in *Zmpste24* KO mice) and expression of *Lmna* (*Lmna* KO mice), it was determined that the source of the cellular and nuclear changes mentioned above is predominantly loss of *Zmpste24* and the accumulation of farnesylated prelamin A, rather than lack of lamin A; had the source of such alterations been solely the absence of *Zmpste24*, no change in the measured fibre parameters should have been noted in FTI-treated muscle fibres. Interestingly, the cellular and nuclear changes found in single muscle fibres from *Zmpste24* KO mice were not witnessed in the presence of progerin ($Lmna^{G609G}$ mice).

4.4.1. Sub-optimal MND sizes in *Zmpste24* KO muscle fibres

In *Zmpste24*-deficient muscle fibres, a lower number of nuclei was observed, with a concomitant increase in NN distances and MND volumes. Due to the nature of this study, it is unknown whether such alterations could be related to a change in nuclear turnover, whereby myonuclei are not incorporated as efficiently, or are extensively lost, as discussed below.

During early development, studies suggest that the source of the low number of nuclei in *Zmpste24*-deficient muscle fibres is inefficient nuclear accretion, observed by a reduction in the satellite cell (SC) pool, as well as lower rates of SC/myoblast activation, proliferation and differentiation (Scharner, 2008; De La Rosa *et al.*, 2013; Song *et al.*, 2013). Under normal conditions, number of myonuclei in mice increases in muscle fibres up to 21 days of age, after which muscle fibres undergo hypertrophy without the addition of myonuclei (White *et al.*, 2010). As activation of SCs and their incorporation into single muscle fibres is impaired in the absence of *Zmpste24* (De La Rosa *et al.*, 2013; Song *et al.*, 2013), it is not surprising that already

at 3-4 weeks of age *Zmpste24* KO mice are smaller and weaker than their WT littermates (Bergo *et al.*, 2002; Pendás *et al.*, 2002). Consequently, it is reasonable to view lack of SC activation as the origin of the low nuclear number in *Zmpste24* KO muscle fibres.

When considering the reasons for inefficient nuclear accretion in *Zmpste24*-deficient muscle fibres during development, the following key facts should be considered. SCs may become activated by stretching of the nuclear membrane (Tatsumi *et al.*, 2001; Wozniak *et al.*, 2005; Enyedi & Niethammer, 2017), which involves the mediation of the mechano-sensitive YAP signalling pathway, amongst other mechano-sensitive genes (Judson *et al.*, 2012; Elosegui-Artola *et al.*, 2017; Panciera *et al.*, 2017). During application of force to the NE, nuclear shape changes, thereby causing stretching of nuclear pores, which in turn, reduces the mechanical resistance to translocation of YAP into the nucleus (Elosegui-Artola *et al.*, 2017). YAP knockdown by anti-Yap shRNAs has been shown to reduce the proliferation of SC-derived myoblasts by ∼40% (Judson *et al.*, 2012). *In vivo* work has shown that inactivation of YAP by tamoxifen, in mice with a conditional knockout of YAP in SCs, impairs muscle regeneration following cardiotoxin-induced injury, by negatively affecting SC proliferation (Sun *et al.*, 2017). It is hence not surprising that the YAP pathway is a critical regulator of myonuclear number and skeletal muscle fibre size (Watt *et al.*, 2015).

Interestingly, the process of YAP import into the nucleus has been shown to be deregulated in myoblasts from L-CMD patients with *LMNA* mutations (ΔK32, R249W and L380S) (Bertrand *et al.*, 2014). In light of the dependence of YAP translocation into the nucleus on nuclear membrane stretching, this is not a surprising result, as such mutations in human myoblasts have been associated with defective ability of cells and nuclei to adapt to substrate stiffness and increased cytoskeletal tension (Bertrand *et al.*, 2014; Schwartz *et al.*, 2017). It would be intriguing to think such changes in YAP signalling could exist in HGPS cells, as at least in theory, if SC activation depends on YAP signalling and the latter depends on the ability of nuclei to respond to mechanical tension (Swift *et al.*, 2013), which is known to be altered in *LMNA* (G609G) HGPS cells (Dahl *et al.*, 2006; Verstraeten *et al.*, 2008), this could potentially account for the low number of nuclei found here in *Zmpste24*-deficient muscle fibres. Nevertheless, the relevance of this theory to the *Zmpste24* KO mouse is unknown, as to the author's knowledge, such studies have never been performed in this model of HGPS.

Alternatively, or in addition to the theory above, it is possible that the incorporation of muscle precursors into muscle fibres is disrupted due to faulty expression of mechano-sensitive genes. For instance, *Lmna* (G609G) human fibroblasts show detachment of chromatin from the lamina and loss of heterochromatin (Shumaker *et al.*, 2006; McCord *et al.*, 2013), which unsurprisingly, as stretching of chromatin results in upregulation of gene transcription (Tajik *et al.*, 2016), leads to altered epigenetic control of mechano-sensitive genes (Shumaker *et al.*, 2006). Nevertheless, these are merely but theories, which suggest that a change in the rate of nuclear incorporation might be a significant cause, whose effect, in *Zmpste24* KO single muscle fibres, is low number of nuclei; specific validation of these theories in this mouse model is, of course, warranted.

Later in life, during adolescence, the low number of nuclei in the *Zmpste24*-deficent muscle fibres could also be explained by loss of nuclei. This could be explained by a dominant negative effect of prelamin A accumulation, as seen by increased structural fragility of the NE (De Vos *et al.*, 2011), delayed recruitment of 53BP1 to sites of DNA lesions and defective DNA repair (Liu *et al.*, 2005), chronic activation of the p53 pathway (Varela *et al.*, 2005), as well as oxidative stress and that leads to cell senescence in cells with prelamin A accumulation (Sieprath *et al.*, 2015). Most of these probably take place in *Zmpste24*-deficient muscle fibres during adolescence. However, as (i) large fibres here were the most affected by the lack of *Zmpste24*, as shown by their low specific force and myosin content, and (ii) large *Zmpste24*-deficient fibres had the same number of nuclei as small fibres, it seems that insufficient nuclear accretion was the predominant factor leading to the observed low number of nuclei in muscle fibres lacking *Zmpste24*. That the number of nuclei in those large fibres was likely insufficient to maintain the function of such muscle fibres of such volume can be supported by their reduced contractile protein content and low specific force.

The maintenance of nuclear number, NN distance and MND size are prerequisites for preserving the intrinsic force-generating capacity of muscle fibres during pathophysiological conditions (Qaisar *et al.*, 2012, 2013; Omairi *et al.*, 2016). Hence, the decrease in the number of nuclei and concomitant increase in NN distance and MND volume in the presence of prelamin A may explain the specific force loss in membrane-permeabilised fibres (where the neuromuscular junction, excitation-contraction coupling and sarcoplasmic reticulum-Ca^{2+} release are not involved). This is in accordance with a recent study investigating myonuclear organisation and

force production in mice lacking myostatin, which suggested that abnormally hypertrophied fibres were limited in their force production through the inability to maintain optimal MND sizes (Qaisar *et al.*, 2012). The absence of myostatin or Zmpste24 may then share similar cascades of sub-optimal or negative cellular events. Reduced incorporation and/or increased loss of myonuclei may require the remaining myonuclei to extend their individual influence to unusually large cytoplasmic volumes, beyond their maximum functional capacity (physiological "ceiling"), preventing the optimal distribution of gene products, protein synthesis and ultimately leading to a sub-optimal density of contractile proteins (i.e., myosin). Therefore, intrinsic myofibre force production is decreased, and this results in skeletal muscle weakness.

4.4.2. Preserved nuclear distribution

As mentioned earlier, myonuclei are well known to be evenly spaced along the surface of muscle fibres. Such distribution is crucial to facilitate lower cytosolic transport distances (Bruusgaard *et al.*, 2003) and to favour a better control of chromosomal architecture and transcriptional regulation (Volk, 2013). Interestingly, the results here show that the overall distribution of nuclei was preserved in all models studied, implying that a proper inter-nuclear communication is maintained (Gordon *et al.*, 1992).

4.4.3. What causes nuclear dysfunction?

As neither a deficiency in lamin A (*Lmna* KO), nor accumulation of progerin ($Lmna^{G609G}$), have affected the myonuclear behaviour and myofibre parameters measured in the present study, it is suggested that the source of the low nuclear number, large MNDs and low specific force found in muscle fibres lacking *Zmpste24* is loss of *Zmpste24* and the accumulation of prelamin A. Specifically, it seems that the farnesylation of prelamin A is a predominant cause, as had the source of such alterations been solely the absence of *Zmpste24*, no change in the measured fibre parameters should have been noted in FTI-treated muscle fibres. Nevertheless, as a WT control was not available for a comparison with the FTI-treated *Zmpste24*-deficient muscle fibres, it is impossible to determine whether the farnesylation of prelamin A is the sole cause of the pathologies observed.

The literature on the *Zmpste24* KO mouse model suggests the accumulation of farnesylated prelamin A is toxic to cells. For instance, the administration of FTIs to these mice has been previously shown to ameliorate the disease (Fong *et al.*, 2006*a*). Moreover, studies on *Zmpste24* KO mice heterozygous for *Lmna* (*Zmpste24*$^{-/-}$ *Lmna*$^{-/+}$) have shown that simply reducing the amount of prelamin A in nuclei partially rescues the progeroid phenotype (Fong *et al.*, 2004, 2006*b*; Varela *et al.*, 2005). Additionally, *Lmna*$^{LCO/LCO}$ mice, which only express lamin C, but not prelamin A or mature lamin A, were entirely healthy and exhibited only very minimal alterations in nuclear shape and nuclear deformability (Fong *et al.*, 2006*b*). Lastly, heterozygosity for *Lmna*$^{LCO/+}$ in *Zmpste24* KO mice (*Zmpste24*$^{-/-}$ *Lmna*$^{LCO/+}$), resulted in mice that were entirely healthy and exhibited only very minimal alterations in nuclear shape and nuclear deformability (Fong *et al.*, 2006*b*). Consequently, the literature above tends to support the notion that the cellular accumulation of farnesylated prelamin A is the main source for the progeroid phenotype in *Zmpste24* KO mice.

With this in mind, a reduction in levels of farnesylated prelamin A might have also been the dominant reason for the rescue of myofibre parameters found in the mosaic mice, which have an equal number of Zmpste24-proficient and Zmpste24-deficient nuclei. On the one hand, the reduction in prelamin A was accompanied by partial expression of lamin A, precluding such a conclusion. On the other hand, *Lmna* KO mice did not show major changes in the measured myofibre parameters, including specific force. Thus, it seems likely that the adverse changes in the mosaic mice were due to prelamin A accumulation.

It is worth noting that whereas mice lacking A-type lamins indeed develop a muscular dystrophy phenotype (Gnocchi *et al.*, 2011), measured parameters from lamin A/C-deficient single muscle fibres were mostly similar to WTs in the present work. It is especially intriguing, as this mouse model has been previously described with significant muscle dysfunction, including reduced specific force of the EDL muscle (Gnocchi *et al.*, 2011). A possible explanation for this is that although the number of nuclei in mouse single muscle fibres appears to stabilise after P21, MNDs continue to expand for possibly more than 60 days following birth (White *et al.*, 2010). As the mice studied here were 5-weeks old and as *Lmna* KO mice have been noted with severe growth retardation (Nikolova *et al.*, 2004; Gnocchi *et al.*, 2011), it is possible that studying single muscle fibres at such a developmental stage is inappropriate for studying of MNDs. Noteworthy, the specific colony studied here was noted with numerous myonuclear abnormalities, typically

at the myotendinous junction (MTJ) (Gnocchi *et al.*, 2011); however, nuclear distribution analysis was not performed in their study, and in the current study the MTJ was avoided. Interestingly, another study on the *Lmna* KO mouse model (Mittelbronn *et al.*, 2008) focused primarily on the MTJ and found nuclear abnormalities in the region that resemble those found by Gnocchi *et al.* (2011), but pathology distal to the MTJ was not witnessed, possibly as the MTJ is particularly vulnerable to damage, due to longitudinal force transmission from contractile proteins to the extracellular matrix (ECM) (Tidball, 1991). Thus, it is possible that either the method used in the current work to analyse nuclear parameters is not suitable for this developmental stage, or that by avoiding the MTJ most of the phenotype is practically missed, in terms of the parameters measured in this thesis.

Nevertheless, this would not explain the surprisingly maintained single fibre force in the *Lmna* KO mouse model. Gnocchi *et al.* (2011) found sarcomeric disorganisation at the MTJ, which was used to account for the reduction in whole EDL muscle specific force. However, the current study avoided the MTJ when measuring specific force. Moreover, the fact that the measurements performed here were on single fibres, which exhibit a linear stress-strain relationship, rather than whole muscle, which has a non-linear relationship due to transmission of forces from the tendon and muscle fibres to the ECM (Gillies & Lieber, 2011; Meyer & Lieber, 2011; Gillies *et al.*, 2011), together with the fact that the *Lmna*-deficient muscles displayed lipid and collagen deposition at the MTJ (Gnocchi *et al.*, 2011), which could further affect the measured force through the ECM (Patel & Lieber, 1997; Gillies & Lieber, 2011), render this comparison in specific force rather difficult, if not impossible. Therefore, further research is required to account for the discrepancies between the phenotypes of *Lmna*-deficient and *Zmpste24*-deficient single muscle fibres.

Lastly, it is intriguing that the accumulation of progerin in $Lmna^{G609G}$ did not elicit similar patterns to those found in *Zmpste24* KO muscle fibres, predominantly as both are models of HGPS that accumulate farnesylated prelamin A, albeit progerin has a deletion of 50 amino acids near its C-terminal domain. Additionally, *Lmna* (G609G) mice have been noted to share a common transcriptional signature with the *Zmpste24* KO progeria model (Osorio *et al.*, 2011). The main difference between the two mouse models is that, whereas both can express lamin C, the expression of lamin A is perturbed, leading to accumulation of a native (*Zmpste24* KO) or mutated farnesylated prelamin A. As mentioned above, the absence of *Zmpste24* could not have

been the only reason for the phenotype of *Zmpste24* KO muscle fibres, as had it been true the treatment with FTIs should not have caused any difference in MND volumes and specific force. However, as *Lmna*^{G609G} showed normal number of nuclei, MNDs and specific force, it certainly seems that the aetiology of muscle dysfunction may be different between *Zmpste24* KO and *Lmna*^{G609G} mice. This may be epitomised in *Lmna*$^{HG/+}$ mice, which unlike *Lmna*^{G609G} mice, exclusively express farnesylated progerin, without simultaneous expression of lamin C, and do not develop grip strength abnormalities even when they are very debilitated (Yang *et al.*, 2006). Importantly, and similarly to *Zmpste24* KO mice, it appears to be the farnesylation of progerin that contributes to the severe progeroid phenotype in these mice (Yang *et al.*, 2005, 2011). Consequently, further close comparison of different mouse models with lamin A/C mutations will be required to delineate all these differences.

4.4.4. Altered gene expression and myosin content

If nuclei in *Zmpste24*-deficient muscle fibres were indeed performing beyond their maximum functional capacity, it is expected that those nuclei should have been working at 100% efficiency, in order to maintain the fibres' force generating capacity (Kirby *et al.*, 2016). However, as seen by the relative reduction in the active portion of AcH3 nuclei in *Zmpste24*-deficent muscle fibres, as well as the maintained genomic repression by H3K27me3, the nuclei were likely not functioning, or unable to function, at maximum capacity.

Normal nuclear response to mechanical stress requires proteins that tether the nucleus to the cell, thereby providing the nucleus with structural integrity and mechanical connectivity with the cell (Schirmer & Gerace, 2005; Kirby & Lammerding, 2018), in order to affect the expression of mechano-sensitive genes (Lammerding *et al.*, 2004; Swift *et al.*, 2013). One mechanism that could possibly account for the altered levels of AcH3 in *Zmpste24* KO muscle fibres is faulty connection of the NE with the cytoskeleton. It has been demonstrated that farnesylated prelamin A upregulates and recruits SUN1 to the NE in human myoblasts (Mattioli *et al.*, 2011). As correct localisation of nesprin-1 depends on that of SUN1/2 in skeletal muscle fibres (Lei *et al.*, 2009) and nesprin-1 associates with microtubules *via* a nesprin-dependent recruitment of kinesin-1 (Wilson & Holzbaur, 2015), PCM-1 (Espigat-Georger *et al.*, 2016), pericentrin and Akap450 (Gimpel *et al.*, 2017), it is possible that nuclei in *Zmpste24*-deficient muscle fibres were

not able to respond to mechanical cues, possibly explaining the shifted levels of AcH3 in these muscle fibres. Nevertheless, this is merely a theory that should be specifically investigated.

With the above in mind, it is not surprising that all the parameters demonstrating the deleterious effects related to the *Zmpste24* deficiency are exaggerated in larger fibres. Smaller *Zmpste24*-deficient muscle fibres showed a normal number of nuclei, MND, contractile protein content and relatively normal muscle fibre function, when compared to WT fibres, despite the relative inability of their nuclei to respond to mechanical cues. However, further hypertrophy of muscle fibres, in the absence of nuclear accretion and reduced ability of nuclei to sense mechanical stress, appears to have led to larger MNDs and NN distances, as well as low contractile protein content and specific force. Importantly, the fact that progerin and prelamin A are phenotypically dissimilar does not necessarily mean that *Zmpste24* KO mice are not suitable for ageing research, as prelamin A has been noted to accumulate in vascular smooth muscle cells (VSMCs) of elderly individuals, promoting atherosclerotic lesions (Ragnauth *et al.*, 2010), as well as calcification of human aortic VSMCs (Liu *et al.*, 2013).

4.5. Conclusion

The present work was performed to unravel the mechanisms that link the processing of lamin A with myonuclear organisation and functional capabilities of single muscle fibres in HGPS and normal ageing. Results showed that the loss of *Zmpste24* and accumulation of farnesylated prelamin A in single muscle fibres is a major determinant in dysregulating myonuclear abundance, NN distance, MND size, contractile protein content and intrinsic force-generating capacity. This newly identified mechanism may contribute to muscle fibre weakness in HGPS and ageing. Future research should investigate the specific involvement of prelamin A farnesylation and loss of Zmpste24 in *Zmpste24* KO mice to further characterise the involvement of each in the pathology.

Chapter 5: Nuclear organisation in human ageing myofibres

5.1. Introduction

The current thesis endeavoured to characterise the connection between ageing and disuse-related misprocessing of lamin A with myonuclear organisation and muscle weakness in isolated single muscle fibres. In the previous chapter, the specific effect of prelamin A and progerin on nuclear organisation and specific force were investigated. This was done because premature ageing syndromes share molecular and cellular mechanisms with many ageing-associated diseases (Janin *et al.*, 2017; Kubben & Misteli, 2017), including accumulation of prelamin A and progerin, a condition noted during normal ageing (Scaffidi & Misteli, 2006; López-Otín *et al.*, 2013; Kubben & Misteli, 2017). The current chapter attempted to investigate whether a link indeed exists between myonuclear organisation and single muscle fibre weakness in human muscle ageing and disuse, as has been found in the prelamin A-accumulating single muscle fibres from *Zmpste24* KO mice.

In many countries, life expectancy and the number of people in older age have increased significantly in the last decades. However, healthspan, that is the length of time one lives without ageing-associated chronic disease, has remained virtually the same since the middle of the 20th century, despite the significant increase in life expectancy in that period. As a result, governments are required more than ever to medically and financially support an increasing number of older unhealthy citizens, who could nowadays be living with ageing-related chronic diseases for 20 years and longer, which current figures show is ∼23% of one's life expectancy at

birth in the UK (ONS, 2017; Harridge & Lazarus, 2017). The goal for health services should therefore be to maximise health expectancy to a similar number of years as life expectancy (Figure 1.11). This would result in a significant reduction in the number of years one is found in a state of morbidity, which could save a tremendous amount of money to health services and citizens alike.

Past studies on muscle ageing suffer from two major limitations. Firstly, literature on human ageing is not only limited by differences in genetics between individuals, nutrition, healthcare and socioeconomic position (Kuh *et al.*, 2014), but is also skewed by the relative lack of longitudinal studies (Harridge & Lazarus, 2017). Secondly, most ageing studies are conducted on sedentary elderly cohorts, which comprise of a combination of biological ageing and muscle disuse. Muscle disuse has been shown to negatively impact skeletal muscle contractile function (Callahan *et al.*, 2014), whereas physical activity is widely associated with numerous health benefits (Powell *et al.*, 2011). An alternative view suggests the default for humans is to be physically active, as our ancestors have always led a physically active lifestyle to survive, and thus, muscle inactivity or even a sedentary lifestyle should be considered as a risk factor for age-related diseases (Harridge & Lazarus, 2017). In light of this, research on human ageing should be to not simply "increase human longevity regardless of the consequences, but to increase active longevity free from disability and functional dependence" (Hayflick, 2000:269). To accomplish this goal, ageing research should differentiate between biological ageing and muscle disuse, by studying physically active elderly populations that are not confounded by the adverse physiological alterations resulting from muscle disuse (Pollock *et al.*, 2015, 2018*b*).

Increasing age is often accompanied by a decline in physical function due, in part, to sarcopenia, a condition that is characterised by progressive loss of skeletal muscle mass and strength (Frontera & Ochala, 2015). At the cellular level, sarcopenia has been associated with an intrinsic deterioration of the force-generating capacity of individual myofibres, however, the reasons remain obscure (Harridge *et al.*, 1996; Frontera *et al.*, 2000; D'Antona *et al.*, 2003; Ochala *et al.*, 2007). Such force loss has been suggested to be due to a reduction in MHC concentration in human single muscle fibres that is modulated by both biological ageing and muscle disuse (D'Antona *et al.*, 2003, 2007*b*). However, the reasons for the reduction in MHC concentrations, and therefore muscle strength, are unknown.

One possible explanation for the reduction in contractile protein content could be nuclear mispositioning in single muscle fibres. As demonstrated by Cristea *et al.* (2010), single muscle fibres from the vastus lateralis muscles of elderly men and women exhibit altered nuclear organisation and nuclear clustering, coinciding with reduced myonuclear domain (MND) volumes and smaller fibre cross-sectional areas (CSA) (Bruusgaard *et al.*, 2006; Qaisar *et al.*, 2013). Nuclear mispositioning and/or enlarged MNDs are likely to affect nuclear synthetic capacity and production of contractile proteins at the myofibre level (Cristea *et al.*, 2010), as has been shown in the previous chapter. Additionally, increasing accumulation of prelamin A/progerin with age has been documented in various cells from healthy young and ageing cohorts (McClintock *et al.*, 2007; Olive *et al.*, 2010*a*; López-Otín *et al.*, 2013), and as been demonstrated in chapter 4, this may be a source of myonuclear disorganisation in single muscle fibres in premature ageing syndromes.

Although Cristea *et al.* (2010) had isolated single muscle fibres from healthy elderly sedentary men and women with no history of any metabolic, locomotor, or neuromuscular disorder, it is unknown whether the observed sarcopenic changes were directly related to biological ageing or other confounding factors, such as long-term muscle disuse (Greig *et al.*, 1994; Qaisar *et al.*, 2013; Pollock *et al.*, 2015, 2018*b*, 2018*a*; Harridge & Lazarus, 2017; Lazarus & Harridge, 2017). Consequently, it is impossible to distinguish the effects of biological ageing on nuclear organisation in that study, and the altered nuclear organisation witnessed might be related to muscle disuse. This is further complicated by the fact that Karlsen *et al.* (2015) had not found a difference between MND volumes of sedentary young, trained young, sedentary elderly and trained elderly individuals; the effect on nuclear distribution, however, had not been investigated. It is also unclear whether prelamin A accumulates due to biological ageing or muscle disuse.

Consequently, in the present investigation, the hypothesis was that age and chronic physical inactivity can lead to changes in nuclear organisation in single muscle fibres. To verify that, membrane-permeabilised single myofibres were isolated from young sedentary individuals and from older participants of various levels of physical activity (Table 5.1), ranging from vigorous exercisers (master cyclists) to sedentary and hip fracture patients (model of muscle disuse). 3D spatial arrangement of myonuclei in the acquired single muscle fibres was then evaluated (Cristea *et al.*, 2010; Qaisar *et al.*, 2013) and analysis of global transcriptional activity,

using acetyl histone H3 (AcH3) as a marker of activation of transcriptional activity (Gnocchi *et al.*, 2011), was performed.

5.2. Methods

5.2.1. Subjects

Four mixed gender groups were recruited to participate in the current study (Table 5.1). The first group, used as controls, consisted of eight healthy young individuals (mean age: 33.13 ± 8.04 years). The other three cohorts were comprised of elderly individuals with different levels of physical activity. The most active elderly group consisted of previously characterised (Pollock *et al.*, 2015, 2018*b*, 2018*a*; Kalakoutis, 2017; Duggal *et al.*, 2018) five physically active individuals who were amateur, non-elite master cyclists. The sedentary elderly group consisted of three healthy individuals (mean age: 72.67 ± 3.79 years). The least active, and used as a model for muscle disuse, was a previously characterised cohort, comprised of three patients in the present study, who underwent dynamic hip screw insertion surgery (mean age: 77.33 ± 16.50 years) (Kalakoutis, 2017).

Participants were considered healthy if they met the criteria outlined by Greig *et al.* (1994). Based on a health questionnaire, participants were excluded from a "healthy" classification if they smoked or consumed alcohol excessively, had known hypertension or any known cardiovascular, musculoskeletal or neurological conditions, or if they were acutely and/or chronically on any medication.

The young cohort was considered healthy, but not necessarily sedentary, as two of the participants had been participating in low-level recreational sport activities (<2 sessions/week) at the time of the study. Thus, the young cohort consisted of low-level physically active and sedentary individuals. No statistically significant difference was noted for any parameter measured here between these two individuals and the rest of the sedentary cohort.

Master cyclists were included if they were able to cycle 100 km in under 6.5 hours (males) or 60 km in under 5.5 hours (females). To be included in the study, participants must have had

completed this distance within the specified time on two occasions in the three weeks prior to the date of participation in the study.

Elderly individuals undergoing hip surgery aged 55 years or older were identified by Mr Onur Berber or Mr Marc George, who were members of their healthcare team. Patients underwent mental health screening to ensure they were able to provide informed consent prior to surgery. The patients also completed a basic physical health questionnaire and were considered eligible if they did not suffer from any neuromuscular disease. The hip fracture patients were recruited on the basis that they were likely to be frail individuals, and due to their age sometimes had underlying health conditions (Table 5.2). In terms of musculoskeletal health status, all patients were previously diagnosed with osteoporosis and patient HF5 had additionally been diagnosed with rheumatoid arthritis. Thus, this group makes up a rather heterogeneous elderly group.

Muscle biopsies were obtained from all the participants, from the vastus lateralis muscle, using the Bergström needle technique, as described in section 2.1.2. In patients undergoing surgery for hip fractures, samples from the vastus lateralis were obtained during surgery. Prior to participation, written informed consent was obtained from all subjects. All procedures were approved by the King's College London ethics committee (reference numbers 12/LO/0457 and 16/LO/0250) and conformed to the Declaration of Helsinki.

5.2.2. Solutions

Relaxing solutions contained 4 mM Mg-ATP, 1 mM free Mg^{2+}, 20 mM imidazole, 7 mM EGTA, 14.5 mM creatine phosphate, and KCl to adjust the ionic strength to 180 mM and pH to 7.0. The concentration of free Ca^{2+} was $10^{-9.00}$ M.

Table 5.1: Participant information

Condition	ID	Age (Years)	Gender	No. myofibres
Young	Y1	25	F	16
	Y2	27	M	17
	Y3	22	M	18
	Y4	32	F	17
	Y5	35	F	17
	Y6	42	F	16
	Y7	38	F	17
	Y8	44	F	18
Mean ± SD		**33.13 ± 8.04**		**17.00 ± 0.76**
Master cyclist	MC1	71	M	18
	MC2	76	F	17
	MC3	79	F	12
	MC4	75	M	12
	MC5	73	M	15
Mean ± SD		**74.80 ± 3.03**		**14.80 ± 2.77**
Sedentary elderly	O1	70	M	17
	O2	71	F	16
	O3	77	M	17
Mean ± SD		**72.67 ± 3.79**		**16.67 ± 0.58**
Hip fracture	HF2	59	F	18
	HF3	91	M	17
	HF5	82	F	17
Mean ± SD		**77.33 ± 16.50**		**17.33 ± 0.58**

Table 5.2: Clinical history of hip surgery patients
RhA = Rheumatoid Arthritis; MS = Multiple Sclerosis; PD = Parkinson's Disease.

	Patient HF2	**Patient HF3**	**Patient HF5**
Cardiac history	None	None	None
Vascular history	None	None	None
Chest history	None	None	None
Smoke	None	None	Unknown
Diabetes	None	None	Type 2
Major illness history	None	Hartmann's operation	RhA
Psychiatric history	None	None	None
Osteoarthritis/RhA	None	None	RhA
Fracture history	Patella 2007	None	Unknown
Bone health	Osteoporosis	Osteoporosis	Osteoporosis
Spinal history	None	None	None
Musculoskeletal surgery	None	None	RhA
Hypertension	Yes	Yes	Yes
Recent acute illness	None	None	None
Regular medication	Perindopril, Amlodipine, Etidronate, Adcal	Furosemide, Paracetamol, Colecalciferon, Docusate	Metformin, Denusomab, Levothyroxin, Allopurinol
Recent (5 year) hospital stay	None	None	None
Physical disabilities	None	Hearing	None
MS/PD	None	None	None
General illness affecting mobility	None	None	RhA
1-year fall frequency	None	Recurrent falls	None
Height (cm)	164	Unknown	152
Weight (kg)	53	Unknown	57.15
BMI	19.70	Unknown	24.70

5.2.3. Muscle fibre permeabilisation

Muscle fibres were permeabilised as described in section 2.2. Briefly, following dissection of the vastus lateralis muscle, muscle samples were placed in relaxing solution at 4°C. Bundles of approximately 50 myofibres were dissected free and then tied with surgical silk to glass capillary tubes at slightly stretched lengths. They were then treated with skinning solution (relaxing solution containing glycerol; 50:50 v/v) for 24 hours at 4°C, after which they were transferred to -20°C or processed further with sucrose, snap frozen in liquid nitrogen-chilled propane and stored at -80°C for long-term storage.

5.2.4. Nuclear organisation in single myofibres

Single muscle fibres were dissected and mounted at a fixed sarcomere length of ≈2.20 µm on copper meshes for electron microscopy (SPI G100 2010C-XA, width, 3 mm), which had been glued to No. 1.5 (0.17 mm thickness) high-precision coverslips, using a stereomicroscope (Zeiss Stemi 2000-C with a Zeiss SteREO CL 1500 ECO light source) and fine dissection tweezers (Ideal-tek High Precision 5.SA) (chapter 3). The fibres were then incubated in a solution containing rhodamine phalloidin (RP; 1:100, Cat. #00027, Biotium) and DAPI (1:1000, Cat. #D3571, Molecular Probes) (section 2.3.1). Image stacks of 100 fluorescent images were acquired for each channel (1 µm *z* increments), using an inverted spinning disk confocal microscope (Zeiss Axiovert 200) equipped with a 20x objective lens (Zeiss FLUAR 20x/0.75, air) and an EXFO X-Cite® 120 mercury halide arc lamp (Table 2.5 and section 2.4.1). Sarcomere length was determined from a single brightfield image per fibre. Images were analysed as described in sections 3.5.1 and 2.4.1, using a custom-made MATLAB script (MATLAB® R2017a, MathWorks, Inc.). Figures were made using Prism v7 (GraphPad Software), Fiji (Schindelin *et al.*, 2012; Rueden *et al.*, 2017) and Photoshop CS6 (Adobe Systems, Inc.). Number of samples can be found in Table 5.1.

5.2.5. Immunofluorescence

Single muscle fibres were dissected and mounted on grids, as described above. Protocol and antibodies used for indirect immunofluorescence (IF) can be found in section 2.3.2. Number of samples studied is available in Table 5.3. Quantitative imaging of acetyl histone H3 was performed using an inverted spinning disk confocal microscope (Yokogawa CV1000), with a disk

pinhole size of 25 µm. The microscope was equipped with a 60x objective (Olympus UPlanSApo 60x/1.35, oil) and excitation lasers of 405 nm and 488 nm, matched with BP447/60 and BP525/50 emission filters. Images were acquired by an electron multiplying charge-coupled device (EM-CCD) camera (ImagEM-1K C9100-14, Hamamatsu), attached to a PC running CellVoyager™ CV1000 Software (Yokogawa). In order to determine global nuclear transcriptional activity in single nuclei, a stack of 50 images, 0.1 µm *z* steps, was acquired in the respective channel for each nucleus, using fixed illumination settings (section 3.4.2). Linearity of increasing camera exposure to a fixed antibody concentration, as well as *vice versa* was validated (De Vos *et al.*, 2010) (section 3.4.2). Skinned muscle fibres did not display any Pax7 positive satellite cells, in line with the literature (Konigsberg *et al.*, 1975; Cristea *et al.*, 2010; Ross *et al.*, 2018). Images were analysed using a custom-made Fiji macro (section 3.5.2), Huygens Deconvolution (Scientific Volume Imaging) and Prism v7 (GraphPad Software).

Table 5.3: Number of samples studied for acetyl-histone H3 quantification

Condition	Young	Master cyclist	Sedentary elderly	Hip fracture
No. participants	8	5	3	3
No. myofibres	32	16	10	24
No. nuclei	229	157	82	301

5.2.6. Statistical analysis

Statistical analysis and production of graphs were performed using Prism v7 (GraphPad Software), as described in section 2.4. Data from individual muscle fibres and cohorts was pooled together for each condition, in line with common practice in the field of both humans and animals (D'Antona *et al.*, 2003, 2007*b*, 2007*a*; Bruusgaard *et al.*, 2005, 2006, 2010, 2012; Frontera *et al.*, 2008; Cristea *et al.*, 2010; McCarthy *et al.*, 2011; Egner *et al.*, 2013, 2016; Karlsen *et al.*, 2015; Ross *et al.*, 2017*b*, 2018; Levy *et al.*, 2018; Buono *et al.*, 2018; Fongy *et al.*, 2019; Dungan *et al.*, 2019). Data are presented as mean ± SEM and as individual data points.

5.3. Results

Similarly to chapter 4, the results section is composed of a rather large number of figures associated with each cohort. Therefore, overview figures will be presented here; large versions of individual graphs within such figures may be found in Appendix 5.

5.3.1. Chronic muscle disuse increases the number of myonuclei

312 membrane-permeabilised muscle fibres were mounted at a fixed sarcomere length (≈2.20 µm; Figure 5.1). As previously described (Cristea et al. 2010), the number of nuclei per mm fibre length was linearly correlated with the CSA (Figure 5.2A) and volume (Figure 5.2B) of the same myofibres in the young and older sedentary individuals. The same pattern was noted in single muscle fibres from the master cyclist cohort. In contrast, in hip fracture patients this relationship was absent; their fibres had smaller volumes and an increased number of nuclei (mainly in smaller fibres). The regression lines were, therefore, significantly different between hip fracture patients and all the other groups.

The average MND size for individual fibres was linearly correlated with the CSA (Figure 5.2C) and volume (Figure 5.2D) of the same myofibres in the young and master cyclist cohorts. The hip fracture patients showed the most significant ($p < 0.0001$) linear correlation compared to all other groups, demonstrating very small MND sizes, especially in smaller fibres, corresponding with the higher number of nuclei found in those fibres. Interestingly, the regression line of the older sedentary group was not significant, thus, demonstrating a weak association between MND and fibre size in older sedentary individuals, in contrast to a previous report (Cristea *et al.*, 2010). The regression lines were, therefore, significantly different between hip fracture patients and all the other groups.

5.3.2. Biological ageing impairs nuclear positioning

To precisely characterise the spatial arrangement of myonuclei relative to one another, nearest neighbour distances (NNs) were calculated using the 3D co-ordinates of individual nuclei within each single muscle fibre. The results were similar to those obtained for MND. Indeed, NN per unit CSA (Figure 5.2E) and volume (Figure 5.2F) were significantly shorter in hip fracture patients than in all the other groups, especially in smaller fibre sizes. Regression lines of all other groups were similar to each other and dissimilar to the hip fracture cohort. To evaluate the regularity of nuclear positioning within myofibres, an order score was calculated (Bruusgaard *et al.*, 2003). The order score was significantly lower in all elderly groups than in young individuals (Figure 5.2G). This implies that the regular spacing between myonuclei is disrupted during the biological ageing process.

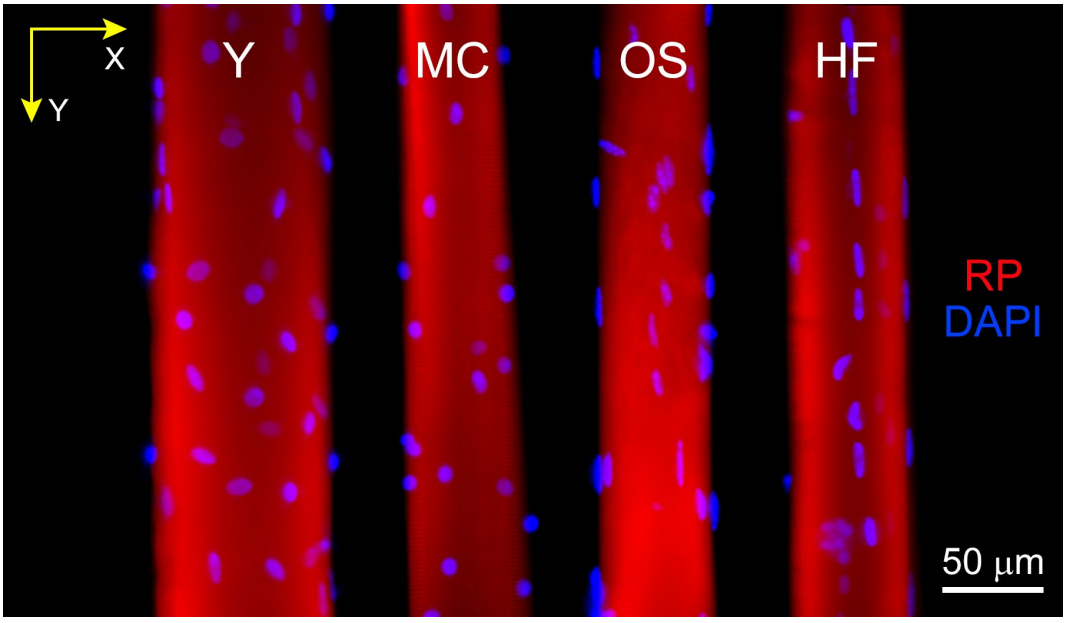

Figure 5.1: Typical confocal images of myofibres from young and elderly cohorts
Maximum intensity projection of muscle fibres stained for nuclei (DAPI, blue) and actin (Rhodamine Phalloidin; RP, red) and imaged using 20x objective lens. Y = Young, MC = Master Cyclists, OS = Older Sedentary, HF = Hip Fracture.

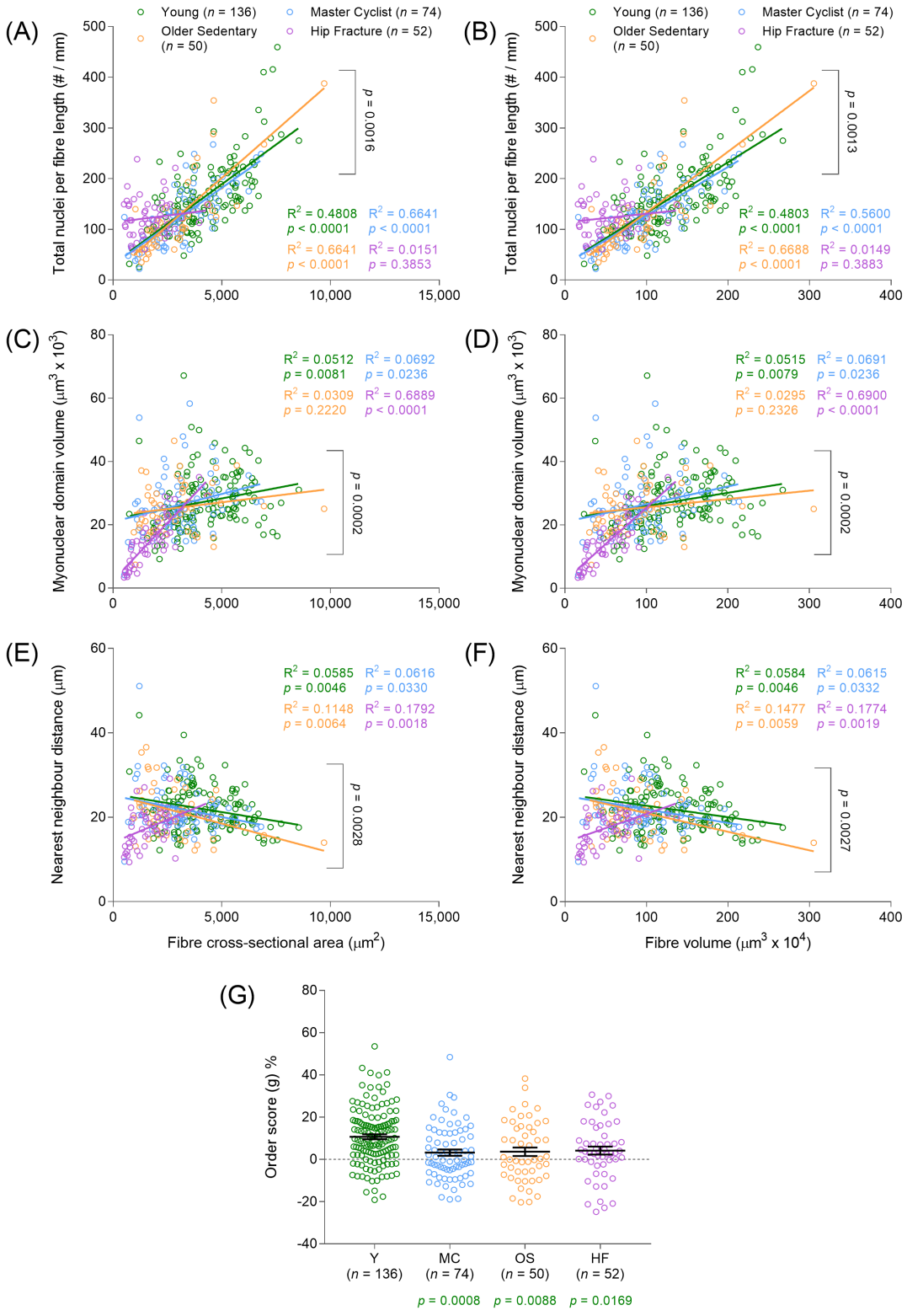

Figure 5.2: Nuclear organisation in single myofibres from young and elderly cohorts

Data points represent single myofibres. Myonuclear parameters per fibre CSA (A, C, E) and volume (B, D, F). Pearson correlation was performed to evaluate linear relationships; (G) Nuclear distribution in fibres. Error bars show mean ± SEM. *p* values of ANOVAs are colour-coded against corresponding groups.

5.3.3. Transcription is predominantly affected by physical activity

The abnormality in nuclear distribution witnessed in the elderly groups may be accompanied by modified global gene transcription. To address this possibility, muscle fibres were incubated in antibodies against acetyl histone H3 (AcH3; Lys9/Lys14; Figure 5.3 through Figure 5.6) as a marker of activation of transcriptional activity (Gnocchi *et al.*, 2011). The mean intensity of AcH3 within nuclei classified as positive for AcH3, measured by setting a cut-off point for nuclei above 1000 greys of background level, was similar in young and master cyclists, but both cohorts were significantly different than older sedentary and hip fracture patients, with the latter two groups showing similar levels of AcH3 (Figure 5.7A). However, nuclei from master cyclists exhibited a much higher percentage of AcH3-positive nuclei than all other groups (Figure 5.7B).

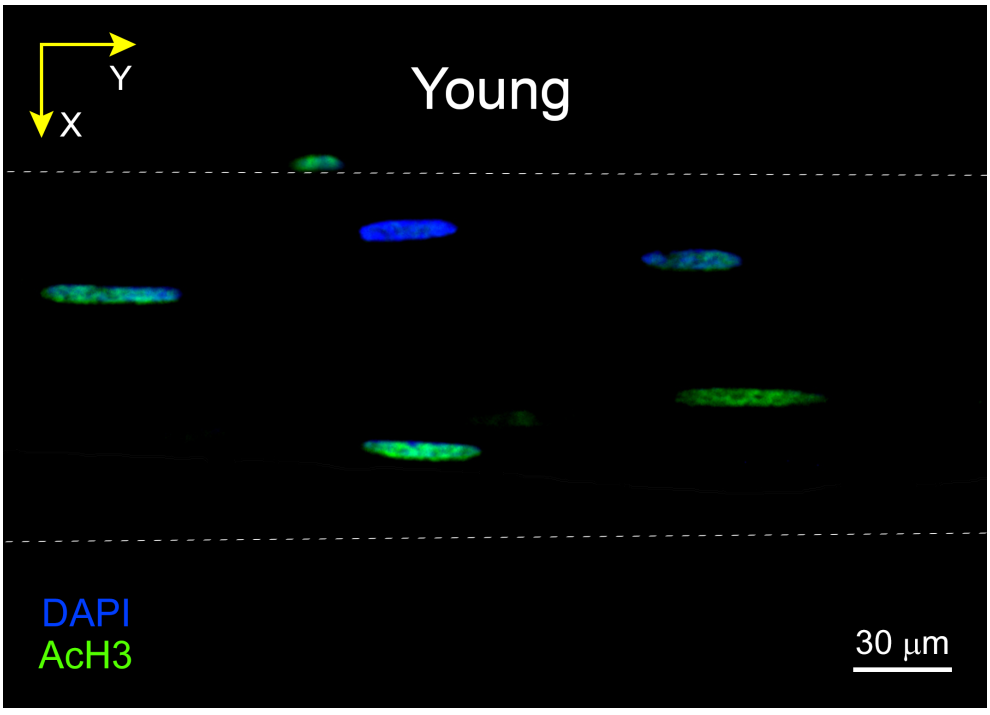

Figure 5.3: DNA acetylation in single myofibres from young individuals
Maximum intensity *z* projection (MIP) of a fibre (space enclosed between contour lines) stained for nuclei (DAPI, blue) and acetyl histone H3 (AcH3, green), imaged using a 60x objective lens.

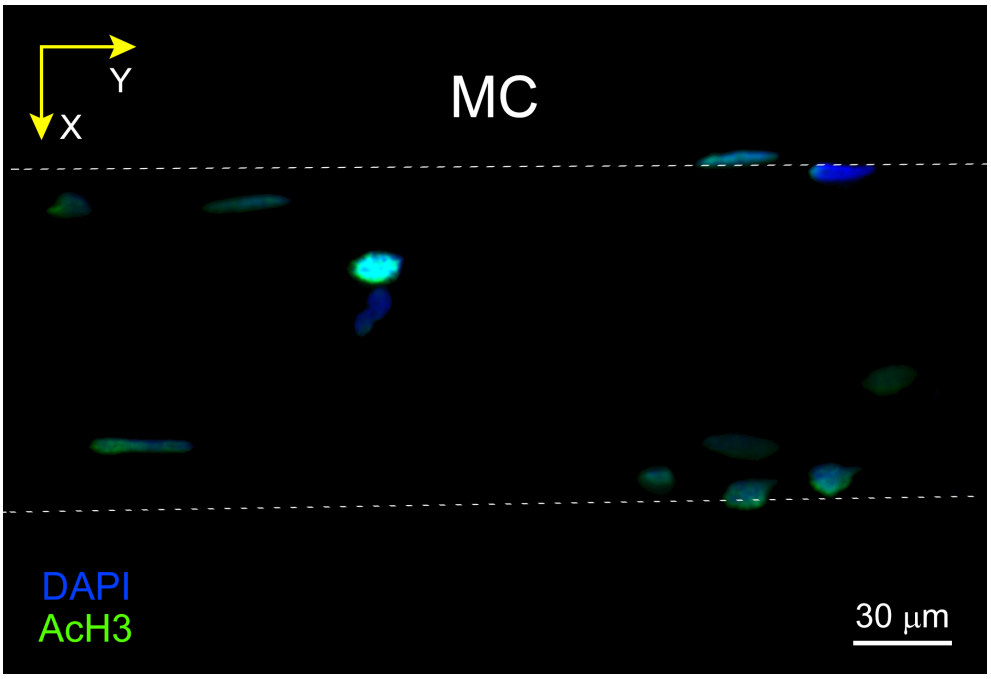

Figure 5.4: DNA acetylation in single myofibres from master cyclists
Maximum intensity *z* projection (MIP) of a fibre (space enclosed between contour lines) stained for nuclei (DAPI, blue) and acetyl histone H3 (AcH3, green), imaged using a 60x objective lens.

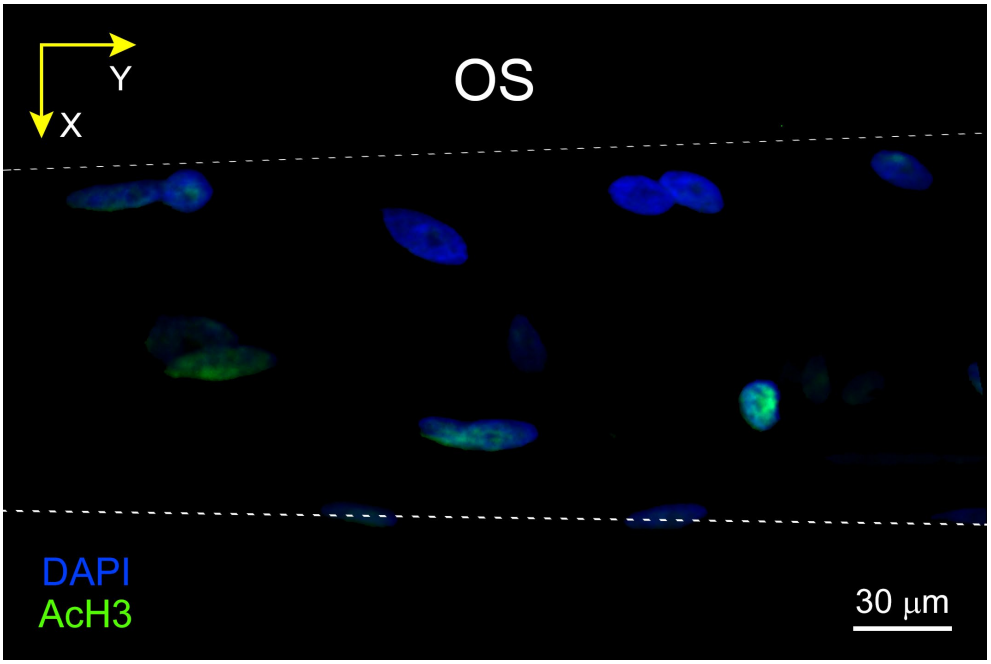

Figure 5.5: DNA acetylation in single myofibres from older sedentary individuals
Maximum intensity *z* projection (MIP) of a fibre (space enclosed between contour lines) stained for nuclei (DAPI, blue) and acetyl histone H3 (AcH3, green), imaged using a 60x objective lens.

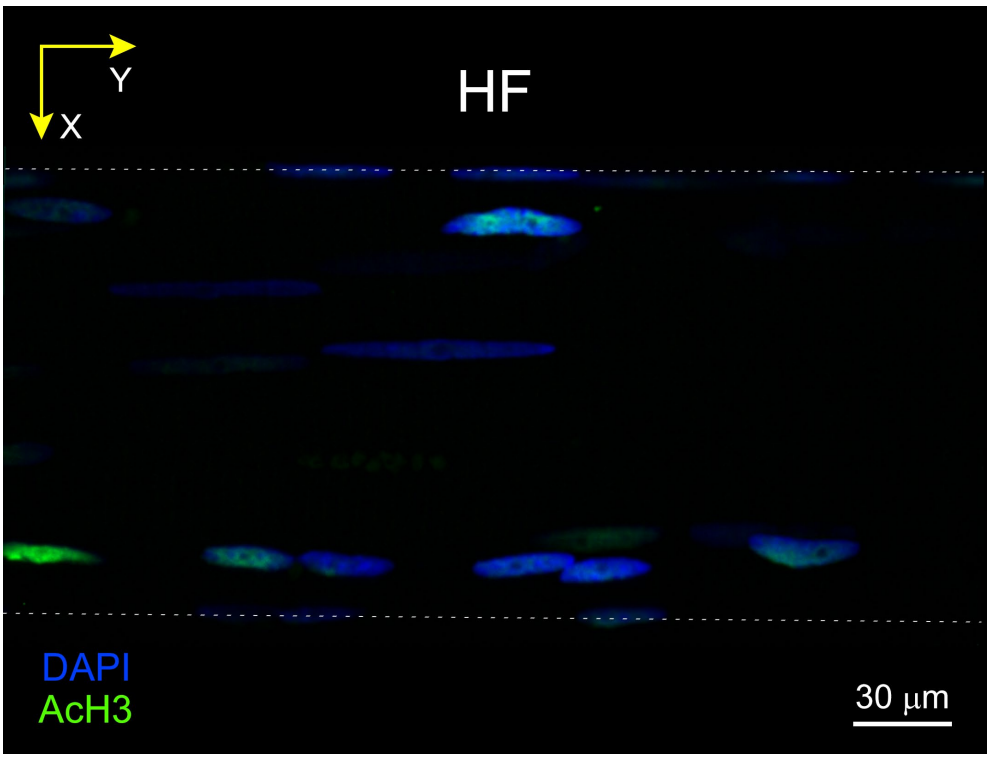

Figure 5.6: DNA acetylation in single myofibres from hip fracture patients
Maximum intensity *z* projection (MIP) of a fibre (space enclosed between contour lines) stained for nuclei (DAPI, blue) and acetyl histone H3 (AcH3, green), imaged using a 60x objective lens.

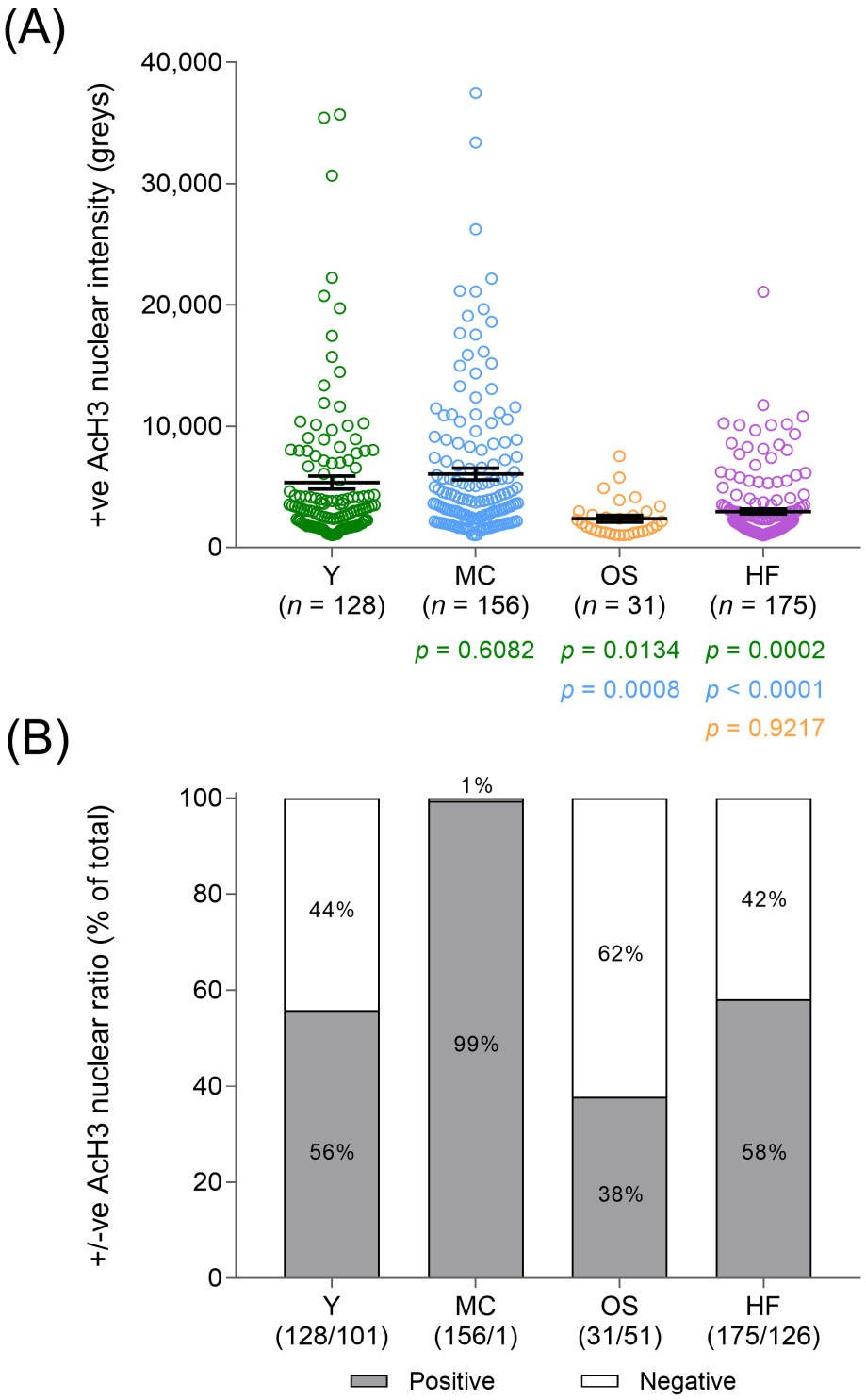

Figure 5.7: Altered transcriptional balance in nuclei from elderly individuals

Y = Young, MC = Master Cyclists, OS = Older Sedentary, HF = Hip Fracture. (A) Data points represent individual nuclei with positive (+ve) levels (>1000 greys) of acetyl-histone H3 (AcH3). Error bars show mean ± SEM. Statistical tests included normality tests and ANOVAs; (B) Positive (+ve) nuclei >1000 greys, negative (-ve) nuclei <1000 greys. The cut-off point was selected based on measured background levels of all studied single muscle fibres. *p* values are colour-coded against corresponding groups.

5.4. Discussion

The present study aimed to verify whether chronic physical activity/inactivity and age can lead to changes in nuclear organisation in single muscle fibres and whether such changes are positively related to the presence of prelamin A in myonuclei. Results showed an elevated number of nuclei in single muscle fibres from hip fracture patients, as well as nuclear mispositioning in all the elderly cohorts, in agreement with Cristea *et al.* (2010). Further, transcriptional activity in the master cyclist cohort was ~2x that of all other groups. Therefore, the results in this study suggest that biological ageing and muscle disuse do not share the same myonuclear alterations, demonstrating the importance of differentiating between the two conditions in ageing research.

5.4.1. MND is dependent on activity level, but not age

Analysis of number of nuclei, MNDs and NNs in single muscle fibres from young individuals and elderly cohorts representing a range of physical activity has revealed that number of nuclei and MND volumes are normal compared to young individuals in active and sedentary elderly individuals, but altered as a result of muscle disuse in elderly individuals. The increase in number of nuclei and the concomitant decrease in MND volumes in hip fracture patients mainly affected smaller fibres (Figure 5.2).

The concept of a "muscle memory", from a cellular perspective, has been suggested to take place in single muscle fibres (Gundersen, 2016). It manifests as the retention of nuclei during atrophic periods of the muscle (though not necessarily for the entire lifespan). This has been demonstrated in cultured single muscle fibres, where number of nuclei had remained the same during ~50% reduction in fibre size (Duddy *et al.*, 2011). It has been further confirmed *ex vivo* in single muscle fibres from rat diaphragm following a 2-week denervation period, resulting in >50% reduction in fibre CSA (Aravamudan *et al.*, 2006), as well as in muscle fibres from mature mice following 120 days of muscle denervation, leading to >50% reduction in fibre CSA (Wada *et al.*, 2002). Other *in vivo* reports in mice have shown that nuclei acquired during overload are not lost in detraining, demonstrating some redundancy in number of nuclei in the resulting smaller fibres (Gundersen & Bruusgaard, 2008; Bruusgaard *et al.*, 2010; Egner *et al.*, 2013; Gundersen, 2016); this phenomenon has also been confirmed in humans (Kadi *et al.*, 2004).

Thus, it has been suggested that the number of myonuclei in a single muscle fibre may represent the largest fibre volume in the history of that single muscle fibre (Gundersen, 2016).

In the context of the work performed here, and following the concept of the aforementioned muscle memory, the higher nuclear number and lower MND sizes in smaller fibres from hip fracture patients should be viewed not so much as an increase *per se* in the number of nuclei, but rather as a retention of the number of nuclei from the time the muscle fibres were larger. As the patients are a model of muscle disuse, a simultaneous reduction of fibre size with activity level is expected. The results of this chapter further reveal that chronic aerobic exercise in older age does not necessarily have an effect on the number of myonuclei in single muscle fibres, supporting the results of the study by Karlsen *et al.* (2015). Long-distance cycling is not expected to result in hypertrophied muscle fibres and therefore maintenance of MND sizes is expected. Consequently, from a functional perspective, these results suggest that chronic aerobic physical activity may preserve the mass of single muscle fibres in older age, whilst maintaining optimal MND volumes. Inactivity, on the other hand, appears to result in a reduction of muscle fibre volume, which especially at older age, could lead to muscle weakness and frailty.

5.4.2. Aberrant nuclear distribution in all elderly cohorts

As observed by the lower order scores in all the elderly cohorts, nuclei in single muscle fibres from elderly individuals are equally disorganised, regardless of the level of physical activity (Figure 5.2G). This was a surprising result, as it was presumed that if number of nuclei and MND were positively correlated with increasing fibre volume (Figure 5.2B and Figure 5.2D, respectively) in master cyclists, but not in hip fracture patients, nuclear distribution should follow the same trend. Such a result demonstrates the specific effect of biological ageing on nuclear organisation. It further reveals the importance of investigating nuclear distribution and not solely MNDs when attempting to determine the spatial nuclear communication on single muscle fibres.

Nevertheless, this result is also interesting, as nuclear movement in muscle fibres is likely to be reliant on myofibrillar contraction (Roman *et al.*, 2017). Thus, it would be expected that nuclei would be able to move more easily in highly active muscle fibres, unless interactions between the nuclear envelope, microtubules and actin filaments are altered in biological ageing

as they are in nuclear envelopathies (Chi *et al.*, 2009*a*; Volk, 2013; Chen *et al.*, 2014*b*; Meinke *et al.*, 2014; Espigat-Georger *et al.*, 2016; Janin *et al.*, 2017; Gimpel *et al.*, 2017; Kim *et al.*, 2017). This change in nuclear organisation could possibly explain the reduction in specific force of single muscle fibres from hip fracture patients and the trend for a reduction in master cyclists, noted previously in my samples (Kalakoutis, 2017). Altered nuclear organisation could result in lower contractile protein content, as seen in chapter 4. Although Kalakoutis (2017) had indeed quantified myosin content in these samples and did not find differences between young, master cyclist and hip fracture cohorts, it was done by gel densitometry, which may not have been sufficiently sensitive to find mild alterations in myosin content, as could be achieved using proteomics analyses.

Another possible explanation for this result could be the difference in fibre types between the cohorts. Previous investigations on my samples showed a predominance of Type I fibres in the master cyclists, 85.9% (Kalakoutis, 2017) and ~68% (Pollock *et al.*, 2018*b*), as well as 72.2% in hip fracture patients (Kalakoutis, 2017). However, samples from the young individuals have been noted with almost a 50/50 proportion of Type I/Type II fibres (Kalakoutis, 2017), with the latter known to show a more ordered nuclear organisation (Bruusgaard *et al.*, 2003; Cristea *et al.*, 2010). Thus, the difference in order score between young and elderly cohorts may have simply reflected fibre-type differences in nuclear distribution. Future research should strive to increase the number of fibres studied in each group and fibre-type the additional fibres. This should allow for correlations to be made between fibre types and nuclear distribution, to identify whether such differences are due to fibre types or biological ageing.

5.4.3. High transcriptional activity in physically active elderly individuals

The mean intensity of AcH3 within nuclei classified as positive for AcH3 was similar in young and master cyclists, but both cohorts were significantly different than older sedentary and hip fracture patients, with the latter two groups showing similar levels of AcH3 (Figure 5.7A). Moreover, the ratio of AcH3-positive/negative nuclei was predominantly affected by the level of physical activity, rather than biological ageing (Figure 5.7B). A previous investigation of the hip fracture and master cyclist muscle samples studied here had demonstrated a reduction in

fibre specific force from hip fracture patients and a mere trend for a reduction in master cyclists (Kalakoutis, 2017). When viewed from the perspective of global transcription in muscle fibres, it is possible that the preservation of specific force in the latter group is not the result of increasing the amount of DNA in the muscle (e.g. more nuclei), but rather by increasing the transcriptional activity of existing nuclei, as viewed by more than double the ratio of AcH3-positive nuclei in these athletes, compared to all other groups. This could also potentially aid in counterbalancing the effect of nuclear disorganisation seen in ageing. As it has been previously shown in mice that myonuclei are capable of upregulating transcription by up to 7x during overload-induced hypertrophy (Kirby *et al.*, 2016), such differences in AcH3 intensity between the master cyclists and all other cohorts are likely to reflect the chronic aerobic exercise performed by such individuals. Future research should validate these result with western blots (Rumbaugh & Miller, 2011).

5.5. Conclusion

The present study aimed to verify whether chronic physical activity/inactivity and age can lead to changes in nuclear organisation in single muscle fibres and whether such changes are positively related to the presence of prelamin A in myonuclei. Results showed an elevated number of nuclei in single muscle fibres from hip fracture patients, as well as nuclear mispositioning in all the elderly cohorts, in agreement with Cristea *et al.* (2010). Further, transcriptional activity in the master cyclist cohort was ∼2x that of all other groups. Therefore, the results in this study suggest that biological ageing and muscle disuse do not share the same myonuclear alterations, demonstrating the importance of differentiating between the two conditions in ageing research.

Future studies should investigate a larger number of muscle fibres, whilst correlating the results with fibre-types. Additionally, it would be useful to quantify levels of prelamin A/progerin to investigate whether expression of these and/or *Zmpste24* are dependent on ageing and physical activity. Lastly, it would be useful to perform proteomics analyses in all groups in order to validate whether such myonuclear alterations correspond with a reduction in contractile protein content and the previously mentioned (Kalakoutis, 2017) decrease in specific force in hip fracture patients.

Chapter 6: General discussion

6.1. Summary of results

Given that research on ageing is confounded with that of muscle inactivity, informative studies of MND in sarcopenic single muscle fibres are scarce. To the best of the author's knowledge, no studies that differentiate sarcopenia from muscle inactivity, in the context of myonuclear distribution on single muscle fibres, and not simply MND, have ever been published. In addition, the source of sarcopenia-related low specific force, MHC concentration and their association with lamin A misprocessing in single muscle fibres is unknown. Thus, this project aimed to characterise the connection between ageing and disuse-related lamin A misprocessing with myonuclear organisation and concentration of MHC in isolated single muscle fibres.

Overall working hypothesis: the nuclear lamina is disrupted in response to biological ageing, a condition exacerbated by muscle disuse. This modifies myonuclear positioning in individual muscle fibres and ultimately affects synthesis and content of contractile proteins, leading to low specific force in single muscle fibres.

Specific aim 1: as a method to determine the 3D spatial organisation of myonuclei in skinned single muscle fibres using confocal microscopy was not within reach for this project, method development was the first objective of this work (chapter 3);

Specific aim 2: determine whether the presence of prelamin A can modulate myonuclear positioning and functional capacity of mouse single muscle fibres (chapter 4);

Specific aim 3: determine whether biological ageing and muscle disuse lead to altered myonuclear organisation in human isolated myofibres (chapter 5).

The method developed here was perfected over the four years of this PhD, by testing it in various conditions, muscle disorders and species. Over time, optimisations have led to a method that can be performed routinely with minimal considerations, as its strengths and weaknesses have been exposed during the iterations. This method was therefore used in the production of this thesis, various publications related to this work and a significant body of work in progress with various collaborators. This method is not perfect, of course, and as discussed in chapter 23, could be improved by increasing its speed, precision and functionality (see section 3.5.1.4). This could be mainly achieved by improving the light penetration through the muscle fibre, by using a microscope more suitable for the task, as well as using red-shifted antibodies. These could help convert the method to automatic image analysis, which could greatly improve the method and add accuracy and precision to the programme, which could in turn, help discovering more subtle differences between muscle fibres. Nevertheless, considering the task at hand was to develop a method that encompasses knowledge in physiology, microscopy and computer programming, when the original training of the author was solely in physiology, this method is considered a major success in the current project. Most importantly, it has allowed the author to produce a significant amount of data in a reliable manner and unravel possible mechanisms by which nuclear organisation and prelamin A could lead to muscle fibre weakness in premature ageing conditions and biological ageing.

Specifically, in chapter 4 (mice), it was found that postnatal absence of *Zmpste24* and accumulation of farnesylated prelamin A in myonuclei can lead to a low number of nuclei and enlarged MNDs in single muscle fibres, but without noting an effect on nuclear optimal distribution. This occurred with a concomitant decrease in transcriptional activity, a reduction in contractile protein content and low specific force in single muscle fibres. The phenotype of *Zmpste24* KO muscle fibres was found to be improved by treatment with FTIs, however, the extent to which the fibres improved is unfortunately unknown, due to lack of WT counterparts. Nevertheless, mosaic mice, which have an equal number of *Zmpste24*-expressing and *Zmpste24*-non expressing nuclei, did not exhibit any myonuclear alterations or changes in specific force. Interestingly, mutations in *Lmna* showed results that were dissimilar to those acquired in the *Zmpste24* models studied in this work, as neither *Lmna* KO nor $Lmna^{G609G}$ demonstrated any changes comparable to those from *Zmpste24* KO mice. As a result, it was concluded that the combination of prelamin A farnesylation with loss of *Zmpste24* had resulted in the noted adverse alterations in nuclear organisation and specific force in *Zmpste24* KO mice (Figure 6.1). It was

additionally concluded that the aetiology of progerin and prelamin A accumulation in cells seem to result in different consequences, which could indeed overall lead to a similar disease, however, the process leading to the disease could be slightly different, despite both affecting the NE.

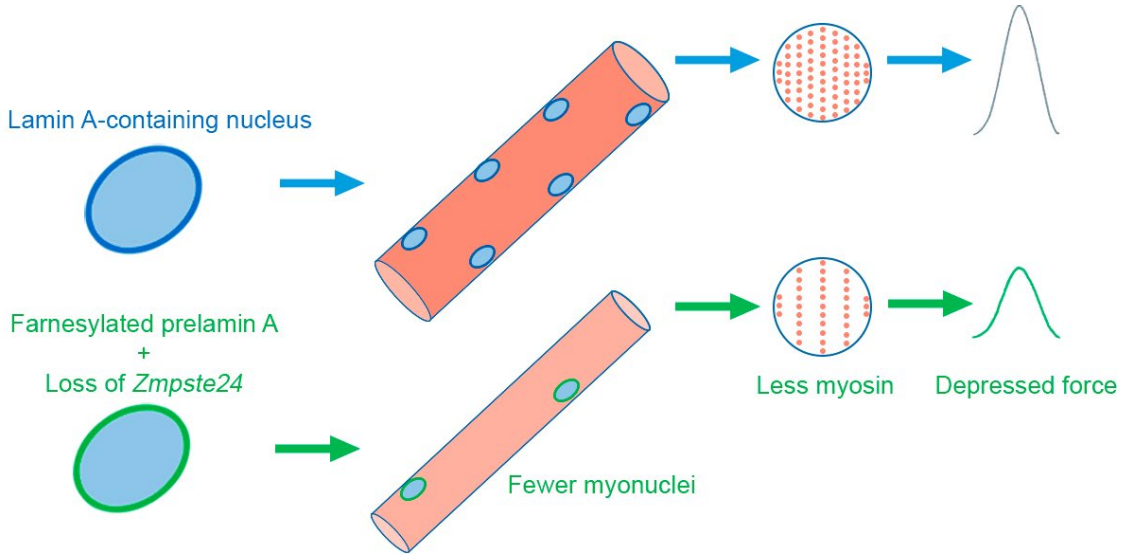

Figure 6.1: Model based on current project
A muscle fibre with normal expression of lamin A has a normal number of myonuclei and therefore, myosin concentration and specific force are normal. However, when *Zmpste24* is absent and farnesylated prelamin A accumulates in the nucleus, fewer nuclei are found on the fibre, MNDs are large and myosin concentration is reduced, leading to low specific force.

In chapter 5 (humans), strong correlation was maintained between muscle fibre size and MND volumes in biological ageing. However, in muscle disuse, a reduction in fibre size was noted and the relatively higher number of nuclei that would be expected in fibres of such sizes possibly reflected a time when the fibres were larger, as per the concept of "muscle memory" (Gundersen, 2016). Interestingly, though nuclear disorganisation seemed to prevail in biological ageing, regardless of the level of physical activity, the latter showed a strong positive impact on levels of transcription; transcriptional activity is therefore likely disassociated from biological ageing.

It would have been beneficial for the study had a young trained group been added for comparisons and had the hip fracture group been a better muscle model of muscle disuse (e.g.

wheelchair-bound elderly individuals). Moreover, it would be highly useful to increase the number of individuals in each cohort, not only as the results would likely be more representative, but also as the age range within each group could tighten and become more representative for a specific decade of life. Lastly, prelamin A and progerin levels should have been quantified for each group, which could have opened numerous opportunities for correlations with other nuclear parameters (e.g. MNDs and order score).

The result that nuclei were disorganised in the master cyclists is almost the only example of biological ageing in that cohort. Previous work on this cohort has documented enhanced cardiorespiratory fitness, reduced cardiometabolic risk (Pollock *et al.*, 2015, 2018*a*), superior immunity and a reduction in markers of immunosenescence (Duggal *et al.*, 2018). Moreover, little evidence of age-related changes in muscle properties (vastus lateralis) has been noted, including fibre-type compositions ratio, absence of type II fibre atrophy, normal capillarity, normal concentration of mitochondrial proteins (Pollock *et al.*, 2018*b*) and greatly enhanced expression of PGC-1α (unpublished data).

When collectively considering the studies in chapter 4 and chapter 5, two main findings regarding sedentary ageing arise. Firstly, biological ageing appears to be accompanied by nuclear disorganisation in single muscle fibres. Interestingly, faulty nuclear movement in ageing does not appear to be limited to myonuclei, as neutrophil chemotaxis has been shown to be reduced in both velocity and accuracy in the elderly (Sapey *et al.*, 2014; Bartlett *et al.*, 2016, 2018), partly as neutrophils are less able to respond to mechanical cues and communicate less efficiently as a population (Oakes *et al.*, 2009; Hazeldine *et al.*, 2014; Niethammer, 2016). Therefore, the effect of ageing on nuclear/cell movement and mechanics does not solely affect myonuclei, but many other cell-types as well (Phillip *et al.*, 2015). The altered distribution of myonuclei in muscle fibres could be originating from numerous sources acting in concert during the ageing process to result in such disordered arrangement. Potential sources may include, (i) altered interactions between the nuclear envelope and the various filamentous networks of the cell, as occurs in nuclear envelopathies, which affect nuclear mechanics and mechano-sensing (Chi *et al.*, 2009*a*; Volk, 2013; Chen *et al.*, 2014*b*; Meinke *et al.*, 2014; Falcone *et al.*, 2014; Espigat-Georger *et al.*, 2016; Janin *et al.*, 2017; Roman *et al.*, 2017; Corne *et al.*, 2017; Gimpel *et al.*, 2017; Kim *et al.*, 2017); (ii) faulty communication of myonuclei with myofibroblasts, which have been shown to regulate peripheral nuclear positioning in single muscle fibres *via* a

fibronectin-integrin-Cdc42 pathway that controls nuclear movement to the periphery by organising desmin, thereby inducing myofibril crosslinking around myonuclei (Roman *et al.*, 2018; Mandigo & Folker, 2018).

The second finding to note regarding ageing is that although prelamin A has indeed been documented to accumulate in cells during the ageing process (Ragnauth *et al.*, 2010; Liu *et al.*, 2013), in most cases it is actually progerin that is found in ageing studies (Carrero *et al.*, 2016; Kubben & Misteli, 2017). Interestingly, strong correlation between the amounts of progerin in nuclei, nuclear abnormalities and severity of clinical phenotypes in progeria syndromes has been noted in humans (Barthélémy *et al.*, 2015). However, this was not the case in the *Lmna*^{G609G} mouse studied in this work. It is important to note in this regard that although the results appear to contrast, this may not necessarily be the case, as they could result from differences in species (humans vs mice), tissues (fibroblasts vs muscle fibres) and technique (cell culture vs single muscle fibres). It is indeed unfortunate prelamin A and progerin were not quantified in chapter 5, as this could have greatly promoted the understanding of the results in the context of mice vs humans. Specifically, it could have aided in revealing whether the low order score noted only in the elderly cohorts was the result of accumulation of prelamin A or progerin (or neither).

It is therefore believed that the primary question originating from these studies is whether and what chronic accumulation of prelamin A or progerin during biological ageing and muscle disuse would cause over time to the number of nuclei and contractile protein content in single muscle fibres. As prelamin A has been shown to increase apoptosis and senescence (Verstraeten *et al.*, 2008; Sieprath *et al.*, 2012, 2015), would the number of nuclei decrease and protein content follow? This is an excellent example of the weakness of cross-sectional studies in ageing and the requirement for longitudinal studies. It would be extremely beneficial to track the patients and athletes studied in chapter 5 across a few years to understand the difference between biological ageing and muscle disuse in humans, in the context of nuclear envelope proteins and MNDs.

6.2. Caveats and future work

Future work should focus on three major aspects: (i) improve the functionality of the method to study nuclear organisation in single muscle fibres; (ii) deepen the understanding of the mechanisms that cause prelamin A to accumulate and reduce the number of nuclei in single muscle fibres; (iii) continue to characterise the specific effects of biological ageing and muscle disuse in human ageing.

6.2.1. Method improvements

The future direction of the method was discussed in section 3.5.1.4. In summary, the method could benefit from 2-3 improvements, which would enhance its speed, functionality and reliability.

6.2.1.1. Full automation

Currently, the main limitation of the method is the axial resolution of the microscope. If the quality of images produced at deep focal planes is enhanced, full automation of the programme for analysing 3D nuclear organisation would become possible. This could be accounted for by improved image processing techniques, or straight from the source by using a microscope with greater axial resolution (e.g. multi-photon), which can produce stacks of images suffering from fewer aberrations, that are more representative of ground truth. If stacks present with fewer aberrations, automatic processing of images using simple tools would become possible. Analysis would therefore entail direct image processing instead of processing of matrices of co-ordinates. As a result, batches of images could be processed automatically without the requirement for user input and supervision.

6.2.1.2. Specific MNDs

Average MND has so far served as an invaluable measure of nuclear organisation, especially when combined with nearest neighbour measurements and order-score. However, the unfortunate nature of averages is a reduction in spatial resolution, which in turn could lead to

masking of information. In relation to MND, the use of an average MND for all nuclei residing within a single muscle fibre means that any mild dissimilarities of domains between nuclei are masked to meet an average. It is therefore believed that calculating specific MNDs would be a better alternative, as the specific volume of the fibre each nucleus governs would be known (as shown in Figure 6.2). The way to achieve that is described thoroughly in Karlsson (2008) and the method was used in the following studies (Edlund & Lindblad, 2008; Liu *et al.*, 2009; Cristea *et al.*, 2010). Briefly, following pre-processing, the method entails modelling of the fibre as an elliptical cylinder from its *xz* slices, as each image contains an ellipse. At this stage, both nuclear co-ordinates and fibre edges are known. Thus, specific MNDs can be calculated by Euclidean distance transform, summing the number of voxels within each domain and multiplying the result by the volume of each voxel. Consequently, the specific MND of each nucleus becomes known.

6.2.1.3. Correlating MNDs with nuclear parameters

Once an individual MND is calculated, it could be correlated with other parameters within that volume. In this regard, it would be interesting to reveal whether larger nuclei are capable of supporting larger MNDs and whether MND volume correlates with the transcriptional activity and level of prelamin A in its associated nucleus. Such questions are difficult to answer when studying a population, but are simpler to tackle using individual MNDs. Thus, such correlations would exploit the abilities of the programmes created in this work for analysis of nuclei as a population and as individuals and enhance the knowledge of MNDs in single muscle fibres.

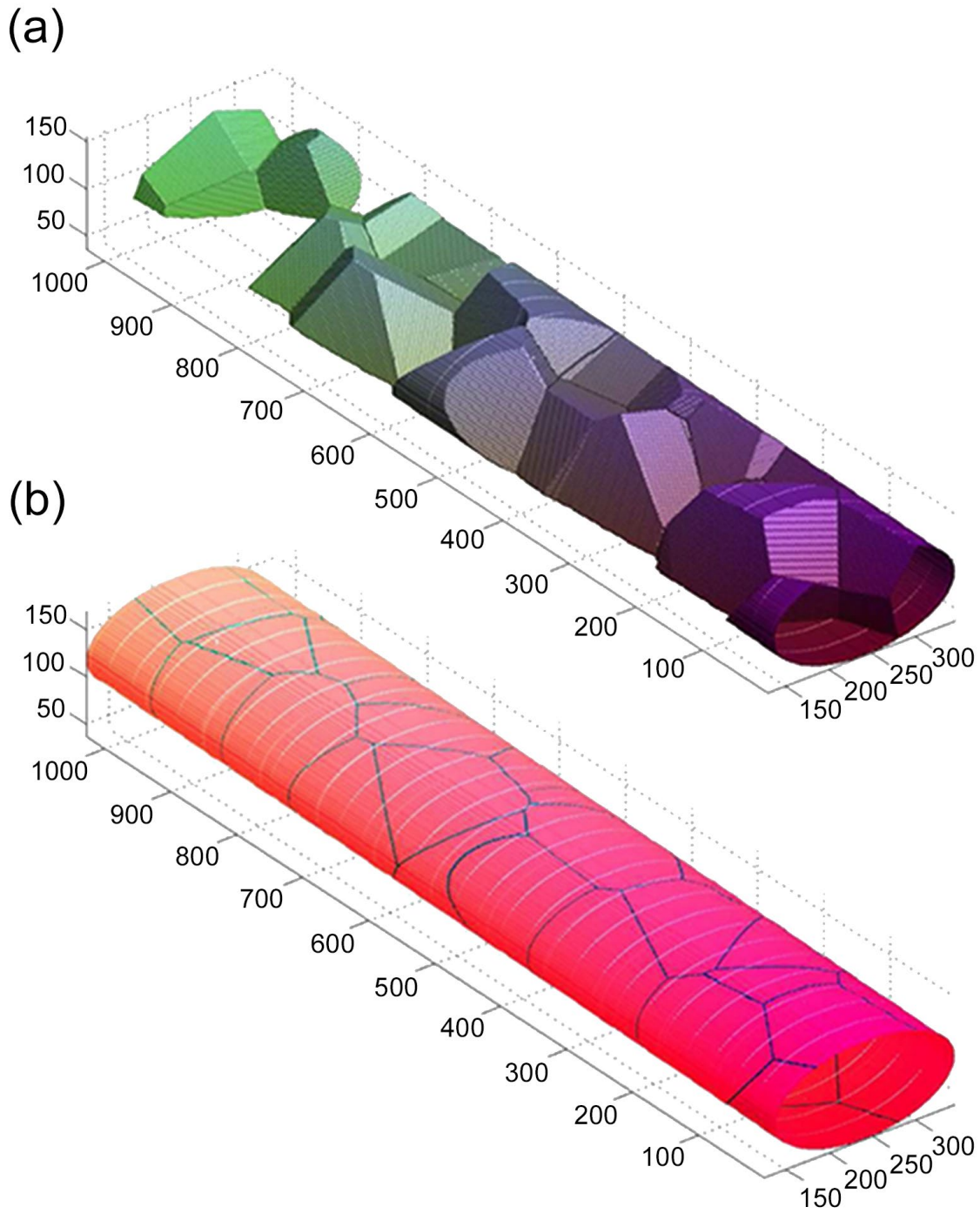

Figure 6.2: Myonuclear domain of individual nuclei in a single myofibre

(a) Image shows myonuclear domain volumes of some nuclei in a single muscle fibre. Each volume represents the domain of a single nucleus found at the centroid of that volume; (b) Myonuclear domain surfaces of nuclei in a single muscle fibre. Each area represents the surface domain of its nucleus. Adapted from Karlsson (2008).

6.2.2. Prelamin A accumulation in mice

6.2.2.1. Future work on current study

The study in chapter 4 could continue in many directions. Firstly, the work on *Zmpste24* KO mice treated with FTIs should be performed not only against a vehicle-treated control, but also against a WT. This would, of course, reveal whether treatment with FTIs is sufficient to fully rescue all measured fibre parameters back to WT levels. Moreover, it will render the results of the current work clearer, as it could be understood whether the myofibre phenotype discovered here in *Zmpste24* KO mice is the result of accumulation of farnesylated prelamin A or loss of *Zmpste24*. After all, although FTI-treated single muscle fibres from *Zmpste24* KO mice were indeed of better state than vehicle-treated fibres, it is unknown whether they were fully rescued to WT levels; yet, mosaic mice were shown to be similar to WT in all measured parameters. Such a study would greatly improve the results acquired in the current project.

Secondly, it would be useful to validate the results of the transcriptional activity, namely acetyl histone H3 (AcH3) and H3K27me3, performed in *Zmpste24* KO animals. Due to the nature of antibody-binding, caution is required when using fluorescence intensity to estimate the concentration of proteins. Thus, only large differences are considered biological and not methodological (Jonkman *et al.*, 2014). It would therefore be preferable to validate the results acquired here with another method, e.g. western blots and densitometry (Rumbaugh & Miller, 2011).

Lastly, it would be useful to research the expression of mechano-sensitive genes in *Zmpste24*-deficient muscle fibres. This would require non-skinned intact fibres, isolated using collagenase, as they retain all the cytoplasmic factors within the cell (Moyle & Zammit, 2014). Thus, transcriptomics analyses could be performed on individual muscle fibres to identify whether the expression of mechano-sensitive genes are affected in the presence of prelamin A. Moreover, it would be possible to analyse the expression of yes-associated protein 1 (YAP1) in normal conditions, knockdown of *Zmpste24* and following rescue. Analysis of the results would be by transcriptomics, western blots and immunofluorescence (IF), by creating a ratio between cytoplasmic and nuclear YAP1 intensity (Sun *et al.*, 2017).

6.2.2.2. Prelamin A in varying ages and activity levels

A study similar to the human work, conducted in chapter 5, could be performed in a more controlled environment to understand the cause of prelamin A accumulation in single muscle fibres. To achieve that, young and older mice with varying levels of physical activity should be used, to identify whether prelamin A accumulates in myonuclei as a result of muscle disuse or biological ageing in mice. Even simple tools, such as a wheel in the cage, could be used to account for sedentarity. Chronic muscle disuse could be also performed to a more extreme level than is possible in humans, by functionally overloading one limb and comparing MNDs and accumulation prelamin A with the other limb. Moreover, this could be a fitting study to compare the expression of mechano-sensitive genes between the four models of age and physical activity. Importantly, the study could provide a platform that is either cross-sectional (harvesting mice at the end of lifespan), semi-longitudinal (harvesting some mice during lifespan and others at the end of lifespan) or longitudinal using the *in vivo* method by Bruusgaard *et al.* (2003).

6.2.2.3. Muscle-specific accumulation of prelamin A in adulthood

The specific mechanisms by which long-term accumulation of prelamin A in skeletal muscle, that commences in adulthood and is dissociated from any debilitating effects of prelamin A in other tissues, e.g. kyphosis and smooth muscle alterations, would be also useful to research. This could be researched using a mouse model with a conditional muscle-specific knockout of *Zmpste24* (Brayson & Shanahan, 2017). However, though this would indeed help show specific muscle alterations, whether such tissue-specific changes are relevant to ageing is arguable, as muscle disuse and ageing cause deterioration of many tissues simultaneously and are not selective to a single tissue (Bartlett *et al.*, 2016, 2018; Harridge & Lazarus, 2017; Duggal *et al.*, 2018). More importantly, a conditional KO that is initiated in adulthood would probably mimic muscle ageing better than a KO since birth, as the accumulation of prelamin A would not interfere with the accretion of satellite cells in single muscle fibres during post-natal development (Zammit *et al.*, 2006; White *et al.*, 2010). The conditional KO should take place in adulthood (2-4 months of age) and persist throughout the lifespan of the mouse. Using a semi-longitudinal approach, mice should be harvested 4 weeks following the KO, then at 12 months, 18 months, 24 months and if possible, every 2 months following. Similarly to the study suggested previously, it might be useful to separate the mice into 2 groups and place wheels in the cages

of one of the groups. Thus, this study would, firstly, model prelamin A accumulation specifically in adult muscle and, secondly, would be conducted in a mouse whose behaviour is more similar to its natural environment, due to its ability to exercise voluntarily. The conditional KO also has the benefit for easier breeding, which is a significant difficulty in the *Zmpste24* KO mice. Analysis of nuclear organisation should take place at each time-point and results should be compared with the *Zmpste24* KO model used here.

6.2.3. Human ageing

6.2.3.1. Future work on current study

As the study on humans is currently at a much earlier stage than the one on mice, additional work should be done to complete the characterisation of the cohorts in the study. Firstly, similar investigations that were conducted in chapter 4 should be repeated in chapter 5, including IF quantification of H3K27me3 and prelamin A/progerin, as well as proteomics analysis to assess the myosin concentration in the samples. Secondly, future research should strive to increase the number of fibres studied in each group and fibre-type the additional fibres. This should allow for correlations to be made between fibre types and nuclear distribution, to elucidate whether the differences noted were due to fibre types or biological ageing. Thirdly, with regards to AcH3 activity in all cohorts, a larger number of nuclei should be studied and results should be validated with western blots and densitometry (Rumbaugh & Miller, 2011).

The final comments about the current study are with respect to its planning. Due to time-constraints and lack of samples a “young” group was created, instead of “young active” and “young sedentary”. Though no differences were noted in any parameter studied here between the two individuals who had been participating in low-level recreational sport activities (<2 sessions/week) at the time of the study and the rest of the cohort, this is not to say that there is no need for a young cyclist group as well. This would make the results of the study more reliable and representative of muscle activity/inactivity in young and older age. In addition, the hip fracture group was a rather heterogenous cohort. The aim of using such participants was to study frail individuals, however, strictly speaking, patients undergoing hip surgery may not have been frail for very long. Thus, using a group of individuals who can be guaranteed to be both elderly and frail (e.g. wheelchair-bound, not as a result of neuromuscular disorders) may be

better. Such individuals were the original participants I wished to research in the human study, however, acquiring ethical approval was proven increasingly complicated.

Another interesting aspect to research is whether the results seen in chapter 5 are different to single muscle fibres from young and elderly weightlifters. A previous report had demonstrated that an 85 years old weightlifter was as powerful as a 65 years old control subject, representing apparent age advantage of ∼20 years for the weightlifters (Pearson *et al.*, 2002). As type II muscle fibres are thought to be more affected in the elderly population (Larsson *et al.*, 1979; Lexell *et al.*, 1988; Andersen, 2003; Nilwik *et al.*, 2013) and resistance training is a potent activator of a hypertrophic response in type II muscle fibres (Damas *et al.*, 2018), it might be that weightlifting is better at maintaining nuclear organisation and single muscle fibre function than long-distance cycling during ageing.

Lastly, as a great requirement for longitudinal studies exists in the literature, where possible, muscle biopsies should be acquired every few years from participants that have been previously studied to monitor the progression of ageing in those cohorts. As the above suggestions are already a significant body of work and the cohorts are currently under-characterised, the suggested work above should be conducted prior to investigating the reason for the reduced nuclear distribution in all the elderly cohorts studied here.

References

Aagaard P, Simonsen EB, Andersen JL, Magnusson P & Dyhre-Poulsen P (2002). Increased rate of force development and neural drive of human skeletal muscle following resistance training. *J Appl Physiol* **93,** 1318–1326.

Abbott KL, Friday BB, Thaloor D, Murphy TJ & Pavlath GK (1998). Activation and Cellular Localization of the Cyclosporine A-sensitive Transcription Factor NF-AT in Skeletal Muscle Cells ed. Yamamoto KR. *Mol Biol Cell* **9,** 2905–2916.

Agley CC, Rowlerson AM, Velloso CP, Lazarus NR & Harridge SDR (2013). Human skeletal muscle fibroblasts, but not myogenic cells, readily undergo adipogenic differentiation. *J Cell Sci* **126,** 5610–5625.

Akhtar A (2015). The flaws and human harms of animal experimentation. *Camb Q Healthc Ethics* **24,** 407–419.

Alam SG, Zhang Q, Prasad N, Li Y, Chamala S, Kuchibhotla R, KC B, Aggarwal V, Shrestha S, Jones AL, Levy SE, Roux KJ, Nickerson JA & Lele TP (2016). The mammalian LINC complex regulates genome transcriptional responses to substrate rigidity. *Sci Rep* **6,** 38063.

Alexander EL & Sanders SK (1977). F(ab')2 reagents are not required if goat, rather than rabbit, antibodies are used to detect human surface immunoglobulin. *J Immunol* **119,** 1084–1088.

Allen DL, Monke SR, Talmadge RJ, Roy RR & Edgerton VR (1995). Plasticity of myonuclear number in hypertrophied and atrophied mammalian skeletal muscle fibers. *J Appl Physiol* **78,** 1969–1976.

Allen DL, Roy RR & Edgerton VR (1999). Myonuclear domains in muscle adaptation and disease. *Muscle Nerve* **22,** 1350–1360.

Allen JR, Ross ST & Davidson MW (2013). Sample preparation for single molecule localization microscopy. *Phys Chem Chem Phys* **15,** 18771–18783.

Amthor H, Macharia R, Navarrete R, Schuelke M, Brown SC, Otto A, Voit T, Muntoni F, Vrbóva G, Partridge T, Zammit P, Bunger L & Patel K (2007). Lack of myostatin results in excessive muscle growth but impaired force generation. *Proc Natl Acad Sci U S A* **104,** 1835–1840.

Amthor H, Otto A, Vulin A, Rochat A, Dumonceaux J, Garcia L, Mouisel E, Hourdé C, Macharia R, Friedrichs M, Relaix F, Zammit PS, Matsakas A, Patel K & Partridge T (2009). Muscle hypertrophy driven by myostatin blockade does not require stem/precursor-cell activity. *Proc Natl Acad Sci U S A* **106,** 7479–7484.

Andersen JL (2003). Muscle fibre type adaptation in the elderly human muscle. *Scand J Med Sci Sports* **13,** 40–47.

Aniansson a, Grimby G & Hedberg M (1992). Compensatory muscle fiber hypertrophy in elderly men. *J Appl Physiol* **73,** 812–816.

Aravamudan B, Mantilla CB, Zhan W-Z & Sieck GC (2006). Denervation effects on myonuclear domain size of rat diaphragm fibers. *J Appl Physiol* **100,** 1617–1622.

Argüello A, López-Fernández JL & Rivero JL (2001). Limb myosin heavy chain isoproteins and muscle fiber types in the adult goat (Capra hircus). *Anat Rec* **264,** 284–293.

Ariel P (2017). A beginner's guide to tissue clearing. *Int J Biochem Cell Biol* **84,** 35–39.

Artaza JN, Bhasin S, Mallidis C, Taylor W, Ma K & Gonzalez-Cadavid NF (2002). Endogenous expression and localization of myostatin and its relation to myosin heavy chain distribution in C2C12 skeletal muscle cells. *J Cell Physiol* **190,** 170–179.

Ashpole NM, Sanders JE, Hodges EL, Yan H & Sonntag WE (2015). Growth hormone, insulin-like growth factor-1 and the aging brain. *Exp Gerontol* **68,** 76–81.

Auld AL & Folker ES (2016). Nucleus-dependent sarcomere assembly is mediated by the LINC complex. *Mol Biol Cell* **27,** 2351–2359.

Azibani F, Muchir A, Vignier N, Bonne G & Bertrand AT (2014). Striated muscle laminopathies. *Semin Cell Dev Biol* **29,** 107–115.

Bakker EA, Lee D, Sui X, Eijsvogels TMH, Ortega FB, Lee I-M, Lavie CJ & Blair SN (2018). Association of Resistance Exercise With the Incidence of Hypercholesterolemia in Men. *Mayo Clin Proc* **93,** 419–428.

Baldwin KM & Haddad F (2001). Effects of different activity and inactivity paradigms on myosin heavy chain gene expression in striated muscle. *J Appl Physiol* **90,** 345–357.

Balikov DA, Brady SK, Ko UH, Shin JH, de Pereda JM, Sonnenberg A, Sung H-J & Lang MJ (2017). The nesprin-cytoskeleton interface probed directly on single nuclei is a mechanically rich system. *Nucleus* **8,** 534–547.

Banerjee I, Zhang J, Moore-Morris T, Pfeiffer E, Buchholz KS, Liu A, Ouyang K, Stroud MJ, Gerace L, Evans SM, McCulloch A & Chen J (2014). Targeted Ablation of Nesprin 1 and Nesprin 2 from Murine Myocardium Results in Cardiomyopathy, Altered Nuclear Morphology and Inhibition of the Biomechanical Gene Response. *PLoS Genet*; DOI: 10.1371/journal.pgen.1004114.

Barthélémy F, Navarro C, Fayek R, Da Silva N, Roll P, Sigaudy S, Oshima J, Bonne G, Papadopoulou-Legbelou K, Evangeliou AE, Spilioti M, Lemerrer M, Wevers RA, Morava E, Robaglia-Schlupp A, Lévy N, Bartoli M & De Sandre-Giovannoli A (2015). Truncated prelamin A expression in HGPS-like patients: a transcriptional study. *Eur J Hum Genet* **23,** 1051–1061.

Bartlett C, Simpson K & Turner AN (2012). Patient access to complex chronic disease records on the Internet. *BMC Med Inform Decis Mak* **12,** 87.

Bartlett DB, Fox O, McNulty CL, Greenwood HL, Murphy L, Sapey E, Goodman M, Crabtree N, Thøgersen-Ntoumani C, Fisher JP, Wagenmakers AJM & Lord JM (2016). Habitual physical activity is associated with the maintenance of neutrophil migratory dynamics in healthy older adults. *Brain Behav Immun* **56,** 12–20.

Bartlett DB, Willis LH, Slentz CA, Hoselton A, Kelly L, Huebner JL, Kraus VB, Moss J, Muehlbauer MJ, Spielmann G, Kraus WE, Lord JM & Huffman KM (2018). Ten weeks of high-intensity interval walk training is associated with reduced disease activity and improved innate immune function in older adults with rheumatoid arthritis: a pilot study. *Arthritis Res Ther* **20,** 127.

Barton-Davis, Shoturma & Sweeney (1999). Contribution of satellite cells to IGF-I induced hypertrophy of skeletal muscle. *Acta Physiol Scand* **167,** 301–305.

Bassey EJ & Harries UJ (1993). Normal values for handgrip strength in 920 men and women aged over 65 years, and longitudinal changes over 4 years in 620 survivors. *Clin Sci (Lond)* **84,** 331–337.

Bayol S, Jones D, Goldspink G & Stickland NC (2004). The influence of undernutrition during gestation on skeletal muscle cellularity and on the expression of genes that control muscle growth. *Br J Nutr* **91,** 331.

Bergo MO, Gavino B, Ross J, Schmidt WK, Hong C, Kendall L V, Mohr A, Meta M, Genant H, Jiang Y, Wisner ER, Van Bruggen N, Carano R a D, Michaelis S, Griffey SM & Young SG (2002). Zmpste24 deficiency in mice causes spontaneous bone fractures, muscle weakness, and a prelamin A processing defect. *Proc Natl Acad Sci U S A* **99,** 13049–13054.

Bertrand AT, Ziaei S, Ehret C, Duchemin H, Mamchaoui K, Bigot A, Mayer M, Quijano-Roy S, Desguerre I, Lainé J, Ben Yaou R, Bonne G & Coirault C (2014). Cellular microenvironments reveal defective mechanosensing responses and elevated YAP signaling in LMNA-mutated muscle precursors. *J Cell Sci* **127,** 2873–2884.

Biggs DSC (2010). A Practical Guide to Deconvolution of Fluorescence Microscope Imagery. *Micros Today* **18,** 10–14.

Bischoff R (1975). Regeneration of single skeletal muscle fibers in vitro. *Anat Rec* **182,** 215–235.

Bischoff R (1986). Proliferation of muscle satellite cells on intact myofibers in culture. *Dev Biol* **115,** 129–139.

Bojkowska K, Santoni De Sio F, Barde I, Offner S, Verp S, Heinis C, Johnsson K & Trono D (2011). Measuring in vivo protein half-life. *Chem Biol* **18,** 805–815.

Booth-Gauthier E a, Du V, Ghibaudo M, Rape AD, Dahl KN & Ladoux B (2013). Hutchinson-Gilford progeria syndrome alters nuclear shape and reduces cell motility in three dimensional model substrates. *Integr Biol* **5,** 569–577.

Booth FW, Roberts CK & Laye MJ (2012). Lack of exercise is a major cause of chronic diseases. *Compr Physiol* **2,** 1143–1211.

Bottinelli R (2001). Functional heterogeneity of mammalian single muscle fibres: do myosin isoforms tell the whole story? *Pflugers Arch* **443,** 6–17.

Bottinelli R & Reggiani C (2000). Human skeletal muscle fibres: Molecular and functional diversity. *Prog Biophys Mol Biol* **73,** 195–262.

Brack AS (2005). Evidence that satellite cell decrement contributes to preferential decline in nuclear number from large fibres during murine age-related muscle atrophy. *J Cell Sci* **118,** 4813–4821.

Brack AS, Conboy MJ, Roy S, Lee M, Kuo CJ, Keller C & Rando T a (2007). Increased Wnt signaling during aging alters muscle stem cell fate and increases fibrosis. *Science* **317,** 807–810.

Braten O, Livneh I, Ziv T, Admon A, Kehat I, Caspi LH, Gonen H, Bercovich B, Godzik A, Jahandideh S, Jaroszewski L, Sommer T, Kwon YT, Guharoy M, Tompa P & Ciechanover A (2016). Numerous proteins with unique characteristics are degraded by the 26S proteasome following monoubiquitination. *Proc Natl Acad Sci* **113,** E4639–E4647.

Brayson D & Shanahan CM (2017). Current insights into LMNA cardiomyopathies: Existing models and missing LINCs. *Nucleus* **8,** 17–33.

Brenner B (1986). The cross-bridge cycle in muscle. Mechanical, biochemical, and structural studies on single skinned rabbit psoas fibers to characterize cross-bridge kinetics in muscle for correlation with the actomyosin-ATPase in solution. *Basic Res Cardiol* **81 Suppl 1,** 1–15.

Bridge DT & Allbrook D (1970). Growth of striated muscle in an Australian marsupial (Setonix brachyurus). *J Anat* **106,** 285–295.

Broers JL V., Ramaekers FCS, Bonne G, Yaou R Ben & Hutchison CJ (2006). Nuclear lamins: laminopathies and their role in premature ageing. *Physiol Rev* **86,** 967–1008.

Broers JLV, Peeters EAG, Kuijpers HJH, Endert J, Bouten CVC, Oomens CWJ, Baaijens FPT & Ramaekers FCS (2004). Decreased mechanical stiffness in LMNA-/- cells is caused by defective nucleo-cytoskeletal integrity: Implications for the development of laminopathies. *Hum Mol Genet* **13,** 2567–2580.

Brooke MH & Kaiser KK (1970). Three “myosin adenosine triphosphatase” systems: the nature of their pH lability and sulfhydryl dependence. *J Histochem Cytochem* **18,** 670–672.

Bruusgaard JC, Brack a S, Hughes SM & Gundersen K (2005). Muscle hypertrophy induced by the Ski protein: cyto-architecture and ultrastructure. *Acta Physiol Scand* **185,** 141–149.

Bruusgaard JC, Egner IM, Larsen TK, Dupre-Aucouturier S, Desplanches D & Gundersen K (2012). No change in myonuclear number during muscle unloading and reloading. *J Appl Physiol* **113,** 290–296.

Bruusgaard JC & Gundersen K (2008). In vivo time-lapse microscopy reveals no loss of murine myonuclei during weeks of muscle atrophy. *J Clin Invest* **118,** 1450–1457.

Bruusgaard JC, Johansen IB, Egner IM, Rana ZA & Gundersen K (2010). Myonuclei acquired by overload exercise precede hypertrophy and are not lost on detraining. *Proc Natl Acad Sci U S A* **107,** 15111–15116.

Bruusgaard JC, Liestøl K, Ekmark M, Kollstad K & Gundersen K (2003). Number and spatial distribution of nuclei in the muscle fibres of normal mice studied in vivo. *J Physiol* **551,** 467–478.

Bruusgaard JC, Liestøl K & Gundersen K (2006). Distribution of myonuclei and microtubules in live muscle fibers of young, middle-aged, and old mice. *J Appl Physiol* **100,** 2024–2030.

Buch A, Carmeli E, Boker LK, Marcus Y, Shefer G, Kis O, Berner Y & Stern N (2016). Muscle function and fat content in relation to sarcopenia, obesity and frailty of old age--An overview. *Exp Gerontol* **76,** 25–32.

Buller AJ, Eccles JC & Eccles RM (1960). Interactions between motoneurones and muscles in respect of the characteristic speeds of their responses. *J Physiol* **150,** 417–439.

Buono S, Ross JA, Tasfaout H, Levy Y, Kretz C, Tayefeh L, Matson J, Guo S, Kessler P, Monia BP, Bitoun M, Ochala J, Laporte J & Cowling BS (2018). Reducing dynamin 2 (DNM2) rescues DNM2-related dominant centronuclear myopathy. *Proc Natl Acad Sci U S A* **2,** 1–6.

Burkholder TJ & Lieber RL (2001). Sarcomere length operating range of vertebrate muscles during movement. *J Exp Biol* **204,** 1529–1536.

Burtner CR & Kennedy BK (2010). Progeria syndromes and ageing: what is the connection? *Nat Rev Mol Cell Biol* **11,** 567–578.

Buxboim A, Irianto J, Swift J, Athirasala A, Shin J-W, Rehfeldt F & Discher DE (2017). Coordinated increase of nuclear tension and lamin-A with matrix stiffness outcompetes lamin-B receptor that favors soft tissue phenotypes. *Mol Biol Cell* **28,** 3333–3348.

Buxboim A, Swift J, Irianto J, Spinler KR, Dingal PCDP, Athirasala A, Kao YRC, Cho S, Harada T, Shin JW & Discher DE (2014). Matrix elasticity regulates lamin-A,C phosphorylation and turnover with feedback to actomyosin. *Curr Biol* **24,** 1909–1917.

Cabrić M & James NT (1983). Morphometric analyses on the muscles of exercise trained and untrained dogs. *Am J Anat* **166,** 359–368.

Callahan DM, Miller MS, Sweeny AP, Tourville TW, Slauterbeck JR, Savage PD, Maugan DW, Ades PA, Beynnon BD & Toth MJ (2014). Muscle disuse alters skeletal muscle contractile function at the molecular and cellular levels in older adult humans in a sex-specific manner. *J Physiol* **592,** 4555–4573.

Canepari M, Pellegrino MA, D'Antona G & Bottinelli R (2010). Skeletal muscle fibre diversity and the underlying mechanisms. *Acta Physiol* **199,** 465–476.

Canepari M, Rossi R, Pellegrino MA, Orrell RW, Cobbold M, Harridge S & Bottinelli R (2005). Effects of resistance training on myosin function studied by the in vitro motility assay in young and older men. *J Appl Physiol* **98,** 2390–2395.

Cao K, Capell BC, Erdos MR, Djabali K & Collins FS (2007). A lamin A protein isoform overexpressed in Hutchinson-Gilford progeria syndrome interferes with mitosis in progeria and normal cells. *Proc Natl Acad Sci U S A* **104,** 4949–4954.

Capell BC, Erdos MR, Madigan JP, Fiordalisi JJ, Varga R, Conneely KN, Gordon LB, Der CJ, Cox AD & Collins FS (2005). Inhibiting farnesylation of progerin prevents the characteristic nuclear blebbing of Hutchinson-Gilford progeria syndrome. *Proc Natl Acad Sci U S A* **102,** 12879–12884.

Caremani M, Melli L, Dolfi M, Lombardi V & Linari M (2015). Force and number of myosin motors during muscle shortening and the coupling with the release of the ATP hydrolysis products. *J Physiol* **593,** 3313–3332.

Carrero D, Soria-Valles C & López-Otín C (2016). Hallmarks of progeroid syndromes: lessons from mice and reprogrammed cells. *Dis Model Mech* **9,** 719–735.

Carriero A, Jonkers I & Shefelbine SJ (2011). Mechanobiological prediction of proximal femoral deformities in children with cerebral palsy. *Comput Methods Biomech Biomed Engin* **14,** 253–262.

Castro-Abril HA, Gutiérrez ML & Garzón-Alvarado DA (2016). Proximal femoral growth plate mechanical behavior: Comparison between different developmental stages. *Comput Biol Med* **76,** 192–201.

Chapman M a, Zhang J, Banerjee I, Guo LT, Zhang Z, Shelton GD, Ouyang K, Lieber RL & Chen J (2014). Disruption of both nesprin 1 and desmin results in nuclear anchorage defects and fibrosis in skeletal muscle. *Hum Mol Genet* **23,** 5879–5892.

Cheek DB, Holt AB, Hill DE & Talbert JL (1971). Skeletal Muscle Cell Mass and Growth: The Concept of the Deoxyribonucleic Acid Unit. *Pediatr Res* **5,** 312–328.

Chen N, Chen M, Liu S, Guo Q, Chen Z & Wang T (2014*a*). Change in refractive index of muscle tissue during laser-induced interstitial thermotherapy. *Biomed Mater Eng* **24,** 807–813.

Chen ZJ, Wang WP, Chen YC, Wang JY, Lin WH, Tai LA, Liou GG, Yang CS & Chi YH (2014*b*). Dysregulated interactions between lamin A and SUN1 induce abnormalities in the nuclear envelope and endoplasmic reticulum in progeric laminopathies. *J Cell Sci* **127,** 1792–1804.

Chi Y-H, Chen Z-J & Jeang K-T (2009*a*). The nuclear envelopathies and human diseases. *J Biomed Sci* **16,** 96.

Chi Y-H, Cheng LI, Myers T, Ward JM, Williams E, Su Q, Faucette L, Wang J-Y & Jeang K-T (2009*b*). Requirement for Sun1 in the expression of meiotic reproductive genes and piRNA. *Development* **136,** 965–973.

Ciechanover A (2005). Proteolysis: From the lysosome to ubiquitin and the proteasome. *Nat Rev Mol Cell Biol* **6,** 79–86.

Ciechanover A (2015). The unravelling of the ubiquitin system. *Nat Rev Mol Cell Biol* **16,** 322–324.

Ciechanover A & Kwon YT (2017). Protein Quality Control by Molecular Chaperones in Neurodegeneration. *Front Neurosci* **11,** 1–18.

Collins CA & Zammit PS (2009). Isolation and grafting of single muscle fibres. ed. Audet J & Stanford WL. *Methods Mol Biol* **482,** 319–330.

Corbin K, Pinkard H, Peck S, Beemiller P & Krummel MF (2014). Assessing and benchmarking multiphoton microscopes for biologists. In *Methods in Cell Biology*, 1st edn., pp. 135–151. Elsevier Inc. Available at: http://dx.doi.org/10.1016/B978-0-12-420138-5.00008-2.

Corne TDJ, Sieprath T, Vandenbussche J, Mohammed D, te Lindert M, Gevaert K, Gabriele S, Wolf K & De Vos WH (2017). Deregulation of focal adhesion formation and cytoskeletal tension due to loss of A-type lamins. *Cell Adh Migr* **11,** 447–463.

Corrigan DP, Kuszczak D, Rusinol AE, Thewke DP, Hrycyna C a, Michaelis S & Sinensky MS (2005). Prelamin A endoproteolytic processing in vitro by recombinant Zmpste24. *Biochem J* **387,** 129–138.

Crisp M, Liu Q, Roux K, Rattner JB, Shanahan C, Burke B, Stahl PD & Hodzic D (2006). Coupling of the nucleus and cytoplasm: Role of the LINC complex. *J Cell Biol* **172,** 41–53.

Cristea A, Qaisar R, Edlund PK, Lindblad J, Bengtsson E & Larsson L (2010). Effects of aging and gender on the spatial organization of nuclei in single human skeletal muscle cells. *Aging Cell* **9,** 685–697.

Curl CL, Bellair CJ, Harris T, Allman BE, Harris PJ, Stewart AG, Roberts A, Nugent KA & Delbridge LMD (2005). Refractive index measurement in viable cells using quantitative phase-amplitude microscopy and confocal microscopy. *Cytometry A* **65,** 88–92.

Curtin NA, Diack RA, West TG, Wilson AM & Woledge RC (2015). Skinned fibres produce the same power and force as intact fibre bundles from muscle of wild rabbits. *J Exp Biol* **218,** 2856–2863.

Cuthbertson D, Smith K, Babraj J, Leese G, Waddell T, Atherton P, Wackerhage H, Taylor PM & Rennie MJ (2005). Anabolic signaling deficits underlie amino acid resistance of wasting, aging muscle. *FASEB J* **19,** 422–424.

Cutler AA, Jackson JB, Corbett AH & Pavlath GK (2018). Non-equivalence of nuclear import among nuclei in multinucleated skeletal muscle cells. *J Cell Sci* **131,** jcs207670.

D'Antona G, Brocca L, Pansarasa O, Rinaldi C, Tupler R & Bottinelli R (2007*a*). Structural and functional alterations of muscle fibres in the novel mouse model of facioscapulohumeral muscular dystrophy. *J Physiol* **584,** 997–1009.

D'Antona G, Lanfranconi F, Pellegrino MA, Brocca L, Adami R, Rossi R, Moro G, Miotti D, Canepari M & Bottinelli R (2006). Skeletal muscle hypertrophy and structure and function of skeletal muscle fibres in male body builders. *J Physiol* **570,** 611–627.

D'Antona G, Pellegrino MA, Adami R, Rossi R, Carlizzi CN, Canepari M, Saltin B & Bottinelli R (2003). The effect of ageing and immobilization on structure and function of human skeletal muscle fibres. *J Physiol* **552,** 499–511.

D'Antona G, Pellegrino MA, Carlizzi CN & Bottinelli R (2007*b*). Deterioration of contractile properties of muscle fibres in elderly subjects is modulated by the level of physical activity. *Eur J Appl Physiol* **100,** 603–611.

Dahl KN, Scaffidi P, Islam MF, Yodh AG, Wilson KL & Misteli T (2006). Distinct structural and mechanical properties of the nuclear lamina in Hutchinson-Gilford progeria syndrome. *Proc Natl Acad Sci U S A* **103,** 10271–10276.

Damas F, Libardi CA, Ugrinowitsch C, Vechin FC, Lixandrão ME, Snijders T, Nederveen JP, Bacurau A V., Brum P, Tricoli V, Roschel H, Parise G & Phillips SM (2018). Early- and later-phases satellite cell responses and myonuclear content with resistance training in young men. *PLoS One* **13,** e0191039.

Davidson PM, Sliz J, Isermann P, Denais C & Lammerding J (2015). Design of a microfluidic device to quantify dynamic intra-nuclear deformation during cell migration through confining environments. *Integr Biol (Camb)* **7,** 1534–1546.

Davies BSJ, Coffinier C, Yang SH, Barnes RH, Jung H-J, Young SG & Fong LG (2011). Investigating the purpose of prelamin A processing. *Nucleus* **2,** 4–9.

Davies BSJ, Fong LG, Yang SH, Coffinier C & Young SG (2009). The posttranslational processing of prelamin A and disease. *Annu Rev Genomics Hum Genet* **10,** 153–174.

Davis AS, Richter A, Becker S, Moyer JE, Sandouk A, Skinner J & Taubenberger JK (2014). Characterizing and Diminishing Autofluorescence in Formalin-fixed Paraffin-embedded Human Respiratory Tissue. *J Histochem Cytochem* **62,** 405–423.

Dechat T, Gajewski A, Korbei B, Gerlich D, Daigle N, Haraguchi T, Furukawa K, Ellenberg J & Foisner R (2004). LAP2alpha and BAF transiently localize to telomeres and specific regions on chromatin during nuclear assembly. *J Cell Sci* **117,** 6117–6128.

Dechat T, Gesson K & Foisner R (2010). Lamina-independent lamins in the nuclear interior serve important functions. *Cold Spring Harb Symp Quant Biol* **75,** 533–543.

Dechat T, Korbei B, Vaughan O a, Vlcek S, Hutchison CJ & Foisner R (2000). Lamina-associated polypeptide 2alpha binds intranuclear A-type lamins. *J Cell Sci* **113 Pt 19,** 3473–3484.

Dechat T, Pfleghaar K, Sengupta K, Shimi T, Shumaker DK, Solimando L & Goldman RD (2008). Nuclear lamins: major factors in the structural organization and function of the nucleus and chromatin. *Genes Dev* **22,** 832–853.

Decroix L, Van Muylder V, Desender L, Sampaolesi M & Thorrez L (2015). Tissue clearing for confocal imaging of native and bio-artificial skeletal muscle. *Biotech Histochem* **90,** 424–431.

Degens H & Alway SE (2006). Control of muscle size during disuse, disease, and aging. *Int J Sports Med* **27,** 94–99.

Delbarre E, Tramier M, Coppey-Moisan M, Gaillard C, Courvalin J-C & Buendia B (2006). The truncated prelamin A in Hutchinson-Gilford progeria syndrome alters segregation of A-type and B-type lamin homopolymers. *Hum Mol Genet* **15,** 1113–1122.

Demetrius L (2005). Of mice and men. *EMBO Rep* **6,** S39–S44.

Denais CM, Gilbert RM, Isermann P, McGregor AL, te Lindert M, Weigelin B, Davidson PM, Friedl P, Wolf K & Lammerding J (2016). Nuclear envelope rupture and repair during cancer cell migration. *Science* **352,** 353–358.

Dialynas G, Shrestha OK, Ponce JM, Zwerger M, Thiemann DA, Young GH, Moore SA, Yu L, Lammerding J & Wallrath LL (2015). Myopathic Lamin Mutations Cause Reductive Stress and Activate the Nrf2/Keap-1 Pathway. *PLOS Genet* **11,** e1005231.

Dirckx JJJ, Kuypers LC & Decraemer WF (2005). Refractive index of tissue measured with confocal microscopy. *J Biomed Opt* **10,** 044014.

Duddy W, Duguez S, Johnston H, Cohen T V, Phadke A, Gordish-Dressman H, Nagaraju K, Gnocchi V, Low S & Partridge T (2015). Muscular dystrophy in the mdx mouse is a severe myopathy compounded by hypotrophy, hypertrophy and hyperplasia. *Skelet Muscle* **5,** 1–18.

Duddy WJ, Cohen T, Duguez S & Partridge T a. (2011). The isolated muscle fibre as a model of disuse atrophy: Characterization using PhAct, a method to quantify f-actin. *Exp Cell Res* **317,** 1979–1993.

Duggal NA, Pollock RD, Lazarus NR, Harridge S & Lord JM (2018). Major features of immunesenescence, including reduced thymic output, are ameliorated by high levels of physical activity in adulthood. *Aging Cell*; DOI: 10.1111/acel.12750.

Dulbecco R (1952). Production of Plaques in Monolayer Tissue Cultures by Single Particles of an Animal Virus. *Proc Natl Acad Sci U S A* **38,** 747–752.

Dungan CM, Murach KA, Frick KK, Jones SR, Crow SE, Englund DA, Vechetti IJ, Figueiredo VC, Levitan BM, Satin J, McCarthy JJ & Peterson CA (2019). Elevated Myonuclear Density During Skeletal Muscle Hypertrophy In Response to Training Is Reversed During Detraining. *Am J Physiol Cell Physiol*; DOI: 10.1152/ajpcell.00050.2019.

Eastwood AB, Wood DS, Bock KL & Sorenson MM (1979). Chemically skinned mammalian skeletal muscle I. The structure of skinned rabbit psoas. *Tissue Cell* **11,** 553–566.

Edlund PK & Lindblad J (2008). Non-uniform 3D distance transform for anisotropic signal correction in confocal image volumes of skeletal muscle cell nuclei. *2008 5th IEEE Int Symp Biomed Imaging From Nano to Macro, Proceedings, ISBI*1363–1366.

Egner IM, Bruusgaard JC, Eftestol E & Gundersen K (2013). A cellular memory mechanism aids overload hypertrophy in muscle long after an episodic exposure to anabolic steroids. *J Physiol* **591,** 6221–6230.

Egner IM, Bruusgaard JC & Gundersen K (2016). Satellite cell depletion prevents fiber hypertrophy in skeletal muscle. *Development* **143,** 2898–2906.

Ehler E & Gautel M (2008). The Sarcomere and Sarcomerogenesis. In *Advances in experimental medicine and biology*, pp. 1–14. Available at: http://www.ncbi.nlm.nih.gov/pubmed/19181089.

Elosegui-Artola A, Andreu I, Beedle AEM, Lezamiz A, Uroz M, Kosmalska AJ, Oria R, Kechagia JZ, Rico-Lastres P, Le Roux A-L, Shanahan CM, Trepat X, Navajas D, Garcia-Manyes S & Roca-Cusachs P (2017). Force Triggers YAP Nuclear Entry by Regulating Transport across Nuclear Pores. *Cell* **171,** 1397-1410.e14.

Endo M (1977). Calcium release from the sarcoplasmic reticulum. *Physiol Rev* **57,** 71–108.

Endo M, Tanaka M & Ogawa Y (1970). Calcium induced release of calcium from the sarcoplasmic reticulum of skinned skeletal muscle fibres. *Nature* **228,** 34–36.

Enesco M & Puddy D (1964). Increase in the number of nuclei and weight in skeletal muscle of rats of various ages. *Am J Anat* **114,** 235–244.

Eng JK, McCormack AL & Yates JR (1994). An approach to correlate tandem mass spectral data of peptides with amino acid sequences in a protein database. *J Am Soc Mass Spectrom* **5,** 976–989.

Ennion S, Sant'ana Pereira J, Sargeant a J, Young a & Goldspink G (1995). Characterization of human skeletal muscle fibres according to the myosin heavy chains they express. *J Muscle Res Cell Motil* **16,** 35–43.

Enyedi B & Niethammer P (2017). Nuclear membrane stretch and its role in mechanotransduction. *Nucleus* **8,** 156–161.

Eriksson M, Brown WT, Gordon LB, Glynn MW, Singer J, Scott L, Erdos MR, Robbins CM, Moses TY, Berglund P, Dutra A, Pak E, Durkin S, Csoka AB, Boehnke M, Glover TW & Collins FS (2003). Recurrent de novo point mutations in lamin A cause Hutchinson-Gilford progeria syndrome. *Nature* **423,** 293–298.

Ertürk A, Lafkas D & Chalouni C (2014). Imaging cleared intact biological systems at a cellular level by 3DISCO. *J Vis Exp*1–12.

Espigat-Georger A, Dyachuk V, Chemin C, Emorine L & Merdes A (2016). Nuclear alignment in myotubes requires centrosome proteins recruited by nesprin-1. *J Cell Sci* **129,** 4227–4237.

Evans VJ, Earle WR, Sanford KK, Shannon JE & Waltz HK (1951). The preparation and handling of replicate tissue cultures for quantitative studies. *J Natl Cancer Inst* **11,** 907–927.

Falcone S, Roman W, Hnia K, Gache V, Didier N, Lainé J, Auradé F, Marty I, Nishino I, Charlet-Berguerand N, Romero NB, Marazzi G, Sassoon D, Laporte J & Gomes ER (2014). N-WASP is required for Amphiphysin-2/BIN1-dependent nuclear positioning and triad organization in skeletal muscle and is involved in the pathophysiology of centronuclear myopathy. *EMBO Mol Med* **6,** 1455–1475.

Fankoua S-O, Bitja Nyom AR, Bahanak D ne dort, Bilong Bilong CF & Pariselle A (2017). Influence of preservative and mounting media on the size and shape of monogenean sclerites. *Parasitol Res* **116,** 2277–2281.

Ferraz-Pereira KN, da Silva Aragão R, Verdier D, Toscano AE, Lacerda DC, Manhães-de-Castro R & Kolta A (2015). Neonatal low-protein diet reduces the masticatory efficiency in rats. *Br J Nutr* **114,** 1515–1530.

Ferri P, Barbieri E, Burattini S, Guescini M, D'Emilio A, Biagiotti L, Del Grande P, De Luca A, Stocchi V & Falcieri E (2009). Expression and subcellular localization of myogenic regulatory factors during the differentiation of skeletal muscle C2C12 myoblasts. *J Cell Biochem* **108,** 1302–1317.

Fiorotto ML, Davis TA, Sosa HA, Villegas-Montoya C, Estrada I & Fleischmann R (2014). Ribosome abundance regulates the recovery of skeletal muscle protein mass upon recuperation from postnatal undernutrition in mice. *J Physiol* **592,** 5269–5286.

Fischer RS, Wu Y, Kanchanawong P, Shroff H & Waterman CM (2011). Microscopy in 3D: A biologist's toolbox. *Trends Cell Biol* **21,** 682–691.

Folgueras AR, Freitas-Rodríguez S, Velasco G & López-Otín C (2018). Mouse Models to Disentangle the Hallmarks of Human Aging. *Circ Res* **123,** 905–924.

Folker ES & Baylies MK (2013). Nuclear positioning in muscle development and disease. *Front Physiol* **4,** 363.

Folker ES, Östlund C, Luxton GWG, Worman HJ & Gundersen GG (2011). Lamin A variants that cause striated muscle disease are defective in anchoring transmembrane actin-associated nuclear lines for nuclear movement. *Proc Natl Acad Sci USA* **108,** 131–136.

Fong LG, Frost D, Meta M, Qiao X, Yang SH, Coffinier C & Young SG (2006*a*). A protein farnesyltransferase inhibitor ameliorates disease in a mouse model of progeria. *Science* **311,** 1621–1623.

Fong LG, Ng JK, Lammerding J, Vickers TA, Meta M, Coté N, Gavino B, Qiao X, Chang SY, Young SR, Yang SH, Stewart CL, Lee RT, Bennett CF, Bergo MO & Young SG (2006*b*). Prelamin A and lamin A appear to be dispensable in the nuclear lamina. *J Clin Invest* **116,** 743–752.

Fong LG, Ng JK, Meta M, Coté N, Yang SH, Stewart CL, Sullivan T, Burghardt A, Majumdar S, Reue K, Bergo MO & Young SG (2004). Heterozygosity for Lmna deficiency eliminates the progeria-like phenotypes in Zmpste24-deficient mice. *Proc Natl Acad Sci U S A* **101,** 18111–18116.

Fongy A, Falcone S, Lainé J, Prudhon B, Martins-Bach A & Bitoun M (2019). Nuclear defects in skeletal muscle from a Dynamin 2-linked centronuclear myopathy mouse model. *Sci Rep* **9,** 1580.

Frenette J & Côté (2000). Modulation of Structural Protein Content of the Myotendinous Junction Following Eccentric Contractions. *Int J Sports Med* **21,** 313–320.

Fridén J & Lieber RL (1998). Segmental muscle fiber lesions after repetitive eccentric contractions. *Cell Tissue Res* **293,** 165–171.

Fries JF (1980). Aging, natural death, and the compression of morbidity. *N Engl J Med* **303,** 130–135.

Frock RL, Kudlow B a, Evans AM, Jameson S a, Hauschka SD & Kennedy BK (2006). Lamin A / C and emerin are critical for skeletal muscle satellite cell differentiation. *Genes Dev* **20,** 486–500.

Frontera WR, Hughes VA, Fielding RA, Fiatarone MA, Evans WJ & Roubenoff R (2000). Aging of skeletal muscle: a 12-yr longitudinal study. *J Appl Physiol* **88,** 1321–1326.

Frontera WR, Hughes VA, Lutz KJ & Evans WJ (1991). A cross-sectional study of muscle strength and mass in 45- to 78-yr-old men and women. *J Appl Physiol* **71,** 644–650.

Frontera WR & Larsson L (1997). Contractile studies of single human skeletal muscle fibers: a comparison of different muscles, permeabilization procedures, and storage techniques. *Muscle Nerve* **20,** 948–952.

Frontera WR & Ochala J (2015). Skeletal muscle: a brief review of structure and function. *Calcif Tissue Int* **96,** 183–195.

Frontera WR, Reid KF, Phillips EM, Krivickas LS, Hughes VA, Roubenoff R & Fielding RA (2008). Muscle fiber size and function in elderly humans: a longitudinal study. *J Appl Physiol* **105,** 637–642.

Fry CS, Lee JD, Jackson JR, Kirby TJ, Stasko SA, Liu H, Dupont-Versteegden EE, McCarthy JJ & Peterson CA (2014*a*). Regulation of the muscle fiber microenvironment by activated satellite cells during hypertrophy. *FASEB J* **28,** 1654–1665.

Fry CS, Noehren B, Mula J, Ubele MF, Westgate PM, Kern P a & Peterson C a (2014*b*). Fibre type-specific satellite cell response to aerobic training in sedentary adults. *J Physiol* **592,** 2625–2635.

García-Plazaola JI, Fernández-Marín B, Duke SO, Hernández A, López-Arbeloa F & Becerril JM (2015). Autofluorescence: Biological functions and technical applications. *Plant Sci* **236,** 136–145.

Gautel M & Djinovic-Carugo K (2016). The sarcomeric cytoskeleton: from molecules to motion. *J Exp Biol* **219,** 135–145.

Gautsch TA, Kandl SM, Donovan SM & Layman DK (1999). Growth hormone promotes somatic and skeletal muscle growth recovery in rats following chronic protein-energy malnutrition. *J Nutr* **129,** 828–837.

Geiger PC, Cody MJ, Macken RL & Sieck GC (2000). Maximum specific force depends on myosin heavy chain content in rat diaphragm muscle fibers. *J Appl Physiol* **89,** 695–703.

Gerhard-Herman M, Smoot LB, Wake N, Kieran MW, Kleinman ME, Miller DT, Schwartzman A, Giobbie-Hurder A, Neuberg D & Gordon LB (2012). Mechanisms of premature vascular aging in children with Hutchinson-Gilford progeria syndrome. *Hypertens (Dallas, Tex 1979)* **59,** 92–97.

Gesson K, Rescheneder P, Skoruppa MP, von Haeseler A, Dechat T & Foisner R (2016). A-type lamins bind both hetero- and euchromatin, the latter being regulated by lamina-associated polypeptide 2 alpha. *Genome Res* **26,** 462–473.

Giddings CJ & Gonyea WJ (1992). Morphological observations supporting muscle fiber hyperplasia following weight-lifting exercise in cats. *Anat Rec* **233,** 178–195.

Gillies AR, Bushong EA, Deerinck TJ, Ellisman MH & Lieber RL (2014). Three-Dimensional Reconstruction of Skeletal Muscle Extracellular Matrix Ultrastructure. *Microsc Microanal* **20,** 1835–1840.

Gillies AR, Chapman MA, Bushong EA, Deerinck TJ, Ellisman MH & Lieber RL (2017). High resolution three-dimensional reconstruction of fibrotic skeletal muscle extracellular matrix. *J Physiol* **595,** 1159–1171.

Gillies AR & Lieber RL (2011). Structure and function of the skeletal muscle extracellular matrix. *Muscle Nerve*n/a-n/a.

Gillies AR, Smith LR, Lieber RL & Varghese S (2011). Method for decellularizing skeletal muscle without detergents or proteolytic enzymes. *Tissue Eng Part C Methods* **17,** 383–389.

Gimpel P, Lee YL, Sobota RM, Calvi A, Koullourou V, Patel R, Mamchaoui K, Nédélec F, Shackleton S, Schmoranzer J, Burke B, Cadot B & Gomes ER (2017). Nesprin-1α-Dependent Microtubule Nucleation from the Nuclear Envelope via Akap450 Is Necessary for Nuclear Positioning in Muscle Cells. *Curr Biol* **27,** 2999-3009.e9.

Gnocchi VF, Scharner J, Huang Z, Brady K, Lee JS, White RB, Morgan JE, Sun YB, Ellis JA & Zammit PS (2011). Uncoordinated transcription and compromised muscle function in the Lmna-null mouse model of Emery-Dreifuss muscular dystrophy. *PLoS One* **6,** 1–12.

Goh Q & Millay DP (2017). Requirement of myomaker-mediated stem cell fusion for skeletal muscle hypertrophy. *Elife* **6,** 1–19.

Goldberg MW, Huttenlauch I, Hutchison CJ & Stick R (2008). Filaments made from A- and B-type lamins differ in structure and organization. *J Cell Sci* **121,** 215–225.

Goldfarb LG & Dalakas MC (2009). Tragedy in a heartbeat: malfunctioning desmin causes skeletal and cardiac muscle disease. *J Clin Invest* **119,** 1806–1813.

Goldman RD, Shumaker DK, Erdos MR, Eriksson M, Goldman AE, Gordon LB, Gruenbaum Y, Khuon S, Mendez M, Varga R & Collins FS (2004). Accumulation of mutant lamin A causes progressive changes in nuclear architecture in Hutchinson-Gilford progeria syndrome. *Proc Natl Acad Sci U S A* **101,** 8963–8968.

Gollapudi SK & Lin DC (2009). Experimental determination of sarcomere force-length relationship in type-I human skeletal muscle fibers. *J Biomech* **42,** 2011–2016.

Gonzalez-Suarez I, Redwood AB, Perkins SM, Vermolen B, Lichtensztejin D, Grotsky D a, Morgado-Palacin L, Gapud EJ, Sleckman BP, Sullivan T, Sage J, Stewart CL, Mai S & Gonzalo S (2009). Novel roles for A-type lamins in telomere biology and the DNA damage response pathway. *EMBO J* **28,** 2414–2427.

Goodwin PC (2014). Quantitative deconvolution microscopy. In *Methods in Cell Biology*, 1st edn., pp. 177–192. Elsevier Inc. Available at: http://dx.doi.org/10.1016/B978-0-12-420138-5.00010-0.

Gordon AM, Huxley AF & Julian FJ (1966). The variation in isometric tension with sarcomere length in vertebrate muscle fibres. *J Physiol* **184,** 170–192.

Gordon H, Ralston E & Hall ZW (1992). Cooperation between the products of different nuclei in hybrid myotubes produces localized acetylcholine receptor clusters. *Proc Natl Acad Sci U S A* **89,** 6595–6598.

Gordon LB, Shappell H, Massaro J, D'Agostino RB, Brazier J, Campbell SE, Kleinman ME & Kieran MW (2018). Association of Lonafarnib Treatment vs No Treatment With Mortality Rate in Patients With Hutchinson-Gilford Progeria Syndrome. *JAMA* **319,** 1687–1695.

Greig CA, Young A, Skelton DA, Pippet E, Butler FM & Mahmud SM (1994). Exercise studies with elderly volunteers. *Age Ageing* **23,** 185–189.

Greising SM, Call J a., Lund TC, Blazar BR, Tolar J & Lowe D a. (2012). Skeletal muscle contractile function and neuromuscular performance in Zmpste24 −/− mice, a murine model of human progeria. *Age (Omaha)* **34,** 805–819.

Gruenbaum Y & Aebi U (2014). Intermediate filaments: a dynamic network that controls cell mechanics. *F1000Prime Rep* **6,** 54.

Gu W et al. (2005). A highly potent and selective farnesyltransferase inhibitor ABT-100 in preclinical studies. *Anticancer Drugs* **16,** 1059–1069.

Guilluy C, Osborne LD, Van LL, Sharek L, Superfine R, Garcia-Mata R & Burridge K (2014). Isolated nuclei adapt to force and reveal a mechanotransduction pathway in the nucleus. *NatCell Biol* **16,** 376–381.

Gundersen K (2016). Muscle memory and a new cellular model for muscle atrophy and hypertrophy. *J Exp Biol* **219,** 235–242.

Gundersen K & Bruusgaard JC (2008). Nuclear domains during muscle atrophy: nuclei lost or paradigm lost? *J Physiol* **586,** 2675–2681.

Gundersen K, Sanes JR & Merlie JP (1993). Neural regulation of muscle acetylcholine receptor epsilon- and alpha-subunit gene promoters in transgenic mice. *J Cell Biol* **123,** 1535–1544.

Haase K, Macadangdang JKL, Edrington CH, Cuerrier CM, Hadjiantoniou S, Harden JL, Skerjanc IS & Pelling AE (2016). Extracellular Forces Cause the Nucleus to Deform in a Highly Controlled Anisotropic Manner. *Sci Rep* **6,** 21300.

Hall ZW & Ralston E (1989). Nuclear domains in muscle cells. *Cell* **59,** 771–772.

Hameed M, Harridge SDR & Goldspink G (2002). Sarcopenia and Hypertrophy: A Role for Insulin-Like Growth Factor-1 in Aged Muscle? *Exerc Sport Sci Rev* **30,** 15–19.

Hansen-Smith FM, Picou D & Golden MH (1979). Muscle satellite cells in malnourished and nutritionally rehabilitated children. *J Neurol Sci* **41,** 207–221.

Haque F, Lloyd DJ, Smallwood DT, Dent CL, Shanahan CM, Fry AM, Trembath RC & Shackleton S (2006). SUN1 interacts with nuclear lamin A and cytoplasmic nesprins to provide a physical connection between the nuclear lamina and the cytoskeleton. *Mol Cell Biol* **26,** 3738–3751.

Hardy D, Besnard A, Latil M, Jouvion G, Briand D, Thépenier C, Pascal Q, Guguin A, Gayraud-Morel B, Cavaillon J-M, Tajbakhsh S, Rocheteau P & Chrétien F (2016). Comparative Study of Injury Models for Studying Muscle Regeneration in Mice. *PLoS One* **11,** e0147198.

Harhouri K, Frankel D, Bartoli C, Roll P, De Sandre-Giovannoli A & Lévy N (2018). An overview of treatment strategies for Hutchinson-Gilford Progeria Syndrome. *Nucleus* **9,** 1–27.

Harman D (1998). Aging: phenomena and theories. *Ann N Y Acad Sci* **854,** 1–7.

Harridge SDR, Bottinelli R, Canepari M, Pellegrino MA, Reggiani C, Esbjörnsson M & Saltin B (1996). Whole-muscle and single-fibre contractile properties and myosin heavy chain isoforms in humans. *Pflugers Arch Eur J Physiol* **432,** 913–920.

Harridge SDR & Lazarus NR (2017). Physical Activity, Aging, and Physiological Function. *Physiology* **32,** 152–161.

Harrison RG, Greenman MJ, Mall FP & Jackson CM (1907). Observations of the living developing nerve fiber. *Anat Rec* **1,** 116–128.

Hatch EM & Hetzer MW (2016). Nuclear envelope rupture is induced by actin-based nucleus confinement. *J Cell Biol* **215,** 27–36.

Haxton HA (1944). Absolute muscle force in the ankle flexors of man. *J Physiol* **103,** 267–273.

Hayflick L (2000). The future of ageing. *Nature* **408,** 267–269.

Hazeldine J, Harris P, Chapple IL, Grant M, Greenwood H, Livesey A, Sapey E & Lord JM (2014). Impaired neutrophil extracellular trap formation: a novel defect in the innate immune system of aged individuals. *Aging Cell* **13,** 690–698.

Hebbes TR, Thorne AW & Crane-Robinson C (1988). A direct link between core histone acetylation and transcriptionally active chromatin. *EMBO J* **7,** 1395–1402.

Heintzmann R & Ficz G (2013). Breaking the resolution limit in light microscopy. In *Methods in Cell Biology*, 4th edn., pp. 525–544. Elsevier Inc. Available at: http://dx.doi.org/10.1016/B978-0-12-407761-4.00022-1.

Helmchen F & Denk W (2005). Deep tissue two-photon microscopy. *Nat Methods* **2,** 932–940.

Hepple RT & Rice CL (2016). Innervation and neuromuscular control in ageing skeletal muscle. *J Physiol* **594,** 1965–1978.

Hershko A (1998). The ubiquitin system. *Ubiquitin Biol Cell*. Available at: http://link.springer.com/chapter/10.1007/978-1-4899-1922-9_1.

Hex N, Bartlett C, Wright D, Taylor M & Varley D (2012). Estimating the current and future costs of Type 1 and Type 2 diabetes in the UK, including direct health costs and indirect societal and productivity costs. *Diabet Med* **29,** 855–862.

Hikida R, Walsh S & Barylski N (1998). Is hypertrophy limited in elderly muscle fibers? A comparison of elderly and young strength-trained men. *Basic Appl Myol* **8,** 419–427.

Hikida RS, Staron RS, Hagerman FC, Walsh S, Kaiser E, Shell S & Hervey S (2000). Effects of high-intensity resistance training on untrained older men. II. Muscle fiber characteristics and nucleo-cytoplasmic relationships. *J Gerontol A Biol Sci Med Sci* **55,** B347-54.

Hill A V. (1938). The Heat of Shortening and the Dynamic Constants of Muscle. *Proc R Soc B Biol Sci* **126,** 136–195.

Hill M & Goldspink G (2003). Expression and Splicing of the Insulin-Like Growth Factor Gene in Rodent Muscle is Associated with Muscle Satellite (stem) Cell Activation following Local Tissue Damage. *J Physiol* **549,** 409–418.

Ho CY, Jaalouk DE, Vartiainen MK & Lammerding J (2013). Lamin A/C and emerin regulate MKL1-SRF activity by modulating actin dynamics. *Nature* **497,** 507–511.

Höök P, Sriramoju V & Larsson L (2001). Effects of aging on actin sliding speed on myosin from single skeletal muscle cells of mice, rats, and humans. *Am J Physiol Cell Physiol* **280,** C782-8.

Houthaeve G, Robijns J, Braeckmans K & De Vos WH (2018). Bypassing Border Control: Nuclear Envelope Rupture in Disease. *Physiology* **33,** 39–49.

Huxley AF (1957). Muscle structure and theories of contraction. *Prog Biophys Biophys Chem* **7,** 255–318.

Huxley AF & Niedergerke R (1958). Measurement of the striations of isolated muscle fibres with the interference microscope. *J Physiol* **144,** 403–425.

Huxley AF & Simmons RM (1971). Proposed mechanism of force generation in striated muscle. *Nature* **233,** 533–538.

I. Wada K, Katsuta S & Soya H (2003). Natural Occurrence of Myofiber Cytoplasmic Enlargement Accompanied by Decrease in Myonuclear Number. *Jpn J Physiol* **53,** 145–150.

Ishido M, Kami K & Masuhara M (2004). Localization of MyoD, myogenin and cell cycle regulatory factors in hypertrophying rat skeletal muscles. *Acta Physiol Scand* **180,** 281–289.

Itano N, Okamoto S, Zhang D, Lipton S a & Ruoslahti E (2003). Cell spreading controls endoplasmic and nuclear calcium: a physical gene regulation pathway from the cell surface to the nucleus. *Proc Natl Acad Sci U S A* **100,** 5181–5186.

Izumi M, Vaughan O a, Hutchison CJ & Gilbert DM (2000). Head and/or CaaX domain deletions of lamin proteins disrupt preformed lamin A and C but not lamin B structure in mammalian cells. *Mol Biol Cell* **11,** 4323–4337.

Jackson JR, Mula J, Kirby TJ, Fry CS, Lee JD, Ubele MF, Campbell KS, McCarthy JJ, Peterson C a & Dupont-Versteegden EE (2012). Satellite cell depletion does not inhibit adult skeletal muscle regrowth following unloading-induced atrophy. *Am J Physiol Cell Physiol* **303,** C854-61.

Janesick JR (1997). CCD transfer method: standard for absolute performance of CCDs and digital CCD camera systems. Available at: https://doi.org/10.1117/12.275190.

Janin A, Bauer D, Ratti F, Millat G & Méjat A (2017). Nuclear envelopathies: a complex LINC between nuclear envelope and pathology. *Orphanet J Rare Dis* **12,** 147.

Janin A & Gache V (2018). Nesprins and Lamins in Health and Diseases of Cardiac and Skeletal Muscles. *Front Physiol* **9,** 1277.

Johnson WL & Straight AF (2013). Fluorescent protein applications in microscopy. In *Methods in Cell Biology*, 4th edn., pp. 99–123. Elsevier Inc. Available at: http://dx.doi.org/10.1016/B978-0-12-407761-4.00005-1.

Jones D, Round J & de Haan A (2004). *Skeletal Muscle from Molecules to Movement*, 1st edn. Elsevier. Available at: http://linkinghub.elsevier.com/retrieve/pii/B9780443074271X50018.

Jonkman J & Brown CM (2015). Any Way You Slice It-A Comparison of Confocal Microscopy Techniques. *J Biomol Tech* **26,** 54–65.

Jonkman J, Brown CM & Cole RW (2014). Quantitative confocal microscopy. Beyond a pretty picture. In *Methods in Cell Biology*, 1st edn., pp. 113–134. Elsevier Inc. Available at: http://dx.doi.org/10.1016/B978-0-12-420138-5.00007-0.

Judson RN, Tremblay AM, Knopp P, White RB, Urcia R, De Bari C, Zammit PS, Camargo FD & Wackerhage H (2012). The Hippo pathway member Yap plays a key role in influencing fate decisions in muscle satellite cells. *J Cell Sci* **125,** 6009–6019.

Kadi F (2008). Cellular and molecular mechanisms responsible for the action of testosterone on human skeletal muscle. A basis for illegal performance enhancement. *Br J Pharmacol* **154,** 522–528.

Kadi F, Charifi N, Denis C, Lexell J, Andersen JL, Schjerling P, Olsen S & Kjaer M (2005). The behaviour of satellite cells in response to exercise: what have we learned from human studies? *Pflugers Arch* **451,** 319–327.

Kadi F, Eriksson A, Holmner S, Butler-Browne GS & Thornell L-E (1999). Cellular adaptation of the trapezius muscle in strength-trained athletes. *Histochem Cell Biol* **111,** 189–195.

Kadi F, Schjerling P, Andersen LL, Charifi N, Madsen JL, Christensen LR & Andersen JL (2004). The effects of heavy resistance training and detraining on satellite cells in human skeletal muscles. *J Physiol* **558,** 1005–1012.

Kalakoutis M (2017). *Specific force in human single muscle fibres with specific referencce to ageing* (thesis). King's College London Faculty.

Kallman DA, Plato CC & Tobin JD (1990). The role of muscle loss in the age-related decline of grip strength: cross-sectional and longitudinal perspectives. *J Gerontol* **45,** M82-8.

Karlsen A, Couppé C, Andersen JL, Mikkelsen UR, Nielsen RH, Magnusson SP, Kjaer M & Mackey AL (2015). Matters of fiber size and myonuclear domain: Does size matter more than age? *Muscle Nerve* **52,** 1040–1046.

Karlsson P (2008). *Methods and models for 2D and 3D image analysis in microscopy, in particular for the study of muscle cells* (thesis). Uppsala University.

Keeling MC, Flores LR, Dodhy AH, Murray ER & Gavara N (2017). Actomyosin and vimentin cytoskeletal networks regulate nuclear shape, mechanics and chromatin organization. *Sci Rep* **7,** 5219.

Keller HE (2006). Objective Lenses for Confocal Microscopy. In *Handbook Of Biological Confocal Microscopy*, pp. 145–161. Springer US, Boston, MA. Available at: http://link.springer.com/chapter/10.1007/978-0-387-45524-2_7%5Cnhttp://link.springer.com/10.1007/978-0-387-45524-2_7.

Kennedy AB, Lavie CJ & Blair SN (2018). Fitness or Fatness: Which Is More Important? *JAMA* **319,** 231–232.

Kim J-K, Louhghalam A, Lee G, Schafer BW, Wirtz D & Kim D-H (2017). Nuclear lamin A/C harnesses the perinuclear apical actin cables to protect nuclear morphology. *Nat Commun* **8,** 2123.

Kim KM, Lim S, Oh TJ, Moon JH, Choi SH, Lim JY, Kim KW, Park KS & Jang HC (2018). Longitudinal Changes in Muscle Mass and Strength, and Bone Mass in Older Adults: Gender-Specific Associations Between Muscle and Bone Losses. *J Gerontol A Biol Sci Med Sci* **73,** 1062–1069.

Kind J, Pagie L, Ortabozkoyun H, Boyle S, de Vries SS, Janssen H, Amendola M, Nolen LD, Bickmore WA & van Steensel B (2013). Single-cell dynamics of genome-nuclear lamina interactions. *Cell* **153,** 178–192.

Kirby TJ & Lammerding J (2018). Emerging views of the nucleus as a cellular mechanosensor. *Nat Cell Biol* **20,** 373–381.

Kirby TJ, Patel RM, McClintock TS, Dupont-Versteegden EE, Peterson CA & McCarthy JJ (2016). Myonuclear transcription is responsive to mechanical load and DNA content but uncoupled from cell size during hypertrophy ed. Marshall W. *Mol Biol Cell* **27,** 788–798.

Klein CS, Rice CL & Marsh GD (2001). Normalized force, activation, and coactivation in the arm muscles of young and old men. *J Appl Physiol* **91,** 1341–1349.

Konigsberg IR (1963). Clonal analysis of myogenesis. *Science* **140,** 1273–1284.

Konigsberg UR, Lipton BH & Konigsberg IR (1975). The regenerative response of single mature muscle fibers isolated in vitro. *Dev Biol* **45,** 260–275.

Korhonen MT, Mero A & Suominen H (2003). Age-related differences in 100-m sprint performance in male and female master runners. *Med Sci Sports Exerc* **35,** 1419–1428.

Kubben N & Misteli T (2017). Shared molecular and cellular mechanisms of premature ageing and ageing-associated diseases. *Nat Rev Mol Cell Biol* **18,** 595–609.

Kugelberg E (1973). Histochemical composition, contraction speed and fatiguability of rat soleus motor units. *J Neurol Sci* **20,** 177–198.

Kuh D, Karunananthan S, Bergman H & Cooper R (2014). A life-course approach to healthy ageing: maintaining physical capability. *Proc Nutr Soc* **73,** 237–248.

De La Rosa J, Freije JMP, Cabanillas R, Osorio FG, Fraga MF, Fernández-García MS, Rad R, Fanjul V, Ugalde AP, Liang Q, Prosser HM, Bradley A, Cadiñanos J & López-Otín C (2013). Prelamin A causes progeria through cell-extrinsic mechanisms and prevents cancer invasion. *Nat Commun*; DOI: 10.1038/ncomms3268.

Lambert TJ & Waters JC (2014). Assessing camera performance for quantitative microscopy. In *Methods in Cell Biology*, 1st edn., pp. 35–53. Elsevier Inc. Available at: http://dx.doi.org/10.1016/B978-0-12-420138-5.00003-3.

Lammerding J, Schulze PC, Takahashi T, Kozlov S, Sullivan T, Kamm RD, Stewart CL & Lee RT (2004). Lamin A/C deficiency causes defective nuclear mechanics and mechanotransduction. *J Clin Invest* **113,** 370–378.

Larsson L, Grimby G & Karlsson J (1979). Muscle strength and speed of movement in relation to age and muscle morphology. *J Appl Physiol* **46,** 451–456.

Larsson L & Moss RL (1993). Maximum velocity of shortening in relation to myosin isoform composition in single fibres from human skeletal muscles. *J Physiol* **472,** 595–614.

de Las Heras JI, Zuleger N, Batrakou DG, Czapiewski R, Kerr ARW & Schirmer EC (2017). Tissue-specific NETs alter genome organization and regulation even in a heterologous system. *Nucleus* **8,** 81–97.

Latouche C, Jowett JBM, Carey AL, Bertovic DA, Owen N, Dunstan DW & Kingwell B a (2013). Effects of breaking up prolonged sitting on skeletal muscle gene expression. *J Appl Physiol* **114,** 453–460.

Lattanzi G, Benedetti S, Bertini E, Boriani G, Mazzanti L, Novelli G, Pasquali R, Pini A & Politano L (2011). Laminopathies: many diseases, one gene. Report of the first Italian Meeting Course on Laminopathies. *Acta Myol myopathies cardiomyopathies Off J Mediterr Soc Myol* **30,** 138–143.

Lautscham LA, Kämmerer C, Lange JR, Kolb T, Mark C, Schilling A, Strissel PL, Strick R, Gluth C, Rowat AC, Metzner C & Fabry B (2015). Migration in Confined 3D Environments Is Determined by a Combination of Adhesiveness, Nuclear Volume, Contractility, and Cell Stiffness. *Biophys J* **109,** 900–913.

Lazarus NR & Harridge SDR (2010). Exercise, physiological function, and the selection of participants for aging research. *J Gerontol A Biol Sci Med Sci* **65,** 854–857.

Lazarus NR & Harridge SDR (2017). Declining performance of master athletes: silhouettes of the trajectory of healthy human ageing? *J Physiol* **595,** 2941–2948.

de Leeuw R, Gruenbaum Y & Medalia O (2018). Nuclear Lamins: Thin Filaments with Major Functions. *Trends Cell Biol* **28,** 34–45.

Lei K, Zhang X, Ding X, Guo X, Chen M, Zhu B, Xu T, Zhuang Y, Xu R & Han M (2009). SUN1 and SUN2 play critical but partially redundant roles in anchoring nuclei in skeletal muscle cells in mice. *Proc Natl Acad Sci U S A* **106,** 10207–10212.

Levy Y, Ross JA, Niglas M, Snetkov VA, Lynham S, Liao C, Puckelwartz MJ, Hsu Y, McNally EM, Alsheimer M, Harridge SDR, Young SG, Fong LG, Español Y, Lopez-Otin C, Kennedy BK, Lowe DA & Ochala J (2018). Prelamin A causes aberrant myonuclear arrangement and results in muscle fiber weakness. *JCI insight*; DOI: 10.1172/jci.insight.120920.

Lexell J, Taylor CC & Sjöström M (1988). What is the cause of the ageing atrophy? *J Neurol Sci* **84,** 275–294.

Li M, Ogilvie H, Ochala J, Artemenko K, Iwamoto H, Yagi N, Bergquist J & Larsson L (2015). Aberrant post-translational modifications compromise human myosin motor function in old age. *Aging Cell* **14,** 228–235.

Li P, Stumpf M, Müller R, Eichinger L, Glöckner G & Noegel AA (2017). The function of the inner nuclear envelope protein SUN1 in mRNA export is regulated by phosphorylation. *Sci Rep* **7,** 9157.

Lin F & Worman HJ (1993). Structural organization of the human gene encoding nuclear lamin A and nuclear lamin C. *J Biol Chem* **268,** 16321–16326.

Lindqvist J, Cheng AJ, Renaud G, Hardeman EC & Ochala J (2013). Distinct underlying mechanisms of limb and respiratory muscle fiber weaknesses in nemaline myopathy. *J Neuropathol Exp Neurol* **72,** 472–481.

Lindqvist J, Levy Y, Pati-Alam A, Hardeman EC, Gregorevic P & Ochala J (2016). Modulating myosin restores muscle function in a mouse model of nemaline myopathy. *Ann Neurol*n/a-n/a.

Link J, Leubner M, Schmitt J, Göb E, Benavente R, Jeang KT, Xu R & Alsheimer M (2014). Analysis of Meiosis in SUN1 Deficient Mice Reveals a Distinct Role of SUN2 in Mammalian Meiotic LINC Complex Formation and Function. *PLoS Genet* **10,** 14–21.

Lipton B & Schultz E (1979). Developmental fate of skeletal muscle satellite cells. *Science (80-)* **205,** 1292–1294.

Liu B et al. (2005). Genomic instability in laminopathy-based premature aging. *Nat Med* **11,** 780–785.

Liu J-X, Höglund A-S, Karlsson P, Lindblad J, Qaisar R, Aare S, Bengtsson E & Larsson L (2009). Myonuclear domain size and myosin isoform expression in muscle fibres from mammals representing a 100,000-fold difference in body size. *Exp Physiol* **94,** 117–129.

Liu J, Rolef Ben-Shahar T, Riemer D, Treinin M, Spann P, Weber K, Fire A & Gruenbaum Y (2000). Essential roles for Caenorhabditis elegans lamin gene in nuclear organization, cell cycle progression, and spatial organization of nuclear pore complexes. *Mol Biol Cell* **11,** 3937–3947.

Liu Y, Drozdov I, Shroff R, Beltran LE & Shanahan CM (2013). Prelamin A accelerates vascular calcification via activation of the DNA damage response and senescence-associated secretory phenotype in vascular smooth muscle cells. *Circ Res* **112,** e99-109.

Liu Y, Rusinol A, Sinensky M, Wang Y & Zou Y (2006). DNA damage responses in progeroid syndromes arise from defective maturation of prelamin A. *J Cell Sci* **119,** 4644–4649.

López-Otín C, Blasco MA, Partridge L, Serrano M & Kroemer G (2013). The hallmarks of aging. *Cell* **153,** 1194–1217.

Lowe DA, Surek JT, Thomas DD & Thompson L V (2001). Electron paramagnetic resonance reveals age-related myosin structural changes in rat skeletal muscle fibers. *Am J Physiol Cell Physiol* **280,** C540-7.

Lowe DA, Thomas DD & Thompson L V (2002). Force generation, but not myosin ATPase activity, declines with age in rat muscle fibers. *Am J Physiol Cell Physiol* **283,** C187-92.

MacConnachie HF, Enesco M & P LC (1964). The mode of increase in the number of skeletal muscle nuclei in the postnatal rat. *Am J Anat* **114,** 245–253.

Makhija E, Jokhun DS & Shivashankar G V. (2016). Nuclear deformability and telomere dynamics are regulated by cell geometric constraints. *Proc Natl Acad Sci U S A* **113,** E32-40.

Mandigo TR & Folker ES (2018). A Touch from Myofibroblasts Puts the Squeeze on Myonuclei. *Dev Cell* **46,** 3–4.

Maniotis a J, Chen CS & Ingber DE (1997). Demonstration of mechanical connections between integrins, cytoskeletal filaments, and nucleoplasm that stabilize nuclear structure. *Proc Natl Acad Sci U S A* **94,** 849–854.

Mantilla CB, Sill R V., Aravamudan B, Zhan W-Z & Sieck GC (2008). Developmental effects on myonuclear domain size of rat diaphragm fibers. *J Appl Physiol* **104,** 787–794.

Marieb EN & Hoehn K (2015). *Human Anatomy & Physiology*, 10th edn. Pearson Education, Inc., New York.

Mattioli E, Andrenacci D, Mai A, Valente S, Robijns J, De Vos WH, Capanni C & Lattanzi G (2019). Statins and Histone Deacetylase Inhibitors Affect Lamin A/C - Histone Deacetylase 2 Interaction in Human Cells. *Front cell Dev Biol* **7,** 6.

Mattioli E, Columbaro M, Capanni C, Maraldi NM, Cenni V, Scotlandi K, Marino MT, Merlini L, Squarzoni S & Lattanzi G (2011). Prelamin A-mediated recruitment of SUN1 to the nuclear envelope directs nuclear positioning in human muscle. *Cell Death Differ* **18,** 1305–1315.

Mauro A (1961). Satellite cell of skeletal muscle fibers. *J Biophys Biochem Cytol* **9,** 493–495.

McCall GE, Allen DL, Linderman JK, Grindeland RE, Roy RR, Mukku VR & Edgerton VR (1998). Maintenance of myonuclear domain size in rat soleus after overload and growth hormone/IGF-I treatment. *J Appl Physiol* **84,** 1407–1412.

McCarthy JJ, Dupont-Versteegden EE, Fry CS, Murach KA & Peterson CA (2017). Methodological issues limit interpretation of negative effects of satellite cell depletion on adult muscle hypertrophy. *Development* **144,** 1363–1365.

McCarthy JJ, Mula J, Miyazaki M, Erfani R, Garrison K, Farooqui AB, Srikuea R, Lawson B a, Grimes B, Keller C, Van Zant G, Campbell KS, Esser K a, Dupont-Versteegden EE & Peterson C a (2011). Effective fiber hypertrophy in satellite cell-depleted skeletal muscle. *Development* **138,** 3657–3666.

McClintock D, Ratner D, Lokuge M, Owens DM, Gordon LB, Collins FS & Djabali K (2007). The mutant form of lamin A that causes Hutchinson-Gilford progeria is a biomarker of cellular aging in human skin. *PLoS One* **2,** e1269.

McCord RP, Nazario-Toole A, Zhang H, Chines PS, Zhan Y, Erdos MR, Collins FS, Dekker J & Cao K (2013). Correlated alterations in genome organization, histone methylation, and DNA-lamin A/C interactions in Hutchinson-Gilford progeria syndrome. *Genome Res* **23,** 260–269.

McGreevy JW, Hakim CH, McIntosh MA & Duan D (2015). Animal models of Duchenne muscular dystrophy: from basic mechanisms to gene therapy. *Dis Model Mech* **8,** 195–213.

McPherron AC, Lawler AM & Lee S-J (1997). Regulation of skeletal muscle mass in mice by a new TGF-p superfamily member. *Nature* **387,** 83–90.

Van der Meer SFT, Jaspers RT & Degens H (2011). Is the myonuclear domain size fixed? *J Musculoskelet Neuronal Interact* **11,** 286–297.

Meinke P, Mattioli E, Haque F, Antoku S, Columbaro M, Straatman KR, Worman HJ, Gundersen GG, Lattanzi G, Wehnert M & Shackleton S (2014). Muscular Dystrophy-Associated SUN1 and SUN2 Variants Disrupt Nuclear-Cytoskeletal Connections and Myonuclear Organization. *PLoS Genet*; DOI: 10.1371/journal.pgen.1004605.

Méjat A, Decostre V, Li J, Renou L, Kesari A, Hantaï D, Stewart CL, Xiao X, Hoffman E, Bonne G & Misteli T (2009). Lamin A/C-mediated neuromuscular junction defects in Emery-Dreifuss muscular dystrophy. *J Cell Biol* **184,** 31–44.

Méjat A & Misteli T (2010). LINC complexes in health and disease. **1,** 40–52.

Men Y, Young A, Stokes M & Crowe M (1985). The size and strength of the quadriceps muscles of old. *Clin Physiol* **5,** 145–154.

Merlie JP & Sanes JR (1985). Concentration of acetylcholine receptor mRNA in synaptic regions of adult muscle fibres. *Nature* **317,** 66–68.

Messier B & Leblond CP (1960). Cell proliferation and migration as revealed by radioautography after injection of thymidine-H3 into male rats and mice. *Am J Anat* **106,** 247–285.

Meyer GA & Lieber RL (2011). Elucidation of extracellular matrix mechanics from muscle fibers and fiber bundles. *J Biomech* **44,** 771–773.

Michaelis I, Kwiet A, Gast U, Boshof A, Antvorskov T, Jung T, Rittweger J & Felsenberg D (2008). Decline of specific peak jumping power with age in master runners. *J Musculoskelet Neuronal Interact* **8,** 64–70.

Michaelis S & Hrycyna CA (2013). Biochemistry. A protease for the ages. *Science* **339,** 1529–1530.

Mislow JMK, Holaska JM, Kim MS, Lee KK, Segura-Totten M, Wilson KL & McNally EM (2002). Nesprin-1α self-associates and binds directly to emerin and lamin A in vitro. *FEBS Lett* **525,** 135–140.

Mittelbronn M, Sullivan T, Stewart CL & Bornemann A (2008). Myonuclear degeneration in LMNA null mice. *Brain Pathol* **18,** 338–343.

Monici M (2005). Cell and tissue autofluorescence research and diagnostic applications. *Biotechnol Annu Rev* **11,** 227–256.

Moriuchi T, Kuroda M, Kusumoto F, Osumi T & Hirose F (2016). Lamin A reassembly at the end of mitosis is regulated by its SUMO-interacting motif. *Exp Cell Res* **342,** 83–94.

Moss FP (1968*a*). The relationship between the dimensions of the fibres and the number of nuclei during restricted growth, degrowth and compensatory growth of skeletal muscle. *Am J Anat* **122,** 565–571.

Moss FP (1968*b*). The relationship between the dimensions of the fibres and the number of nuclei during normal growth of skeletal muscle in the domestic fowl. *Am J Anat* **122,** 555–563.

Moss FP & Leblond CP (1970). Nature of dividing nuclei in skeletal muscle of growing rats. *J Cell Biol* **44,** 459–462.

Moss FP & Leblond CP (1971). Satellite cells as the source of nuclei in muscles of growing rats. *Anat Rec* **170,** 421–435.

Moyle LA & Zammit PS (2014). Isolation, culture and immunostaining of skeletal muscle fibres to study myogenic progression in satellite cells. *Methods Mol Biol* **1210,** 63–78.

Muir AR, Kanji AH & Allbrook D (1965). The structure of the satellite cells in skeletal muscle. *J Anat* **99,** 435–444.

Murach KA, Englund DA, Dupont-Versteegden EE, McCarthy JJ & Peterson CA (2018). Myonuclear Domain Flexibility Challenges Rigid Assumptions on Satellite Cell Contribution to Skeletal Muscle Fiber Hypertrophy. *Front Physiol* **9,** 635.

Murphy DB & Davidson MW (2012). *Fundamentals of Light Microscopy and Electronic Imaging*. John Wiley & Sons, Inc., Hoboken, NJ, USA. Available at: http://doi.wiley.com/10.1002/9781118382905.

Murray JM (2013). Practical aspects of quantitative confocal microscopy. In *Methods in Cell Biology*, 4th edn., pp. 427–440. Elsevier Inc. Available at: http://dx.doi.org/10.1016/B978-0-12-407761-4.00018-X.

Naetar N, Ferraioli S & Foisner R (2017). Lamins in the nuclear interior - life outside the lamina. *J Cell Sci* **130,** 2087–2096.

Nagata Y, Partridge TA, Matsuda R & Zammit PS (2006). Entry of muscle satellite cells into the cell cycle requires sphingolipid signaling. *J Cell Biol* **174,** 245–253.

Navarro CL et al. (2004). Lamin A and ZMPSTE24 (FACE-1) defects cause nuclear disorganization and identify restrictive dermopathy as a lethal neonatal laminopathy. *Hum Mol Genet* **13,** 2493–2503.

Navarro CL et al. (2013). New ZMPSTE24 (FACE1) mutations in patients affected with restrictive dermopathy or related progeroid syndromes and mutation update. *Eur J Hum Genet* **24,** 1002–1011.

Nemeth PM, Solanki L, Gordon D a, Hamm TM, Reinking RM & Stuart DG (1986). Uniformity of metabolic enzymes within individual motor units. *J Neurosci* **6,** 892–898.

Newlands S, Levitt LK, Robinson CS, Karpf ABC, Hodgson VRM, Wade RP & Hardeman EC (1998). Transcription occurs in pulses in muscle fibers. *Genes Dev* **12,** 2748–2758.

Niethammer P (2016). Neutrophil mechanotransduction: A GEF to sense fluid shear stress. *J Cell Biol* **215,** 13–14.

Nikolova V, Leimena C, McMahon AC, Tan JC, Chandar S, Jogia D, Kesteven SH, Michalicek J, Otway R, Verheyen F, Rainer S, Stewart CL, Martin D, Feneley MP & Fatkin D (2004). Defects in nuclear structure and function promote dilated cardiomyopathy in lamin A/C-deficient mice. *J Clin Invest* **113,** 357–369.

Nilwik R, Snijders T, Leenders M, Groen BBL, van Kranenburg J, Verdijk LB & Van Loon LJC (2013). The decline in skeletal muscle mass with aging is mainly attributed to a reduction in type II muscle fiber size. *Exp Gerontol* **48,** 492–498.

Nolte A, Pawley JB & Höring L (2006). Non-Laser Light Sources for Three-Dimensional Microscopy. In *Handbook Of Biological Confocal Microscopy*, pp. 126–144. Springer US, Boston, MA. Available at: http://link.springer.com/10.1007/978-0-387-45524-2_6.

Ntziachristos V (2010). Going deeper than microscopy: the optical imaging frontier in biology. *Nat Methods* **7,** 603–614.

O'Connor RS, Mills ST, Jones KA, Ho SN & Pavlath GK (2006). A combinatorial role for NFAT5 in both myoblast migration and differentiation during skeletal muscle myogenesis. *J Cell Sci* **120,** 149–159.

Oakes PW, Patel DC, Morin NA, Zitterbart DP, Fabry B, Reichner JS & Tang JX (2009). Neutrophil morphology and migration are affected by substrate elasticity. *Blood* **114,** 1387–1395.

Ochala J, Frontera WR, Dorer DJ, Van Hoecke J & Krivickas LS (2007). Single skeletal muscle fiber elastic and contractile characteristics in young and older men. *J Gerontol A Biol Sci Med Sci* **62,** 375–381.

Ochala J, Gokhin DS, Pénisson-Besnier I, Quijano-Roy S, Monnier N, Lunardi J, Romero NB & Fowler VM (2012*a*). Congenital myopathy-causing tropomyosin mutations induce thin filament dysfunction via distinct physiological mechanisms. *Hum Mol Genet* **21,** 4473–4485.

Ochala J, Ravenscroft G, Laing NG & Nowak KJ (2012*b*). Nemaline myopathy-related skeletal muscle α-actin (ACTA1) mutation, Asp286Gly, prevents proper strong myosin binding and triggers muscle weakness. *PLoS One* **7,** e45923.

Ohira Y, Tanaka T, Yoshinaga T, Kawano F, Nomura T, Nonaka I, Allen DL, Roy RR & Edgerton VR (2001). Ontogenetic, gravity-dependent development of rat soleus muscle. *Am J Physiol Cell Physiol* **280,** C1008-16.

Olive M, Harten I, Mitchell R, Beers JK, Djabali K, Cao K, Erdos MR, Blair C, Funke B, Smoot L, Gerhard-Herman M, Machan JT, Kutys R, Virmani R, Collins FS, Wight TN, Nabel EG & Gordon LB (2010*a*). Cardiovascular pathology in Hutchinson-Gilford progeria: correlation with the vascular pathology of aging. *Arterioscler Thromb Vasc Biol* **30,** 2301–2309.

Olive M, Harten I, Mitchell R, Beers JK, Djabali K, Cao K, Erdos MR, Blair C, Funke B, Smoot L, Gerhard-Herman M, MacHan JT, Kutys R, Virmani R, Collins FS, Wight TN, Nabel EG & Gordon LB (2010*b*). Cardiovascular pathology in Hutchinson-Gilford progeria: Correlation with the vascular pathology of aging. *Arterioscler Thromb Vasc Biol* **30,** 2301–2309.

Oliveira VC, Carrara RCV, Simoes DLC, Saggioro FP, Carlotti CG, Covas DT & Neder L (2010). Sudan Black B treatment reduces autofluorescence and improves resolution of in situhybridization specific fluorescent signals of brain sections. *Histol Histopathol* **25,** 1017–1024.

Omairi S et al. (2016). Enhanced exercise and regenerative capacity in a mouse model that violates size constraints of oxidative muscle fibres. *Elife* **5,** 1–25.

ONS (2017). *Life expectancy (LE), healthy life expectancy (HLE) and disability-free life expectancy (DFLE) at birth and age 65 by sex, UK, 2014 to 2016*. Office for National Statistics.

Oreopoulos J, Berman R & Browne M (2014). Spinning-disk confocal microscopy. present technology and future trends. In *Methods in Cell Biology*, 1st edn., pp. 153–175. Elsevier Inc. Available at: http://dx.doi.org/10.1016/B978-0-12-420138-5.00009-4.

Osorio FG, Navarro CL, Cadinanos J, Lopez-Mejia IC, Quiros PM, Bartoli C, Rivera J, Tazi J, Guzman G, Varela I, Depetris D, de Carlos F, Cobo J, Andres V, De Sandre-Giovannoli A, Freije JMP, Levy N & Lopez-Otin C (2011). Splicing-Directed Therapy in a New Mouse Model of Human Accelerated Aging. *Sci Transl Med* **3,** 106ra107-106ra107.

Overend TJ, Cunningham DA, Kramer JF, Lefcoe MS & Paterson DH (1992). Knee extensor and knee flexor strength: cross-sectional area ratios in young and elderly men. *J Gerontol* **47,** M204-10.

Padmakumar VC, Libotte T, Lu W, Zaim H, Abraham S, Noegel A a, Gotzmann J, Foisner R & Karakesisoglou I (2005). The inner nuclear membrane protein Sun1 mediates the anchorage of Nesprin-2 to the nuclear envelope. *J Cell Sci* **118,** 3419–3430.

Pallafacchina G, Blaauw B & Schiaffino S (2013). Role of satellite cells in muscle growth and maintenance of muscle mass. *Nutr Metab Cardiovasc Dis* **23 Suppl 1,** S12-8.

Pallafacchina G, François S, Regnault B, Czarny B, Dive V, Cumano A, Montarras D & Buckingham M (2010). An adult tissue-specific stem cell in its niche: a gene profiling analysis of in vivo quiescent and activated muscle satellite cells. *Stem Cell Res* **4,** 77–91.

Pan C, Cai R, Quacquarelli FP, Ghasemigharagoz A, Lourbopoulos A, Matryba P, Plesnila N, Dichgans M, Hellal F & Ertürk A (2016). Shrinkage-mediated imaging of entire organs and organisms using uDISCO. *Nat Methods* **13,** 859–867.

Panciera T, Azzolin L, Cordenonsi M & Piccolo S (2017). Mechanobiology of YAP and TAZ in physiology and disease. *Nat Rev Mol Cell Biol* **18,** 758–770.

Parise G & Yarasheski KE (2000). The utility of resistance exercise training and amino acid supplementation for reversing age-associated decrements in muscle protein mass and function. *Curr Opin Clin Nutr Metab Care* **3,** 489–495.

Patel TJ & Lieber RL (1997). Force transmission in skeletal muscle: from actomyosin to external tendons. *Exerc Sport Sci Rev* **25,** 321–363.

Pavlath GK, Rich K, Webster SG & Blau HM (1989). Localization of muscle gene products in nuclear domains. *Nature* **337,** 570–573.

Peachey LD (1965). The sarcoplasmic reticulum and transverse tubules of the frog's sartorius. *J Cell Biol* **25,** Suppl:209-31.

Pearson SJ, Young A, Macaluso A, Devito G, Nimmo MA, Cobbold M & Harridge SDR (2002). Muscle function in elite master weightlifters. *Med Sci Sports Exerc* **34,** 1199–1206.

Pendás AM, Zhou Z, Cadiñanos J, Freije JMP, Wang J, Hultenby K, Astudillo A, Wernerson A, Rodríguez F, Tryggvason K & López-Otín C (2002). Defective prelamin A processing and muscular and adipocyte alterations in Zmpste24 metalloproteinase-deficient mice. *Nat Genet* **31,** 94–99.

Petrella JK, Kim J, Cross JM, Kosek DJ & Bamman MM (2006). Efficacy of myonuclear addition may explain differential myofiber growth among resistance-trained young and older men and women. *Am J Physiol Metab* **291,** E937–E946.

Phillip JM, Aifuwa I, Walston J & Wirtz D (2015). The Mechanobiology of Aging. *Annu Rev Biomed Eng* **17,** 113–141.

Piazzesi G, Reconditi M, Linari M, Lucii L, Bianco P, Brunello E, Decostre V, Stewart A, Gore DB, Irving TC, Irving M & Lombardi V (2007). Skeletal muscle performance determined by modulation of number of myosin motors rather than motor force or stroke size. *Cell* **131,** 784–795.

Piazzesi G, Reconditi M, Linari M, Lucii L, Sun Y-B, Narayanan T, Boesecke P, Lombardi V & Irving M (2002). Mechanism of force generation by myosin heads in skeletal muscle. *Nature* **415,** 659–662.

Piekarowicz K, Machowska M, Dzianisava V & Rzepecki R (2019). Hutchinson-Gilford Progeria Syndrome-Current Status and Prospects for Gene Therapy Treatment. *Cells* **8,** 88.

Place N et al. (2015). Ryanodine receptor fragmentation and sarcoplasmic reticulum Ca 2+ leak after one session of high-intensity interval exercise. *Proc Natl Acad Sci*201507176.

Pollock RD, Carter S, Velloso CP, Duggal NA, Lord JM, Lazarus NR & Harridge SDR (2015). An investigation into the relationship between age and physiological function in highly active older adults. *J Physiol* **593,** 657–680.

Pollock RD, Duggal NA, Lazarus NR, Lord JM & Harridge SDR (2018*a*). Cardiorespiratory fitness not sedentary time or physical activity is associated with cardiometabolic risk in active older adults. *Scand J Med Sci Sports* **28,** 1653–1660.

Pollock RD, O'Brien KA, Daniels LJ, Nielsen KB, Rowlerson A, Duggal NA, Lazarus NR, Lord JM, Philp A & Harridge SDR (2018*b*). Properties of the vastus lateralis muscle in relation to age and physiological function in master cyclists aged 55-79 years. *Aging Cell* **17,** e12735.

Powell KE, Paluch AE & Blair SN (2011). Physical activity for health: What kind? How much? How intense? On top of what? *Annu Rev Public Health* **32,** 349–365.

Power GA, Dalton BH, Behm DG, Vandervoort AA, Doherty TJ & Rice CL (2010). Motor unit number estimates in masters runners: use it or lose it? *Med Sci Sports Exerc* **42,** 1644–1650.

Power GA, Dalton BH & Rice CL (2013). Human neuromuscular structure and function in old age: A brief review. *J Sport Heal Sci* **2,** 215–226.

Puckelwartz MJ, Kessler E, Zhang Y, Hodzic D, Randles KN, Morris G, Earley JU, Hadhazy M, Holaska JM, Mewborn SK, Pytel P & McNally EM (2009). Disruption of nesprin-1 produces an Emery Dreifuss muscular dystrophy-like phenotype in mice. *Hum Mol Genet* **18,** 607–620.

Qaisar R & Larsson L (2014). What determines myonuclear domain size? *Indian J Physiol Pharmacol* **58,** 1–12.

Qaisar R, Renaud G, Hedstrom Y, Pöllänen E, Ronkainen P, Kaprio J, Alen M, Sipilä S, Artemenko K, Bergquist J, Kovanen V & Larsson L (2013). Hormone replacement therapy improves contractile function and myonuclear organization of single muscle fibres from postmenopausal monozygotic female twin pairs. *J Physiol* **591,** 2333–2344.

Qaisar R, Renaud G, Morine K, Barton ER, Sweeney HL & Larsson L (2012). Is functional hypertrophy and specific force coupled with the addition of myonuclei at the single muscle fiber level? *FASEB J* **26,** 1077–1085.

Quigley A, Dong YY, Pike ACW, Dong L, Shrestha L, Berridge G, Stansfeld PJ, Sansom MSP, Edwards AM, Bountra C, von Delft F, Bullock AN, Burgess-Brown NA & Carpenter EP (2013). The structural basis of ZMPSTE24-dependent laminopathies. *Science* **339,** 1604–1607.

Raab M, Gentili M, de Belly H, Thiam HR, Vargas P, Jimenez AJ, Lautenschlaeger F, Voituriez R, Lennon-Duménil AM, Manel N & Piel M (2016). ESCRT III repairs nuclear envelope ruptures during cell migration to limit DNA damage and cell death. *Science* **352,** 359–362.

Raffaello A, Milan G, Masiero E, Carnio S, Lee D, Lanfranchi G, Goldberg AL & Sandri M (2010). JunB transcription factor maintains skeletal muscle mass and promotes hypertrophy. *J Cell Biol* **191,** 101–113.

Ragnauth CD, Warren DT, Liu Y, McNair R, Tajsic T, Figg N, Shroff R, Skepper J & Shanahan CM (2010). Prelamin a acts to accelerate smooth muscle cell senescence and is a novel biomarker of human vascular aging. *Circulation* **121,** 2200–2210.

Rajgor D, Mellad J a., Autore F, Zhang Q & Shanahan CM (2012). Multiple novel nesprin-1 and nesprin-2 variants act as versatile tissue-specific intracellular scaffolds. *PLoS One*; DOI: 10.1371/journal.pone.0040098.

Ralston E & Hall ZW (1989*a*). Intracellular and surface distribution of a membrane protein (CD8) derived from a single nucleus in multinucleated myotubes. *J Cell Biol* **109,** 2345–2352.

Ralston E & Hall ZW (1989*b*). Transfer of a protein encoded by a single nucleus to nearby nuclei in multinucleated myotubes. *Science (80-)* **244,** 1066–1069.

Ralston E & Hall ZW (1992). Restricted distribution of mRNA produced from a single nucleus in hybrid myotubes. *J Cell Biol* **119,** 1063–1068.

Ramamurthy B, Höök P, Jones AD & Larsson L (2001). Changes in myosin structure and function in response to glycation. *FASEB J* **15,** 2415–2422.

Ramos-Vara JA & Miller MA (2014). When Tissue Antigens and Antibodies Get Along: Revisiting the Technical Aspects of Immunohistochemistry-The Red, Brown, and Blue Technique. *Vet Pathol* **51,** 42–87.

Relaix F & Zammit PS (2012). Satellite cells are essential for skeletal muscle regeneration: the cell on the edge returns centre stage. *Development* **139,** 2845–2856.

Richardson DS & Lichtman JW (2015). Clarifying Tissue Clearing. *Cell* **162,** 246–257.

Richmond E & Rogol AD (2016). Treatment of growth hormone deficiency in children, adolescents and at the transitional age. *Best Pract Res Clin Endocrinol Metab* **30,** 749–755.

Risson V et al. (2009). Muscle inactivation of mTOR causes metabolic and dystrophin defects leading to severe myopathy. *J Cell Biol* **187,** 859–874.

Rittweger J, di Prampero PE, Maffulli N & Narici M V. (2009). Sprint and endurance power and ageing: an analysis of master athletic world records. *Proceedings Biol Sci* **276,** 683–689.

Robijns J, Molenberghs F, Sieprath T, Corne TDJ, Verschuuren M & De Vos WH (2016). In silico synchronization reveals regulators of nuclear ruptures in lamin A/C deficient model cells. *Sci Rep* **6,** 30325.

Robson MI, de Las Heras JI, Czapiewski R, Lê Thành P, Booth DG, Kelly DA, Webb S, Kerr ARW & Schirmer EC (2016). Tissue-Specific Gene Repositioning by Muscle Nuclear Membrane Proteins Enhances Repression of Critical Developmental Genes during Myogenesis. *Mol Cell* **62,** 834–847.

Rodriguez S, Coppedè F, Sagelius H & Eriksson M (2009). Increased expression of the Hutchinson-Gilford progeria syndrome truncated lamin A transcript during cell aging. *Eur J Hum Genet* **17,** 928–937.

Roman W, Martins JP, Carvalho FA, Voituriez R, Abella JVG, Santos NC, Cadot B, Way M & Gomes ER (2017). Myofibril contraction and crosslinking drive nuclear movement to the periphery of skeletal muscle. *Nat Cell Biol* **19,** 1189–1201.

Roman W, Martins JP & Gomes ER (2018). Local Arrangement of Fibronectin by Myofibroblasts Governs Peripheral Nuclear Positioning in Muscle Cells. *Dev Cell*1–10.

Rosenblatt JD, Lunt AI, Parry DJ & Partridge TA (1995). Culturing satellite cells from living single muscle fiber explants. *In Vitro Cell Dev Biol Anim* **31,** 773–779.

Ross JA, Levy Y, Lawlor MW & Ochala J (2017*a*). Myostatin Inhibition as a Therapeutic Strategy for Skeletal Muscle Myopathies–Effects on Nuclear Organisation. *FASEB J* **31,** 1022.19-1022.19.

Ross JA, Levy Y, Svensson K, Philp A, Schenk S & Ochala J (2018). SIRT1 regulates nuclear number and domain size in skeletal muscle fibers. *J Cell Physiol*1–7.

Ross JA, Pearson A, Levy Y, Cardel B, Handschin C & Ochala J (2017*b*). Exploring the Role of PGC-1α in Defining Nuclear Organisation in Skeletal Muscle Fibres. *J Cell Physiol* **232,** 1270–1274.

Ross ST, Allen JR & Davidson MW (2014). Practical considerations of objective lenses for application in cell biology. In *Methods in Cell Biology*, 1st edn., pp. 19–34. Elsevier Inc. Available at: http://dx.doi.org/10.1016/B978-0-12-420138-5.00002-1.

Roth SM, Martel GF & Rogers M a (2000). Muscle biopsy and muscle fiber hypercontraction: a brief review. *Eur J Appl Physiol* **83,** 239–245.

Roy RR, Monke SR, Allen DL & Edgerton VR (1999). Modulation of myonuclear number in functionally overloaded and exercised rat plantaris fibers. *J Appl Physiol* **87,** 634–642.

Rueden CT, Schindelin J, Hiner MC, DeZonia BE, Walter AE, Arena ET & Eliceiri KW (2017). ImageJ2: ImageJ for the next generation of scientific image data. *BMC Bioinformatics* **18,** 529.

Rui Y, Bai J & Perrimon N (2010). Sarcomere formation occurs by the assembly of multiple latent protein complexes. *PLoS Genet*; DOI: 10.1371/journal.pgen.1001208.

Rumbaugh G & Miller CA (2011). Epigenetic changes in the brain: measuring global histone modifications. *Methods Mol Biol* **670,** 263–274.

Salamon M, Millino C, Raffaello A, Mongillo M, Sandri C, Bean C, Negrisolo E, Pallavicini A, Valle G, Zaccolo M, Schiaffino S & Lanfranchi G (2003). Human MYO18B, a Novel Unconventional Myosin Heavy Chain Expressed in Striated Muscles Moves into the Myonuclei upon Differentiation. *J Mol Biol* **326,** 137–149.

Salmon ED, Shaw SL, Waters JC, Waterman-Storer CM, Maddox PS, Yeh E & Bloom K (2013). A high-resolution multimode digital microscope system. In *Methods in Cell Biology*, 4th edn., pp. 179–210. Elsevier Inc. Available at: http://dx.doi.org/10.1016/B978-0-12-407761-4.00009-9.

De Sandre-Giovannoli A, Bernard R, Cau P, Navarro C, Amiel J, Boccaccio I, Lyonnet S, Stewart CL, Munnich A, Le Merrer M & Lévy N (2003). Lamin a truncation in Hutchinson-Gilford progeria. *Science* **300,** 2055.

Sanes JR, Johnson YR, Kotzbauer PT, Mudd J, Hanley T, Martinou JC & Merlie JP (1991). Selective expression of an acetylcholine receptor-lacZ transgene in synaptic nuclei of adult muscle fibers. *Development* **113,** 1181–1191.

Sanoudou D, Haslett JN, Kho AT, Guo S, Gazda HT, Greenberg SA, Lidov HGW, Kohane IS, Kunkel LM & Beggs AH (2003). Expression profiling reveals altered satellite cell numbers and glycolytic enzyme transcription in nemaline myopathy muscle. *Proc Natl Acad Sci* **100,** 4666–4671.

Sapey E, Greenwood H, Walton G, Mann E, Love A, Aaronson N, Insall RH, Stockley RA & Lord JM (2014). Phosphoinositide 3-kinase inhibition restores neutrophil accuracy in the elderly: toward targeted treatments for immunosenescence. *Blood* **123,** 239–248.

Sartori R, Milan G, Patron M, Mammucari C, Blaauw B, Abraham R & Sandri M (2009). Smad2 and 3 transcription factors control muscle mass in adulthood. *Am J Physiol Cell Physiol* **296,** C1248-57.

Saunders CA, Harris NJ, Willey PT, Woolums BM, Wang Y, McQuown AJ, Schoenhofen A, Worman HJ, Dauer WT, Gundersen GG & Luxton GWG (2017). TorsinA controls TAN line assembly and the retrograde flow of dorsal perinuclear actin cables during rearward nuclear movement. *J Cell Biol* **216,** 657–674.

Sawano S, Komiya Y, Ichitsubo R, Ohkawa Y, Nakamura M, Tatsumi R, Ikeuchi Y & Mizunoya W (2016). A one-step immunostaining method to visualize rodent muscle fiber type within a single specimen. *PLoS One* **11,** 1–19.

Scaffidi P & Misteli T (2006). Lamin A-dependent nuclear defects in human aging. *Science* **312,** 1059–1063.

Scaffidi P & Misteli T (2008). Lamin A-dependent misregulation of adult stem cells associated with accelerated ageing. *Nat Cell Biol* **10,** 452–459.

Scharner J (2008). *Defective adult muscle satellite cells in Zmpste24 deficient mice* (thesis). The University of Hong Kong.

Scharner J & Zammit PS (2011). The muscle satellite cell at 50: the formative years. *Skelet Muscle* **1,** 28.

Schiaffino S, Bormioli SP & Aloisi M (1976). The fate of newly formed satellite cells during compensatory muscle hypertrophy. *Virchows Arch B, Cell Pathol* **21,** 113–118.

Schiaffino S, Dyar K a, Ciciliot S, Blaauw B & Sandri M (2013). Mechanisms regulating skeletal muscle growth and atrophy. *FEBS J* **280,** 4294–4314.

Schiaffino S & Partridge T (2008). *Skeletal Muscle Repair and Regeneration*. Springer Netherlands, Dordrecht. Available at: http://link.springer.com/10.1007/978-1-4020-6768-6 [Accessed December 9, 2014].

Schindelin J, Arganda-Carreras I, Frise E, Kaynig V, Longair M, Pietzsch T, Preibisch S, Rueden C, Saalfeld S, Schmid B, Tinevez J-Y, White DJ, Hartenstein V, Eliceiri K, Tomancak P & Cardona A (2012). Fiji: an open-source platform for biological-image analysis. *Nat Methods* **9,** 676–682.

Schirmer EC & Gerace L (2005). The nuclear membrane proteome: extending the envelope. *Trends Biochem Sci* **30,** 551–558.

Schmalbruch H & Hellhammer U (1976). The number of satellite cells in normal human muscle. *Anat Rec* **185,** 279–287.

Schmalbruch H & Hellhammer U (1977). The number of nuclei in adult rat muscles with special reference to satellite cells. *Anat Rec* **189,** 169–175.

Schreiner SM, Koo PK, Zhao Y, Mochrie SGJ & King MC (2015). The tethering of chromatin to the nuclear envelope supports nuclear mechanics. *Nat Commun* **6,** 7159.

Schwartz C, Fischer M, Mamchaoui K, Bigot A, Lok T, Verdier C, Duperray A, Michel R, Holt I, Voit T, Quijano-Roy S, Bonne G & Coirault C (2017). Lamins and nesprin-1 mediate inside-out mechanical coupling in muscle cell precursors through FHOD1. *Sci Rep* **7,** 1253.

Schwartz LM, Brown C, McLaughlin K, Smith W & Bigelow C (2016). The myonuclear domain is not maintained in skeletal muscle during either atrophy or programmed cell death. *Am J Physiol Cell Physiol* **311,** C607–C615.

Seals DR, Justice JN & LaRocca TJ (2016). Physiological geroscience: targeting function to increase healthspan and achieve optimal longevity. *J Physiol* **594,** 2001–2024.

Seiden D (1976). A quantitative analysis of muscle cell changes in compensatory hypertrophy and work-induced hypertrophy. *Am J Anat* **145,** 459–465.

Serebryannyy L & Misteli T (2018). Protein sequestration at the nuclear periphery as a potential regulatory mechanism in premature aging. *J Cell Biol* **217,** 21–37.

Shackleton S, Smallwood DT, Clayton P, Wilson LC, Agarwal a K, Garg A & Trembath RC (2005). *Compound heterozygous ZMPSTE24 mutations reduce prelamin A processing and result in a severe progeroid phenotype.*

Shafiq SA & Gorycki MA (1965). Regeneration in skeletal muscle of mouse: Some electron-microscope observations. *J Pathol Bacteriol* **90,** 123–127.

Shafiq SA, Gorycki MA & Mauro A (1968). Mitosis during postnatal growth in skeletal and cardiac muscle of the rat. *J Anat* **103,** 135–141.

Shafiq SA, Gorycki MA & Milhorat AT (1967). An electron microscopic study of regeneration and satellite cells in human muscle. *Neurology* **17,** 567–567.

Shah SB, Davis J, Weisleder N, Kostavassili I, McCulloch AD, Ralston E, Capetanaki Y & Lieber RL (2004). Structural and functional roles of desmin in mouse skeletal muscle during passive deformation. *Biophys J* **86,** 2993–3008.

Shah SB & Lieber RL (2003). Simultaneous imaging and functional assessment of cytoskeletal protein connections in passively loaded single muscle cells. *J Histochem Cytochem* **51,** 19–29.

Shevchenko A, Tomas H, Havlis J, Olsen J V. & Mann M (2006). In-gel digestion for mass spectrometric characterization of proteins and proteomes. *Nat Protoc* **1,** 2856–2860.

Shimi T, Kittisopikul M, Tran J, Goldman AE, Adam SA, Zheng Y, Jaqaman K & Goldman RD (2015). Structural organization of nuclear lamins A, C, B1, and B2 revealed by superresolution microscopy. *Mol Biol Cell* **26,** 4075–4086.

Shimi T, Pfleghaar K, Kojima SI, Pack CG, Solovei I, Goldman AE, Adam SA, Shumaker DK, Kinjo M, Cremer T & Goldman RD (2008). The A- and B-type nuclear lamin networks: Microdomains involved in chromatin organization and transcription. *Genes Dev* **22,** 3409–3421.

Shtengel G, Wang Y, Zhang Z, Goh WI, Hess HF & Kanchanawong P (2014). Imaging cellular ultrastructure by PALM, iPALM, and correlative iPALM-EM. In *Methods in Cell Biology*, 1st edn., pp. 273–294. Elsevier Inc. Available at: http://dx.doi.org/10.1016/B978-0-12-420138-5.00015-X.

Shumaker DK, Dechat T, Kohlmaier A, Adam SA, Bozovsky MR, Erdos MR, Eriksson M, Goldman AE, Khuon S, Collins FS, Jenuwein T & Goldman RD (2006). Mutant nuclear lamin A leads to progressive alterations of epigenetic control in premature aging. *Proc Natl Acad Sci U S A* **103,** 8703–8708.

Sieck GC, Fournier M, Prakash YS & Blanco CE (1996). Myosin phenotype and SDH enzyme variability among motor unit fibers. *J Appl Physiol* **80,** 2179–2189.

Sieprath T, Corne TD, Nooteboom M, Grootaert C, Rajkovic A, Buysschaert B, Robijns J, Broers JL, Ramaekers FC, Koopman WJ, Willems PH & De Vos WH (2015). Sustained accumulation of prelamin A and depletion of lamin A/C both cause oxidative stress and mitochondrial dysfunction but induce different cell fates. *Nucleus* **6,** 236–246.

Sieprath T, Darwiche R & De Vos WH (2012). Lamins as mediators of oxidative stress. *Biochem Biophys Res Commun* **421,** 635–639.

Snider NT & Omary MB (2014). Post-translational modifications of intermediate filament proteins: mechanisms and functions. *Nat Rev Mol Cell Biol* **15,** 163–177.

Snijders T, Smeets JSJ, van Kranenburg J, Kies AK, van Loon LJC & Verdijk LB (2016). Changes in myonuclear domain size do not precede muscle hypertrophy during prolonged resistance-type exercise training. *Acta Physiol (Oxf)* **216,** 231–239.

Snijders T, Verdijk LB & van Loon LJC (2009). The impact of sarcopenia and exercise training on skeletal muscle satellite cells. *Ageing Res Rev* **8,** 328–338.

Solovei I, Wang AS, Thanisch K, Schmidt CS, Krebs S, Zwerger M, Cohen T V., Devys D, Foisner R, Peichl L, Herrmann H, Blum H, Engelkamp D, Stewart CL, Leonhardt H & Joffe B (2013). LBR and lamin A/C sequentially tether peripheral heterochromatin and inversely regulate differentiation. *Cell* **152,** 584–598.

Song M, Lavasani M, Thompson SD, Lu A, Ahani B & Huard J (2013). Muscle-derived stem/progenitor cell dysfunction in Zmpste24-deficient progeroid mice limits muscle regeneration. *Stem Cell Res Ther* **4,** 33.

Soria-Valles C et al. (2016). Novel LMNA mutations cause an aggressive atypical neonatal progeria without progerin accumulation. *J Med Genet* **53,** 776–785.

Spear ED, Hsu E-T, Nie L, Carpenter EP, Hrycyna CA & Michaelis S (2018). ZMPSTE24 missense mutations that cause progeroid diseases decrease prelamin A cleavage activity and/or protein stability. *Dis Model Mech* **11,** dmm033670.

Sprott H, Salemi S, Gay RE, Bradley LA, Alarcón GS, Oh SJ, Michel BA & Gay S (2004). Increased DNA fragmentation and ultrastructural changes in fibromyalgic muscle fibres. *Ann Rheum Dis* **63,** 245–251.

Stålberg E (1979). Single fibre electromyography. *Trends Neurosci*; DOI: 10.1016/0166-2236(79)90075-4.

Staszewska I, Fischer I & Wiche G (2015). Plectin isoform 1-dependent nuclear docking of desmin networks affects myonuclear architecture and expression of mechanotransducers. *Hum Mol Genet* **1,** 1–53.

van Steensel B & Belmont AS (2017). Lamina-Associated Domains: Links with Chromosome Architecture, Heterochromatin, and Gene Repression. *Cell* **169,** 780–791.

Stephens AD, Banigan EJ, Adam SA, Goldman RD & Marko JF (2017). Chromatin and lamin A determine two different mechanical response regimes of the cell nucleus. *Mol Biol Cell* **28,** 1984–1996.

Stickland NC, Widdowson EM & Goldspink G (1975). Effects of severe energy and protein deficiencies on the fibres and nuclei in skeletal muscle of pigs. *Br J Nutr* **34,** 421–428.

Stienen GJM (2000). Chronicle of skinned muscle fibres. *J Physiol* **527 Pt 1,** 1.

Stroud MJ, Feng W, Zhang J, Veevers J, Fang X, Gerace L & Chen J (2017). Nesprin 1α2 is essential for mouse postnatal viability and nuclear positioning in skeletal muscle. *J Cell Biol* **216,** 1915–1924.

Sun C, De Mello V, Mohamed A, Ortuste Quiroga HP, Garcia-Munoz A, Al Bloshi A, Tremblay AM, von Kriegsheim A, Collie-Duguid E, Vargesson N, Matallanas D, Wackerhage H & Zammit PS (2017). Common and Distinctive Functions of the Hippo Effectors Taz and Yap in Skeletal Muscle Stem Cell Function. *Stem Cells* **35,** 1958–1972.

Swedlow JR (2013). Quantitative fluorescence microscopy and image deconvolution. In *Methods in Cell Biology*, 4th edn., pp. 407–426. Elsevier Inc. Available at: http://dx.doi.org/10.1016/B978-0-12-407761-4.00017-8.

Swift J, Ivanovska IL, Buxboim A, Harada T, Dingal PCDP, Pinter J, Pajerowski JD, Spinler KR, Shin J-W, Tewari M, Rehfeldt F, Speicher DW & Discher DE (2013). Nuclear Lamin-A Scales with Tissue Stiffness and Enhances Matrix-Directed Differentiation. *Science (80-)* **341,** 1240104–1240104.

Tajik A, Zhang Y, Wei F, Sun J, Jia Q, Zhou W, Singh R, Khanna N, Belmont AS & Wang N (2016). Transcription upregulation via force-induced direct stretching of chromatin. *Nat Mater* **15,** 1–20.

Tatsumi R, Sheehan SM, Iwasaki H, Hattori A & Allen RE (2001). Mechanical stretch induces activation of skeletal muscle satellite cells in vitro. *Exp Cell Res* **267,** 107–114.

Theer P, Hasan MT & Denk W (2003). Two-photon imaging to a depth of 1000 microm in living brains by use of a Ti:Al2O3 regenerative amplifier. *Opt Lett* **28,** 1022–1024.

Therizols P, Illingworth RS, Courilleau C, Boyle S, Wood AJ & Bickmore WA (2014). Chromatin decondensation is sufficient to alter nuclear organization in embryonic stem cells. *Science* **346,** 1238–1242.

Thiam H-R, Vargas P, Carpi N, Crespo CL, Raab M, Terriac E, King MC, Jacobelli J, Alberts AS, Stradal T, Lennon-Dumenil A-M & Piel M (2016). Perinuclear Arp2/3-driven actin polymerization enables nuclear deformation to facilitate cell migration through complex environments. *Nat Commun* **7,** 10997.

Tidball JG (1991). Myotendinous junction injury in relation to junction structure and molecular composition. *Exerc Sport Sci Rev* **19,** 419–445.

Tokumasu F & Dvorak J (2003). Development and application of quantum dots for immunocytochemistry of human erythrocytes. *J Microsc* **211,** 256–261.

Toth JI, Yang SH, Qiao X, Beigneux AP, Gelb MH, Moulson CL, Miner JH, Young SG & Fong LG (2005). Blocking protein farnesyltransferase improves nuclear shape in fibroblasts from humans with progeroid syndromes. *Proc Natl Acad Sci U S A* **102,** 12873–12878.

Turgay Y, Eibauer M, Goldman AE, Shimi T, Khayat M, Ben-Harush K, Dubrovsky-Gaupp A, Sapra KT, Goldman RD & Medalia O (2017). The molecular architecture of lamins in somatic cells. *Nature* **543,** 261–264.

Uhler C & Shivashankar G V. (2017). Chromosome Intermingling: Mechanical Hotspots for Genome Regulation. *Trends Cell Biol* **27,** 810–819.

Ungricht R & Kutay U (2017). Mechanisms and functions of nuclear envelope remodelling. *Nat Rev Mol Cell Biol* **18,** 229–245.

Varela I, Cadiñanos J, Pendás AM, Gutiérrez-Fernández A, Folgueras AR, Sánchez LM, Zhou Z, Rodríguez FJ, Stewart CL, Vega J a, Tryggvason K, Freije JMP & López-Otín C (2005). Accelerated ageing in mice deficient in Zmpste24 protease is linked to p53 signalling activation. *Nature* **437,** 564–568.

Verheul a J, Mantilla CB, Zhan W-Z, Bernal M, Dekhuijzen PNR & Sieck GC (2004). Influence of corticosteroids on myonuclear domain size in the rat diaphragm muscle. *J Appl Physiol* **97,** 1715–1722.

Verstraeten VLRM, Broers JLV, van Steensel MAM, Zinn-Justin S, Ramaekers FCS, Steijlen PM, Kamps M, Kuijpers HJH, Merckx D, Smeets HJM, Hennekam RCM, Marcelis CLM & van den Wijngaard A (2006). Compound heterozygosity for mutations in LMNA causes a progeria syndrome without prelamin A accumulation. *Hum Mol Genet* **15,** 2509–2522.

Verstraeten VLRM, Ji JY, Cummings KS, Lee RT & Lammerding J (2008). Increased mechanosensitivity and nuclear stiffness in Hutchinson-Gilford progeria cells: Effects of farnesyltransferase inhibitors. *Aging Cell* **7,** 383–393.

Vidak S & Foisner R (2016). Molecular insights into the premature aging disease progeria. *Histochem Cell Biol* **145,** 401–417.

Viegas MS, Martins TC, Seco F & do Carmo A (2007). An improved and cost-effective methodology for the reduction of autofluorescence in direct immunofluorescence studies on formalin-fixed paraffin-embedded tissues. *Eur J Histochem* **51,** 59–66.

Viguie CA, Lu DX, Huang SK, Rengen H & Carlson BM (1997). Quantitative study of the effects of long-term denervation on the extensor digitorum longus muscle of the rat. *Anat Rec* **248,** 346–354.

Volk T (2013). Positioning nuclei within the cytoplasm of striated muscle fiber: cooperation between microtubules and KASH proteins. *Nucleus* **4,** 18–22.

De Vos WH, Houben F, Kamps M, Malhas A, Verheyen F, Cox J, Manders EMM, Verstraeten VLRM, van Steensel MAM, Marcelis CLM, van den Wijngaard A, Vaux DJ, Ramaekers FCS & Broers JL V (2011). Repetitive disruptions of the nuclear envelope invoke temporary loss of cellular compartmentalization in laminopathies. *Hum Mol Genet* **20,** 4175–4186.

De Vos WH, Van Neste L, Dieriks B, Joss GH & Van Oostveldt P (2010). High content image cytometry in the context of subnuclear organization. *Cytometry A* **77,** 64–75.

Wada K-I, Takahashi H, Katsuta S & Soya H (2002). No decrease in myonuclear number after long-term denervation in mature mice. *Am J Physiol Cell Physiol* **283,** C484-8.

Wallgren-Pettersson C, Rapola J & Donner M (1988). Pathology of congenital nemaline myopathy. *J Neurol Sci* **83,** 243–257.

Wang N, Tytell JD & Ingber DE (2009). Mechanotransduction at a distance: mechanically coupling the extracellular matrix with the nucleus. *Nat Rev Mol Cell Biol* **10,** 75–82.

Wang S, Stoops E, Cp U, Markus B, Reuveny A, Ordan E & Volk T (2018). Mechanotransduction via the LINC complex regulates DNA replication in myonuclei. *J Cell Biol*jcb.201708137.

Wang Y, Lichter-Konecki U, Anyane-Yeboa K, Shaw JE, Lu JT, Östlund C, Shin J-Y, Clark LN, Gundersen GG, Nagy PL & Worman HJ (2016). A mutation abolishing the ZMPSTE24 cleavage site in prelamin A causes a progeroid disorder. *J Cell Sci* **129,** 1975–1980.

Wang Y, Ostlund C, Choi JC, Swayne TC, Gundersen GG & Worman HJ (2012). Blocking farnesylation of the prelamin A variant in Hutchinson-Gilford progeria syndrome alters the distribution of A-type lamins. *Nucleus* **3,** 452–462.

Wang Z, Cui J, Wong WM, Li X, Xue W, Lin R, Wang J, Wang P, Tanner JA, Cheah KSE, Wu W & Huang J-D (2013). Kif5b controls the localization of myofibril components for their assembly and linkage to the myotendinous junctions. *Development* **140,** 617–626.

Waters JC (2009). Accuracy and precision in quantitative fluorescence microscopy. *J Cell Biol* **185,** 1135–1148.

Waters JC (2013). Live-cell fluorescence imaging. In *Methods in Cell Biology*, 4th edn., pp. 125–150. Elsevier Inc. Available at: http://dx.doi.org/10.1016/B978-0-12-407761-4.00006-3.

Waters JC & Wittmann T (2014). Concepts in quantitative fluorescence microscopy. In *Methods in Cell Biology*, 1st edn., pp. 1–18. Elsevier Inc. Available at: http://dx.doi.org/10.1016/B978-0-12-420138-5.00001-X.

Watt KI, Turner BJ, Hagg A, Zhang X, Davey JR, Qian H, Beyer C, Winbanks CE, Harvey KF & Gregorevic P (2015). The Hippo pathway effector YAP is a critical regulator of skeletal muscle fibre size. *Nat Commun* **6,** 6048.

Welle S, Bhatt K, Pinkert CA, Tawil R & Thornton CA (2007). Muscle growth after postdevelopmental myostatin gene knockout. *Am J Physiol Endocrinol Metab* **292,** E985-91.

White RB, Biérinx A-S, Gnocchi VF & Zammit PS (2010). Dynamics of muscle fibre growth during postnatal mouse development. *BMC Dev Biol* **10,** 21.

Wilhelmsen K, Litjens SHM, Kuikman I, Tshimbalanga N, Janssen H, Van Bout I Den, Raymond K & Sonnenberg A (2005). Nesprin-3, a novel outer nuclear membrane protein, associates with the cytoskeletal linker protein plectin. *J Cell Biol* **171,** 799–810.

Wilkie GS, Korfali N, Swanson SK, Malik P, Srsen V, Batrakou DG, de las Heras J, Zuleger N, Kerr ARW, Florens L & Schirmer EC (2011). Several novel nuclear envelope transmembrane proteins identified in skeletal muscle have cytoskeletal associations. *Mol Cell Proteomics* **10,** M110.003129.

Wilson MH & Holzbaur ELF (2015). Nesprins anchor kinesin-1 motors to the nucleus to drive nuclear distribution in muscle cells. *Development* **142,** 218–228.

Winchester PK & Gonyea WJ (1992). A quantitative study of satellite cells and myonuclei in stretched avian slow tonic muscle. *Anat Rec* **232,** 369–377.

Winegard KJ, Hicks AL, Sale DG & Vandervoort AA (1996). A 12-year follow-up study of ankle muscle function in older adults. *J Gerontol A Biol Sci Med Sci* **51,** B202-7.

Winje IM, Bengtsen M, Eftestøl E, Juvkam I, Bruusgaard JC & Gundersen K (2018). Specific labelling of myonuclei by an antibody against pericentriolar material 1 on skeletal muscle tissue sections. *Acta Physiol*; DOI: 10.1111/apha.13034.

Wolf DE (2013). Fundamentals of fluorescence and fluorescence microscopy. In *Methods in Cell Biology*, 4th edn., pp. 69–97. Elsevier Inc. Available at: http://dx.doi.org/10.1016/B978-0-12-407761-4.00004-X.

Wood DS, Zollman J, Reuben JP & Brandt PW (1975). Human skeletal muscle: properties of the "chemically skinned" fiber. *Science* **187,** 1075–1076.

Worman HJ (2012). Nuclear lamins and laminopathies. *J Pathol* **226,** 316–325.

Worman HJ & Michaelis S (2018). Permanently Farnesylated Prelamin A, Progeria, and Atherosclerosis. *Circulation* **138,** 283–286.

Wozniak AC, Kong J, Bock E, Pilipowicz O & Anderson JE (2005). Signaling satellite-cell activation in skeletal muscle: Markers, models, stretch, and potential alternate pathways. *Muscle and Nerve* **31,** 283–300.

Wu W, Muchir A, Shan J, Bonne G & Worman HJ (2011). Mitogen-Activated Protein Kinase Inhibitors Improve Heart Function and Prevent Fibrosis in Cardiomyopathy Caused by Mutation in Lamin A/C Gene. *Circulation* **123,** 53–61.

Wydner KL, McNeil JA, Lin F, Worman HJ & Lawrence JB (1996). Chromosomal assignment of human nuclear envelope protein genes LMNA, LMNB1, and LBR by fluorescence in situ hybridization. *Genomics* **32,** 474–478.

Xie W, Chojnowski A, Boudier T, Lim JSY, Ahmed S, Ser Z, Stewart C & Burke B (2016). A-type Lamins Form Distinct Filamentous Networks with Differential Nuclear Pore Complex Associations. *Curr Biol* **26,** 2651–2658.

Yablonka-Reuveni Z (1995). Development and postnatal regulation of adult myoblasts. *Microsc Res Tech* **30,** 366–380.

Yadav P, Shefelbine SJ & Gutierrez-Farewik EM (2016). Effect of growth plate geometry and growth direction on prediction of proximal femoral morphology. *J Biomech* **49,** 1613–1619.

Yamamoto DL, Csikasz RI, Li Y, Sharma G, Hjort K, Karlsson R & Bengtsson T (2008). Myotube Formation on Micro-patterned Glass: Intracellular Organization and Protein Distribution in C2C12 Skeletal Muscle Cells. *J Histochem Cytochem* **56,** 881–892.

Yamamoto N, Miyazaki H, Shimada M, Nakagawa N, Sawada SS, Nishimuta M, Kimura Y, Kawakami R, Nagayama H, Asai H, Lee I-M, Blair SN & Yoshitake Y (2018). Daily step count and all-cause mortality in a sample of Japanese elderly people: a cohort study. *BMC Public Health* **18,** 540.

Yang SH, Bergo MO, Toth JI, Qiao X, Hu Y, Sandoval S, Meta M, Bendale P, Gelb MH, Young SG & Fong LG (2005). Blocking protein farnesyltransferase improves nuclear blebbing in mouse fibroblasts with a targeted Hutchinson-Gilford progeria syndrome mutation. *Proc Natl Acad Sci U S A* **102,** 10291–10296.

Yang SH, Chang SY, Andres DA, Spielmann HP, Young SG & Fong LG (2010). Assessing the efficacy of protein farnesyltransferase inhibitors in mouse models of progeria. *J Lipid Res* **51,** 400–405.

Yang SH, Chang SY, Ren S, Wang Y, Andres DA, Spielmann HP, Fong LG & Young SG (2011). Absence of progeria-like disease phenotypes in knock-in mice expressing a non-farnesylated version of progerin. *Hum Mol Genet* **20,** 436–444.

Yang SH, Meta M, Qiao X, Frost D, Bauch J, Coffinier C, Majumdar S, Bergo MO, Young SG & Fong LG (2006). A farnesyltransferase inhibitor improves disease phenotypes in mice with a Hutchinson-Gilford progeria syndrome mutation. *J Clin Invest* **116,** 2115–2121.

Yarasheski KE (2003). Exercise, aging, and muscle protein metabolism. *J Gerontol A Biol Sci Med Sci* **58,** M918-22.

Young SG, Fong LG & Michaelis S (2005). Prelamin A, Zmpste24, misshapen cell nuclei, and progeria--new evidence suggesting that protein farnesylation could be important for disease pathogenesis. *J Lipid Res* **46,** 2531–2558.

Young SG, Meta M, Yang SH & Fong LG (2006). Prelamin A farnesylation and progeroid syndromes. *J Biol Chem* **281,** 39741–39745.

Zammit PS, Partridge TA & Yablonka-Reuveni Z (2006). The Skeletal Muscle Satellite Cell: The Stem Cell That Came in From the Cold. *J Histochem Cytochem* **54,** 1177–1191.

Zane L, Sharma V & Misteli T (2014). Common features of chromatin in aging and cancer: cause or coincidence? *Trends Cell Biol* **24,** 686–694.

Zhang J, Felder A, Liu Y, Guo LT, Lange S, Dalton ND, Gu Y, Peterson KL, Mizisin AP, Shelton GD, Lieber RL & Chen J (2009). Nesprin 1 is critical for nuclear positioning and anchorage. *Hum Mol Genet* **19,** 329–341.

Zhang Q, Bethmann C, Worth NF, Davies JD, Wasner C, Feuer A, Ragnauth CD, Yi Q, Mellad J a., Warren DT, Wheeler M a., Ellis J a., Skepper JN, Vorgerd M, Schlotter-Weigel B, Weissberg PL, Roberts RG, Wehnert M & Shanahan CM (2007*a*). Nesprin-1 and -2 are involved in the pathogenesis of Emery Dreifuss muscular dystrophy and are critical for nuclear envelope integrity. *Hum Mol Genet* **16,** 2816–2833.

Zhang Q, Ragnauth CD, Skepper JN, Worth NF, Warren DT, Roberts RG, Weissberg PL, Ellis J a & Shanahan CM (2005). Nesprin-2 is a multi-isomeric protein that binds lamin and emerin at the nuclear envelope and forms a subcellular network in skeletal muscle. *J Cell Sci* **118,** 673–687.

Zhang X, Xu R, Zhu B, Yang X, Ding X, Duan S, Xu T, Zhuang Y & Han M (2007*b*). Syne-1 and Syne-2 play crucial roles in myonuclear anchorage and motor neuron innervation. *Development* **134,** 901–908.

Zhang Y-Q & Sarge KD (2008). Sumoylation regulates lamin A function and is lost in lamin A mutants associated with familial cardiomyopathies. *J Cell Biol* **182,** 35–39.

Zhou C, Li C, Zhou B, Sun H, Koullourou V, Holt I, Puckelwartz MJ, Warren DT, Hayward R, Lin Z, Zhang L, Morris GE, McNally EM, Shackleton S, Rao L, Shanahan CM & Zhang Q (2017). Novel nesprin-1 mutations associated with dilated cardiomyopathy cause nuclear envelope disruption and defects in myogenesis. *Hum Mol Genet* **26,** 2258–2276.

Zhou C, Rao L, Warren DT, Shanahan CM & Zhang Q (2018). Mouse models of nesprin-related diseases. *Biochem Soc Trans*BST20180085.

Zhou Z, Du X, Cai Z, Song X, Zhang H, Mizuno T, Suzuki E, Yee MR, Berezov A, Murali R, Wu S-L, Karger BL, Greene MI & Wang Q (2012). Structure of Sad1-UNC84 homology (SUN) domain defines features of molecular bridge in nuclear envelope. *J Biol Chem* **287,** 5317–5326.

Appendix 1: Nuclear organisation MATLAB script

8.1. Introduction to the MATLAB script

The script below, named NO (Nuclear Organisation), is the original code the author had developed for the derivation of fibre properties and spatial nuclear organisation.

The script is divided into sections, each with a specific purpose, denoted by its heading. Comments have been placed within the script, to enhance accessibility to the code. As the code was copied directly from MATLAB, its layout and colours are in the same format as MATLAB. Colour labelling is summarised in the table below.

The code begins with a brief introduction to the programme, which explains the functions of the programme, the author and the date of last update, in line with common practice. Following the introduction, the programme reads and stores the previously acquired co-ordinates from the Excel file of the specific fibre in a variable termed 'Original_Fibre_File' and computes the structural properties of the fibre, as well as the spatial arrangement of its nuclei. Finally, it writes all the data into the Excel file of the fibre ('Original_Fibre_File'), as well as into a collective data file (named ‘CDFile’ in the script), which summarises the data from all the previously analysed fibres.

Table 8.1: Colour coding in MATLAB

Colour	Definition
Green	Comment
Black	Command
Blue	Selection statement (e.g. “if” statements)
Red	String (i.e. words/sentences)

8.2. MATLAB script – nuclear organisation in single muscle fibres

Introductory comments

```
% NO (Nuclear Organisation) uses co-ordinates in confocal images to
% calculate three dimensional morphometrical parameters of muscle fibres and
% correlates the results with their nuclear organisation.

% Input = co-ordinates (xyz) of a single muscle fibre and its nuclei,
% extracted from stacks of confocal images into Microsoft Excel.

% Output = fibre morphometrical parameters (e.g. diameter, volume etc.) and
% nuclear organisation (e.g. mean near neighbour distance, order score
% etc.).

% Yotam Levy
% yotamlevy@gmail.com

% Last update: 14 March 2018
```

Clear and close everything

```
clear % Clears the Workspace
clc % Clears the Command Window
close all % Closes any open windows
```

Define paths to the Excel files containing co-ordinates from confocal images

```
% Data file of the fibre to be analysed
Original_Fibre_File = fullfile('Fibre File.xlsx');

% Summary file collecting data from all samples (Collective Data File)
CDFile = fullfile('Collective Data File.xlsx');
```

Store and process the 'Collective' sheet from the collective data file (CDFile)

```
% The collective sheet contains pooled data from all fibres

% Read Excel file
Excel_CDFile_Original = xlsread(CDFile, 'Collective', 'A2:AK500');

% Extract the fibres' details from the data (fibre number, calibration etc.)
Excel_CDFile_Details = Excel_CDFile_Original(1:end,1:5);

% Erase the fibres' details and calibration factors from the data
Excel_CDFile_Data = Excel_CDFile_Original(1:end,6:end);

% Find NaNs (non-numbers or empty cells) in the sheet
[row, col] = find(isnan(Excel_CDFile_Data));

% Test whether NaNs should be removed from the sheet to allow processing
if isempty(row) ==0

    Excel_Extra_Size = NaN((max(row) - min(row)), (max(col)));
    Size_Excel_Extra_Size = size(Excel_Extra_Size);
    Excel_CDFile_Data = Excel_CDFile_Data...
        (1:end-((Size_Excel_Extra_Size(1,1)+1)), 1:end);

end

% At this stage the sheet is stored and ready for the addition of the fibre
% to be analysed.
```

Store and process the matrix of nuclear co-ordinates

```
% Read Excel file
nn_xyz = xlsread(Original_Fibre_File, 'Nc xyz', 'C2:K300');

% Test whether the fibre to be analysed had been marked as discarded (i.e
% the sheet is empty)
if nn_xyz == 0,0;
    Excel_CDFile_Data(end+1,:) = 0;
    % Adds a row of zeros at the bottom of the collective sheet to
    % represent the discarded fibre
```

```
    % Need to add NaNs to 'Excel_CDFile_Data'?
    if isempty(row) == 0
        % Evaluates whether NaNs are needed in 'Excel_CDFile_Data' in order
        % to copy the variable into the Excel spreadsheet
        Excel_CDFile_Data = [Excel_CDFile_Data; Excel_Extra_Size];
        Excel_CDFile_Data = [Excel_CDFile_Details Excel_CDFile_Data];

        % Is the first row of the dataset to be copied similar to the
        % original? Used to test the original data had not suffered a bug
        % during processing
        if Excel_CDFile_Data(1, :) == Excel_CDFile_Original(1, :)
            % Add the dataset to the collective Excel spreadsheet
             xlswrite(CDFile, Excel_CDFile_Data, 'Collective', 'A2');
             error(['This fibre has been noted as discarded! '...
                 'Collective Data File has been updated. For details '...
                 'see datasheet of corresponding fibre.']);
        else error(['First row of new dataset does not match first row '...
            'of original dataset! Excel files have not been updated.']);
        end

    else Excel_CDFile_Details(end+1, :) = NaN;
        % Added zeros to 'Excel_CDFile_Data' so must equalise size of
        % matrices
        Excel_CDFile_Data = [Excel_CDFile_Details Excel_CDFile_Data];

        % Is the first row of the dataset to be copied similar to the
        % original?
        if Excel_CDFile_Data(1, :) == Excel_CDFile_Original(1, :)

            % Add the dataset to the collective Excel spreadsheet
             xlswrite(CDFile, Excel_CDFile_Data, 'Collective', 'A2');
             error(['This fibre has been noted as discarded! '...
                 'Collective Data File has been updated. For details '...
                 'see datasheet of corresponding fibre.']);

        else error(['First row of new dataset does not match first row '...
                'of original dataset! Excel files have not been updated.']);
        end
    end
end

% Below only takes place if the fibre had not been discarded. Otherwise,
% the programme stops running at this point.

% Extract the xy calibration factor and bins for DAPI from 'nn_xyz'
DAPI_xy_cal_factor = nn_xyz(1,8);
DAPI_xy_bins = nn_xyz(1,9);

% Remove the DAPI xy calibration factors and bins from 'nn_xyz'
nn_xyz = nn_xyz(1:end,1:3);

% At this stage the matrix of nuclear co-ordinates ('nn_xyz') is stored in
```

```
% a form that allows further processing. It contains nothing but nuclear
% co-ordinates.
```

Nearest neighbour calculations

```
% Euclidean distance matrix of the nuclei
nn_dist_all = sqrt(sum(bsxfun(@minus,permute(nn_xyz,[1 3 2]), ...
    permute(nn_xyz,[3 1 2])).^2,3));

% Locate the self-self distances in the matrix 'nn_dist_all' and define
% them as Inf (infinity)
nn_dist_all(1:length(nn_dist_all)+1:end) = Inf;

% Which nucleus is the closest? Returns the index number of a nucleus
% ('nn') and distance ('nn_dist') to the closest co-ordinate
[nn_dist, nn] = min(nn_dist_all,[],1);

% Calculations of nn distances - mean, std and std/nn ratio
nn_mean = mean(nn_dist);
nn_std = std(nn_dist);
nn_ratio = 100 * (nn_std / nn_mean); % Result should be in %

% Count the total number of nuclei
nn_total_Nc = numel(nn_xyz(:,1));
```

Store and process the matrix of the fibre co-ordinates

```
% Read Excel file
fibre_xyz = xlsread(Original_Fibre_File, 'Fibre xyz', 'C2:E13');

% Extract the sarcomere xy co-ordinates
sarcomere_xy = fibre_xyz(7:8,1:2);

% Extract the calibration factors and bins for Phalloidin and Brightfield
Phalloidin_xy_cal_factor = fibre_xyz(9,1);
BR_xy_cal_factor = fibre_xyz(11,1);
Phalloidin_xy_bins = fibre_xyz(10,1:2);
BR_xy_bins = fibre_xyz(12,1:2);

% Remove the sarcomere co-ordinates, Phalloidin and BR calibration and bins
% from the fibre matrix
fibre_xyz = fibre_xyz(1:6,:);

% At this stage the matrix of fibre co-ordinates ('fibre_xyz') is stored in
% a form that allows further processing. It contains nothing but fibre
% co-ordinates.
```

Muscle fibre calculations

```
% Sarcomere length
% Calculated by measuring the distance between the 1st band and 10th band
% in the fibre and divide the result by 10 to acuqire the average length
    sarcomere_length = (sqrt((sarcomere_xy(1,1) - sarcomere_xy(2,1)) ^2 ...
        + (sarcomere_xy(1,2) - sarcomere_xy(2,2)) ^2)) / 10;

% Axes of the fibre
% Calculate the Euclidean distance between all the co-ordinates in the
% fibre matrix. Length of axes is then found within the resulting
% matrix
fibre_dist_all = sqrt(sum(bsxfun(@minus,permute(fibre_xyz,[1 3 2]), ...
    permute(fibre_xyz,[3 1 2])).^2,3));

% Fibre length (y dimension in the original confocal image)
fibre_length = ((fibre_dist_all(1,3) + fibre_dist_all(2,4)) / 2);

% Fibre diameter and radius (x dimension)
fibre_diameter = ((fibre_dist_all(1,2) + fibre_dist_all(3,4)) / 2);
fibre_radius = fibre_diameter/2;

% Fibre depth (z dimension)
fibre_xyz_max_z = max(fibre_xyz(:,3)); % Highest z coordinate in the z column
fibre_xyz_min_z = min(fibre_xyz(:,3));% Lowest z coordinate in the z column
fibre_depth = fibre_xyz_max_z - fibre_xyz_min_z;

% Test whether all the nuclei are located inside the fibre. If not,
% correct fibre depth accordingly.
nn_xyz_max_z = max(nn_xyz(:,3)); % Highest nucleus in the z column
nn_xyz_min_z = min(nn_xyz(:,3)); % Lowest nucleus in the z column

if  fibre_depth < ((nn_xyz_max_z - nn_xyz_min_z) + 3)
    fibre_depth = (nn_xyz_max_z - nn_xyz_min_z) + 3;
    warning(['Measured fibre depth (%d µm) is smaller than top-bottom '...
        'nuclei distance +3 µm (%d µm). '...
        'Result has been converted accordingly.'], ...
        fibre_xyz_max_z - fibre_xyz_min_z, fibre_depth)
end

% Fibre cross sectional area (CSA)
fibre_CSA = pi * (0.5 * fibre_diameter) * (0.5 * fibre_depth);
% Uses the formula for area of an ellipse, A = pi*ab, where a =
% semi-major axis, b = semi-minor axis

% Fibre volume
fibre_volume = fibre_CSA * fibre_length;
fibre_volume_adj = fibre_volume * 1e-4;
% Result should be in µm3 x 1e+4

% Fibre circumference
h = (fibre_diameter - fibre_depth)^2 / (fibre_diameter + fibre_depth)^2;
fibre_circ = pi * (fibre_diameter + fibre_depth) * ...
    (1 + (3 * h) / (10 + sqrt(4 - 3 * h)));
```

```
% Fibre surface area
fibre_SA = fibre_circ * fibre_length;
fibre_SA_adj = fibre_SA * 1e-2;
% Result should be in µm2 x 1e+2

% At this stage, all nuclear and fibre calculations have been completed.
% Correlations between them can commence.
```

Correlations between the fibre and its nuclei

```
% nn mean distances with fibre volume
nn_mean_per_fibre_volume = nn_mean / fibre_volume;
nn_mean_per_fibre_volume_adj = nn_mean_per_fibre_volume * 1e+5;
% Result should be in µm-2 x 1e-5

% nn mean distances with fibre CSA
nn_mean_per_fibre_CSA = nn_mean / fibre_CSA;
nn_mean_per_fibre_CSA_adj = nn_mean_per_fibre_CSA * 1e+3;
% Result should be in µm-1 x 1e-3

% nn SD distances with fibre volume
nn_std_per_fibre_volume = nn_std / fibre_volume;
nn_std_per_fibre_volume_adj = nn_std_per_fibre_volume * 1e+5;
% Result should be in µm-2 x 1e-5

% nn SD distances with fibre CSA
nn_std_per_fibre_CSA = nn_std / fibre_CSA;
nn_std_per_fibre_CSA_adj = nn_std_per_fibre_CSA * 1e+3;
% Result should be in µm-1 x 1e-3

% Number of nuclei with fibre volume
Nc_per_fibre_volume = nn_total_Nc / fibre_volume;
Nc_per_fibre_volume_adj = Nc_per_fibre_volume * 1e+6;
% Result should be in µm3 x 1e-6

% Number of nuclei with fibre CSA
Nc_per_fibre_CSA = nn_total_Nc / fibre_CSA;
Nc_per_fibre_CSA_adj = Nc_per_fibre_CSA * 1e+3;
% Result should be in µm2 x 1e-3

% Number of nuclei with fibre length
Nc_per_fibre_length = nn_total_Nc / fibre_length;
Nc_per_fibre_length_adj = Nc_per_fibre_length * 1e+3;
% Result should be in mm

% Number of nuclei with surface area
Nc_per_fibre_SA = nn_total_Nc / fibre_SA;
Nc_per_fibre_SA_adj = Nc_per_fibre_SA * 1e+5;
% Result should be in µm2 x 1e-5

% Average myonuclear domain (MND) volume
```

```
Nc_MND_volume = fibre_volume / nn_total_Nc;
Nc_MND_volume_adj = Nc_MND_volume * 1e-3;
% Result should be in µm3 x 1e+3

% Average MND surface area
Nc_MND_SA = fibre_SA / nn_total_Nc;
Nc_MND_SA_adj = Nc_MND_SA * 1e-2;
% Result should be in µm2 x 1e+2

% MND volume with fibre CSA
MND_volume_per_CSA = Nc_MND_volume / fibre_CSA;
MND_volume_per_CSA_adj = MND_volume_per_CSA;
% Result should be in µm

% MND volume with fibre SA
MND_volume_per_SA = Nc_MND_volume / fibre_SA;
MND_volume_per_SA_adj = MND_volume_per_SA * 1e+2;
% Result should be in µm x 1e-2

% MND surface area with fibre CSA
MND_SA_per_CSA = Nc_MND_SA / fibre_CSA;
MND_SA_per_CSA_adj = MND_SA_per_CSA * 1e+1;
% Result should be in Ratio x 1e-1


% Order score g(ME)

% This part (order score) was adapted with permission from Jo Bruusgaard.
% Original publication: Bruusgaard et al (2003), J Physiol
% Author: Andreas V. SolbrÃ¥
% Contact: a.v.solbra@fys.uio.no

[g, M_E, M_R, M_O] = NND_analysis(nn_xyz, fibre_radius, fibre_length);
% g = order score, M_E = experimental mean nn distance,
% M_R = random mean nn distance, M_O = optimal nn distance

g = g * 100;
% variable "g" should be represented as % improvement from random
% distribution
```

Copy all the acquired information to the collective Excel file

```
% Create variables containing the data for Excel ('Original_Fibre_File')
Excel_NN_xyz_Data = [nn' nn_dist']; % Creates a single variable for all
% the nn data to build upon
Excel_NN_xyz_Data(1,3) = nn_mean;
Excel_NN_xyz_Data(2:end,3) = NaN; % Converts the '0s' in 2:end of the
% nn_mean column to NaN
Excel_NN_xyz_Data(1,4) = nn_std;
Excel_NN_xyz_Data(2:end,4) = NaN; % Converts the '0s' in 2:end of the
% nn_std column to NaN
```

```
% Create variables containing the summary of the data for Excel
% ('Original_Fibre_File' (later-on) and 'CDFile' )
Excel_NN_Summary_Data = [DAPI_xy_cal_factor Phalloidin_xy_cal_factor ...
   BR_xy_cal_factor nn_total_Nc nn_mean nn_std nn_ratio fibre_length ...
   fibre_diameter fibre_depth fibre_CSA fibre_circ fibre_volume_adj ...
   fibre_SA_adj nn_mean_per_fibre_volume_adj nn_mean_per_fibre_CSA_adj ...
   nn_std_per_fibre_volume_adj nn_std_per_fibre_CSA_adj ...
   Nc_per_fibre_volume_adj Nc_per_fibre_CSA_adj Nc_per_fibre_length_adj ...
   Nc_per_fibre_SA_adj Nc_MND_volume_adj Nc_MND_SA_adj...
   MND_volume_per_CSA_adj MND_volume_per_SA_adj MND_SA_per_CSA_adj...
   sarcomere_length M_E M_R M_O g];

% Add the fibre's summary data ('Excel_NN_Summary_Data') to
% 'Excel_CDFile_Data' (for the Collective Data Sheet)

% Need to add NaNs to 'Excel_CDFile_Data'?
if isempty(row) == 0
% Evaluates whether NaNs are needed in 'Excel_CDFile_Data' in order
% to copy the variable into the Excel spreadsheet
    Excel_CDFile_Data = [Excel_CDFile_Data; Excel_NN_Summary_Data];
    Excel_CDFile_Data = [Excel_CDFile_Data; Excel_Extra_Size];
    Excel_CDFile_Data = [Excel_CDFile_Details Excel_CDFile_Data];

   % Is the first row of the dataset to be copied similar to the original?
   if Excel_CDFile_Data(1, :) == Excel_CDFile_Original(1, :)
       Repeated_Analysis = ismember...
           (Excel_NN_Summary_Data, Excel_CDFile_Original);
       Repeated_Analysis = sum(Repeated_Analysis);

       % Has the fibre already been analysed?
       if Repeated_Analysis > 10
           error(['This dataset has already been analysed! '...
               'Excel files have not been updated.'])
       else xlswrite(CDFile, Excel_CDFile_Data, 'Collective', 'A2');
       % Adds the summary data to 'CDFile'
       end

   else error(['First row of new dataset does not match first row '...
              'of original dataset! Excel files have not been updated.']);
   end

else Excel_CDFile_Details(end+1, :) = NaN;
      % Added 'Excel_NN_Summary_Data' to 'Excel_CDFile_Data' so must
      % equalise size of matrices
      Excel_CDFile_Data = [Excel_CDFile_Data; Excel_NN_Summary_Data];
      Excel_CDFile_Data = [Excel_CDFile_Details Excel_CDFile_Data];

     % Is the first row of the dataset to be copied similar to the original?
     if Excel_CDFile_Data(1, :) == Excel_CDFile_Original(1, :)
         Repeated_Analysis = ismember...
             (Excel_NN_Summary_Data, Excel_CDFile_Original);
         Repeated_Analysis = sum(Repeated_Analysis);

          % Has the fibre already been analysed?
```

```
            if Repeated_Analysis > 10
                error(['This dataset has already been analysed! '...
                    'Excel files have not been updated.'])
            else xlswrite(CDFile, Excel_CDFile_Data, 'Collective', 'A2');
            % Adds the summary data to 'CDFile'
            end

        else error(['First row of new dataset does not match first row '...
                'of original dataset! Excel files have not been updated.']);
        end
end
```

Copy all the acquired information to the fibre's Excel file

```
xlswrite(Original_Fibre_File, Excel_NN_xyz_Data, 'Nc xyz', 'F2');

% Remove the XY calibration factors from 'Excel_NN_Summary_Data'
Excel_NN_Summary_Data = Excel_NN_Summary_Data(:, 4:end);
xlswrite(Original_Fibre_File, Excel_NN_Summary_Data, 'Summary', 'A2');
```

Separate the data into the different genetic conditions

```
% Create variables for the various Excel sheets for CDFile
Excel_CDFile_Condition1 = zeros(100, 37);
Excel_CDFile_Condition2 = zeros(100, 37);
Excel_CDFile_Condition3 = zeros(100, 37);
Excel_CDFile_Condition4 = zeros(100, 37);

% Copy the different rows to the corresponding variables according to
% genetic condition
for m = 1:numel(Excel_CDFile_Data(:, 1))
    if Excel_CDFile_Data(m, 3) == 1
         Excel_CDFile_Condition1(m, :) = Excel_CDFile_Data(m, :);
    elseif Excel_CDFile_Data(m, 3) == 2
         Excel_CDFile_Condition2(m, :) = Excel_CDFile_Data(m, :);
    elseif Excel_CDFile_Data(m, 3) == 3
         Excel_CDFile_Condition3(m, :) = Excel_CDFile_Data(m, :);
    elseif Excel_CDFile_Data(m, 3) == 4
         Excel_CDFile_Condition4(m, :) = Excel_CDFile_Data(m, :);
    else error(['Could not copy data from the collective data sheet '...
            'to the corresponding Excel sheets. Information about '...
            'condition (e.g. WT) for one or more fibres is missing. '...
            'Collective and fibre sheets HAVE been updated.'])
    end
end

% Erase rows with zeros (discarded fibres)
Excel_CDFile_Condition1...
    (any(Excel_CDFile_Condition1(:, 1:37) == 0, 2), :) = [];
```

```
Excel_CDFile_Condition2...
    (any(Excel_CDFile_Condition2(:, 1:37) == 0, 2), :) = [];
Excel_CDFile_Condition3...
    (any(Excel_CDFile_Condition3(:, 1:37) == 0, 2), :) = [];
Excel_CDFile_Condition4...
    (any(Excel_CDFile_Condition4(:, 1:37) == 0, 2), :) = [];
```

Add the data into the corresponding sheets in the collective data file

```
if isempty(Excel_CDFile_Condition1) == 0
    xlswrite(CDFile, Excel_CDFile_Condition1, 'Condition 1 (All)', 'A2');
end

if isempty(Excel_CDFile_Condition2) == 0
    xlswrite(CDFile, Excel_CDFile_Condition2, 'Condition 2 (All)', 'A2');
end

if isempty(Excel_CDFile_Condition3) == 0
    xlswrite(CDFile, Excel_CDFile_Condition3, 'Condition 3 (All)', 'A2');
end

if isempty(Excel_CDFile_Condition4) == 0
    xlswrite(CDFile, Excel_CDFile_Condition4, 'Condition 4 (All)', 'A2');
end
```

The functions below were added with permission to the script above and were written by Andreas V. Solbrå, collaborator of Jo Bruusgaard, University of Oslo (Bruusgaard *et al.*, 2003). For further details see Appendix 2.

Order score main function

```
function [g, M_E, M_R, M_O] = NND_analysis( points, R, L )
%   NND_ANALYSIS This analyses the distribution of points on the surface
%   of a cylinder of radius R and length L.
%   points must be an Mx3 matrix containing all positions of the points
%   R is the radius of the cylinder
%   L is the length of the cylinder
% Author: Andreas V. Solbra
% contact: a.v.solbra@fys.uio.no

N = length(points);

[ neighbor_idx, nearest_dist, dist] = NND(points);
M_E = mean(nearest_dist);

rr = linspace(0, 2*max(nearest_dist));
[ f ] = pdf_random_points_on_cylinder(rr, N, R, L);
M_R = trapz(rr, rr.*f);

M_O = NND_optimal_distribution( L,R,N );

g = (M_E - M_R)/(M_O - M_R);

end
```

Nearest Neighbour calculation

```
function [ neighbor_idx, nearest_dist, dist ] = NND( x )
%   NND(x) finds the distances and indices of nearest neighbors
%   in a set of points, as well as a matrix containing all distances
%   Author: Andreas V. Solbra
%   Date: 01-12-2015 (dd-mm-yyyy)
%
%   Description:
%   Input matrix must be Nx3
%
%   Example:
%   x = rand(4,3);
%   [idx,nearest_dist, dist] = nearest_neighbor(x);
% Author: Andreas V. Solbra
% contact: a.v.solbra@fys.uio.no


if (size(x,2) ~= 3)
    msg = 'Input matrix has wrong dimensions! Must be Nx3.';
    error(msg)
end

y = pdist(x);
Y = squareform(y);
```

```
Y(logical(eye(size(Y)))) = Inf;
[nearest_dist,neighbor_idx] = min(Y);
Y(logical(eye(size(Y)))) = 0;
dist=Y;
end
```

Random distribution calculation

```
function [ f ] = pdf_random_points_on_cylinder(rr, N, R, L)
%PDF_RANDOM_POINTS_ON_CYLINDER(rr, N, R, L) Generates the pdf of the NND
%for N random points on a cylinder of length L and radius R.
%   rr is a vector with the points where the pdf should be evaluated.
%   Example use:
%   rr = linspace(0,200,201);
%   N = 10;
%   L = 100;
%   R = 20;
%   f = pdf_random_points_on_cylinder(rr, N, R, L);
%   plot(rr, f)
% Author: Andreas V. SolbrÃ¥
% contact: a.v.solbra@fys.uio.no

n = length(rr);
F = zeros(1,n);
for i=1:n
    r = rr(i);
    r1 = linspace(0,min(L,r),n);
    h = (2/L)*(1-r1/L).*(2/pi).*asin(min(2*R, sqrt(r^2-r1.^2))/(2*R));
    F(i) = trapz(r1,h);

end

p = 1-F;
pN = p.^N;


dp = diff(1-pN)/(rr(2)-rr(1));
dp(end+1) = dp(end);

f = dp;

end
```

Optimal distribution calculation

```
function d= NND_optimal_distribution( L,R,N )
%UNIFORM_DISTANCE(L,R,N) Finds the NND for N points on a cylinder of length
%L and radius R, if the points are spread out on a d
%

% Author: Andreas V. SolbrÃ¥
% contact: a.v.solbra@fys.uio.no

C = 2*pi*R;
A = L*C;

r = C/L;

Nx = round(sqrt(N/r));
Ny = round(Nx*r);

dx = L/Nx;
dy = C/Ny;

d = mean([dx,dy]);
end
```

Published with MATLAB® R2017a

Appendix 2: Order-score calculations

The information in this appendix was provided by the creator of the order-score functions, Andreas V. Solbrå, collaborator of Jo Bruusgaard, University of Oslo (Bruusgaard *et al.*, 2003). The functions were used with permission in the script to calculate nuclear distribution in single muscle fibres (Appendix 1). The description below remains loyal to the source, despite minor insignificant language adjustments (e.g. American-English spelling).

9.1. Methods: Statistical analysis

Nuclei are usually distributed close to the surface of the fibre. For each muscle fibre, an idealized circular cylinder segment with constant radius was constructed. The length and radius of the cylinder were found by the Imaris software. From these parameters, the distance from each nucleus to its nearest neighbour was compared to the cases of:

- Nuclei spread uniformly at random on the cylinder surface;
- Nuclei spread optimally to minimize transport distances.

In principle, one could use the distances as measured along the surface of the parameterised cylinder in the statistical analysis. However, as this allows for possible errors in the surface parameters due to the uncertainties in the nuclei position, we have here chosen to use the direct, Euclidean distances.

For the chosen distance measurement, one can show that the nearest neighbour distance probability density function for the case of N nuclei spread randomly on a cylinder segment of radius R and length L, is given by (see section 9.2 for derivation of this expression):

$$f_{cyl}(r) = \frac{d}{dr}\left(1 - P(NND(x_i) > r)\right) \quad (1)$$

Where

$$P(NND(x_i) > r) = 1 - \frac{4}{\pi L^2}\int_0^{min\{L,r\}} \int_0^{min\left\{2R,\sqrt{r^2-r_1^2}\right\}} \frac{L - r_1}{\sqrt{4R^2 - r_2^2}} dr_2 dr_1 \quad (2)$$

It is difficult to determine the optimal distribution of nuclei to minimize transport distances. Here we follow Bruusgaard *et al.* (2003), which suggest using a hexagonal grid pattern on the cylinder surface. There are several ways to create such a pattern. The way chosen here was to create a rectangular grid off equispaced points, with NL points along the length of the cylinder, and *NC* points along the circumference, such that $NC/NL \approx C/L$ and $NCNL \approx N$, where *C* is the circumference of a circle with radius *R*, $C = 2\pi R$. Ideally, these would be exactly equal, but this is not possible for all sets of *L*, *R* and *N*. Afterwards, every second line of points either along the circumference a distance $\Delta C = C/(2N_c)$. These points now define the centres of approximately regular hexagons.

In order to measure how ordered the nuclei distribution for a particular fibre is the mean nearest neighbour distance was calculated for the experimental data, as well as for the random and optimal distribution using parameters from the experiment. We denote the experimental, random and optimal means by M_E, M_R and M_O. An "orderness-score", $g(M_E)$, was then calculated as

$$g(M_E, M_R, M_O) = \frac{M_E - M_R}{M_O - M_R}$$

In the case where the experimental nuclei are clustered, this score may be negative.

9.2. Mathematical derivation

Here we will derive equation (2). We begin by considering the nearest neighbour distance (NND) probability density function (PDF) for points on a line. For two points x and y uniformly randomly placed on a line segment of length *L*, the probability density for the distance between the two points, $r_1 = |x - y|$ is

$$g_l(r_1)dr_1 = \frac{2}{L}(1 - r_1/L)dr_1 \tag{3}$$

For Euclidean distances on a circle of radius *R*, if two points are selected at uniformly random angles, then the probability density of the chord length is

$$g_c(r_2)dr_2 = \frac{2}{\pi\sqrt{4R^2 - r_2^2}}dr_2 \tag{4}$$

for $0 \leq r_2 \leq 2R$.

For two points on the surface of the complete cylinder, what is the probability that the distance between the points is larger than some value r?

$$P(r_1^2 + r_2^2 > r^2) = 1 - P(r_1^2 + r_2^2 < r^2) \tag{5}$$

$$= 1 - \int_0^{min\{L,r\}} \int_0^{min\left\{2R, \sqrt{r^2 - r_1^2}\right\}} g_c(r_2)g_1(r_1)dr_2dr_1 \tag{6}$$

$$= 1 - \int_0^{min\{L,r\}} g_1(r_1) \int_0^{min\left\{2R, \sqrt{r^2 - r_1^2}\right\}} \frac{2}{\pi\sqrt{4R^2 - r_2^2}}dr_2dr_1 \tag{7}$$

We can solve part of the integral analytically as

$$P(r_1^2 + r_2^2 > r^2) = 1 - \int_0^{min\{L,r\}} g_1(r_1)\frac{2}{\pi}\left[\sin^{-1}\left(r_2/(2R)\right)\right]_0^{min\left\{2R,\sqrt{r^2-r_1^2}\right\}} dr_1 \quad (8)$$

$$= 1 - \int_0^{min\{L,r\}} g_1(r_1)\frac{2}{\pi}\sin^{-1}\left(min\left\{2R,\sqrt{r^2-r_1^2}\right\}/(2R)\right) dr_1 \quad (9)$$

The last integral can be solved analytically.

For a collection of *N* particles, the probability that none are closer than r is

$$P(NND(x_i) > r) = P(r_1^2 + r_2^2 > r^2)^{N-1}$$

and the PDF for $NND(x_i)$ is

$$f_{cyl}(r) = \frac{d}{dr}\left(1 - P(NND(x_i) > r)\right) \quad (10)$$

Appendix 3: Nuclear pixel intensity Fiji script

10.1. Introduction to the Fiji scripts

The scripts in the following sections are typical examples of the scripts used for this project. They are presented in the same order they were run (as described above). The first script requires longer time to run, as reading/writing 50-100 images at a time is significantly more taxing for a computer than processing a couple of maximum intensity projection (MIP) images. For producing the most accurate regions of interest (ROIs), it is best that the second script is run following deconvolution. A description of the colour-scheme of the codes is provided below.

Table 10.1: Colour coding in Fiji

Colour	Definition
Green	Comment
Black	Variable
Blue	Selection statement (e.g. “if” statements)
Dark yellow	Built-in functions
Pink	String (i.e. words/sentences)

10.2. Dark-field and flat-field

```
/* Macro to correct stacks of images for background and flat-field
 * Yotam Levy
 * 20.05.18
 */

print("\\Clear");

// Select input and output directories
input = getDirectory("Input directory");
output = getDirectory("Output directory");

// Select dark and flat-field images
Darkinput = File.openDialog("Select your dark image");
Flatinput = File.openDialog("Select your flat-field image");

// Choose suffix to find in directories
Dialog.create("File type");
Dialog.addString("File suffix: ", ".TIF", 40);
Dialog.show();
suffix = Dialog.getString();

setBatchMode(true);

// Open dark and flat-field images
open(Darkinput);
DarkName=getInfo("image.filename");
open(Flatinput);
FlatName=getInfo("image.filename");

// Get mean pixel intensity of the flat-field image
getStatistics(area, FlatNameMeanPixel);

// Process folder
processFolder(input);

function processFolder(input) {
	setBatchMode(true);
	list = getFileList(input);

	for (i = 0; i < list.length; i++) {
		if(File.isDirectory(input + list[i]))
			processFolder("" + input + list[i]);

		if(endsWith(list[i], suffix))
			processFile(input, output, list[i]);
	}
}
```

```
// Process file
function processFile(input, output, filename) {
        open(input + filename);
        selectWindow(filename);
        OrgImgInfo = getInfo("image.description");

        // Subtract dark image from each image in the stack
        imageCalculator("Subtract stack", filename, DarkName);
        BackCorrImage = getTitle();

        // Divide each image in the stack by the flat-field image
        run("Calculator Plus", "i1=[BackCorrImage] i2=FlatName operation=[Divide:  i2 =
(i1/i2) x k1 + k2] k1=FlatNameMeanPixel k2=0");
        BackFlatCorrImage = getTitle();
        selectWindow(BackFlatCorrImage);
        setSlice(90);
        resetMinAndMax();

        // Save and exit
        setMetadata("Info", OrgImgInfo);
        saveAs("Tiff", output + filename);
        close();
}

print("Done!");
```

10.3. Nuclear pixel intensities

```
/* Macro to measure nuclear parameters from MIPs of nuclear stacks
 * Yotam Levy
 * 20.05.18
 */

print("\\Clear");

// Set all required configurations
// Set binary options
run("Options...", "iterations=1 count=1 black do=Nothing");
// Set the required measurements
run("Set Measurements...", "mean standard min redirect=None decimal=4");
// Set the structure of the dataset
run("Input/Output...", "jpeg=85 gif=-1 file=.csv use_file copy_column copy_row
save_column save_row");

// Create results tables
Table.create("Results Channel 1");
Table.create("Results Channel 2");
```

```
// Select input and output directories
input = getDirectory("Input directory");
output = getDirectory("Output directory");

// Choose suffix for channel 1 (e.g. DAPI)
Dialog.create("File type");
Dialog.addString("File suffix: ", "DAPI.tif", 40);
Dialog.show();
suffix1 = Dialog.getString();

// Choose suffix for channel 2 (e.g. AF594)
Dialog.create("File type");
Dialog.addString("File suffix: ", "AF594.tif", 40);
Dialog.show();
suffix2 = Dialog.getString();

// Process folder
processFolder(input);

function processFolder(input) {
	setBatchMode(true);
	list = getFileList(input);

	for (i = 0; i < list.length; i++) {
		if(File.isDirectory(input + list[i]))
			processFolder("" + input + list[i]);

		if(endsWith(list[i], suffix))
			processFile(input, output, list[i]);
	}
}

// Process file
function processFile(input, output, filename) {

	// Open images
	ch1inputfilename = input + filename;
	open(ch1inputfilename);
	ch1filenameWoExt = File.nameWithoutExtension;
	ch2filename = replace(filename, suffix1, suffix2);
	ch2inputfilename = input + ch2filename;
	open(ch2inputfilename);
	ch2filenameWoExt = File.nameWithoutExtension;

	// Create max MIP images for both channels

		// Channel 1
		selectWindow(filename);
		run("Z Project...", "projection=[Max Intensity]");
		rename(ch1filenameWoExt + "_MIP");
		ch1MIPName = getTitle();
		ch1MIPID = getImageID();
		close(filename);
```

```
		// Channel 2
		selectWindow(ch2filename);
		run("Z Project...", "projection=[Max Intensity]");
		rename(ch2filenameWoExt + "_MIP");
		ch2MIPName = getTitle();
		ch2MIPID = getImageID();
		close(ch2filename);

	// Create ROIs from Channel 1 MIP

		// Duplicate Channel 1 MIP for creating ROIs
		selectWindow(ch1MIPName);
		run("Duplicate...", ch1MIPName + " ");
		rename(ch1MIPName + "_binary");
		ch1MIPBinaryName = getTitle();
		ch1MIPBinaryID = getImageID();

		// Make binary image
		run("Enhance Contrast...", "saturated=1 normalize");
		run("8-bit");
		setThreshold(3, 255);
		run("Convert to Mask");
		run("Fill Holes");

		// Create ROIs from binary image
		selectWindow(ch1MIPBinaryName);
		run("Analyze Particles...", "size=50-Infinity pixel exclude include
add");
		close(ch1MIPBinaryName);

	// Use ROIs to measure set parameters in both channels and save ROI images

		// DAPI
		IJ.renameResults("Results Channel 1", "Results");
		selectWindow(ch1MIPName);
		roiManager("Measure");
		roiManager("Show All without labels");
		roiManager("Show All with labels");
		selectWindow(ch1MIPName);
		run("Flatten");
		saveAs("Jpeg", output + ch1filenameWoExt + "_ROIs");
		ch1ROIName = getTitle();
		ch1ROIID = getImageID();
		close(ch1MIPName);
		close(ch1ROIName);
		IJ.renameResults("Results", "Results Channel 1");

		// Channel 2
		IJ.renameResults("Results Channel 2", "Results");
		selectWindow(ch2MIPName);
		roiManager("Measure");
		roiManager("Show All without labels");
		roiManager("Show All with labels");
```

```
                selectWindow(ch2MIPName);
                run("Flatten");
                saveAs("Jpeg", output + ch2filenameWoExt + "_ROIs");
                ch2ROIName = getTitle();
                ch2ROIID = getImageID();
                close(ch2MIPName);
                close(ch2ROIName);
                IJ.renameResults("Results", "Results Channel 2");

        // Clear ROI list
        roiManager("Delete");
}

// Save results tables
selectWindow("Results Channel 1");
saveAs("Results", output + "Results Channel 1.csv");
selectWindow("Results Channel 2");
saveAs("Results", output + "Results Channel 2.csv");

// Close all open windows
run("Close All");
close("*.csv");

selectWindow("Log");
print("Done!");
```

Appendix 4: Effects of prelamin A on myonuclear and muscle fibre function

The current appendix consists of larger versions of graphs that are contained within the summary figures of the mouse models studied in chapter 4. Thus, only figures that were reduced in size will be found here. Each set of graphs is categorised by its respective mouse model.

11.1. *Zmpste24* KO

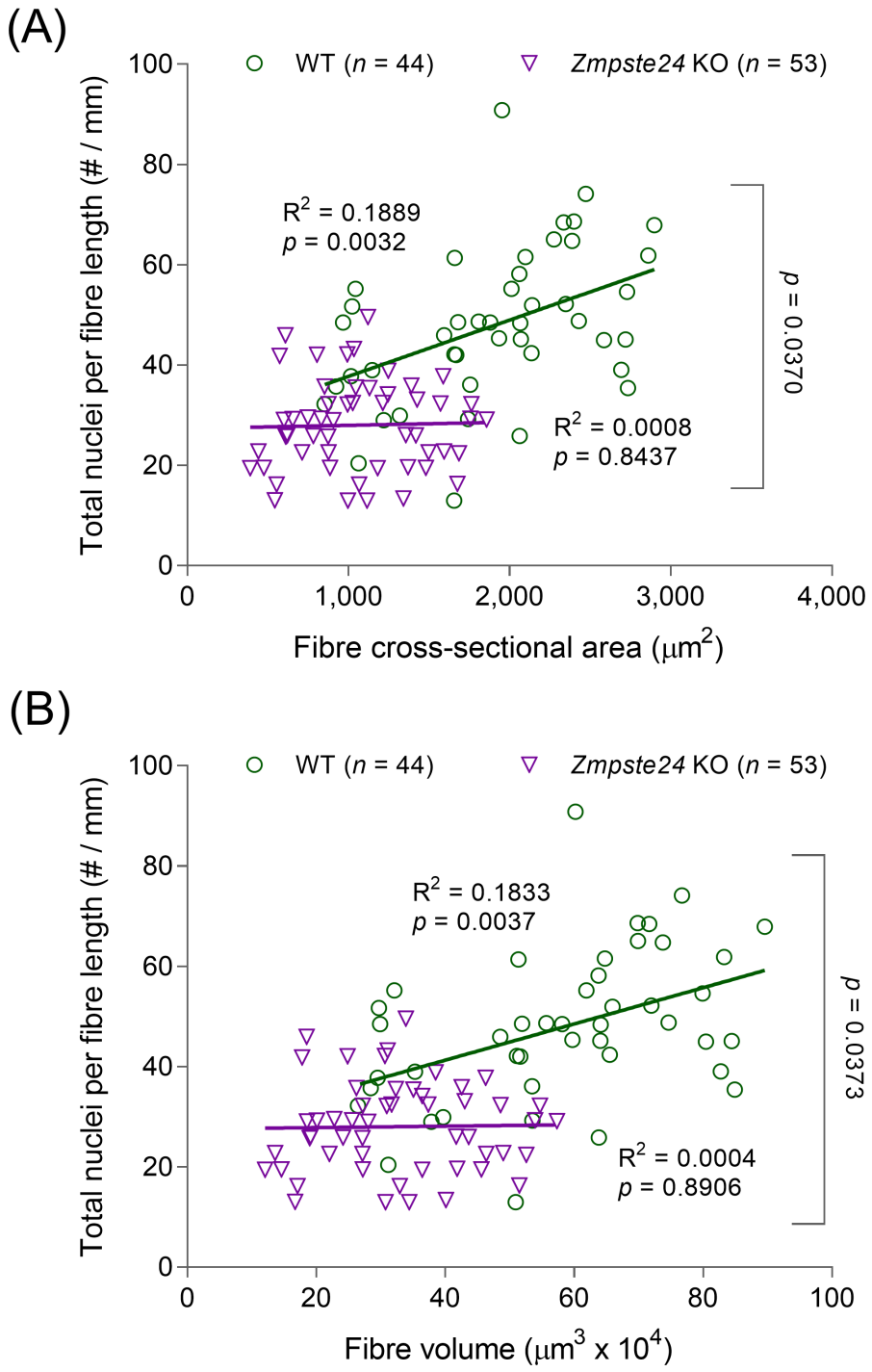

Figure 11.1: Reduced number of nuclei in *Zmpste24*-deficient single myofibres

Data points represent individual single muscle fibres. Pearson product moment correlation was performed to evaluate linear relationships.

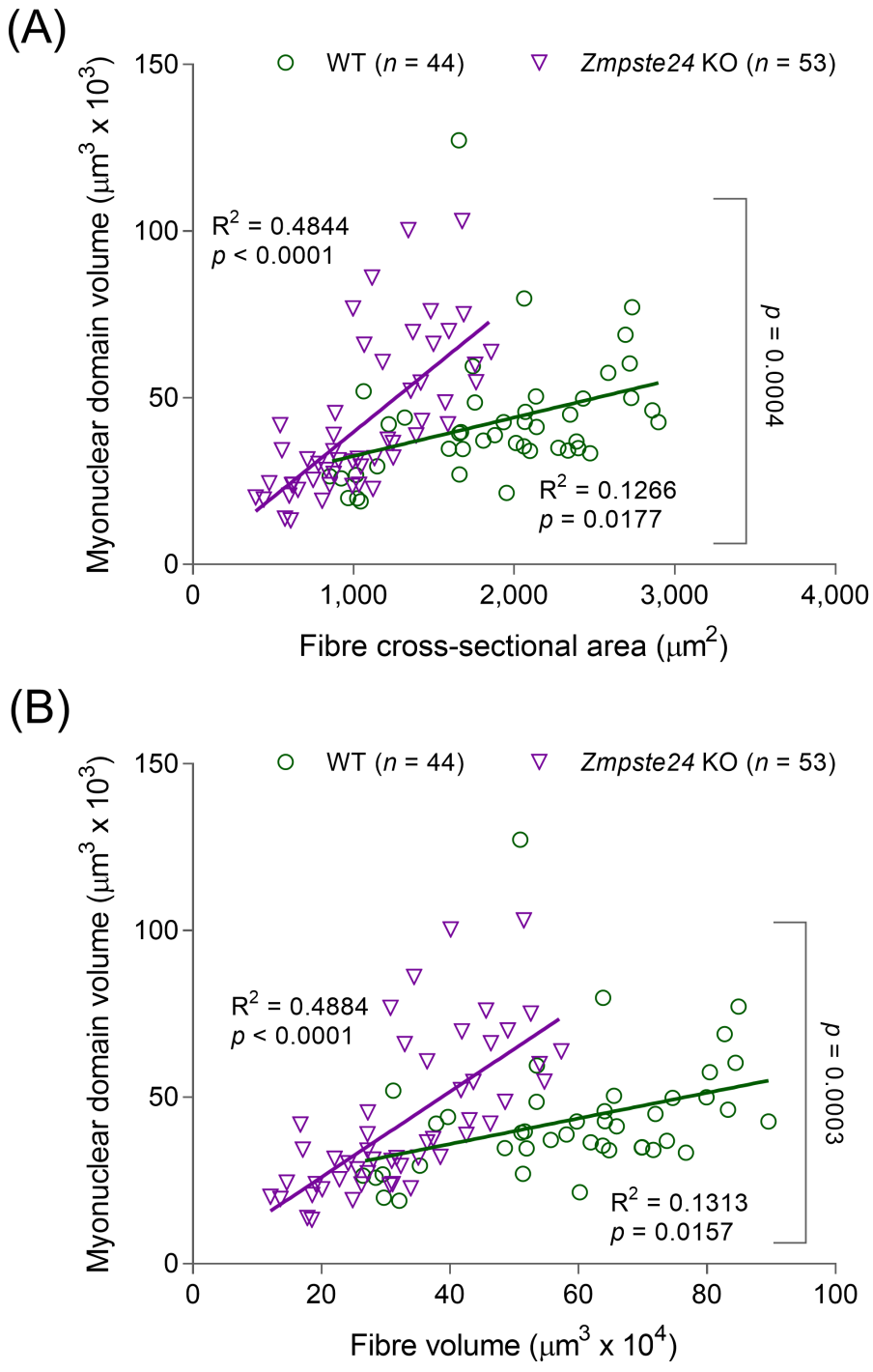

Figure 11.2: Enlarged MNDs in *Zmpste24*-deficient single myofibres

Data points represent individual single muscle fibres. Pearson product moment correlation was performed to evaluate linear relationships.

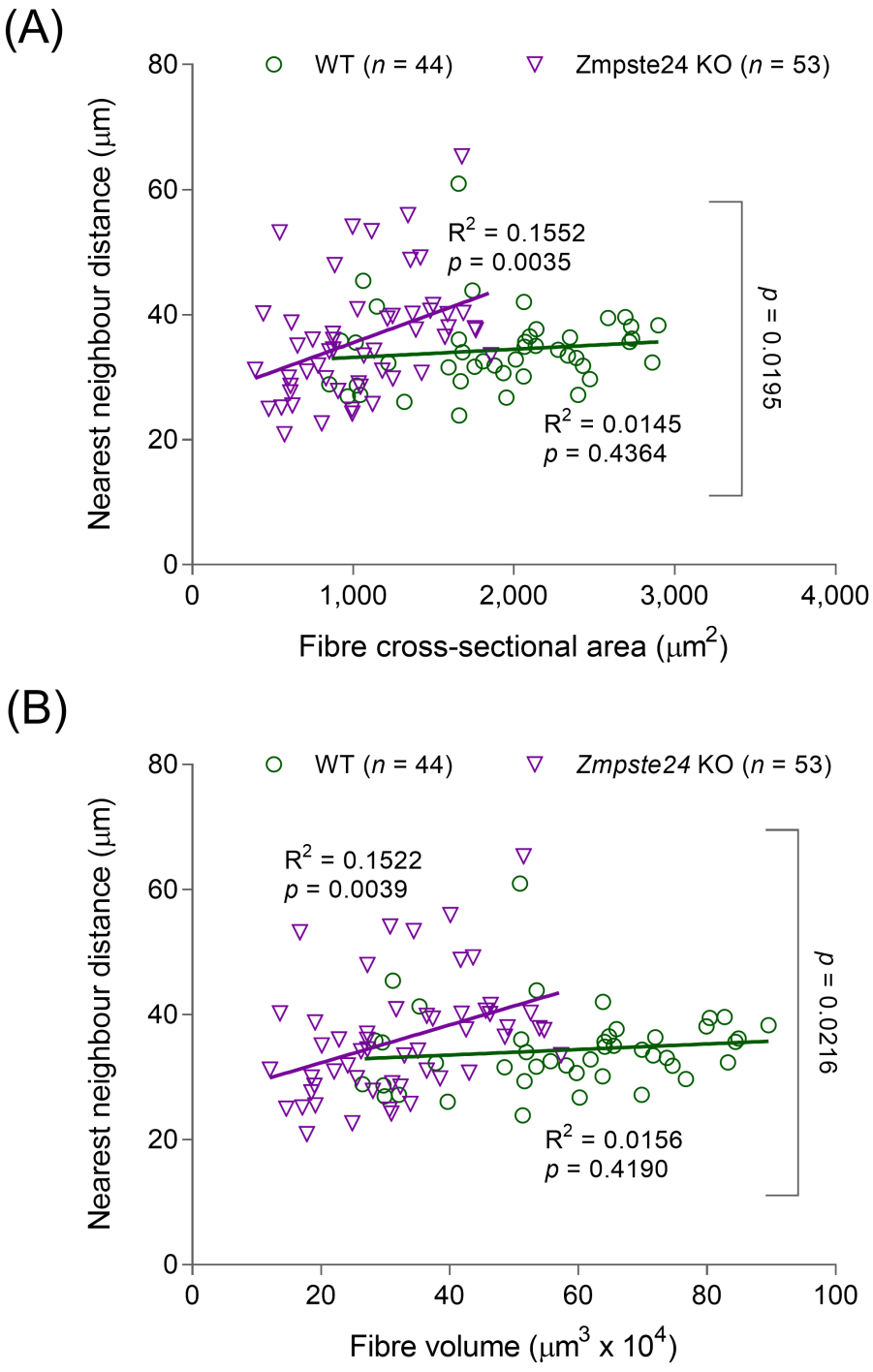

Figure 11.3: Increased nuclear distances in *Zmpste24*-deficient single myofibres

Data points represent individual single muscle fibres. Pearson product moment correlation was performed to evaluate linear relationships.

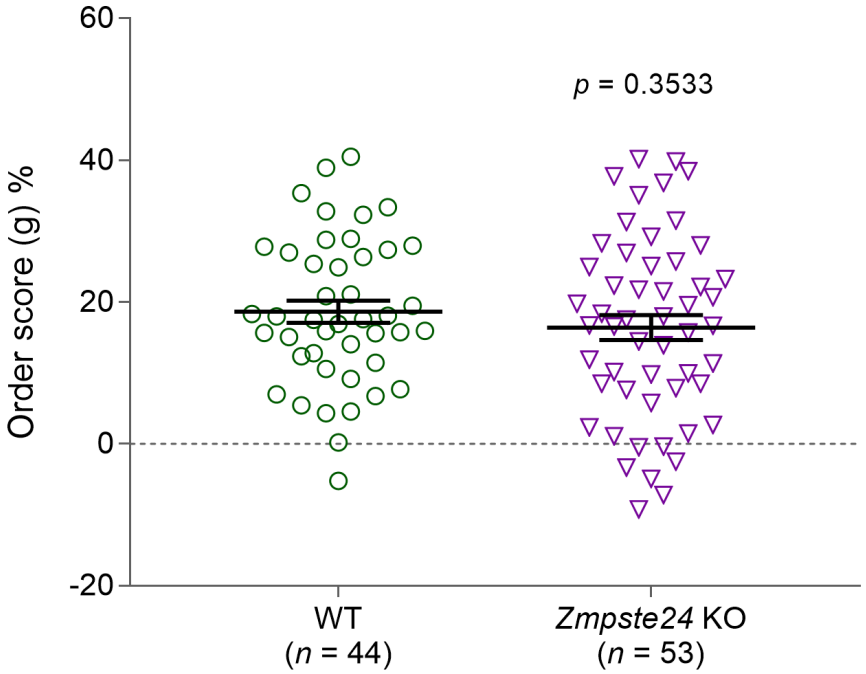

Figure 11.4: Normal nuclear distribution in *Zmpste24*-deficient single myofibres
Data points represent individual single muscle fibres. Error bars show mean ± SEM. Statistical tests included normality tests and t-tests.

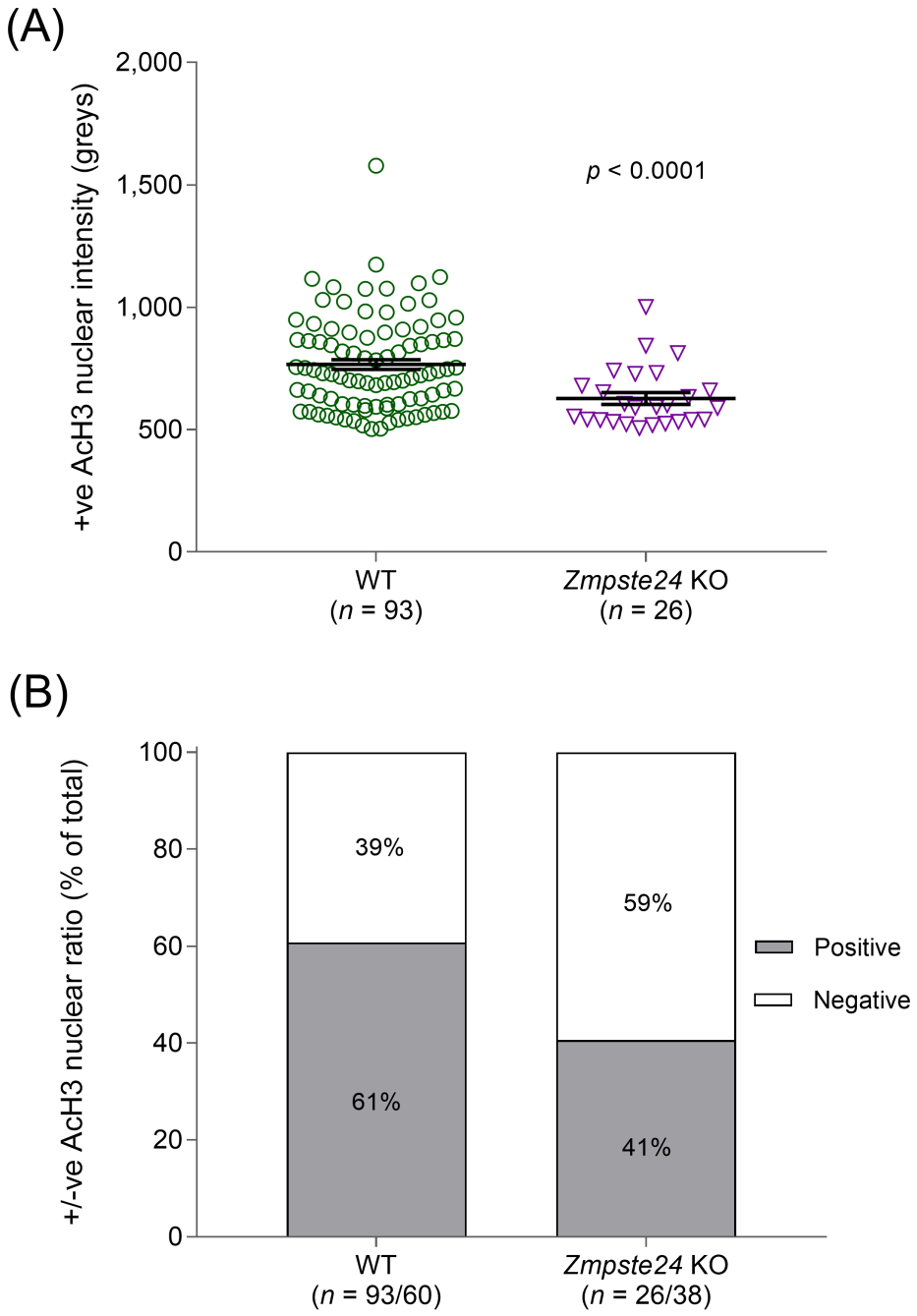

Figure 11.5: Altered acetyl-histone H3 levels in nuclei lacking *Zmpste24*

(A) Data points represent individual nuclei with positive (+ve) level (>500 greys) of acetyl-histone H3 (AcH3). Error bars show mean ± SEM. Statistical tests included normality tests and t-tests; (B) Positive (+ve) nuclei >500 greys, negative (-ve) nuclei <500 greys. The cut-off point of 500 greys was selected based on measured background levels of all studied single muscle fibres.

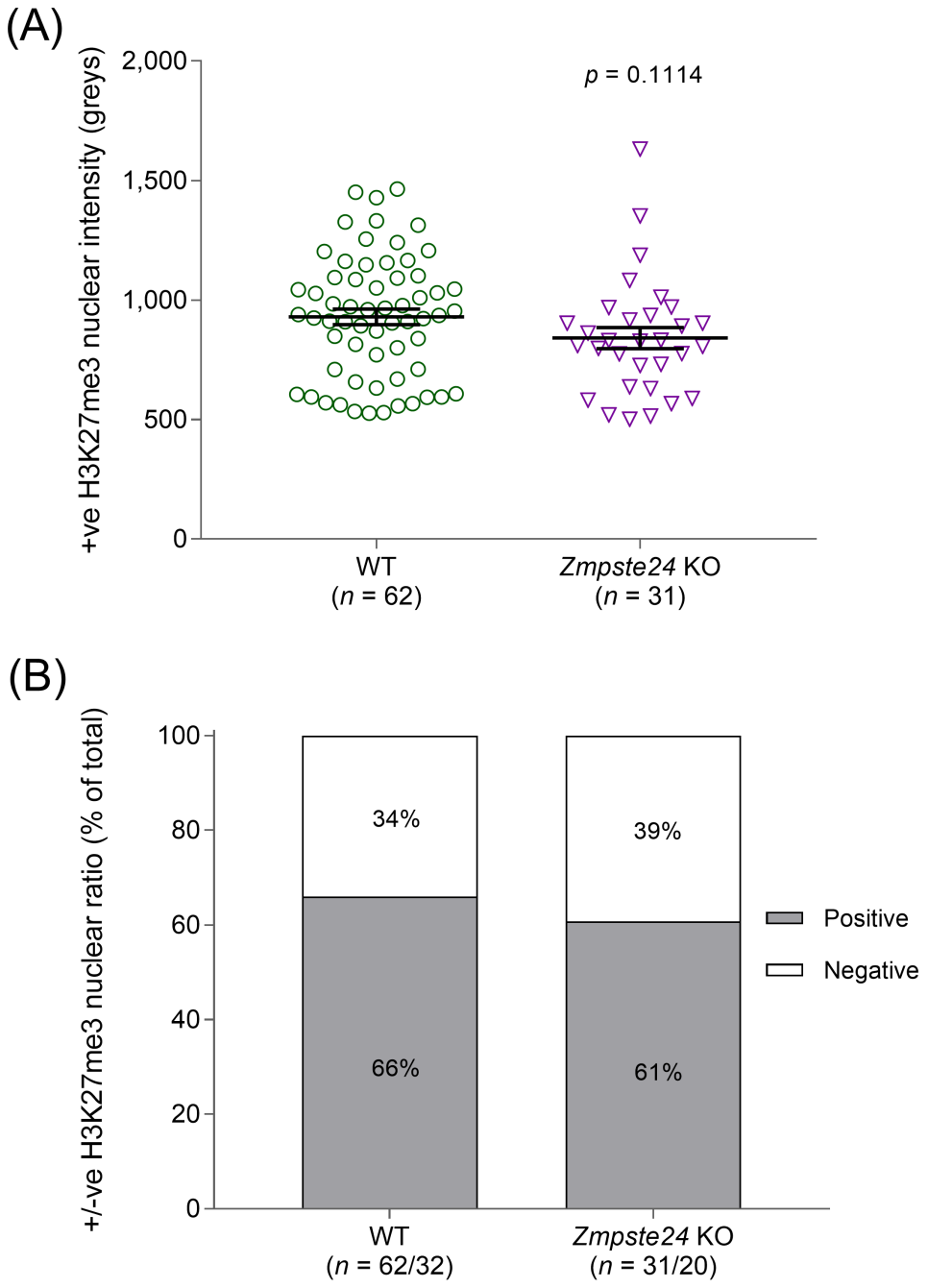

Figure 11.6: Normal H3K27me3 levels in nuclei lacking *Zmpste24*

(A) Data points represent individual nuclei with positive (+ve) level (>500 greys) of acetyl-histone H3 (AcH3). Error bars show mean ± SEM. Statistical tests included normality tests and t-tests; (B) Positive (+ve) nuclei >500 greys, negative (-ve) nuclei <500 greys. The cut-off point of 500 greys was selected based on measured background levels of all studied single muscle fibres.

11.2. Mosaic

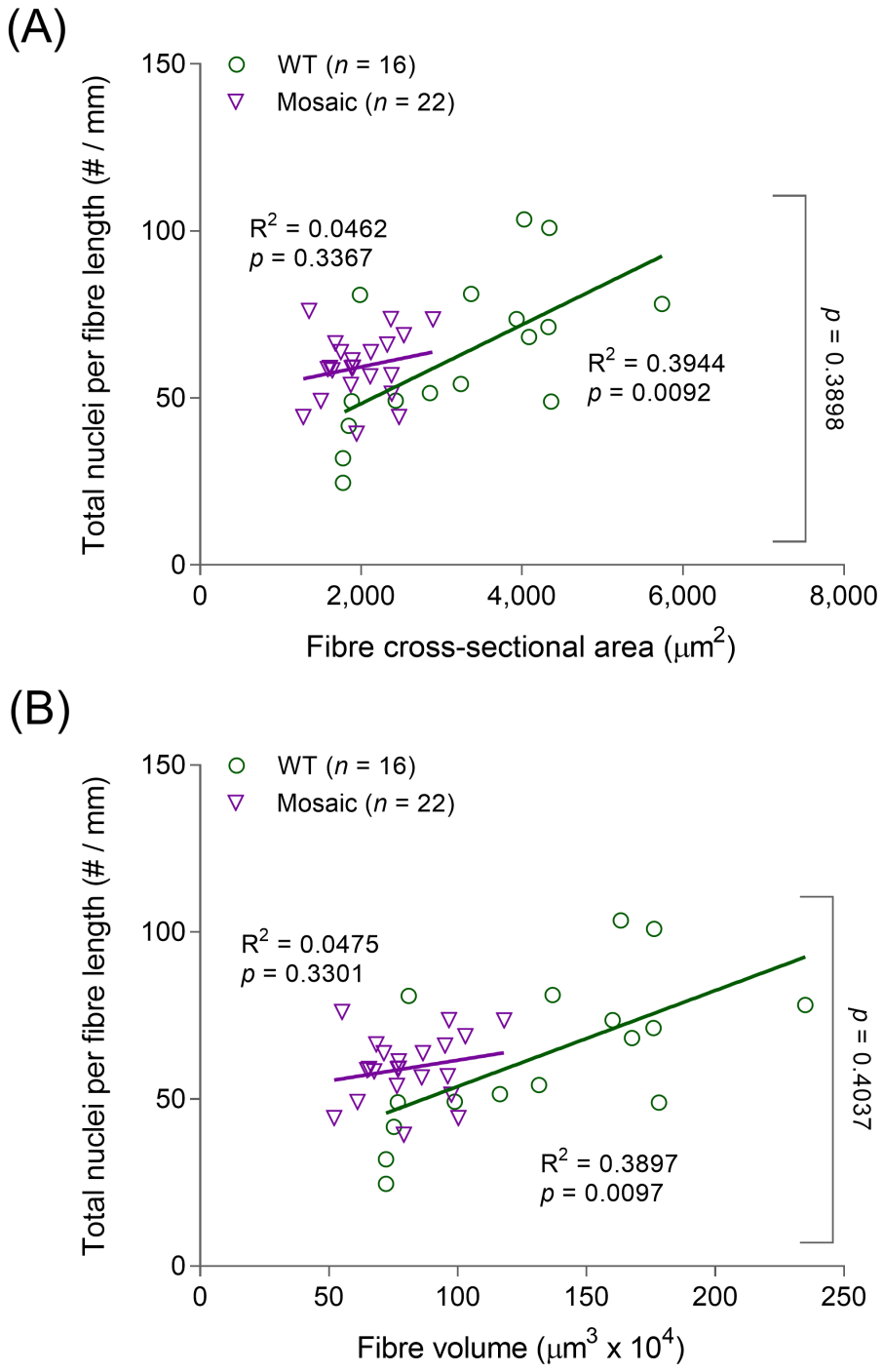

Figure 11.7: Normal number of nuclei in mosaic single myofibres

Data points represent individual single muscle fibres. Pearson product moment correlation was performed to evaluate linear relationships.

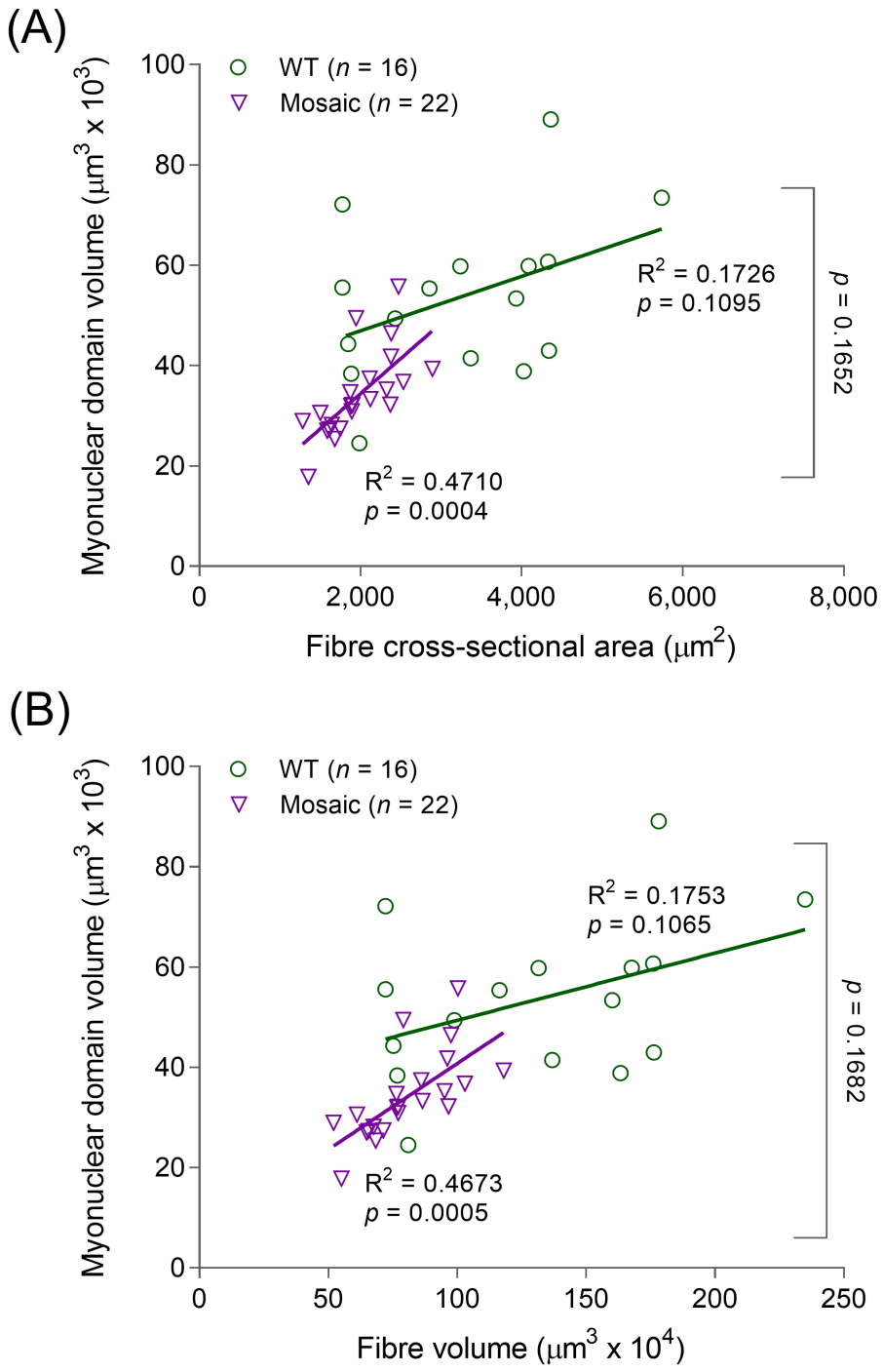

Figure 11.8: Normal MNDs in mosaic single myofibres

Data points represent individual single muscle fibres. Pearson product moment correlation was performed to evaluate linear relationships.

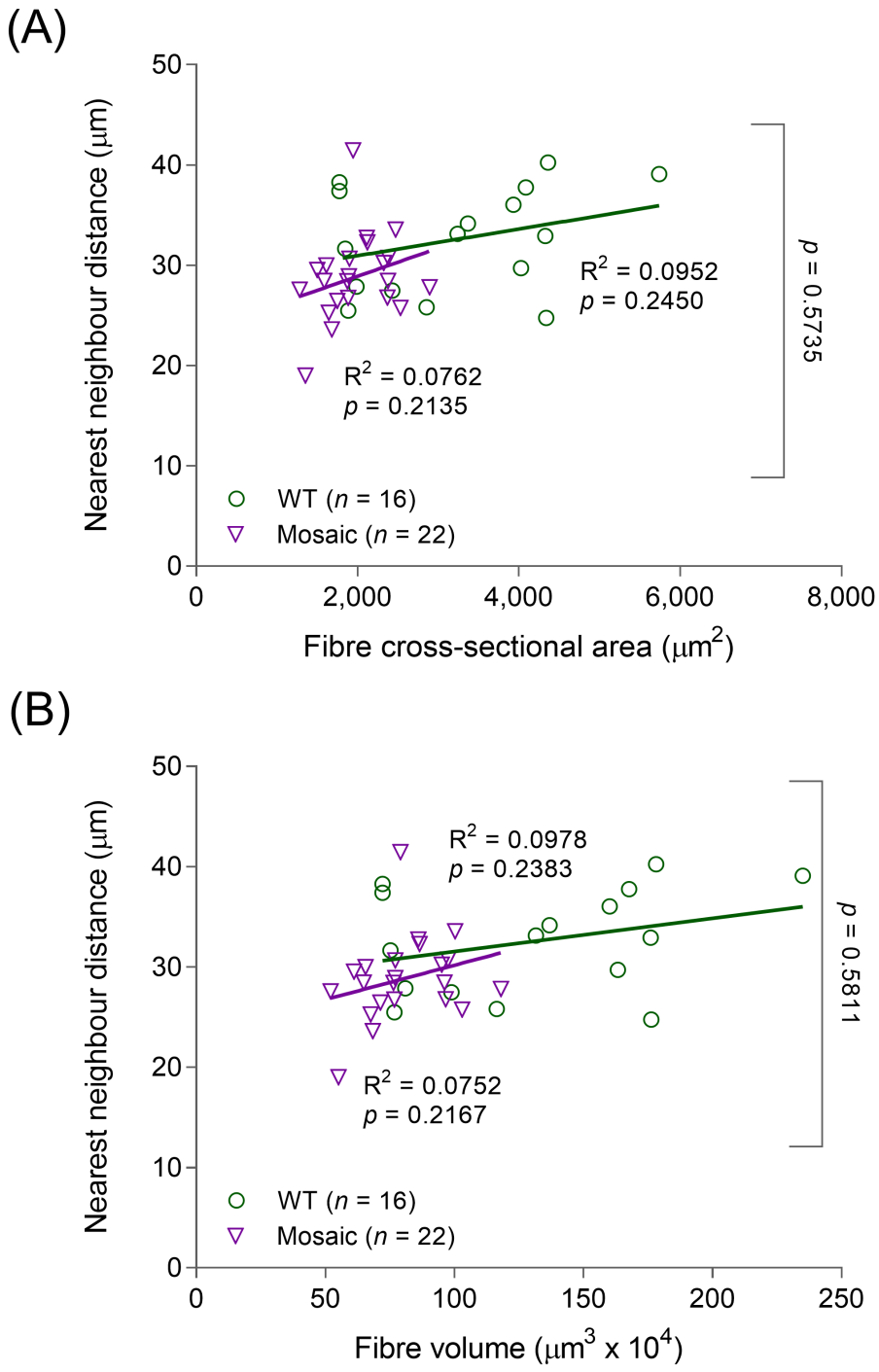

Figure 11.9: Normal nuclear distances in mosaic single myofibres

Data points represent individual single muscle fibres. Pearson product moment correlation was performed to evaluate linear relationships.

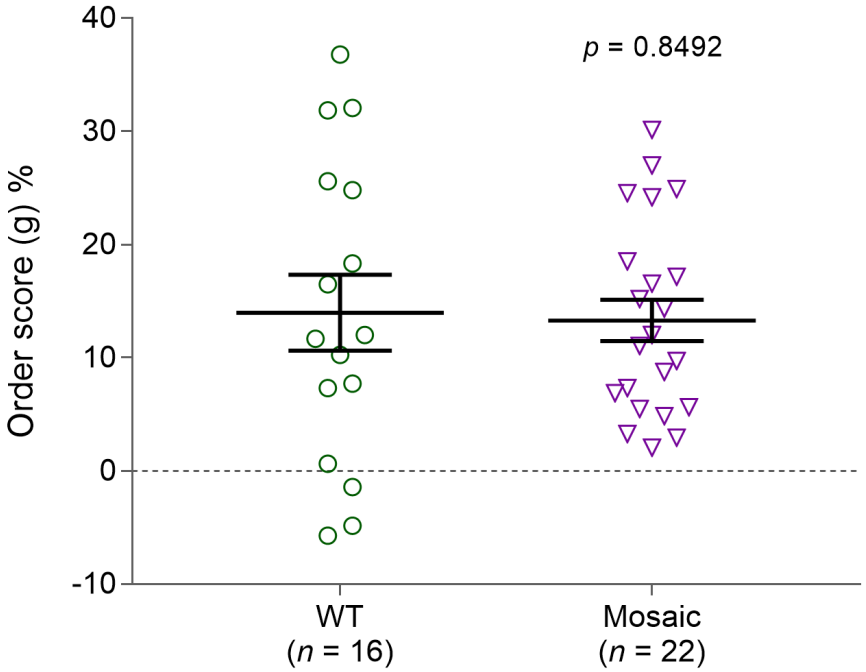

Figure 11.10: Normal nuclear distribution in mosaic single myofibres

Data points represent individual single muscle fibres. Error bars show mean ± SEM. Statistical tests included normality tests and t-tests.

11.3. *Zmpste24* KO FTIs

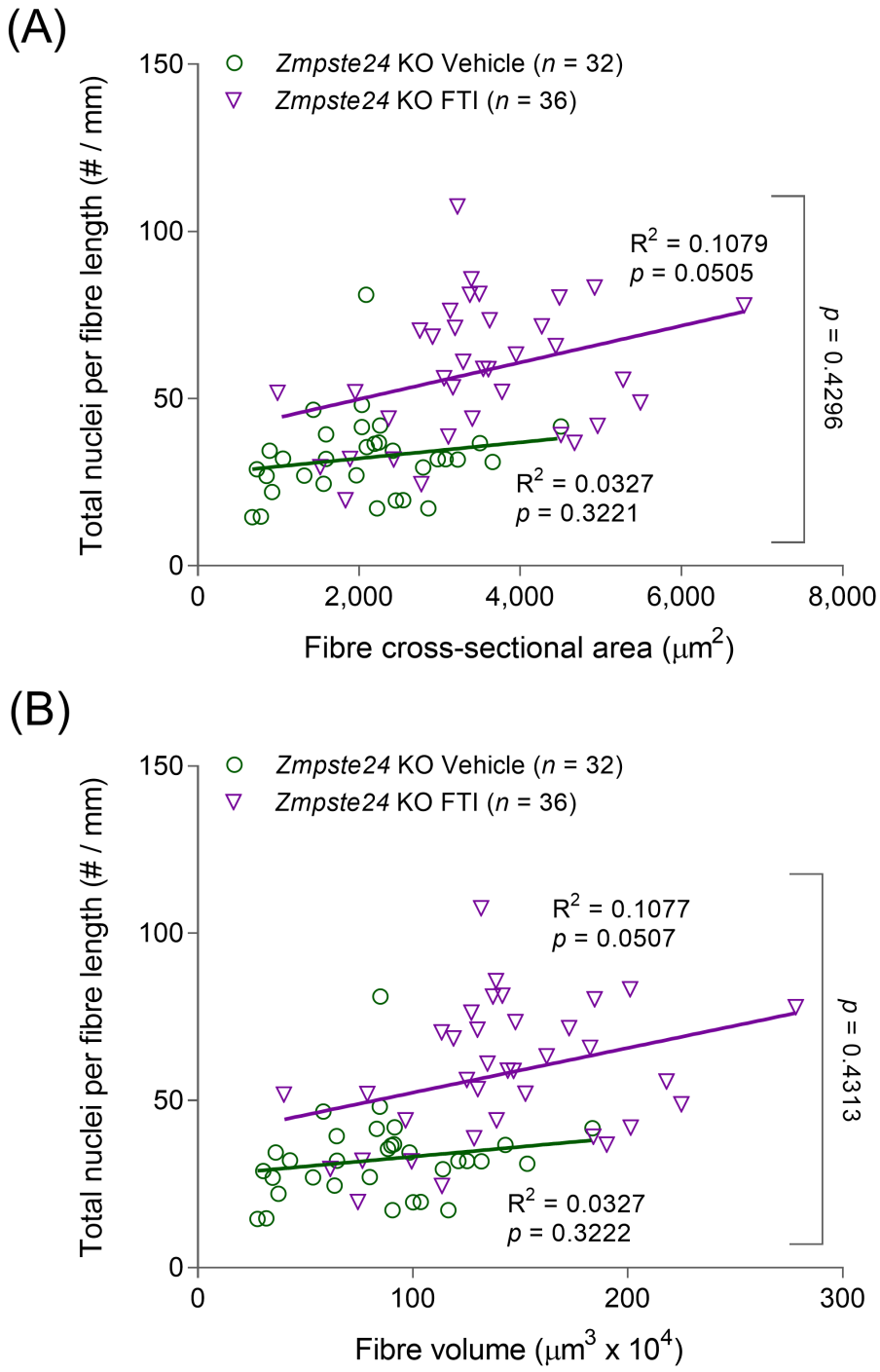

Figure 11.11: Normal number of nuclei in FTI-treated *Zmpste24*-deficient myofibres

Data points represent individual single muscle fibres. Pearson product moment correlation was performed to evaluate linear relationships.

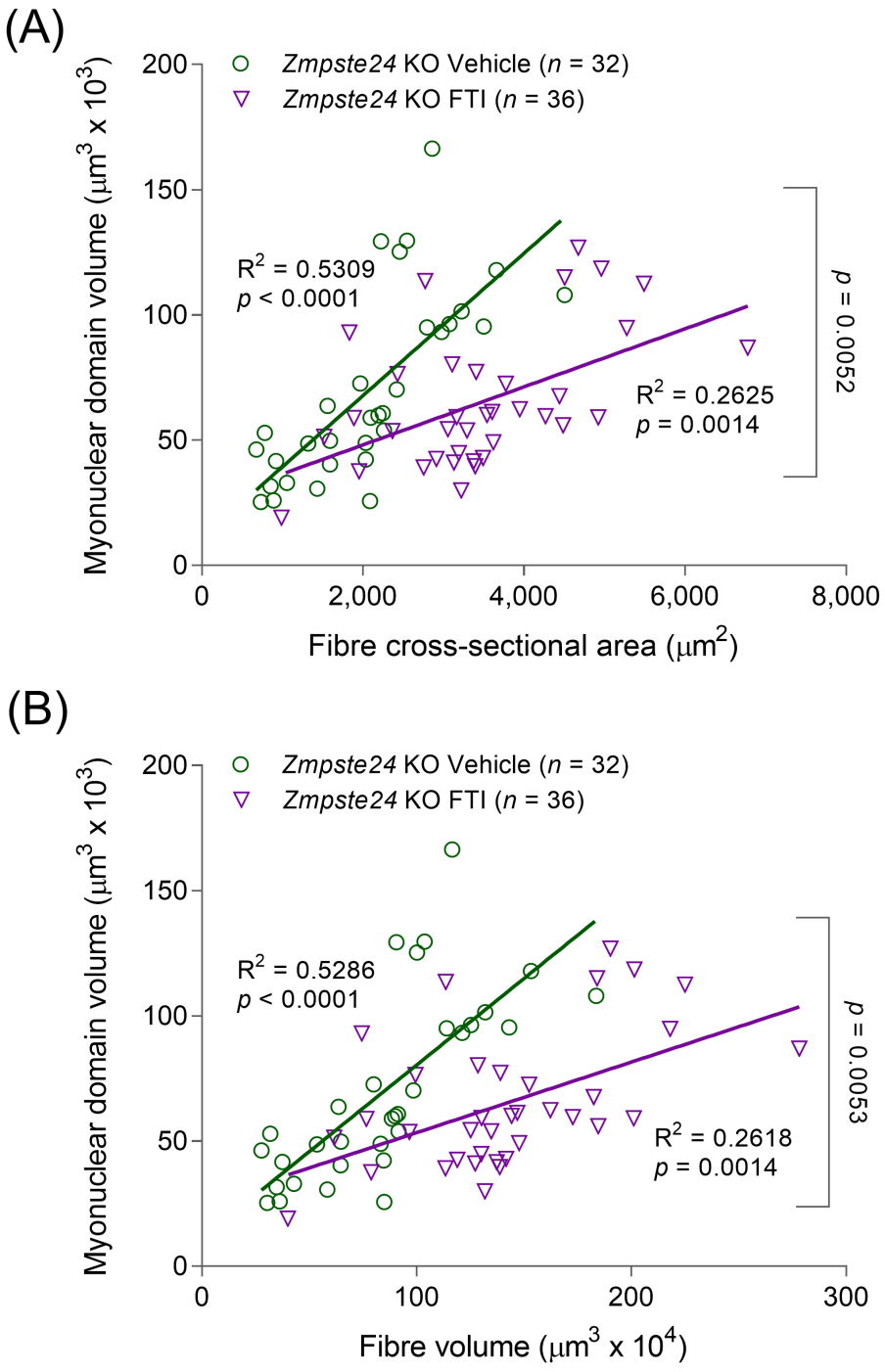

Figure 11.12: Normal MNDs in FTI-treated *Zmpste24*-deficient myofibres

Data points represent individual single muscle fibres. Pearson product moment correlation was performed to evaluate linear relationships.

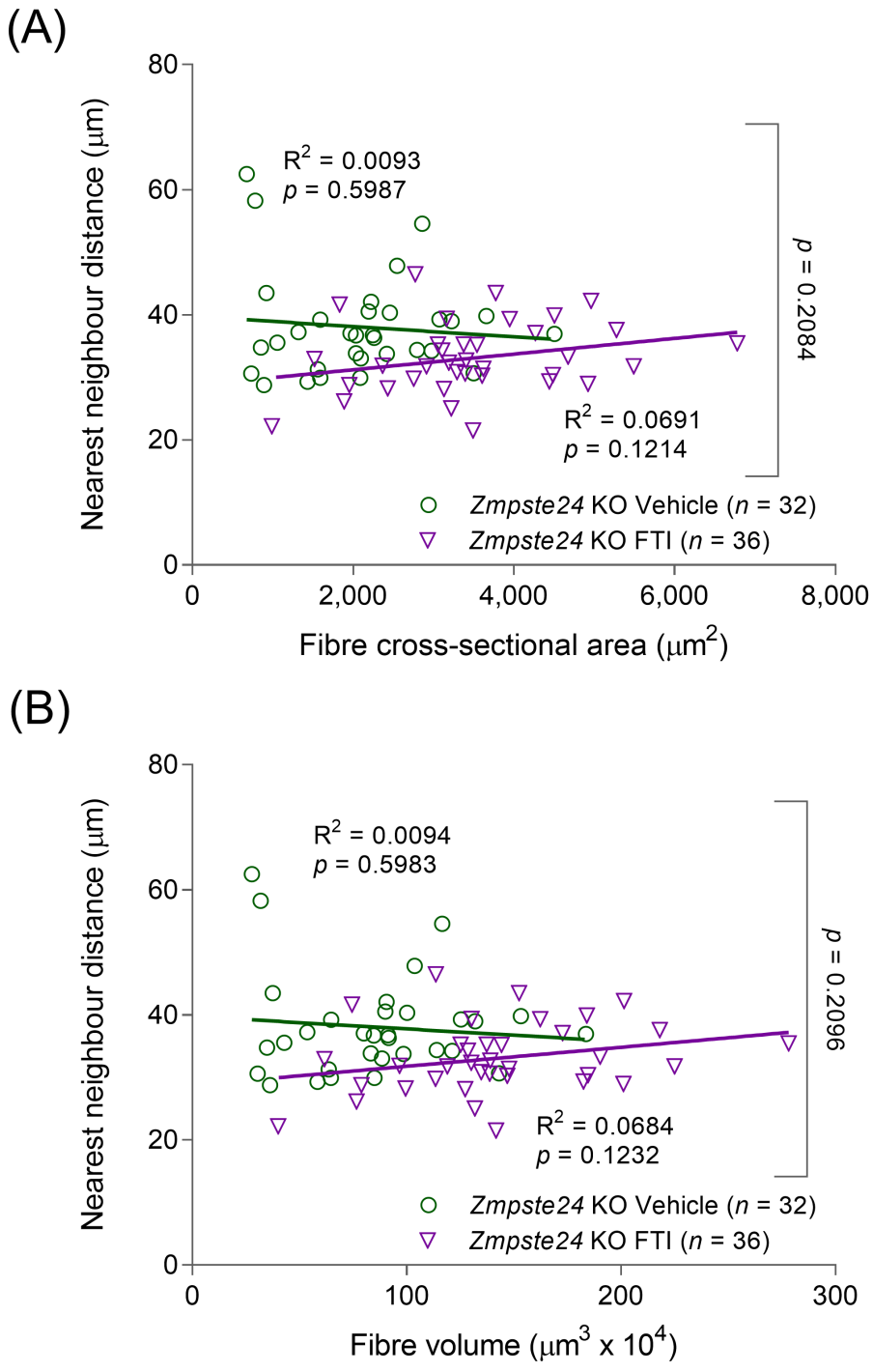

Figure 11.13: Normal nuclear distances in FTI-treated *Zmpste24*-deficient myofibres
Data points represent individual single muscle fibres. Pearson product moment correlation was performed to evaluate linear relationships.

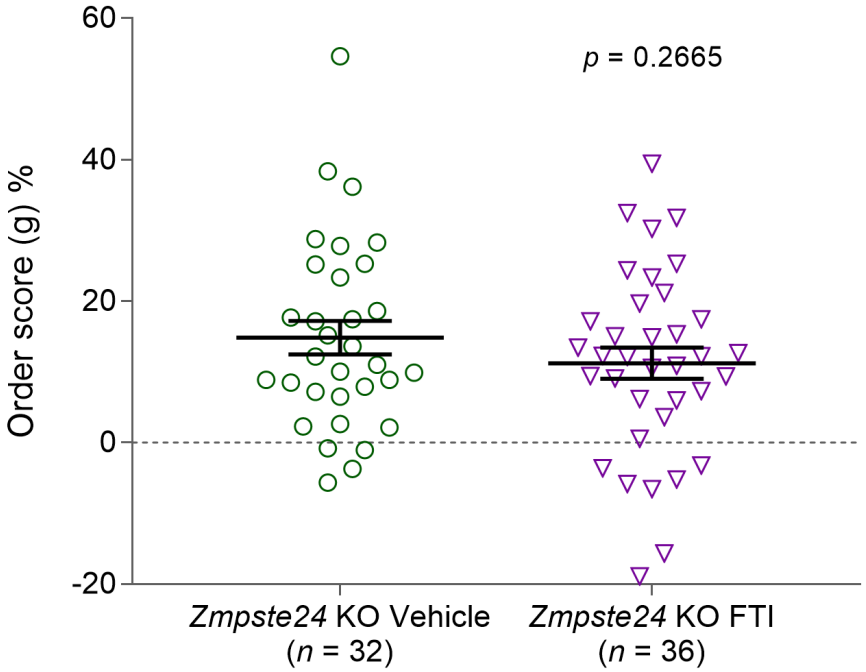

Figure 11.14: Nuclear distribution in FTI-treated *Zmpste24*-deficient myofibres

Data points represent individual single muscle fibres. Error bars show mean ± SEM. Statistical tests included normality tests and t-tests.

11.4. *Lmna* KO

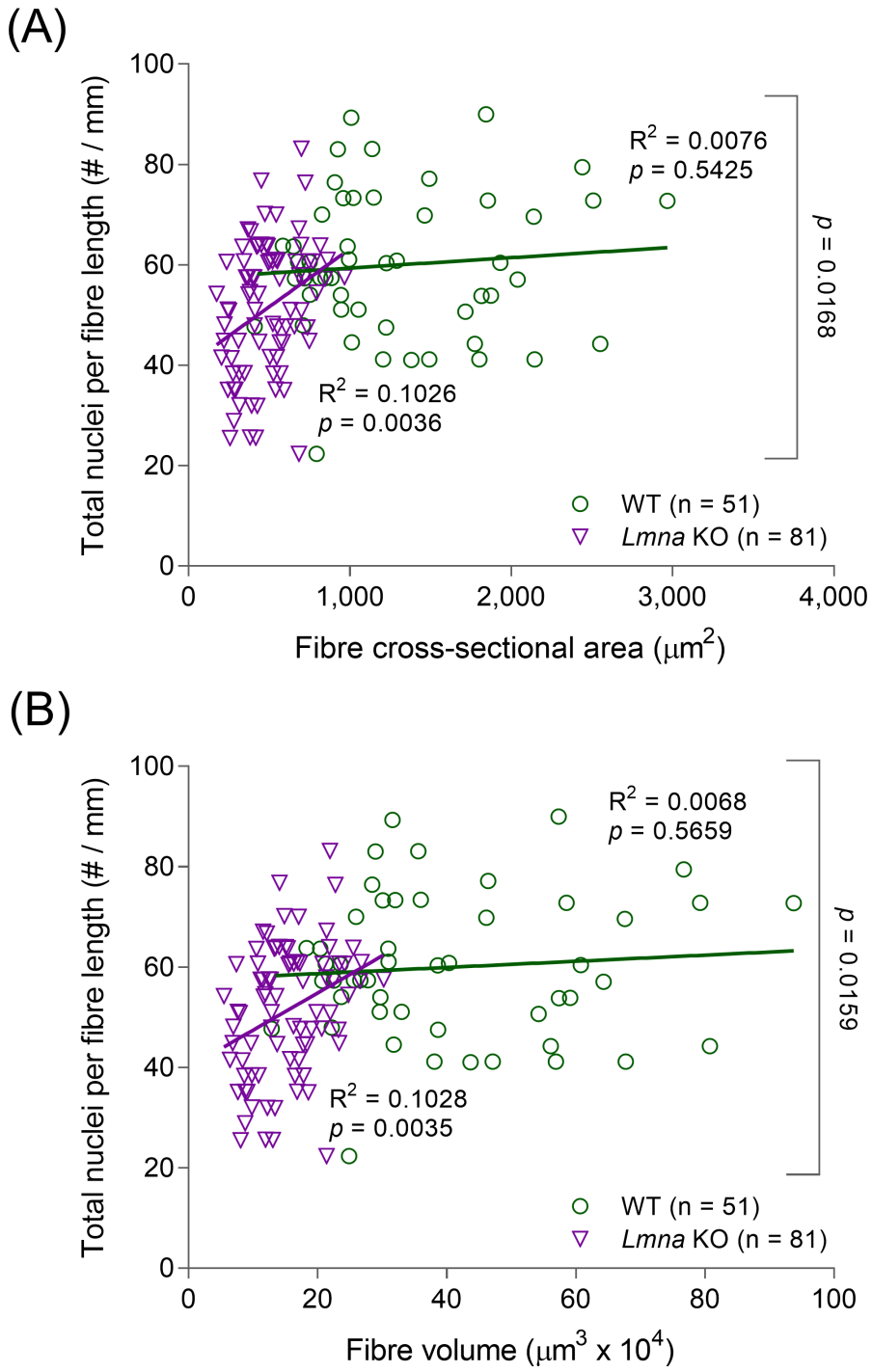

Figure 11.15: Lower number of nuclei in lamin A-deficient single myofibres

Data points represent individual single muscle fibres. Pearson product moment correlation was performed to evaluate linear relationships.

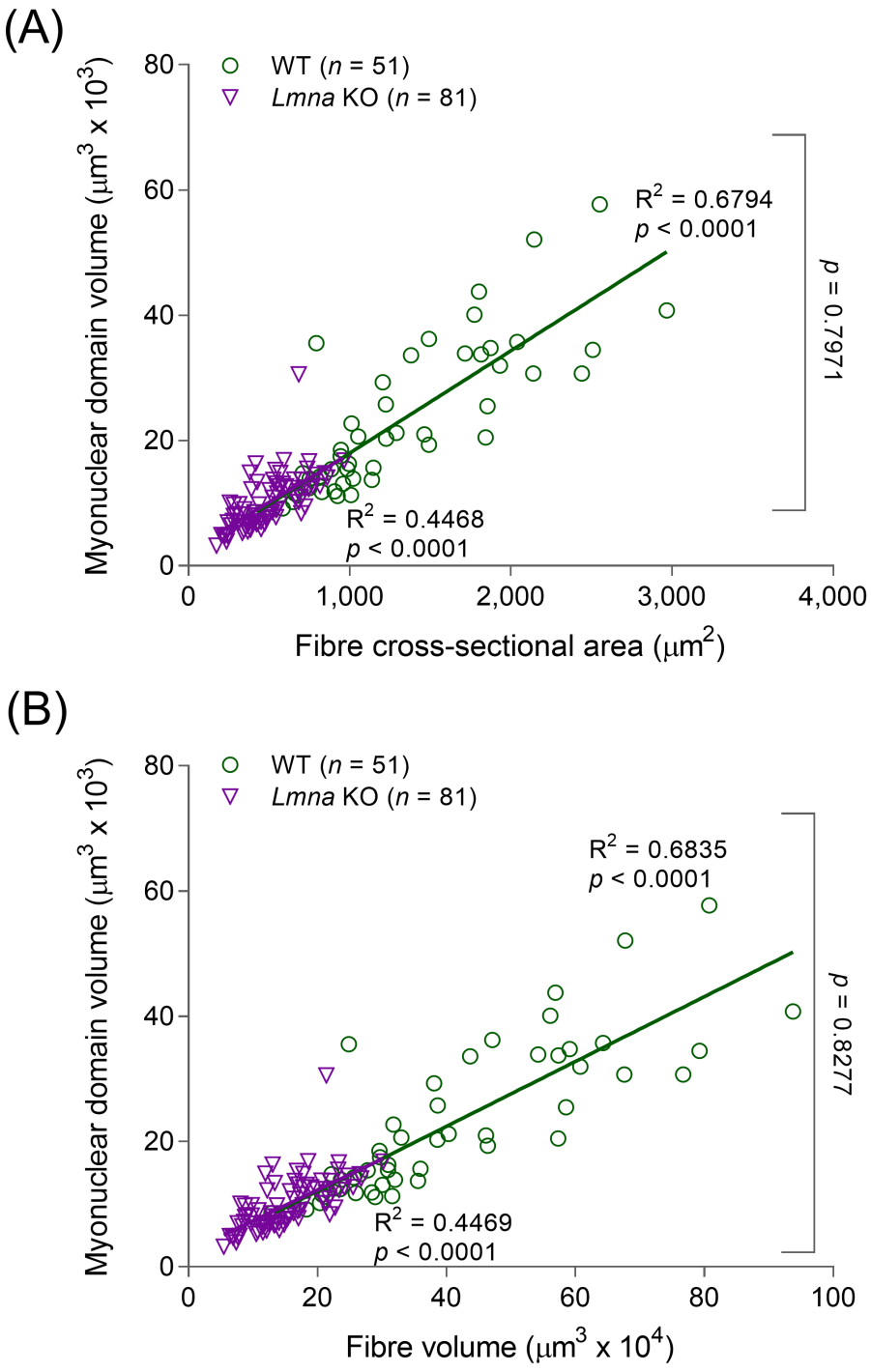

Figure 11.16: Normal MNDs in lamin A-deficient single myofibres

Data points represent individual single muscle fibres. Pearson product moment correlation was performed to evaluate linear relationships.

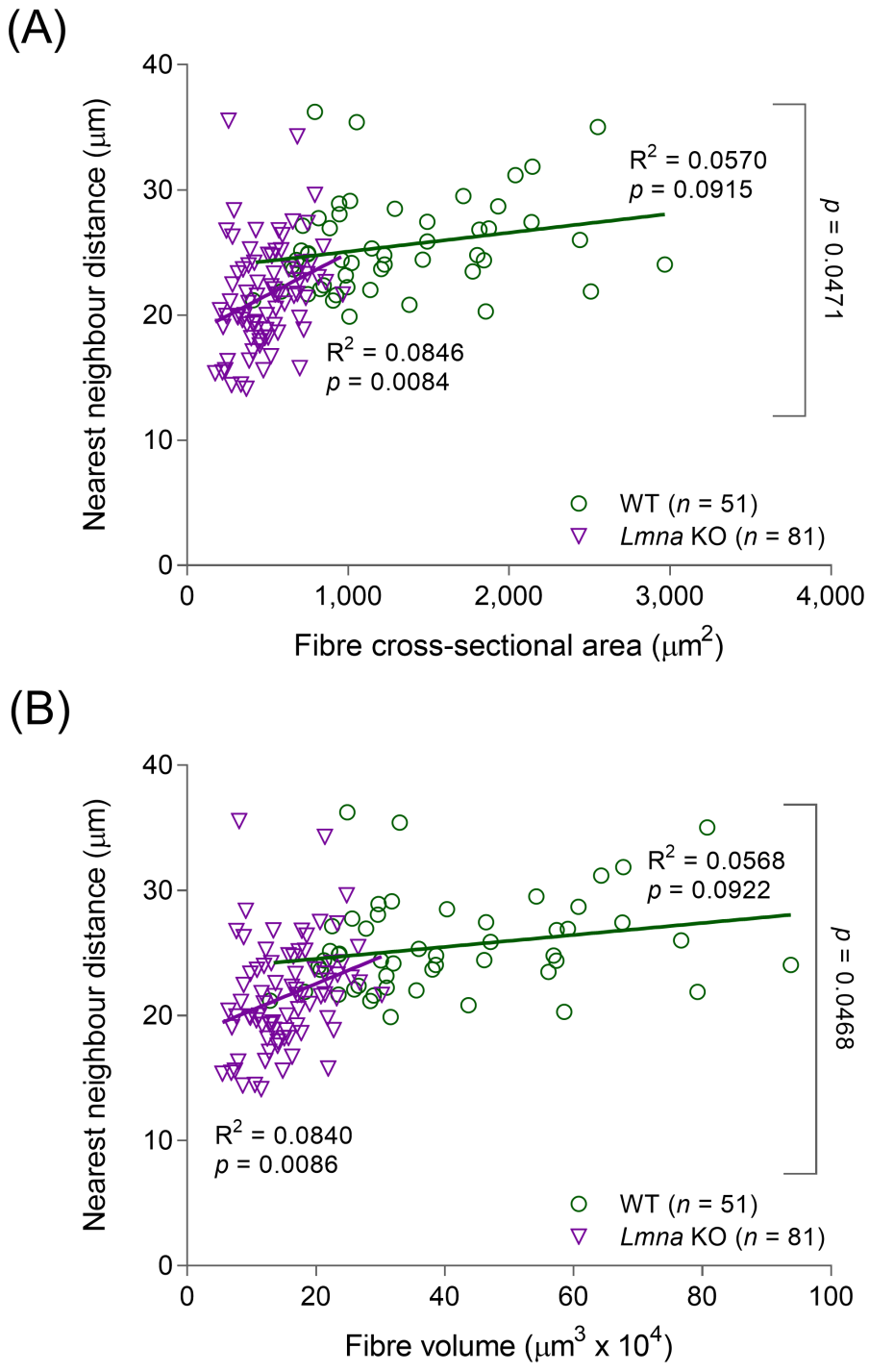

Figure 11.17: Normal nuclear distances in lamin A-deficient single myofibres
Data points represent individual single muscle fibres. Pearson product moment correlation was performed to evaluate linear relationships.

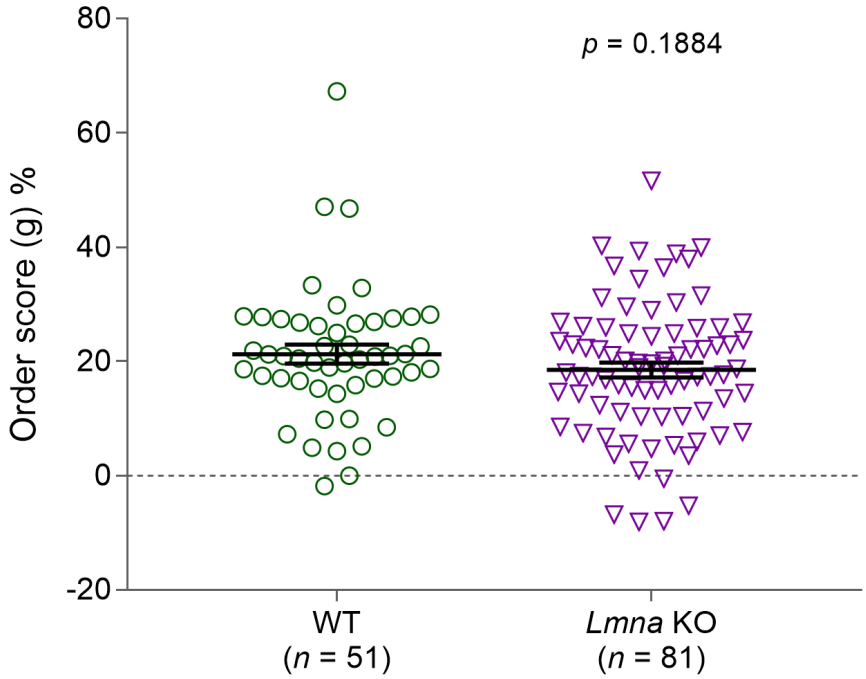

Figure 11.18: Normal nuclear distribution in lamin A-deficient single myofibres
Data points represent individual single muscle fibres. Error bars show mean ± SEM. Statistical tests included normality tests and t-tests.

11.5. *Lmna*^{G609G}

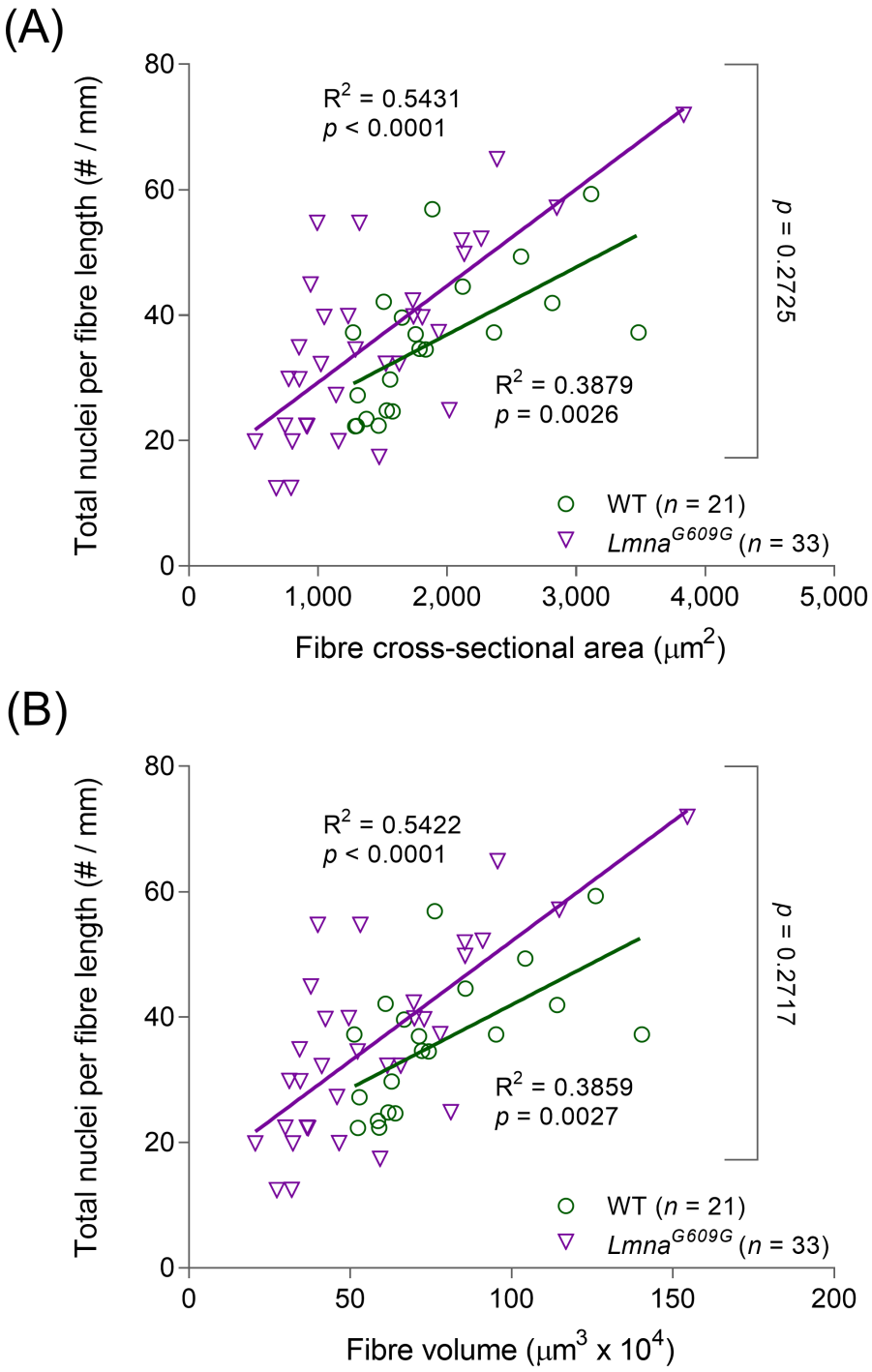

Figure 11.19: Normal number of nuclei in *Lmna*^{G609G} single myofibres

Data points represent individual single muscle fibres. Pearson product moment correlation was performed to evaluate linear relationships.

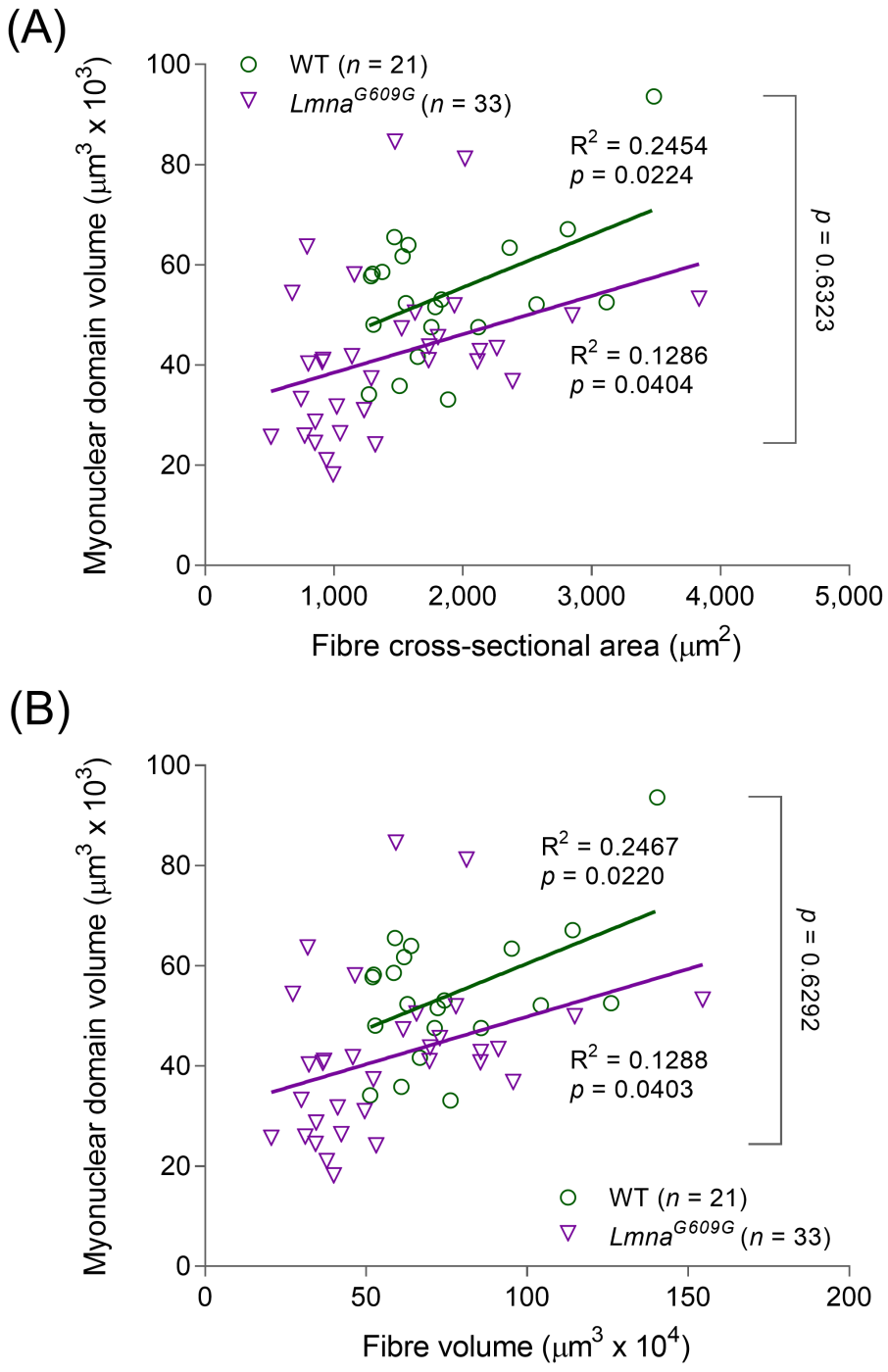

Figure 11.20: Normal MNDs in *Lmna*^{G609G} single myofibres

Data points represent individual single muscle fibres. Pearson product moment correlation was performed to evaluate linear relationships.

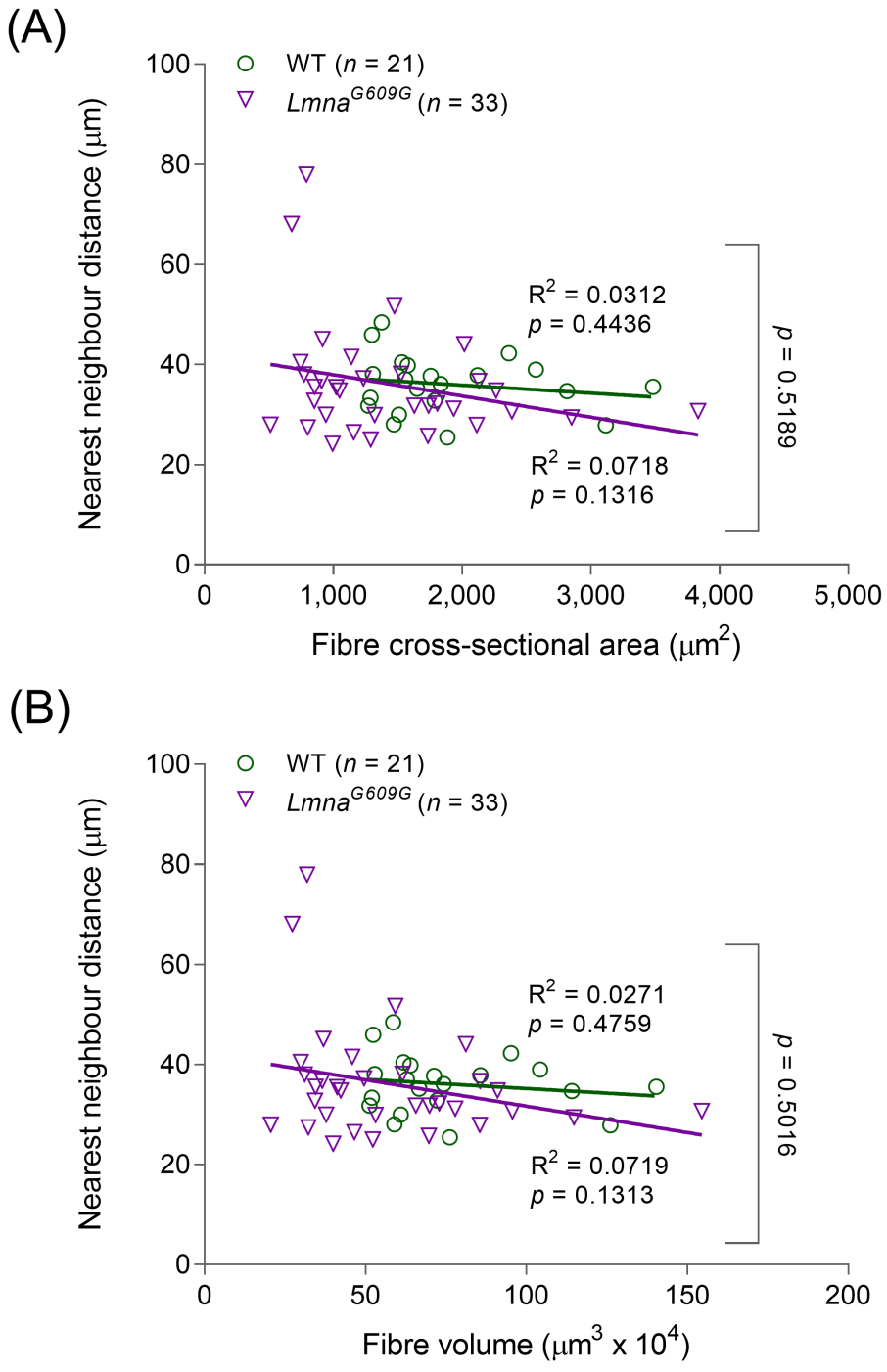

Figure 11.21: Normal nuclear distances in *Lmna*^{G609G} single myofibres

Data points represent individual single muscle fibres. Pearson product moment correlation was performed to evaluate linear relationships.

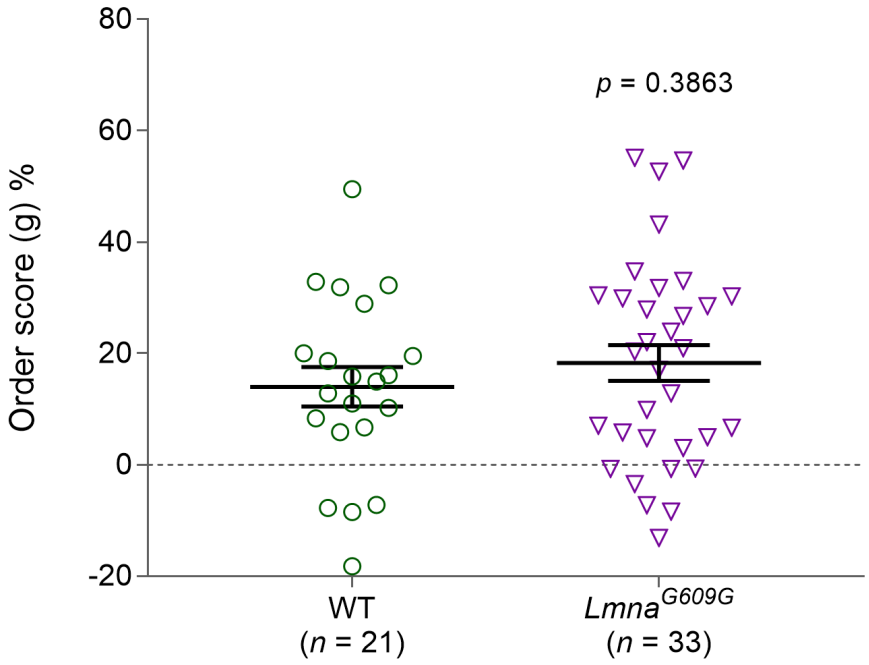

Figure 11.22: Normal nuclear distribution in *Lmna*^{G609G} single myofibres

Data points represent individual single muscle fibres. Error bars show mean ± SEM. Statistical tests included normality tests and t-tests.

Appendix 5: Nuclear organisation in human ageing muscle

The current appendix consists of larger versions of graphs that are contained within the summary figures of the cohorts studied in chapter 5. Thus, only figures that were reduced in size will be found here.

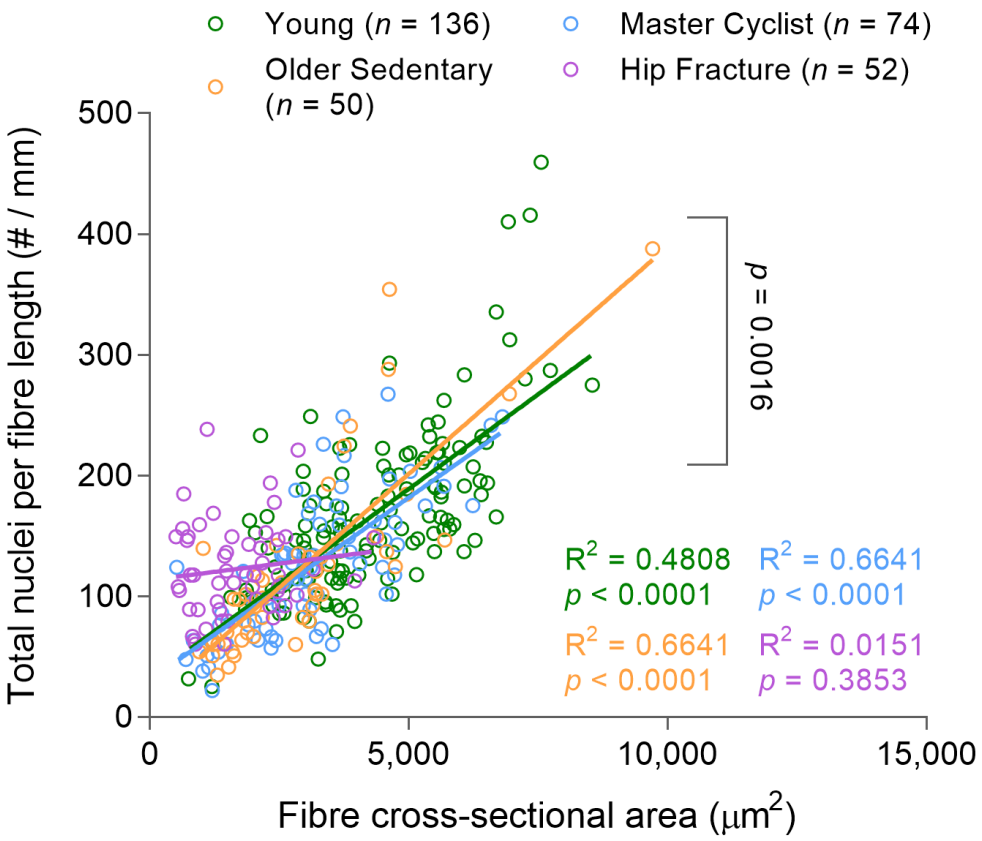

Figure 12.1: Higher number of nuclei/single fibre CSA in HF patients

CSA = cross-sectional area, HF = Hip Fracture. Data points represent individual muscle fibres. Pearson product moment correlation was performed to evaluate linear relationships. R^2 and *p* values are colour-coded against corresponding groups.

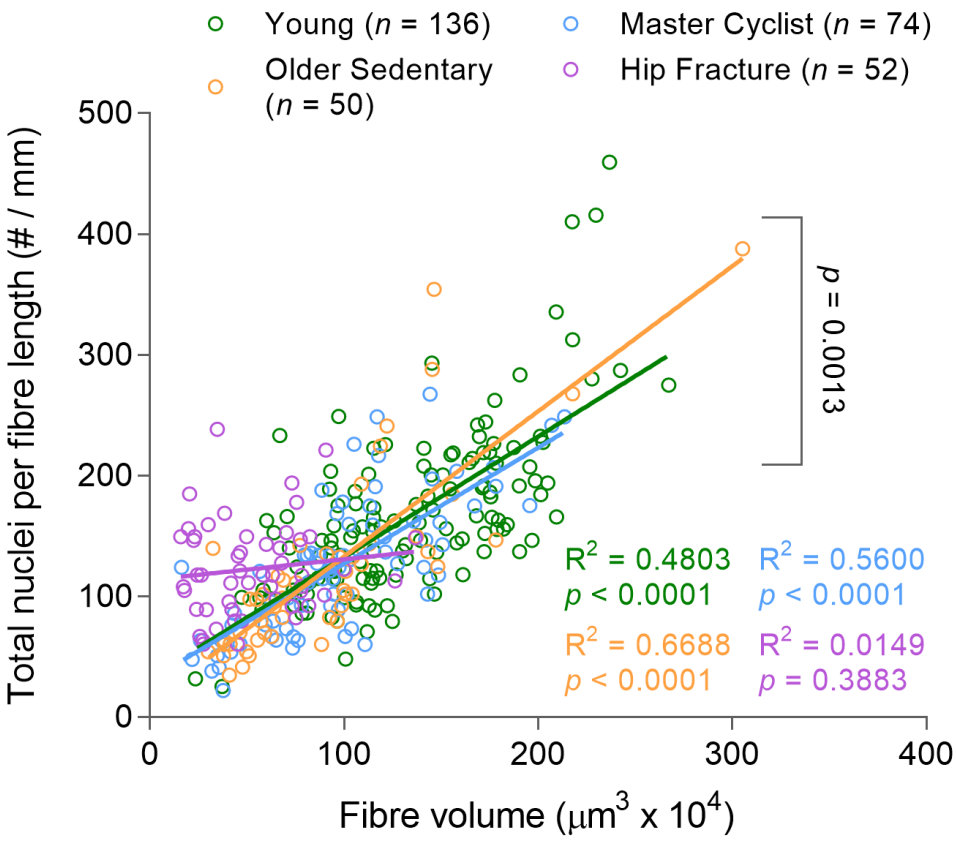

Figure 12.2: Higher number of nuclei/single fibre volume in HF patients

HF = Hip Fracture. Data points represent individual muscle fibres. Pearson product moment correlation was performed to evaluate linear relationships. R^2 and *p* values are colour-coded against corresponding groups.

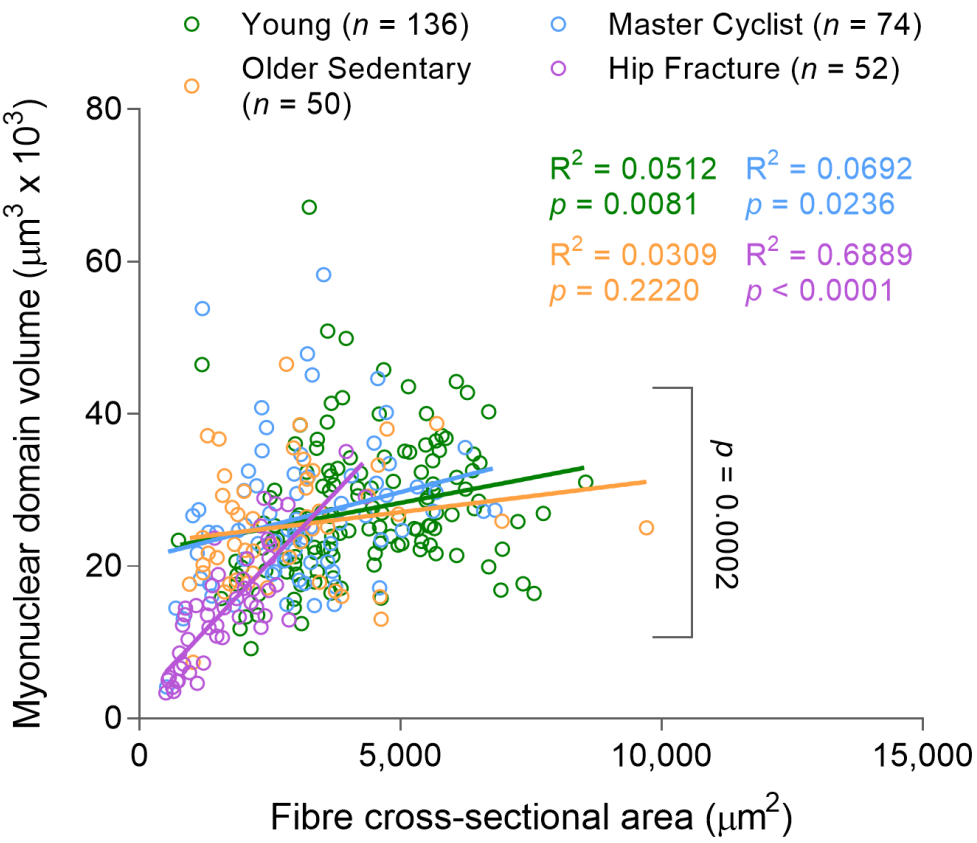

Figure 12.3: Smaller myonuclear domains/single fibre CSA in HF patients

CSA = cross-sectional area, HF = Hip Fracture. Data points represent individual muscle fibres. Pearson product moment correlation was performed to evaluate linear relationships. R^2 and *p* values are colour-coded against corresponding groups.

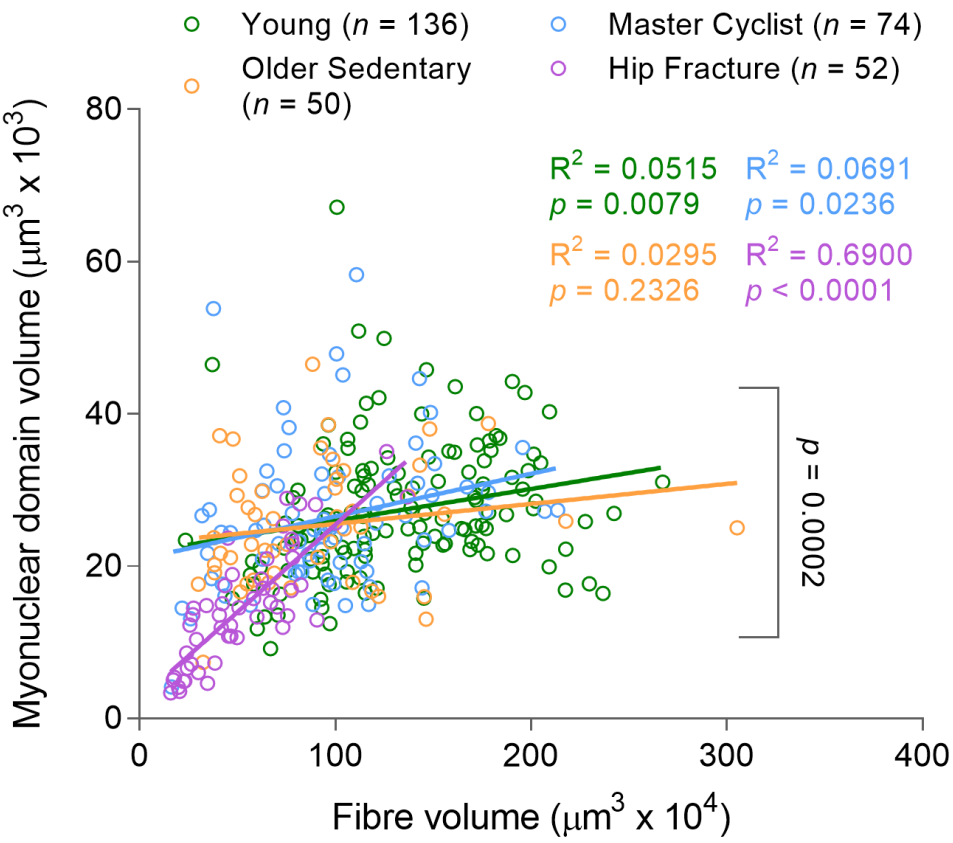

Figure 12.4: Smaller myonuclear domains/single fibre volume in HF patients

HF = Hip Fracture. Data points represent individual muscle fibres. Pearson product moment correlation was performed to evaluate linear relationships. R^2 and *p* values are colour-coded against corresponding groups.

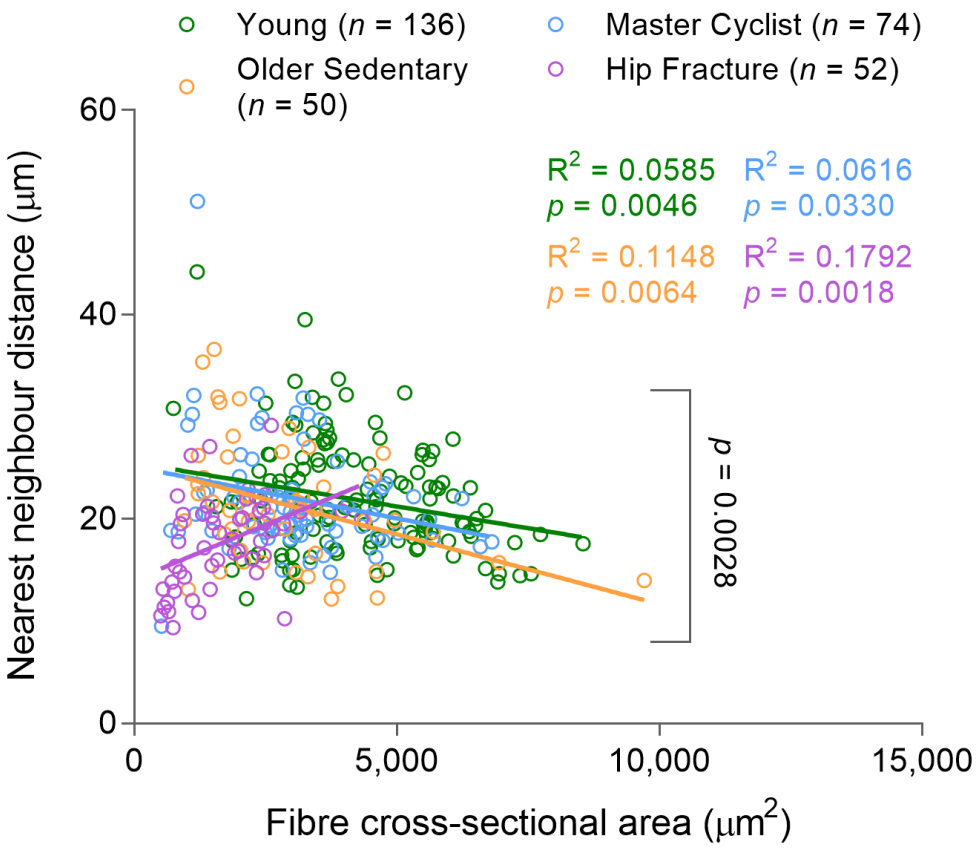

Figure 12.5: Shorter nuclear distances/single fibre CSA in HF patients

CSA = cross-sectional area, HF = Hip Fracture. Data points represent individual muscle fibres. Pearson product moment correlation was performed to evaluate linear relationships. R^2 and *p* values are colour-coded against corresponding groups.

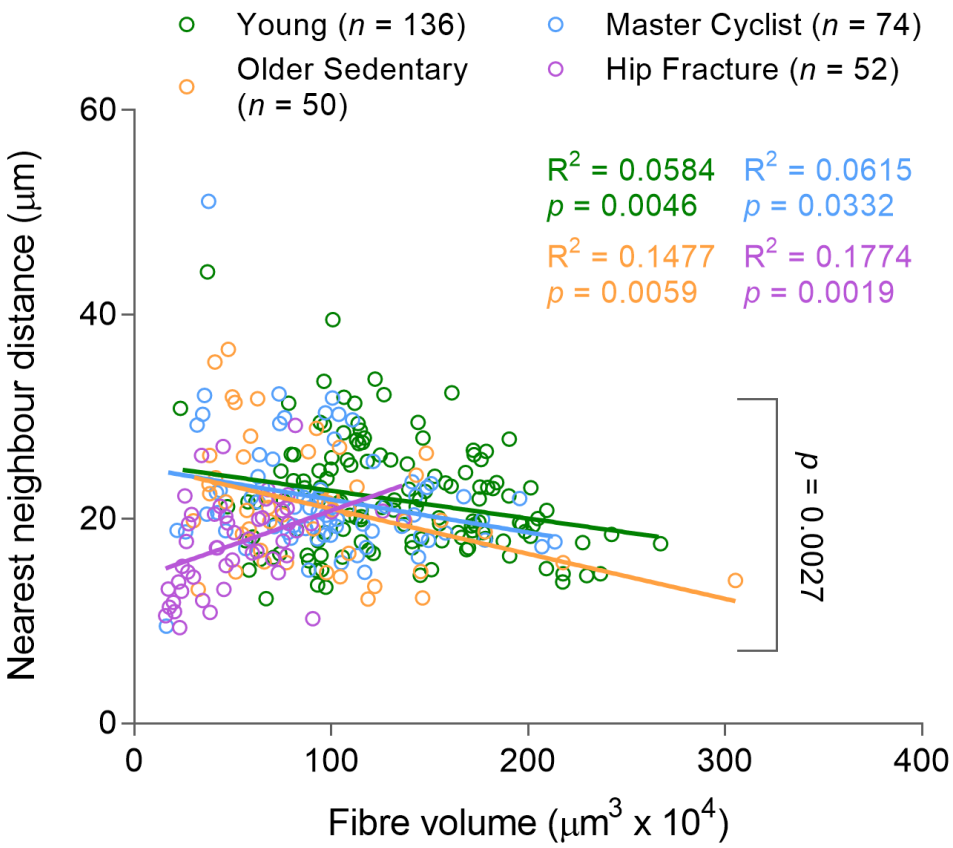

Figure 12.6: Shorter nuclear distances/single fibre volume in HF patients

HF = Hip Fracture. Data points represent individual muscle fibres. Pearson product moment correlation was performed to evaluate linear relationships. R^2 and *p* values are colour-coded against corresponding groups.

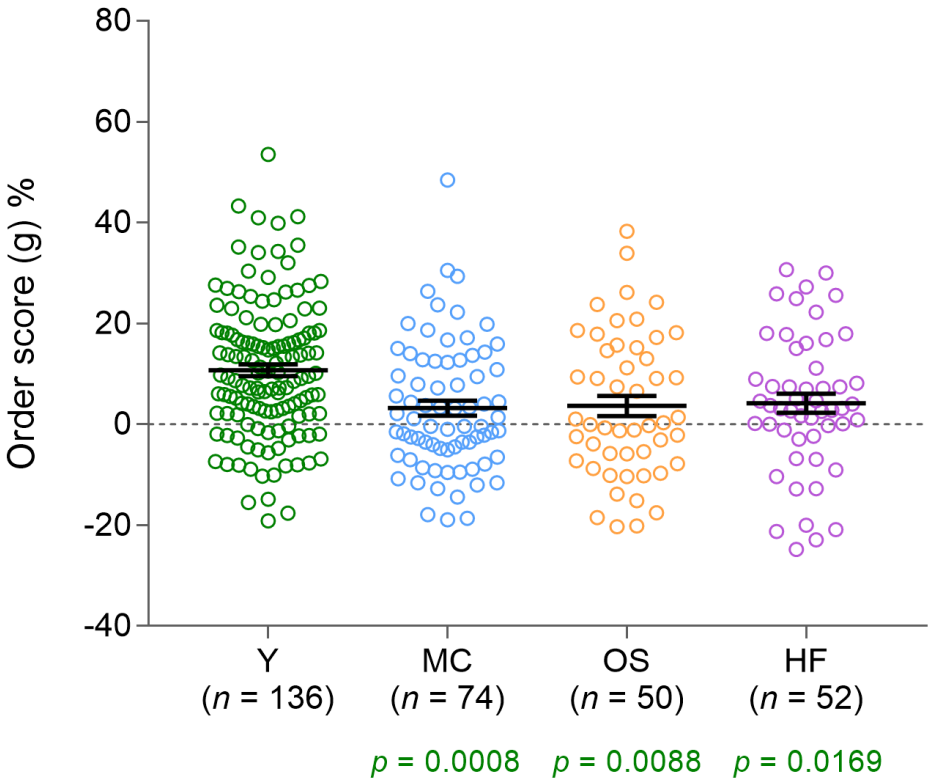

Figure 12.7: Disrupted nuclear distribution in myofibres from elderly individuals
Y = Young, MC = Master Cyclists, OS = Older Sedentary, HF = Hip Fracture. Data points represent individual muscle fibres. Error bars show mean ± SEM. Statistical tests included normality tests and ANOVAs. *p* values are colour-coded against corresponding groups.